

Chemistry of Chromophore Bridged Biradicals

– Synthesis and Properties

Dissertation zur Erlangung des
naturwissenschaftlichen Doktorgrades der
Julius–Maximilians–Universität Würzburg

vorgelegt von
Rodger Rausch
aus Ingolstadt

Würzburg 2021

Eingereicht bei der Fakultät für Chemie und Pharmazie am:

21.01.2021

Gutachter der schriftlichen Arbeit:

1. Gutachter: Prof. Dr. Frank Würthner
2. Gutachter: Prof. Dr. Ingo Fischer

Prüfer des öffentlichen Promotionskolloquiums:

1. Prüfer: Prof. Dr. Frank Würthner
2. Prüfer: Prof. Dr. Ingo Fischer
3. Prüfer: Priv.-Doz. Dr. Florian Beuerle

Datum des öffentlichen Promotionskolloquiums:

12.03.2021

Doktorurkunde ausgehändigt am:

List of Abbreviations

Abs.	absorbance
Ac	acetyl
AIBN	azobisisobutyronitrile
a. u.	arbitrary unit
B3LYP	Becke-3-parameter-Lee-Yang-Parr (exchange-correlation functional)
BAnth	bisanthene
BEC	Bose-Einstein condensate
BHT	butylated hydroxytoluene (2,6-di- <i>tert</i> -butyl-4-methylphenol)
BLA	bond length alternation
BODIPY	boron dipyrromethene
Bpin	4,4,5,5-tetramethyl-1,3,2-dioxaborolan-2-yl
br.	broad
BS	broken symmetry
Calcd.	calculated
CASSCF	complete active space self-consistent field
Cbz	carbazole
CCDC	Cambridge Crystallographic Data Centre
Cor	corannulene
CS	closed-shell
CT	charge transfer
CV	cyclic voltammetry
CW	continuous wave
DAE	diarylethene
dba	dibenzylideneacetone
DCM	dichloromethane
DCTB	<i>trans</i> -2-[3-(4- <i>tert</i> -butylphenyl)-2-methyl-2-propenylidene]malononitrile

DFT	density functional theory
DIPP	2,6-diisopropylphenyl
DMF	<i>N,N'</i> -Dimethylformamide
DMSO	Dimethylsulfoxide
DPP	diketopyrrolopyrrole
dppf	1,1'-bis(diphenylphosphino)ferrocene
DPV	differential pulse voltammetry
DTT	dithienothiophene
EPR	electron paramagnetic resonance spectroscopy (= ESR)
eq.	equivalents
ESI	electrospray ionization
Et	ethyl
EWG	electron withdrawing group
exc.	excitation
exp.	experimental
Fc	ferrocene
FL	fluorescence
Fu	furyl
FWHM	full width at half maximum
GS	ground state
HC	hydrocarbon
Hex	hexyl
HOMA	harmonic oscillator model of aromaticity
HOMO	highest occupied molecular orbital
HQ	heteroquinone
HRMS	high-resolution mass spectrometry
IIn	isoindigo
IUPAC	International Union of Pure and Applied Chemistry
LUMO	lowest unoccupied molecular orbital

<i>m</i>	<i>meta</i>
MALDI	matrix assisted laser desorption ionisation
Mes	mesityl (= 2,4,6-trimethylphenyl)
MS	mass spectrometry
NBI	naphthalene bisimide
NHC	<i>N</i> -heterocyclic carbene
NIR	near-infrared
NMR	nuclear magnetic resonance
NN	nitronyl nitroxide
NOON	natural orbital occupation number
MV	mixed valent
NICS	nucleus-independent chemical shift
norm.	normalised
<i>o</i>	<i>ortho</i>
OD	optical density
OEG	oligoethylene glycol
ORTEP	Oak Ridge thermal-ellipsoid plot
OS	open-shell
OTFT	organic thin film transistor
<i>p</i>	<i>para</i>
PAH	polycyclic aromatic hydrocarbon
PAK	Polyzyklischer aromatischer Kohlenwasserstoff
PBI	perylene bisimide
Ph	phenyl
ppm	parts per million
PTFE	polytetrafluoroethylene
ref.	reference
rt	room temperature
s	singlet

SCFET	single-crystal field-effect transistor
SEC	spectroelectrochemistry
SET	single electron transfer
SF	spin flip
sim.	simulated
SOMO	singly occupied molecular orbital
SPhos	2-dicyclohexylphosphino-2',6'-dimethoxybiphenyl
t	triplet
TBAF	tetra- <i>n</i> -butylammonium fluoride
TBAH	tetra- <i>n</i> -butylammonium hydroxide
TBAPF ₆	tetra- <i>n</i> -butylammonium hexafluorophosphate
TBDMS	<i>tert</i> -butyldimethylsilyl
TD	time-dependent
TDMAE	tetrakis(dimethylamino)ethylene
TEMPO	(2,2,6,6-tetramethylpiperidin-1-yl)oxyl
TEOS	tetraethyl orthosilicate
Th	thienyl
THF	tetrahydrofuran
TIPS	tri- <i>iso</i> -propylsilyl
TMS	tetramethylsilane
ToF	time of flight
TTF	tetrathiafulvalene
UV	ultraviolet
vis	visible
vs.	versus
VT	variable temperature
QDM	quinodimethane

List of variables and constants

c	concentration
C	Curie constant
δ	chemical shift
d	distance
ΔE_{ST}	singlet-triplet energy gap
E	potential
g	Landé factor, EPR g -factor (= g_{iso})
k_B	Boltzmann constant ($1.380649 \cdot 10^{-23} \text{ J K}^{-1}$)
J	spin-spin exchange interaction (NMR, EPR)
λ	wavelength
μ_B	Bohr magneton ($9.274010 \cdot 10^{-24} \text{ J T}^{-1}$)
μ_e	electron mobility
μ_{eff}	effective magnetic moment
μ_h	hole mobility
n	amount of substance
$\tilde{\nu}$	wavenumber
R	ideal gas constant ($8.314463 \text{ J mol}^{-1} \text{ K}^{-1}$)
S	total spin
Φ_{FL}	fluorescence quantum yield
$\tau_{1/2}$	half-life in solution
T	temperature
χ	magnetic susceptibility
y_0	singlet biradical character
y_1	singlet tetraradical character
y_2	singlet hexaradical character
y_3	singlet octaradical character

Common energy values of ΔE_{ST} in literature and their unit conversion

eV	kJ mol ⁻¹	kcal mol ⁻¹	cm ⁻¹	$k_B T$ @298.15K	Upper state occupation [%] @298.15K
0.001	0.096	0.023	8.066	0.039	49.0
0.002	0.193	0.046	16.13	0.078	48.1
0.005	0.482	0.115	40.33	0.195	45.2
0.008	0.772	0.184	64.52	0.311	42.3
0.010	0.965	0.231	80.66	0.389	40.4
0.010	1.000	0.239	83.59	0.403	40.0
0.020	1.930	0.461	161.3	0.778	31.5
0.026	2.479	0.592	207.2	1.000	26.9
0.043	4.184	1.000	349.8	1.674	15.6
0.050	4.824	1.153	403.3	1.946	12.5
0.080	7.719	1.845	645.2	3.114	4.25
0.100	9.649	2.306	806.6	3.892	2.00
0.150	14.47	3.459	1210	5.838	0.291
0.200	19.30	4.612	1613	7.784	0.042
0.300	28.95	6.918	2420	11.68	0.001
0.400	38.59	9.224	3226	15.57	< 0.0001
0.500	48.24	11.53	4033	19.46	< 10 ⁻⁶
0.700	67.54	16.14	5646	27.25	< 10 ⁻⁹
0.900	86.84	20.75	7259	35.03	< 10 ⁻¹³
1.000	96.49	23.06	8066	38.92	< 10 ⁻¹⁴
1.100	106.1	25.37	8872	42.81	< 10 ⁻¹⁶
1.300	125.4	29.98	10485	50.60	< 10 ⁻¹⁹
1.500	144.7	34.59	12098	58.38	< 10 ⁻²³
2.000	193.0	46.12	16131	77.84	< 10 ⁻³¹

Table of Contents

Chapter 1 – Introduction and Aim of Thesis	1
Chapter 2 – State of knowledge.....	5
2.1 Nomenclature, terminology and key properties.....	5
2.2 Important classes and design principles of diradicals.....	10
2.2.1 Towards carbon centred diradicals and open-shell PAHs.....	10
2.2.1.1 Triphenylmethane-based biradicals.....	10
2.2.1.2 Acenes and (Di-)Indenoacenes.....	13
2.2.1.3 Bisphenalenes.....	17
2.2.1.4 Zethrenes	18
2.2.1.5 Pristine quinodimethanes and their incorporation into macrocyclic structures.....	20
2.2.1.6 Twofold dicyanomethylene functionalised compounds.....	23
2.2.2 Phenoxy based biradicals and quinones	27
2.2.2.1 Introduction	27
2.2.2.2 Heteroquinones and oligo(hetero)aromatic biradicals.....	28
2.2.2.3 Sterically hindered quinones	32
2.2.2.4 π -Extended phenoxy biradicals and quinones.....	34
2.2.2.5 Non-Kekulé phenoxy diradicals.....	40
2.2.2.6 Synthesis and optical properties of phenoxy diradicals	41
2.2.3 Nitronyl nitroxide (bi)radicals – synthesis and properties	46
2.2.3.1 Synthetic strategies towards nitronyl nitroxide radicals.....	46
2.2.3.2 Magnetic properties of nitronyl nitroxide (bi-)radicals.....	51
2.2.4 Further spin-bearing moieties.....	54
2.3 Methods for the analysis of (bi)radicals.....	55
2.3.1 NMR spectroscopy	55
2.3.2 EPR spectroscopy.....	57
2.3.3 Stability analysis via UV/vis absorption spectroscopy	58
2.3.4 Spectro-electrochemistry (SEC) of biradicals	60
2.3.5 X-ray diffraction analysis of diradicals and quinones.....	61
2.3.6 Quantum chemical investigation of diradicals	61
Chapter 3	63
Chapter 4	73
4.1 Abstract.....	73

4.2	Introduction.....	74
4.3	Results and discussion	78
4.4	Conclusion	90
Chapter 5	91
5.1	Abstract.....	91
5.2	Introduction.....	92
5.3	Results and discussion	93
5.3.1	Synthesis.....	93
5.3.2	UV/vis absorption and fluorescence spectroscopy	95
5.3.3	Cyclic voltammetry (CV) and differential pulse voltammetry (DPV)	98
5.3.4	¹ H NMR and EPR spectroscopy	100
5.3.5	Single crystal X-ray diffraction analysis	102
5.4	Conclusion	105
5.5	Experimental section.....	106
5.6	Supporting Information.....	112
5.7	Acknowledgements.....	112
Chapter 6	– Summary and Conclusion	113
Chapter 7	– Zusammenfassung und Fazit.....	119
Chapter 8	– Appendix	125
8.1	Supporting Information for <i>Chapter 3</i>	125
8.1.1	Materials and methods.....	125
8.1.2	Syntheses	127
8.1.2.1	Synthesis of 4	127
8.1.2.2	Synthesis of 1	128
8.1.2.3	Synthesis of 2	129
8.1.2.4	Synthesis of OS-2^{••}	130
8.1.3	Sample preparation.....	131
8.1.3.1	Generation of (di)anions 1⁻ and 2²⁻	131
8.1.3.2	Generation of radical 1[•]	132
8.1.3.3	Generation of biradical OS-2^{••}	133
8.1.4	X-Ray diffractometry	135
8.1.5	Mass spectrometry.....	137
8.1.6	UV/vis/NIR spectroscopy and spectroelectrochemistry	138
8.1.7	NMR spectroscopy	148

8.1.8	EPR spectroscopy.....	154
8.1.9	DFT calculations	155
8.1.10	Examples for recent singlet open-shell biradicals	157
8.2	Supporting Information for <i>Chapter 4</i>	158
8.2.1	Materials and methods	158
8.2.2	Syntheses.....	161
8.2.2.1	Synthesis of DPP1	162
8.2.2.2	Synthesis of DPP2	163
8.2.2.3	Synthesis of DPP2q	164
8.2.2.4	Synthesis of DPP3	165
8.2.2.5	Synthesis of DPP3q	166
8.2.2.6	Preparation of a DPP1^{••} sample.....	167
8.2.3	Mass spectrometry.....	168
8.2.4	Single crystal X-ray diffraction.....	169
8.2.5	UV/vis/NIR spectroscopy and spectroelectrochemistry.....	173
8.2.6	NMR spectroscopy	181
8.2.7	Band gap analysis and cyclic voltammetry (CV).....	189
8.2.8	EPR spectroscopy.....	193
8.2.9	Computational chemistry	195
8.3	Supporting Information for <i>Chapter 5</i>	200
8.3.1	Materials and methods	200
8.3.2	Syntheses.....	203
8.3.3	Mass spectrometry.....	205
8.3.4	NMR spectroscopy	211
8.3.5	X-ray analysis.....	226
8.3.6	UV/vis/NIR spectroscopy	231
8.3.7	Cyclic voltammetry	236
8.3.8	EPR spectroscopy.....	239
Chapter 9 – Individual contribution.....		241
Chapter 10 – Danksagung.....		245
Chapter 11 – List of Publications		249
Chapter 12 – Bibliography.....		251

Chapter 1 – Introduction and Aim of Thesis

“In the case of all things which have several parts and in which the totality is not, as it were, a mere heap, but the whole is something beside the parts, there is a cause; for even in bodies’ contact is the cause of unity in some cases, and in others viscosity or some other such quality.” Aristotle, 350 BC^[1]

This section cited from Aristotle’s famous philosophical opus “metaphysics” is commonly shortened as “the whole is greater than the sum of its parts”, however this simplification may not convey the greater meaning. In this regard, Aristotle’s conclusion can be understood as unique properties developing out of the totality of the assembled components and the force that binds them together. And just as the Greek syllable “bi” means more than just the second and ninth letter in the alphabet added mathematically but “twice” or “twofold”, so do biradicals offer much more than simply two radical entities put together. Instead, the two electrons – the unpaired state of a covalent bond – can interact with each other and therefore endow biradicals with remarkable stability and make them the archetype of a ferro- or antiferromagnetic coupler.

Apart from their theoretical relevance, biradicals are important reaction intermediates and increasingly spark interest as open-shell materials.^[2] (Bi-)radical generation and recombination (i. e. bond formation) or saturation are crucial steps in numerous important thermolytical or photochemical processes like the Norrish-type-II reaction^[3-6] or the Masamune Bergman cyclisation^[7-11] as well as in combustion^[12, 13] and atmospheric^[14, 15] chemistry. Despite their long history, biradicals have been discovered late as a material class due to their highly reactive behaviour. Nevertheless, this did not prevent biradicals to raise continuous attention over the past decades as promising candidates for non-linear optics,^[16, 17] energy storage,^[18, 19] singlet fission^[20] and spintronic materials^[21]. However, until today, it is rather challenging to advance these highly reactive compounds towards stable materials. Accordingly, the (ambient) stability of biradicals is one of the most important determinants for any open-shell organic material and stabilization is a fundamental challenge to meet. Nevertheless, the chemistry of biradicals led to a plethora of molecules based on numerous different design principles and hence resulting in a broad variety of stabilities and properties. Thus, it is the intention of *Chapter 2* to give a brief overview on the development of structural classes and molecular properties.

It will also be pointed out in *Chapter 2* that electron deficient π -scaffolds are capable of stabilizing (bi)radicals *via* efficient spin delocalization. However, whereas larger π -systems gain stability with half-life times up to several days, smaller but evenly electron deficient π -systems decompose within hours.^[22–24] Furthermore, less electron poor but larger open-shell PAHs tremendously gain stability.^[25] Hence, it is reasonable to conclude that an extraordinarily high degree of electron deficiency is not always necessary for spin delocalization, but rather harmful regarding stability and causing increased reactivity. Accordingly, the question arises, whether or not it is possible to maintain the stability of biradicals for at least several days, with a moderately electron deficient and small sized π -core.

Therefore, the first aim of this thesis was to design a balanced small π -system with moderate electron deficiency but still significant spin delocalization at the same time. For this purpose, the isoindigo (II_n) scaffold was considered to be ideal. Accordingly, it is the aim of *Chapter 3* to describe the synthesis and characterization of open-shell **OS-2^{••}** and draw a comparison between the biradical and the respective monoradical **1[•]** (Chart 1.1).

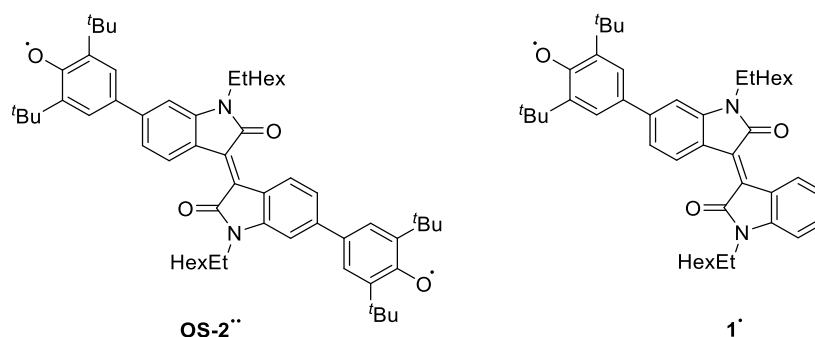


Chart 1.1 | Structural formula of isoindigo phenoxy (bi)radicals **OS-2^{••}** and **1[•]** discussed in *Chapter 3*.

Like shown for **OS-2^{••}** in *Chapter 3*, Kekulé-type (singlet) biradicals are in resonance with closed-shell quinoidal mesomeric structures, which often leads to a significant gain in persistence. However, there is a smooth transition from distinctly interacting but still unpaired electron spins to a dominating closed-shell quinoidal structure. Whether an open-shell biradical or a closed-shell quinoidal structure prevails, is determined by several factors like the π -system's size,^[26–31] constitutional isomerism^[25, 32–36] or substituent effects^[37]. Additionally, already starting in the 1950s Clar highlighted the importance of benzenoid sextets^[38–40] for the stabilization of polycyclic aromatic hydrocarbons. Thus, it is all the more remarkable that the impact of a systematic variation of aromaticity within a biradicaloid framework was so far not investigated.

Therefore, the linker-aromaticity in a series of diketopyrrolopyrrole (DPP) bridged phenoxy biradical(oid)s **DPP1^{••}**, **DPP2q** and **DPP3q** was tuned by incorporation of phenyl, thiophene and furane spacers (Chart 1.2). Presenting the synthesis and characterisation as well as gaining deeper insights into the electronic factors, individually stabilizing open-shell biradicals or closed-shell quinoidal states in DPP bridged phenoxy biradicals and quinones is the intention of *Chapter 4*.

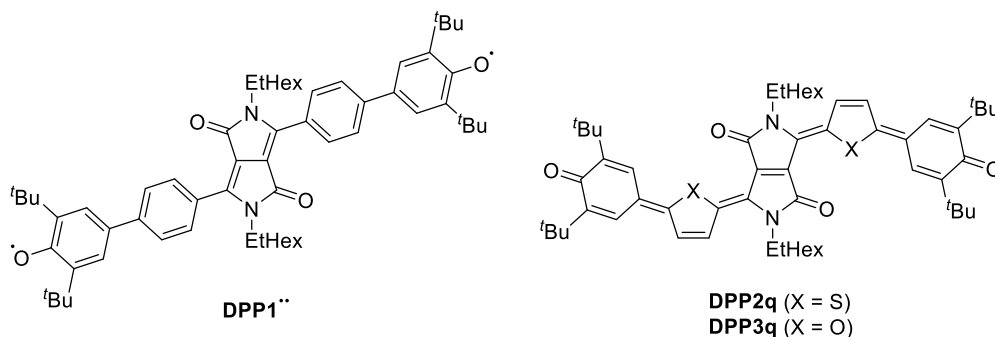


Chart 1.2 | Structural formula of DPP bridged phenoxy biradical **DPP1^{••}** and heteroaromatic quinones **DPP2q** and **DPP3q**.

Phenoxy radical decoration of pigment chromophores is on the one hand a convenient approach in order to achieve spin functionalization, but on the other hand increases decomposition rates – in particular in a non-inert environment.^[41] Thus, further kinetic and thermodynamic stabilization is necessary in order to advance these inherently unstable compounds into useful materials or applications. Furthermore, pronounced electronic coupling of phenoxy spin centres with the chromophore cores leads to tremendous changes of absorption spectral properties like large shifts of absorption maxima wavelengths or even rise of completely new spectral signatures. In order to enable a better predictability of optical properties, maintaining the unique magnetic characteristics of biradicals (i. e. twofold spin decoration) while electronically decoupling the spin centres would be desirable. Promising candidates for this purpose are nitronyl nitroxide (NN) biradicals, as they feature spin delocalization limited to an O-N-C-N-O pentad, covalent attachments and strong intramolecular magnetic coupling.

Thus, in *Chapter 5* the synthesis and investigation of twofold NN decorated perylene bisimide (PBI), isoindigo and diketopyrrolopyrrole derivatives **PBI-NN**, **IIn-NN**, **PhDPP-NN**, **ThDPP-NN** and **FuDPP-NN** was tackled (Chart 1.3). In addition, the optical and magnetic properties of these interesting compounds as well as challenges during the synthesis of this electron deficient biradicals will be discussed.

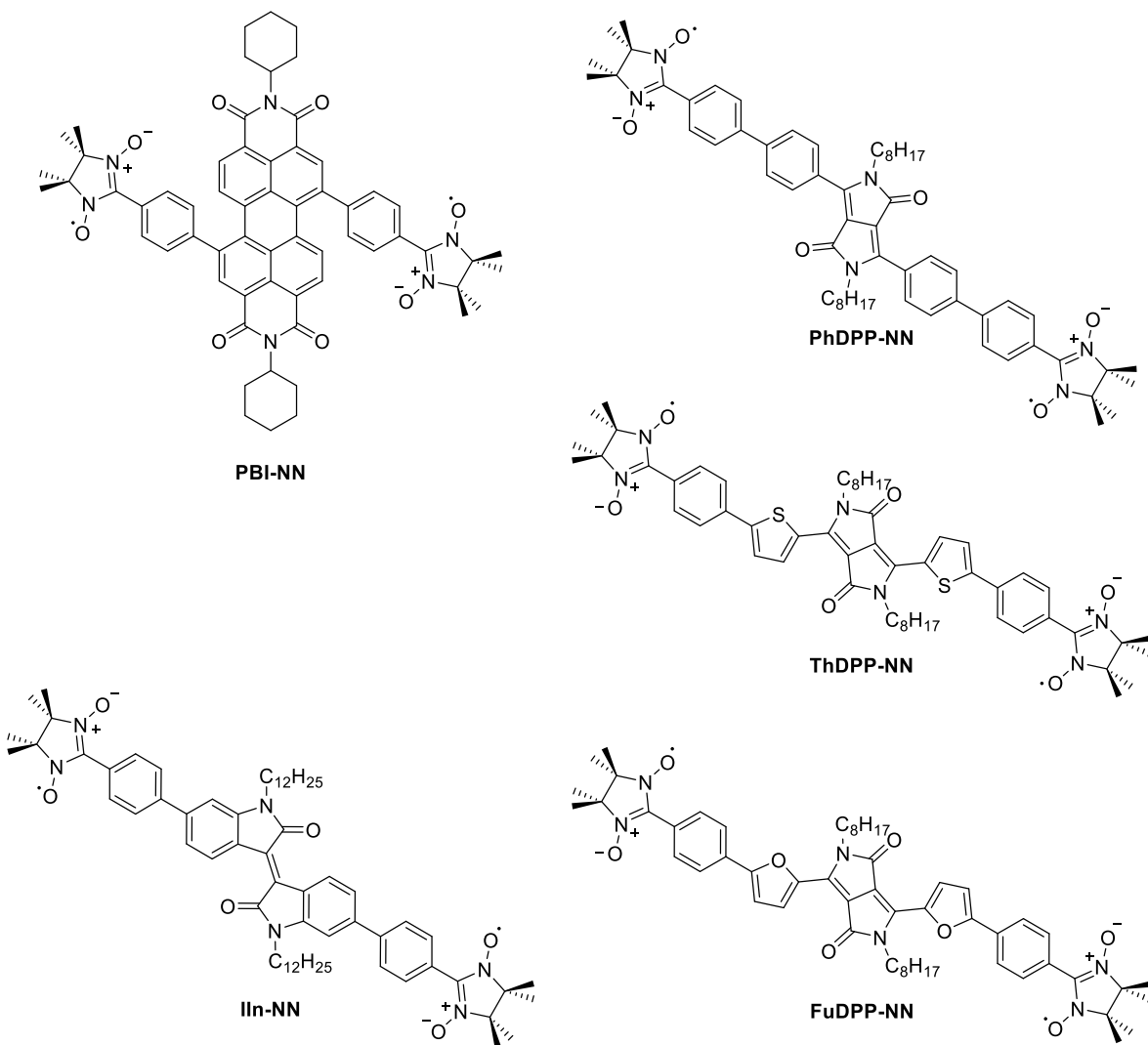


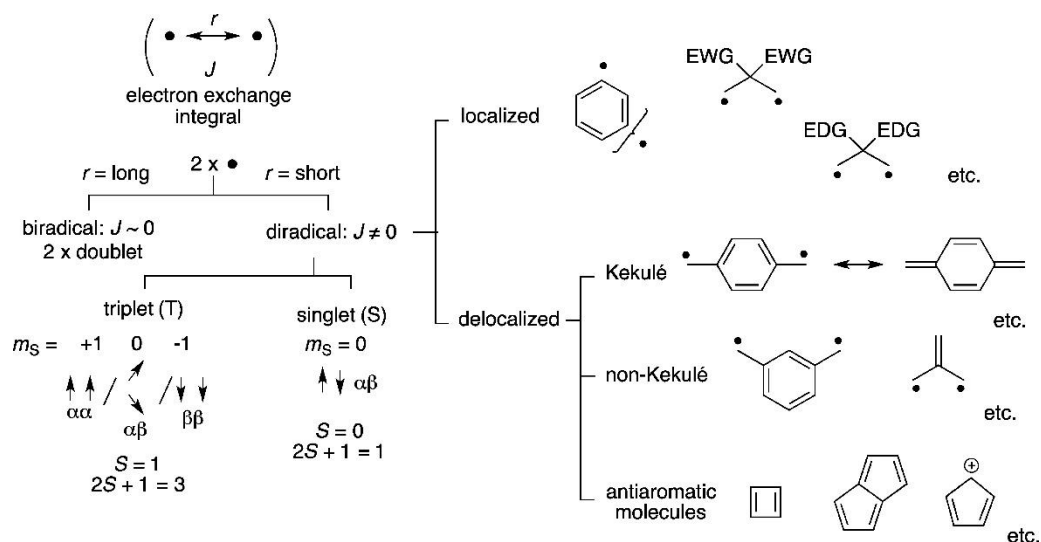
Chart 1.3 | Structural formula of pigment chromophore bridged nitronyl nitroxide biradicals **PBI-NN**, **IIn-NN**, **PhDPP-NN**, **ThDPP-NN** and **FuDPP-NN**.

Finally, a conclusive summary will be drawn in *Chapters 6* and *7* in German and English language.

Chapter 2 – State of knowledge

2.1 Nomenclature, terminology and key properties

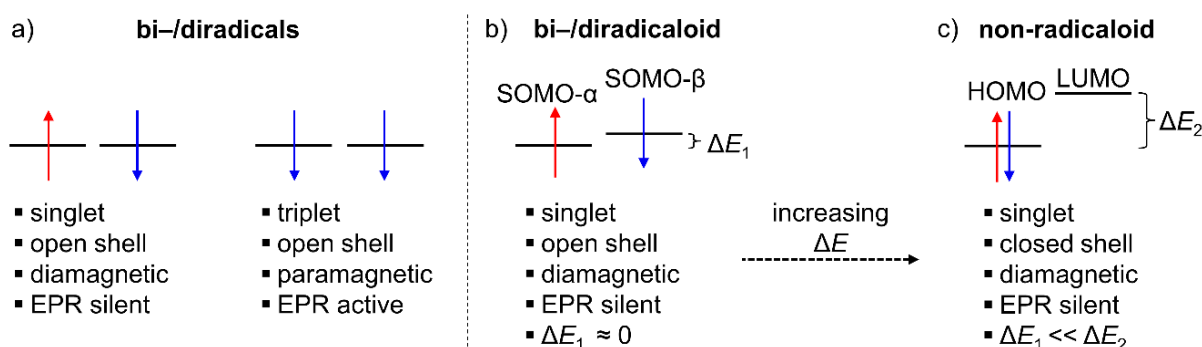
Radicals are paramagnetic molecules with an odd total number of electrons. Besides their electrical charge, free electrons bear a spin information and a magnetic momentum. Thus, additionally to charge related phenomena, magnetic exchange interactions have to be considered in radical chemistry. Structures functionalised with two spin centres are denominated biradical(oid)s or diradical(oid)s (Scheme 2.1).^[2]



Scheme 2.1 | Suggested diradical classification according to Abe.^[2] However, it does not strictly follow the IUPAC recommendations. Adapted with permission from ref. [2]. Copyright 2013 American Chemical Society.

The chemical as well as physical properties of these compounds are determined significantly by the interaction between both radical centres.^[42] Accordingly, molecules are called **biradicals**, if the distance between both spin centres is very large, and thus spin-spin interactions are only weak, but still measurable. In contrast, **diradicals** are characterised by a large energy value for the electron exchange integral J (Scheme 2.1).^[43] In both cases, but more easily detectable among diradicals, singlet (spin multiplicity = 1) and triplet (spin multiplicity = 3) spin states can be distinguished. The two spins in singlet biradicals are oriented antiparallel (e.g. $\uparrow\downarrow$), leading to a total spin $S = 0$, and thus no resonance signals can be detected by EPR spectroscopy (Scheme 2.2). Accordingly, in triplet diradicals with

parallel spin orientation (e.g. $\uparrow\uparrow$) the total spin amounts to $S = 1$, leading to well detectable resonance signals in the respective EPR spectra.^[2] In general, for triplet biradicals ferromagnetic coupling is observed, whereas singlet biradicals feature anti-ferromagnetic coupling.^[44] Finally, structures in which the singly occupied molecular orbitals (SOMO) are energetically not degenerated, but in very close proximity, are called **diradicaloids** (Scheme 2.2b).^[45] In this case, the only minor energetic difference between both orbitals results in an almost equal orbital occupation. However, with an increasing energy difference, there is a smooth transition from SOMO to HOMO and LUMO and accordingly from diradicaloid to non-radicaloid.



Scheme 2.2 | Selected electronic configurations of bi-/diradicals (a), bi-/diradicaloids (b) and non-radicaloids (c).

In recent literature, the terms “biradical”, “diradical” and “bi-/diradicaloid” are often mixed up or used synonymously, although formal definitions for each of these terms were recommended in a “Gold Book” by the International Union of Pure and Applied Chemistry (IUPAC): The term “biradical” is defined as a molecular entity with two radical centres, which interact nearly independently of each other.^[46] The exact meaning of “nearly” remained vague in this context but is slightly specified, as the spin interaction should be judged with respect to $k_B T$. Thus, it is appropriate to apply the term “biradical” in particular for molecules, where room temperature caused (de-)population effects of spin states can be observed. Diradicals are more generally defined by the IUPAC as molecules bearing two spin sites with at least two different multiplicity states (e.g. singlet and triplet).^[47] It is obvious that both definitions do not exclude each other (Figure 2.1), but the term “biradical” refers to a more specific and measurable temperature-dependent magnetic effect. However, already in 1995 IUPAC stated, that the term “diradical” is preferably used for exactly this kind of molecules (“biradicals”) as well.^[47] According to the 2007 IUPAC recommendation, both terms “biradicaloid” and “diradicaloid” are synonyms and describe molecules with significant radical-radical interaction.^[48]

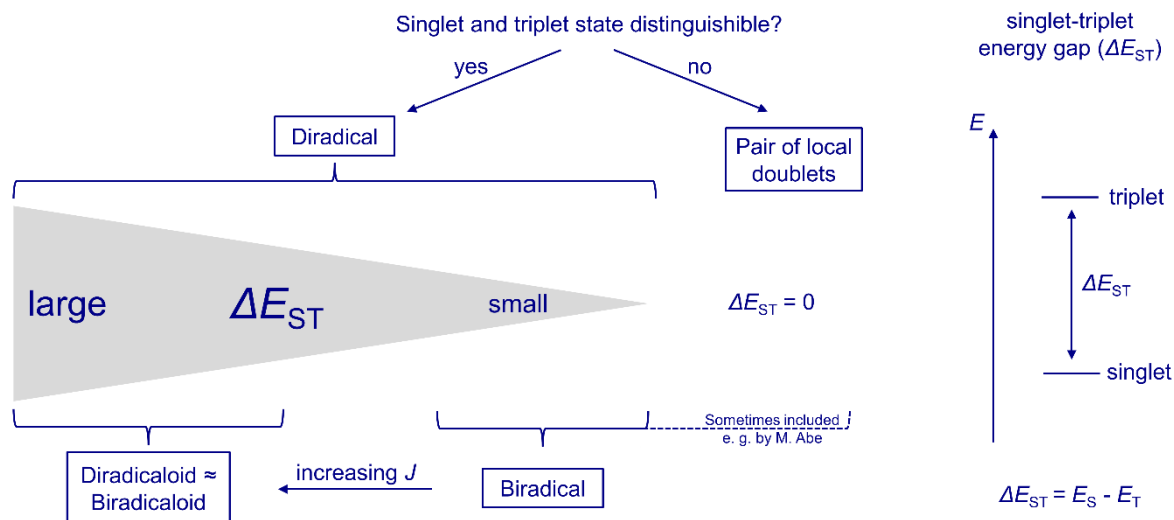


Figure 2.1 | Suggested diradical classification for this thesis in accordance with IUPAC recommendations (left) as well as schematic illustration of the singlet-triplet energy gap (right).

The **singlet-triplet energy gap** ΔE_{ST} is the energy difference between the lowest energy singlet and triplet state (Figure 2.1). It can be estimated experimentally via variable temperature (VT) EPR spectroscopy or superconducting quantum interference device (SQUID) magnetisation measurements (see the methods part for details). In literature, different units were used for this energy, and unfortunately, SI units are not the most common ones. As the IUPAC recommends benchmarking ΔE_{ST} with respect to $k_B T$ (*vide supra*), the energy amount of $k_B T$ at room temperature is informative, which equals 25.69 meV ($= 2.479 \text{ kJ mol}^{-1} = 0.592 \text{ kcal mol}^{-1} = 207 \text{ cm}^{-1}$). Due to the advantage of a per molecule unit, ΔE_{ST} will mainly be given in (milli) electron volts and in kilojoule per mole in this work.

In summary, the denomination “diradical” is the more general description for molecules with two interacting spin centres whereas the term biradical should be used in cases where the singlet-triplet energy gap (ΔE_{ST}) is small and thus changes in the occupation of spin states is caused easily by moderate temperature variation. Therefore, and in accordance with the IUPAC recommendations, the term biradical will be used in this thesis for an open-shell ground state molecule bearing two spin sites with a singlet-triplet energy gap that can be thermally overcome at room temperature or in a moderate temperature range between $-100 \text{ }^\circ\text{C}$ and $+100 \text{ }^\circ\text{C}$.

Electron spins located along a conjugated chain of atoms are oriented antiparallel and thus alternate up and down.^[49] For this reason, only biradicals in which both spin centers are linked by an even number of atoms like in **3** can undergo an intramolecular recombination and form a closed-shell mesomeric

resonance structure (Chart 2.1a). These compounds are called **Kekulé-type** molecules and commonly exhibit a singlet ground state multiplicity (terminal spins are oriented anti-parallel blue and red in **3**, Chart 2.1a).^[50–53] Well-known representatives of this class of molecules are quinodimethanes (QDM) *ortho*- or *para*-xylylene **5** and **6**, which however, have a closed-shell ground state (Chart 2.1b). In contrast, triplet diradicals like polyene **4** or *meta*-xylylene **7** cannot be stabilized via intramolecular recombination and consequently are denominated **non-Kekulé-type** molecules (terminal spins are oriented parallel: blue and blue, Chart 2.1a, b).^[54, 55] Due to their distinct paramagnetic character, non-Kekulé-type diradicals are more reactive and tend to dimerise or decompose.^[56–58]

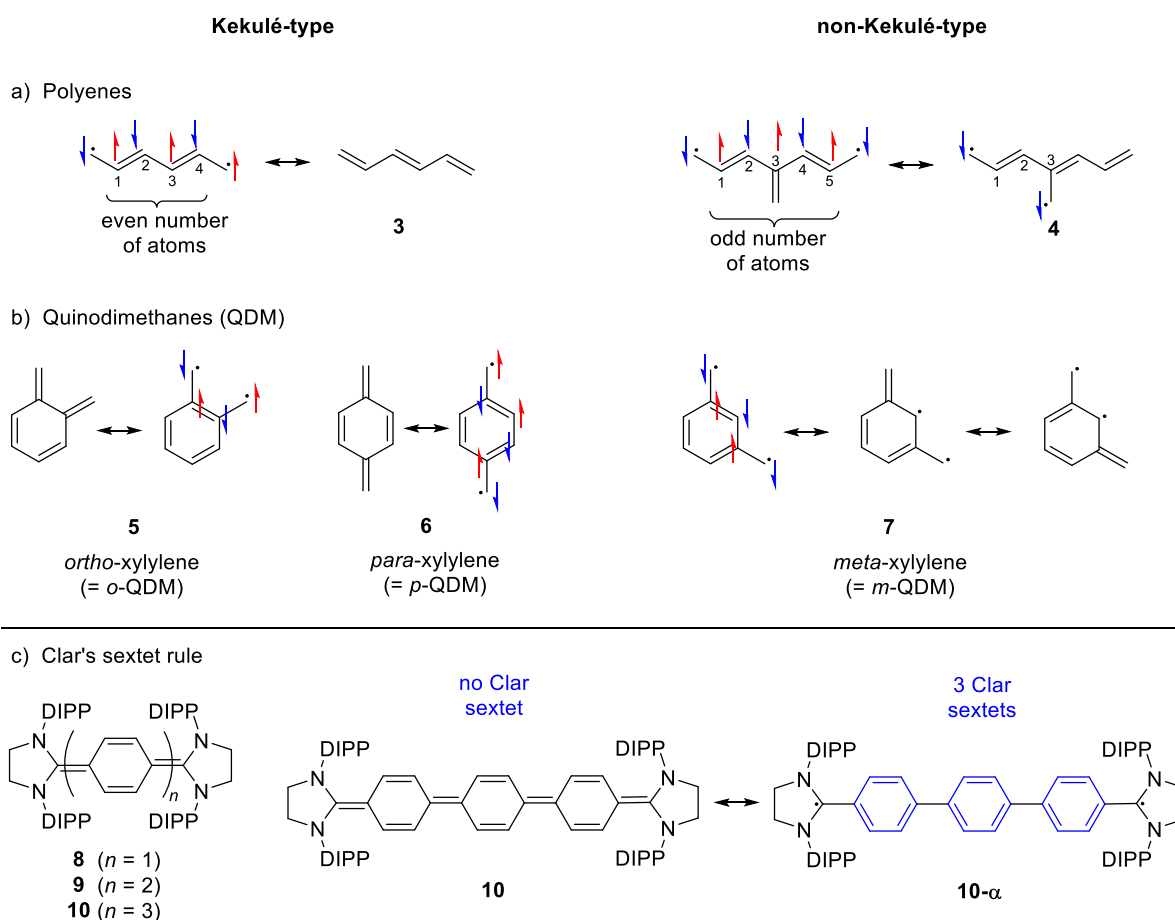


Chart 2.1 | Selected open and/or closed-shell resonance structures of polyenes **3** and **4** (a), of *ortho*-, *para*- and *meta*-xylylene **5**, **6** and **7** (b) as well as of NHC-based diradicaloids **8**, **9** and **10** (c).^[59–61] Red and blue arrows indicate spin polarization and resulting ferro- and antiferromagnetic coupling. Blue hexagons highlight Clar sextets.

Almost every conjugated molecule can be represented by more than one mesomeric structure like NHC-based diradicaloids **8–10** (Chart 2.1c).^[59–61] However, not all of these resonance structures are equal in

energy. A concept to identify favoured structures was developed by Clar, which is commonly known as **Clar's sextet rule**.^[38–40] According to Clar, structures with a higher number of benzenoid sextets are more stable. For instance, in a NHC-based terphenyl diradical, the open-shell state **10- α** is more stable compared to closed-shell **10** due to three additional Clar sextets. Frequently – like e.g. in all xylylene isomers (Chart 2.1b) – the open-shell structures comprise a higher number of benzenoid hexagons compared to the closed-shell states and thus gain stability. Accordingly, Clar's sextet rule is a powerful and fundamentally important principle in biradical chemistry, frequently serving as an explanation for the stabilisation of open-shell states.

As Kekulé-type diradicals can be represented by open and closed-shell resonance structures, which – in addition – commonly both contribute to the ground state, the **singlet biradical character y_0** was introduced as a measure for the extent of the open-shell contribution. The biradical character ranges from zero for a completely closed-shell molecule to one for a fully open-shell material^[2] and is usually accessed by quantum chemical analysis of the natural orbital occupation number (NOON)^[52] or experimentally from the one and two-photon absorption energy as well as the singlet-triplet energy gap.^[62]

Finally, a central measure for the ambient stability of biradicals in solution is the **minimum half-life in solution $\tau_{1/2}$** . In default of an established standard test, stability is most commonly determined by UV/vis/NIR absorption spectroscopy (see the methods part for details).

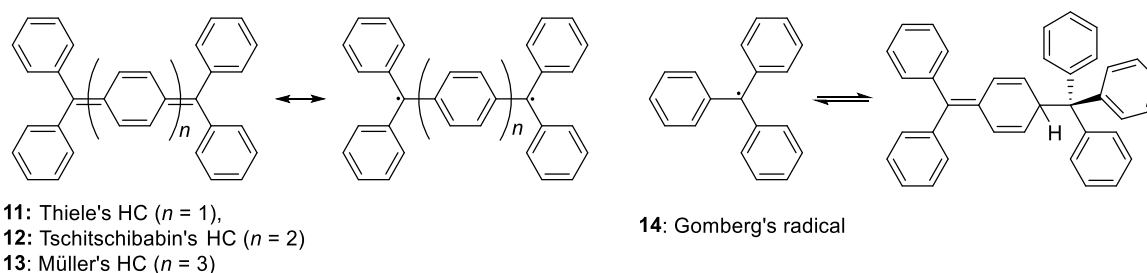
2.2 Important classes and design principles of diradicals

In the following sections, important classes of (organic) diradicals will be presented, thereby illustrating common structural design principles and structure-property relationships. Thus, this part is not intended to be an enumeration, but to clarify the specific effects caused by steric factors and electronic modifications. As the number of known open-shell compounds is tremendous and several examples can be categorized into more than one substance class (e.g. carbon- vs. oxygen-centred radicals, zethrenes vs. acenes, etc.), not each individual biradical characteristic (γ_0 , ΔE_{ST} , half-life in solution) will be discussed in this overview, but information of relevance for this thesis only.

2.2.1 Towards carbon centred diradicals and open-shell PAHs

2.2.1.1 Triphenylmethane-based biradicals

Since their discovery more than one century ago by Thiele in 1904^[63] and Tschitschibabin in 1907^[64], biradicaloid organic molecules continuously raised attention among organic chemists and material scientists. Both hydrocarbons **11** and **12** are named after their discoverers and differ only in the number of bridging phenylene units (Scheme 2.3). They can be understood as conjugated triaryl methane dimers based on Gomberg's radical **14**^[65–67] but – in contrast to **14** – do not show any dimerisation tendency. Although both **11** and **12** feature a closed-shell ground state, Tschitschibabin's HC shows a particularly higher reactivity, which originates from significant biradical contributions in the ground state.^[50, 68, 69]



Scheme 2.3 | Open- and closed-shell resonance structures of Thiele's,^[63] Tschitschibabin's^[64] and Müller's^[70] hydrocarbon **11**, **12** and **13** as well as Gomberg's radical **14** in a dimerisation equilibrium.

Upon insertion of an additional phenylene bridge, Müller's HC **13** is obtained, which represents the first open-shell derivative out of this series.^[70, 71] This can be rationalized by an increasing number of aromatic sextets stabilizing the open-shell configuration (Clar's sextet rule).^[39] Accordingly, a spin crossover from

closed-shell quinoidal to open-shell biradical was achieved in the hydrocarbon series presented by Thiele, Tschitschibabin and Müller, upon elongation of the *para*-phenylene oligomer unit. A similar spin crossover was observed recently for diamino carbene based analogues as well.^[59–61] A certain improvement regarding ambient stability of triaryl methane radicals was later achieved upon perchlorination of the aryl units, which lowers the electron density, promotes spin delocalization and/or enables charge separation.^[72, 73]

Until today, structural motives based on Thiele's and Tschitschibabin's hydrocarbon have not lost attraction and led to largely extended π -systems like **15**, **16** and **17** with bridging anthracene units instead of the phenylene-based historic counterpart (Figure 2.2).^[74–76] The ground state of **15** is closed-shell quinoidal, but the open-shell singlet state is only 165 meV (= 15.9 kJ mol⁻¹) higher in energy. Accordingly, even minor structural changes can invert the relative position of energy levels and result in a spin crossover, as demonstrated by formally biphenyl-fused analogous fluorenyl derivative **16**, which is a triplet ground state biradical.

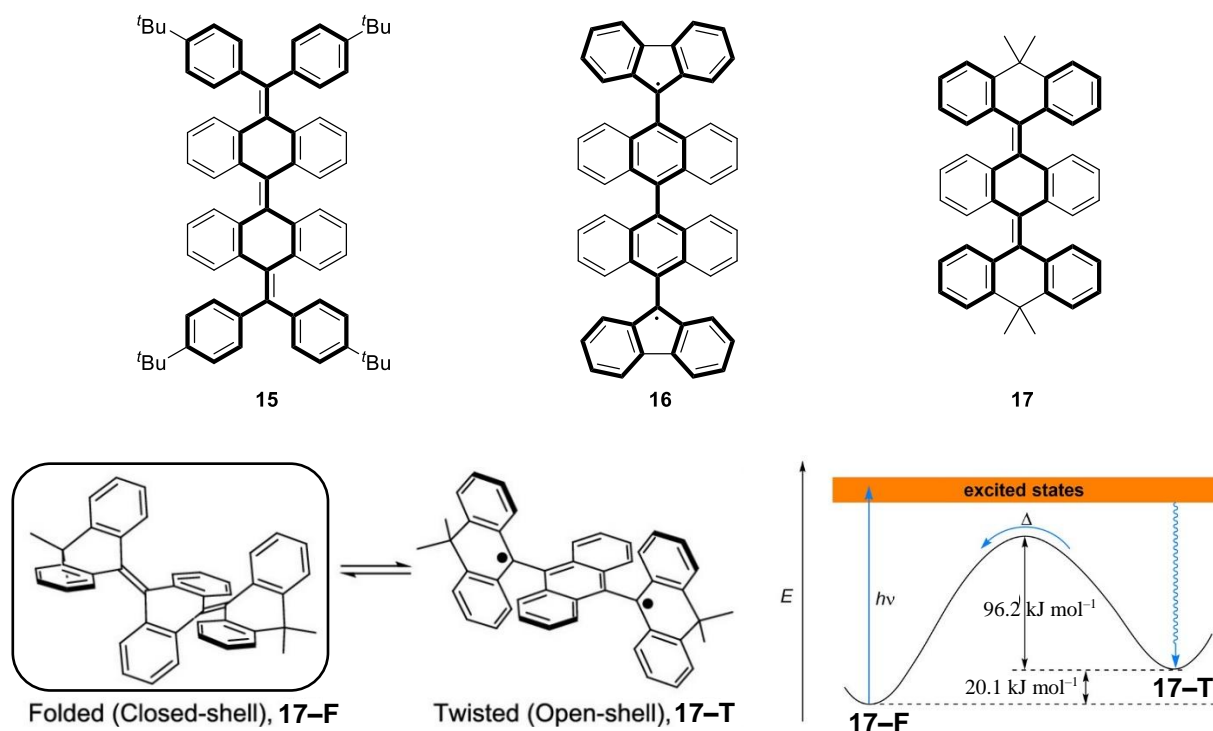


Figure 2.2 | Biradicaloid systems **15**,^[74] **16**^[74] and **17**^[75] based on Tschitschibabin's and Thiele's hydrocarbon (top, incorporated scaffolds of **12** and **11** are highlighted in bold). Additionally shown is the switching process of **17**^[75] between a folded form **17-F** and a twisted form **17-T** as well as schematic representation of the energy profile for the switching cycle (bottom, from left to right). Adapted with permission from ref. [75]. Copyright 2020 American Chemical Society.

The open-shell states of PAHs **15**, **16** and **17** are characterized by a geometry with orthogonal π -surfaces: The bridging anthracene cores are oriented perpendicular to the neighbouring anthracene or terminal diphenylmethane units. In contrast, the quinoidal states feature much smaller dihedral twist angles but are highly contorted structures as well due to steric repulsion.^[75] This overcrowding results in a huge energy barrier for the transition of the orthogonal open-shell state to the more planarised quinoidal one. Both conformations represent local minima resulting in a bistability of states as has been demonstrated in the case of thermally/photochemically switchable **17**.^[75] Tristicyclic aromatic ene (TAE) **17** features a closed-shell quinoidal ground state **17-F**, which however is only 208 meV (= 20.1 kJ mol⁻¹) lower in energy than the respective open-shell state **17-T** (Figure 2.2, bottom). The activation barrier for the conformational isomerization at 300 K was found to be 997 meV (= 96.2 kJ mol⁻¹) leading to a half-life of 2 h for the open-shell conformation and thus a remarkable persistence of this kinetic state. Nevertheless, steric overcrowding is not large enough to endow **17** with an open-shell ground state, but still enables a significant stabilization of the biradical conformation.

An open-shell ground state was achieved in a related series of higher oligo(9,10-anthryl)_n derivatives **18** and **19** (Chart 2.2) with a total number of three and four 9,10-anthryl units.^[77]

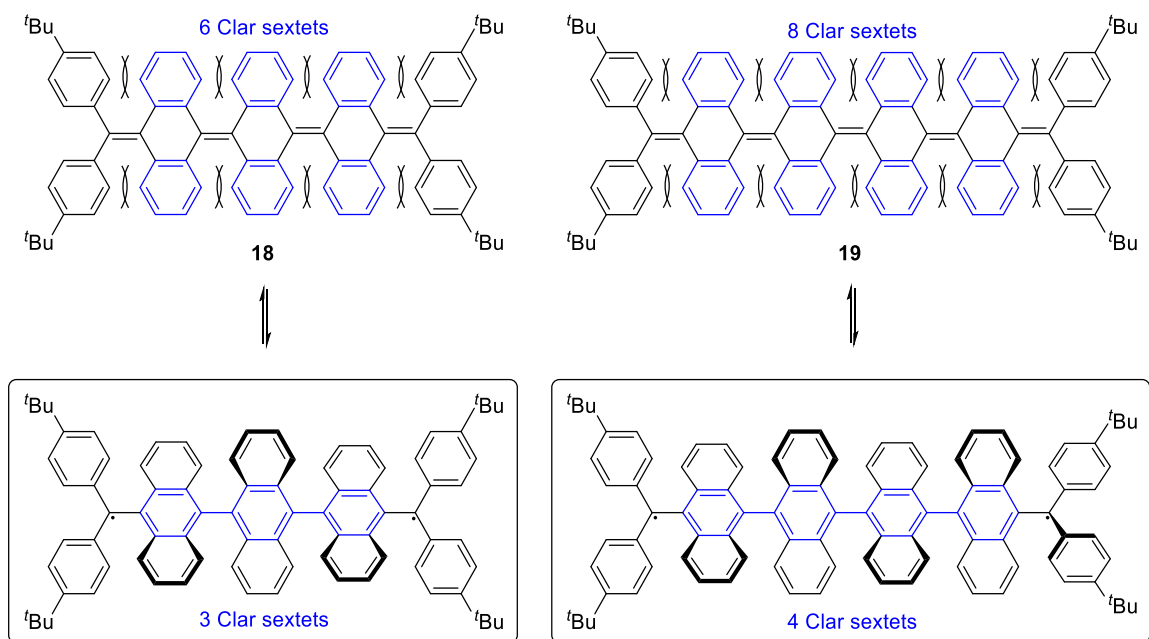


Chart 2.2 | Open- and closed-shell valence isomers of oligo(9,10-anthryl)_n derivatives **18** and **19**.^[77]

This is remarkable, since the stabilisation of the open-shell state in **18** and **19** cannot be explained by a larger number of Clar sextets, as there are more benzenoid hexagons in the closed-shell state (Chart 2.2, highlighted in blue). Thus, the authors concluded that increasing steric repulsion of the “wing-like” anthracene units overweighs the effect of Clar sextets and overcrowding is the main driving force towards the biradical character in this series.

2.2.1.2 Acenes and (Di-)Indenoacenes

As observed upon *para*-phenylene elongation, a spin crossover from closed-shell PAHs to open-shell biradicals can be imagined by a benzannulation approach in the (poly)acene series (Chart 2.3).^[78, 79] Acenes, representing planar, conjugated molecules, formally match the Hückel criteria for aromaticity, which however only apply for monocyclic compounds.^[80–82] Consequently, all closed-shell resonance structures of (linear) acenes can accommodate only one Clar sextet, as illustrated for anthracene **20** and pentacene **22** (Chart 2.3). Consequently, the number of benzenoid hexagons in acenes only increases in open-shell resonance structures like in diradicals **20- α** and **22- α** or in tetradical **22- β** , which, however, do not stabilise the molecule but enhances its reactivity. In contrast, the nonlinear arrangement of hexagons enables an increasing number of aromatic sextets in closed-shell structures, as can be seen by comparing isomeric anthracene **20** and phenanthrene **21**.^[83, 84] Despite the possible contribution of open-shell states to the ground state, up to pentacene all acenes are quite stable materials and according to computational analysis mainly closed-shell molecules.^[85, 98] Starting with hexacene, open-shell contributions to the electronic ground state increase and the singlet-triplet energy gap decreases with the length of linear extension reaching an almost constant plateau value of about 240 meV (= 23.2 kJ mol⁻¹) beyond octacene ($n = 7$, Chart 2.3).^[2, 85] The synthesis of larger polyacenes is challenging due to their low solubility combined with high sensitivity, which steadily increases with the number of annulated rings. The generation of unsubstituted higher acenes is therefore limited to surface- or matrix-based approaches.^[86–89] However, introduction of sterically demanding protecting groups shielding the reactive π -scaffold and/or rising oxidation potentials by extensive fluorine substitution like in nonacene derivative **23** (Chart 2.3) allowed a preparative isolation.^[90–92] Magnetic spectroscopic investigations as well as the reduced stability of **23** hint towards an open-shell ground state, however, this aspect was not clarified in detail.

Similar to the effect achieved by introduction of fluorine substituents, oxidation resistance of acenes can also be increased by incorporation of heteroatoms into the PAH scaffold. For instance, the group of Bunz demonstrated that the exchange of two or four CH-groups by nitrogen atoms leads to a significant

lowering of the LUMO levels resulting in highly oxidation resistant azaacenes.^[93] Furthermore, these compounds frequently feature ambipolar properties making them promising candidates for both n- and p-type semiconductors. Thus, Zhang and co-workers determined for azaacene **24** balanced hole and electron mobility of $\mu_h = 0.11$ and $\mu_e = 0.15$ cm²/Vs.^[94] Apart from more electron deficient designs, further stabilization was achieved as well by sulfur-doped acenes *via* an increasing number of Clar sextets^[95, 96] like in **25** or with structural incorporation of benzothiophene units.^[97] However, most of these (hetero-) acenes represent closed-shell (quinoidal) compounds.

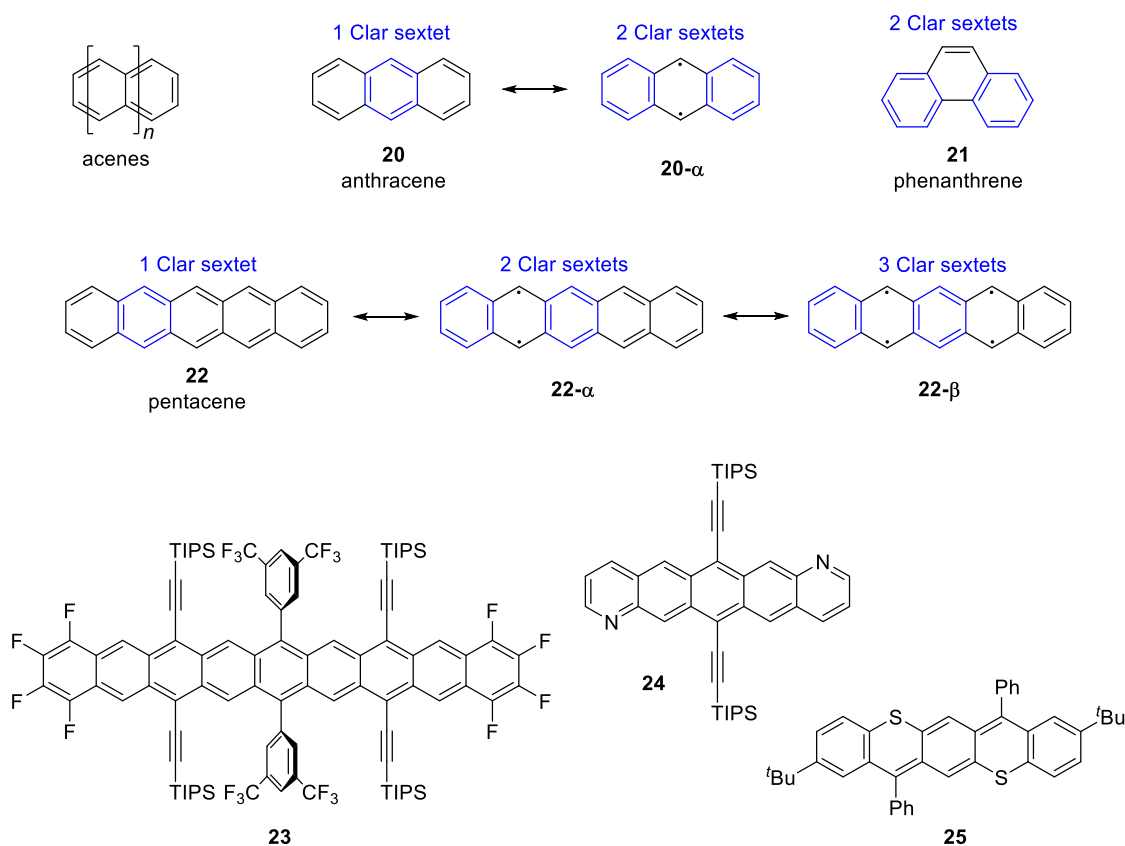
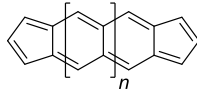


Chart 2.3 | General structure of acenes as well as open and/or closed-shell resonance structures of anthracene **20**,^[84] phenanthrene **21**^[84] and pentacene **22**^[85] as well as nonacene derivative **23**,^[92] diazapentacene **24**^[94] and sulfur-doped **25**.^[96]

A significant enhancement of the open-shell character in the polyacene series was predicted upon capping the terminal acene rings with cyclopentadienyl units, presumably due to a spin concentration effect (*vide infra*).^[98] Already with four annulated benzene rings (Table 2.1, $n = 3$), a dominating biradical character of 60% is predicted, reaching 90% with seven hexagons (Table 2.1, $n \geq 6$).

Table 2.1 | Size-dependent increase of singlet biradical character y_0 in antiaromatic cyclopentadiene capped acenes.

n	1	2	3	4	5	6	7	8	9	10	11
y_0	0.21	0.39	0.60	0.74	0.84	0.90	0.93	0.95	0.96	0.96	0.97



However, the cyclopentadiene termination leads to antiaromatic structures and “exposed” carbon sites with increased spin density and thus high reactivity. Steric shielding of these reactive positions while gaining additional π -surface was later achieved by further π -extension beyond the terminal five membered rings. Accordingly, Haley and co-workers presented diindeno-fused anthracene derivative **26** (Figure 2.3a),^[32] in which the authors considered spin concentration at the non-fused pentagon carbon atom within their molecular design and thus attached bulky mesityl groups sterically protecting these sites (Figure 2.3b). Consequently, **26** is exceptionally stable with a half-life in solution of 64 days and features a pronounced biradical character of $y_0 = 0.62$ due to aromatic stabilization of the open-shell state as evidenced by an XY-scan of the nucleus-independent chemical shifts (NICS, Figure 2.3c). This NICS-scan revealed a high degree of aromaticity in the central as well as both terminal rings (D and A, Figure 2.3a, c).

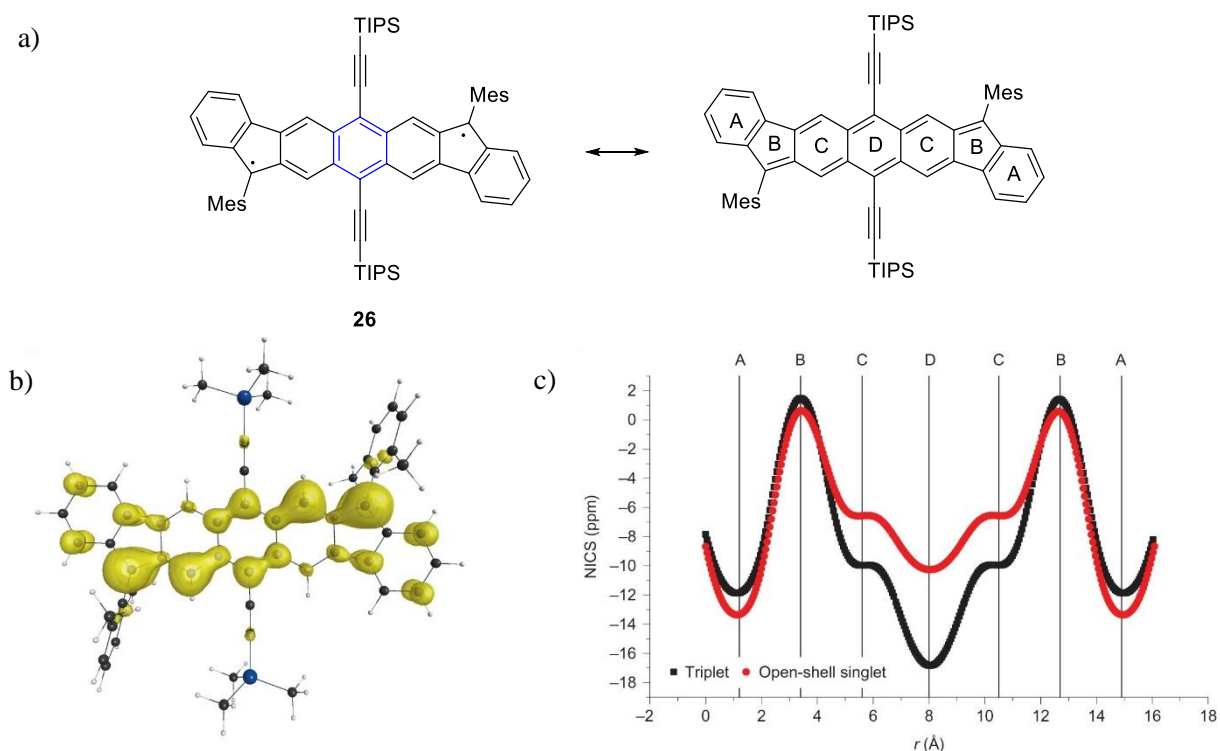


Figure 2.3 | Open- and closed-shell resonance structures of diindenofused anthracene derivative **26** (a),^[32] as well as odd electron density plot of (simplified) **26** on the LC–UBLYP/6–311+G(d,p) level of theory (b) and NICS-XY scans of the open-shell singlet and triplet states of **26** (c). Capital letters A, B, C and D in (c) refer to the rings of **26** in (a). Adapted with permission from ref. [32]. Copyright 2016 Springer Nature.

Apart from **26**, a plethora of structures has been developed based on (di)indenofused acenes as well as larger π -systems.^[34] Indenofluorenes are the smallest representatives of this class and comprise a fused indene and fluorene scaffold, but their properties strongly depend on the exact molecular constitution (Chart 2.4).^[33, 99–101] Indeno[1,2-*a*]fluorene **27** and indeno[2,1-*b*]fluorene **28** are rare examples of *meta*-substituted quinodimethanes (QDM), which are able to form a closed-shell Kekulé structure. However, the closed-shell resonance structures of **27** and **28** are energetically disfavoured, as the number of Clar sextets is tripled in the open-shell state (Chart 2.4, top). Accordingly, **27** and **28** feature significantly increased biradical characters of $y_0 = 0.65$ – 0.80 compared to 0.25 – 0.29 for the derivatives **29**, **30** and **31** based on an *ortho*- and *para*-QDM substitution pattern (Chart 2.4, bottom). Additionally, by applying Ovchinnikov's spin polarization rule^[102] (spin orientation is alternating along a conjugated chain of atoms (*vide supra*), illustrated by red and blue arrows), a triplet open-shell state is correctly predicted for indeno[1,2-*a*]fluorene **27**, which was confirmed with magnetic spectroscopy and is well in line with the observed enhanced reactivity.^[33]

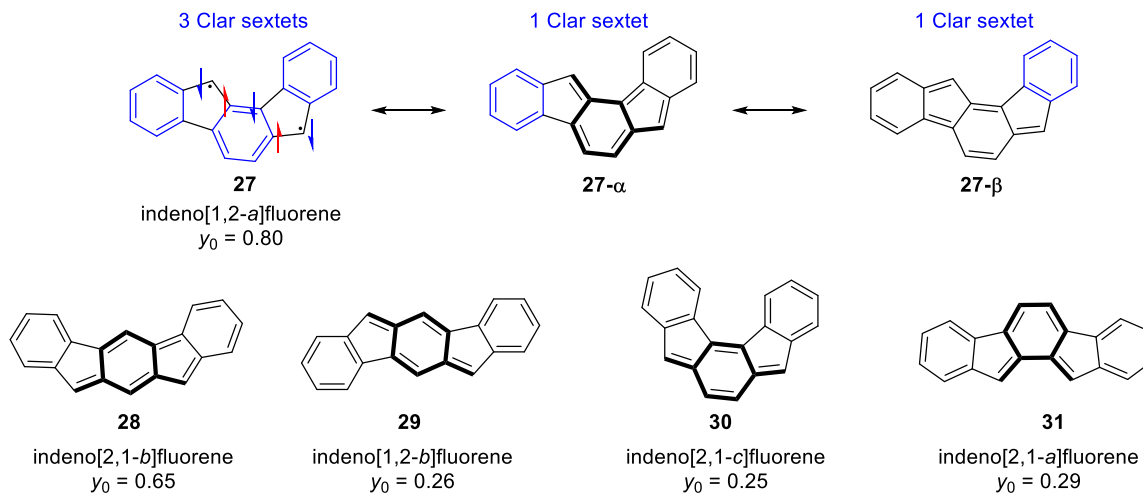


Chart 2.4 | Different indenofluorene isomers^[33, 99–101] and resonance structures of indeno[1,2-*a*]fluorene **27**.^[33] Red and blue arrows indicate ferromagnetic coupling and QDM substructures are highlighted in bold.

Like demonstrated with the remarkably stable open-shell diindenofused anthracene **26** (Figure 2.3) exhibiting a half-life time of more than two months in non-degassed CH_2Cl_2 solution^[32] as well as with other indenofused PAHs^[25], larger π -surfaces enable significant thermodynamic stabilization of biradicals, presumably by enhanced delocalization. Furthermore, structural isomerism, π -extension via benzannulation and sulfur doping allows a rational fine-tuning of biradical properties like the singlet-triplet energy gap or the singlet biradical character in indenofluorene chemistry.^[36, 103–105]

2.2.1.3 Bisphenalenes

The non-linear arrangement of fused rings offers an additional approach for the design of open-shell compounds and can generate unique orbital symmetries like in phenalenyl radical **32** and bisphenalene based biradicals (Figure 2.4, top).^[30, 106] The free electron can be localised at seven positions in **32** resulting in efficient delocalisation and thus enhanced stability. Accordingly, biradicals **33**, **34** and **35** (Figure 2.4, middle) are robust materials in the solid state.^[107–110] The molecular packing of **33** is characterised by close intermolecular π - π -interactions (Figure 2.4, bottom) leading to hole mobilities up to $\mu_h = 0.72 \text{ cm}^2/\text{Vs}$ in a single crystal field effect transistors (SC-FET).^[108] As in the case of acenes, the singlet biradical character of bisphenalene based biradicals increases with the size of the central core unit from $y_0 = 0.30$ for the phenyl linked **33**^[109] over $y_0 = 0.50$ for naphthalene bridged **34**^[107] to $y_0 = 0.68$ for anthracene derivative **35**^[110], whereas the ΔE_{ST} decreases from of 312 meV (= 30.1 kJ mol⁻¹) over 195 meV (= 18.8 kJ mol⁻¹) to 126 meV (= 12.1 kJ mol⁻¹), respectively.

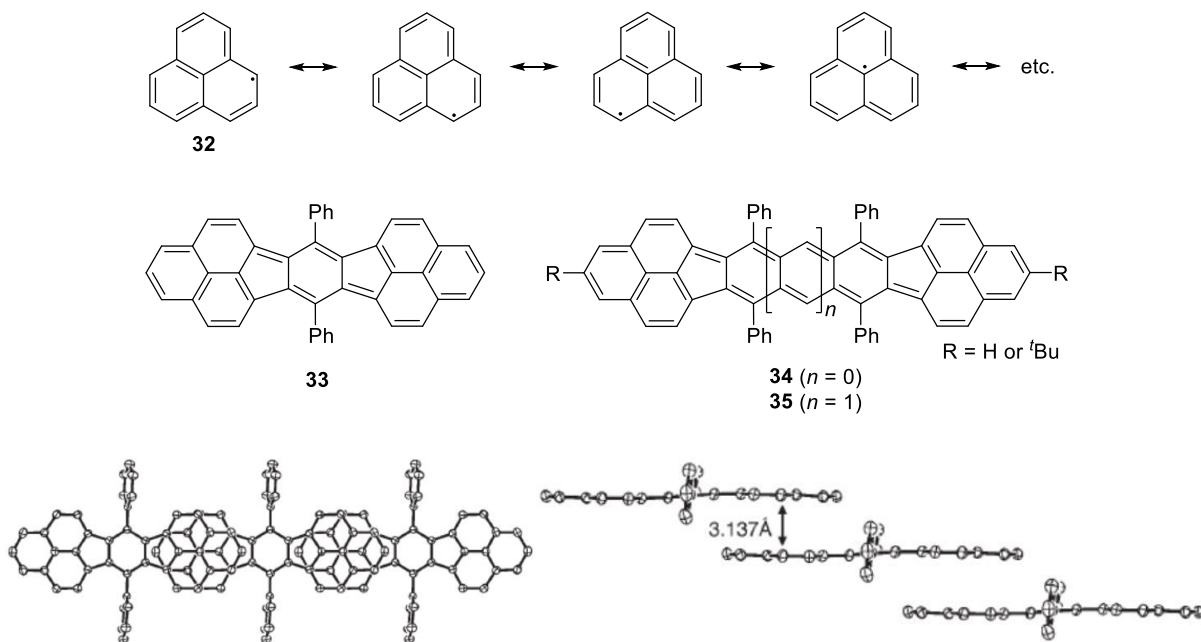


Figure 2.4 | Selected resonance structures of the phenalenyl radical **32** (top) and bisphenalene based biradicals **33**,^[109] **34**^[107] and **35**^[110] (middle) as well as solid state molecular packing of bisphenalene derivative **33** in top and side view (bottom, from left to right). Adapted with permission from ref. [109]. Copyright 2005 John Wiley and Sons Inc.

2.2.1.4 Zethrenes

Terminal capping of acenes with two phenalene units formally leads to “Z-shaped acenes”, which are denominated as zethrenes. The simplest representative of this series is zethrene **36** itself ($n = 1$, Chart 2.5a) and was first synthesized by Clar^[40] in 1955. However the synthesis remained low yielding until a drastic improvement was accomplished in 2010 by Wu.^[111]

Based on his zethrene research and taking further π -extended derivatives into account, Clar concluded his aforementioned famous theory about stabilization through aromaticity: PAH **37** features only two aromatic sextets (Chart 2.5a, highlighted in blue) and is much less stable than **38** which has four benzenoid sextets.^[38] Accordingly, structures with a higher number of benzenoid hexagons are more stable than structures with a lower number. More generally speaking, the structure with the highest number of benzenoid sextets is according to Clar the most stable one. Clar’s rule has also been used in order to evaluate the stability of different mesomeric structures and serves as a common explanation for the ground state stabilization of open-shell compounds (*vide supra*).

In recent years, several zethrene derivatives like bisimide **39** (Chart 2.5b) were synthesized by the group of Wu, which also achieved a certain advancement regarding photostability and solubility compared to unsubstituted **36**, although the central butadiene unit remained a weak point due to the lack of aromatic stabilisation.^[112] The higher homologue, heptazethrene **40** (Chart 2.5b) is one of the first representatives with an open-shell ground state and a small ΔE_{ST} of 73 meV ($= 7.0 \text{ kJ mol}^{-1}$).^[22] Indeed, the open-shell valence isomer of heptazethrene bisimide **40** gains stability from an additional central Clar sextet compared to the quinoidal closed-shell structure. However, the total number of benzenoid sextets is not the only determinant for the spin configuration^[113] of the ground state: Alkyne substituted heptazethrene derivative **41** (Chart 2.5b), which is analogous to **40**, is mainly a closed-shell quinoidal compound with only 16% biradical contribution.^[29] Accordingly, this example demonstrates that electron poor imide substituents are capable of additionally stabilizing the open-shell resonance structure in biradical(oid)s.^[114] Further elongation of the “bridging acene” leads to a more pronounced biradical character of $y_0 = 0.43$ in the octazethrene derivative **42**.^[29]

So far it was demonstrated that the size of the π -system and in particular the length of the incorporated acene substructures significantly influences the spin configuration of the ground state. Additionally, electron-poor substituents stabilize open-shell states. However, as pointed out already in the section about indenofluorenes, the impact of the specific hexagon arrangement and thus the substitution pattern cannot be neglected in zethrene chemistry as well.

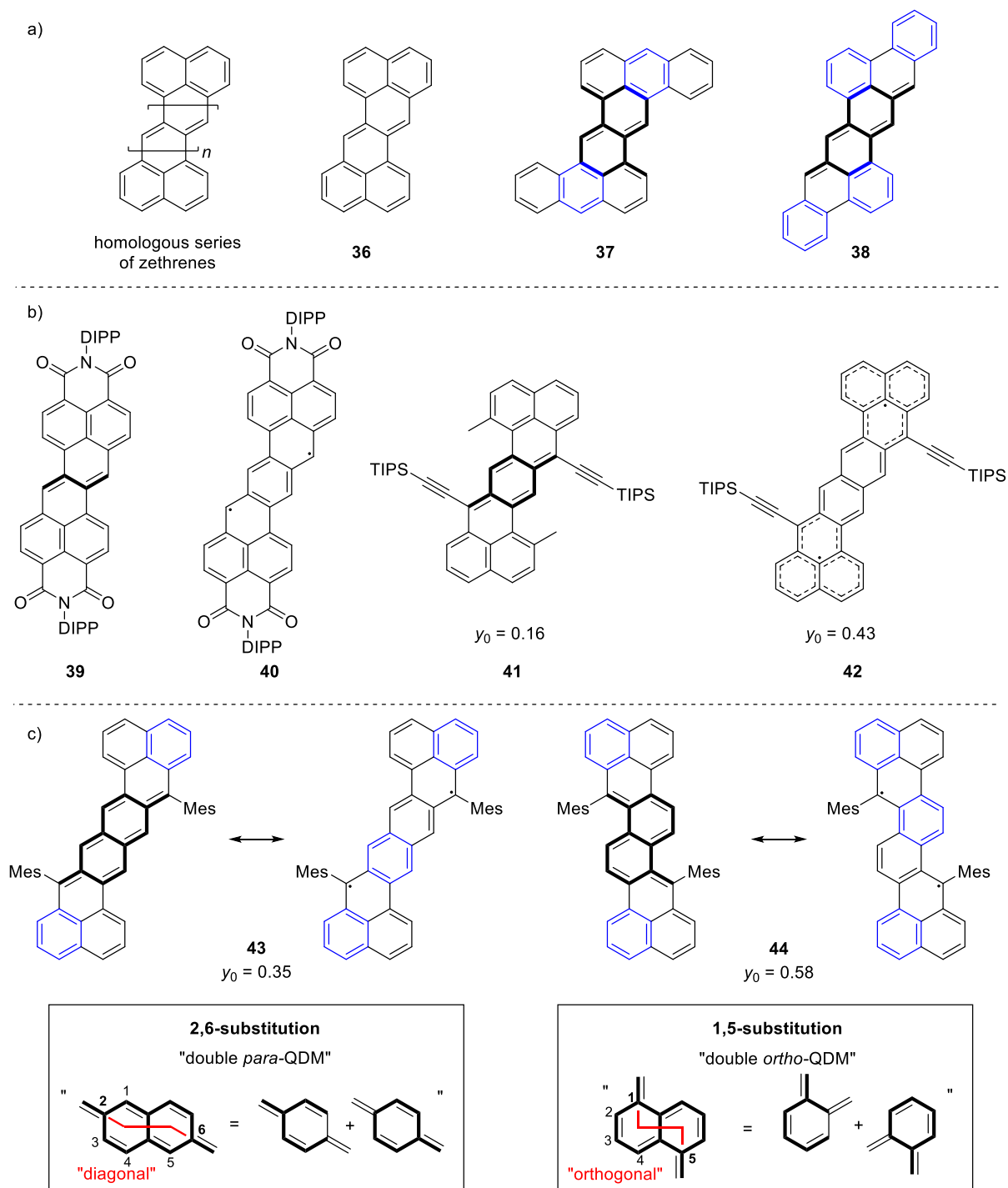


Chart 2.5 | Open- and/or closed-shell resonance structures of zethrene **36**^[38] and historic benzannulated derivatives **37**^[38] and **38**^[38] investigated by Clar (a), of zethrene bisimide **39**,^[112] heptazethrene derivatives **40**,^[22] **41**^[29] and octazethrene **42**^[29] (b) as well as of isomeric octazethrenes **43**^[31] and **44**^[31] (c). Benzenoid sextets are highlighted in blue.

Based on octazethrenes **43** and **44** (Chart 2.5c)^[31] and confirmed by recent investigations on dicyclopenta-naphthalenes,^[115] Wu and co-workers further demonstrated that the substitution pattern itself crucially determines the electronic ground state composition and thus the stability of naphthoquinodimethane-bridged PAHs: The “zig-zag”-shaped 1,5-substituted isomer **44** is highly labile with a pronounced biradical character of $y_0 = 0.58$, whereas the 2,6-substituted naphthoquinodimethane **43** is a stable compound with only 35% biradical character. Due to the equal number of Clar sextets in both isomers (two in the closed-shell state and three in the open-shell state), the destabilization of the 1,5-isomer has to arise out of the substitution pattern itself. Upon taking a closer look, it becomes apparent that the “diagonal” 2,6-substitution pattern in **43** (Chart 2.5c, highlighted in red) can be understood as a “fused double *para*-quinodimethane”, whereas the “orthogonal” 1,5-isomer resembles a structure of two superimposed *ortho*-QDM moieties. Thus, the different stability of **43** and **44** follows the higher reactivity observed for *ortho*-quinodimethanes, compared to the *para*-derivatives, which is commonly explained by the much more diene-like conjugation in *ortho*-QDMs.^[116, 117] A similar effect might additionally explain the higher stability of Clar’s **38** compared to **37** (Chart 2.5a, naphthoquinodimethane structures highlighted in bold).

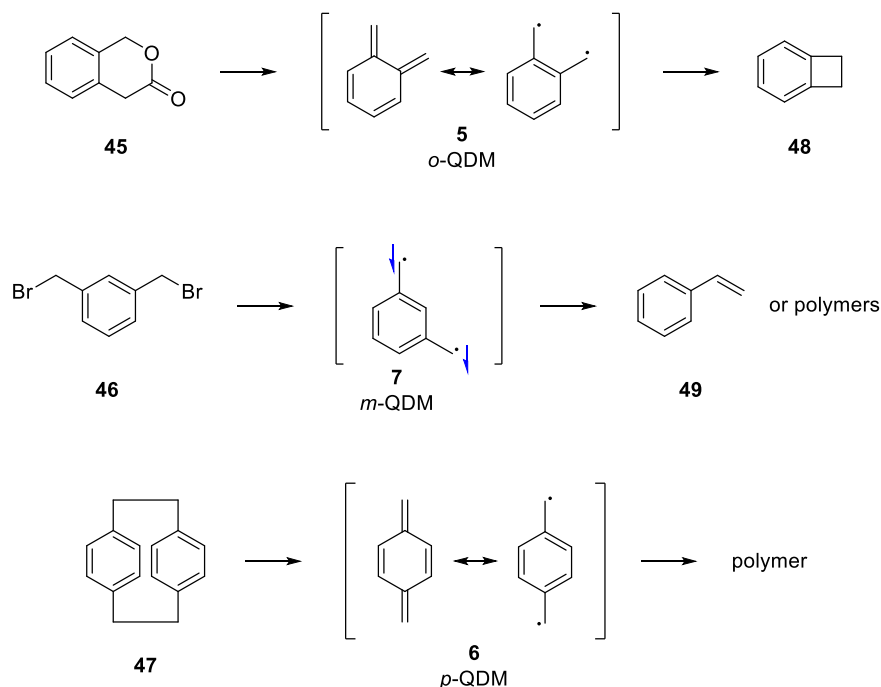
As already mentioned for the structural class of (extended) indenofluorenes (*vide supra*), incremental tuning of ΔE_{ST} , y_0 and the compound’s stability is also possible with longitudinally and laterally expanded zethrenes.^[118–120]

2.2.1.5 Pristine quinodimethanes and their incorporation into macrocyclic structures

Almost every biradical(oid) PAH presented so far comprises the quinodimethane (QDM) structural motif, which is the determining substructure of (oligo)acenes, zethrenes or diindenoacenes, and thus represents one of the most studied building block in biradical chemistry.^[121] But despite their presence in this broad variety of open-shell PAHs, “pure”, i. e. unsubstituted quinodimethanes are rare. The most simple QDMs are the three xylylene isomers **5**, **6** and **7**, which were already mentioned in the beginning of this chapter (Chart 2.1).

The pristine xylylenes exhibit high reactivity and are studied in regard of reactive intermediates.^[116] As demonstrated by Fischer, Petersen, Mitrić, Rijs and co-workers they can be generated by flash vacuum pyrolysis of the respective lactone **45**, dibromide **46** or cyclophane **47**, (Scheme 2.4).^[122] Respective monoradicals are accessible *via* pyrolysis of (methylphenyl)ethyl nitrites^[123]. Closed-shell *o*-QDM **5** and triplet diradical **7** show an enhanced tendency towards isomerisation^[122] under formation of benzocyclobutane **48** and styrene **49**, respectively, or – like in the case of *meta*- and *para*-QDMs **7** and

6 – tend to undergo polymerization.^[122, 124] It is hence not surprising, that substituted derivatives like the above-mentioned hydrocarbons of Thiele, Tschitschibabin and Müller or cyclic quinodimethanes are much more common and persistent. The reactivity of diradicals containing different quinodimethane substructures decreases in the order *m*-QDM > *o*-QDM > *p*-QDM as was observed in particular among zethrene and indenofluorene chemistry (*vide supra*). In this regard, McCarthy, Schmidt and co-workers computed the energy differences between **5**, **6** and **7** using a G3SX composite model.^[125] Indeed, the authors confirmed that *o*-QDM is 269 meV (= 26 kJ mol⁻¹) higher in energy than *p*-QDM and *meta*-substituted **7** is even 1.17 eV (= 113 kJ mol⁻¹) higher than *o*-QDM. Accordingly, the sensitivity of larger structures can be traced back frequently to the high reactivity of small QDMs, which they are composed of.



Scheme 2.4 | Generation of quinodimethanes **5**, **6** and **7** by flash vacuum pyrolysis of **45**, **46** and **47** as well as decomposition/isomerisation products **48** and **49**.^[122] Blue arrows indicate ferromagnetic coupling.

Only recently, the group of Wu and co-workers synthesized and investigated several *para*- and *meta*-xylylene derivatives incorporated into larger macrocyclic structures (Chart 2.6). Cyclo-*para*-phenylmethin **50** can be described by a closed-shell resonance structure, but features several open-shell contributions as well.^[126] The singlet biradical character of macrocycle **50** was determined to be $y_0 = 0.49$, but also higher degree (poly-)radicals contribute to the ground state resulting in remarkably

large tetra- and hexa-radical characters of $y_1 = 0.47$ and $y_2 = 0.29$, respectively. The pronounced polyradical character of **50** can be rationalized by an increasing number of Clar sextets for higher open-shell structures.

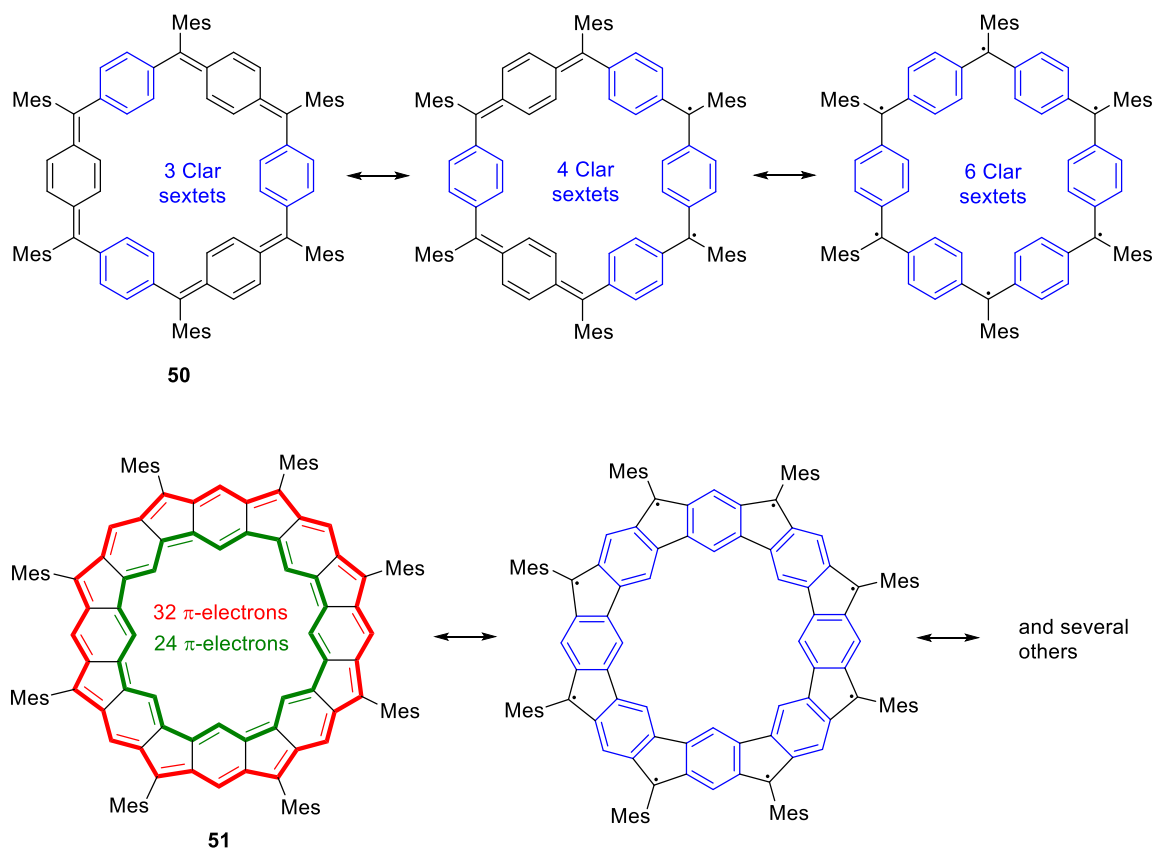


Chart 2.6 | Selected open- and closed-shell resonance structures of macrocyclic quinodimethane **50**^[126] (top) and **51**^[127] (bottom). Red and green bonds highlight large anti-aromatic [32] and [24]annulene substructures.

In addition, global aromaticity effects have to be taken into account for the proper description of *meta*-fused macrocycle **51**.^[127] The closed-shell resonance structure can be understood as an [24]annulene (Chart 2.6, highlighted in green) within, but decoupled from an [32]annulene (Chart 2.6, highlighted in red). Following the $4n$ Baird's aromaticity rule, this resonance structure can be considered as "anti-Hückel"-aromatic and is thus energetically not favoured.^[128–130] Consequently, and further stabilized by several Clar sextets in the open-shell state, macrocycle **51** features multiple high poly radical characters of $y_0 = 0.79$, $y_1 = 0.56$, $y_2 = 0.56$ and $y_3 = 0.45$.

2.2.1.6 Twofold dicyanomethylene functionalised compounds

As pointed out in the section about zethrene bisimides, electron-withdrawing substituents are capable of stabilizing open-shell spin states. For this reason, di- and tetracyano-substituted quinodimethanes *inter alia* based on oligomeric heteroaromatics (which originally have been investigated as organic semiconductors) are of high interest as a design principle for biradicals as well. In addition, quinoidal oligothiophenes are easily accessible *via* nucleophilic substitution or transition metal catalysed cross coupling reaction of brominated thiophene derivatives with deprotonated malononitrile and subsequent dehydrogenation. Following this strategy, a series of bis(dicyanomethylene) substituted oligothiophenes with up to six thiophene units was synthesized by Otsubo and co-workers (Chart 2.7).^[131]

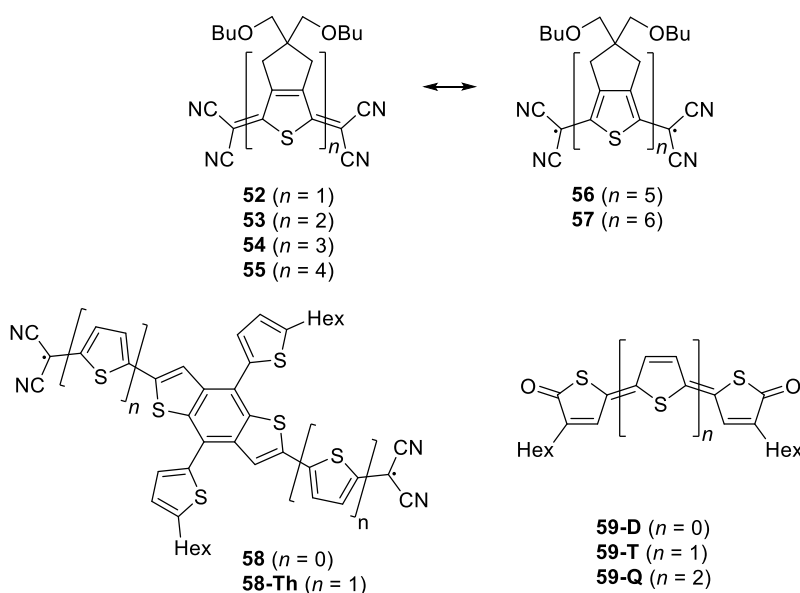


Chart 2.7 | Open- and closed-shell resonance structures of twofold dicyanomethylene-substituted oligothiophenes **52–57** (top) and formula of quinoidal benzodithiophenes **58** and **58-Th** as well as carbonyl-terminated oligothiophenes **59-D**, **59-T** and **59-Q** (bottom).^[131, 132, 134]

Whereas the lower oligomers **52–55** with up to four thiophene units clearly show diamagnetic behaviour, the pentamer **56** as well as hexamer **57** exhibit pronounced EPR signals and are NMR silent. Accordingly, a spin crossover from closed-shell quinoidal to open-shell biradical was achieved upon insertion of one additional thiophene unit into the tetramer. The authors concluded the increasing aromaticity with every heteroaromatic ring added being crucial for the spin crossover from **55** → **56**, like it was observed for the elongation of Tschitschibabin’s to Müller’s hydrocarbon before.^[131] Consequently, the rather small thienoquinoidal systems **59-D**, **59-T** and **59-Q** (Chart 2.7) investigated by Takimiya and co-workers with up to four thiophene units do not show any biradical contribution to the ground state.^[132, 133] However, a spin crossover can be observed upon elongation of a

benzodithiophene system. The insertion of two additional thiophene units into twofold dicyanomethylene substituted benzodithiophene **58** leads to open-shell compound **58-Th** (Chart 2.7) with a pronounced singlet biradical character of $y_0 = 0.59$, whereas the ground state of the smaller derivative is closed-shell.^[134]

Conceptually related to the thiophene series is the sequence of perylene oligomers **60–65** (Figure 2.5), which can be understood as a π -extended congener of the *para*-phenylene oligomers presented earlier.^[135, 136] The ground state of bis(dicyanomethylene) perylene **60** is closed-shell quinoidal, whereas the dimer **61** ($y_0 = 0.85$), trimer **62** ($y_0 = 0.99$) and tetramer **63** ($y_0 = 0.99$) are singlet biradicals with spin density mainly located at the terminal perylene units (Figure 2.5, inset). Notably, pentamer **64** and hexamer **65** are triplet biradicals reflecting the fact that in a widely separated two-spin system, the triplet state is lower in energy than the singlet state following Hund's rule.^[135] Furthermore, the open-shell states in **61–65** are significantly favoured due to several degrees of rotational freedom along the bond connecting the perylene subunits leading to a significant reduction of steric strain. This becomes apparent, as the analogous fused tetraylene **66** (Figure 2.5) is fully closed-shell and the open-shell character of hexarylene system **67** is marginally ($y_0 = 0.06$).^[137]

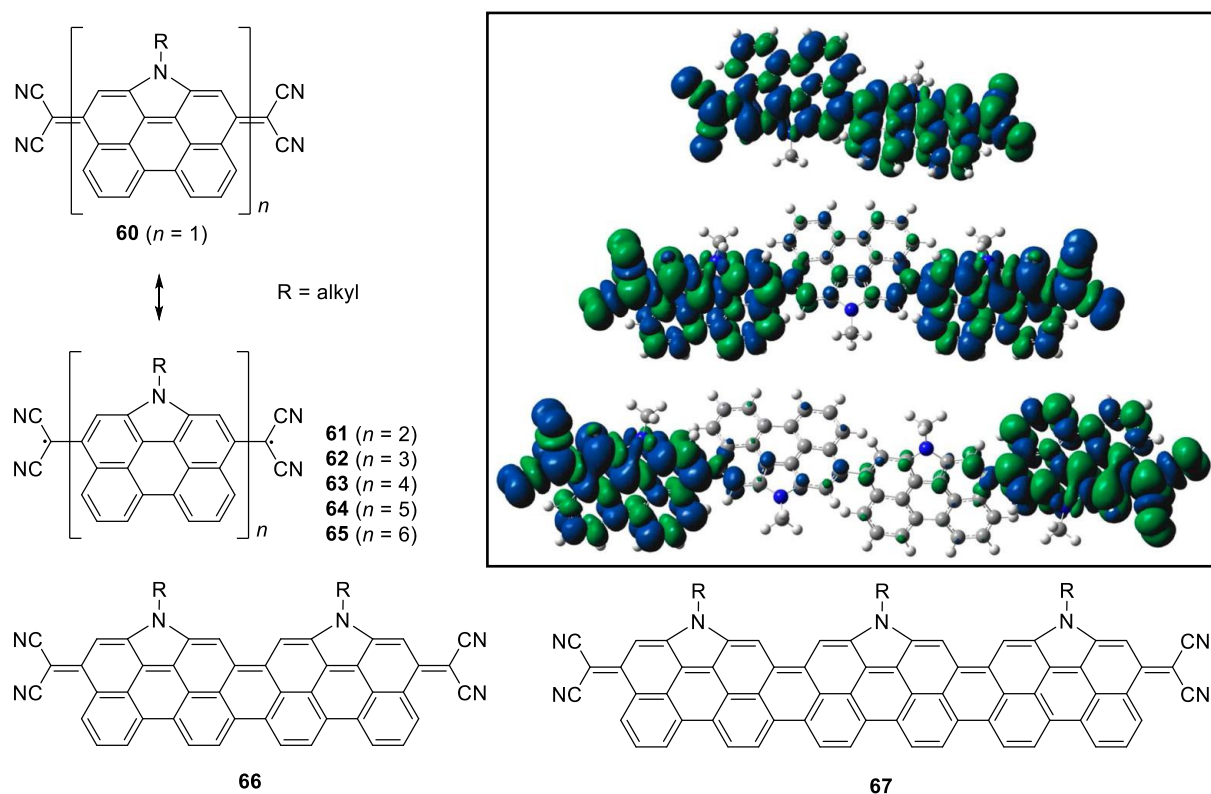


Figure 2.5 | Structures of twofold dicyanomethylene substituted perylene oligomers **60–65**,^[135] as well as fused derivatives **66**^[137] and **67**.^[137] Inset: Calculated spin density of **61**, **62** and **63** (from the top). Adapted with permission from ref. [135]. Copyright 2013 American Chemical Society.

In addition to the quinoidal and the biradical form, a zwitterionic mesomeric structure can be drawn in push-pull systems **68–70**, which possibly contributes to the ground state as well (Figure 2.6). However, quantum chemical analysis on the LC–UBLYP ($\mu = 0.33$)/6–311+G* level of theory revealed that the biradical characters remain almost unchanged with pronounced open-shell contributions of $y_0 = 0.899$ for dimer **69** ($n = 2$) and $y_0 = 0.995$ for trimer **70** ($n = 3$).^[138] Thus, the charge-separated state is widely suppressed by a biradical state due to decreasing spin and charge interaction upon chain elongation, which becomes apparent by decreasing Hirshfeld charges as well (Figure 2.6).

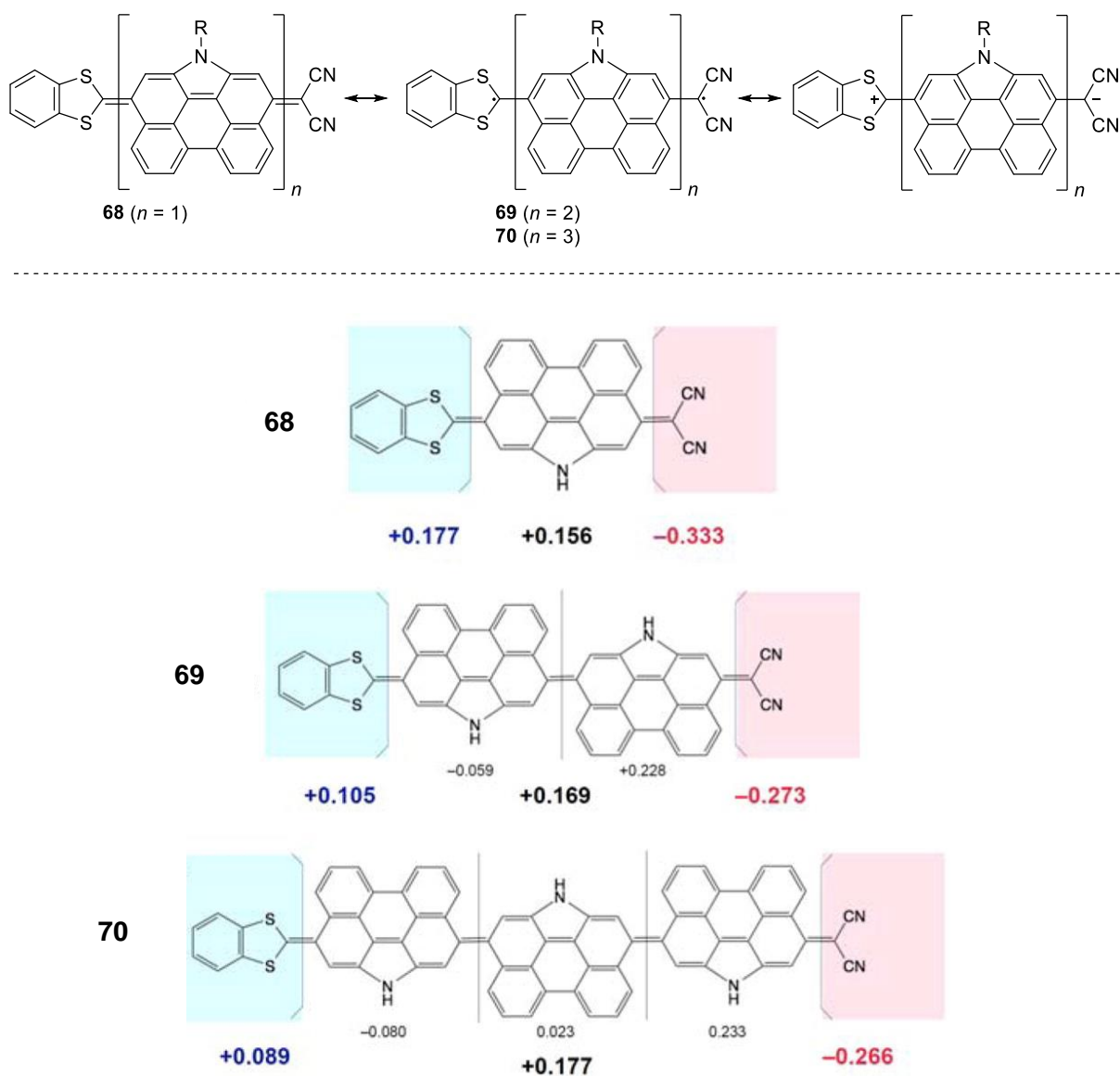


Figure 2.6 | Selected resonance structures of donor-acceptor-substituted perylene oligomers **68–70**^[138] (top) and calculated Hirshfeld charges of **68**, **69** and **70** (from the top). Adapted with permission from ref. [138]. Copyright 2015 American Chemical Society.

In summary, quinoidal dicyanomethylene substituted oligomers frequently feature open-shell contributions in the ground state – in particular upon crossing a certain degree of π -extension, which however is specific to every substance class. As dicyanomethylene-substituted compounds are often considered as promising acceptor materials or as n-type semiconductors in organic electronic applications, more electron poor π -bridges might be beneficial in order to further increase the molecules electron accepting properties. In this regard, the electron poor chromophore core diketopyrrolopyrrole (DPP) was incorporated into a quinoidal framework of four cyano groups.^[139] Resulting compound **71** (Chart 2.8) shows excellent electron mobility up to $\mu_e = 0.55 \text{ cm}^2/\text{Vs}$ in OTFTs but is characterized by a closed-shell ground state, as has been evidenced by single crystal X-ray diffraction.^[140]

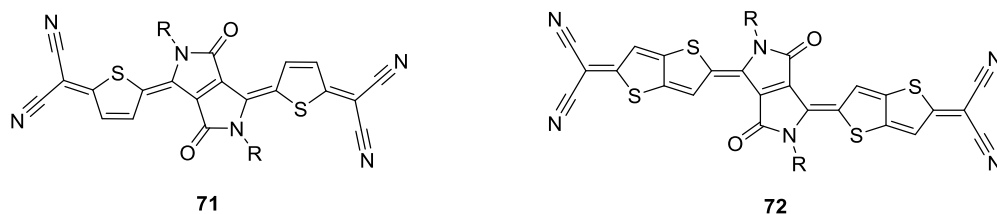


Chart 2.8 | Structures of quinoidal thiophene and thienothiophene containing DPPs **71**^[140] and **72**.^[141]

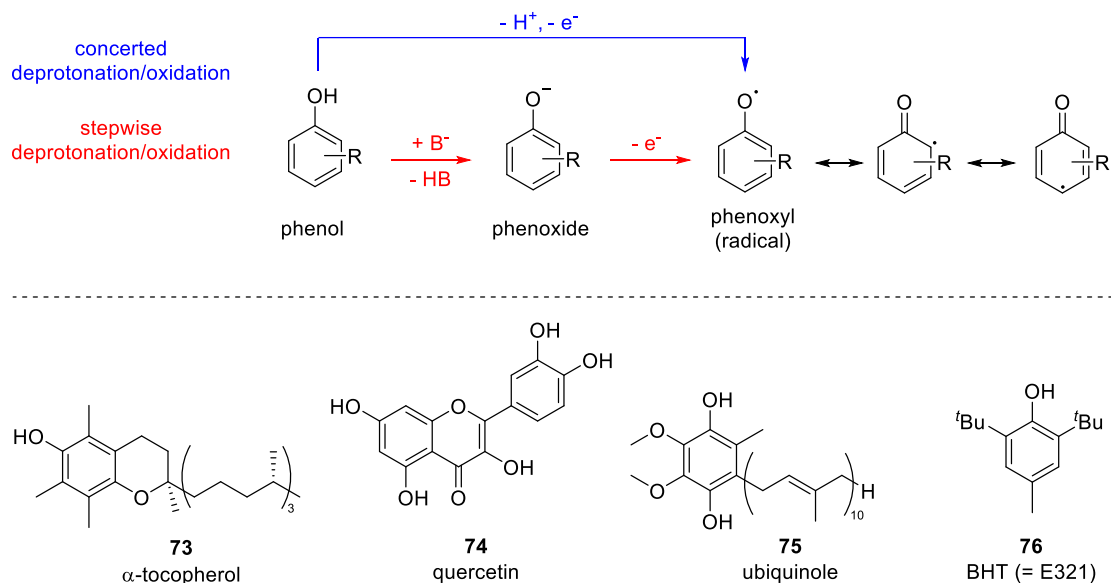
Similar to the benzodithiophene couple **58** and **58-Th** (Chart 2.7), the interplay between open-shell biradical and closed-shell quinoidal form was investigated in detail with experimental and theoretical methods for the larger thienothiophene containing **72**.^[141] However, in contrast to **58-T**, no spin crossover could be achieved and it was demonstrated that the ground state of **72** is closed-shell quinoidal as well. Accordingly, so far no open-shell DPP biradical is known.

2.2.2 Phenoxy-based biradicals and quinones

2.2.2.1 Introduction

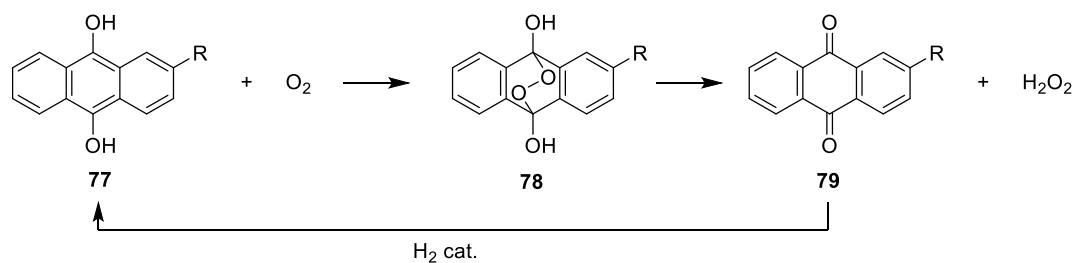
In addition to the rich chemistry of carbon centred biradical(oid)s based on quinodimethanes, another class of important structural architectures in this field are the oxygen analoga of QDMs – the structural class of quinones. All principles outlined so far influencing the relative energetical position of open and closed-shell resonance structures and thus determining the spin configuration of the electronic ground state apply for quinones as well. Accordingly, molecules can be dominated by open-shell resonance structures leading to (phen)oxyl biradicals or by closed-shell structures denominated as “real” quinones. Relevant developments in this field will be highlighted in the following section of this thesis.

Phenols in general and phenolates in particular are well known to form (considerably stable) phenoxy radicals upon (proton-coupled) oxidation (Scheme 2.5, top). Accordingly, numerous phenol derivatives can be found in nature as antioxidants^[142] like α -tocopherol (vitamin E) **73**,^[143] quercetin **74**^[144] or tannin^[145] and are intensively studied as redox agents like ubiquinole **75**,^[146] a reduced form of coenzyme Q10 (Scheme 2.5, bottom).^[147] In addition, the extraordinary quenching capability of phenols for reactive oxygen species made them widely used industrially^[148] as food or fuel preservatives like e.g. 4-methyl-2,6-di-*tert*-butyl phenol **76** (butylated hydroxytoluene = BHT (= E321), Scheme 2.5, bottom).^[149, 150]



Scheme 2.5 | Formation of phenoxy radicals upon concerted (blue arrow) or stepwise (red arrows) deprotonation/oxidation (= proton coupled oxidation) of phenols (top) as well as selected natural and artificial phenol-based antioxidants: α -tocopherol **73**,^[143] quercetin **74**,^[144] ubiquinole **75**,^[146] and butylated hydroxytoluene **76** (bottom).^[149, 150]

For instance, in concentrations of approx. 20 mg per litre of fuel, BHT can effectively capture (free) radicals and thus stabilize diesel or jet fuels during storage and combustion, which is necessary in particular in the presence of high percentages of biodiesel.^[151–153] Furthermore, the reversible redox chemistry of quinones is used technically in the anthraquinone process for the production of hydrogen peroxide with an anthrahydroquinone **77**/anthraquinone **79** redox system *via* endoperoxide **78** (Scheme 2.6).^[154]



Scheme 2.6 | Oxidation reaction of anthrahydroquinone **77** to form endoperoxide **78**, which decomposes to anthraquinone **79** and hydrogen peroxide as well as the regeneration cycle *via* catalytic hydrogenation.^[154]

2.2.2.2 Heteroquinones and oligo(hetero)aromatic biradicals

Quinones and phenoxy (bi)radicals occur frequently in natural and artificial redox processes, but are an important material class as well. They sparked great interest in understanding the electronic structure of biradical(oid)s and the molecular determinants influencing their spin states. Twofold phenoxy decorated π -systems can be drawn as open-shell biradicals or as closed-shell quinones (Chart 2.9). However, commonly both structures contribute to the electronic ground state. Which valence state is dominating and thus decisive for the molecular properties depends mainly on the π -core linking both phenoxy moieties. Thus, the next section of this thesis will illustrate insights gained from research covering rather small as well as considerably large π -extended phenoxy biradicals and quinones.

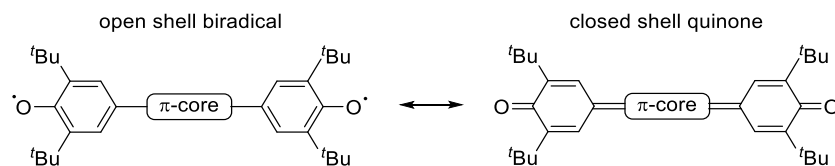
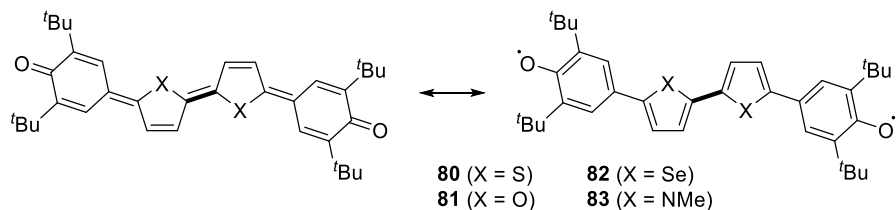


Chart 2.9 | Open- and closed-shell resonance structures of Kekulé-type phenoxy biradicals and quinones.

Heteroquinones (HQ) consist of two terminal phenoxy units bridged by a small heteroaromatic oligomer. Due to the low aromatic stabilization of these rather small oligomeric systems, heteroquinones are commonly closed-shell. A comprehensive series of HQs was studied by Takahashi and co-workers already in 1996 comprising a bithiophene (**80**), bifurane (**81**), biselenophene (**82**) or (*N*-methylated) bipyrrrol moiety (**83**) bridging the two terminal phenoxy units (Chart 2.10, top).^[155] Overall, the group's results indicate the dominance of a closed-shell quinoidal ground state in all four investigated derivatives **80–83**. However, temperature-dependent proton NMR studies revealed a coalescence phenomenon, presumably resulting from rotation around the inner heteroaromatic double bond *via* a biradical state (Chart 2.10, top, highlighted in bold). In this regard, the authors concluded that compound **80** containing two thiophene units might best stabilize this open-shell transition state, as the coalescence temperature is the lowest in this series. However, the focus of this work lay on the investigation of electrochemical properties and thus implications risen by the potential biradicaloid nature of **80–83** were not targeted in detail.

Heteroquinones investigated by Takahashi and co-workers.



Heteroquinones investigated by Canesi and co-workers.

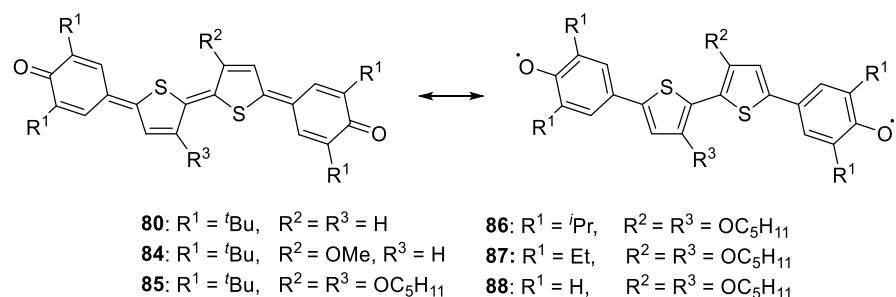


Chart 2.10 | Open- and closed-shell resonance structures of thiophene, selenophene, furane and pyrrole-based heteroquinones **80–83** investigated by Takahashi and co-workers,^[155] (top) and structure variation of heteroquinones **80** and **84–88** investigated by Canesi and co-workers (bottom).^[37] Note that **80** was investigated by both groups.

A systematic combined experimental and theoretical study investigating the biradical properties of bithiophene-bridged heteroquinones was later presented by Canesi and co-workers.^[37] The authors studied the effect of *ortho*-positioned alky chains by a variation from *tert*-butyl over *iso*-propyl and ethyl to unsubstituted phenones and calculated the singlet-triplet gap for each compound. In addition, the

impact of donor substituents attached to the bithiophene core was clarified using one fold methoxy or twofold pentoxy substitution (Chart 2.10, bottom). It is worth to mention that in this 2012 study, the authors re-investigated compound **80**, which was studied by Takahashi already 16 years before.^[155] Geometry optimizations using density functional theory (DFT) calculations on the B3LYP/6–31 level of theory with subsequent analysis of the wave function stability on the broken symmetry (BS) level revealed an open-shell singlet ground state for **80** ($R^1 = t\text{Bu}$, $R^2 = R^3 = \text{H}$) with a rather small ΔE_{ST} of 41 meV ($= 4.0 \text{ kJ mol}^{-1}$) and uncovered a further reduction of the singlet-triplet energy gap to 7.8 meV ($= 0.75 \text{ kJ mol}^{-1}$) for still open-shell **84** ($R^1 = t\text{Bu}$, $R^2 = \text{OMe}$, $R^3 = \text{H}$). Thus, it was concluded that donor substitution destabilises the open-shell state, which is in line with a closed-shell ground state calculated for the twofold pentoxy substituted heteroquinone **85**. As pointed out by the authors themselves, conventional DFT is frequently insufficient to describe the electronic ground state of biradicals precisely. Results that are more accurate can be achieved by applying complete active space self-consistent field (CASSCF) calculations. However, in the study of Canesi and co-workers, only for dipentoxy derivative **88** CASSCF(12,12) calculations were performed confirming the DFT results. Accordingly, in the case of **80** ($R^1 = t\text{Bu}$, $R^2 = R^3 = \text{H}$), there is an ongoing debate on whether the ground state of this molecule is open-shell or closed-shell^[156–158] and recently, Bunz and co-workers computed a singlet biradical character of $y_0 = 0.18$ by using conventional as well as spin-flip DFT.^[159] In contrast to donor substitution, reducing the steric demand of *ortho*-positioned alkyl chains R^1 from *tert*-butyl (**85**) over *iso*-propyl (**86**) and ethyl (**87**) to unsubstituted **88** does not influence the electronic ground state but only results in a drop of solubility (Chart 2.10, bottom).^[37]

Until today, heteroquinones continuously raise attention and new scaffolds with tailed heterocycles are synthesised. In this regard, phenoquinones with a thiazulenic bridge (**89**)^[160] or a tetrathiafulvalene (TTF) “tail” (**90**)^[161] were presented recently (Figure 2.7) and their redox chemistry and molecular structures was studied in detail.

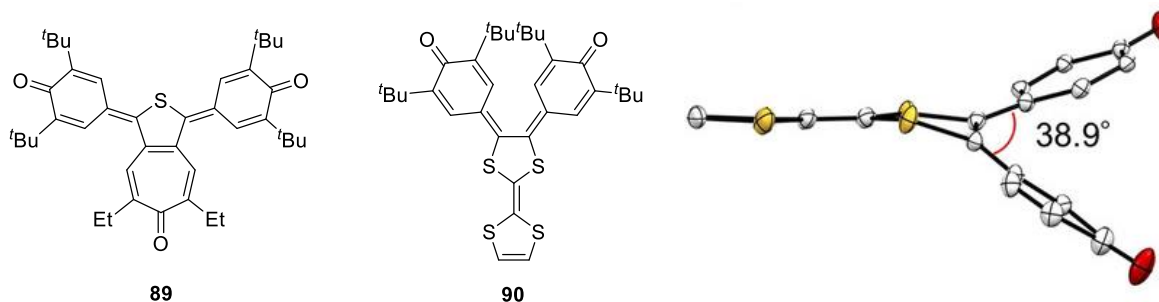


Figure 2.7 | Formula of “tailed” heteroquinones **89**^[160] based on thiazulene and **90**^[161] containing tetrathiafulvalene as well as X-ray crystal structure of **90** (from left to right). Reprinted with permission from ref. [161]. Copyright 2020 John Wiley and Sons Inc.

Despite a large dihedral angle of 38.9° between both phenoxy units in the case of TTF tailed quinone **95** (Figure 2.7, right), the ground state of both compounds **89** and **90** is closed-shell quinoidal. Thus, neither the tetrathiafulvalene nor the thiazulene system shows enough aromaticity to stabilise the open-shell structure. The group of Bunz recently took up the structural motif of bithiophene-linked heteroquinones and combined these with azaacene “tails” of different lengths.^[159] Accordingly, Y-shaped heteroquinone **91** and a series of regioisomeric open-shell phenoxyl biradicals **92–94** were obtained (Figure 2.8).

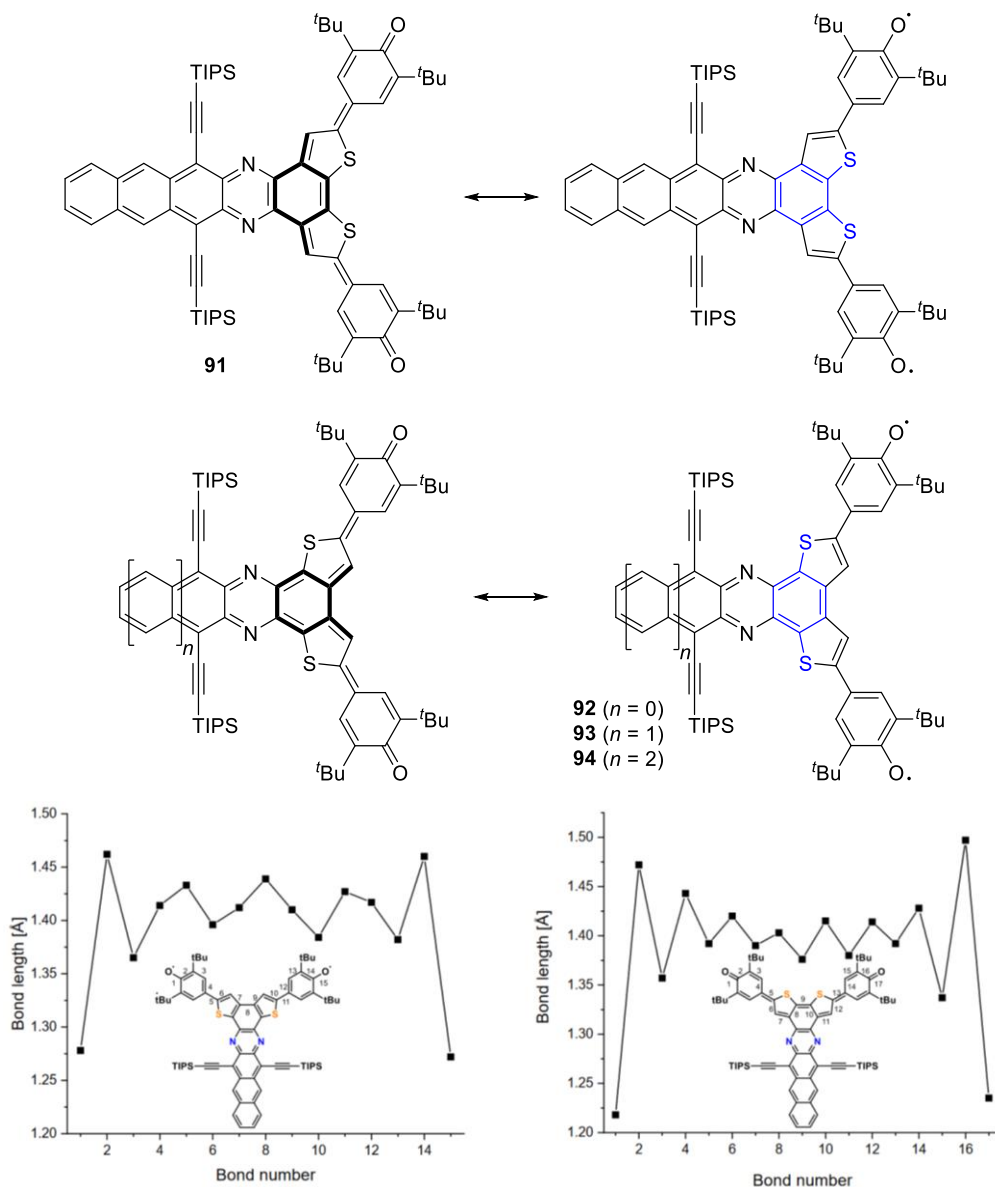
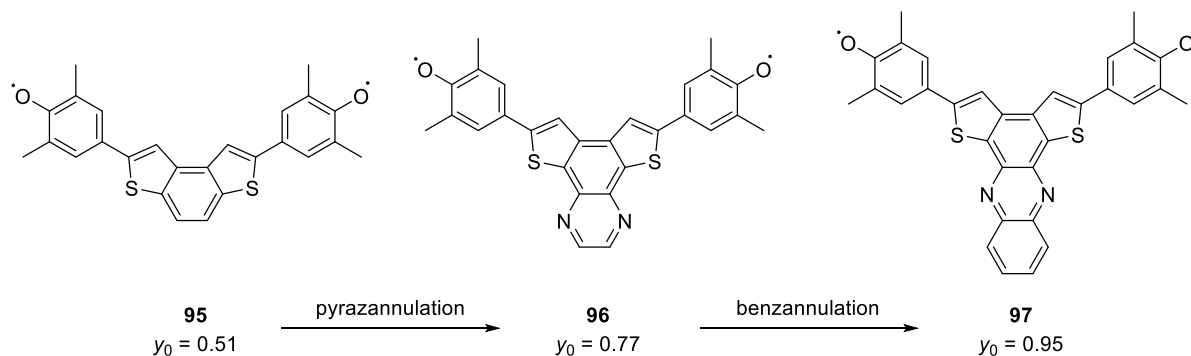


Figure 2.8 | Open- and closed-shell resonance structures of azaacenoquinones **91** (top) and regioisomeric biradicals **92–94** (middle) as well as bond length alternation along the quinoid structure in **94** (bottom, left) and **91** (bottom, right).^[159] The “*ortho*-S,S” (top) as well as “*para*-S,S” (middle) structural motif is highlighted in blue. Reprinted with permission from ref. [159]. Copyright 2020 John Wiley and Sons Inc.

All “*para-S,S*” derivatives (Figure 2.8, middle, highlighted in blue) exhibit pronounced biradical characters of $y_0 = 0.95$ for **92** ($n = 0$), $y_0 = 0.99$ for **93** ($n = 1$) and $y_0 = 0.98$ for **94** ($n = 2$), whereas for the “*ortho-S,S*” regioisomer **91** only a minor biradical contribution of 26% was calculated (Figure 2.8, top, highlighted in blue) on the DFT/CAM–B3LYP/6–311G(d,p) level of theory. The authors were able to substantiate their conclusions drawn from quantum chemical calculations additionally by X-ray analysis of both azapentacene derivatives proofing a distinct bond length alternation in the case of quinoidal **91** and a “single bond broken” biradical structure for **94** (Figure 2.8, bottom). These opposite ground states result from different central quinodimethane isomers: In the hypothetical closed-shell quinoidal forms of **92–94**, the heteroquinone is linked by an *ortho*-QDM unit (Figure 2.8, middle, left, highlighted in bold). In contrast, regioisomer **91** is bridged by a *para*-QDM. As discussed in the section about QDMs, *ortho*-quinodimethanes are energetically unfavoured conformations pushing these biradicaloid compounds towards an open-shell ground state. Contrarily, **91** is stabilised by a *para*-quinodimethane substructure resulting in much higher quinoidal contributions. In addition, the authors clarified the impact of a stepwise expansion of the (aza)acene “tail” on the singlet biradical character (Scheme 2.7). Pyrazannulation (**95** → **96**) and further benzannulation (**96** → **97**) leads to a growing tail and stepwise increase of the singlet biradical character of approx. 20% points per additional ring reaching a plateau of $y_0 \geq 0.95$ for **97** and longer azaacenes.



Scheme 2.7 | Increasing biradical character y_0 upon (hetero)acene length elongation from compound **95** to **97**.^[159]

2.2.2.3 Sterically hindered quinones

Quinoidal compounds are commonly almost planar or feature rather low torsion angles, whereas geometries of biradicals are much more contorted. However, even highly distorted geometries do not in general prevent a closed-shell ground state. For instance, bisanthene **98**^[162] and in particular [6]-radialene **99**^[113] (Figure 2.9, top and middle) – both reported by Wu and co-workers – are closed-shell quinoidal compounds. This is remarkable, as **99** would gain seven additional Clar sextets in the open-shell

hexaradical form **99- α** compared to the closed-shell radicalene form **99**. In addition, from a steric point of view, the hexaradical form **99- α** should be favourable due to less steric strain caused by repulsion of the six di-*tert*-butyl phenyl units. Nevertheless, after selective oxidative generation of **99- α** , a very slow transition to the thermodynamically preferred closed-shell state **99** occurs resulting in a half-life of the hexaradical of 156 min. Accordingly, an energy barrier of 990 meV (= 95.5 kJ mol⁻¹) at 298 K was determined for this valence and conformational isomerisation.

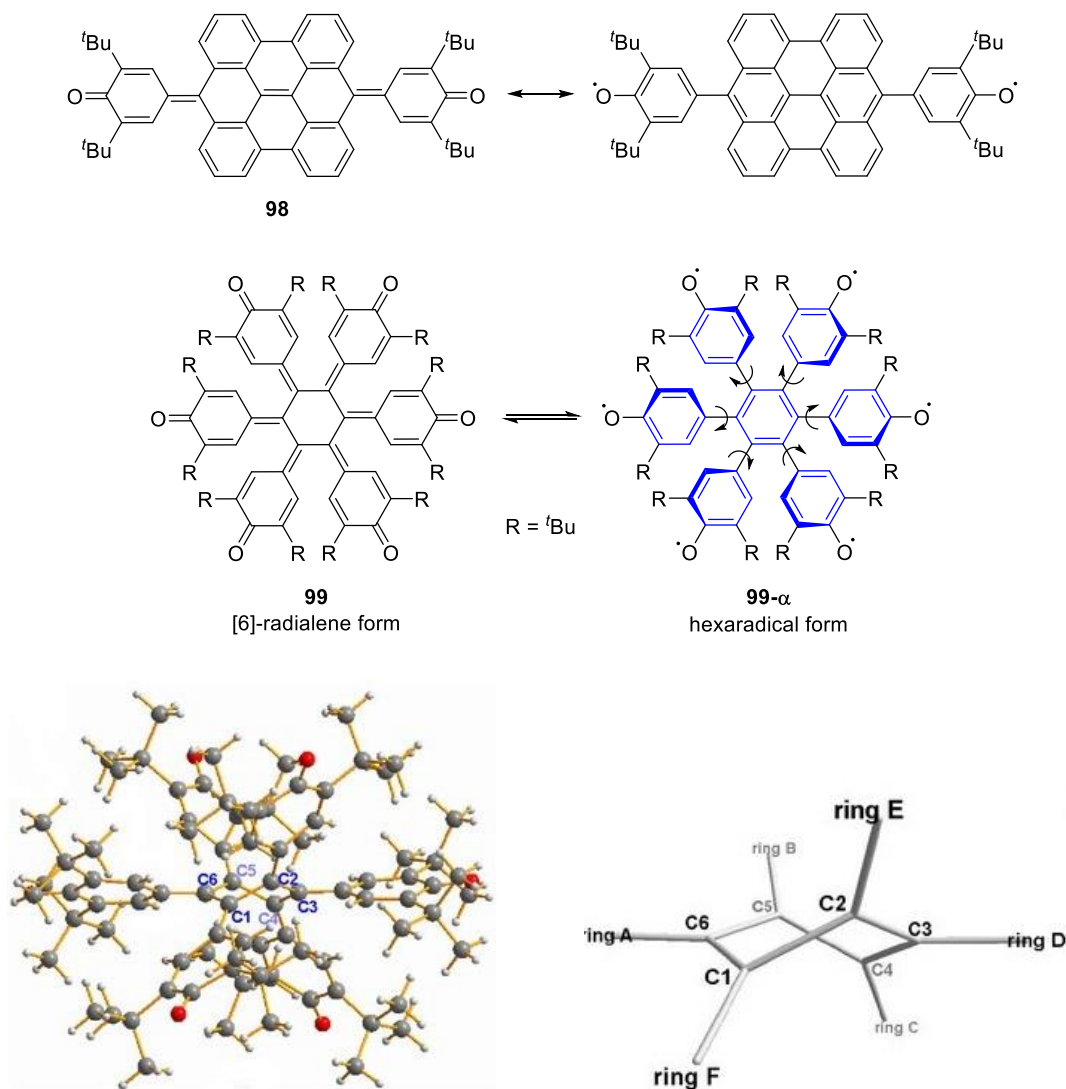


Figure 2.9 | Open- and closed-shell resonance structures of bisanthene **98**^[162] (top) and [6]-radialene **99** (middle)^[113] as well as X-ray crystallographic structure of **99** in side view (bottom, left) with a twisted-boat conformation (bottom, right) of the central six-membered ring. Reprinted with permission from ref. [113].

Single crystal X-ray analysis of **99** revealed a twisted boat conformation of the central six membered ring (Figure 2.9, bottom). This conformation leads to a highly symmetric displacement of the bulky *tert*-butyl phenyl units and thus to a release of steric strain. In addition, dispersion interactions between the twelve *tert*-butyl groups might further stabilise this closed-shell conformation.

2.2.2.4 π -Extended phenoxy biradicals and quinones

Based on bowl-shaped corannulene, in 2010 Morita and co-workers presented one of the first PAHs decorated with two phenoxy radical centres.^[163] The Kekulé type singlet biradical **101** can be represented by several open-shell resonance structures and was obtained by dehydration of the respective bisphenol **100** using lead (IV) oxide (Figure 2.10). Biradical **101** remained unchanged over several weeks at reduced temperature ($-30\text{ }^{\circ}\text{C}$) even under ambient conditions indicating a remarkably high stability. Due to the large π -surface, the spin density is significantly delocalized mainly over the top four rings (A, B, C and F, Figure 2.10, inset) of the corannulene moiety with highest densities located at the phenoxy moieties as revealed by quantum chemical calculations on the UB3LYP/6–31G(d,p) level of theory.

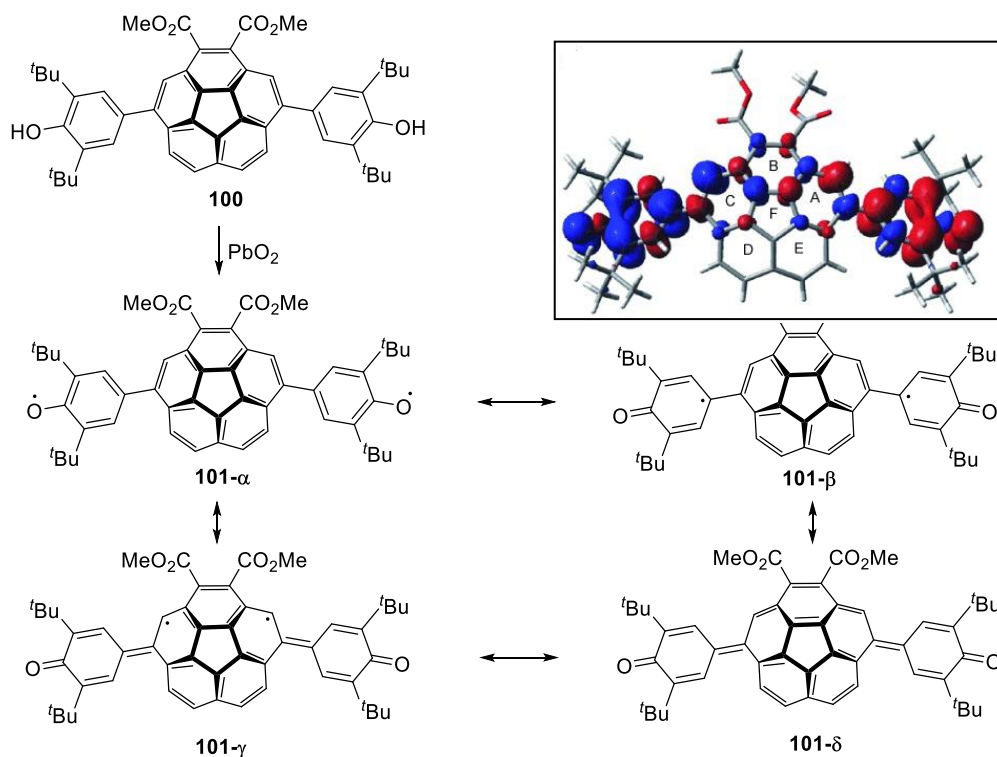


Figure 2.10 | Open- and closed-shell resonance structures of corannulene-based phenoxy biradical **101**^[163] as well as its synthesis by oxidation of bisphenol **100**.^[163] Inset: Calculated spin-density distributions of **101** in the singlet state on the UB3LYP/6–31G(d,p) level of theory. Red colour indicates positive and blue negative spin densities. Reproduced with permission from ref. [163]. Copyright 2010 John Wiley and Sons Inc.

Due to the exceptional stability of **101**, the authors were able to grow single crystals suitable for X-ray diffraction analysis, which revealed three crystallographically independent molecular structures of **101**, which only marginally differ from each other with respect to bond lengths and angles in a stack-like arrangement (Figure 2.11c). In this rare example, it was possible, to investigate the bonding situation and identify relevant mesomeric structures contributing most to the electronic ground state of **101**. In particular, bonds C10-C18 and C4-C13 between the corannulene and phenoxy subunits (Figure 2.11b) show an average length of 1.455 Å, which is only slightly shorter than the respective bonds in bisphenole **100** with 1.485 Å and thus indicates a dominating single bond character. In contrast, carbon oxygen bonds C1-O1 and C7-O2 have double-bond character and can be best described as C=O bonds. Based on this, the authors concluded that mainly mesomeric structure **101-β** but also **101-α** and **101-γ** (Figure 2.10) contribute to the ground state. Accordingly, based on X-ray structure analysis and quantum chemical calculations, a singlet biradical character of $y_0 = 0.80\text{--}0.85$ was determined for **101** along with a small ΔE_{ST} of 70 meV ($= 6.7 \text{ kJ mol}^{-1}$). The partial but only minor quinoidal contribution is reflected by the lower C9-C10-C18-C17 dihedral twist angles of 20–26° between the corannulene and phenoxy units compared to 37.7° in bisphenole **100**, whereas a more planar geometry would be expected for a closed-shell molecule (*vide infra*).

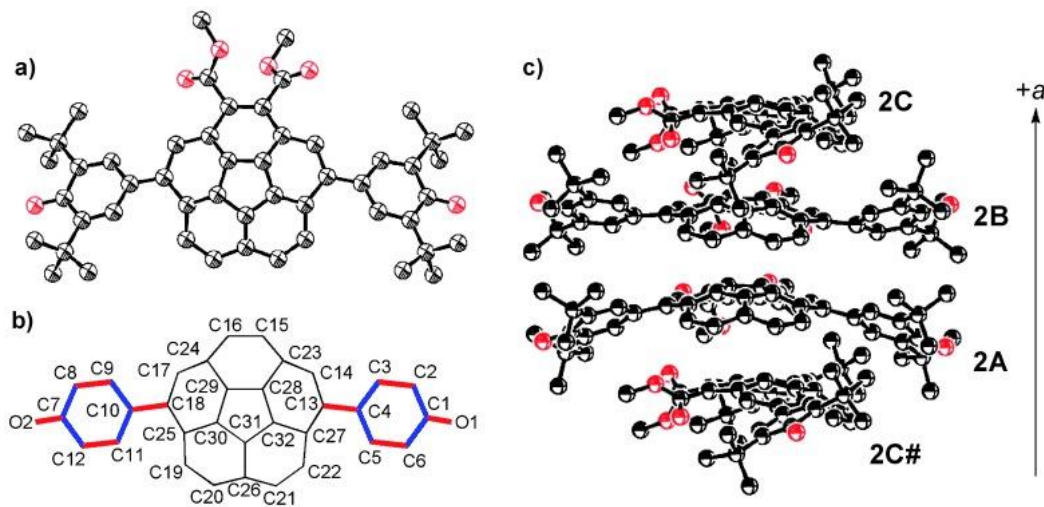


Figure 2.11 | Molecular structure (a) and packing (c) of biradical **101**^[163] obtained by single crystal X-ray analysis as well as carbon atom numbering (b). Red bonds are shorter and blue bonds are longer than the corresponding bonds in precursor **100**^[163] (Figure 2.7). Reprinted with permission from ref. [163]. Copyright 2010 John Wiley and Sons Inc.

Due to the two carboxylic acid ester functions, it is justified to classify corannulene biradical **101** as a slightly electron deficient system. As shown in the context of zethrene bisimides, the attachment of

acceptor substituents to π -systems increases spin delocalization and favours open-shell states. Accordingly, linker units between both phenoxy radical centres with electron deficient character should lead to both enhanced spin delocalization and protection from oxidative degradation. For this purpose, imide decorated pigment chromophores seemed to be promising candidates. Therefore, in 2015 the groups of Würthner and Kim presented the first perylene bisimide-based phenoxy biradical,^[23] a concept which was later taken over by Wu and Kim and applied to naphthalene bisimides as well.^[24] Perylene bisimide biradical **102** (Figure 2.12) was obtained by proton coupled oxidation of the respective bisphenol^[164] with lead (IV) oxide.^[23] Indeed, an analysis of the spin density distribution on the UCAM–B3LYP/6–31G(d) level of theory revealed widespread spin delocalization over both phenoxy subunits and the perylene core (Figure 2.12, right). In addition, a rather small singlet-triplet energy gap ΔE_{ST} of 41 meV ($= 4.0 \text{ kJ mol}^{-1}$) and a large biradical character of $y_0 = 0.72$ was determined. The authors further quantified the ambient stability of **102** in solution by kinetic analysis of time-dependent UV/vis/NIR absorption spectral data and obtained a minimum half-life of $\tau_{1/2} = 54 \text{ h}$. Due to the lack of a standardized stability test and detailed information in the Morita paper^[163], any comparison between the stability of **102** and **101** has to be treated with caution. Nevertheless, it is reasonable to assume that PBI biradical **102** exhibits lower stability in solution than the respective derivative **101** (Figure 2.10) as isolation out of solution was successful in the case of corannulene but not for the perylene bisimide biradical. A plausible explanation for this might be an increased reactivity of the phenoxy radical units caused by the highly electron poor PBI core compared to **101**. Despite the similar π -surface size of perylene and corannulene, it can be concluded, that electron deficient systems like **102** are beneficial in regard of significant spin delocalization. However, this electron deficient character increases the radical's sensitivity leading to overall lower stability compared to moderately e^- -poor systems like **101**.

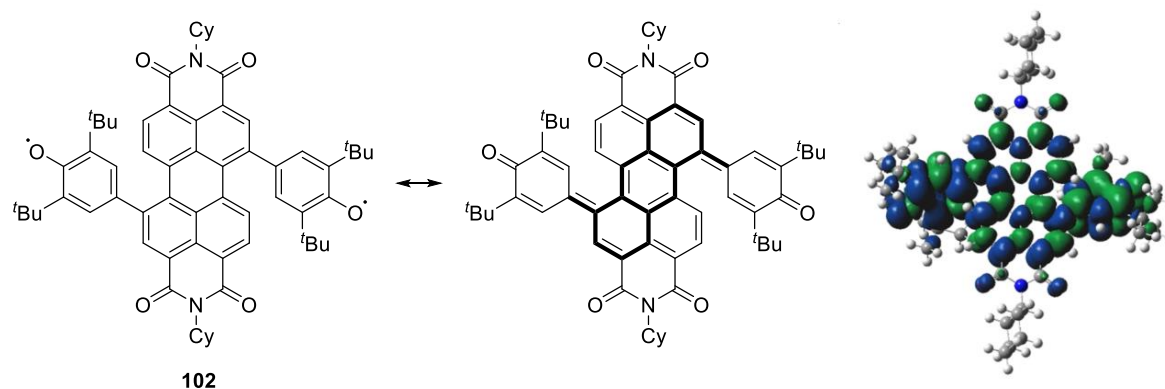


Figure 2.12 Open- and closed-shell resonance structures (left and middle) as well as calculated spin density distribution on the UCAM–B3LYP/6–31G(d) level of theory (right) of perylene bisimide-based biradical **102**.^[23] Blue and green surface colours represent positive and negative spin densities, respectively. Reprinted with permission of ref. [23]. Copyright 2015 John Wiley and Sons Inc.

Kim and co-workers together with the group of Wu investigated an analogous naphthalene bisimide derivative **103** (Figure 2.13)^[24] with a bisected π -surface compared to PBI biradical **102**. The authors calculated for **103** a similar y_0 of 0.69 but an almost doubled singlet-triplet energy gap ΔE_{ST} of 82 meV ($= 7.9 \text{ kJ mol}^{-1}$) and absorption spectral analysis revealed a reduced half-life of $\tau_{1/2} = 10 \text{ h}$. On first glance – despite the reduced size of the conjugated system in the NBI compared to PBI – the overall molecular structure and in particular, the acceptor substitution appears equal in both bisimides **102** and **103**. However, upon a detailed look on the substitution pattern, remarkable differences become apparent: NBI **103** comprises a 2,6-substitution pattern i. e. a “diagonal” arrangement of substituents. As pointed out above, the “diagonal” substitution of the naphthalene core is more stable and characterized by a lower biradical contribution than the respective “orthogonal” 1,5-substituted isomer (*vide supra*). In contrast, PBI biradical **102** shows an “orthogonal” substitution of the incorporated anthracene core. Although a direct comparison of the naphtho- and anthracene core is challenging and was not investigated experimentally so far, a 1,5-anthracene substitution pattern is known to feature a pronounced biradical character.^[165] Thus, based on the substitution pattern, one would expect rather a reduction of stability in the case of “orthogonally” substituted PBI **102** compared to diagonal NBI **103**. The fact that **103** is more stable than the respective NBI derivative thus can be explained by the larger π -surface, highlighting the importance of an electron deficient, but large conjugated π -core for effective spin delocalisation and thus stabilisation.

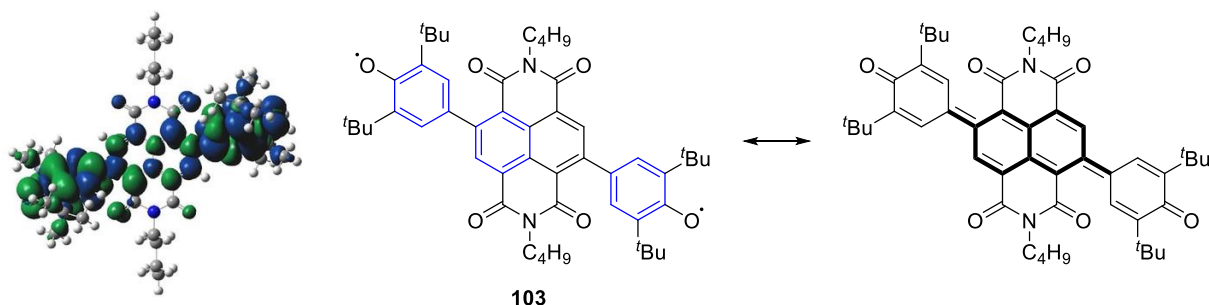


Figure 2.13 | Calculated spin density distribution (left) as well as open- and closed-shell resonance structures (middle and right) of biradical **103** calculated on the UB3LYP/6-31G(d,p) level of theory.^[24] Green and blue surface colours indicate positive and negative spin densities, respectively. Reprinted with permission from ref. [24]. Copyright 2017 John Wiley and Sons Inc.

Despite the rather small size of the naphthalene core, the aromatic stabilisation gained from three additional Clar sextets in the open-shell state is large enough to make NBI **103** a singlet biradical. Further reducing the number of benzenoid hexagons to the two phenoxy groups themselves frequently leads to

closed-shell compounds like several heteroquinones (*vide infra*). Nevertheless, by exploiting specific polarity and geometry phenomena, even the ground state of “small” quinoidal systems can be tuned towards open-shell biradicals. In this regard, based on a the rather rigid and planar boron dipyrromethene (BODIPY) scaffold, Wu and co-workers presented a twofold phenoxyl decorated quinoidal system **104**, which shows different ground states depending on the solvent polarity (Figure 2.14).^[166]

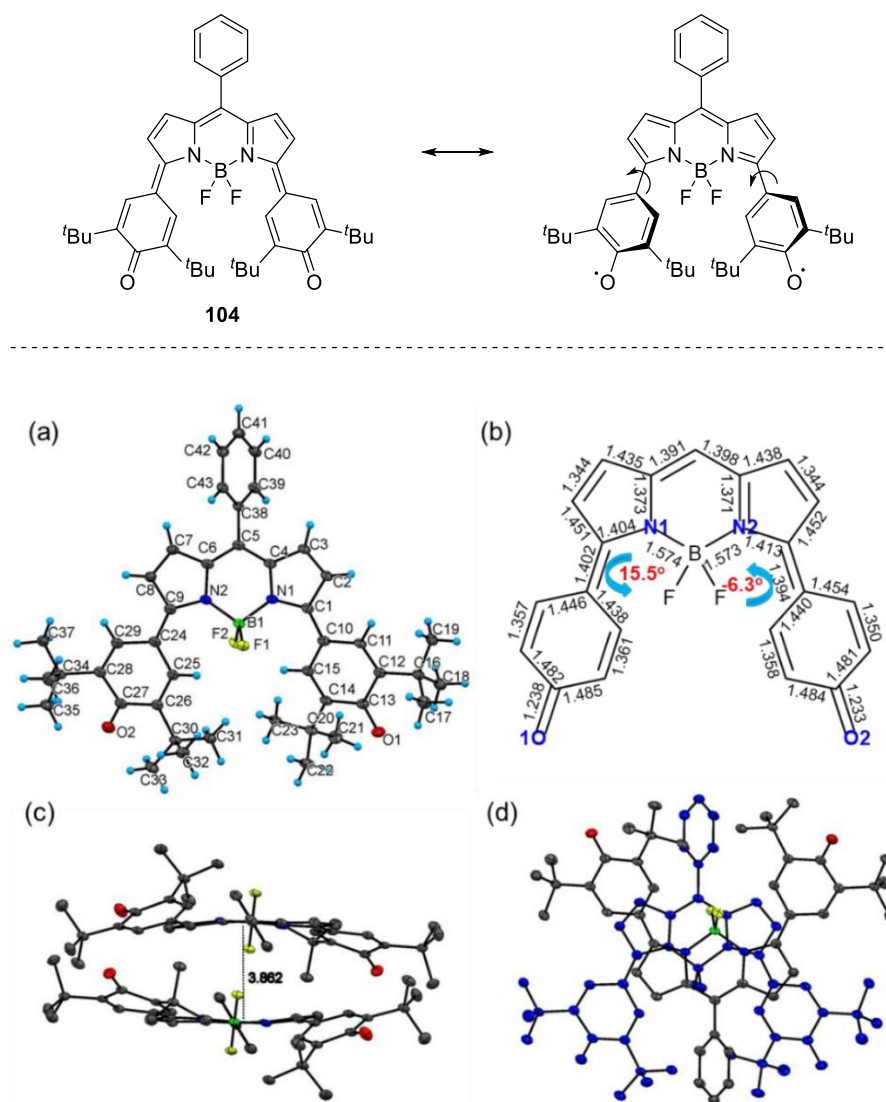


Figure 2.14 | Open- and closed-shell resonance structures of BODIPY bridged phenoxyl biradical(oid) **104**^[166] (top, arrows indicate rotational freedom) as well as X-ray crystallographic structure (a), selected bond lengths and dihedral angles (b) and top view (c) as well as side view (d) of the dimeric packing structure of **104** (bottom, hydrogen atoms are omitted for clarity). Reprinted from (open access) ref. [166].

In apolar benzene, sharp signals can be detected in the aromatic region of the ^1H NMR spectrum of **104** and the solution is EPR silent. In contrast, a DMF solution of **104** shows a pronounced EPR signal and aromatic resonance signals in the respective proton NMR are significantly broadened. Additionally, further VT-NMR and EPR experiments support the assumption of a dominating closed-shell quinoidal ground state in apolar solvents, but revealed large open-shell contributions in more polar environments. The authors rationalized this “solvato-magnetism” by the presence of a large dipole moment of 9.9 Debye in **104**, leading to dimer-like structures with a cancelled dipole moment as evidenced in the solid state by X-ray analysis (Figure 2.14c and d). Accordingly, only polar solvents like DMF are capable of stabilizing the “monomeric” structure. Notably, the quinoidal valence isomer of **104** is not completely planar, but small dihedral twist angles of 6.3-15.5° between the phenoxy unit and the BODIPY bridge (C25-C24-C9-N2 and C15-C10-C1-N1, Figure 2.14a and b) were observed in the dimer structure due to steric demand. In addition, quantum chemical calculations on the UCAM–B3LYP/6–31G(d,p) level of theory revealed a strong dependence of the biradical character in **104** of the phenoxy plane orientation: Upon increasing the dihedral angle from 17.6 to 77.6°, the biradical character rises from $y_0 = 0.27$ to $y_0 = 0.84$, respectively. Hence, the group of Wu successfully utilised the interplay of solvent polarity and geometry adjustment and thus obtained a solvato-magnetic switch.

2.2.2.5 Non-Kekulé phenoxyl diradicals

So far, mainly Kekulé type biradicals were presented, which are commonly much more stable than the respective non-Kekulé-type biradicals and thus represent the majority of current biradical research. Nevertheless, several phenoxyl biradicals have been investigated as well, which cannot be represented by a closed-shell resonance structure. Seminal examples of this class are the Yang biradical **105**,^[167] bisgalvinoxyl **106**^[168] and *para*-phenylene bridged bisgalvinoxyl **107** (Chart 2.11).^[169] In accordance with Ovchinnikov's parity model,^[102, 170] compound **105** is a triplet ground state diradical, which even resists recrystallization from boiling benzene.

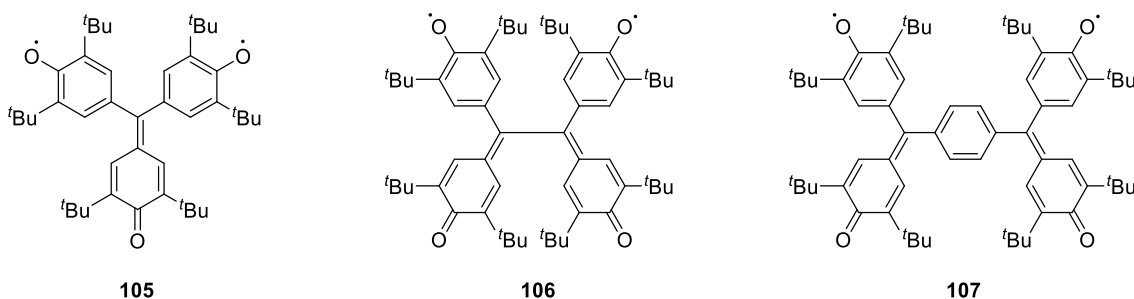
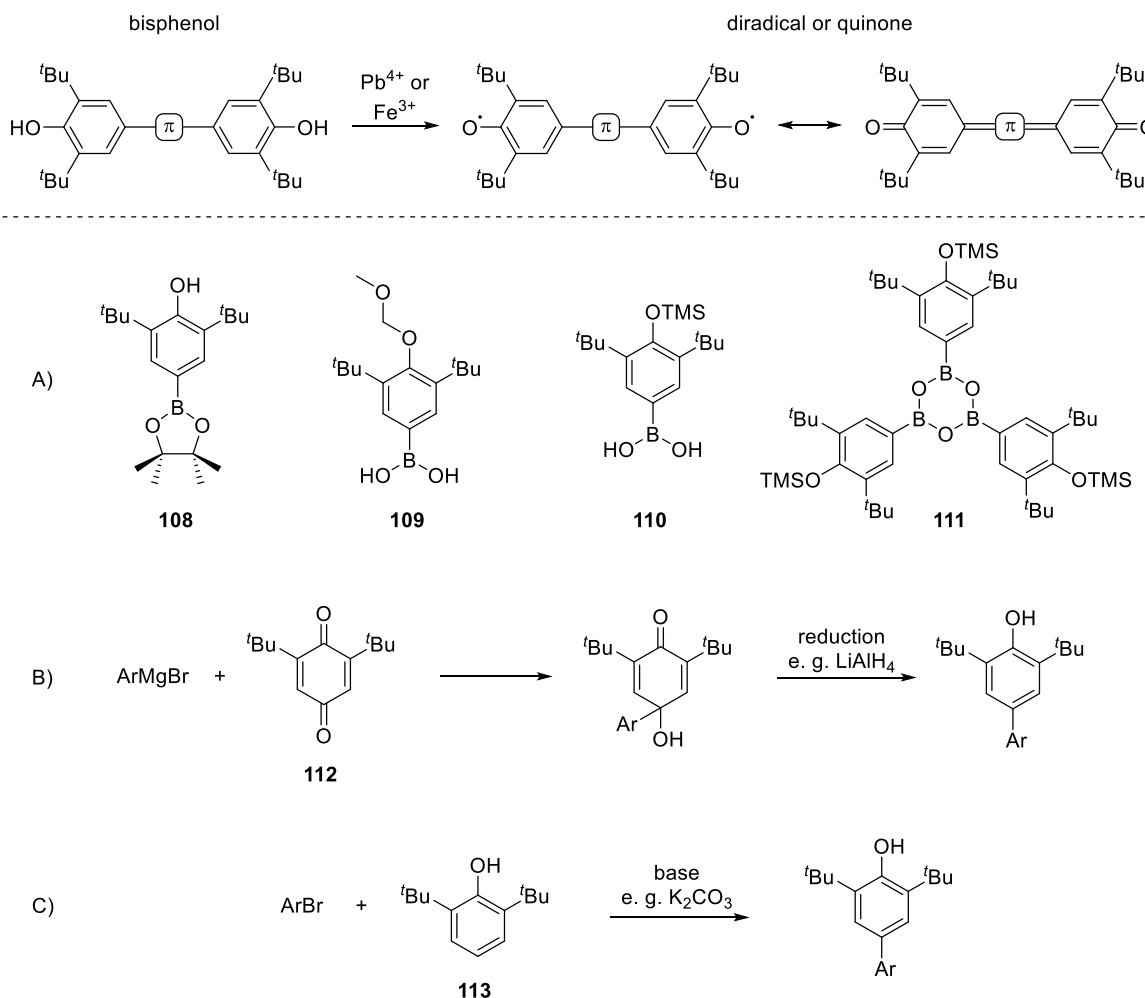


Chart 2.11 | Structures of stable galvinoxyl-based non-Kekulé-type diradicals **105**,^[167] **106**^[168] and **107**.^[169]

Furthermore, polyradicals^[171] and spin decorated porphyrins^[172] have been synthesized based on the galvinoxyl structural motif and exhibit good stabilities. However, as these are only of minor importance in current diradical research, no further details will be provided in this overview.

2.2.2.6 Synthesis and optical properties of phenoxy diradicals

In this part, the synthesis and optical properties of known phenoxy-based diradicals will be briefly discussed. In general, phenoxy diradical(oid)s can be obtained in high yield by oxidation of the respective bisphenols using lead (IV) or iron (III) compounds like PbO_2 , $\text{Pb}(\text{OAc})_4$ or $\text{K}_3[\text{Fe}(\text{CN})_6]/\text{KOH}$ (Scheme 2.8, top).^[23, 24, 159, 173]

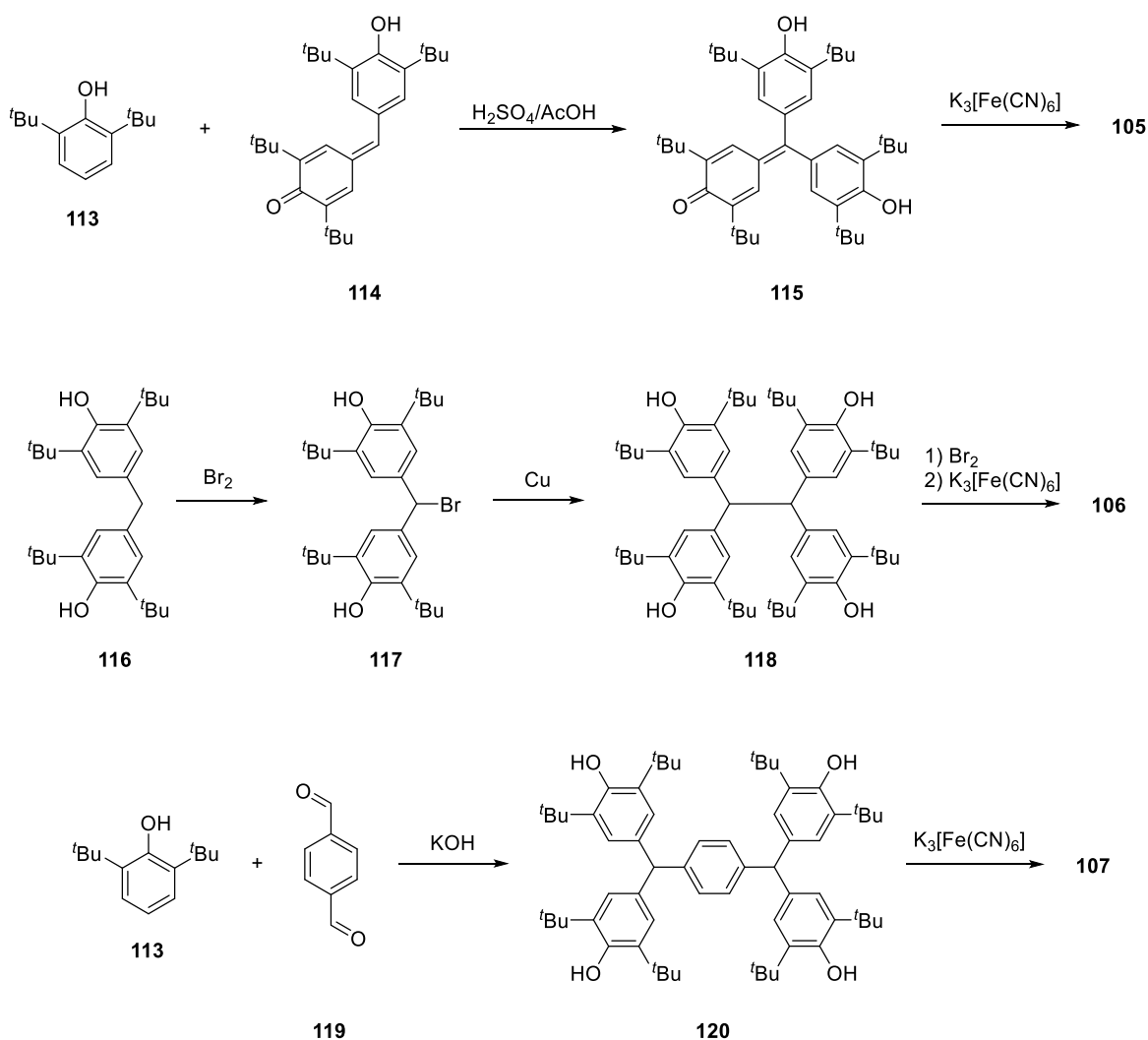


Scheme 2.8 | Generation of diradicals and quinones by dehydrogenation of bisphenols with high-valent metal ions (top) and synthetic strategies towards these π -extended bisphenols by using boronic acid derivatives **108–111** (A), *via* addition of Grignard reagents to quinone **112** (B)^[174, 175] or direct C-H -arylation of phenol **113** (C).^[164, 176]

The respective bisphenols can be synthesised *via* transition metal catalysed cross coupling reactions of arylhalides with the corresponding boronic acids, esters or anhydrides of 4-boron substituted 2,6-di-*tert*-butyl phenols and *O*-protected derivatives **108–111** (A, Scheme 2.8).^[24, 159, 163, 166, 177] Alternatively, the addition of metal organic compounds like Grignard reagents to quinone **112** with subsequent reduction

with LiAlH_4 was used in order to introduce the 2,6-di-*tert*-butyl phenol substituent (B, Scheme 2.8).^[174, 175] Furthermore, in the case of a 1,7-dibromo substituted PBI and several other aryl halides, a direct CH -arylation of phenol **113** was achieved under basic conditions (C, Scheme 2.8).^[164, 176]

Galvinoxyl-based (bi)radicals are commonly obtained *via* condensation reactions or reductive dimerisation and subsequent oxidation of the respective bis- and tetrakisphenols. Accordingly, the Yang diradical **105** (Chart 2.11) was first obtained by condensation of phenol **113** and methide **114** yielding bisphenol **115**, which was further oxidized with ferricyanide leading to diradical **105** (Scheme 2.9, top).^[167]



Scheme 2.9 | Synthetic strategies towards galvinoxyl diradical precursors **115**,^[167] **118**^[168] and **120**^[178] *via* condensation or reductive homo coupling reactions. Subsequent oxidation of **115**, **118** and **120** with ferricyanide yields biradicals **105**,^[167] **106**^[168] and **107**, respectively.^[169, 178]

Analogously, tetrakisphenols **118** and **120** were obtained by bromination of **116** and subsequent Ullmann homocoupling of **117** or by condensation of phenol **113** and terephthalaldehyde **119**, respectively (Scheme 2.9, middle and bottom).^[167–169, 178]

Spectral signatures of phenoxy biradicals and quinones

The attachment of phenol-substituents and the oxidation to the respective phenoxy radicals provides a simple possibility of spin functionalising small-sized π -systems or PAHs. In addition to the large changes regarding the magnetic properties, colour changes and complete transformations of absorption spectral profiles are observed frequently upon phenoxy decoration. The following section is intended to provide an overview about the optical properties of biradicals and quinones – in particular in comparison to the respective bisphenols.

Upon oxidation of bisphenol **100** (Figure 2.15, red line) to biradical **101**, a rise of an additional absorption band at 652 nm can be detected (Figure 2.15, green line).^[163] Notably, this new absorption band of **101** shows a weak vibrational pattern and is significantly bathochromically shifted by more than 200 nm ($\Delta\tilde{\nu}_{\text{abs}} \approx 6900 \text{ cm}^{-1}$) with respect to the absorption edge of **100**. Notably, the authors did not discuss optical properties in their original work; however a broad absorption band in the lower wavelength region is a common feature of π -extended phenoxy biradicals and quinones.^[177]

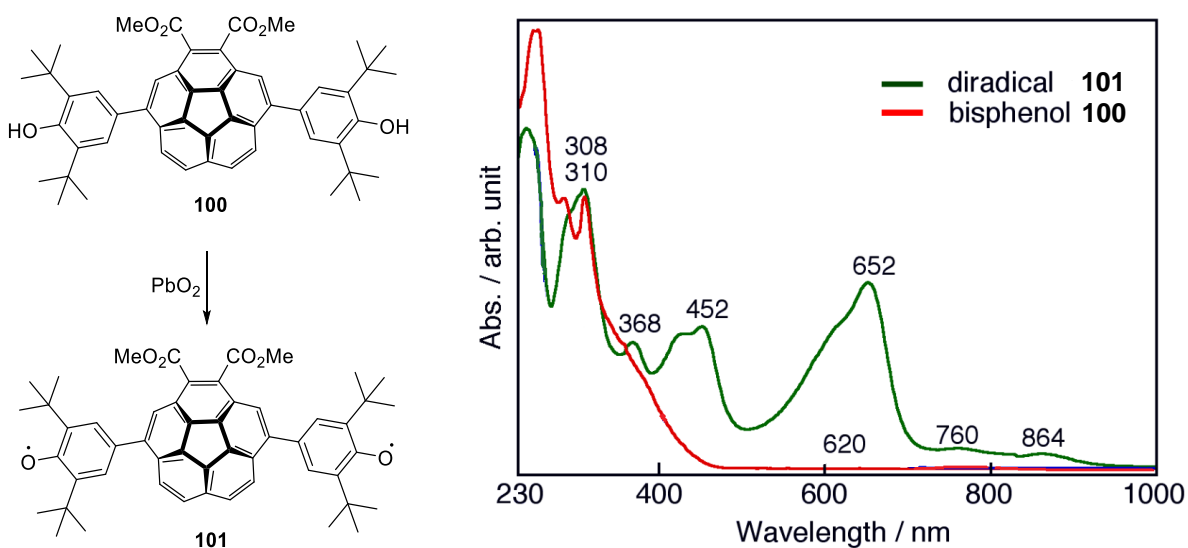


Figure 2.15 | Synthesis of corannulene biradical **101** by oxidation of bisphenol **100** (left) and UV/vis/NIR absorption spectra (right) of **100** (red line) as well as biradical **101** (green line) in CH_2Cl_2 .^[163] In addition, selected wavelengths are given in the graph. Adapted with permission from ref. [163]. Copyright 2010 John Wiley and Sons Inc.

Similar effects were observed upon oxidation of PBI linked bisphenol **121** under formation of biradical **102** (Figure 2.16, top) and upon generation of NBI biradical **103** via oxidation of bisphenol **122** (Figure 2.16, middle).^[23, 24] A sharp absorption maximum can be detected for **102** at 783 nm and for NBI **103** at 677 nm. Both maxima are significantly redshifted compared to the respective bisphenols by 4500 cm^{-1} and 5600 cm^{-1} , respectively.

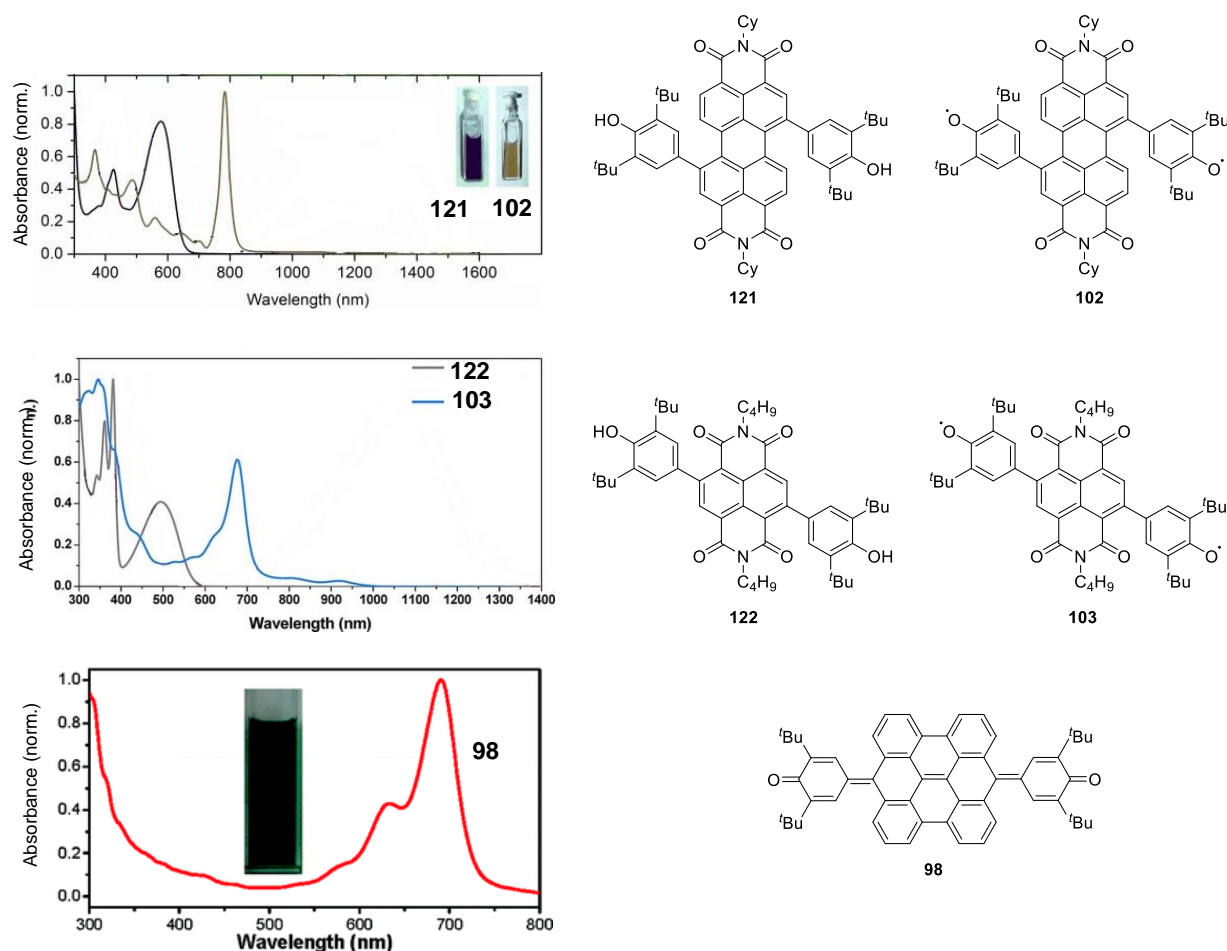
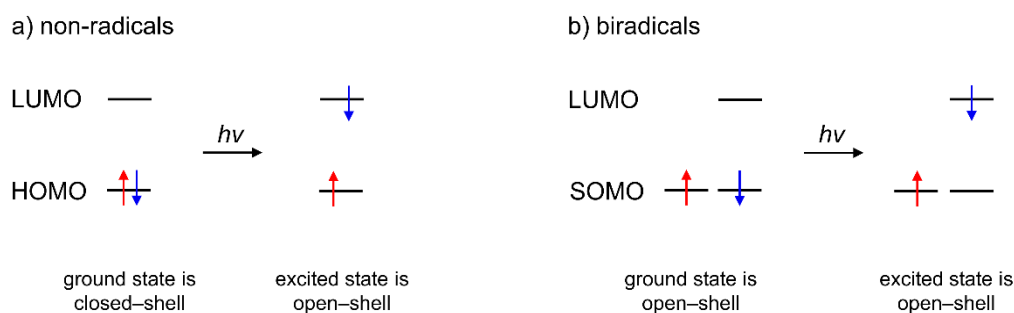


Figure 2.16 | UV/vis/NIR absorption spectra of PBI bisphenol **121**^[23] (top, violet line, in toluene) and biradical **102**^[23] (top, beige line, in toluene), of NBI bisphenol **122**^[24] (middle, grey line, in CH_2Cl_2) and biradical **103**^[24] (middle, blue line, in CH_2Cl_2) and of bisanthene quinone **98** (bottom, in CH_2Cl_2). Adapted with permission from ref. [23] Copyright 2015 John Wiley and Sons Inc., ref. [24] Copyright 2017 John Wiley and Sons Inc. and ref. [162] Copyright 2009 American Chemical Society.

In biradicals, the lowest energy absorption band is frequently ascribed to a SOMO-LUMO transition (Scheme 2.10a).^[23, 173] However, in contrast to closed shell molecules, this lowest energy excitation is not accompanied by overcoming a (large) spin pairing energy, as the ground as well as the excited state are unpaired biradical states (Scheme 2.10b). In addition, the free electron spins of biradicals are

frequently delocalised over significant parts of the conjugated π -systems resulting in rather widespread SOMO profiles. Quantum chemical calculations for the PBI biradical **102** revealed that this holds true for the LUMOs as well.^[23] Therefore, it is reasonable to assume that the bonding situation and geometry in the ground as well as in the first excited state remains almost unchanged resulting in a rather vertical excitation. Consequently, the lowest energy absorption bands of biradicals appear quite sharp with a full width at half maximum (FWHM) of approx. 390 cm^{-1} PBI biradical **102**.^[23]



Scheme 2.10 | Schematic representation of the excitation process upon light absorption in non-radicals (a) and in biradicals (b).

However, sharp absorption bands with slightly more pronounced vibrational progression are frequently observed for mainly closed-shell quinones like bisanthene **98** as well (Figure 2.16, bottom).^[159, 162] A potential explanation for this might be the still reduced spin pairing energy in this systems compared to completely diamagnetic ground state compounds. Apparently, the difference in absorption spectral properties between closed shell quinones and open shell biradicals is rather small; in particular compared to the tremendous spectral changes observed upon the transition from bisphenols to biradicals/quinones (*vide supra*). The large bathochromic shifts up to 7000 cm^{-1} can be rationalised by increasing conjugation and thus rigidification in the dehydrogenated state.^[162, 163] In summary, phenoxy biradicals and quinones feature rather sharp, intense absorption bands with varying degrees of vibrational progression. These bands are red shifted compared to the respective bisphenols by an average of 200 nm.

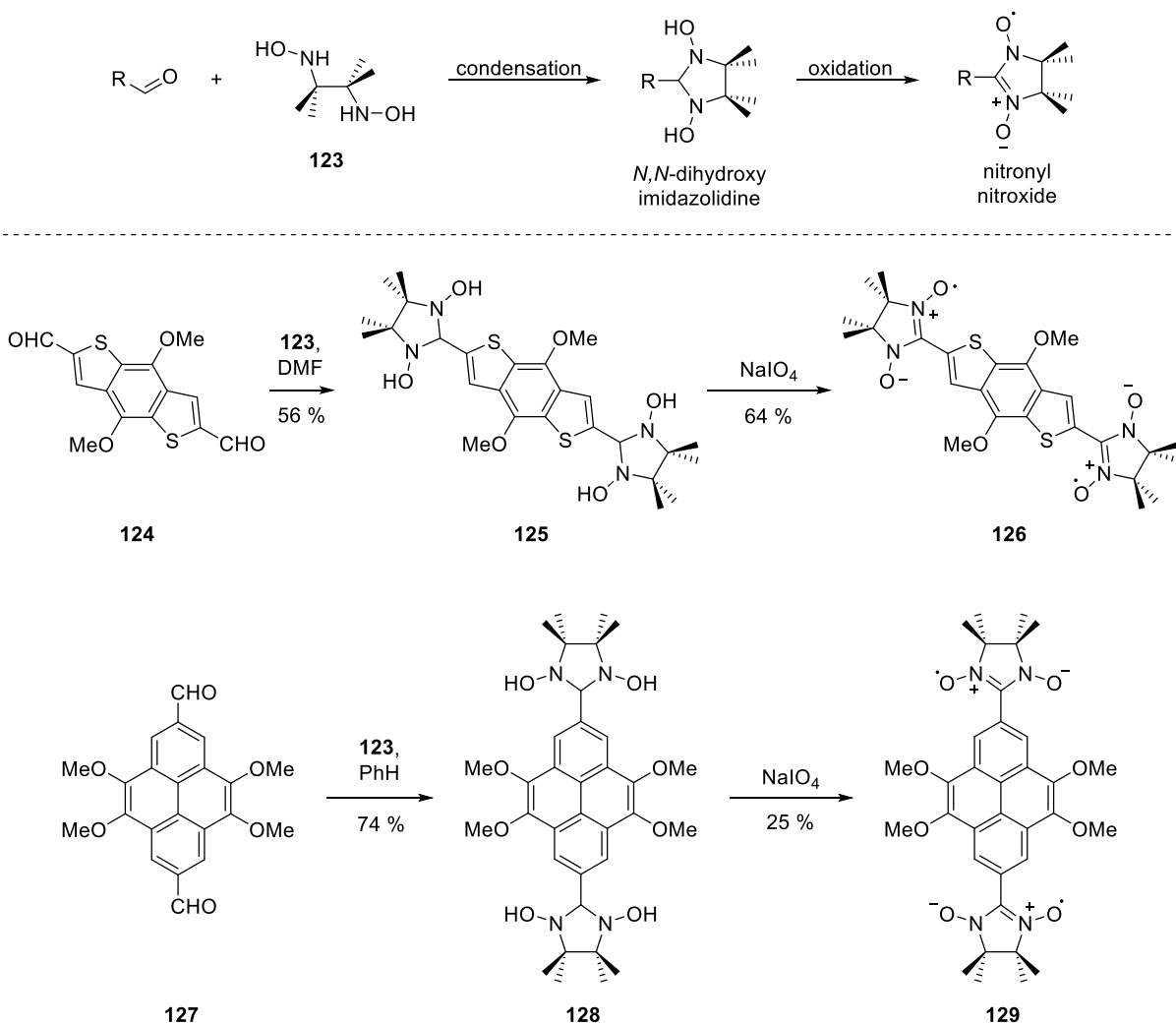
2.2.3 Nitronyl nitroxide (bi)radicals – synthesis and properties

Decoration of π -scaffolds with phenoxyl radicals is a convenient approach in order to achieve spin functionalization, but leads to a significant decrease of stability.^[24, 41] In order to retain magnetic properties and increase kinetic stability, more stable radical centres have been developed. In this regard, an outstanding representative is the class of nitronyl nitroxides (NN), which are stabilised by pronounced spin delocalisation over an O-N-C-N-O pentad. Nitronyl nitroxides are robust molecules withstanding ambient oxygen and moisture. However, the synthesis can be challenging, in particular in the case of electron deficient substrates. Therefore, in the following section, the current state of synthetic methods for nitronyl nitroxides will be presented.

2.2.3.1 Synthetic strategies towards nitronyl nitroxide radicals

One of the most common methods for the synthesis of NNs is a two-step process starting with condensation of a respective aldehyde with bishydroxylamine derivative **123** yielding the corresponding *N,N*-dihydroxy imidazolidines (Scheme 2.11, top). Subsequent oxidation of the *N,N*-dihydroxy imidazolidines finally leads to the nitronyl nitroxide radicals. Following this strategy, NN biradicals **126** and **129** containing a benzodithiophene^[179] and pyrene^[180] moiety have been synthesized from dialdehydes **124** and **127**, respectively (Scheme 2.11, bottom). A drawback of this method is the required previous synthesis of the respective aldehydes from the corresponding arylhalides before, resulting in an overall yield of only 13% from the respective pyrene diiodide to biradical **129**. In addition, the synthesis of bishydroxyl amine **123** by selective reduction of 2,3-dimethyl-2,3-dinitrobutane with zinc is less reliable due to a strong dependence of the yield from the individual metal batch and **123** is a highly unstable compound, which does not tolerate harsh reaction conditions.^[181, 182] Nevertheless, the “aldehyde condensation route” is still widely applied and several nitronyl nitroxide (poly)radicals have been successfully synthesised with this approach.^[183–186]

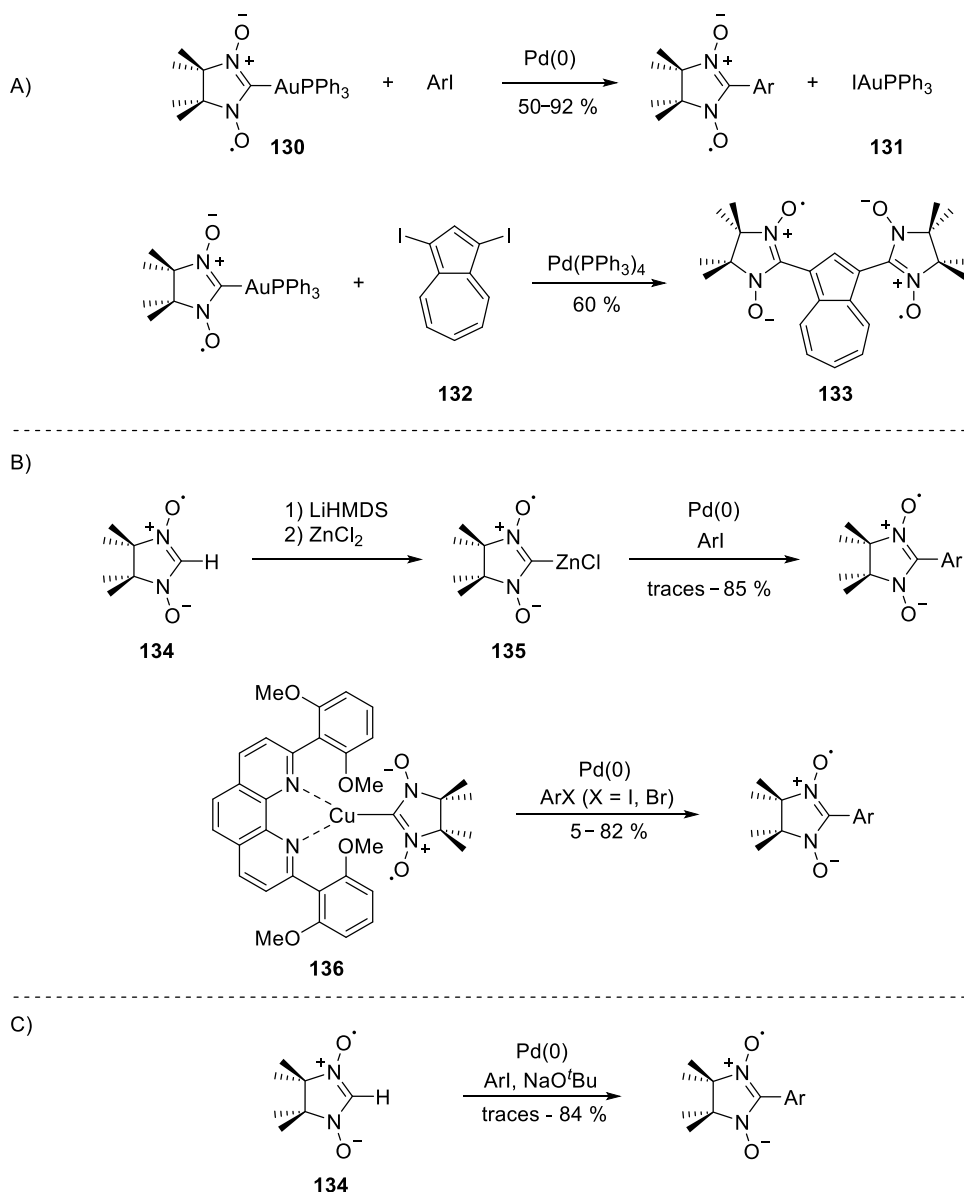
In particular, due to frequently occurring limitations regarding stability, accessibility and solubility of the respective aldehydes, alternative routes have been developed. A great advancement was achieved upon introduction of metal organic reagents and transition metal catalysed synthetic protocols, which target the direct attachment of the nitronyl nitroxide moiety to halide functionalised π -systems.^[187] In this regard, a phosphine stabilized gold-nitronyl nitroxide complex **130** was applied by Okada in 2014 and later utilized for the twofold spin functionalisation of diiodoazulene **132** (route A, Scheme 2.12).^[188]



Scheme 2.11 | General synthetic strategy towards nitronyl nitroxides *via* condensation of the respective aldehyde with bishydroxylamine **123** to afford N,N -dihydroxy imidazolidine, followed by subsequent oxidation to the nitronyl nitroxide (top). Also shown are applications of this procedure for the synthesis of biradicals **126**^[179] and **129**^[180] from dialdehydes **124**^[179] and **127**^[180] (middle and bottom), containing a benzodithiophene and pyrene bridge, respectively.

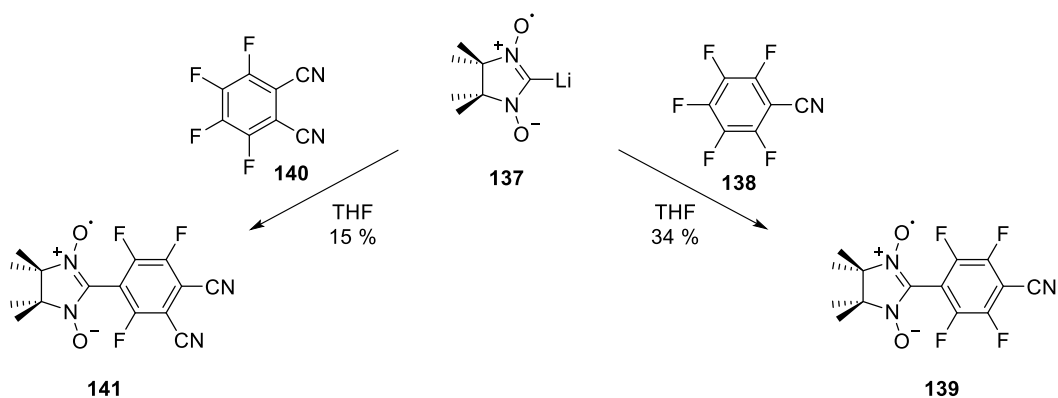
Despite the good yields of up to 92 %, ^[189] a huge drawback of this route is the stoichiometric use of a rather expensive gold complex **130**. To overcome this limitation, alternative approaches based on zinc reagent **135**^[190] and copper complex **136**^[191] have been developed (route B, Scheme 2.12). Both reactions tolerate a broad scope of substrates including acyl-, nitro- or alkoxy-substituted derivatives and are widely applicable on aryl, biphenyl or heterocyclic compounds. Notably, yields over 80% can be achieved with both reactions, which in addition do not show any dependence on specific substituent effects. However, highly active iodine compounds are necessary for sufficient conversion and only traces of product are formed upon using the respective bromo compounds.

Only recently, Naota and co-workers presented a coupling approach utilizing a “non-transition metal nucleophile” (route C, Scheme 2.12).^[192] As a key step, the C-H-acidic precursor **134** is *in situ* deprotonated with sodium *tert*-butoxide and subjected to a palladium(0) catalysed coupling reaction. The authors achieved high yields >80% for small nitro- and cyano-substituted compounds, but slightly lower ones of 60–64 % for unsubstituted naphthyl or triphenylene halides.^[192]



Scheme 2.12 | Synthesis of biradical **133**^[188] using gold reagent **130**^[188] (route A, top) and alternative approaches towards nitronyl nitroxides based on zinc or copper organic compounds **135**^[190] and **136**^[191] (route B, middle) as well as Naota’s “non-transition metal nucleophile” strategy of direct arylation of **134** (route C, bottom).^[192]

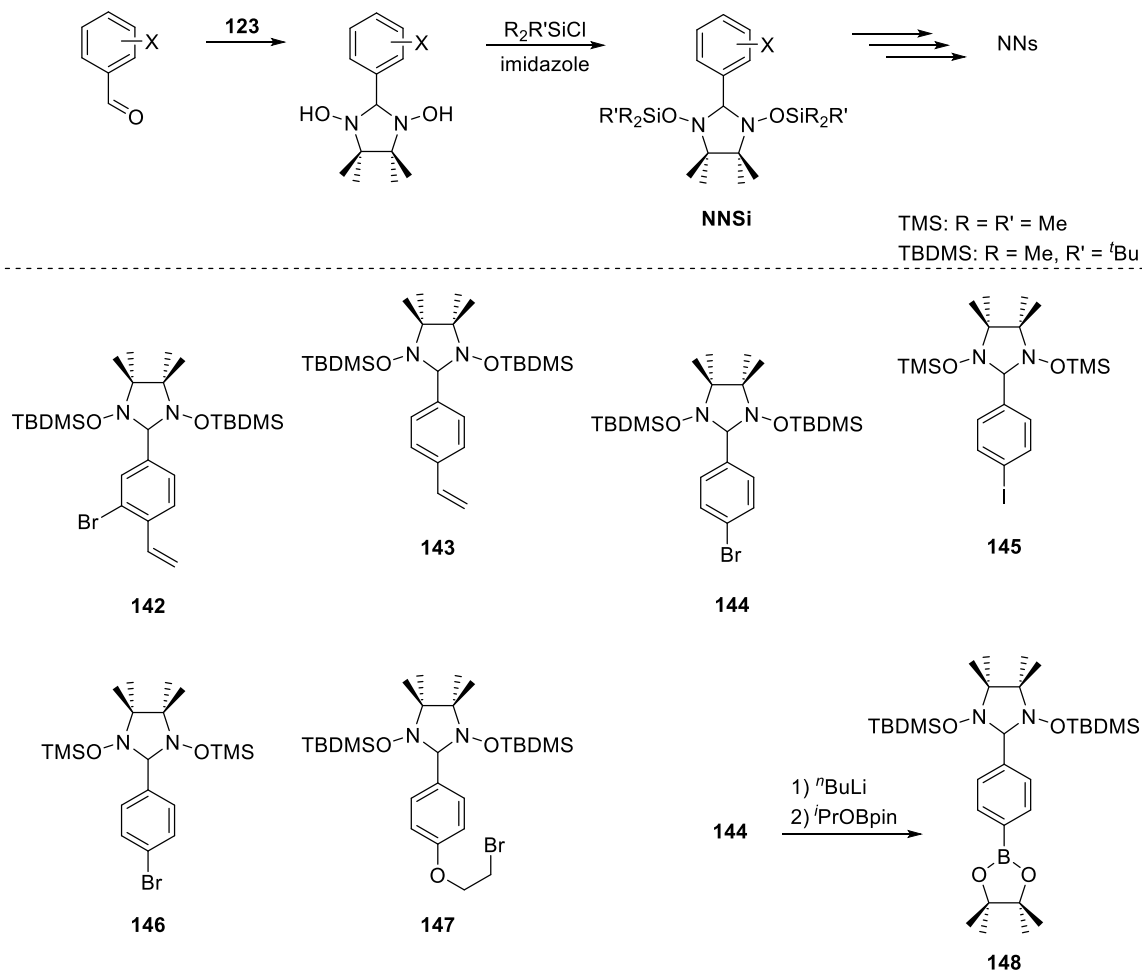
In case of highly activated and fluorine rich compounds like perfluorobenzonitrile **138** or perfluorophthalonitrile **140**, organo-lithium compound **137** can be used directly in NN-aryl-coupling reactions (Scheme 2.13), which follow a nucleophilic fluoride substitution mechanism without the need of additional transition metal catalysts.^[193, 194] However, this reaction investigated by Tretyakov and co-workers provides nitronyl nitroxide biradicals **139** and **141** with only 10–34% yield and is limited to the very specific type of perfluorinated substrates.



Scheme 2.13 | Synthesis of electron poor nitronyl nitroxides **139**^[194] and **141**^[193] by nucleophilic aromatic fluoride substitution of perfluorinated **138** and **140**, respectively.

All procedures for the synthesis of nitronyl nitroxides presented so far tackle the introduction of the radical moiety or the *N,N*-dihydroxy imidazolidine ring as a final step. A reason for this might be the sensitivity of nitronyl nitroxides and in particular of the respective *N,N*-dihydroxy imidazolidine precursors (Scheme 2.11, top) towards decomposition in the presence of strong acids or bases.^[190, 193] Therefore, reaction designs based on *O*-silyl protected *N,N*-dihydroxy imidazolidines (**NNSi**) were developed, which allow chemical modifications and synthetic steps after their introduction (Scheme 2.14, top). In this regard, styrene derivatives **142**^[195] and **143**^[196] (Scheme 2.14) were polymerised *via* a poly-Heck reaction and chain-growth polymerisation with AIBN as radical initiator in boiling benzene, respectively.^[195, 196] Furthermore, a whole sequence of reactions including highly basic reagents like NaO^tBu and BuLi was conducted with **144**^[197] after silyl protection and TMS protected **145** was subjected to Sonogashira coupling reactions showing the excellent stability of these silyl ethers.^[198] Further *O*-silylated NN precursors like **146** were used in Negishi-type cross coupling reactions^[199] or like **147** for the built-up of oligodesoxynucleotides (Scheme 2.14).^[200, 201] A further step towards a convenient and generalisable approach for the synthesis of nitronyl nitroxides was finally achieved by

Baumgarten and co-workers, who developed boronic acid ester **148** that is suitable for Suzuki-Miyaura coupling.^[202]



Scheme 2.14 | General synthetic procedure towards *O*-silyl protected nitronyl nitroxide precursors **NNSi** (top) as well as selected representatives **142–147**^[195–201] of this class. Also shown is the synthesis of boronic acid pinacol ester **148** *via* borylation of **144**.^[202]

2.2.3.2 Magnetic properties of nitronyl nitroxide (bi-)radicals

Nitronyl nitroxide radicals are known to feature remarkably high ambient and thermal stability. In this regard, Rajca and co-workers just recently presented a triplet ground state diradical with an onset of decomposition at ~ 160 °C under inert conditions.^[203] In addition, NNs are stable in various media including most organic solvents, but water as well.^[204] Many nitronyl nitroxide biradicals linked by (small) PAH cores do not show tremendous differences regarding their magnetic properties. For instance, they feature comparable g_{iso} values of 2.006–2.007, hyperfine splitting constants a_{N} around 3.7 G and intramolecular exchange interactions $|2J/g\mu_{\text{B}}|$ in the 10^5 G order of magnitude.^[179, 180, 188]

With a systematic phenylene-ethynylene-based elongation approach, the group of Matsuda demonstrated that the spin-spin exchange interaction strength in conjugated NN biradicals strongly depends on the distance of both radical centres.^[198] Starting with “four phenylene-three ethynylene” spaced NN diradical **149**, a nine-line EPR spectrum was recorded revealing strong intramolecular magnetic coupling of $|2J/g\mu_{\text{B}}| = 1800$ G i. e. $|J| \gg a_{\text{N}}$ (Figure 2.18). Upon elongation of the spacer, a continuous decrease of spin coupling strength was observed: 120 G in the case of five phenyl spaced **150**, 8.0 G for “six phenylene - five ethynylene” **151** and only 0.53 G for **152** bearing seven phenylene spacers. It is worth to mention that in the last case a five line hyperfine splitting pattern is dominating i. e. $|J| \approx a_{\text{N}}$, which is well known from non-conjugated NN biradicals or mono-radicals. Accordingly, the intramolecular spin-spin exchange interaction becomes almost negligible compared to the hyperfine splitting constant even in conjugated NN biradicals, when the distance between both radical centres is large enough.

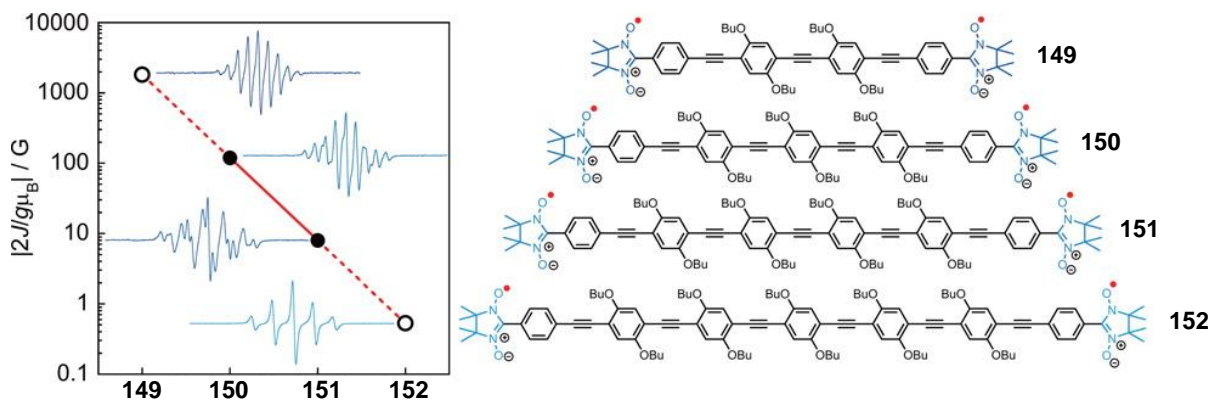


Figure 2.18 | Correlation of the exchange interaction with the number of phenylene ethynylene moieties (left) and respective biradical structural formula of **149–152** (right).^[198] Adapted with permission from ref. [198]. Copyright 2013 American Chemical Society.

A similar transformation of the hyperfine splitting pattern was obtained by Baumgarten and co-workers with non-conjugated hexaethylene glycol bridged NN biradical **153** revealing a temperature dependence of the spin coupling strength (Figure 2.19a).^[204] The authors identified two conformational states for **153**, i. e. a stretched state A at lower temperatures of 210 K with weakly to non-interacting terminal nitronyl nitroxide moieties ($|J| \approx a_N$) and a bent state B at 300 K, which is characterised by close proximity of both NN caps leading to pronounced through space intramolecular spin-spin exchange interactions and $|J| \gg a_N$ (Figure 2.19b). Both states can be distinguished by significantly different hyperfine splitting patterns in the respective EPR spectra (Figure 2.19c). If the electron spin only couples to two nitrogen atoms, five lines are observed in the EPR spectrum, as ^{14}N is a $S = 1$ core and the total number of lines follows the “ $2S + 1$ ” rule.^[204] Spin coupling to four ^{14}N nuclei – in contrast – results in the appearance of nine lines. Indeed, at 300 K, nine lines can be detected for **153** and thus “biradical behaviour” is dominating, whereas at 210 K only five lines occur in the respective EPR spectrum. This temperature effect was explained by increasing flexibility of the OEG chain.

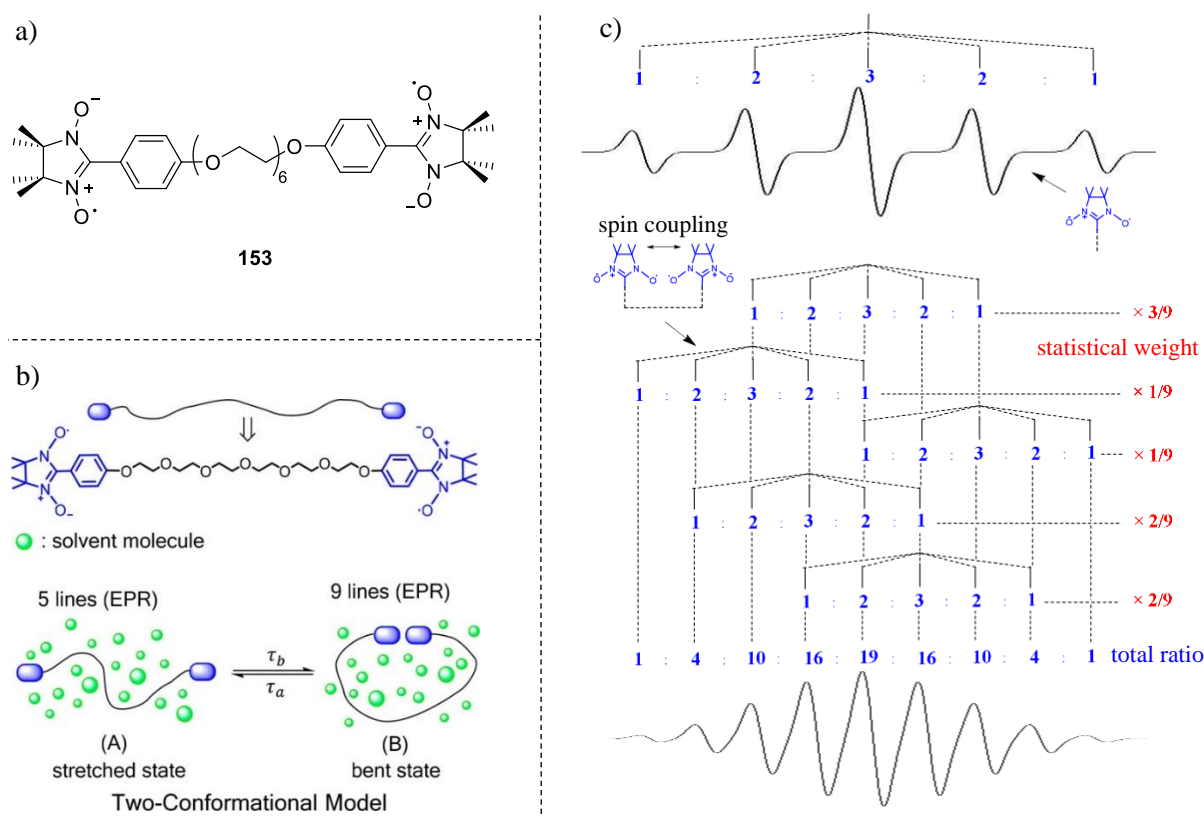


Figure 2.19 | Chemical structure of hexaethylene glycol linked NN biradical **153** (a), diagrammatic sketch of two-conformational model (b) and relative intensity ratio of EPR spectral lines of a nitronyl nitroxide diradical with strong spin exchange coupling (c).^[204] Adapted with permission from ref. [204]. Copyright 2018 American Chemical Society.

A gradual transition from nine to five lines was additionally illustrated by a simulation of EPR spectra with different proportions of spin coupling interactions (Figure 2.20).^[204] According to this simulation, decreasing the spin-spin exchange interaction from 100% to 0% will result in vanishing of the second, fourth, sixth and eighth EPR line. Conversely, a hyperfine splitting pattern containing nine lines is a proof of strong magnetic coupling revealing the presence of a diradical.

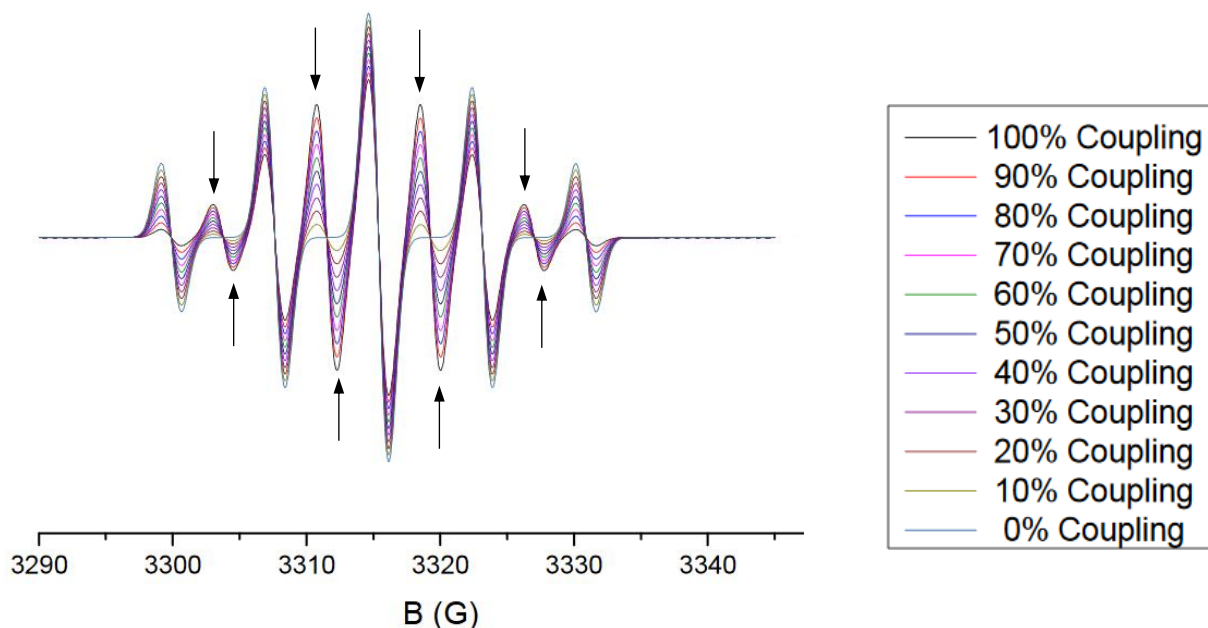


Figure 2.20 | Simulated EPR spectra of **153** in acetonitrile with different proportions of spin coupling interactions of diradicals from 0% to 100%.^[204] Arrows indicate vanishing EPR lines with decreasing spin coupling. Reprinted with permission from ref. [204]. Copyright 2018 American Chemical Society.

The group of Irie presented thiophene-spaced diaryl ethene (DAE)-based nitronyl nitroxide biradicals with no (**154**), two (**155**) or four (**156**) thiophene linkers, which are photoswitchable and enable the modulation of the magnetic coupling strength by changing the conjugation path (Figure 2.21).^[205, 206] In all three biradicals, spin-spin exchange interactions are much larger in the closed form compared to the open form due to more efficient conjugation. In this regard, for DAE **156** ($n = 2$) bearing four thiophene spacers, the most drastic switching effect was observed with a 150-fold increase in magnetic coupling. The authors further illustrated the different spin coupling intensities with highly diverging EPR spectra, as for the open form of **156** five lines can be detected (Figure 2.21, top, right), whereas **156** in the closed form is characterised by a nine line spectrum (Figure 2.21, bottom, right). Accordingly, in the open form spin coupling to two equivalent nitrogen nuclei is observed, whereas the closed form represents a

diradical with spin coupling to all four equivalent ^{14}N cores. Replacing the thiophene units in **156** by *para*-phenylene linkers results in photoswitchable DAE derivatives as well.^[207] However, as *para*-phenylene is a much weaker magnetic coupler than thiophene, only a 30-times increase in magnetic interaction can be measured upon “closing”.^[207]

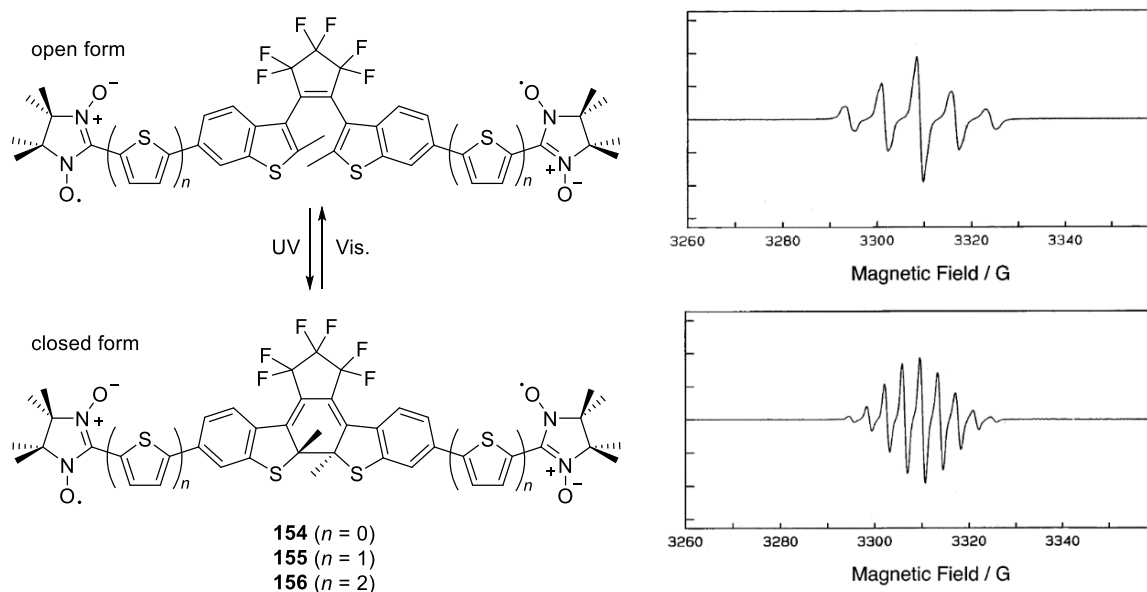


Figure 2.21 | Photoswitchable biradicals **154–156**^[205, 206] in open (top, left) and closed form (bottom, left) as well as the respective EPR spectra of open **156** (top, right) and closed **156** (bottom, right) in benzene solution at room temperature (9.32 GHz). Reprinted with permission from ref. [206]. Copyright 2013 American Chemical Society.

2.2.4 Further spin-bearing moieties

Apart from the so far described inherently open shell PAHs as well as phenoxy and nitronyl nitroxides, other radical centres are occasionally investigated in literature. In this context, verdazyl, imidazolyl, thiadiazolyl, iminonitroxide, nitroxide and TEMPO radicals (Chart 2.12, from left to right) have to be mentioned. They are of certain relevance, however their importance stands back behind phenoxy and nitronyl nitroxide radicals – in particular in the context of this thesis. Therefore, they will not be further discussed in detail.

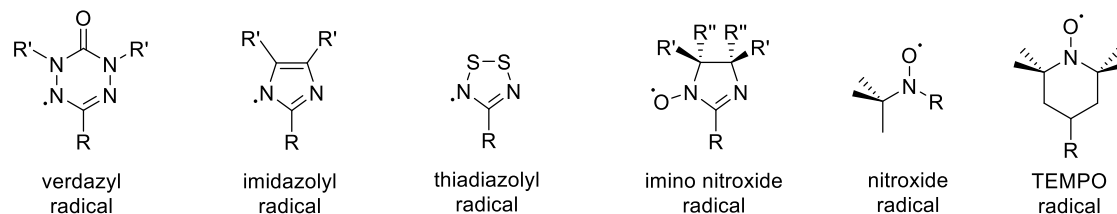


Chart 2.12 | Structures of further radical centres occasionally investigated in literature.

2.3 Methods for the analysis of (bi)radicals

Radicals are spin-bearing sites and therefore carry a magnetic momentum in addition to the negative electric charge of the electron. Therefore, they commonly exhibit paramagnetic properties, which can be explored in particular with magnetic spectroscopy. Whereas species with a total spin of zero are called diamagnetic and can be studied best by NMR spectroscopy, paramagnetic compounds feature pronounced EPR signals, but are NMR silent.^[2] The two methods are complementary but both allow to gain insight into the ground state spin configuration and spin orbital energetics. Hence, common NMR and EPR techniques for the investigation of (bi)radicals will be described in the following section. In addition, the stability of biradicals is commonly evaluated by time dependent UV/vis absorption spectroscopy, which will be also described in this section.

2.3.1 NMR spectroscopy

In the presence of doublet or triplet species, a distinct signal broadening is observed in the respective ¹H NMR spectra. In general, only resonance signals of atoms directly bearing the free electron should appear broadened.^[107] However, due to conjugation and thus spin delocalisation, signal broadening is frequently observed for all atoms, which are conjugated to the radical centre. This is *de facto* the case for all resonance signals appearing in the “aromatic region” of the respective proton NMR spectrum. In contrast, isolated (i. e. non-conjugated) NMR active nuclei, like the protons of alkyl chains show well detectable resonance signals.^[23]

As mentioned above, this broadening effect is only caused by paramagnetic species like doublets or triplets, but not by diamagnetic singlets. In biradicals, singlet and triplet states are not equal in energy, but commonly close enough that the energetic difference can be thermally overcome. Therefore, variation of temperature results in thermal depopulation or population of the ground and higher energetic states (Figure 2.22a, b). Accordingly, it is possible to determine the electronic character (i. e. singlet or triplet) of the ground state of a biradical and to qualitatively estimate the energetic difference between the singlet and triplet state (ΔE_{ST}).^[2] If the ground state of a biradical is a singlet state and ΔE_{ST} is rather small (e.g. in the same order of magnitude as $k_B T$), a thermal population of the triplet state is possible. Therefore, the amount of triplet increases with temperature and NMR signal intensity decreases (Figure 2.22a). Conversely, triplet ground state biradicals show an increasing NMR signal intensity upon raising the temperature (Figure 2.22b). For example, the aromatic ¹H NMR resonance signals of biradical **26** broaden and even vanish at elevated temperature of 150 °C (Figure 2.22c, d) revealing a singlet multiplicity of the ground state.^[32]

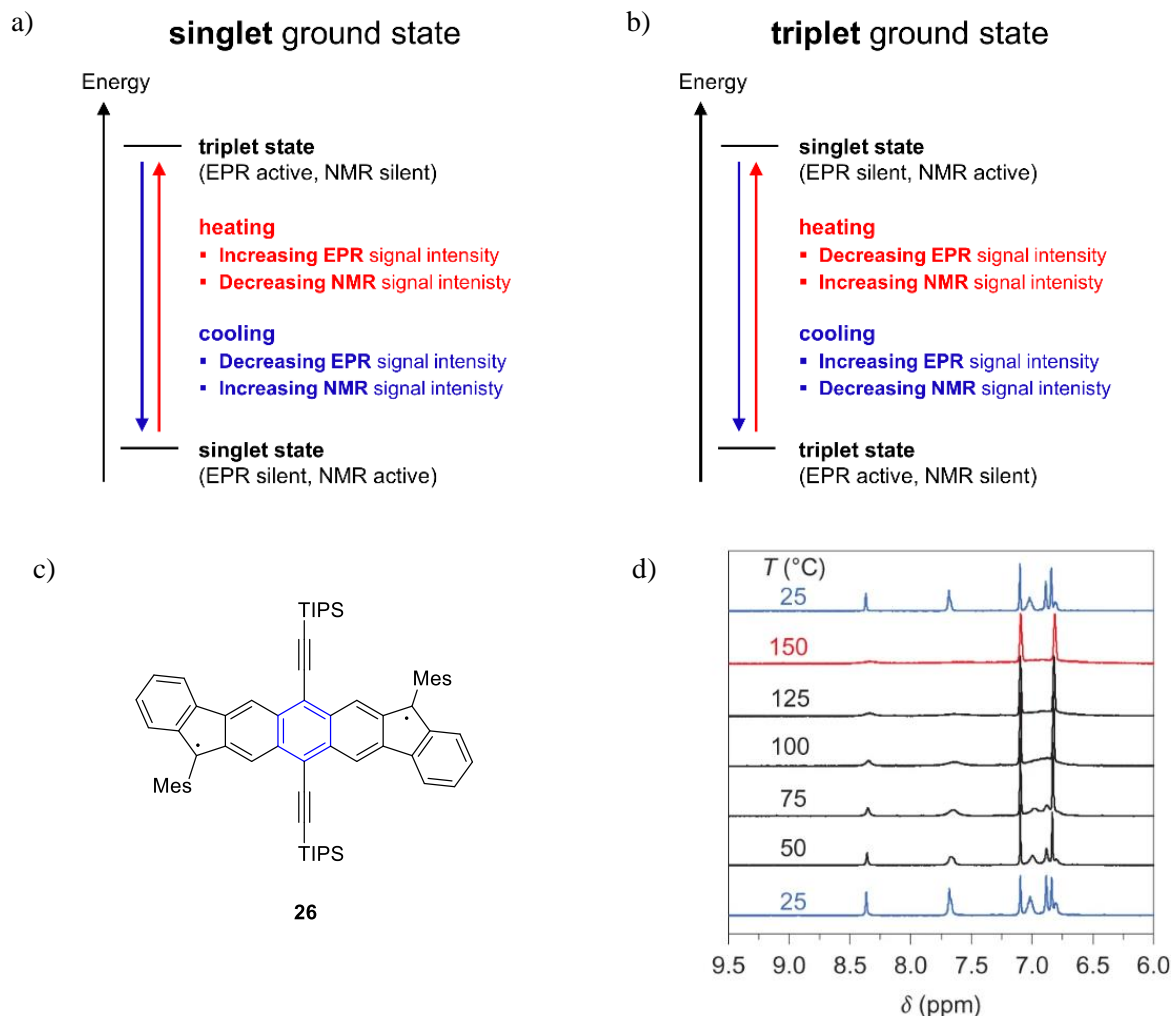


Figure 2.22 | Implications of singlet (a) or triplet ground states (b) of biradicals for temperature-dependent magnetic spectroscopic techniques VT-NMR and -EPR. Additionally shown is the structure (c) and the aromatic region of the ^1H NMR spectra of diindenofused anthracene biradical **26** at various temperatures (d).^[32] Adapted with permission from ref. [32]. Copyright 2016 Springer Nature.

The presence of paramagnetic compounds leads to a measurable shift of the solvent residual signal (e.g. of CHCl_3 in CDCl_3) compared to the pure solvent in the proton NMR spectra. Based on this paramagnetic shift, Evans developed a method for the determination of the magnetic susceptibility of a molecule.^[208–212] Despite the fact that this method works only precisely for monoradicals, the Evans method gained certain importance in the field of biradical investigations, as monoradicals often serve as reference compounds.^[23] For a sufficiently precise measurement of the paramagnetic shift, an internal reference signal is needed, which must not be in direct contact with the radical itself. This is achieved by addition of a sealed capillary containing pure solvent into the sample and measuring both (solution and solvent

capillary) in one NMR tube. Accordingly, two solvent residual signals can be detected and the paramagnetic shift can be calculated from the displacement of both resonance signals. Taking this shift, the exact molar concentration, the spectrometer frequency and solvent constants into account, the molar magnetic susceptibility and thus the average number of unpaired electrons in a molecule can be calculated. Further details, as well as a full derivation of all relevant equations is given in *Chapter 8.1*.

2.3.2 EPR spectroscopy

The electron spin in radicals can be oriented up ($S = +1/2$) or down ($S = -1/2$), resulting in two different spin orbitals, which usually are energetically degenerated, but show an energetic separation in the presence of an external magnetic field. This phenomenon is known as the Zeeman effect and causes the appearance of spin transitions detectable with EPR spectroscopy (Figure 2.23, left).^[2] Accordingly, paramagnetic species like radicals absorb microwave irradiation for which the resonance condition (1) has to be fulfilled:

$$\Delta E = h\nu = Bg_e\mu_B \quad (1)$$

With B as the magnetic flux, g_e as the Landé factor of the electron and μ_B as the Bohr magneton. For technical reasons, commonly the first derivative of the absorption is detected. Depending on the spin coupling between the radical and magneto active nuclei like ^1H or ^{14}N , a certain hyperfine splitting pattern is observed, as mentioned in the context of nitronyl nitroxide biradical properties.

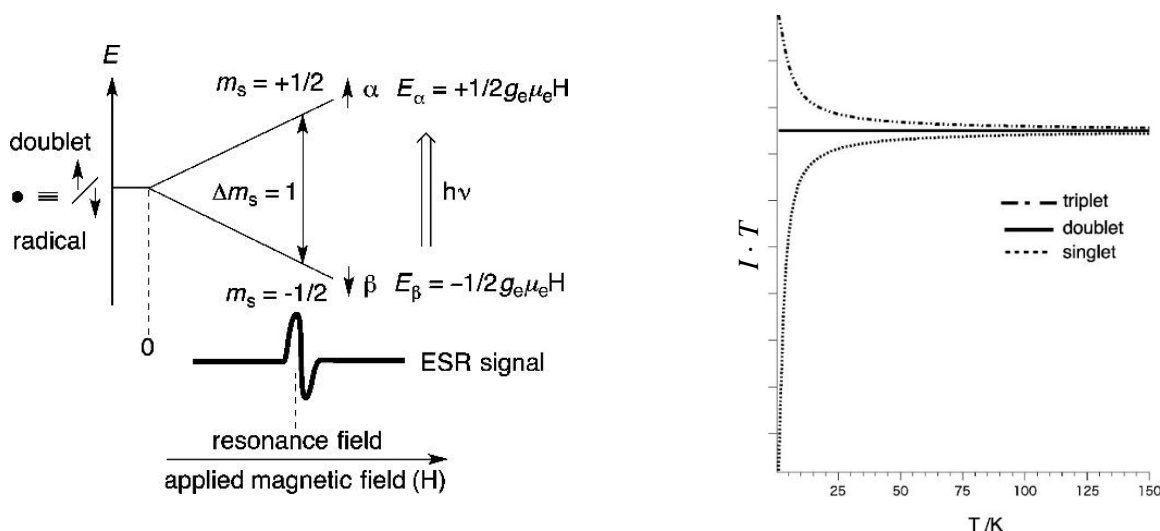


Figure 2.23 | Zeeman splitting of the spin orbitals of a radical in an external magnetic field and derived EPR signal (left) as well as typical temperature-dependent changes of EPR signal intensities ($I \cdot T$) for triplet- and singlet-ground-state diradicals (right). Adapted with permission from ref. [2]. Copyright 2013 American Chemical Society.

Monoradicals with a total spin of $S = \pm 1/2$ have a multiplicity of 2 and therefore are doublet states (Figure 2.23). In the respective EPR spectra, the product of signal intensity and absolute temperature $I \cdot T$ is constant for such doublets (Figure 2.23, right). In contrast, in diradicals, the total spin either equals zero in case of an antiparallel spin orientation resulting in a singlet state or the total spin is one resulting in a triplet state. Opposite to the trends observed in NMR spectroscopy, $I \cdot T$ decreases upon rising temperature in triplet biradicals and increases in singlet biradicals, as the EPR signal originates only from the triplet species (Figure 2.23, right). The changes of signal intensity times the absolute temperature $I \cdot T$ during variation of the measurement temperature can be utilised for a quantitative analysis of the energy difference between singlet and triplet state ($\Delta E_{ST} = 2J_{ab}$). The $I \cdot T$ vs. T curves can be fitted with the Bleaney-Bowers equation (2) where C is the Curie constant, J_{ab} the exchange integral and R the gas constant.^[213]

$$I * T = C \frac{3 \exp\left(\frac{2J_{ab}}{RT}\right)}{1 + 3 \exp\left(\frac{2J_{ab}}{RT}\right)} \quad (2)$$

2.3.3 Stability analysis via UV/vis absorption spectroscopy

The (ambient) stability of biradicals can be analysed by time-dependent UV/vis absorption spectroscopy. A sharp absorption band, which is bathochromically shifted compared to the respective bisphenole is characteristic for most phenoxyl biradicals (*vide supra*) and can be used to monitor the decomposition process.^[23] An analysis of this time dependence at a properly chosen wavelength (i. e. commonly the sharp absorption maximum) allows the determination of the half-life time in solution. It is apparently important that the decay of absorbance is only caused by decomposition of the biradical. In the case of PBI biradical **102** (Figure 2.24), a slow decrease of intensity was recorded over several hours. (Figure 2.24, left).

For the kinetic analysis of the decomposition process, the change of biradical concentration over time is monitored. According to the Lambert-Beer law, the observed absorption is proportional to the concentration in solution. In order to evaluate the measured changes in concentration, $[A]_0 - [A]_t$ is plotted versus time for a zero-order kinetic, $\ln \frac{[A]_0}{[A]_t}$ vs. t in case of a first-order kinetic or $\frac{1}{[A]_t} - \frac{1}{[A]_0}$ vs. t for a second-order kinetic process (Table 2.2). Since several reactions pathways like proton abstraction from the solvent, fragmentation, rearrangements or recombination occur during degradation of (bi)radicals, the underlying kinetic is complex and in general unknown. Therefore, data fitting according to zero-, first- and second-order kinetics are performed in order to get an estimation of the apparent half-

life time. Therefore, changes in concentration are fitted with all three kinetic models and the quality of each fit is then judged using Pearson's correlation coefficient (Pearson R^2). As the half-life times obtained in this way usually do not differ significantly, it is an accepted practice to give the lowest half-life time determined with these three models as a minimum value.

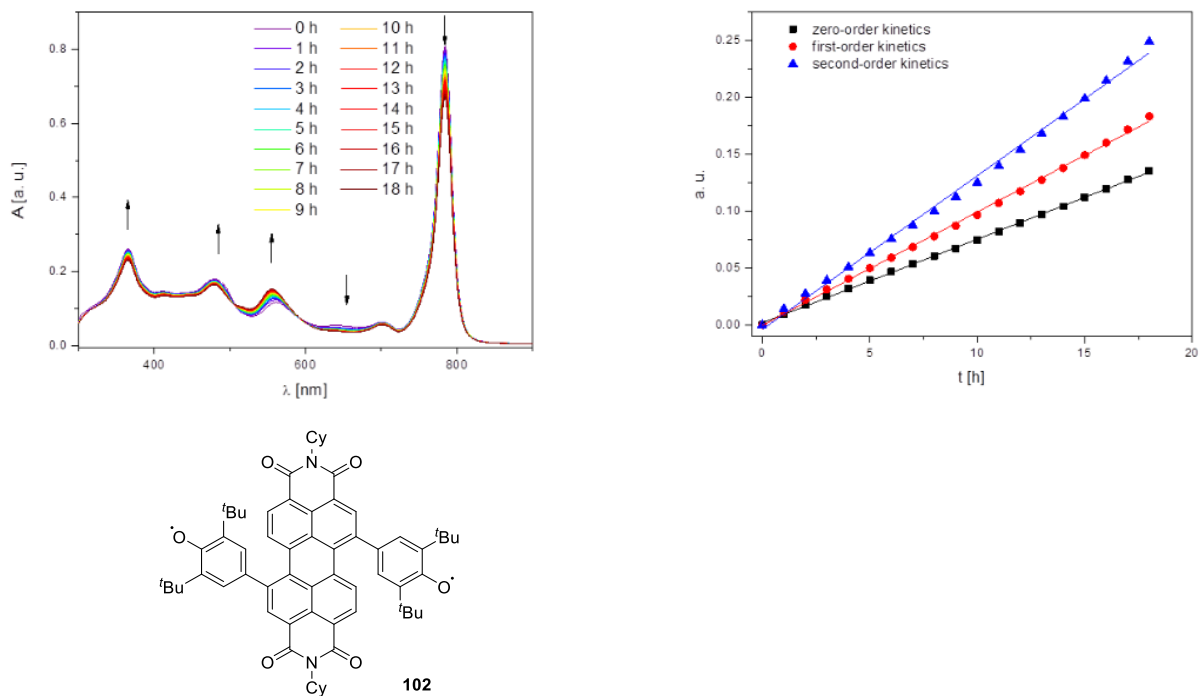


Figure 2.24 | Time-dependent UV/Vis/NIR absorption spectral changes of **102**^[23] (top, left) upon decomposition and spectral changes of **102** at 784 nm plotted versus time using zero-, first- and second-order rate equations (top, right). Reprinted with permission from ref. [23]. Copyright 2015 John Wiley and Sons Inc.

Table 2.2 | Rate laws of a zero-, first- and second-order kinetic decomposition process and derived half-life times.

order of rate law	rate law	linearised rate equation	half-life time
zero order	$-\frac{d[A]}{dt} = k$	$[A]_0 - [A]_t = kt$	$\tau_{\frac{1}{2}} = \frac{[A]_0}{2k}$
first order	$-\frac{d[A]}{dt} = k[A]$	$\ln \frac{[A]_0}{[A]_t} = kt$	$\tau_{\frac{1}{2}} = \frac{\ln 2}{k}$
second order	$-\frac{d[A]}{dt} = k[A]^2$	$\frac{1}{[A]_t} - \frac{1}{[A]_0} = kt$	$\tau_{\frac{1}{2}} = \frac{1}{k[A]_0}$

$[A]$ is the molar concentration of the radical. $[A]_0$ equals the initial concentration at $t = 0$ and $[A]_t$ is the concentration at time t .

2.3.4 Spectro-electrochemistry (SEC) of biradicals

Oxidation and reduction processes of chromophores frequently cause drastic changes of the respective optical properties. Furthermore, in the case of biradicals, redox processes are commonly the final synthetic step to generate the open shell system. For instance, phenoxyl biradicals are mainly accessed by deprotonation and oxidation of the respective bisphenols. Investigations of these redox processes can give valuable hints towards the redox sensitivity of (bi)radicals. In this regard, recording absorption spectra while applying a reducing or oxidising electrical potential is a key technique and commonly performed in a spectroelectrochemical (SEC) setup. SEC cells consist out of a working, a counter and a reference electrode, which are placed in an optical transparent cuvette and connected to a potentiostat. Often, a planar disc working electrode is applied and the measurement performed in reflection mode. With such a SEC setup, the stepwise oxidation process of phenolate $\mathbf{102}^{2-}$ to radical anion $\mathbf{102}^{\cdot-}$ with concomitant rise of a NIR band at 1396 nm and further oxidation to PBI biradical $\mathbf{102}$ with a characteristic sharp absorption band at 783 nm was monitored (Figure 2.25).^[23]

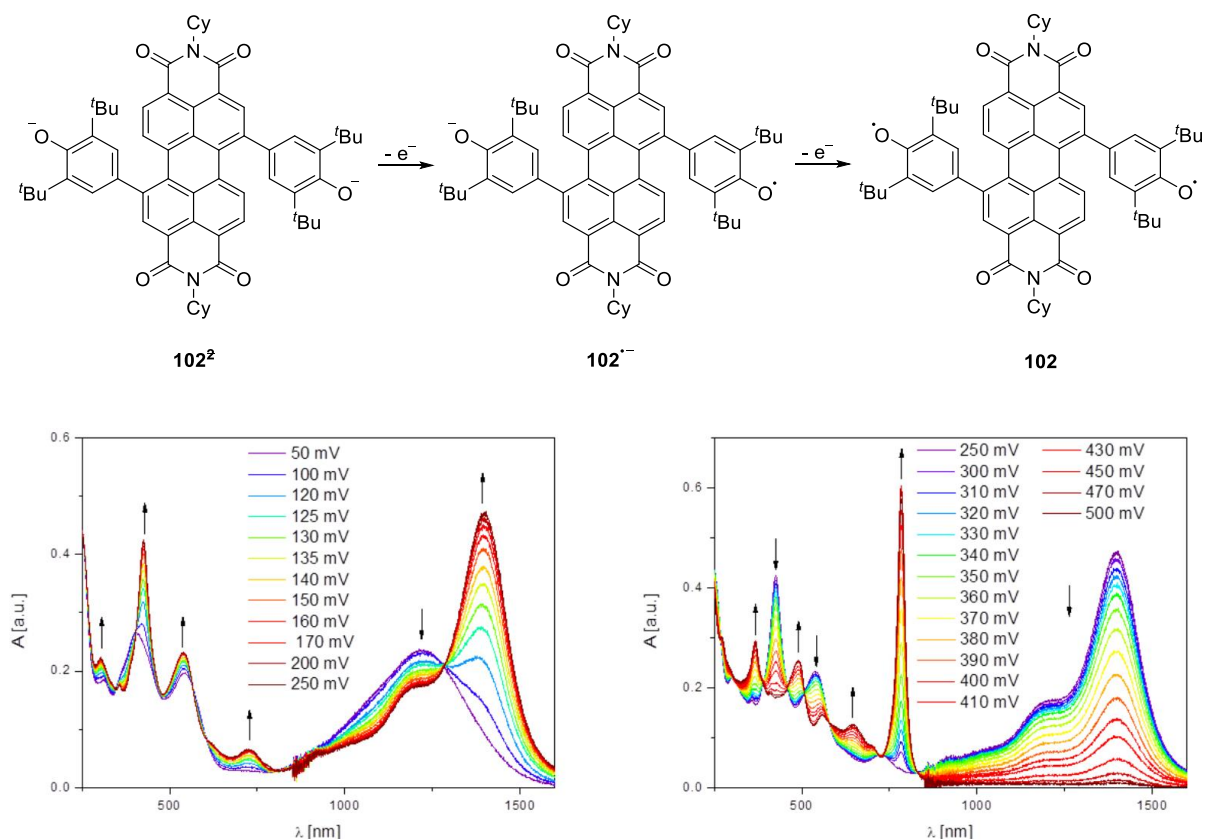


Figure 2.25 | Stepwise oxidation process of dianion $\mathbf{102}^{2-}$ to mixed valent $\mathbf{102}^{\cdot-}$ and subsequently biradical $\mathbf{102}$ as well as respective UV/Vis/NIR absorption spectral changes of $\mathbf{102}^{2-}$ upon electrochemical oxidation.^[23] Arrows indicate spectral changes with increasing positive potential. Reprinted with permission from ref. [23]. Copyright 2015 John Wiley and Sons Inc.

2.3.5 X-ray diffraction analysis of diradicals and quinones

X-ray diffraction analysis of single crystals enables an experimental access to the molecular structure. In the field of diradicals, the precise determination of bond lengths *via* X-ray analysis is a considerably important experimental method in order to distinguish a closed-shell quinoidal from an open-shell diradical state. Quinones and quinoidal compounds like **91** are characterised by a pronounced bond length alternation (BLA) along a conjugated path between both radical centres (Figure 2.26, left).^[159] In contrast, the structure of diradicals is frequently “single bond broken”, like by bonds 5 and 11 in **94** due to the more pronounced aromatic character (Figure 2.26, right). Therefore, X-ray diffraction analysis is a powerful tool in order to assign a predominant quinoidal or biradical character and to determine y_0 .^[163]

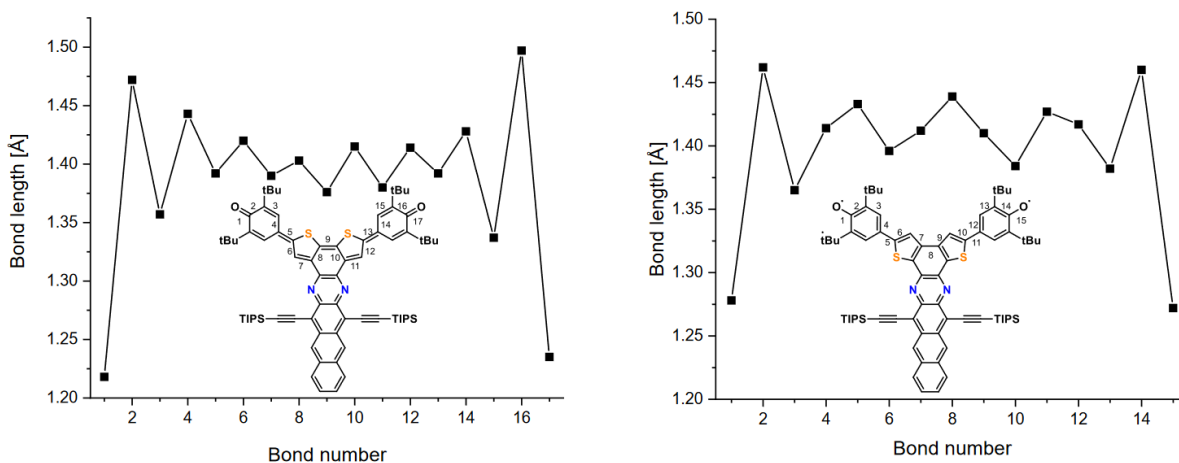


Figure 2.26 | Bond length alternation along the quinoid structure in **91** (left) and biradical **94** (right).^[159] Adapted with permission from ref. [159]. Copyright 2020 John Wiley and Sons Inc.

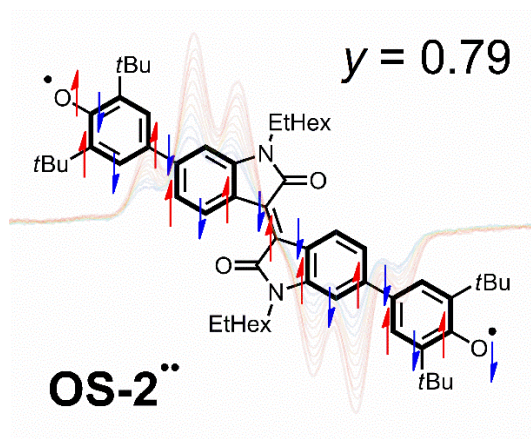
2.3.6 Quantum chemical investigation of diradicals

Biradicals are molecular systems with two electrons occupying two (almost) degenerate molecular frontier orbitals. Therefore, respective wave functions are not dominated by a single configuration, but rather include several leading determinants.^[2] For this reason, biradicals usually cannot be described sufficiently using conventional DFT or single-reference wavefunction-based methods, which, however, are frequently used in current literature.^[214, 215] More precise results can be obtained by applying e.g. the spin-flip (SF) TD-DFT approach.^[216] Additional details on the importance of a proper theoretical description and drawbacks of conventional DFT and single-reference wavefunction-based methods are explained in *Chapter 4* of this thesis.

Chapter 3

Stable Organic (Bi)Radicals by Delocalization of Spin Density into the Electron-Poor Chromophore Core of Isoindigo

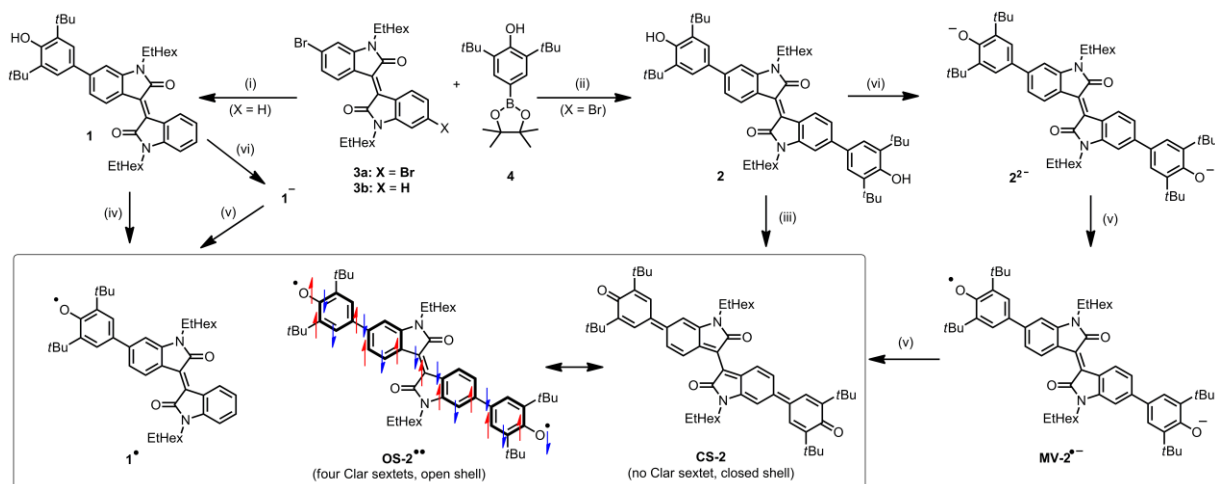
This chapter was partly communicated in: Rausch, R., Schmidt, D., Bialas, D., Krummenacher, I., Braunschweig, H., Würthner, F. *Chem. Eur. J.* **2018**, 24, 3420–3424. Reprinted with permission of *Chem. Eur. J.* **2018**, 24, 3420–3424 (= ref. [173]). Copyright 2018 John Wiley and Sons Inc.



Abstract: The first isoindigo (bi)radicals were obtained by proton coupled oxidation of their 4-hydroxyaryl substituted precursors. Optical and magnetic spectroscopic studies revealed a singlet open-shell biradicaloid electronic ground state for the bisphenoxy-isoindigo ($\langle s^2 \rangle = 1.20$) with a small singlet-triplet energy gap of 0.065 eV and a large biradical character of $y = 0.79$ that was corroborated by temperature-dependent EPR spectroscopy and quantum chemical calculations. The concept of kinetic blocking of the radical centers and delocalization of spin density into the electron-withdrawing chromophore core of isoindigo offers an entry into a new class of exceptionally stable open-shell functional materials based on organic colorants.

Since the discovery of the first biradicaloid polycyclic aromatic hydrocarbon (PAH) by Tschitschibabin in 1907,^[64] the interest in organic open-shell π -conjugated compounds has increased tremendously due to their unique optical, electronic and magnetic properties.^[2] Usually, open-shell PAHs exhibit redox amphoterism,^[217] comparatively small HOMO–LUMO energy gaps,^[218] enhanced second hyperpolarizability^[219] and large two-photon absorption cross-sections^[220] which makes them interesting for the development of new ambipolar field-effect transistors,^[221] second generation solar cells based on singlet fission,^[20] non-linear optics,^[16, 17] energy storage^[18, 19] or electronic devices^[108] as well as for organic spintronics.^[21] Generally, the degree of biradical character y_0 can range from zero (completely closed-shell) to one (completely open-shell) with overall spin angular momenta of $S = 0$ for singlet and $S = 1$ for triplet states which can be predicted by applying Ovchinnikov's parity model.^[102, 170] However, an unambiguous characterization of the ground state electronic structure of open-shell PAHs is rather challenging due to their inherent instability.^[222] Thus, much efforts have been invested in the last decades to stabilize such intrinsically reactive materials by kinetic blocking of the radical centers and/or thermodynamic stabilization by introduction of electron withdrawing substituents and π -electron delocalization.^[163, 223] Based on this strategy, reasonably stable open-shell PAHs have been synthesized using quinodimethanes,^[224] bisphenalenyles,^[225, 226] zethrenes^[227] or diindeno fused π -scaffolds with significant open-shell biradicaloid character.^[25, 32] Only recently, we and others have introduced 2,6-di-*tert*-butylphenoxy substituents into electron deficient rylene bisimides or PAHs to generate singlet open-shell biradicals with record biradical characters of up to $y = 0.83$ which, however decomposed very fast.^[23, 24, 163] Therefore, we directed our attention on another versatile organic colorant, i.e. isoindigo (In), a derivative of the most important dye in history^[228] and targeted the development of stable (bi)radicals based on this dye.

In this contribution, we communicate the isolation and characterization of an exceptionally stable isoindigo biradical **OS-2 $\cdot\cdot$** by successive deprotonation and oxidation of a 6,6'-di(4-hydroxyaryl)-substituted In-derivative. To approach the synthesis of isoindigo (bi)radicals **1 \cdot** and **OS-2 $\cdot\cdot$** we introduced sterically demanding 2,6-di-*tert*-butylphenol substituents into the appropriately brominated In-precursors **3a** and **3b** (Scheme 3.1).



Scheme 3.1 | Synthetic routes to isoindigo (bi)radicals **1*** and **OS-2****. (i) $[\text{Pd}_2(\text{dba})_3]$, $\text{P}(o\text{-tol})_3$, $n\text{Bu}_4\text{NOH}$, H_2O , PhMe , 90°C , 14 h, 66%; (ii) $[\text{Pd}_2(\text{dba})_3]$, $\text{P}(o\text{-tol})_3$, $n\text{Bu}_4\text{NOH}$, H_2O , PhMe , 90°C , 14 h, 68%; (iii) PbO_2 , CH_2Cl_2 , rt, 0.5 h, 97%, (iv) PbO_2 , CH_2Cl_2 , (v) $\text{Pb}(\text{OAc})_4$, CH_2Cl_2 , (vi) TBAF, CH_2Cl_2 . Steps (i), (ii) and (iii) describe synthesis conditions, whereas (iv), (v) and (vi) are conditions applied for generating the following species. Blue and red arrows indicate spin polarization and illustrate antiferromagnetic coupling.

By applying typical Suzuki-Miyaura cross coupling reaction conditions using **4** as readily accessible boronic acid ester, IIn derivatives **1** and **2** were isolated in 66% and 68% yield, respectively (Supporting Information, Scheme 8.1.1–8.1.3). Both compounds were characterized by NMR spectroscopy, mass spectrometry as well as elemental analysis and their solid state structures were unambiguously determined by single crystal X-ray diffraction (Figure 3.1). All bond lengths and angles of the isoindigo scaffolds of **1** and **2** are comparable to those of the parent chromophore bearing no additional functionalities. Although the dihedral twist angles of **2** ($2 \times 19.6(2)^\circ$) are considerably larger than those of **1** ($6.1(3)^\circ$ and $9.5(3)^\circ$), both materials closely resemble the γ -phase of parent isoindigo with two crystallographically independent molecules and twist angles between 6.23° and 19.38° .^[229] The 2,6-di-*tert*-butylphenol substituents are rotated out of the IIn- π -surfaces by approximately 38.3° (**1**) and 25.0° (**2**). IIn-derivative **1** with only one 2,6-di-*tert*-butylphenol substituent forms slipped-stacked one dimensional OH–O hydrogen bonded single strands with longitudinally displaced chromophores (Supporting Information, Figure 8.1.1). Adjacent strands are thereby arranged antiparallel in a staircase-like packing arrangement. In contrast, the twofold substituted IIn **2** forms rotoinverted π -dimers with an average π – π -distance of 3.4 \AA and a rotational displacement of approximately 62.4° (Supporting Information, Figure 8.1.2).

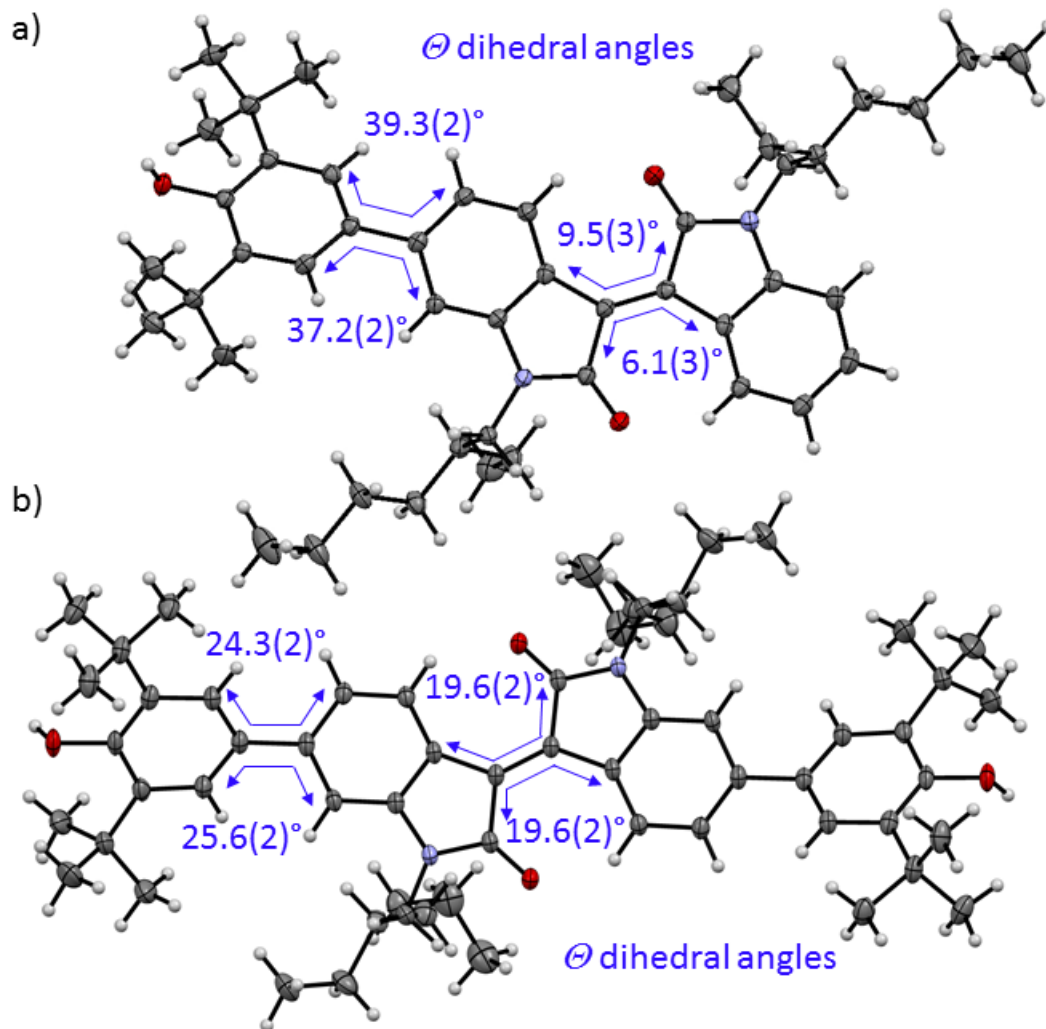


Figure 3.1 | Solid state molecular structures of **1** (a) and **2** (b) determined by single crystal X-ray diffraction (ellipsoids set to 50 % probability, carbon gray, nitrogen blue, oxygen red, hydrogen white).

The optical properties of non-fluorescent dyes **1** and **2** were investigated by UV/vis/NIR spectroscopy in dichloromethane solutions at room temperature (Figure 3.2 and Supporting Information, Table 8.1.4). The absorption spectra of both chromophores are characterized by broad absorption bands in the visible spectral range with each two maxima located at 514, 421 nm (**1**) and 537, 437 nm (**2**), respectively, which are bathochromically shifted compared to the 6,6'-unsubstituted In derivative (496 and 394 nm).^[230, 231]

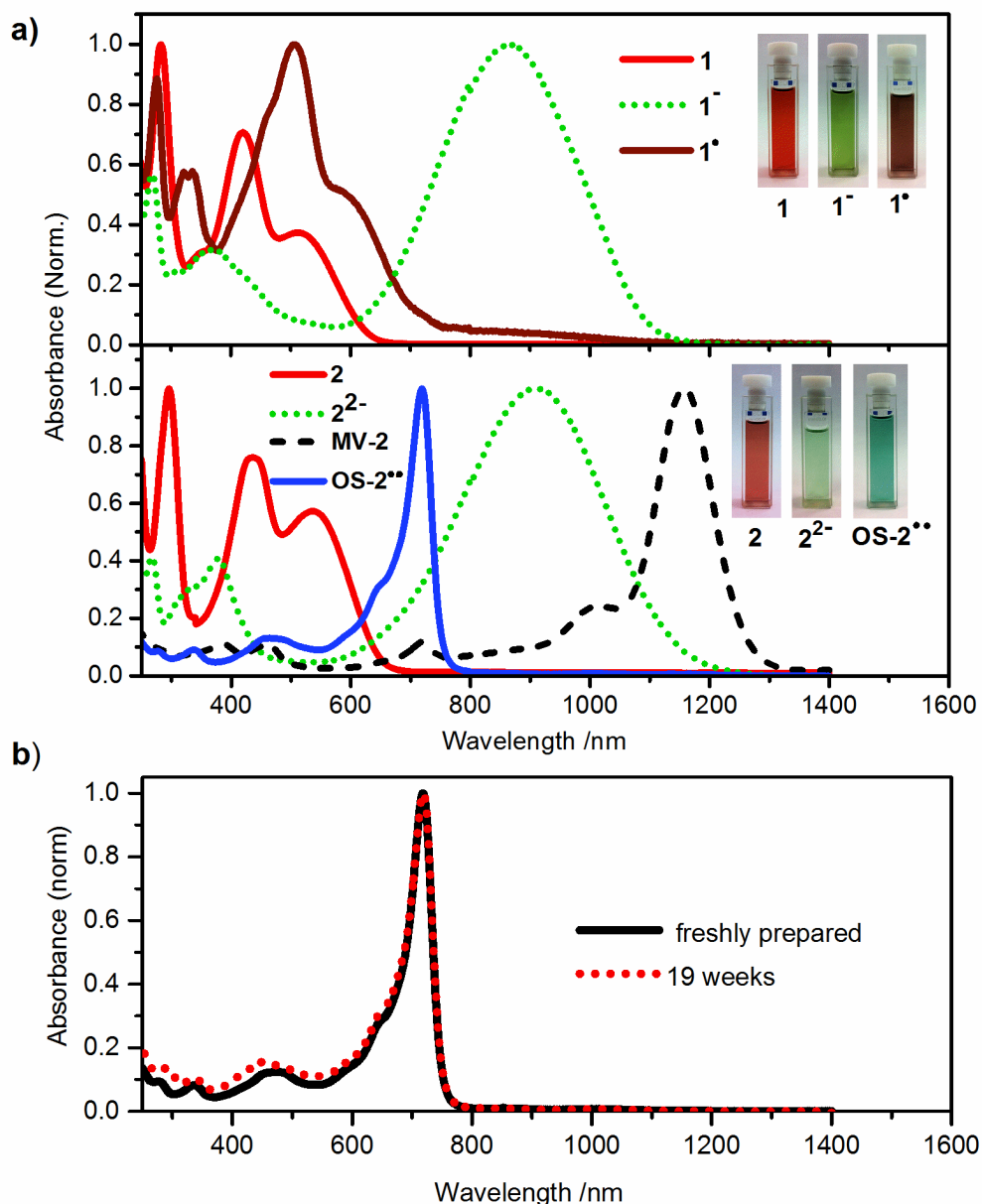


Figure 3.2 | Normalized UV/vis/NIR absorption spectra of neutral IIns **1** and **2** (red solid lines, from the top), (di)anionic species **1⁻** and **2²⁻** (green dotted lines, from the top), radical **1[•]** (brown solid line, top), mixed-valence **MV-2[•]** (black dashed line, below) and biradical **OS-2^{••}** (blue solid line, below) (a) and of a redissolved sample of **OS-2^{••}** in dichloromethane after storing the isolated solid for 19 weeks (red dotted line) under an atmosphere of nitrogen (b).

Due to the strongly acidic character of the 4-hydroxyaryl substituents, both compounds can readily be deprotonated upon addition of tetra-*n*-butylammonium fluoride (TBAF) to generate their corresponding (di)anions **1⁻** and **2²⁻** (Supporting Information, Scheme 8.1.5). The deprotonation is accompanied by

drastic color changes from deep red to pale green and the absorption spectral changes were therefore monitored by UV/vis/NIR spectroscopy (Supporting Information, Figure 8.1.5). Stepwise addition of TBAF to solutions of **1** and **2** causes a decrease of the initial absorption bands with a concomitant rise of broad charge transfer (CT) bands in the NIR region between 600 and 1200 nm which are attributed to pronounced charge transfer from the electron-rich phenoxide substituents to the electron-poor In cores. The spectral signatures of neutral **1** and **2** can however be recovered by adding equimolar amounts of trifluoroacetic acid to solutions of **1**⁻ and **2**²⁻ in dichloromethane, corroborating the reversibility of the deprotonation/protonation processes (Supporting Information, Figure 8.1.5). During our base titration of **2**, we observed an additional even more red-shifted shoulder at around 1150 nm that continuously increased over time but is absent in the UV/vis/NIR absorption spectra of freshly prepared solutions of **2**²⁻ (Supporting Information, Figure 8.1.5). Since this emerging band can be attributed to the mixed valent species **MV-2**⁻ (*vide infra*) arising from autoxidation of **2**²⁻ under ambient conditions, the stability of the (di)anion itself has been monitored by UV/vis/NIR absorption spectroscopy (Supporting Information, Figure 8.1.6). Most interestingly, the autoxidation of **2**²⁻ to **MV-2**⁻ proceeds for 33 hours followed by disproportionation and reprotonation of **MV-2**⁻ under formation of **2** and biradical **OS-2**^{••}. The latter exhibits a characteristic absorption band at 719 nm (*vide infra*) and its spontaneous formation already indicates a remarkable stability. This process can be decelerated considerably in the absence of oxygen as it has been demonstrated in degassed CH₂Cl₂ solutions.

Neutral monoradical **1**[•] and biradical **OS-2**^{••} can also be generated by reacting **1**⁻ and **2**²⁻ with lead(IV) tetraacetate in dichloromethane solutions or heterogeneously by adding lead(IV) oxide to the corresponding dichloromethane solutions of **1** and **2** followed by filtration of the excess of oxidant (Supporting Information, Scheme 8.1.6 and 8.1.7). The molecular compositions of **1**[•] and **OS-2**^{••} were proven by high resolution ESI-ToF mass spectrometry (Supporting Information Figure 8.1.4) and after evaporation of the solvent under an atmosphere of nitrogen, **OS-2**^{••} could even be isolated as a dark green solid in quantitative yields. Both compounds exhibit exceptional stabilities compared to many other organic materials with open-shell (bi)radicaloid electronic ground states. As evidenced by kinetic analyses of the gradual changes in their time-dependent UV/vis/NIR absorption spectra, **1**[•] and **OS-2**^{••} are highly stable in solution even under ambient conditions. Monoradical **1**[•] slowly decomposes under these conditions with a minimum half-life of 6.6 days (in CH₂Cl₂) whereas **OS-2**^{••} exhibits a minimum half-life of more than 28 days in CCl₄ (21 d in CH₂Cl₂, 7.3 d in PhH, Supporting Information Figure 8.1.7, 8.1.8 and Table 8.1.1–8.1.3). Protected from air and moisture **OS-2**^{••} was stored under an atmosphere of nitrogen for 19 weeks without any sign of decomposition. Accordingly, thin films of **OS-2**^{••} spin-coated under inert conditions or redissolved samples of the appropriately stored material display

the same absorption spectral features like freshly prepared solutions (Figure 3.2 and Supporting Information, Figure 8.1.8).

Upon stepwise addition of $[\text{Pb}(\text{OAc})_4]$ solutions to $\mathbf{1}^-$ and $\mathbf{2}^{2-}$, the broad CT-bands at 867 ($\mathbf{1}^-$) and 905 nm ($\mathbf{2}^{2-}$) gradually decrease whereas new absorption bands arise in the visible and NIR-spectral range for monoradical $\mathbf{1}^\bullet$ and biradical $\mathbf{OS-2}^{\bullet\bullet}$, respectively (Supporting Information, Figure 8.1.9). Whereas $\mathbf{1}^\bullet$ is characterized by multiple transitions at 276, 321, 336, 504 and 590 nm, $\mathbf{OS-2}^{\bullet\bullet}$ exhibits a more red-shifted and unusual narrow absorption band at 719 nm (full width at half maximum FWHM = 930 cm^{-1}) with a significantly increased extinction coefficient of $123500 \text{ M}^{-1} \text{ cm}^{-1}$. The intermediate appearance of the singly oxidized mixed-valent species $\mathbf{MV-2}^{\bullet-}$ during titration of $\mathbf{2}^{2-}$ with $[\text{Pb}(\text{OAc})_4]$, could be substantiated based on its characteristic optical signature in the NIR region with an absorption maximum located at 1158 nm (Supporting Information Figure 8.1.9). The generation of $\mathbf{1}^\bullet$ and $\mathbf{OS-2}^{\bullet\bullet}$ as well as $\mathbf{MV-2}^{\bullet-}$ has further been proven by spectroelectrochemical experiments performed on (di)anions $\mathbf{1}^-$ and $\mathbf{2}^{2-}$ in which equal absorption spectra were obtained after increasing the potential to 560 ($\mathbf{1}^\bullet$), 260 ($\mathbf{MV-2}^{\bullet-}$), and 400 mV ($\mathbf{OS-2}^{\bullet\bullet}$), respectively (vs. Pt pseudo reference electrode, Supporting Information, Figure 8.1.10). The absorption spectra of both, the chemical and the electrochemical oxidations are thereby characterized by several isosbestic points indicating well defined one electron oxidation processes.

To confirm quantitative radical formation using PbO_2 , the number of unpaired electrons per molecule $\mathbf{1}^\bullet$ was investigated by ^1H NMR spectroscopic experiments according to Evans method (Supporting Information, Figure 8.1.15). Thereby a paramagnetic shift of 10.3 Hz was observed, which is directly related to an effective magnetic moment of $1.81 \mu_B$ originating from 1.07 unpaired electrons per molecule and provides unambiguous evidence for a single oxidation of $\mathbf{1}$. Likewise, the singlet open-shell biradicaloid character of $\mathbf{OS-2}^{\bullet\bullet}$ was elucidated by temperature dependent ^1H NMR spectroscopic studies. In contrast to *II*n-derivative $\mathbf{2}$ with well-resolved resonances in the aromatic shift region (Figure 3.3), no signals can be observed for $\mathbf{OS-2}^{\bullet\bullet}$ at room temperature. However, upon decreasing the temperature to 181 K, signal intensity gradually increases until five well-separated aromatic resonances each with an integration of two can be detected for the ten protons of the isoindigo core and the phenoxy substituents. Such a behavior is typically observed for organic biradicals with singlet open-shell electronic ground states and small singlet-triplet energy gaps that give rise to thermally excited triplet species, which reduce NMR signal intensity.

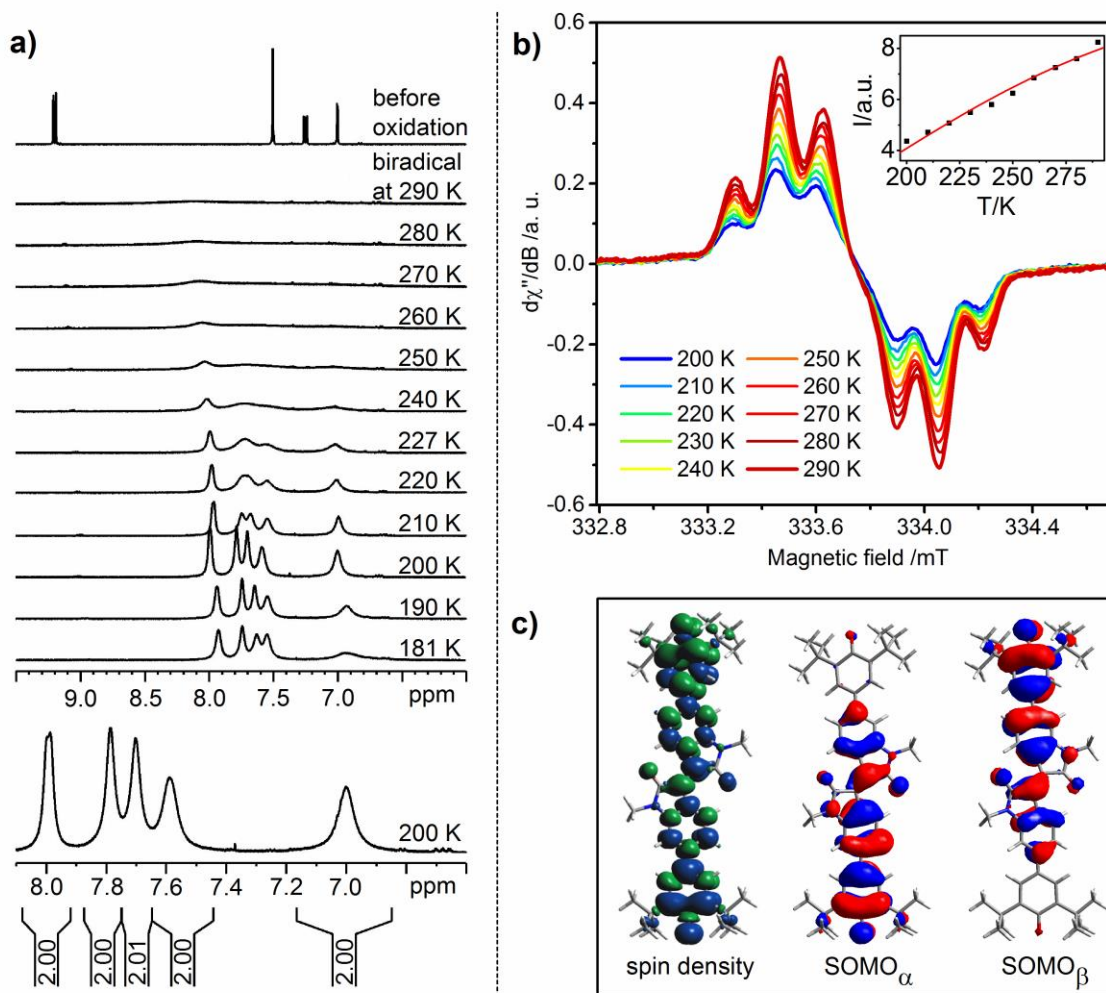


Figure 3.3 | ^1H NMR spectra of isoindigo biradical **OS-2** $^{\bullet\bullet}$ (a) at different temperatures (181 K up to 290 K) in CD_2Cl_2 (5.1 mM, 600.1 MHz, top) and integrated ^1H NMR spectrum of **OS-2** $^{\bullet\bullet}$ (5.1 mM in CD_2Cl_2 , 600.1 MHz, aromatic region) at 200 K (bottom). Continuous-wave (CW) X-band EPR spectra of **OS-2** $^{\bullet\bullet}$ in CH_2Cl_2 solution at various temperatures (b). Inset: Fitting of the integrated EPR signal intensities versus the temperature. Calculated SOMOs (isovalue 0.02 a. u.) and spin density distribution of **OS-2** $^{\bullet\bullet}$ (c) (isovalue 0.001 a. u.; UB3LYP/6-31G(d)).

To further investigate the magnetic properties of these (bi)radicals and to experimentally assess the ΔE_{ST} of **OS-2** $^{\bullet\bullet}$, EPR spectroscopy was performed on dichloromethane solutions of both compounds. The room temperature EPR spectrum of **1** $^{\bullet}$ is centered around $g_{iso} = 2.004$ and features fairly broad lines (Supporting Information, Figure 8.1.20) attributable to the coupling of the unpaired electron to ^1H nuclei of the phenoxy substituent and the chromophore core, consistent with the calculated spin density distribution (Supporting Information, Figure 8.1.23). The dominant couplings arise from the hyperfine interaction with four sets of non-equivalent aromatic protons of the phenoxy group ($A(^1\text{H}) = 5.8$ MHz) and one oxindole subunit ($A(^1\text{H}) = 2.9, 4.2,$ and 5.0 MHz). An analysis of the hyperfine pattern of biradical **OS-**

2^{••} gave virtually identical parameters at room temperature, suggesting that the spin-bearing sites are only weakly interacting. Due to the four stabilizing aromatic Clar sextets in **OS-2**^{••} and the antiferromagnetic exchange coupling of the two unpaired electrons, **OS-2**^{••} is hence best described as a singlet open-shell biradical. In agreement with its singlet open-shell biradical character and our NMR spectroscopic study (*vide supra*), the EPR signal intensity of **OS-2**^{••} continuously decreases upon cooling the sample to 200 K (Figure 3.3 and Supporting Information, Figure 8.1.20). A quantitative analysis by fitting the data to Bleaney-Bowers equation revealed a singlet-triplet energy gap of 0.065 eV.

Similarly, quantum chemical DFT calculations on the UB3LYP/6–31G(d) level of theory predict a singlet open-shell electronic ground state for **OS-2**^{••} ($\langle s^2 \rangle = 1.20$) with a ΔE_{ST} of 0.056 eV, a large biradical character of $y = 0.79$ and no bond length alternation in the geometry optimized structure of **OS-2**^{••}. The calculated spin density distribution of monoradical **1**[•] and biradical **OS-2**^{••} is delocalized over the whole chromophore (Figure 3.3 and Supporting Information, Figure 8.1.23). Moreover, the singly occupied molecular orbitals (SOMOs) of **OS-2**^{••} are characterized by disjoint profiles as one would expect for a singlet open-shell biradical with weak exchange coupling and a small ΔE_{ST} . The UV/vis/NIR absorption spectra of **1**[•] and **OS-2**^{••} were finally simulated with time-dependent DFT calculations and are in agreement with the experimental data (Supporting Information, Figures 8.1.21 and 8.1.22). Accordingly, the lowest-energy transition of **OS-2**^{••} at 719 nm originates predominantly from the characteristic $SOMO_{\alpha}$ – $LUMO_{\alpha}$ transition and exhibits the highest oscillator strength ($f = 1.16$). In contrast, the most intensive absorption bands of **1**[•] located at 504 ($f = 0.45$) and 590 nm ($f = 0.23$) mainly arise from $SOMO-3_{\beta}$ – $LUMO_{\beta}$, $SOMO_{\alpha}$ – $LUMO_{\alpha}$, and $SOMO_{\beta}$ – $LUMO_{\beta}$.

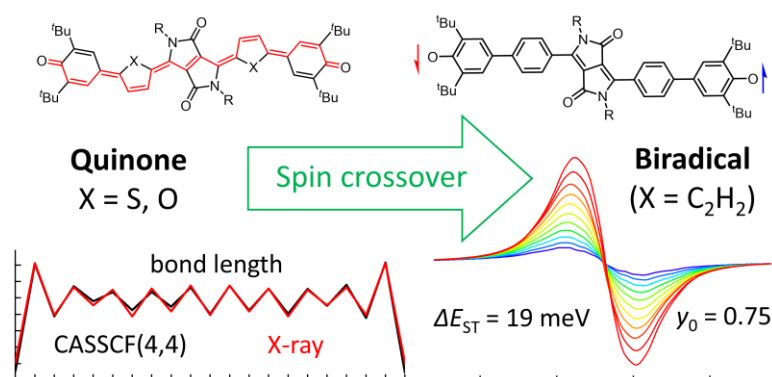
Molecules with a large biradical character and a small singlet-triplet energy gap like **OS-2**^{••} are usually characterized by comparatively short lifetimes. Thus super-heptazethrenes^[227] and phenoxy substituted rylene bisimides^[23, 24] and corannulenes^[163] with similar molecular properties ($\Delta E_{ST} = 0.041$ – 0.082 eV, $y = 0.64$ – 0.83) readily decompose within hours under ambient conditions in solution and/or weeks in the solid state. Conversely, so far available materials with comparable stabilities like **OS-2**^{••} ($\tau_{1/2} =$ several weeks in solution and infinite in the solid state) exhibit considerably larger singlet-triplet energy gaps, smaller biradical characters or require substantial spin delocalization.^[25] For instance, biradicaloid diindeno-fused polycyclic aromatic hydrocarbons or superbenzoquinones exhibit much higher ΔE_{ST} of 0.181–0.183 eV (Supporting Information, Figure 8.1.24).^[24, 25, 32] Accordingly, isoindigo biradical **OS-2**^{••} is an outstanding example combining a large biradical character ($y_0 = 0.79$), a small singlet-triplet energy gap ($\Delta E_{ST} = 0.056$ eV) and an exceptional stability, while being structurally comparatively compact.

In summary unprecedented isoindigo (bi)radicals **1**[•] and **OS-2**^{••} were reported. **OS-2**^{••} revealed a singlet open-shell electronic ground state ($\langle s^2 \rangle = 1.20$) with a small singlet-triplet energy gap of 0.065 eV that enables a thermal switching of the magnetic response. Despite its large biradical character of $y = 0.79$, **OS-2**^{••} is exceptionally stable due to rearomatization of the central benzene rings and spin delocalization from the phenoxyl radical centers into the electron-withdrawing Π n chromophore core. Accordingly, more robust open-shell materials for organic spintronics become accessible with the help of electron poor π -scaffolds as given by many organic colorants.

Chapter 4

Tuning phenoxy-substituted diketopyrrolopyrroles from quinoidal to biradical ground states through (hetero-)aromatic linkers

This chapter was partly communicated in: Rausch, R., Röhr, M. I. S., Schmidt, D., Krummenacher, I., Braunschweig, H., Würthner, F. *Chem. Sci.* **2021**, *12*, 793–802. Adapted and reprinted with permission of *Chem. Sci.* **2021**, *12*, 793–802. Published by The Royal Society of Chemistry.



4.1 Abstract

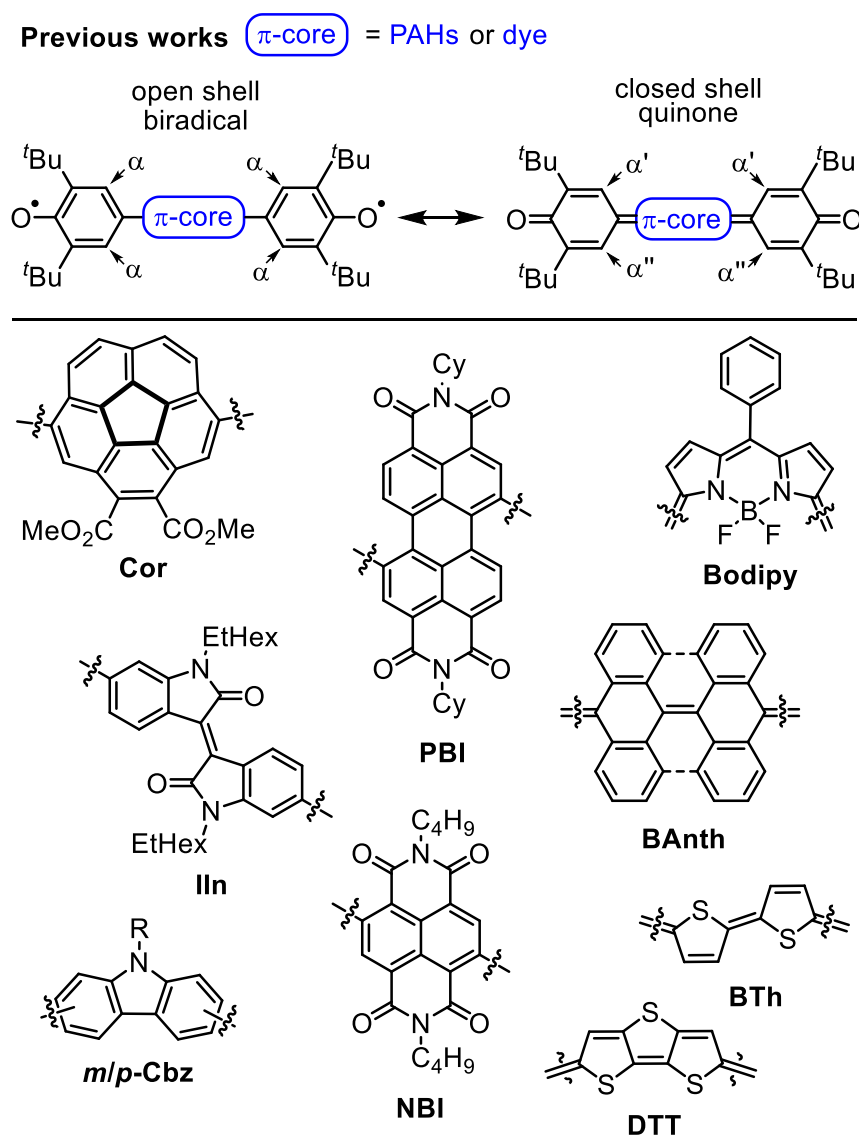
Strongly fluorescent halochromic 2,6-di-*tert*-butyl-phenol-functionalised phenyl-, thienyl- and furyl-substituted diketopyrrolopyrrole (DPP) dyes were deprotonated and oxidised to give either phenylene-linked **DPP1**^{••} biradical ($y_0 = 0.75$) with a singlet open-shell ground state and a thermally populated triplet state ($\Delta E_{ST} = 19 \text{ meV}$; 1.8 kJ mol^{-1} ; $0.43 \text{ kcal mol}^{-1}$) or thienylene/furylene-linked **DPP2q** and **DPP3q** compounds with closed-shell quinoidal ground states. Accordingly, we identified the aromaticity of the conjugated (hetero-)aromatic bridge to be key for modulating the electronic character of these

biradicaloid compounds and achieved a spin crossover from closed-shell quinones **DPP2q** and **DPP3q** to open-shell biradical **DPP1^{••}** as confirmed by optical and magnetic spectroscopic studies (UV/vis/NIR, NMR, EPR) as well as computational investigations (spin-flip TD-DFT calculations in combination with CASSCF(4,4) and harmonic oscillator model of aromaticity (HOMA) analysis). Spectroelectrochemical studies and comproportionation experiments further prove the reversible formation of mixed-valent radical anions for the **DPP2q** and **DPP3q** quinoidal compounds with absorption bands edging into the NIR spectral region.

4.2 Introduction

Despite of the long history,^[64] open-shell organic molecules gained tremendous interest in recent years due to their unique electronic, magnetic and optical properties, which mainly arise from weakly coupled electron spins.^[2] Biradicals are the smallest units to allow investigations of intramolecular spin interactions.^[232] They commonly feature small HOMO-LUMO energy gaps^[218], enhanced second hyperpolarisability^[219], redox amphoterism^[217] and large two-photon absorption cross-sections^[220]. While on the one hand these properties make biradicals promising candidates for organic spintronics^[21], molecular magnetism^[233], energy storage^[18] and electronic devices^[108], it is the unpaired electron spins, on the other hand, that drastically increase the reactivity and accelerate decomposition. Therefore, incorporation of biradicals into Kekulé-type quinoidal resonance structures is a common design strategy to stabilise these inherently highly reactive species. However, this brings up the question which factors favour biradicals and which ones quinodimethanes (\approx biradicaloids), as well as how to distinguish experimentally between both of these singlet states.^[2] In general, quinodimethane-like compounds can be described by closed-shell Kekulé structures, as open-shell biradicals or as a superposition of both.^[121, 234] Singlet biradicals are molecules with a singlet multiplicity of the lowest energy state but an open-shell configuration and are described by the respective biradical character y_0 , which ranges from zero for closed-shell to one for completely open-shell compounds.^[2] They are further characterised by the singlet-triplet energy gap ΔE_{ST} , which typically lies between 10 and 500 meV ($= 0.96\text{--}48 \text{ kJ mol}^{-1}$; $0.23\text{--}11.5 \text{ kcal mol}^{-1}$).^[135, 227, 235, 236] Within this material class, biradical(oid)s composed of π -systems substituted with two phenoxy units are among the most outstanding representatives, due to the broad variety of accessible structures, which makes them an ideal model system for experimental and theoretical investigations (Scheme 4.1).^[23, 24, 157, 162, 163, 166, 173, 177] In order to gain insight into the biradical character of these organic compounds, it is crucial to experimentally distinguish the biradical and quinone singlet state. As energy differences between these states tend to be very narrow, an even more careful choice of analytical methods is essential to uncover hidden discrepancies and draw solid conclusions. In general,

biradicals show significantly broadened ^1H NMR spectra^[23, 173] and/or pronounced EPR signals^[166, 173] due to thermal triplet state population. Quinones, in contrast, are commonly EPR silent and characterised by sharp NMR resonance signals.^[157, 162] Additionally, the (in)equivalency of phenyl protons α (Scheme 4.1, top) can be used as an indicator for the molecules' rigidity.^[157, 166]



Scheme 4.1 | (top) Open and closed-shell resonance structures of Kekulé type biradicals and biradicaloids and (bottom) examples of π -extended quinones and biradicals based on planar and bowl shaped polycyclic aromatic hydrocarbons, pigment chromophores and oligomeric heteroaromatics.^[23, 24, 157, 162, 163, 166, 173, 177]

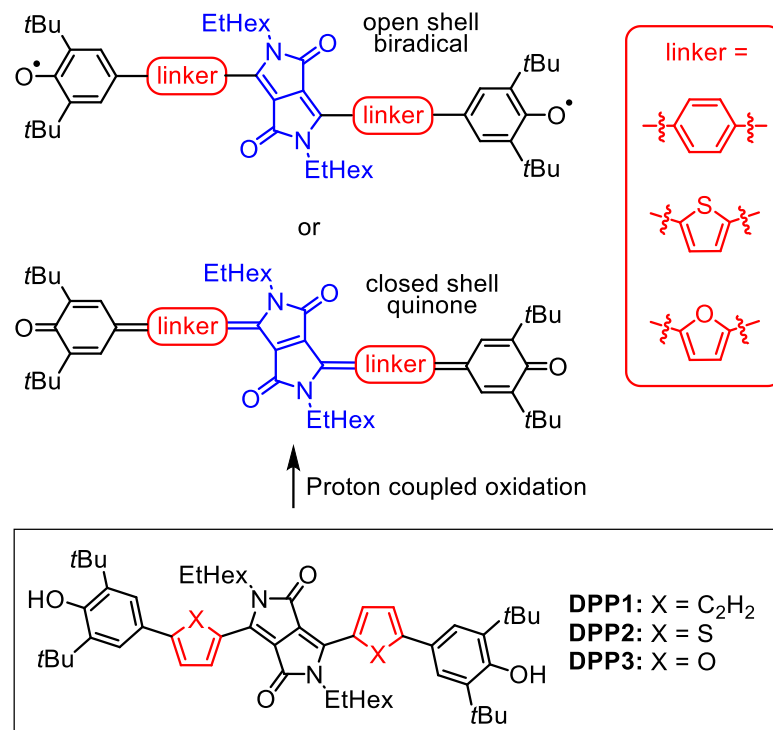
Furthermore, in order to experimentally access the singlet–triplet energy gap (ΔE_{ST}), SQUID (superconducting quantum interference device) or variable temperature (VT) EPR can be utilised, of which the latter one commonly is performed in solution.^[157, 173] In the solid state, further effects like enhanced intermolecular interactions have to be considered.^[177] X-ray analysis is a powerful method to shine light on the electronic ground state, since it allows an experimental bond length determination. Accordingly, the appearance of a distinct bond length alternation (BLA) is commonly a clear hint towards closed-shell quinones^[157, 166], whereas its absence indicates a dominating open-shell biradical character^[163]. Like for the experimental counterpart, also the theoretical description of biradicals requires sophisticated methods, since conventional (single reference) DFT is mainly suitable for closed-shell compounds, monoradicals, decoupled pairs of local doublets or high spin states, but rather inappropriate to properly describe low spin (i. e. singlet) states in biradicals.^[157, 214] Nevertheless, in case of very weakly interacting spin centres in biradicals, conventional DFT can lead to reasonable results in accordance with experimental findings (like for isoindigo derivative **II_n**)^[173], but has to be treated with caution. Due to an increasing number of compounds claimed to be open-shell and a broad variety of methods applied – experimentally as well as theoretically – it is more than ever important to study molecules comprehensively because otherwise a comparison of investigated molecules like those collected in Scheme 1 becomes impossible. In this regard, only investigations applying the same theoretical (and ideally identical experimental) methods to all molecules allow relevant conclusions.^[32] Unfortunately, an increasing number of recent publications still utilises isolated characterisation methods and (completely) neglects double checking of the gained results by comprehensive methods.

In the past, several factors influencing the electronic ground state and hence enabling a spin crossover from closed-shell quinoidal to open-shell biradical of π -conjugated compounds derived from quinodimethanes in general and twofold phenoxy substituted chromophores in particular have been investigated. In this regard, the impact of the number of bridging phenyl units^[26, 237], the connecting π -core (Scheme 4.1, bottom)^[23, 24, 162, 163, 166, 173], hetero atom effects, the number of attached (donor) substituents and the steric demand of *ortho*-positioned alkyl chains protecting the radical centres in such systems^[37, 155, 215] has been investigated. Furthermore, based on numerous longitudinally and laterally extended zethrenes^[29–31, 119], Wu and coworkers as well as Juríček and coworkers have demonstrated, that the size of the π -scaffold can significantly influence the biradical character of these polycyclic aromatic hydrocarbons (PAH). Likewise, Baumgarten, Feng and Müllen and in particular Haley and coworkers utilised structural isomerism and the number of Clar sextets^[39, 238] in various (di)indenoacenes^[25, 32–36] to rationally finetune the ΔE_{ST} of these compounds. However, a spin crossover has so far been mainly observed upon incremental elongation of an acene-like series.^[28]

In this work, we present the first detailed study on a spin crossover for this important class of twofold phenoxy functionalised π -scaffolds. Toward this goal we chose diketopyrrolopyrrole (DPP) as a core unit and carried out a simple linker variation, while maintaining the molecular size (Scheme 4.2). DPPs are highly versatile chromophores with tunable optical and electronic properties^[239–243] and outstanding chemical stability which explains their wide application in coatings^[228] and photoelectric devices^[244–252]. Furthermore, especially quinoidal DPPs and related oligo (hetero-)aromatic compounds have recently raised great attention as redox amphoteric dyes^[133, 141], in organic thin film transistors (OTFTs)^[139, 140, 253, 254] or as near infrared (NIR) emitters^[255]. As DPPs are known both in the “aromatic” and the quinoidal conjugation, they are hence predestinated to study questions related to the biradical/quinone form.

As demonstrated by a recent contribution from Zheng and co-workers^[215] reporting on a similar series of DPPs (including **DPP2** and **DPP3** and their oxidised derivatives with just different alkyl chains) we were not alone with this idea. However, in contrast to the conclusion of these authors that these two molecules upon oxidation exhibit an open-shell ground state, our high level quantum chemical calculations and multifaceted experimental methods revealed just the opposite: The ground state of these compounds is fully closed-shell, i.e. quinoidal, which could be proven among other techniques by a X-ray crystal structure analysis for **DPP3q**. Most interestingly, for the oxidised species from the phenylene-spacer compound **DPP1** (that was missing in the study of Zheng), indeed the desired spin crossover into the biradicaloid ground state can be observed. Thus, our systematic study of these biradicals and quinones with optical and magnetic spectroscopic methods as well as computational investigations with spin-flip TD-DFT calculations in combination with CASSCF(4,4) and harmonic oscillator model of aromaticity (HOMA) analysis allow to rationalise how the aromaticity of the linker unit tunes these DPP dyes from quinoidal to biradicaloid ground states. Accordingly, this is a lucky case where independently acquired results from two different laboratories on partly identical compounds enable insights on the importance of experimental and theoretical methods for obtaining conclusive results in this important field of research.^[256]

This work: Introduction and variation of an aromatic linker



Scheme 4.2 | (top) Schematic illustration of DPP bridged biradicals and quinones, as well as (bottom) structures of synthesised derivatives **DPP1–3**.

4.3 Results and discussion

Diketopyrrolopyrrole derivatives **DPP1–3** were synthesised by Suzuki-Miyaura cross coupling of the respective literature known brominated DPP-precursors **1–3** with boronic ester **4** in 70 %, 53 % and 64 % yield, respectively (Scheme 8.2.1a, ESI†). All new compounds were characterised by ¹H and ¹³C NMR spectroscopy as well as high resolution mass spectrometry. Additionally, the structure of bisphenole **DPP1** could be analysed by single crystal X-ray analysis (Fig. 8.2.4 and 8.2.5, ESI†).^[257] The optical properties of **DPP1–3** in solution and in the solid state were investigated by UV/vis/NIR absorption and steady state fluorescence spectroscopy under ambient conditions (Fig. 4.1 and Table 8.2.3, ESI†).

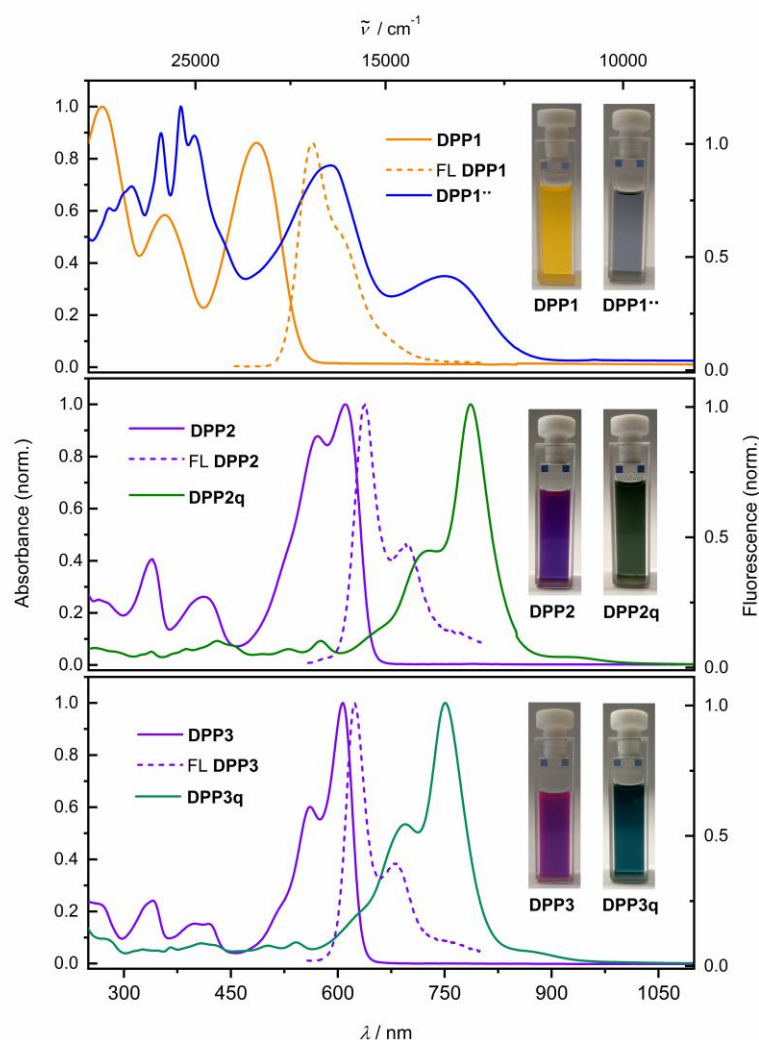


Figure 4.1 | Normalised UV/vis/NIR absorption spectra (CH_2Cl_2 , $c \approx 10 \mu\text{M}$, rt) of **DPP1** (orange solid line, top), **DPP2** (purple solid line, middle) and **DPP3** (purple solid line, bottom) as well as fluorescence spectra of **DPP1–3** (orange and purple dashed lines, from the top). Also shown are the absorption spectra of biradical **DPP1••** (blue solid line, top), and quinones **DPP2q** (dark green solid line, middle) and **DPP3q** (green solid line, bottom) obtained from proton coupled oxidation of **DPP1–3**. Inset: Photographs of the respective cuvettes.

The absorption spectrum of **DPP1** in CH_2Cl_2 (Fig. 4.1 top, orange solid line) is characterised by broad absorption in the UV and visible spectral range with maxima located at 269, 356 and 486 nm. These absorption maxima are only slightly bathochromically shifted compared to the parent chromophore Ph_2DPP ($\lambda_{\text{abs}} = 466 \text{ nm}$).^[258] In contrast, heteroaromatic derivatives **DPP2** (Fig. 4.1 middle, purple solid line) and **DPP3** (Fig. 4.1 bottom, purple solid line) show absorption maxima at 610 nm (**DPP2**) and at 607 nm (**DPP3**) with well resolved vibronic progression, which are significantly redshifted compared to the unsubstituted parent compounds Fu_2DPP and Th_2DPP ($\lambda_{\text{abs}} = 535\text{--}550 \text{ nm}$).^[239, 259] The bathochromic

shift observed in the UV/vis spectra suggests a pronounced electron-donating effect from the terminal 4-hydroxyphenyl units to the DPP chromophore cores. **DPP1–3** show intense fluorescence at 565 nm for **DPP1** ($\Delta\tilde{\nu}_{\text{Stokes}} = 2580 \text{ cm}^{-1}$, $\Phi_{\text{FL}} = 49 \%$, Fig. 4.1 top, orange dashed line), at 638 nm for **DPP2** ($\Delta\tilde{\nu}_{\text{Stokes}} = 719 \text{ cm}^{-1}$; $\Phi_{\text{FL}} = 38 \%$, Fig. 4.1 middle, purple dashed line) and at 624 nm for **DPP3** ($\Delta\tilde{\nu}_{\text{Stokes}} = 449 \text{ cm}^{-1}$; $\Phi_{\text{FL}} = 48 \%$, Fig. 4.1 bottom, purple dashed line). It is noteworthy that despite of the lowering of the band gap in this series of dyes, fluorescence quantum yields remain high and comparable to those reported in literature for the respective unsubstituted chromophores Ph₂DPP, Th₂DPP or Fu₂DPP with much larger band gaps.^[239, 258, 259]

Dehydrogenation of bisphenols occurs easily using proton coupled oxidation, which follows a concerted deprotonation-oxidation mechanism.^[23, 24, 173] Therefore, solutions of **DPP1–3** were treated with basic tetra-*n*-butylammonium fluoride (TBAF) in order to study the occurring spectral changes. Gradual changes in the respective absorption spectra were monitored by UV/vis/NIR spectroscopy (Fig. 8.2.7, ESI†). Upon stepwise addition of a solution of TBAF in CH₂Cl₂, the intensity of the absorption bands of **DPP1**, **DPP2** and **DPP3** decreases with concomitant rise of absorption bands at longer wavelengths at 704 nm for **DPP1**, at 813 nm for **DPP2** and at 789 nm for **DPP3**. The appearance of these bathochromically shifted absorption bands indicates the formation of the respective dianions **DPP1**²⁻, **DPP2**²⁻ and **DPP3**²⁻ and can be explained by the strong charge transfer (CT) from the electron-rich phenoxide substituents to the electron-poor DPP core. Such CT bands are commonly observed in halochromic systems.^[23, 24, 173] Notably, the immediate addition of an equimolar amount of trifluoroacetic acid to freshly prepared solutions of the dianions leads to a complete recovery of the absorption spectral signatures of the corresponding phenols (Fig. 8.2.7, ESI†) and hence reveals the reversibility of the deprotonation process. Additionally, during deprotonation titration experiments of the heteroaromatic derivatives **DPP2** and **DPP3**, a concomitant rise of an additional NIR band at 1083 and 1063 nm, respectively, was observed, which does not appear upon titration of **DPP1** (Fig. 8.2.7, ESI†). The appearance of these bands indicates the formation of mixed valent radical anions **MV-DPP2** and **MV-DPP3** upon autoxidation. As these mixed valent species arise upon oxidation of dianions **DPP2**²⁻ and **DPP3**²⁻ under ambient conditions, we monitored UV/vis/NIR absorption spectral changes over time (Fig. 8.2.8, ESI†) to study the extent of this oxidation process. Within 17 h (**DPP2**²⁻) and 4 h (**DPP3**²⁻), the bands attributed to the presence of radical anions **MV-DPP2** and **MV-DPP3** rise continuously, followed by a subsequent decrease. Analogous time-dependent monitoring of **DPP1**²⁻ (Fig. 8.2.8a, b, ESI†) merely shows a decrease of CT band intensity upon oxidation, which is much slower than the processes observed for the heteroaromatic derivatives. It is worth to mention, that there is no hint for the formation of an analogous mixed valent species upon autoxidation of **DPP1**²⁻. Taking the different extent and rates of

the autoxidation processes into account, it can be concluded that the phenolate's sensitivity towards oxidation is decreasing in the order $\text{DPP3}^{2-} > \text{DPP2}^{2-} > \text{DPP1}^{2-}$. This trend was proven to hold true for neutral bisphenoles **DPP1–3** as well by cyclic voltammetry, although the furane and thiophene derivatives feature a quite similar redox behaviour (Fig. 8.2.28 and Table 8.2.4, ESI†). Accordingly, the disparity between heterocyclic **DPP2/3** and **DPP2q/3q** (S ↔ O) caused by chalcogen effects is much lower than the differences (S/O ↔ Ph) to the aromatic phenyl system **DPP1**.

Our results indicate, that the first (aut-)oxidation step of DPP2^{2-} and DPP3^{2-} involves the formation of radical anions **MV-DPP2** and **MV-DPP3** by single electron transfer (SET). Apparently, a further defined oxidation process cannot be achieved by using ambient oxygen. Therefore, we applied electrochemical oxidation in order to study the stepwise oxidation process and gain further insight into the redox properties. Accordingly, the electro-optical properties of dianions DPP1^{2-} , DPP2^{2-} and DPP3^{2-} were subsequently studied by spectroelectrochemistry (SEC, Fig. 4.2). Initial spectral changes observed for DPP2^{2-} and DPP3^{2-} mainly reproduce the transformations already monitored during their autoxidation (Fig. 4.2c, e and Fig. 8.2.8, ESI†). However, the NIR bands attributed to radical anions **MV-DPP2** and **MV-DPP3** vanish completely upon further raising the potential to 500 mV and 475 mV (*vs.* Pt pseudo reference electrode, Fig. 4.2d, f, red solid line), respectively, and simultaneously, the appearance of new absorption bands with maxima at 782 nm (**DPP2**) and 751 nm (**DPP3**) (Fig. 4.2d, f, blue solid line) can be observed, which resemble by spectral shape and vibronic structure those of **DPP2** and **DPP3**, but are significantly red shifted. The formed species represent quinones **DPP2q** and **DPP3q** (*vide infra*) with outstanding high molar extinction coefficients, i. e. tripled and doubled compared to **DPP2** and **DPP3**, respectively (Table 8.2.3, ESI†). Also for DPP1^{2-} a new optical signature (Fig. 4.2b, blue solid line) emerges upon electrochemical oxidation with increasing potential to 450 mV, which could not be observed during autoxidation experiments (Fig. 8.2.8, ESI†) and can be attributed to the formation of **DPP1^{••}** (*vide infra*). The resulting absorption spectrum is significantly broadened in the visible region and shows pronounced panchromaticity with intense maxima at 380 and 588 nm and a band of lower intensity in the NIR region (749 nm). The appearance of several isosbestic points for all three dianions DPP1–3^{2-} indicates clearly defined oxidation processes. Our results indicate the formation of mixed valent radical anions **MV-DPP2** and **MV-DPP3** as well as twofold oxidised species **DPP1^{••}**, **DPP2q** and **DPP3q** by electrochemical oxidation of **DPP1–3**.

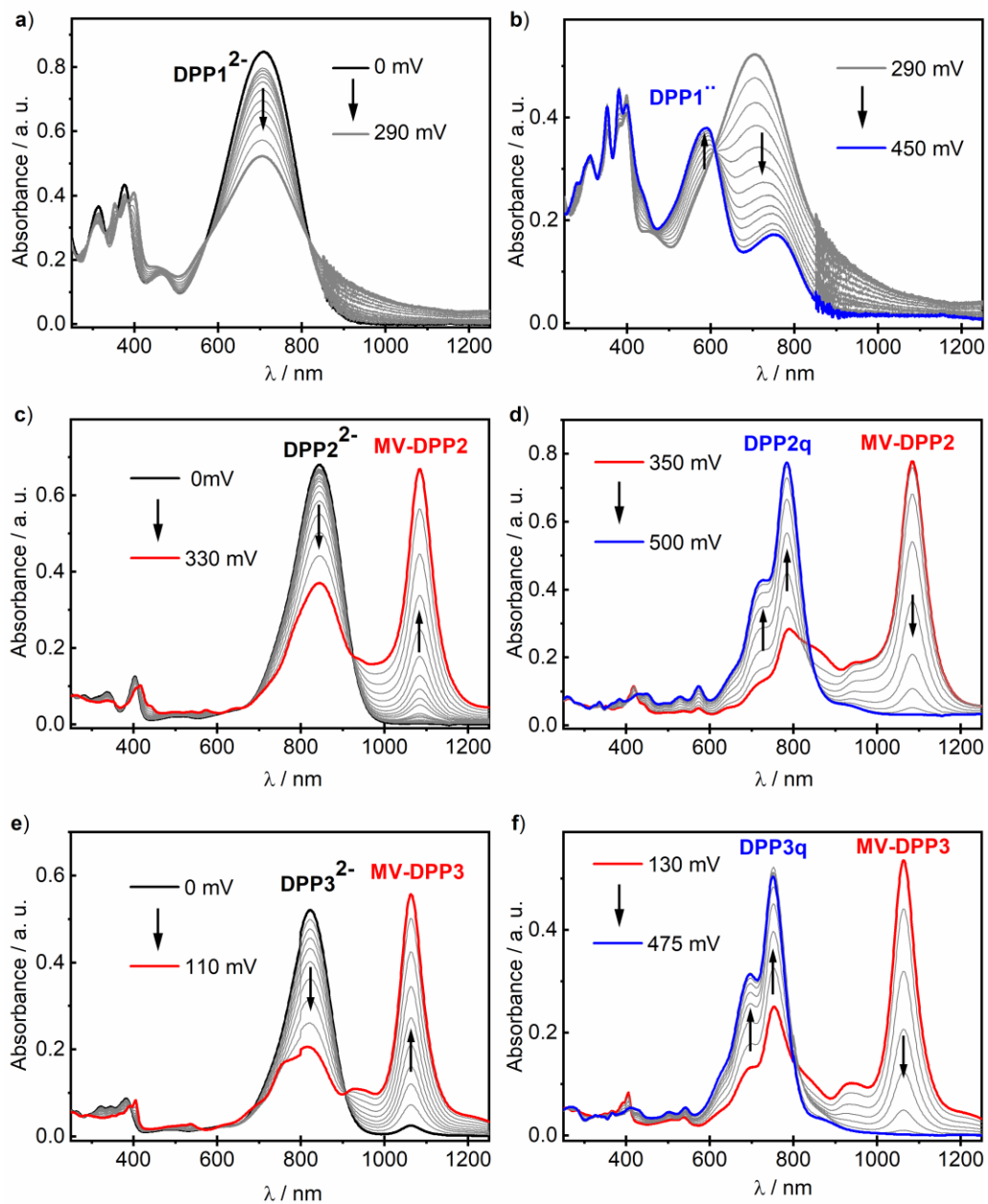


Figure 4.2 | UV/vis/NIR absorption spectral changes of (a, b) DPP1²⁻, (c, d) DPP2²⁻ and (e, f) DPP3²⁻ ($c \approx 3$ mM in CH₂Cl₂, rt, 0.2 M ⁿBu₄NPF₆) upon electrochemical oxidation in a spectroelectrochemical setup. Arrows indicate spectral changes with increasing positive potential.

In order to enable in-depth studies, we attempted to obtain these species on a preparative scale as well by applying a suitable chemical oxidant. Accordingly, biradical **DPP1^{••}** and quinones **DPP2q** and **DPP3q** were synthesised almost quantitatively by oxidation of **DPP1** with potassium ferricyanide and by dehydrogenation of **DPP2** and **DPP3** using lead(IV) oxide (Scheme 8.2.1b, ESI†), which could not be applied to **DPP1** as it caused decomposition. All products feature the same UV/vis/NIR absorption spectral signatures as observed for the electrochemically generated ones (Fig. 8.2.9, ESI†). By selective reduction of **DPP2q** and **DPP3q** with (Me₂N)₂C=C(NMe₂)₂ (TDMAE), as well as by comproportionation of **DPP2²⁻** or **DPP3²⁻** with **DPP2q** or **DPP3q**, respectively, we could furthermore generate mixed valent compounds **MV-DPP2** and **MV-DPP3** (Schemes 8.2.8–8.2.11 and Fig. 8.2.12–8.2.13, ESI†), which, however, could not be isolated. Nevertheless, the result proves that comproportionation of (extended) quinones and bisphenoxides offers an efficient and convenient access to highly desirable radical anions^[260] in appropriately functionalised chromophores.

Whereas **DPP2q** and **DPP3q** could be easily isolated out of solution by evaporation of the solvent (CH₂Cl₂) and even be crystallised (**DPP3q**, Fig. 4.3), attempts to isolate **DPP1^{••}** failed and significant bleaching of the solution was observed instead even under inert conditions in degassed CCl₄ and more accelerated upon raising temperature to reflux. For this reason, isolation or recrystallization was not successful as well. Hence, to quantify the stability of **DPP1^{••}**, **DPP2q** and **DPP3q** in solution and in the solid state under ambient conditions, time-dependent UV/vis/NIR absorption spectra were recorded. The spectral signatures of **DPP2q** and **DPP3q** in solution and in the solid state remain unchanged over several days (Fig. 8.2.10, ESI†), and thus prove the high stability of these compounds. In contrast, **DPP1^{••}** decomposes within minutes in the solid state and within hours in solution as band intensities gradually decrease over time (Fig. 8.2.11, ESI†). By fitting the time-dependent data, a minimum half-life of 78 h in CCl₄ and 39 h in CH₂Cl₂ was obtained for **DPP1^{••}** at room temperature (Fig. 8.2.11 and Table 8.2.1–8.2.2, ESI†). Such a fast decomposition within the timescale of days compared to stable **DPP2q** and **DPP3q**, can be explained with a considerably higher reactivity of **DPP1^{••}**, presumably caused by the distinct biradical character. Life times in the range of hours to days are indeed typical for phenoxy-based biradicals.^[23, 24]

Representatively for both quinones, the solid state structure of **DPP3q** could be determined by single crystal X-ray diffraction analysis (Fig. 4.3). Furane derivative **DPP3q** features an almost planar π -surface with negligible dihedral twist angles between 0.7(3)° and 1.7(3)° (Fig. 4.3a, b). In addition, a distinct bond length alternation over the whole chromophore can be observed (Fig. 4.3c), which is well in line with the quinoidal character of **DPP3q** concluded by NMR spectroscopy (*vide infra*). The parallel

displaced chromophores with an average π - π -distance of 3.19 Å form staircase like strands, which are oriented in a herringbone-type packing (Fig. 8.2.6, ESI†).

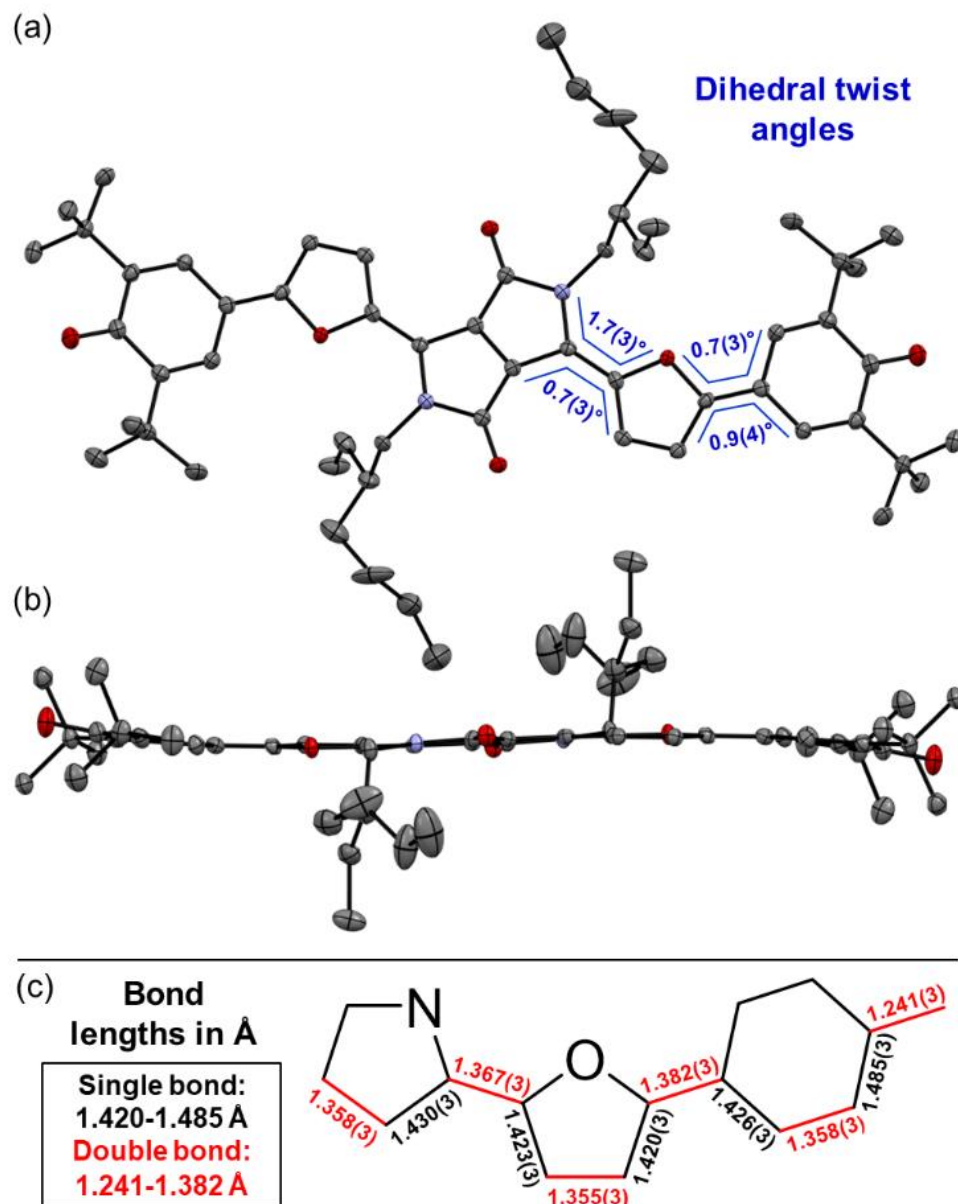


Figure 4.3 | Solid state molecular structure of **DPP3q** in (a) topview and (b) sideview as well as (c) selected bond lengths determined by single crystal X-ray diffraction (ellipsoids set to 50 % probability, carbon gray, nitrogen blue, oxygen red). H atoms and solvent (MeOH) molecules are omitted for clarity.

As **DPP1^{••}** is stable for several hours in solution (CH_2Cl_2) and **DPP2q** and **DPP3q** show no significant decomposition, we were able to investigate the para- and diamagnetic properties of the compounds with electron paramagnetic resonance (EPR) and nuclear magnetic resonance (NMR) spectroscopy (Fig. 4.4). **DPP2q** and **DPP3q** are virtually EPR silent (Fig. 8.2.3 1a, b, ESI†) in CH_2Cl_2 solution, but show a very weak signal in the solid state.

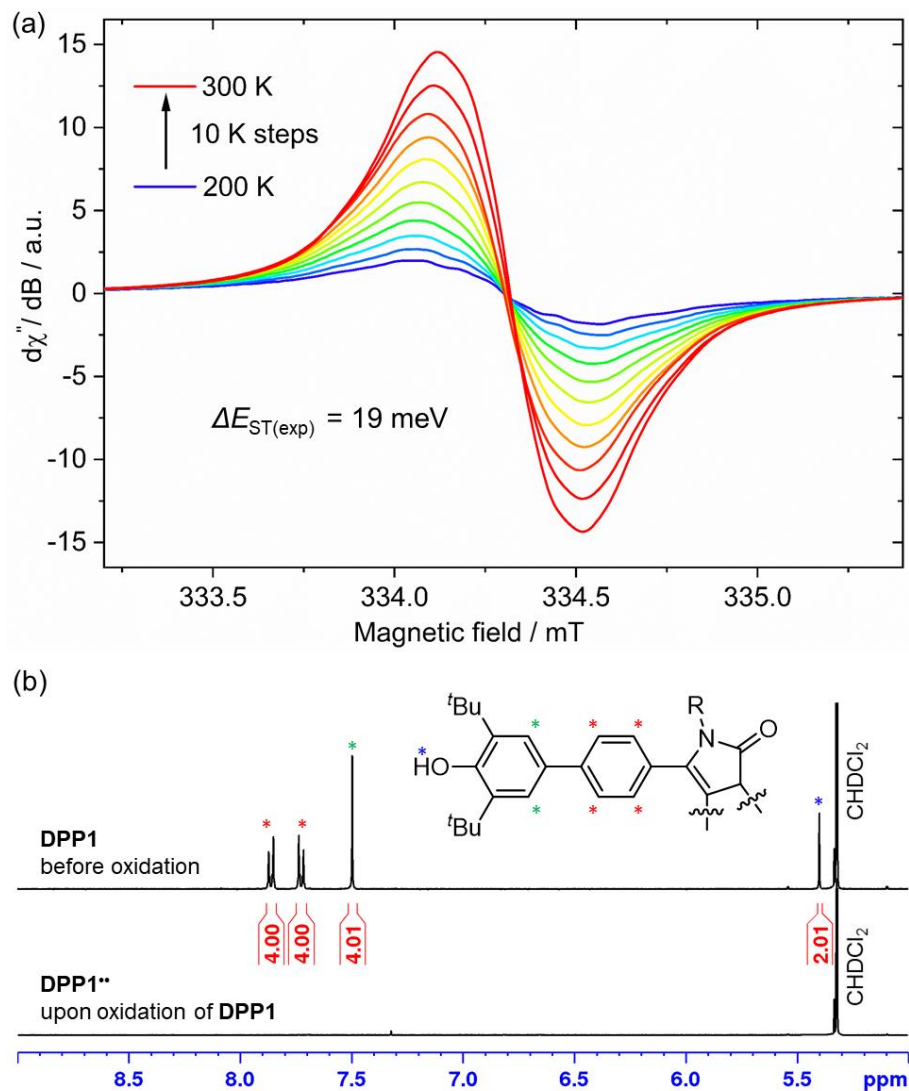


Figure 4.4 | (a) Temperature dependence of the X-band EPR spectrum of **DPP1^{••}** in CH_2Cl_2 ($c \approx 1$ mM) and (b) aromatic region of the ^1H NMR spectrum of **DPP1** (top) and **DPP1^{••}** (bottom) in CD_2Cl_2 at rt.

However, temperature-dependent solid state EPR measurements in the range of 240 to 300 K did not reveal any significant signal intensity change (Fig. 8.2.31c, d, ESI†). Accordingly, no hints for thermal triplet state population were found, which proves an insurmountable ΔE_{ST} and provides further evidence for a diamagnetic character. In contrast, **DPP1^{••}** features a pronounced EPR signal, which is centred at $g_{iso} = 2.0044$ with a peak-to-peak line width of 3.8 G (Fig. 4.4a). Temperature-dependent EPR spectroscopy of **DPP1^{••}** additionally allowed for a quantitative view on the energy difference between the singlet and triplet state. Double integration of EPR signals and data fitting according to the Bleaney-Bowers equation revealed a remarkably low ΔE_{ST} of 19 meV (1.8 kJ mol^{-1} ; $0.43 \text{ kcal mol}^{-1}$, $2J = 147 \text{ cm}^{-1}$) and hence indicates almost decoupled spin centres (Fig. 8.2.30, ESI†). As EPR signal integrals of **DPP1^{••}** increase with temperature, an open-shell singlet ground state can be concluded for **DPP1^{••}**. In compliance with the increasing amount of triplet species at higher temperature, also a pronounced broadening of resonance signals in the aromatic region of the respective ^1H NMR spectra is observed, thereby confirming the substantial paramagnetic character of **DPP1^{••}** at room temperature.^[23, 24, 173] Accordingly, the ^1H NMR spectrum of **DPP1^{••}** in CD_2Cl_2 at 298 K shows very broad signals (Fig. 4.4b), which significantly gain intensity upon decreasing the temperature to 180 K (Fig. 8.2.24, ESI†). This is in accordance with a biradical character in the ground state with a low energy difference to the NMR silent triplet state, which is thermally populated at higher temperature.

In contrast to **DPP1^{••}**, sharp signals are detected for **DPP2q** and **DPP3q** in the aromatic region of the respective ^1H NMR spectra at room temperature. Notably, the resonance signals for the two heteroaryl protons are separated by 1.45 to 1.76 ppm (Fig. 8.2.16–8.2.22, ESI†) with a significantly downfield shifted signal at 9.02 ppm (**DPP2**), 8.34 ppm (**DPP3**), 9.38 ppm (**DPP2q**) and 8.85 ppm (**DPP3q**). This shift can be explained by hydrogen bonding between a heteroaryl H atom and the carbonyl oxygen atom (Fig. 8.2.16–8.2.22, ESI†, hydrogen bonded proton highlighted in blue).^[140, 141] Accordingly, a *N,S*- and *N,O*-*cis* configuration can be concluded for all heteroaromatic derivatives, which was also corroborated by X-ray structure analysis in the case of **DPP3q** (Fig. 4.3). In addition, the resonance signal of the protons of the phenyl moiety in **DPP2** (7.52 ppm) and **DPP3** (7.63 ppm) with a singlet multiplicity splits up into two doublet signals for quinones **DPP2q** and **DPP3q** (Fig. 8.2.16–8.2.22, ESI†). Thus, both protons are chemically not equivalent anymore, which can be explained by the formation of a double bond between the former phenyl and heteroaromatic unit.^[157, 215] Therefore, the rotational freedom of the terminal phenyl unit is significantly hindered, as expected due to the quinoidal character of **DPP2q** and **DPP3q**. At an elevated temperature of 373 K, the resonance signals assigned to the heteroaryl protons of **DPP3q** remain sharp, whereas signals of **DPP2q** show a slight broadening (Fig. 8.2.25–8.2.26, ESI†). In particular, the resonance signals ascribed to the hydrogen bonded protons (*vide supra*) are well detectable, whereas the phenyl proton signal becomes broad in all heteroaromatic quinones.^[215]

Accordingly, the different behavior of phenyl and heteroaryl proton signals upon heating can be explained by a rather rigid DPP core flanked by phenoxy groups with thermally enhanced rotational freedom rather than by a thermal triplet population. Summarising, it can be concluded that the ground state of **DPP2q** and **DPP3q** is dominated by a closed-shell character with a large, thermally insurmountable singlet–triplet energy gap (ΔE_{ST}).

To further shine light onto the electronic ground state character of **DPP1^{••}**, **DPP2q** and **DPP3q**, quantum chemical calculations have been performed. In general, biradicals can be defined as molecular systems with two electrons occupying two (almost) degenerate molecular frontier orbitals.^[2] These orbital (near-)degeneracies result in wave functions, which are not dominated by a single configuration, but rather include several leading determinants. Since the accurate description of low-spin states in organic systems with partial open-shell contributions requires at least two Slater determinants, biradicals usually cannot be described sufficiently using conventional density functional theory (DFT) or single-reference wavefunction-based methods^[214], but considerably more precisely by applying the spin-flip (SF) TD-DFT approach.^[216] This method uses a single-determinant high-spin triplet state as a reference, which is well represented by a single Slater determinant. From that configuration, the target manifold of low-spin states (that is: singlets and low-spin triplet) is generated in a single excitation by applying a linear spin-flipping excitation operator $\hat{R}_{M_S=-1}$:

$$\Psi_{M_S=0}^{s,t} = \hat{R}_{M_S=-1} \Psi_{M_S=1}^t \quad (1)$$

Optimization of the formally first excited state and subsequent analysis of its character allows to determine the electronic configuration in the relaxed ground state structure of the molecule. The geometry optimization of **DPP1^{••}**, **DPP2q** and **DPP3q** has therefore been carried out in the framework of SF-TD-DFT employing the 50/50 functional (50% Hartree-Fock + 8% Slater^[261] + 42% Becke^[262] for exchange and 19% VWN^[263] + 81% LYP^[264] for correlation) along with the def2-SVP^[265] basis set (Fig. 8.2.35, ESI†). Dihedral angles between the terminal phenoxy and bridging phenylene unit in **DPP1^{••}** are significantly reduced to 11.14–14.73° compared to the parent bisphenole **DPP1** (30.2–32.2°, Fig. 8.2.4, ESI†), which can be explained by increasing conjugation in the dehydrogenated state.^[163] In accordance with the single crystal X-ray results for **DPP3q**, the relaxed geometries of **DPP2q** and **DPP3q** exhibit negligible dihedral angles of only 0.5/0.6° and 0.2/0.4°, respectively. Furthermore, we observed a distinct, and continuous bond length alternation over the whole chromophore in **DPP2q** and **DPP3q**. In contrast, BLA is broken in **DPP1^{••}** with significantly elongated bonds e and q indicating a much higher biradical character (Fig. 4.5a).

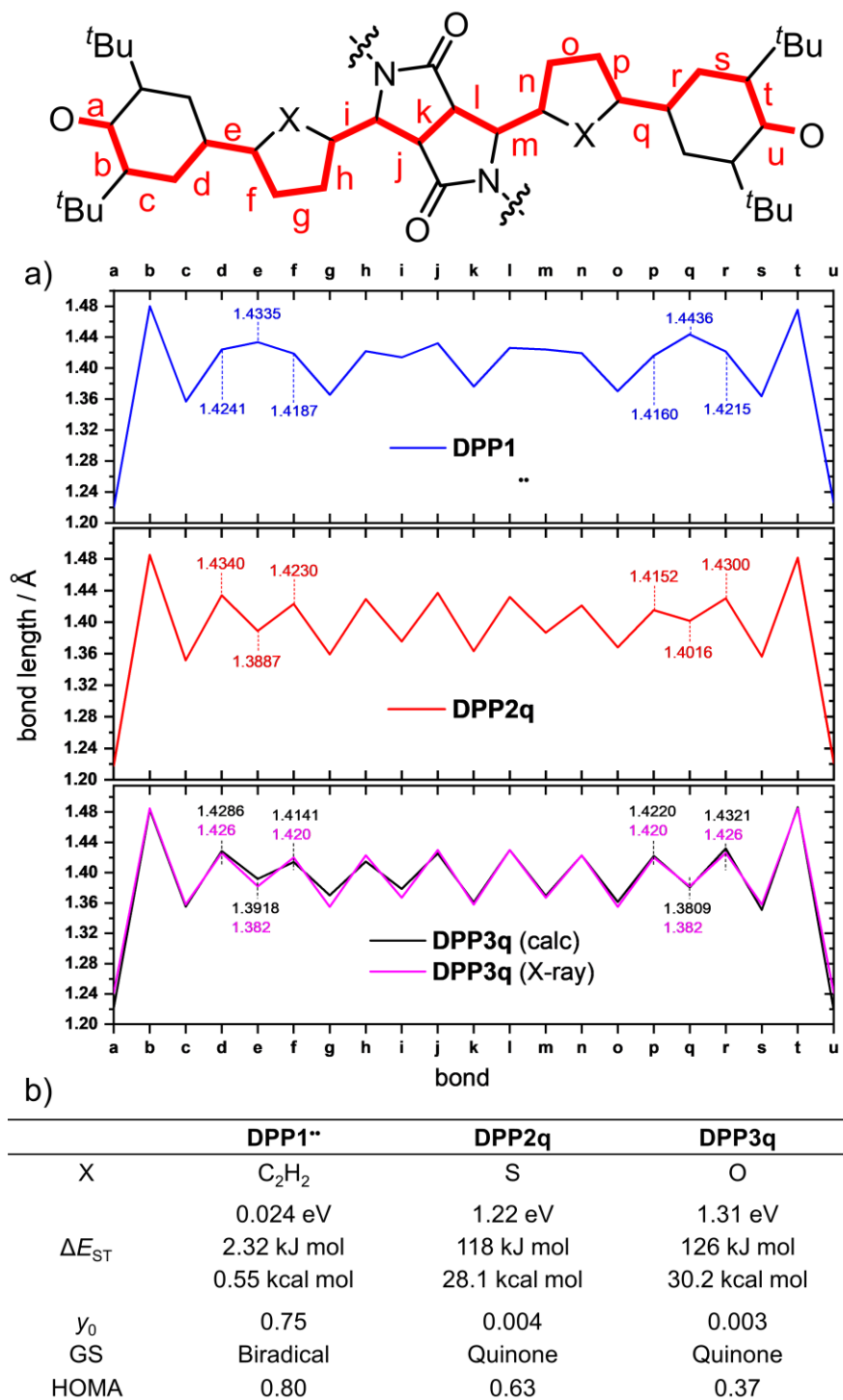


Figure 4.5 | (a) Bond lengths in Å between both oxygen sites in **DPP1^{••}**, **DPP2q** and **DPP3q** (blue, red and black solid line, from the top) as well as (b) calculated biradical/quinoidal properties of **DPP1^{••}**, **DPP2q** and **DPP3q**, ((SF) TD-DFT and CASSCF(4,4)/def2-SVP level of theory). Also shown are the bond lengths determined experimentally by X-ray diffraction (purple solid line). GS = Ground state.

As evidenced by ^1H NMR spectroscopy and X-ray analysis (*vide supra*), the *N,O*- and *N,S-cis* geometry – on which our calculations are based – is dominating in **DPP2q** and **DPP3q**. However, to complete our geometrical analysis, we performed optimisation of the *N,X-trans* geometries as well (Fig. 8.2.37, ESI†). The *trans* geometries were found to be 340 to 400 meV (= 32.8–38.6 kJ mol⁻¹; 7.84–9.22 kcal mol⁻¹) higher in energy, making the *cis* conformation a thermodynamic global minimum. Notably, the impact of the conformation on the bond lengths is very large. Accordingly, BLA is significantly reduced in the hypothetical *trans* geometry which is in good agreement with the respective values obtained by conventional DFT.^[215] For this reason, the real bond length alternation was underestimated in the earlier study by Zheng and co-workers, which is based on the *trans* geometry.^[215]

Additionally, analysis of the spin ($S^2 = 0$) and the natural orbital occupation number was used to determine the electronic ground state configuration and biradical character y_0 .^[52] Both together indicate that the energetically most favorable electronic configuration is governed by a closed-shell occupation of orbitals for **DPP2q** and **DPP3q**, while **DPP1*** is dominated by an open-shell singlet configuration and hence can be described as a singlet biradical. In order to estimate the singlet–triplet energy gaps and quantify the singlet biradical character y_0 , single point CASSCF(4,4)/def2-SVP^[52, 263, 265–269] calculations were employed for all three relaxed geometries, confirming the SF-TD-DFT results. The resulting energy gap is calculated to be 24 meV (2.3 kJ mol⁻¹, 0.54 kcal mol⁻¹) in case of **DPP1*** and 1.22 eV (118 kJ mol⁻¹, 28.1 kcal mol⁻¹)/ 1.31 eV (126 kJ mol⁻¹, 30.2 kcal mol⁻¹) for **DPP2q/DPP3q**, respectively (Fig. 4.5b). The calculated ΔE_{ST} of **DPP1*** is in good accordance with the value obtained experimentally by temperature-dependent EPR spectroscopy. Accordingly, the value of $y_0 = 0.75$ obtained for **DPP1*** clearly indicates the high biradical character of **DPP1***, while y_0 values of 0.004 and 0.003 validate the closed-shell configuration of the quinones **DPP2q** and **DPP3q**, respectively. These findings further support the structures derived from ^1H NMR spectroscopy and X-ray analysis (*vide supra*). The low biradical character calculated for **DPP2q** and **DPP3q** is in contrast to the recent conclusions of Zheng and co-workers^[215] who reported a pronounced biradical character of $y_0 = 0.64$ – 0.65 for related dyes bearing just different alkyl chains. However, these values were calculated by employing conventional DFT calculations, which become less precise in case of stronger spin interactions and low spin states (*vide supra*)^[214], as they are observed in **DPP2q** and **DPP3q**. For the purpose of investigating the role of aromaticity as a key factor for the stabilization of the open-shell configuration in **DPP1***, the “harmonic oscillator model of aromaticity” (HOMA)^[270, 271] value was calculated for all three linkers. HOMA takes into account the deviation of bond length from an “optimal” value expected for a fully aromatic system.^[270, 271]

$$\text{HOMA} = 1 - \sum_i \frac{\alpha_{ij}}{N} (R_{\text{Ref}} - R_{i,j})^2 \quad (2)$$

Here, j is the atom next to atom i , N denotes the total number of atoms, α and R_{Ref} are pre-calculated constants which are presented in the original article for each type of atom pair.^[271] A perfectly aromatic compound thereby has a HOMA value of 1, whereas a non-aromatic compound has a value of 0 or below. For the phenyl linker in **DPP1**^{••} a value of 0.8 was obtained, which clearly indicates the presence of an aromatic benzene ring, thereby stabilising the biradical configuration, while in **DPP2q** and **DPP3q**, HOMA indices of 0.63 and 0.37, respectively, hint towards a much stronger quinoidal character (Fig. 4.5b). All theoretical findings are hence in agreement with the experimental results and our interpretation.

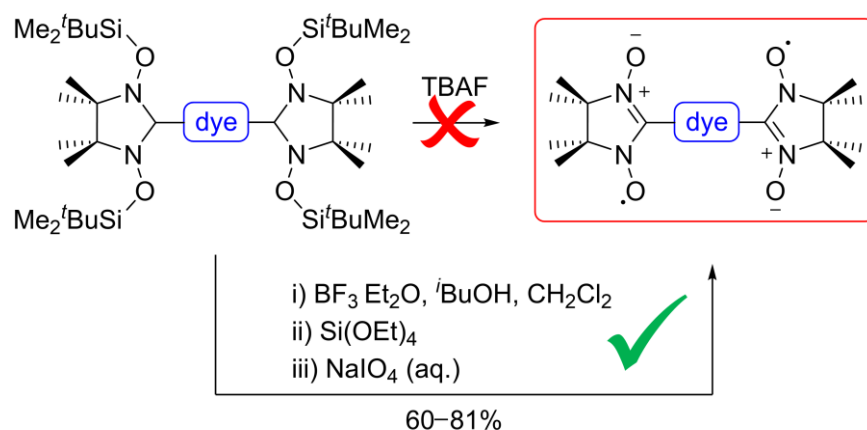
4.4 Conclusion

In conclusion, we reported a series of three with two 2,6-di-*tert*-butylphenoxy groups functionalised diketopyrrolopyrrole dyes **DPP1–3** that on first glance look very similar, but upon deprotonation and oxidation afford electronically very distinct compounds, i. e. biradical **DPP1**^{••} and quinones **DPP2q** and **DPP3q**. Our comprehensive optical and magnetic spectroscopic studies demonstrate the spin crossover from closed-shell quinones **DPP2q** and **DPP3q** to a singlet open-shell biradical **DPP1**^{••} by simple linker variation. Thus, the heteroaromatic thiophene or furane linkers between the DPP core and phenoxy substituent favour a closed-shell ground state, thereby endowing **DPP2q** and **DPP3q** with bench stability and quinoidal structures as evidenced by X-ray diffraction (**DPP3q**) and UV/vis/NIR absorption, EPR and NMR spectroscopy as well as by quantum chemical calculations based on the spin-flip TD-DFT and CASSCF(4,4) level of theory. In contrast, the “isolating” strongly aromatic phenylene bridge endows derivative **DPP1**^{••} with biradical properties with a very small singlet-triplet-energy gap of 19 meV (1.8 kJ mol⁻¹; 0.43 kcal mol⁻¹) and a large biradical character of $y_0 = 0.75$. As a consequence, **DPP1**^{••} loses stability and decomposes within the timescale of days in solution. The aromatic character of the bridging units in **DPP1**^{••}, **DPP2q** and **DPP3q** was investigated using HOMA index values, which show that the established order of aromaticity decrease (phenyl > thiophene > furane) applies for such biradicaloid systems with a central dye unit. Accordingly, we conclude that Clar’s sextet rule^[39] also offers a design principle to derive open-shell colorants with central dye and pigment units. In our example only **DPP1**^{••} with four benzenoid sextets prevailed in an open-shell configuration as a biradical, whereas energy gains through non-benzenoid heteroaromatic furane or thiophene linkers were not large enough to counteract the transformation of the π -electron system into a fully conjugated quinoidal scaffold.

Chapter 5

Nitronyl Nitroxide Bifunctionalized Electron-Poor Chromophores: Synthesis of Stable Dye Biradicals by Lewis Acid Promoted Desilylation

This chapter was partly communicated in: Rausch, R., Krause, A.-M., Krummenacher, I., Braunschweig, H., Würthner, F. *J. Org. Chem.* **2021**, *86*, 2447–2457. Adapted and reprinted with permission of *J. Org. Chem.* **2021**, *86*, 2447–2457. Copyright 2021 The American Chemical Society.



5.1 Abstract

Open shell organic molecules bearing π -cores are of great interest for optical, electronic and magnetic applications, but frequently suffer fast decomposition or lack synthetic accessibility. In this regard, nitronyl nitroxides are promising candidates for stable (bi-)radicals due to their high degree of spin-delocalization along the O-N-C-N-O pentade unit. Unfortunately, they are limited to electron rich systems so far. To overcome this limitation, we developed a synthetic procedure for the twofold spin-decoration of electron-poor chromophores ($E_{\text{red}} = -1158 \text{ mV}$) with nitronyl nitroxide radical moieties via

selective deprotection/oxidation of the respective silylated precursors with boron fluoride and subsequent quenching with tetraethyl orthosilicate. Nitronyl nitroxide biradicals **PBI-NN**, **IIn-NN**, **PhDPP-NN**, **ThDPP-NN** and **FuDPP-NN** bridged by perylene bisimide (PBI), isoindigo (IIn) and diketopyrrolopyrrole (DPP) pigment colorants were finally obtained as bench stable compounds after periodate oxidation with yields of 60–81%. The absorption spectral signatures of the chromophores remain preserved in the open shell state and match the ones of the pristine parent compounds, which allows an *a priori* prediction of their optical properties. Consequently, we achieved twofold spin labeling while keeping the intrinsic properties of the electron-deficient chromophores intact.

5.2 Introduction

Spin functionalized organic colorant materials are of interest due to their unique combination of magnetic, optical and electrochemical properties and feature significant differences regarding the spin-spin coupling strength.^[2, 30, 272] Open shell molecules in general as well as high-spin materials in particular are used for spintronics and molecular magnets and weakly antiferromagnetically coupling materials (i. e. singlet biradicals) are frequently considered as potential Bose-Einstein condensates (BEC).^[170, 233, 273–276] However, biradicals are prevalently highly reactive compounds and often feature low ambient stability. In this regard, nitronyl nitroxides (NN) are appealing radical centers due to their exceptional high kinetic stability^[203, 277, 278] and – in contrast to approaches based on 2,2,6,6-tetramethylpiperidinyloxy (TEMPO)^[279] – provide the possibility of conjugated attachment to π -scaffolds, enabling intramolecular spin coupling. Additionally, NNs are stable in various media^[204] and bear potential for applications like redox polymers^[280] or diarylethene based magnetic photo switches.^[205, 206] In the past, several electron rich PAHs^[232] and π -systems like benzodithiophenes,^[179] pyrene,^[180] azulene,^[188] polyacenes^[183, 184] or graphene-like nanoribbons^[281, 282] as well as alkyne-based molecular wires^[198] have been incorporated as linkers between two nitronyl nitroxide radical centers.

The most common synthetic strategy for NNs thereby involves a condensation reaction of the respective aldehyde with bis(hydroxylamine) derivatives to give the substituted *N,N'*-dihydroxy imidazolidines.^[185] Subsequent oxidation with high valent metal oxides or sodium periodate finally yields the nitronyl nitroxides.^[185] However, this procedure has several limitations including the limited solubility, stability and accessibility of the respective aldehydes. Furthermore, the *N,N'*-dihydroxy imidazolidines as primary reaction products frequently suffer fast decomposition, especially in the presence of electron withdrawing substituents.^[185, 186, 190, 193] Therefore, alternative approaches have been developed, utilizing a direct introduction of the nitronyl nitroxide moiety via transition metal catalyzed coupling

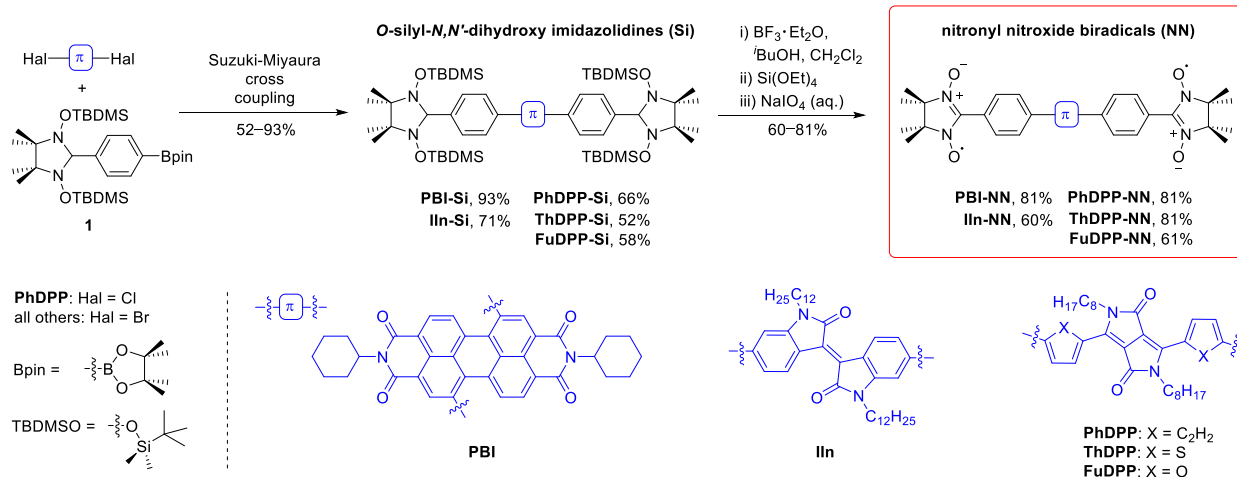
procedures^[192, 283, 284] or the usage of metal-organic gold^[187, 189], copper^[191] or zinc^[190] reagents. In addition, nucleophilic aromatic fluoride substitution^[194] has been successfully used. The drawback of these approaches is that they require highly activated aryl iodides, work for electron rich aromatic systems only, require expensive reagents and/or are limited to very special and inert perfluorinated substrates. Finally, Baumgarten and co-workers presented a boronic acid ester approach, in which a silyl-protected nitronyl nitroxide precursor unit is employed.^[202] By this means, a broadly applicable way for NN functionalization of the respective aryl halides via Suzuki-Miyaura cross coupling reaction followed by radical generation with tetra-*n*-butyl ammonium fluoride (TBAF) became accessible. Although this strategy might be widely applicable, it was so far only deployed to rather electron rich small aromatic oligomers. Hence, nitronyl nitroxide moieties have not yet been linked to the most common electron deficient pigment colorant cores although such radical decorated organic chromophores are considered to be useful for controlling spin polarization in organic semiconductors and modulating the excited states.^[285, 286]

Herein, we present a synthetic strategy toward electron poor nitronyl nitroxide biradicals via Suzuki-Miyaura cross coupling reaction and subsequent Lewis acid promoted deprotection of the resulting *O*-silyl-*N,N'*-dihydroxy imidazolidine precursors. In this way, five nitronyl nitroxide biradicals **PBI-NN**, **IIn-NN**, **PhDPP-NN**, **ThDPP-NN** and **FuDPP-NN** bearing common pigment colorant cores, i. e. perylene bisimide (PBI), isoindigo (IIn) and diketopyrrolopyrrole (DPP), were obtained as bench stable magenta, red, orange, purple and blue solids, respectively (Scheme 5.1). Notably, whereas the established TBAF deprotection procedure^[202] failed for our utilized electron poor systems, a Lewis acid assisted approach provided access to the desired NN biradicals in good to excellent yields.

5.3 Results and discussion

5.3.1 Synthesis

Nitronyl nitroxide precursors *O*-silyl-*N,N'*-dihydroxy imidazolidines **PBI-Si**, **IIn-Si**, **PhDPP-Si**, **FuDPP-Si** and **ThDPP-Si** were synthesized in 52–93% yield via Suzuki-Miyaura cross coupling reaction of boronic acid ester **1**^[202] and the respective halogenated PBI, IIn or DPP dyes (Scheme 5.1 and Scheme 8.3.1).

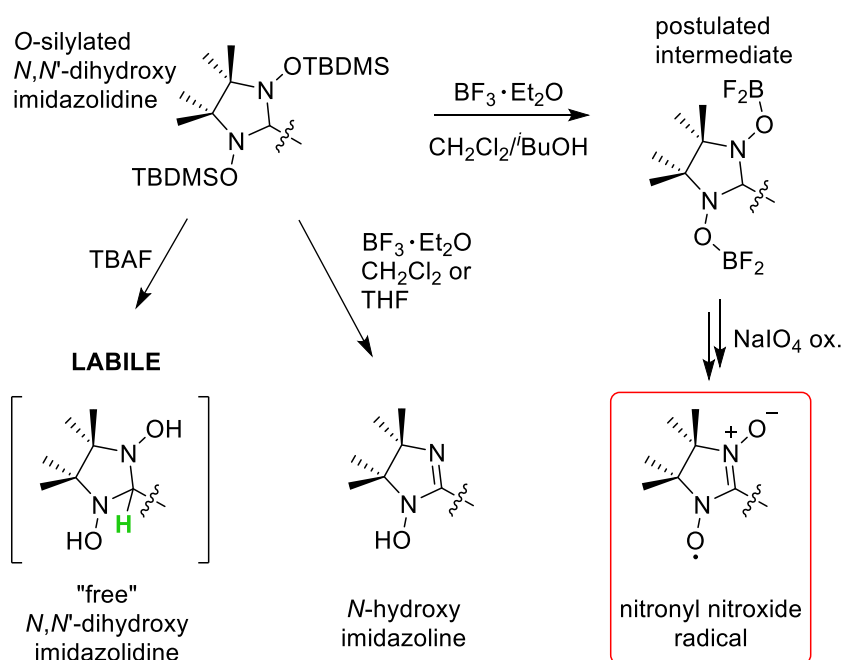


Scheme 5.1 | Synthesis of nitronyl nitroxide biradicals **PBI-NN**, **IIn-NN**, **PhDPP-NN**, **ThDPP-NN** and **FuDPP-NN** via Suzuki-Miyaura cross coupling reaction and subsequent deprotection/oxidation of the respective *O*-silylated *N,N'*-dihydroxy imidazolidines **PBI-Si**, **IIn-Si**, **PhDPP-Si**, **ThDPP-Si** and **FuDPP-Si** by Lewis acid promoted desilylation and periodate oxidation. Suzuki-Miyaura cross coupling conditions: $\text{Pd}(\text{PPh}_3)_4$, Na_2CO_3 , $\text{PhMe}/\text{EtOH}/\text{H}_2\text{O}$ (2:1:1), N_2 (for **PBI-Si**, **IIn-Si** and **FuDPP-Si**); $\text{Pd}(\text{OAc})_2$, SPhos, K_3PO_4 , $\text{THF}/\text{H}_2\text{O}$ (20:1), N_2 (for **PhDPP-Si**); $\text{Pd}(\text{dba})_2$, $\text{P}(o\text{-tol})_3$, Na_2CO_3 , $\text{THF}/\text{H}_2\text{O}$ (20:1), N_2 (for **ThDPP-Si**).

Attempting cleavage of the four *tert*-butyldimethylsilyl (TBDMS) protecting groups by the addition of tetra-*n*-butylammonium fluoride (TBAF) in THF solution following the procedure by Baumgarten and co-workers^[202] neither provided the respective *N,N'*-dihydroxy imidazolidines nor the desired nitronyl nitroxides. Instead, decomposition occurred as revealed by ESI mass spectrometry (Figure 8.3.1–8.3.5). Elimination of water and undefined redox processes are well known degradation pathways in the field of nitronyl nitroxide synthesis and appear frequently both in the presence of acidic and basic media or reagents.^[179, 204, 287] Therefore, the observed accelerated decomposition and enhanced sensitivity towards basic TBAF can possibly be explained by an increased acidity of the free *N,N'*-dihydroxy imidazolidine (Scheme 5.2, left, acidic proton highlighted in green) moieties due to the electron deficient dye cores, which leads to fast elimination of water and further formation of undefined species.^[185, 186, 190, 193]

Nevertheless, we achieved selective desilylation upon using $\text{BF}_3 \cdot \text{Et}_2\text{O}$ as a deprotection agent.^[288] However, in CH_2Cl_2 as well as in THF, mainly *N*-hydroxy imidazolines (Scheme 5.2, middle) as single and twofold water elimination products were formed and detected by ESI HRMS, as shown exemplarily for **PhDPP-Si** (Figure 8.3.6a, b). Hence, it is reasonable to conclude that the Lewis acidity of $\text{BF}_3 \cdot \text{Et}_2\text{O}$ in non- or moderately coordinating DCM or THF is too high, thereby causing dehydration. However, this undesired side reaction was circumvented by using *iso*-butanol (*t*-BuOH) as a suitable co-solvent (20–25 vol.-%), presumably forming a Lewis acid-base adduct^[289, 290] with boron fluoride ($\text{BF}_3 \cdot t\text{-BuOH}$). We assume that the treatment of TBDMS-ethers with BF_3 leads to the formation of difluoro borate esters^[288].

²⁹¹, ²⁹²] (Scheme 5.2, top right) instead of the “free” *N,N'*-dihydroxy imidazolidines. Possibly due to hydrolysis or fragmentation, these esters were not detected by ESI-HRMS. Subsequently, the reaction mixture was quenched after 24 h with tetraethyl orthosilicate (TEOS, Si(OEt)₄) to deactivate boron fluorides and capture HF under base-free conditions. Attempts to isolate the free *N,N'*-dihydroxy imidazolidines, e.g. by column chromatography or precipitation failed, confirming its low stability. Accordingly, we directly applied oxidation with aqueous NaIO₄ after quenching with TEOS. Subsequent purification by silica gel column chromatography provided the desired biradicals **PBI-NN**, **IIn-NN**, **PhDPP-NN**, **ThDPP-NN** and **FuDPP-NN** in remarkably high yields of 60–81% (Scheme 5.1), which were fully characterised by high resolution ESI mass spectrometry, ¹H NMR, electron paramagnetic resonance (EPR) and UV/vis absorption spectroscopy as well as cyclic voltammetry (CV).



Scheme 5.2 | Presumed desilylation pathways of TBDMS protected *N,N'*-dihydroxy imidazolidines upon addition of TBAF and boron fluoride.

5.3.2 UV/vis absorption and fluorescence spectroscopy

In order to explore the optical properties of the nitronyl nitroxide biradicals and the respective *O*-silylated *N,N'*-dihydroxy imidazolidines, UV/vis absorption and steady state fluorescence spectroscopy measurements (Figure 5.1 and Table 5.1) were performed under ambient conditions in CHCl₃ (PBI and IIn) or THF (DPPs) solution (different solvents for solubility reasons). Accordingly, the series of nitronyl

nitroxides covers a broad absorption range with maxima from 417 nm (**IIn-NN**) to 620 nm (**ThDPP-NN**).

Table 5.1 | Electronic absorption and fluorescence spectroscopic characteristics of silylated **PBI-Si**, **IIn-Si**, **PhDPP-Si**, **ThDPP-Si**, **FuDPP-Si** as well as biradicals **PBI-NN**, **IIn-NN**, **PhDPP-NN**, **ThDPP-NN**, **FuDPP-NN** in solution.

chromophore	λ_{abs} [nm]		ϵ [$\text{M}^{-1} \text{cm}^{-1}$]		λ_{em} [nm]		Φ_{FL} [%]		$\Delta\tilde{\nu}_{\text{abs}}^{\text{c}}$ [cm^{-1}]
	Si	NN	Si	NN	Si	NN	Si	NN	
PBI ^a	562	558	29900	22200	614	602	1	1	127
IIn ^a	525	525	12900	14500	–	–	–	–	0
	418	417	24900	31400	–	–	–	–	57
PhDPP ^b	491	497	25600	25600	561	569	94	2	246
ThDPP ^b	606	620	58700	48700	624	–	35	–	373
FuDPP ^b	598	616	89600	90000	607	–	37	–	488

$c \approx 10 \mu\text{M}$, rt. a) in CHCl_3 ; b) in THF; c) $\Delta\tilde{\nu}_{\text{abs}} = |\tilde{\nu}_{\text{abs, NN}} - \tilde{\nu}_{\text{abs, Si}}|$.

Notably, the UV/vis absorption maxima of the nitronyl nitroxides are almost unchanged with respect to the diamagnetic precursors ($\Delta\tilde{\nu}_{\text{abs}} \leq 488 \text{ cm}^{-1}$, Figure 5.1 and Table 5.1) and are slightly bathochromically shifted compared to the unsubstituted parent compounds^[230, 239, 258, 259, 293–295], which can be explained by the extension of the conjugated π -system by the additional phenylene groups. Larger deviations between the biradical and silylated precursors can be detected between 250 and 450 nm, due to the absorption of the nitronyl nitroxide radical unit in the shorter wavelength region.^[185, 204, 296] Furane and thiophene bridged DPP derivatives feature sharp absorption bands with pronounced vibronic progression (Figure 5.1, magenta and green lines), whereas the phenylene derivatives (Figure 5.1, blue lines) are characterized by broad, featureless absorption bands. This different behavior is well known among heteroaromatic diketopyrrolopyrroles and can be explained by the higher degree of planarity due to the sterically less demanding heterocyclic substituents.^[239, 295] The wavelength of the absorption maxima of the DPP derivatives show the order $\text{PhDPP} < \text{FuDPP} < \text{ThDPP}$, which is in agreement with the trend for the parent compounds.^[239, 295] This trend can be rationalized by a higher donor strength of the heteroaromatic compounds compared to PhDPP resulting in a pronounced push-pull interaction with the electron poor chromophore core. The characteristic spectral shape and colour of 6,6'-diaryl-IIn^[173] with two superimposed maxima between 400 and 600 nm and of 1,7-diaryl-PBI^[23] with one broad absorption band between 450 and 580 nm is resembled by the respective nitronyl nitroxide biradicals as

well. Thus, the absorption spectral signatures and maxima wavelengths of **PBI-NN**, **IIn-NN**, **PhDPP-NN**, **ThDPP-NN** and **FuDPP-NN** are hardly affected by chromophore-spin interactions.

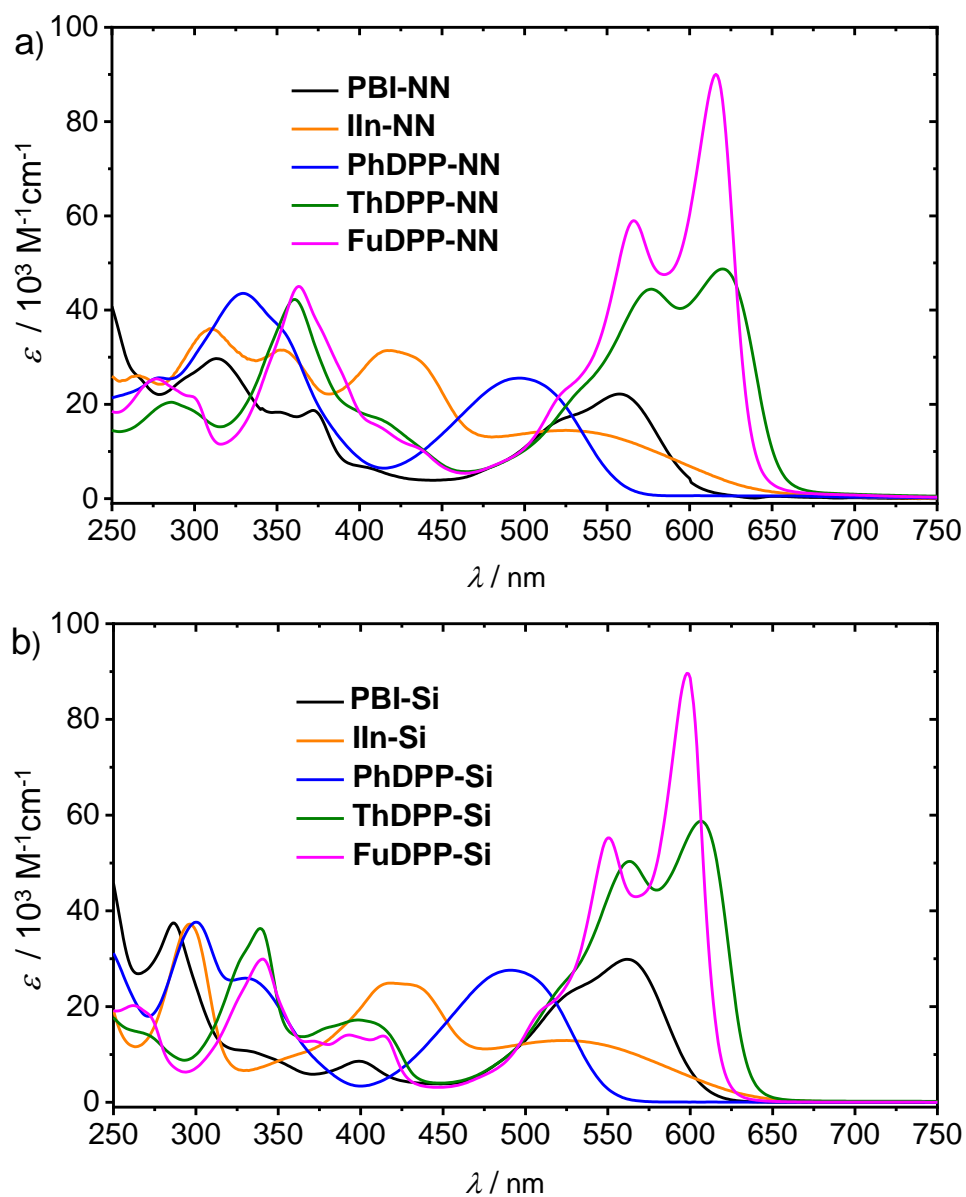


Figure 5.1 | UV/vis absorption spectra of (a) **PBI-NN** (black line), **IIn-NN** (orange line), **PhDPP-NN** (blue line), **ThDPP-NN** (green line) and **FuDPP-NN** (magenta line) and (b) **PBI-Si** (black line), **IIn-Si** (orange line), **PhDPP-Si** (blue line), **ThDPP-Si** (green line) and **FuDPP-Si** (magenta line) in solution (CHCl_3 for PBI and IIn as well as THF for all DPPs, $c \approx 10 \mu\text{M}$, rt).

Remarkably, UV/vis absorption spectra of biradicals **PBI-NN**, **IIn-NN**, **PhDPP-NN**, **ThDPP-NN** and **FuDPP-NN** stored under ambient conditions were recorded after several months and remained completely unchanged, indicating the extraordinary bench stability of these biradicals (Figure 8.3.24–8.3.28). We therefore overcame the tremendous disadvantage of analogous phenoxyl biradicals exhibiting highly different half-lives and rather unpredictable absorption spectra.^[23, 173] Furthermore, we investigated the steady state emission properties of all silyl precursors and nitronyl nitroxides. Like frequently reported for open shell compounds in general^[22, 297], all nitronyl nitroxides show no or only weak fluorescence, whereas **PhDPP-Si**, **FuDPP-Si** and **ThDPP-Si** exhibit decent emission^[239, 295] (Table 5.1 and Figure 8.3.24–8.3.28).

5.3.3 Cyclic voltammetry (CV) and differential pulse voltammetry (DPV)

As evidenced by UV/vis absorption spectroscopy, the optical properties of the five nitronyl nitroxide biradicals are mainly determined by the chromophore core with only minor contributions of the nitronyl nitroxide moieties. We therefore aimed to ascribe redox processes to the respective subunits as well and investigated the electrochemical properties of these biradicals in CH₂Cl₂ solution by cyclic voltammetry (CV) and differential pulse voltammetry (DPV). All NNs feature redox amphoterism with at least two reversible reductions and oxidations (Figure 5.2 and Figure 8.3.29–8.3.30).

Whereas highly different first reduction potentials were observed for the five NN biradicals, covering a range of more than 370 mV, the first oxidation potentials of the nitronyl nitroxides are very similar (Table 8.3.2). As oxidation potentials between 330 and 520 mV are typically observed for NNs in literature, the first oxidation process can be ascribed to the formation of an oxammonium cation from the respective (bi-)radical.^[180, 188, 190, 202, 280, 296, 298] This is further corroborated by analogous CV and DPV studies of the silylated precursors (Figure 8.3.29–8.3.30 and Table 8.3.1), which reveal a similar redox behavior as observed for the respective nitronyl nitroxides, but the pronounced oxidation event at 366–422 mV (all potentials vs. Fc^{0/+}), being observed for all NN, is absent in **PBI-Si**, **IIn-Si** and **PhDPP-Si**. Electron rich **ThDPP-Si** and **FuDPP-Si** exhibit an additional oxidation process between 300 and 400 mV (Figure 8.3.30), which can be ascribed to the DPP chromophore oxidation, although these processes occur at slightly higher potentials (500 mV) in the unsubstituted parent chromophore^[243] due to the smaller π -system. Thus, we conclude a superposition of the nitroxide and chromophore core oxidation in the case of **ThDPP-NN** and **FuDPP-NN** (Figure 5.2 and Figure 8.3.30), being also reflected by the larger relative peak area compared to the other potentials (Figure 5.2).

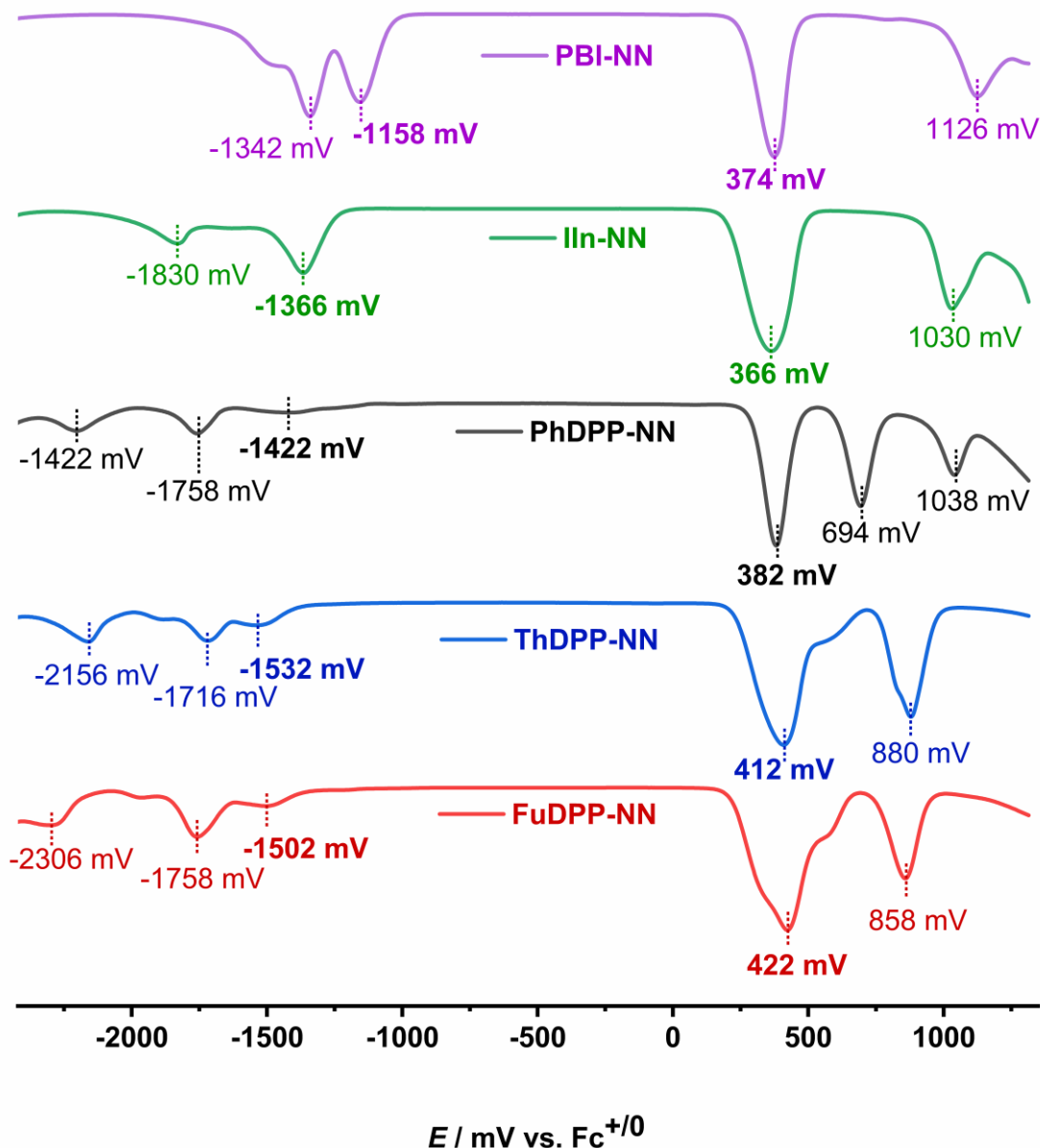


Figure 5.2 | Differential pulse voltammograms (DPV) of **PBI-NN**, **IIn-NN**, **PhDPP-NN**, **ThDPP-NN** and **FuDPP-NN** (from the top) with potentials of reversible reductions and oxidations in (CH_2Cl_2 , $c \approx 20 \mu M$, electrolyte: $0.1 M nBu_4NPF_6$, rt).

The first reduction potentials of all five NN biradicals decrease in the order: **PBI-NN** > **IIn-NN** > **Ph-NN** > **Fu-NN** > **Th-NN**. Hence, **PBI-NN** (−1158 mV) is the most easily reducible biradical, whereas reduction of **ThDPP-NN** as the most electron rich compound appears at the lowest potential (−1532 mV).

In contrast to the oxidation process, reduction potentials of NNs are hardly reported in literature and are thus much less indicative. For instance, reduction potentials between -1270 and -1330 mV have been reported for NN-containing redox polymers or fused thiophene systems,^[280, 298] however, these reduction potentials strongly depend on the π -system. Accordingly, it can be concluded that the electron accepting properties (reduction) are strongly driven by the chromophore core and reflect its electron affinity, whereas the first oxidation potential is determined by the nitronyl nitroxide radical moiety.

5.3.4 ^1H NMR and EPR spectroscopy

In order to examine the magnetic properties of the nitronyl nitroxide biradicals, ^1H NMR and EPR spectroscopy have been performed at room temperature. All nitronyl nitroxides are NMR silent in the aromatic region of the respective ^1H NMR spectrum, whereas well detectable signals are observed in the aliphatic region and can be ascribed to the protons of the alkyl chains (Figure 5.3a bottom and Figure 8.3.9, 8.3.15, 8.3.18 and 8.3.21). Distinct signal broadening is commonly observed for protons of spin bearing aromatic systems and is therefore a strong experimental evidence for a pronounced (bi)radical contribution in the ground state.^[23, 173] In contrast, diamagnetic precursors **PBI-Si**, **IIn-Si**, **PhDPP-Si**, **ThDPP-Si** and **FuDPP-Si** expectedly show well resolved resonance signals (Figure 5.3a top and Figure 8.3.7, 8.3.13, 8.3.16 and 8.3.19) giving no hints for a radical contribution.

In agreement to the results obtained from the NMR studies, intense signals are observed in the electron paramagnetic resonance (EPR) spectra for all nitronyl nitroxides (Figure 5.3b and Figure 8.3.31) confirming a pronounced biradical character. All signals are centered at $g_{\text{iso}} = 2.0066$ – 2.0067 and feature nine lines with almost identical hyperfine splitting constants of $a(^{14}\text{N}) = 10.3$ – 10.6 MHz (≈ 3.7 – 3.8 G, Table 8.3.4). This suggests spin coupling to four equivalent nitrogen nuclei (^{14}N), as such nine-line spectra are commonly observed for twofold nitronyl nitroxide substituted compounds with a strong intramolecular spin exchange interaction of $|J| \gg |a(2\text{N})|$ between the radical sites^[198, 204], which is an experimental proof for the biradical nature of **PBI-NN**, **IIn-NN**, **PhDPP-NN**, **ThDPP-NN** and **FuDPP-NN**. Thus, strong intramolecular spin coupling between the two nitronyl nitroxide units can be concluded.

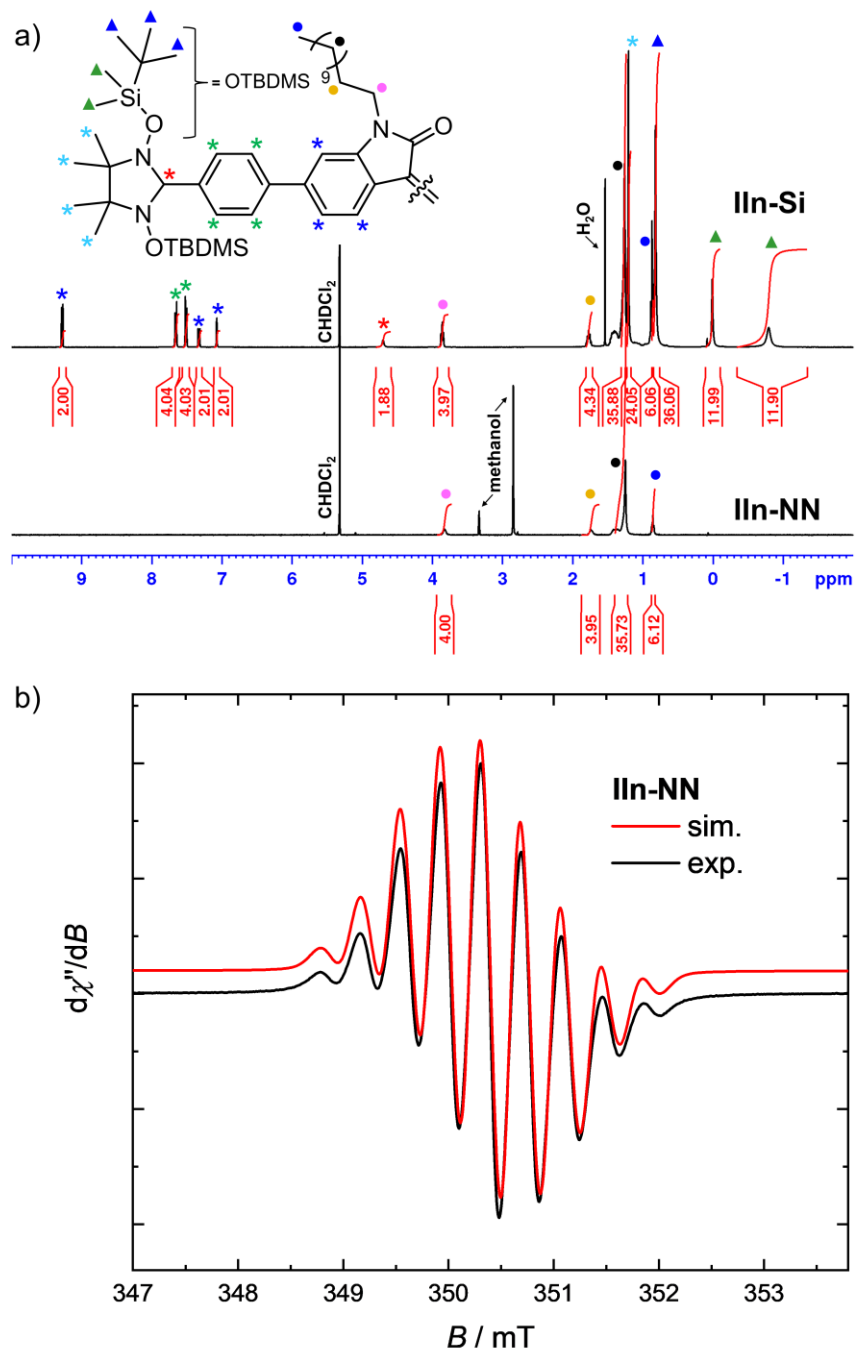


Figure 5.3 | (a) ¹H NMR spectra (400 MHz, 298 K) of **IIIn-Si** (top, CD₂Cl₂) and **IIIn-NN** (bottom, CD₂Cl₂/CD₃OD (9:1), methanol added for solubility reasons). (b) Experimental (black) and simulated (red) continuous-wave (CW) X-band EPR spectra of **IIIn-NN** in a CH₂Cl₂/MeOH (9:1) mixture at room temperature ($c \approx 1$ mM).

5.3.5 Single crystal X-ray diffraction analysis

In addition, the molecular structure of **IIn-NN** was confirmed representatively for all nitronyl nitroxides by single crystal X-ray diffraction analysis (Figure 5.4). Suitable crystals without solvent molecules were obtained by slow diffusion of methanol into a solution of **IIn-NN** in CH_2Cl_2 at 7 °C. The isoindigo biradical crystallises in the triclinic space group ($P\bar{1}$) and shows a stair case like packing arrangement with close distances between next-neighbouring chromophores of 3.26–3.47 Å (π - π -stacking, Figure 5.4a, b and Figure 8.3.22a, b). The determined bond lengths are almost unchanged compared to the unsubstituted parent chromophore^[299] and do not show any quinoidal alternation. In particular, all bonds in the bridging phenylene unit (Figure 5.4c, highlighted in red) exhibit comparable lengths between 1.382 Å and 1.403 Å, indicating a pronounced aromatic character. Accordingly, the two bonds connecting the phenyl bridge with the IIn core and the nitronyl nitroxide moiety (Figure 5.4c, highlighted in blue) show lengths of 1.483 Å and 1.456 Å, which equals a typical single bond length between two sp^2 -hybridized carbon atoms.^[202, 300, 301] Notably, the determined molecular structure is not centrosymmetric (Figure 5.4c) and slightly different bond lengths with an average deviation < 0.005 Å are observed between both parts of the molecule (note that only one part is shown in Figure 5.4c; for details see Figure 8.3.23).

Furthermore, the nitronyl nitroxide moiety and the phenylene linker are not coplanar to the isoindigo core, but show a rotation along the C–C-axis by 13.81–22.80° and 13.78–36.33°, respectively (Figure 5.4c). In addition, both N–O and N–C bonds in the nitronyl nitroxide O–N–C–N–O unit feature almost equal lengths (Figure 5.4c, highlighted in green), which is well in line with a spin delocalization over this pentad.^[202] In summary, our bond length analysis based on X-ray structural information reveals no pronounced quinoidal character and therefore further supports our assumption of a dominating open shell character of **IIn-NN**. Based on the single bond character of the C–C bonds in **IIn-NN** that connects the phenyl group with the NN moiety and the IIn core (Figure 5.4c, highlighted in blue), a singlet closed-shell ground state can be excluded. However, a differentiation between the singlet and triplet open-shell state is not possible based on X-ray analysis. In this regard, Ovchinnikov's parity model^[102] allows a prediction of the terminal spin orientation (Chart 8.3.1).^[202] Based on this model, it is reasonable to assume an antiparallel spin orientation and thus a singlet open shell ground state for all five nitronyl nitroxide biradicals.

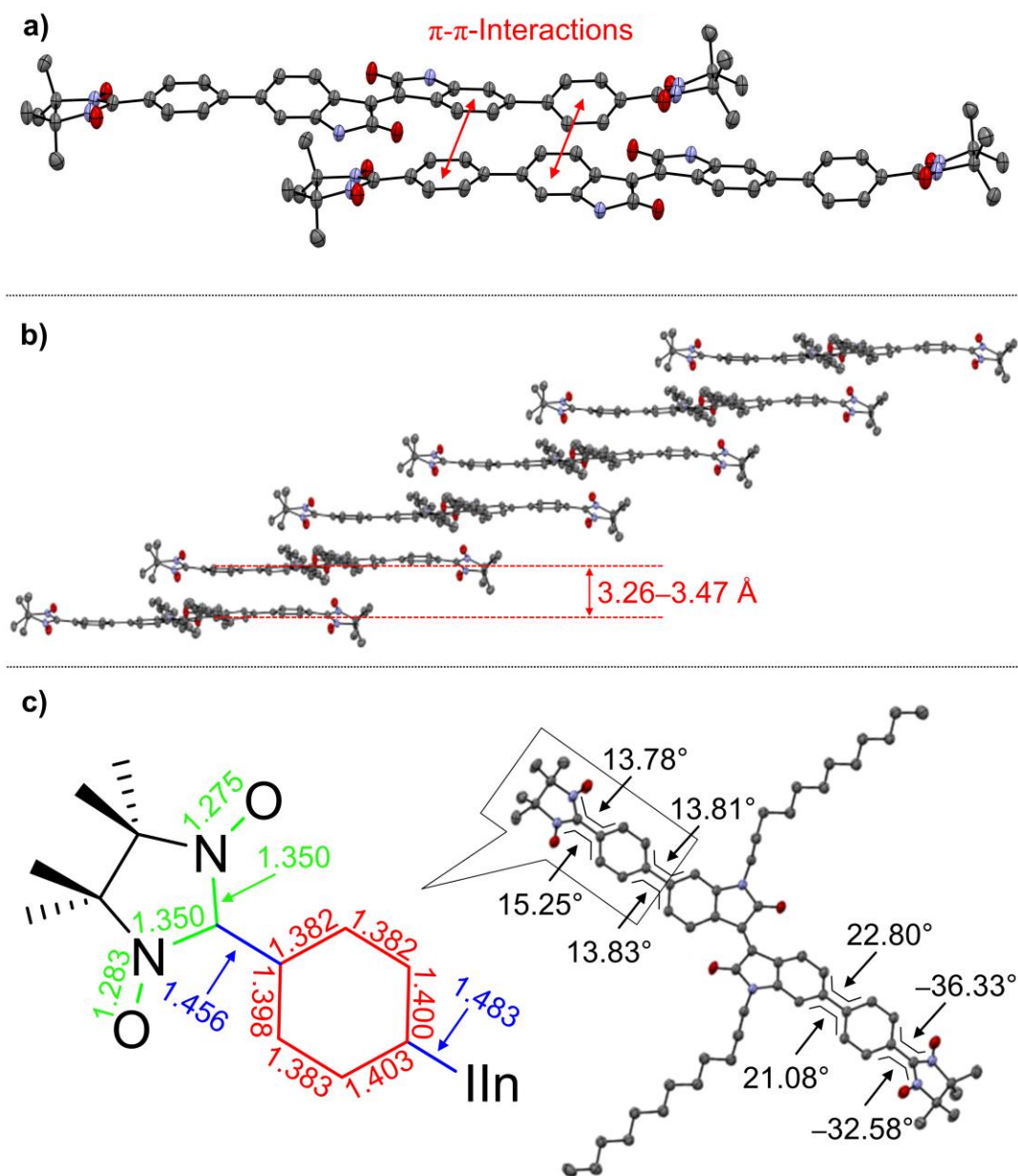
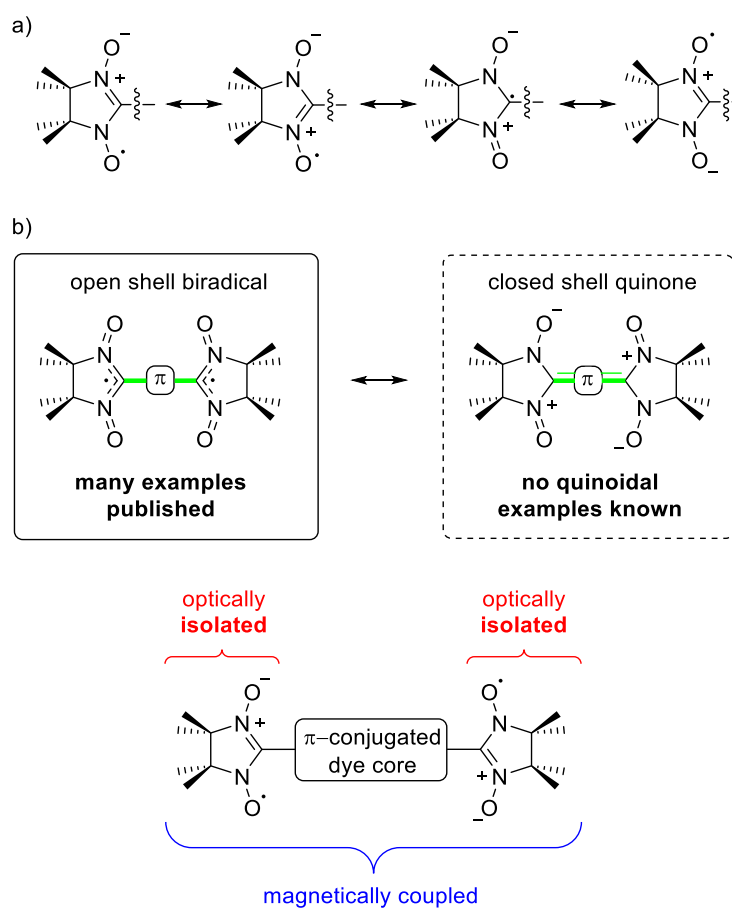


Figure 5.4 | (a) Solid state molecular packing of **II n-NN** with π - π -interactions, (b) side view of **II n-NN** with π - π -distances and (c) solid state molecular structure of **II n-NN** with selected bond lengths in Å and torsion angles determined by single crystal X-ray diffraction (ellipsoids set to 50 % probability, carbon gray, nitrogen blue, oxygen red). H atoms are omitted for clarity.

The spin bearing nitronyl nitroxide O-N-C-N-O pentad is stabilized by several resonance structures (Scheme 5.3a) leading to significant spin delocalization and N-O/N-C bond lengths between single (1.40 ± 0.02 Å/ 1.36 ± 0.02 Å)^[301] and double bond (1.23 ± 0.02 Å/ 1.30 ± 0.02 Å)^[301] as revealed by X-ray

analysis for **II**n-NN (*vide supra*) and other NNs in literature.^[179, 180, 188, 202] However, this delocalization cannot extend into the connecting π -system. Thus, upon formation of a closed shell Kekulé structure with a double bond between the NN unit and the π -core, the π -conjugation path within the nitronyl nitroxide O-N-C-N-O pentad would be disrupted (Scheme 5.3b). Such a switch in resonance has been recently observed for cyanine/merocyanine bifurcated conjugation paths^[302] but is obviously energetically disfavored for nitronyl nitroxides. Accordingly, unlike phenoxy-based biradical(oid)s,^[23, 173] a quinoidal structure (Scheme 5.3b, dashed box) has no significant contribution to the ground state of NN biradicals.^[198] Only single bonded open shell nitronyl nitroxides (Scheme 5.3b, solid box, bond highlighted in green) are reported with bond lengths of 1.452–1.472 Å for moderately to highly electron poor derivatives^[180, 184, 190, 192, 194, 283, 284] and of 1.414–1.433 Å for electron rich^[179, 202] systems (typical bond lengths: $d(\text{C}_{\text{sp}2}=\text{C}_{\text{sp}2}) = 1.32\pm 0.02$ Å and $d(\text{C}_{\text{sp}2}-\text{C}_{\text{sp}2/\text{aryl}}) = 1.46\pm 0.03$)^[300, 301]. Shorter bond lengths in the case of electron rich systems may arise from charge transfer (CT) from the electron rich π -system to the rather electron poor nitronyl nitroxide unit.



Scheme 5.3 | (a) Selected resonance structures of the nitronyl nitroxide radical unit as well as (b) open and closed shell resonance structures of π -bridged NN biradical(oid)s with schematic illustration of optical and magnetic coupling properties.

In addition, the NN pentagon usually shows a contortion towards the attached π -scaffold along the bond highlighted in green (Scheme 5.3b) with dihedral angles of 4–11° for thiophene^[179, 202] and of 15–29° for benzene-based π -cores.^[180, 202] In the case of **IIn-NN**, even larger dihedral angles of 13–36° were determined by X-ray analysis. Thus, the bond order as well as the dihedral angles indicate a significant reduction of conjugation between the NN moiety and the π -scaffold. Accordingly, despite their covalent attachment to the π -conjugated PBI, IIn and DPP dye cores, the nitronyl nitroxide units remain electronically isolated as evidenced by X-ray analysis (**IIn-NN**) and especially UV/vis absorption spectroscopy. For this reason, no electronic coupling between the spin centers and the colorant core can be observed for **PBI-NN**, **IIn-NN**, **PhDPP-NN**, **ThDPP-NN** and **FuDPP-NN**.

Unlike the rather weak electronic radical-chromophore-interactions, spin-spin exchange interactions in (small) conjugated nitronyl nitroxide biradicals can be much more pronounced, presumably due to a tunneling effect.^[198] Therefore, twofold conjugated spin decoration of colorants like PBI, IIn or DPP with nitronyl nitroxide moieties leads to biradicals with large spin-spin exchange interactions but electronically isolated radical centers.

5.4 Conclusion

In conclusion, we have synthesized five novel nitronyl nitroxide biradicals based on perylene bisimide, isoindigo and diketopyrrolopyrrole chromophore scaffolds from the respective *O*-silylated precursors by a sequential one pot Lewis acid promoted deprotection and subsequent periodate oxidation procedure. Notably, we used base-free deactivation of $\text{BF}_3 \cdot \text{Et}_2\text{O}$ with $\text{Si}(\text{OEt})_4$ as a key step to circumvent substrate decomposition. The procedure is applicable for a variety of electron poor pigment colorants systems with yields up to 81%. CV and DPV measurements revealed that the first reduction potentials of **PBI-NN**, **IIn-NN**, **PhDPP-NN**, **ThDPP-NN** and **FuDPP-NN** strongly depend on the chromophore core and cover a potential range of more than 370 mV. The bridging perylene bisimide core endows **PBI-NN** with pronounced electron accepting properties ($E_{\text{red}} = -1158$ mV) and magnetic spectroscopy of all nitronyl nitroxides as well as X-ray diffraction analysis in the case of **IIn-NN** substantiated the open shell character of these biradicals. Accordingly, we successfully preserved the intrinsic optical and electrical chromophore properties whilst strong spin coupling was observed between the two distant radical centers in these electron deficient biradicals. Thus, we presented a general method for the spin decoration of electron-poor π -systems with nitronyl nitroxide radical moieties.

5.5 Experimental section

General Methods. Silica-gel column chromatography was performed on silica gel (particle size of 0.040–0.063 mm) with freshly distilled solvents. ^1H NMR and ^{13}C NMR spectra were recorded on a Bruker Avance III HD 400 spectrometer at 298 K. Chemical shift data are reported in parts per million (ppm, δ scale) downfield (for positive shifts) or upfield (for negative shifts) from tetramethylsilane and referenced internally to the residual proton (for proton NMR) in the solvent (CDCl_3 , $\delta = 7.26$; CD_2Cl_2 , $\delta = 5.32$) or to the carbon resonance (CDCl_3 , $\delta = 77.16$; CD_2Cl_2 , $\delta = 53.84$). The coupling constants are listed in Hertz and multiplicities abbreviated as follows: s = singlet, d = doublet, t = triplet, q = quartet, m = multiplet, vt = virtual, br = broad. MALDI TOF measurements were carried out on a Bruker Daltonics (Autoflex II) mass spectrometer. High-resolution ESI TOF spectra were acquired on a Bruker Daltonics microTOF focus spectrometer. Melting points were measured with an Olympus BX41 polarization microscope connected to a TP84 Linkam scientific temperature regulator. UV/vis absorption spectra were recorded on a JASCO V-770 or V-670 spectrometer (scan rate 400 nm/s). Fluorescence spectra were recorded with a FLS980 Edinburgh Instrument fluorescence spectrometer. Cyclic voltammetry (CV) and differential pulse voltammetry (DPV) were conducted on an EC epsilon standard electrochemical analyzer. A Pt disc electrode was used as the working electrode, a platinum wire as the counter electrode, and a Ag/AgCl reference electrode using the ferrocenium/ferrocene (Fc^+/Fc) redox couple as the internal standard. The measurements were conducted in dichloromethane solutions (0.1 M) and tetra-*n*-butylammonium hexafluorophosphate as an electrolyte with a scan rate of 100 mV/s at room temperature. Boronic acid ester **1**^[202], as well as dibrominated PBI **2**^[303], In **3**^[304] and DPPs **4**, **5** and **6**^[305–307] (Scheme S3) were synthesized according to literature procedures. EPR measurements at X-band (9.38 GHz) were carried out using a Bruker ELEXSYS E580 CW EPR spectrometer equipped with an Oxford Instruments helium cryostat (ESR900) and a MercuryITC temperature controller. Single crystal X-ray diffraction data for **In-NN** were collected at 100 K on a Bruker D8 Quest Kappa diffractometer with a Photon II CPAD detector and multi-layered mirror monochromated CuK_α radiation.

PBI-Si. 1,7-Dibromo-PBI **2** (100 mg, 140 μmol , 1.00 equivalent), boronic acid ester **1** (245 mg, 421 μmol , 3.00 equivalents) and sodium carbonate (446 mg, 4.21 mmol, 30.0 equivalents) were suspended in a mixture of toluene/ethanol/water 2:1:1 (12 mL) under an atmosphere of nitrogen. The reaction mixture was stirred for 20 minutes and subsequently tetrakis(triphenylphosphine)palladium(0) (32.4 mg, 28.1 μmol , 20.0 mol%) dissolved in toluene (0.5 mL) was added. The reaction mixture was heated to 80 °C in an oil bath, stirred for 20 hours and then cooled down to room temperature. The crude product was extracted with Et_2O (2 x 50 mL), the combined organic layers washed with water, dried over MgSO_4 and the solvent removed under reduced pressure. The crude product was purified by silica

gel column chromatography using CH₂Cl₂/cyclohexane (1:3) as an eluent to yield **PBI-Si** as a red solid. Yield: 193 mg (131 μmol, 93 %). m. p. 174–175 °C. ¹H NMR (400 MHz, CD₂Cl₂): δ = 8.42 (s, 2 H), 8.11 (d, *J* = 8.1 Hz, 2 H), 8.05 (d, *J* = 8.1 Hz, 2 H), 7.59–7.51 (m, 8 H), 4.98 (m, 2 H), 4.73 (s, 2 H), 2.59–2.44 (m, 4 H), 1.94–1.84 (m, 4 H), 1.78–1.72 (m, 4 H), 1.51–1.28 (m, 8 H), 1.22 (s, 12 H), 1.20 (s, 12 H), 0.89 (s, 36 H), 0.08 (s, 12 H), –0.55 (s, 12 H). ¹³C NMR (101 MHz, CD₂Cl₂): δ = 164.2, 163.9, 143.0, 141.2, 135.9, 135.1, 132.9, 132.5, 130.7, 129.6 (2 signals), 128.9 (2 signals), 128.0, 123.3, 122.9, 68.6, 30.2, 29.5, 26.9, 26.5, 25.9, 25.0, 18.3, 17.5, –3.5, –4.2. HRMS (ESI-TOF) *m/z*: [M+H]⁺ calcd for C₈₆H₁₂₃N₆O₈Si₄⁺ 1479.8474; Found 1479.8409. MS (MALDI-ToF, neg. mode, CHCl₃) *m/z*: [M][–] Calcd for C₈₆H₁₂₂N₆O₈Si₄[–] 1478.8407; Found 1478.8396. UV/vis (CHCl₃, *c* = 1.00 · 10^{–5} M): λ_{max} [nm] (ε_{max} [M^{–1} cm^{–1}]) = 562 (29900). Fluorescence (CHCl₃, λ_{ex} = 505 nm): λ_{em} [nm] = 614 (Φ_{FL} = 0.01, standard: *N,N*-bis(2,6-diisopropylphenyl)-1,6,7,12-tetraphenoxy-3,4,9,10-perylenetetracarboxylic bisimide, “Lumogen/ perylene red”, CAS: 123174–58–3, Φ_{FL} = 0.96 in CHCl₃).^[308] CV (CH₂Cl₂, *c* = 2 · 10^{–3} M, 0.1 M TBAPF₆, [V] vs. Fc⁺⁰, 298 K): *E*_{1/2 red} = –1.373, –1.174; *E*_{1/2 ox} = 0.901, 1.243.

IIn-Si. 6,6'-dibromo-IIn **3** (150 mg, 198 μmol, 1.00 equivalent), boronic acid ester **1** (351 mg, 595 μmol, 3.00 equivalents) and sodium carbonate (630 mg, 5.95 mmol, 30.0 equivalents) were suspended in a mixture of toluene/ethanol/water 2:1:1 (15 mL) under an atmosphere of nitrogen. The reaction mixture was stirred for 20 minutes and subsequently tetrakis(triphenylphosphine)palladium(0) (22.9 mg, 19.8 μmol, 10.0 mol%) dissolved in toluene (0.5 mL) was added. The reaction mixture was heated to 80 °C in an oil bath, stirred for 20 hours and then cooled down to room temperature. The crude product was extracted with Et₂O (2 x 50 mL), the combined organic layers were washed with water, dried over MgSO₄ and the solvent removed under reduced pressure. The crude product was purified by silica gel column chromatography using CH₂Cl₂/cyclohexane (4:1) as an eluent to yield **IIn-Si** as a red solid. Yield: 213 mg (140 μmol, 71 %). m. p. 151 °C. ¹H NMR (400 MHz, CD₂Cl₂): δ = 9.27 (d, *J* = 8.4 Hz, 2 H), 7.66 (d, *J* = 8.4 Hz, 4 H), 7.51 (d, *J* = 8.4 Hz, 4 H), 7.33 (dd, *J* = 1.4 Hz, *J* = 8.5 Hz, 2 H), 7.08 (d, *J* = 1.4 Hz, 2 H), 4.70 (s, 2 H), 3.86 (t, *J* = 7.3 Hz, 4 H), 1.83–1.71 (m, 4 H), 1.29–1.24 (m, 36 H), 1.21 (s, 24 H), 0.87 (t, *J* = 7.1 Hz, 6 H), 0.82 (s, 36 H), 0.01 (s, 12 H), –0.79 (s, 12 H). ¹³C NMR (101 MHz, CD₂Cl₂): δ = 168.6, 146.0, 145.2, 140.2, 132.8, 131.9, 130.5, 126.5 (2 signals), 121.4, 120.7, 106.5, 68.4, 40.3, 32.3, 30.1 (2 signals), 30.0 (3 signals), 29.8, 28.0, 27.4, 26.4, 24.9, 23.1, 18.2, 17.4, 14.3, –3.7, –4.8. HRMS (ESI-TOF) *m/z*: [M+H]⁺ Calcd for C₉₀H₁₅₁N₆O₆Si₄⁺ 1524.0767; Found 1524.0731. MS (MALDI-ToF, pos. mode, CHCl₃) *m/z*: [M+H]⁺ Calcd for C₉₀H₁₅₁N₆O₆Si₄⁺ 1524.0767; Found 1524.0798. UV/vis (CHCl₃, *c* = 1.00 · 10^{–5} M): λ_{max} [nm] (ε_{max} [M^{–1} cm^{–1}]) = 525 (12900). CV (CH₂Cl₂, *c* = 2 · 10^{–3} M, 0.1 M TBAPF₆, [V] vs. Fc⁺⁰, 298 K): *E*_{1/2 red} = –1.798, –1.326; *E*_{1/2 ox} = 1.062.

PhDPP-Si. Palladium(II) acetate (1.93 mg, 8.60 μmol , 5.00 mol%), DPP **4** (100 mg, 172 μmol , 1.00 equivalent), boronic acid ester **1** (305 mg, 517 μmol , 3.00 equiv.), 2-dicyclohexylphosphino-2',6'-dimethoxybiphenyl (SPhos, 7.06 mg, 17.2 μmol , 10.0 mol%) and potassium phosphate (219 mg, 1.03 mmol, 6.00 equivalents) were suspended in a mixture of THF/water 20:1 (10.5 mL) under an atmosphere of nitrogen. The reaction mixture was stirred at 80 °C in an oil bath for 18 hours. The suspension was cooled down to room temperature and the crude product was extracted with CH_2Cl_2 (2 x 50 mL). The combined organic layers were washed with water, dried over MgSO_4 and the solvent was removed under reduced pressure. The crude product was purified by silica gel column chromatography using CH_2Cl_2 /hexane (gradient from 1:4 to 1:1) as an eluent to yield **PhDPP-Si** as an orange solid. Yield: 162 mg (113 μmol , 66 %). m. p. 222–223 °C. ^1H NMR (400 MHz, CD_2Cl_2): δ = 7.92 (d, J = 8.6 Hz, 4 H), 7.83 (d, J = 8.6 Hz, 4 H), 7.66 (d, J = 8.3 Hz, 4 H), 7.52 (d, J = 8.3 Hz, 4 H), 4.69 (s, 2 H), 3.80 (t, J = 7.7 Hz, 4 H), 1.65–1.56 (m, 4 H), 1.27–1.21 (m, 20 H), 1.20 (s, 24 H), 0.84 (t, J = 6.8 Hz, 6 H), 0.87–0.77 (m, 36 H), –0.00 (s, 12 H), –0.82 (s, 12 H). ^{13}C NMR (101 MHz, CD_2Cl_2): δ = 162.9, 148.2, 143.9, 139.7, 131.9, 129.6 (2 signals), 127.5 (2 signals), 126.6, 110.3, 68.4, 42.1, 32.1, 29.8, 29.5, 29.4, 27.0, 26.4, 24.9, 23.0, 18.2, 17.3, 14.3, –3.7, –4.9. HRMS (ESI-TOF) m/z : $[\text{M}+\text{H}]^+$ Calcd for $\text{C}_{84}\text{H}_{137}\text{N}_6\text{O}_6\text{Si}_4^+$ 1437.9671; Found: 1437.9609. MS (MALDI-ToF, pos. mode, CHCl_3) m/z : $[\text{M}+\text{H}]^+$ Calcd for $\text{C}_{84}\text{H}_{137}\text{N}_6\text{O}_6\text{Si}_4^+$ 1437.9671; Found 1437.9560. UV/vis (THF, $c = 1.00 \cdot 10^{-5}$ M): λ_{max} [nm] (ϵ_{max} [$\text{M}^{-1}\text{cm}^{-1}$]) = 491 (25600). Fluorescence (THF, $\lambda_{\text{ex}} = 470$ nm): λ_{em} [nm] = 561 ($\Phi_{\text{FL}} = 0.94$, standard: *N,N*-bis(2,6-diisopropylphenyl)-3,4,9,10-perylenetetracarboxylic bisimide, “Lumogen/ perylene orange”, CAS: 82953–57–9, $\Phi_{\text{Fl}} = 1.00$ in CHCl_3).^[308] CV (CH_2Cl_2 , $c = 2 \cdot 10^{-3}$ M, 0.1 M TBAPF₆, [V] vs. $\text{Fc}^{+/0}$, 298 K): $E_{1/2\text{red}} = -1.719$; $E_{1/2\text{ox}} = 0.695$, 1.031.

ThDPP-Si. Bis(dibenzylideneacetone)palladium(0) (5.66 mg, 9.85 μmol , 6.67 mol%), DPP **5** (100 mg, 147 μmol , 1.00 equivalent), boronic acid ester **1** (260 mg, 441 μmol , 3.00 equivalents), tris(2-methylphenyl)phosphane (*P(o-tol)*₃, 5.81 mg, 19.1 μmol , 13.0 mol%) and sodium carbonate (276 mg, 2.60 mmol, 17.7 equivalents) were suspended in a mixture of THF/water 20:1 (10.5 mL) under an atmosphere of nitrogen. The reaction mixture was stirred at 80 °C in an oil bath for 18 hours. The suspension was cooled down to room temperature and the crude product was extracted with CH_2Cl_2 (2 x 50 mL). The combined organic layers were washed with water, dried over MgSO_4 and the solvent was removed under reduced pressure. The crude product was purified by silica gel column chromatography using CH_2Cl_2 /hexane (gradient from 1:4 to 1:2) as an eluent to yield **ThDPP-Si** as a blue solid. Yield: 111 mg (76.5 μmol , 52 %). m. p. 96 °C. ^1H NMR (400 MHz, CD_2Cl_2): δ = 8.97 (d, J = 4.2 Hz, 2 H), 7.68 (d, J = 8.3 Hz, 4 H), 7.56–7.52 (m, 2 H), 7.48 (d, J = 8.3 Hz, 4 H), 4.67 (s, 2 H), 4.13 (t, J = 8.0 Hz, 4 H), 1.84–1.74 (m, 4 H), 1.52–1.25 (m, 20 H), 1.19 (s, 24 H), 0.88 (t, J = 6.8 Hz, 6 H), 0.81 (s, 36 H), –0.01 (s, 12 H), –0.79 (s, 12 H). ^{13}C NMR (101 MHz, CD_2Cl_2): δ = 161.5, 150.2, 139.6, 136.9, 133.0,

132.1, 129.1, 125.5 (2 signals), 124.7, 108.4, 68.5, 42.5, 32.2, 30.4, 29.6, 27.3, 26.4, 24.9, 23.0, 18.2, 17.4, 14.3, -3.7, -4.7. HRMS (ESI-TOF) m/z : $[M]^+$ Calcd for $C_{80}H_{132}N_6O_6S_2Si_4^+$ 1448.8721; Found: 1448.8787. MS (MALDI-ToF, neg. mode, $CHCl_3$) m/z : $[M]^-$ Calcd for $C_{80}H_{132}N_6O_6S_2Si_4^-$ 1448.8732; Found 1448.9551. UV/vis (THF, $c = 1.00 \cdot 10^{-5}$ M): λ_{max} [nm] (ϵ_{max} [$M^{-1} cm^{-1}$]) = 606 (58700). Fluorescence (THF, $\lambda_{ex.} = 560$ nm): λ_{em} [nm] = 624 ($\Phi_{FL} = 0.35$, standard: 3,7-bis(diethylamino)-phenoxazinium perchlorate, „Oxazine 1“, CAS: 24796-94-9, $\Phi_{Fl} = 0.11$ in EtOH).^[309] CV (CH_2Cl_2 , $c = 2 \cdot 10^{-3}$ M, 0.1 M TBAPF₆, [V] vs. $Fc^{+/0}$, 298 K): $E_{1/2 red} = -1.602$; $E_{1/2 ox} = 0.384, 0.858$.

FuDPP-Si. DPP **6** (105 mg, 162 μ mol, 1.00 equiv.), boronic acid ester **1** (287 mg, 486 μ mol, 3.00 equiv.) and sodium carbonate (310 mg, 2.92 mmol, 18.0 equiv.) were suspended in a mixture of toluene/ethanol/water 2:1:1 (16 mL) under an atmosphere of nitrogen. The reaction mixture was heated to 80 °C in an oil bath and tetrakis(triphenylphosphine)palladium(0) (18.7 mg, 16.2 μ mol, 10.0 mol%) dissolved in toluene (0.5 mL) was added. After stirring the reaction mixture for 18 hours, the suspension was cooled down to room temperature and the crude product was extracted with Et₂O (2 x 50 mL). The combined organic layers were washed with water, dried over MgSO₄ and the solvent was removed under reduced pressure. The crude product was purified by silica gel column chromatography using CH_2Cl_2 /hexane (1:1) as an eluent to yield **FuDPP-Si** as a blue solid. Yield: 134 mg (94.6 μ mol, 58 %). m. p. 112–113 °C. ¹H NMR (400 MHz, CD_2Cl_2): $\delta = 8.38$ (d, $J = 3.8$ Hz, 2 H), 7.73 (d, $J = 8.4$ Hz, 4 H), 7.50 (d, $J = 8.4$ Hz, 4 H), 7.01 (d, $J = 3.8$ Hz, 2 H), 4.67 (s, 2 H), 4.23 (t, $J = 7.7$ Hz, 4 H), 1.88–1.77 (m, 4 H), 1.40–1.24 (m, 20 H), 1.14 (s, 24 H), 0.86 (t, $J = 7.0$ Hz, 6 H), 0.81 (s, 36 H), 0.00 (s, 12 H), -0.81 (s, 12 H). ¹³C NMR (101 MHz, CD_2Cl_2): $\delta = 161.0, 157.4, 144.4, 132.8, 132.0, 129.4, 124.1$ (2 signals), 122.4, 109.3, 107.2, 68.5, 43.1, 32.3, 30.8, 30.0, 29.8, 27.6, 26.4, 24.8, 23.1, 18.2, 17.4, 14.3, -3.7, -4.7. HRMS (ESI-TOF) m/z : $[M]^+$ Calcd for $C_{80}H_{132}N_6O_8Si_4^+$ 1416.9178; Found 1416.9257. MS (MALDI-ToF, pos. mode, $CHCl_3$) m/z : $[M]^+$ Calcd for $C_{80}H_{132}N_6O_8Si_4^+$ 1416.9178; Found 1416.9215. UV/vis (THF, $c = 1.00 \cdot 10^{-5}$ M): λ_{max} [nm] (ϵ_{max} [$M^{-1} cm^{-1}$]) = 598 (89600). Fluorescence (THF, $\lambda_{ex.} = 560$ nm): λ_{em} [nm] = 607 ($\Phi_{FL} = 0.37$, standard: 3,7-bis(diethylamino)-phenoxazinium perchlorate, „Oxazine 1“, CAS: 24796-94-9, $\Phi_{Fl} = 0.11$ in EtOH).^[309] CV (CH_2Cl_2 , $c = 2 \cdot 10^{-3}$ M, 0.1 M TBAPF₆, [V] vs. $Fc^{+/0}$, 298 K): $E_{1/2 red} = -1.669$; $E_{1/2 ox} = 0.303, 0.631, 0.835$.

PBI-NN. PBI derivative **PBI-Si** (20.0 mg, 13.5 μ mol, 1.00 equivalent) was dissolved in a mixture of isobutanol/ CH_2Cl_2 4:1 (10 mL) and $BF_3 \cdot Et_2O$ (205 μ L, 1.62 mmol, 120 equivalents) was added under ambient conditions. After stirring for 18 h, the reaction mixture was quenched with tetraethoxysilane ($Si(OEt)_4$, 389 μ L, 1.76 mmol, 130 equivalents) and stirred for 1 h. Subsequently, a saturated aqueous $NaIO_4$ solution (20 mL) was added and the reaction mixture stirred vigorously for 18 h. Then the aqueous phase was separated and the organic layer diluted with Et₂O (100 mL), washed with water (100 mL) and

dried over MgSO₄. The solvent was removed under reduced pressure and the crude product purified by silica gel column chromatography using CH₂Cl₂ with 1% of methanol as an eluent to yield **PBI-NN** as a red solid. Yield: 11.2 mg (11.0 μmol, 81 %). m. p. 242 °C. ¹H NMR (400 MHz, CD₂Cl₂/CD₃OD 9:1): δ = 5.04–4.86 (br, 2 H), 2.62–2.38 (br, 4 H), 1.96–1.80 (br, 4 H), 1.75–1.69 (br, 4 H), 1.51–1.37 (br, 4 H), 1.34–1.20 (br, 4 H). HRMS (ESI-TOF) *m/z*: [M+Na]⁺ Calcd for C₆₂H₆₀N₆O₈Na⁺ 1039.4365; Found 1039.4353. MS (MALDI-ToF, neg. mode, CHCl₃) *m/z*: [M]⁻ Calcd for C₆₂H₆₀N₆O₈⁻ 1016.4478; Found 1016.4372. UV/vis (CHCl₃, *c* = 1.00 · 10⁻⁵ M): λ_{max} [nm] (ε_{max} [M⁻¹ cm⁻¹]) = 558 (22200). Fluorescence (CHCl₃, λ_{ex} = 520 nm): λ_{em} [nm] = 602 (Φ_{FL} = 0.01, standard: *N,N'*-bis(2,6-diisopropylphenyl)-1,6,7,12-tetraphenoxy-3,4,9,10-perylenetetracarboxylic bisimide, “Lumogen/ perylene red”, CAS: 123174–58–3, Φ_{FI} = 0.96 in CHCl₃).^[308] CV (CH₂Cl₂, *c* = 2 · 10⁻³ M, 0.1 M TBAPF₆, [V] vs. Fc⁺⁰, 298 K): *E*_{1/2 red} = -1.342, -1.158; *E*_{1/2 ox} = 0.374, 1.126.

In-NN. Isoindigo derivative **In-Si** (20.0 mg, 13.1 μmol, 1.00 equivalent) was dissolved in a mixture of isobutanol/CH₂Cl₂ 4:1 (10 mL) and BF₃ · Et₂O (199 μL, 1.57 mmol, 120 equivalents) was added under ambient conditions. After stirring for 17 h, the reaction mixture was quenched with tetraethoxysilane (Si(OEt)₄, 366 μL, 1.71 mmol, 130 equivalents) and stirred for 1 h. Subsequently, a saturated aqueous NaIO₄ solution (20 mL) was added and the reaction mixture stirred vigorously for 1 h. The aqueous phase was separated and the organic layer diluted with Et₂O (100 mL), washed with water (100 mL) and dried over MgSO₄. The solvent was removed under reduced pressure and the crude product purified by silica gel column chromatography using CH₂Cl₂ with 1% of methanol as an eluent to yield **In-NN** as a red solid. Yield: 8.40 mg (7.91 μmol, 60 %). m. p. 185–186 °C. ¹H NMR (400 MHz, CD₂Cl₂/CD₃OD 9:1): δ = 3.92–3.73 (br, 4 H), 1.86–1.65 (br, 4 H), 1.40–1.22 (br, 36 H), 0.89–0.83 (br, 6 H). HRMS (ESI-TOF) *m/z*: [M]⁺ Calcd for C₆₆H₈₈N₆O₆⁺: 1060.6760; Found 1060.6759. MS (MALDI-ToF, pos. mode, CHCl₃) *m/z*: [M]⁺ Calcd for C₆₆H₈₈N₆O₆⁺ 1060.6760; Found 1060.6709. UV/vis (CHCl₃, *c* = 1.00 · 10⁻⁵ M): λ_{max} [nm] (ε_{max} [M⁻¹ cm⁻¹]) = 419 (31400), 525 (14500). CV (CH₂Cl₂, *c* = 2 · 10⁻³ M, 0.1 M TBAPF₆, [V] vs. Fc⁺⁰, 298 K): *E*_{1/2 red} = -1.830, -1.366; *E*_{1/2 ox} = 0.366, 1.030.

PhDPP-NN. **PhDPP-Si** (20.0 mg, 13.9 μmol, 1.00 equivalents) was dissolved in a mixture of isobutanol/CH₂Cl₂ 10:3 (6.5 mL) and BF₃ · Et₂O (100 μL, 789 μmol, 56.8 equivalents) was added under ambient conditions. After stirring for 18 h, the reaction mixture was quenched with tetraethoxysilane (Si(OEt)₄, 100 μL, 451 μmol, 32.4 equivalents) and stirred for another 3 h. Subsequently, a saturated aqueous NaIO₄ solution (50 mL) was added and the reaction mixture stirred vigorously for 30 min. The aqueous phase was separated and the organic layer diluted with Et₂O (100 mL), washed with water (100 mL) and dried over MgSO₄. The solvent was removed under reduced pressure and the crude product purified by silica gel column chromatography using CH₂Cl₂ with 1% of methanol as an eluent to yield

PhDPP-NN as a red solid. Yield: 11.0 mg (11.3 μmol , 81 %). m. p. 201–202 °C. $^1\text{H NMR}$ (400 MHz, $\text{CD}_2\text{Cl}_2/\text{CD}_3\text{OD}$ 9:1): δ = 3.87–3.75 (br, 4 H), 1.59–1.52 (br, 4 H), 1.26–1.10 (br, 20 H), 0.86–0.78 (br, 6 H). HRMS (ESI-TOF) m/z : $[\text{M}]^+$ Calcd for $\text{C}_{60}\text{H}_{74}\text{N}_6\text{O}_6^+$ 974.5664; Found 974.5606. MS (MALDI-ToF, pos. mode, CHCl_3) m/z : $[\text{M}]^+$ Calcd for $\text{C}_{60}\text{H}_{74}\text{N}_6\text{O}_6^+$ 974.5664, Found 974.5855. UV/vis (THF, $c = 1.00 \cdot 10^{-5}$ M): λ_{max} [nm] (ϵ_{max} [$\text{M}^{-1} \text{cm}^{-1}$]) = 497 (25600). Fluorescence (THF, $\lambda_{\text{ex.}} = 475$ nm): λ_{em} [nm] = 569 ($\Phi_{\text{FL}} = 0.02$, standard: *N,N*-bis(2,6-diisopropylphenyl)-3,4,9,10-perylenetetracarboxylic bisimide, “Lumogen/ perylene orange”, CAS: 82953–57–9, $\Phi_{\text{FL}} = 1.00$ in CHCl_3).^[308] CV (CH_2Cl_2 , $c = 2 \cdot 10^{-3}$ M, 0.1 M TBAPF₆, [V] vs. $\text{Fc}^{+/0}$, 298 K): $E_{1/2 \text{ red}} = -2.206, -1.758, -1.422$; $E_{1/2 \text{ ox}} = 0.382, 0.694, 1.038$.

ThDPP-NN. DPP derivative **ThDPP-Si** (20.0 mg, 13.8 μmol , 1.00 equivalent) was dissolved in a mixture of isobutanol/ CH_2Cl_2 10:3 (6.5 mL) and $\text{BF}_3 \cdot \text{Et}_2\text{O}$ (87.4 μL , 689 μmol , 50.0 equivalents) was added under ambient conditions. After stirring for 17 h, the reaction mixture was quenched with tetraethoxysilane ($\text{Si}(\text{OEt})_4$, 153 μL , 689 μmol , 50.0 equivalents) and stirred for another 3 h. Subsequently, a saturated aqueous NaIO_4 solution (10 mL) was added and the reaction mixture stirred vigorously for 30 min. The aqueous phase was separated and the organic layer diluted with Et_2O (100 mL), washed with water (100 mL) and dried over MgSO_4 . The solvent was removed under reduced pressure and the crude product purified by silica gel column chromatography using CH_2Cl_2 with 2% of methanol as an eluent to yield **ThDPP-NN** as a blue solid. Yield: 11.0 mg (11.1 μmol , 81 %). m. p. 232 °C. $^1\text{H NMR}$ (400 MHz, $\text{CD}_2\text{Cl}_2/\text{CD}_3\text{OD}$ 9:1): δ = 4.26–3.95 (br, 4 H), 1.87–1.70 (br, 4 H), 1.24–1.37 (br, 20 H), 0.90–0.83 (br, 6 H). HRMS (ESI-TOF) m/z : $[\text{M}+\text{H}]^+$ Calcd for $\text{C}_{56}\text{H}_{71}\text{N}_6\text{O}_6\text{S}_2^+$ 987.4871; Found 987.4950. MS (MALDI-ToF, pos. mode, CHCl_3) m/z : $[\text{M}]^+$ Calcd for $\text{C}_{56}\text{H}_{70}\text{N}_6\text{O}_6\text{S}_2^+$ 986.4793; Found 986.4913. UV/vis (THF, $c = 1.00 \cdot 10^{-5}$ M): λ_{max} [nm] (ϵ_{max} [$\text{M}^{-1} \text{cm}^{-1}$]) = 620 (48700). CV (CH_2Cl_2 , $c = 2 \cdot 10^{-3}$ M, 0.1 M TBAPF₆, [V] vs. $\text{Fc}^{+/0}$, 298 K): $E_{1/2 \text{ red}} = -2.156, -1.716, -1.532$; $E_{1/2 \text{ ox}} = 0.412, 0.880$.

FuDPP-NN. DPP derivative **FuDPP-Si** (20.0 mg, 14.1 μmol , 1.00 equivalent) was dissolved in a mixture of isobutanol/ CH_2Cl_2 10:3 (6.5 mL) and $\text{BF}_3 \cdot \text{Et}_2\text{O}$ (100 μL , 789 μmol , 56.0 equivalents) was added under ambient conditions. After stirring for 18 h, the reaction mixture was quenched with tetraethoxysilane ($\text{Si}(\text{OEt})_4$, 200 μL , 902 μmol , 64.0 equivalents) and stirred for another 3 h. Subsequently, a saturated aqueous NaIO_4 solution (50 mL) was added and the reaction mixture stirred vigorously for 30 min. The aqueous phase was separated and the organic layer diluted with Et_2O (100 mL), washed with water (100 mL) and dried over MgSO_4 . The solvent was removed under reduced pressure and the crude product purified by silica gel column chromatography using CH_2Cl_2 with 1% of methanol as an eluent to yield **FuDPP-NN** as a blue solid. Yield: 8.20 mg (8.59 μmol , 61 %). m. p. 227–228 °C. $^1\text{H NMR}$ (400 MHz, $\text{CD}_2\text{Cl}_2/\text{CD}_3\text{OD}$ 9:1): δ = 4.33–4.15 (br, 4 H), 1.93–1.71 (br, 4 H), 1.43–1.21 (br,

20 H), 0.94–0.82 (br, 6 H). HRMS (ESI-TOF) m/z : $[M+H]^+$ Calcd for $C_{56}H_{71}N_6O_8^+$ 955.5328; Found 955.5403. MS (MALDI-ToF, pos. mode, $CHCl_3$) m/z : $[M]^+$ Calcd for $C_{56}H_{70}N_6O_8^+$ 954.5250; Found 954.5504. UV/vis (THF, $c = 1.00 \cdot 10^{-5}$ M): λ_{max} [nm] (ϵ_{max} [$M^{-1} cm^{-1}$]) = 616 (90000). CV (CH_2Cl_2 , $c = 2 \cdot 10^{-3}$ M, 0.1 M TBAPF₆, [V] vs. Fc⁺⁰, 298 K): $E_{1/2 red} = -2.306, -1.758, -1.502$; $E_{1/2 ox} = 0.422, 0.858$.

5.6 Supporting Information

NMR, ESI HRMS, UV/vis, EPR spectra and electrochemical data of new silyl and nitronyl nitroxide compounds as well as the X-ray structure of **IIn-NN**.

5.7 Acknowledgements

We thank the DFG for financial support provided to the research training school GRK 2112 on “Molecular Biradicals”.

Chapter 6 – Summary and Conclusion

Within this PhD thesis, chromophore-bridged biradicals were synthesised and their properties characterised. Therefore, it was necessary to develop novel synthetic procedures and implement several experimental characterisation methods.

In the first project of this work, isoindigo phenoxy biradical **OS-2^{••}** was synthesised by proton-coupled oxidation from its respective bisphenol precursor **2** (Figure 6.1, top and *Chapter 3*) and characterised with optical and magnetic spectroscopic techniques. It is the first open shell compound based on this chromophore and combines an exceptional stability in solution of several weeks and even unlimited shelf life in the solid state (Figure 6.1, bottom) with a large biradical character ($y_0 = 0.79$) and a small singlet-triplet energy gap ($\Delta E_{ST} = 65$ meV).

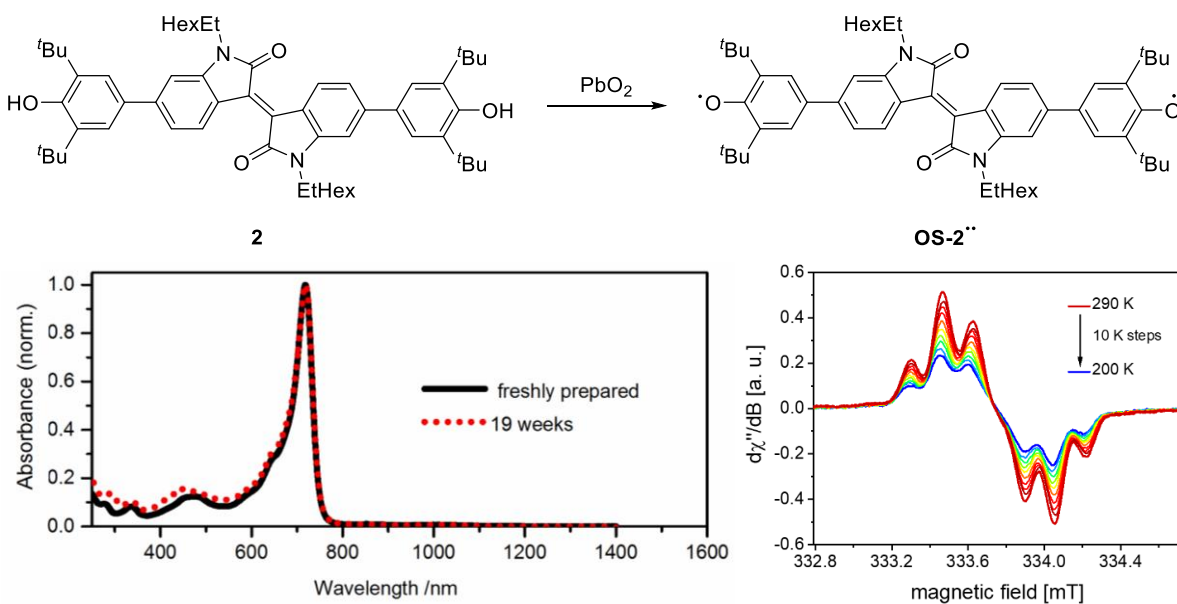


Figure 6.1 | Formation of isoindigo biradical **OS-2^{••}** upon oxidation of **2** with PbO_2 (top) as well as UV/vis/NIR absorption spectra (bottom left) and VT-EPR spectra (bottom, right) of **OS-2^{••}** in CH_2Cl_2 .

Therefore, **OS-2^{••}** is an outstanding representative of the class of pigment chromophore containing phenoxy biradicals combining dye and radical properties in a hitherto unprecedented fashion. In general, molecules with a large biradical character (e.g. $y_0 > 0.70$) and a small singlet-triplet energy gap (e.g. $\Delta E_{ST} < 100$ meV) readily decompose within hours in solution, whereas open-shell materials with half-lives of several weeks exhibit considerably larger singlet-triplet energy gaps, smaller biradical characters and/or require the large π -surface of extended PAHs for spin delocalisation and thus stabilisation.

The extraordinary persistence of **OS-2^{••}** results from widespread spin delocalisation edging from the phenoxy radical centres into the electron-withdrawing isoindigo chromophore core, as evidenced by EPR spectroscopy and an analysis of the hyperfine splitting pattern (Figure 6.1, bottom, right) as well as quantum chemical calculations. Therefore, the concept of kinetic blocking of the radical centres and delocalisation of spin density into the electron-withdrawing chromophore core of isoindigo offers an entry into a new class of highly persistent open-shell functional materials based on organic colorants. Isoindigo biradical **OS-2^{••}** represents an aromatic open-shell compound, although a closed-shell quinoidal ground state dominates in the majority of such small sized π -systems like e.g. in heteroquinones. In this regard, it is reasonable to assume that the biradical properties of **OS-2^{••}** arise from the unique combination of a moderately electron deficient π -system with the gain of aromatic stabilisation energy by four additional Clar sextets in the open-shell state compared to the closed-shell quinoidal state.

In order to gain deeper insights into aromatisation as a key determinant for open-shell ground states, a systematic linker variation in a series of three twofold 2,6-di-*tert*-butylphenoxy functionalised diketopyrrolopyrrole dyes **DPP1–3** (Figure 6.2a and Chapter 4) was the second focus of this thesis. On first glance, all three derivatives look very similar, but upon deprotonation and oxidation, electronically very distinct compounds were obtained. The strongly aromatic phenylene bridge endows derivative **DPP1^{••}** with a pronounced biradical character of $y_0 = 0.75$ and a very small singlet-triplet energy gap of 19 meV (Figure 6.2c). As a consequence, **DPP1^{••}** shows low stability and decomposes in solution within the timescale of days. In contrast, oxidation of heteroaromatic derivatives **DPP2** and **DPP3** bearing thiophene or furane linkers, respectively, afforded closed-shell planar and bench stable quinones **DPP2q** and **DPP3q**, as evidenced *inter alia* by single crystal X-ray analysis (Figure 6.2d). The aromatic character of the bridging units in **DPP1^{••}**, **DPP2q** and **DPP3q** was investigated using HOMA index values, revealing that the established order of aromaticity decrease (phenyl > thiophene > furane) applies for such biradicaloid systems with a central dye unit. Accordingly, Clar's sextet rule also offers a design principle to derive open-shell colorants with central dye and pigment units. In this series only **DPP1^{••}** with four benzenoid sextets prevailed in an open-shell configuration as a biradical, whereas energy gains through non-benzenoid heteroaromatic furane or thiophene linkers were not large enough to counteract the transformation of the π -electron system into a fully conjugated quinoidal scaffold (Figure 6.2b). In addition, it was demonstrated that the significantly larger singlet biradical characters reported by Zheng and co-workers for derivatives of **DPP2q** and **DPP3q** bearing different alkyl chains^[215] results from calculations based on the *N,X*-cis configuration, which is not present in solution or in the solid state and led to misinterpretation.

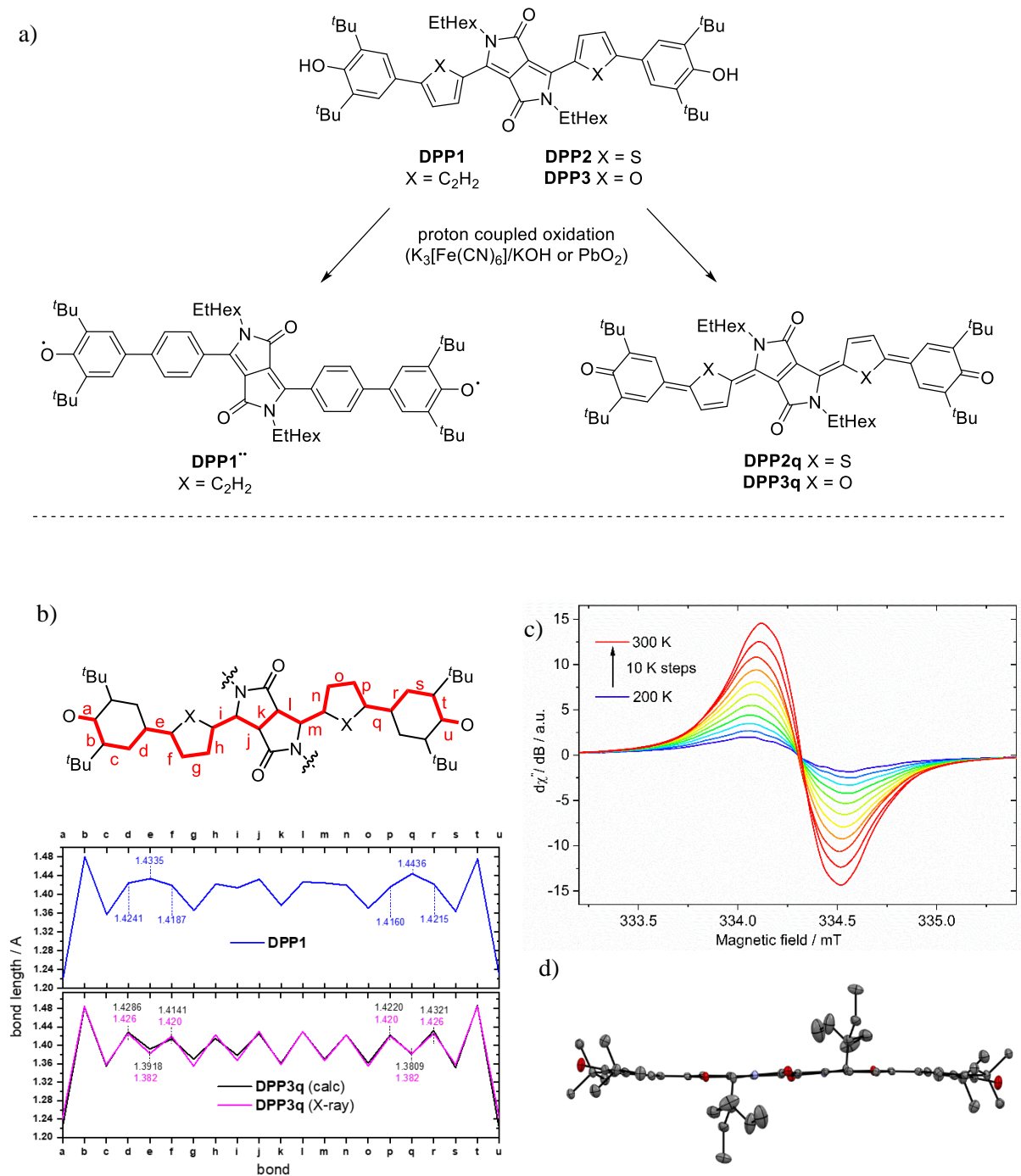
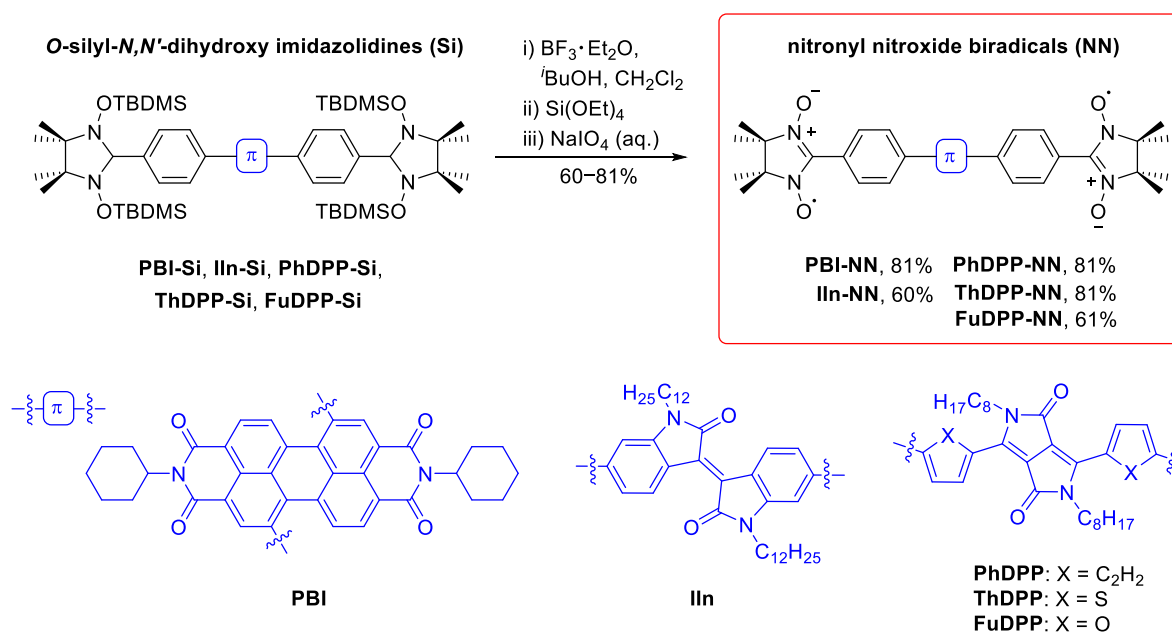


Figure 6.2 | Synthesis of biradical **DPP1^{••}** and quinones **DPP2q** and **DPP3q** by proton coupled oxidation of bisphenols **DPP1–3** (a), conjugated path and calculated bond length alternation of **DPP1^{••}** and **DPP3q** (b), VT-EPR spectra of **DPP1^{••}** in CH_2Cl_2 solution (c) and X-ray structure of **DPP3q** (d).

With perylene bisimide (PBI) biradical **102** (Figure 2.12 in *Chapter 2*) investigated by M.-J. Lin and D. Schmidt^[23], isoindigo (IIn) based **OS-2** and diketopyrrolopyrrole (DPP) bridged **DPP1**, a series of twofold phenoxy decorated pigment chromophores was intensively studied over the last five years. This design principle enables a stepwise adjustment of biradical properties like (ambient) stability, y_0 , ΔE_{ST} , spin delocalisation or optical properties by careful choice of the bridging chromophore core. For instance, half-lives in solution vary from two or three days in the case of PBI or DPP up to several weeks for IIn, while all three systems feature a pronounced singlet biradical character of 0.72–0.79. The singlet-triplet energy gaps of **102**, **OS-2** and **DPP1** stretch from 19 to 65 meV and thus include $k_B T$ under ambient conditions. Accordingly, a temperature responsive behaviour of the magnetic properties was observed for all three derivatives justifying their classification as biradicals. The degree of spin delocalisation increases with the pigment chromophore's electron deficiency (PBI > IIn > DPP) and hence follows the trend **102** > **OS-2** > **DPP1**, as uncovered by an analysis of the hyperfine splitting patterns in the respective EPR spectra of **OS-2** and **DPP1** (Figures 6.1 and 6.2c) and further confirmed by quantum chemical calculations.^[23] The UV/vis absorption maxima of biradicals **102**, **OS-2** and **DPP1** are all redshifted compared to the respective bisphenols due to increased conjugation and charge transfer. Notably, the absorption bands of **102** and **OS-2** are exceptionally sharp with a full width at half maximum (FWHM) of 390 cm^{-1} and 930 cm^{-1} , respectively, presumably due to similar spin delocalisation in the ground and excited state.

Spin decoration of pigment chromophores with phenoxy radical centres leads to rather unpredictable optical properties and frequently a significantly reduced ambient stability. In this regard, nitronyl nitroxides (NN) are radicals capable of overcoming both of these drawbacks. Thus, unprecedented nitronyl nitroxide biradicals **PBI-NN**, **IIn-NN**, **PhDPP-NN**, **ThDPP-NN** and **FuDPP-NN** (Scheme 6.1 and *Chapter 5*) bridged by perylene bisimide (PBI), isoindigo (IIn) and diketopyrrolopyrrole (DPP) pigment colorants are bench stable compounds, which do not show any sign of decomposition over several months even under ambient conditions. The absorption spectral signatures of the pigment chromophores remain preserved in the open shell state and match the ones of the pristine parent compounds, which allows an *a priori* prediction of their optical properties. However, the synthesis of these rather electron poor biradicals turned out to be challenging and was not possible with conventional preparation methods. Finally, all five NN biradicals were obtained from the respective *O*-silylated *N,N'*-dihydroxy imidazolidine precursors **PBI-Si**, **IIn-Si**, **PhDPP-Si**, **ThDPP-Si** and **FuDPP-Si** by a sequential one pot Lewis acid promoted deprotection and subsequent periodate oxidation procedure (Scheme 6.1). Notably, the use of base-free deactivation of BF_3 with fluorophilic $\text{Si}(\text{OEt})_4$ offered a pathway to circumvent substrate decomposition. The newly established procedure appears applicable for

a variety of electron poor pigment colorants with yields up to 81% in the deprotection/oxidation step and overall yields from the aryl halide to the NN biradical of up to 75%. *Inter alia* due to the rather electron poor character of the O-N-C-N-O pentad and sterical reasons, the conjugation between the nitronyl nitroxide moiety and the IIn, PBI or DPP π -cores is significantly reduced and no electronic coupling between these units can be observed. Unlike the weak electronic radical-chromophore interactions, magnetic spin-spin exchange interactions of both nitronyl nitroxide moieties appears strong in all investigated chromophores due to tunnelling effects. Overall, twofold conjugated spin decoration of colorants with nitronyl nitroxide moieties leads to biradicals with electronically isolated but strongly magnetically coupled spin centres. Consequently, high yielding twofold spin labelling of chromophores was achieved while keeping the intrinsic properties of the electron-deficient colorants intact.



Scheme 6.1 | Synthesis of nitronyl nitroxide biradicals **PBI-NN**, **IIn-NN**, **PhDPP-NN**, **ThDPP-NN** and **FuDPP-NN** via deprotection/oxidation of the respective *O*-silylated *N,N'*-dihydroxy imidazolidines **PBI-Si**, **IIn-Si**, **PhDPP-Si**, **ThDPP-Si** and **FuDPP-Si** by Lewis acid promoted desilylation and periodate oxidation.

In summary, within this thesis the scope of pigment chromophore phenoxyl radical decoration was further explored and expanded to IIn as well as DPP colourants. OMA analysis highlighted the importance of aromaticity in order to understand the spin crossover from heteroaromatic quinoidal to aromatic open shell DPPs. Finally, PBI, IIn and DPP biradicals were advanced towards stable materials by introduction of nitronyl nitroxide radical centres.

Chapter 7 – Zusammenfassung und Fazit

Im Rahmen der vorliegenden Doktorarbeit wurden chromophor-verbrückte Biradikale hergestellt und ihre Eigenschaften charakterisiert. Hierzu bedurfte es der Entwicklung neuer synthetischer Methoden sowie der Ausarbeitung zahlreicher experimenteller Techniken zur Charakterisierung.

Innerhalb des ersten Projekts dieser Arbeit konnte das Isoindigo-basierte Phenoxybiradikal **OS-2''** durch protonengekoppelte Oxidation des entsprechenden Bisphenols **2** erhalten (Abbildung 7.1, oben und Kapitel 3) und mittels optischer und magnetischer Spektroskopietechniken charakterisiert werden. Das Biradikal **OS-2''** ist die erste offenschalige Verbindung basierend auf diesem Chromophor und vereint außerordentlich hohe Stabilität über mehrere Wochen hinweg in Lösung und sogar unbegrenzte Lagerungsfähigkeit im Festkörper (Abbildung 7.1, links unten) mit einem großen Biradikalcharakter ($\nu_0 = 0.79$) und einer eher geringen Singulett-Triplett Aufspaltung ($\Delta E_{ST} = 65$ meV).

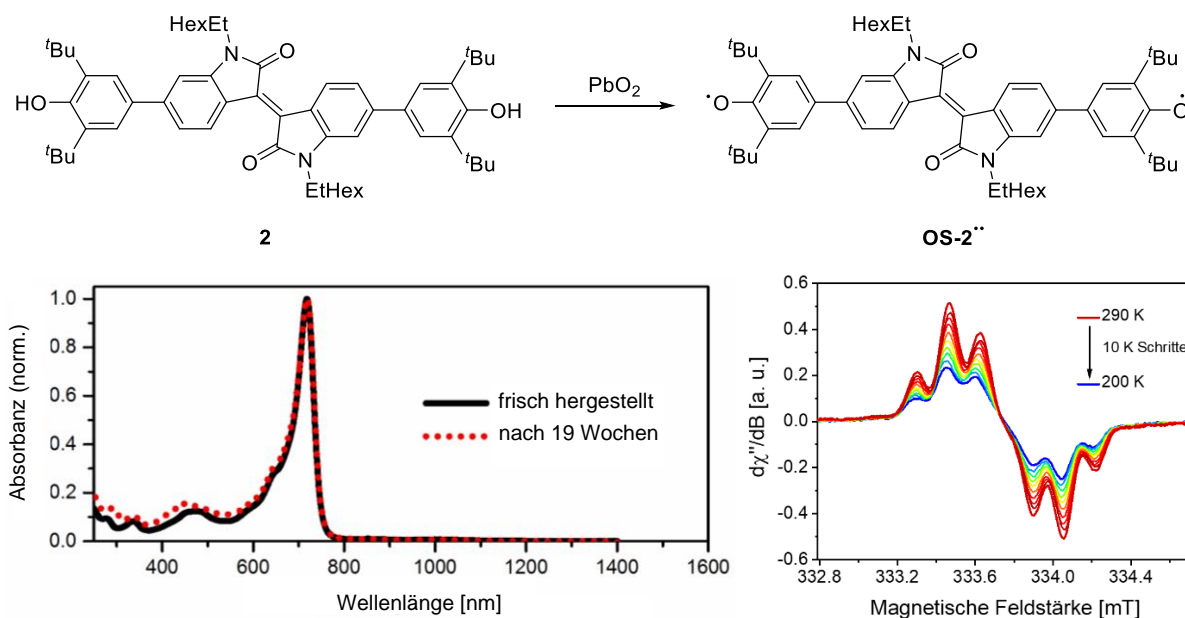


Abbildung 7.1 | Darstellung des Isoindigobiradikals **OS-2''** durch Oxidation von **2** mit PbO_2 (oben) sowie UV/vis/NIR Absorptionsspektren (unten links) und VT-EPR Spektren (unten rechts) von **OS-2''** in CH_2Cl_2 .

In dieser Hinsicht sticht **OS-2''** aus der Klasse der pigmentchromophor-verbrückten Phenoxybiradikale hervor und vermag es, Farbstoff- und Radikal-Eigenschaften in einer bislang unbekanntem Art und Weise miteinander zu verbinden. Ganz allgemein unterliegen Moleküle mit einem ausgeprägten

Biradikalcharakter (z. B. $y_0 > 0.70$) und einer kleinen Singulett-Triplett Aufspaltung (z. B. $\Delta E_{ST} < 100$ meV) in Lösung einer raschen Zersetzung binnen weniger Stunden, wohingegen offenschalige Materialien mit Halbwertszeiten im Bereich einiger Wochen durch eine merklich größere Singulett-Triplett Aufspaltung sowie deutlich niedrigeren Biradikalcharakter gekennzeichnet sind und/oder die ausgedehnte π -Fläche größerer PAKs zur Delokalisierung der Spindichte und somit zur Stabilisierung benötigen. Wie mittels EPR-Spektroskopie und einer Analyse der Hyperfeinstruktur (Abbildung 7.1, rechts unten) sowie mittels quantenchemischen Rechnungen gezeigt werden konnte, beruht die außergewöhnliche Persistenz von **OS-2^{••}** auch auf der weitreichenden Spindelokalisierung vom Phenoxyradikalzentrum bis in den elektronenziehenden Isoindigo-Chromophor hinein. Dementsprechend eröffnet das Konzept der kinetischen Abschirmung von Radikalzentren und der Delokalisation von Spindichte auch über den elektronenziehenden Chromophorkern von Isoindigo den Zugang zu einer neuen Klasse hoch stabiler, offenschaliger Materialien auf Basis organischer Farbstoffe. Das Biradikal **OS-2^{••}** stellt eine offenschalige, aromatische Verbindung dar, obwohl ein geschlossenschaliger Grundzustand bei der Mehrzahl derart kleiner π -Systeme dominiert, wie beispielsweise in Heterochinonen. Aus diesem Grund erscheint es gerechtfertigt anzunehmen, dass die biradikalischen Eigenschaften von **OS-2^{••}** gerade durch die einzigartige Kombination eines moderat elektronenarmen π -Systems mit dem Energiegewinn von vier zusätzlichen Clar-Sextetten im offenschaligen Zustand gegenüber dem geschlossenschaligen entstehen.

Um tiefere Einblicke in die Schlüsselrolle der Aromatizität für einen offenschaligen Grundzustand zu gewinnen, wurde eine systematische Variation der Brückeneinheit in einer Serie von drei jeweils zweifach 2,6-di-*tert*-butylphenoxyyl funktionalisierten Diketopyrrolopyrrol-Farbstoffen **DPP1–3** (Abbildung 7.2a und *Kapitel 4*) vorgenommen, welche den zweiten Schwerpunkt dieser Arbeit bildet. Obschon alle drei Derivate auf den ersten Blick sehr ähnlich wirken, werden nach Deprotonierung und Oxidation elektronisch sehr unterschiedliche Verbindungen erhalten. Die hochgradig aromatische Phenylenbrücke ruft in Derivat **DPP1^{••}** einen ausgeprägten Biradikalcharakter $y_0 = 0.75$ und eine äußerst kleine Singulett-Triplett Aufspaltung von nur 19 meV hervor (Abbildung 7.2c). Infolgedessen zeigt **DPP1^{••}** nur eine geringe Stabilität und unterliegt in Lösung innerhalb von wenigen Tagen der Zersetzung. Im Gegensatz dazu entstehen durch Oxidation der heteroaromatischen Derivate **DPP2** und **DPP3**, welche jeweils Thiophen- bzw. Furanbrücken enthalten, geschlossenschalige, planare und langzeitstabile Chinone, wie unter anderem mittels Röntgenstrukturanalyse gezeigt werden konnte (Abbildung 7.2d). Der aromatische Charakter des Brückenglieds in **DPP1^{••}**, **DPP2q** und **DPP3q** wurde anhand von HOMA Indexwerten untersucht, wobei deutlich wurde, dass die etablierte Reihenfolge abnehmender Aromatizität (Phenyl > Thiophen > Furan) auch für solche biradikaloiden Systeme mit einer zentralen

Farbstoffeinheit gilt. Dementsprechend bietet Clars Sextettregel auch ein Designprinzip für offenschalige Chromophore mit zentraler Farbstoff- oder Pigmenteinheit.

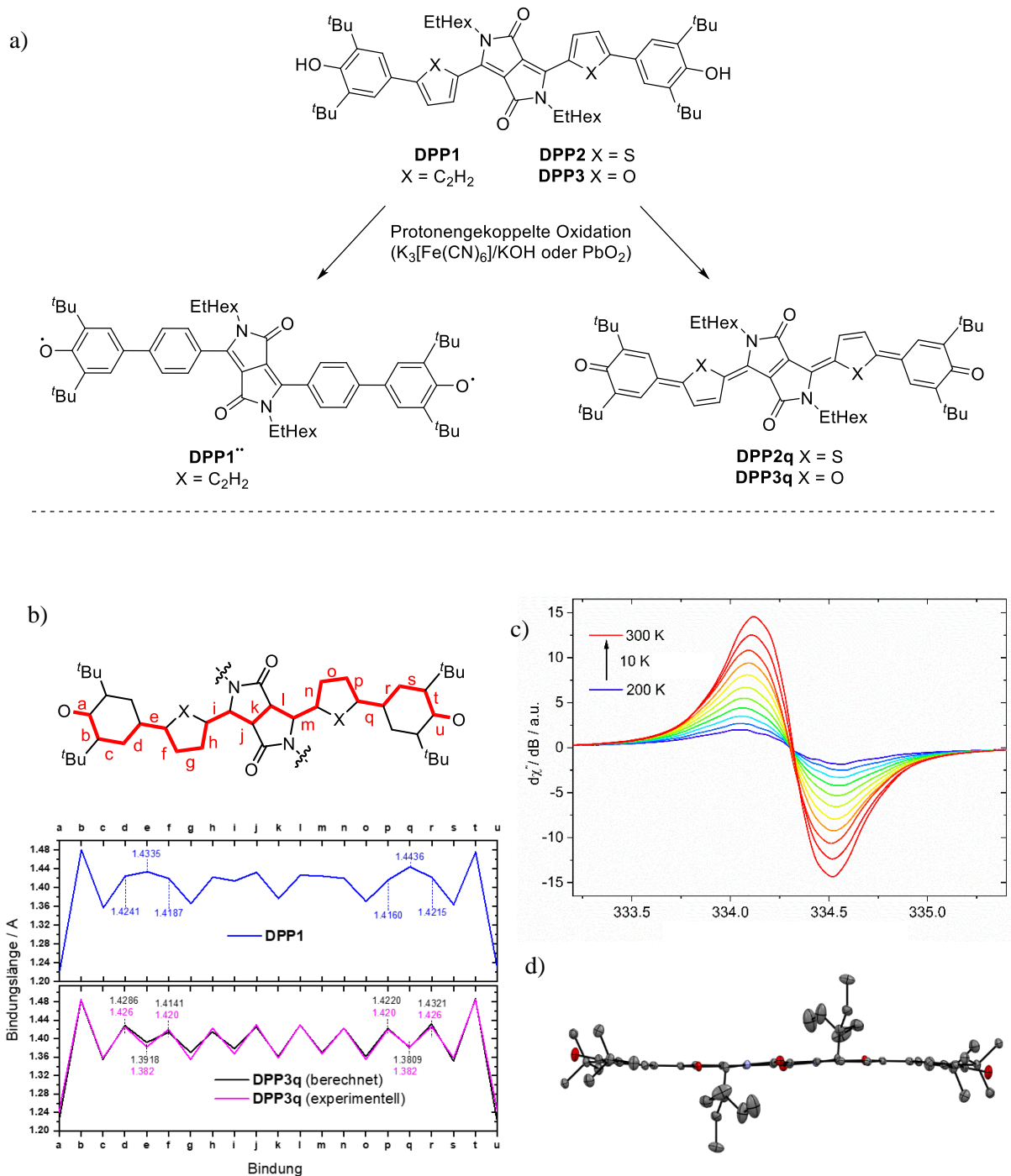


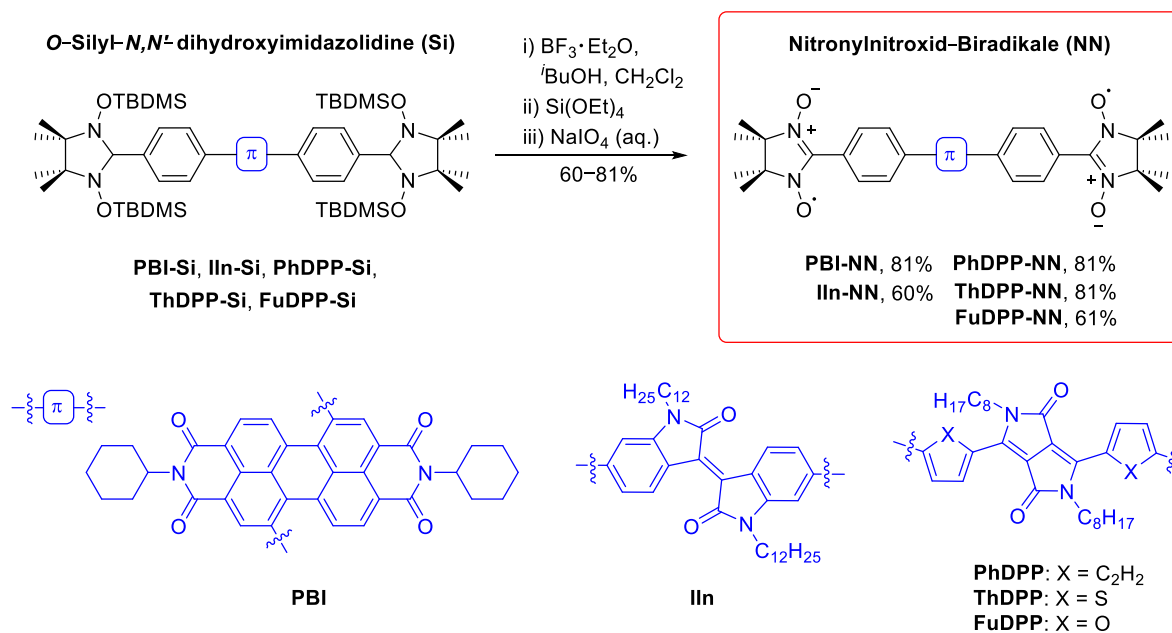
Abbildung 7.2 | Synthese des Biradikals **DPP1^{••}** und der Chinone **DPP2q** und **DPP3q** durch protonengekoppelte Oxidation der Bisphenole **DPP1–3** (a), Konjugationspfad und berechnete Bindungslängenalternanz in **DPP1^{••}** sowie **DPP3q** (b), VT-EPR Spektren von **DPP1^{••}** in CH₂Cl₂ Lösung (c) sowie Kristallstruktur von **DPP3q** (d).

Innerhalb der vorliegenden Serie vermag nur **DPP1^{••}** mit vier benzenoiden Sextetten eine offenschalige Biradikal-Konfiguration zu stabilisieren, wohingegen die Energiegewinne aus den heteroaromatischen Thiophen- und Furanbrücken nicht ausreichend sind, um die Ausbildung eines vollkommen konjugierten Chinongerüsts zu verhindern (Abbildung 7.2b). Überdies konnte gezeigt werden, dass die deutlich größeren Singulett-Biradikalcharakter, welche von Zheng und Mitarbeitern für Derivate von **DPP2q** und **DPP3q** mit anderen Alkylketten berichtet wurden,^[215] lediglich daher rühren, dass deren quantenchemische Berechnungen auf der *N,X*-cis Konfiguration beruhen; diese liegen jedoch weder in Lösung noch im Festkörper tatsächlich vor und führen mithin zu einer Fehlinterpretation.

Mit dem von M.-J. Lin und D. Schmidt untersuchten Perylenbisimid-Biradikal **102** (Abbildung 2.12), dem Isoindigo-basierten **OS-2^{••}** sowie dem Diketopyrrolopyrrol-verbrückten **DPP1^{••}** konnte in den vergangenen fünf Jahren eine Serie von jeweils zweifach phenoxy-substituierten Pigmentchromophoren intensiv untersucht werden. Dieses Designprinzip gestattet dabei eine inkrementelle Anpassung der Biradikaleigenschaften Stabilität, y_0 , ΔE_{ST} , Spindichtedelokalisation und der optischen Eigenschaften durch eine entsprechende Auswahl des verbrückenden Chromophorkerns. Beispielsweise variiert die Halbwertszeit in Lösung von zwei oder drei Tagen im Falle von PBI oder DPP bis hin zu einigen Wochen bei IIn, während alle drei Systeme einen ausgeprägten Singulett-Biradikalcharakter von 0.72–0.79 aufweisen. Die Singulett-Triplett Energien von **102**, **OS-2^{••}** und **DPP1^{••}** reichen dabei von 19 bis 65 meV und schließen somit $k_B T$ unter Standardbedingungen mit ein. Dementsprechend kann auch ein Temperatur-responsives Verhalten der magnetischen Eigenschaften bei allen drei Derivaten beobachtet werden, welches seinerseits die Einklassifizierung als Biradikale bestätigt. Wie überdies mittels einer Analyse der Hyperfeinstrukturen der EPR-Spektren von **OS-2^{••}** und **DPP1^{••}** gezeigt und durch quantenchemische Rechnungen auch für **102** bestätigt werden konnte,^[23] nimmt das Ausmaß der Spindelokalisation mit der Elektronenarmut des Pigmentchromophors (PBI > IIn > DPP) zu und folgt somit der Reihenfolge **102** > **OS-2^{••}** > **DPP1^{••}**. Die UV/vis Absorptionsmaxima der Biradikale **102**, **OS-2^{••}** und **DPP1^{••}** sind durch ausgeprägtere Konjugation und Ladungstransfers im Vergleich zu den entsprechenden Bisphenolen rotverschoben. Bemerkenswert ist dabei, dass die Absorptionsbanden von **102** und **OS-2^{••}** mit Halbwertsbreiten (FWHM) von 390 cm^{-1} , bzw. 930 cm^{-1} außergewöhnlich schmal sind, was durch eine vergleichbare Spindelokalisation sowohl im Grund- als auch im angeregten Zustand erklärt werden kann.

Die Spinfunktionalisierung von Pigmentchromophoren mit Phenoxy-Radikalzentren geht oft mit eher unvorhersehbaren optischen Eigenschaften und einer drastischen Verminderung der allgemeinen Stabilität einher. Nitronyl nitroxide (NN) hingegen sind Radikalzentren, die beide Nachteile zu überwinden vermögen. Entsprechend sind die bislang unbekanntenen Nitronylnitroxid-Biradikale **PBI-**

NN, **IIn-NN**, **PhDPP-NN**, **ThDPP-NN** und **FuDPP-NN** (Schema 7.1 und Kapitel 5), welche einen Perylenbisimid (PBI), Isoindigo (IIn) and Diketopyrrolopyrrol (DPP) Farbstoffkern enthalten, langzeitstabile Verbindungen und zeigen auch nach monatelanger Lagerung unter Umgebungsbedingungen keinerlei Zersetzungserscheinungen. Zudem bleiben die optischen Signaturen der Pigmentchromophore auch im offenschaligen Zustand erhalten und stimmen mit denen der reinen Stammverbindung überein, was eine *a priori* Vorhersage der zu erwartenden optischen Eigenschaften ermöglicht.



Schema 7.1 | Synthese der Nitronylnitroxid-Biradikale **PBI-NN**, **IIn-NN**, **PhDPP-NN**, **ThDPP-NN** und **FuDPP-NN** *via* Entschützung/Oxidation der entsprechenden *O*-Silyl-*N,N'*-dihydroxyimidazolidine **PBI-Si**, **IIn-Si**, **PhDPP-Si**, **ThDPP-Si** und **FuDPP-Si** mittels Lewis-Säure-vermittelter Desilylierung und Periodatoxidation.

Die Synthese dieser elektronenarmen Biradikale gestaltete sich jedoch zunächst schwierig und konnte nicht mittels etablierter Herstellungsverfahren bewerkstelligt werden. Schlussendlich wurden alle fünf NN-Biradikale ausgehend von den entsprechenden *O*-silylierten *N,N'*-Dihydroxyimidazolidin-Vorstufen **PBI-Si**, **IIn-Si**, **PhDPP-Si**, **ThDPP-Si** und **FuDPP-Si** durch eine sequentielle Eintopfreaktion mit Lewis-Säure-vermittelter Entschützung und nachfolgender Periodatoxidation (Schema 7.1) erhalten. Erwähnenswert ist in diesem Zusammenhang auch, dass in der basenfreien Deaktivierung von BF_3 mit fluorophilem $\text{Si}(\text{OEt})_4$ ein Weg zur Umgehung der Substratzerersetzung gefunden wurde. Das somit neu erarbeitete Verfahren scheint breit anwendbar auf eine Vielzahl elektronenarmer Pigmentfarbstoffe und

ermöglicht Ausbeuten bis zu 81% für den Entschützungs- und Oxidationsschritt sowie Gesamtausbeuten vom Arylhalogenid bis zum NN-Biradikal von bis zu 75%. Unter anderem durch den eher elektronenarmen Charakter der O-N-C-N-O-Pentade und zusätzlicher sterischer Gründe ist die Konjugation zwischen der Nitronylnitroxideinheit und den IIn-, PBI- oder DPP- π -Gerüsten deutlich reduziert, sodass nahezu keine elektronische Kopplung zwischen diesen beiden Einheiten beobachtet werden kann. Anders als die schwachen elektronischen Radikal-Chromophor Wechselwirkungen sind die magnetischen Spin-Spin Austauschwechselwirkungen beider Nitronylnitroxid-Gruppen durch Tunneleffekte in allen untersuchten Chromophoren stark ausgeprägt. Insgesamt führt die zweifache, konjugierte Spinfunktionalisierung von Farbstoffen mit Nitronylnitroxideinheiten also zu Biradikalen mit elektronisch entkoppelten, aber magnetisch stark wechselwirkenden Spinzentren. Somit konnte eine zweifache Spinfunktionalisierung von Chromophoren mit hohen Ausbeuten erreicht werden, welche zudem die intrinsischen Eigenschaften dieser elektronenarmen Farbstoffe unberührt lässt.

Zusammenfassend konnte im Rahmen dieser Arbeit der Anwendungsbereich der Phenoxyradikal-Funktionalisierung von Pigmentchromophoren erforscht und auf IIn- sowie DPP-Farbstoffe erweitert werden. Mittels HOMA-Analyse wurde die Bedeutung der Aromatizität für den beobachteten Spinzustandswechsels von heteroaromatischen, quinoidalen zu aromatischen und offenschaligen DPPs theoretische gedeutet. Abschließend konnten PBI-, IIn- und DPP-Biradikale durch die Einführung von Nitronylnitroxid-Radikalzentren zu stabilen Materialien weiterentwickelt werden.

Chapter 8 – Appendix

8.1 Supporting Information for Chapter 3

Please note: This section was partly communicated in *Chem. Eur. J.* **2018**, *24*, 3420–3424. The numeration of compounds in this part refers only to *Chapter 3* and is not necessarily the same as in *Chapter 1* and in particular in *Chapter 2*. Reprinted and adapted with permission from *Chem. Eur. J.* **2018**, *24*, 3420–3424. Copyright 2018 John Wiley and Sons Inc. For the sake of unity of this thesis, several editorial changes have been made, which, however, do not affect substantive amendments.

8.1.1 Materials and methods

Materials. Chemicals, reagents and solvents were purchased from commercial suppliers. Column chromatography was performed on silica gel (particle size 0.040–0.063 mm) with freshly distilled solvents as eluents. Tetrabutylammonium fluoride was purchased as its trihydrate but had a significantly higher water content due to its hygroscopic character. All other commercially available reagents and solvents were of reagent grade and used without further purification.

NMR Spectroscopy. ^1H , ^{11}B and ^{13}C NMR Spectra were recorded on a Bruker Avance III HD 400 or Bruker Avance III HD 600 spectrometer. ^{13}C NMR Spectra are broad band proton decoupled. Chemical shifts (δ) are listed in parts per million (ppm) and are reported relative to tetramethylsilane (TMS). Spectra are referenced internally to residual proton solvent resonances or natural abundance carbon resonances. ^{11}B NMR spectra were referenced to external $\text{BF}_3 \cdot \text{Et}_2\text{O}$. Coupling constants (J) are quoted in Hertz (Hz).

Mass Spectrometry. MALDI-ToF mass spectra were recorded on a Bruker Daltronik GmbH (Autoflex II) mass spectrometer using trans-2-[3-(4-*tert*-butylphenyl)-2-methyl-2-propenylidene]malononitrile (DCTB) as matrix. High resolution ESI-ToF mass spectrometry was carried out on a microToF focus instrument (Bruker Daltronik GmbH).

UV/vis/NIR Absorption Spectroscopy. The solvents for the spectroscopic measurements were of spectroscopic grade. UV/vis/NIR absorption spectra were recorded on a Perkin Elmer Lambda 950 or a Jasco V-670 spectrometer. Measurements in solution were carried out using quartz cuvettes with path

lengths of 10 mm at ambient temperature. Measurements in solid state were performed on freshly spin coated thin films on quartz wavers at ambient temperature ($c = 2 \times 10^{-3}$ M, rpm = 3000, t = 30s).

UV/vis/NIR Spectroelectrochemistry. UV/vis/NIR spectroelectrochemical experiments in reflection mode were performed using an Agilent Cary 5000 Spectrometer and a self-made sample compartment with a layer thickness of 100 μm , consisting of a cylindrical PTFE cell, a sapphire window and an adjustable three in one electrode (6 mm platinum disc working electrode, 1 mm platinum counter and pseudo reference electrode).

DFT Calculations. DFT calculations were performed using the Gaussian 09 program package^[310] with (U)B3LYP^[262, 264, 311] as functionals and 6-31G(d)^[312, 313] as basis set. The structures were geometry optimized, followed by frequency calculations on the optimized structures, which confirmed the existence of minima. Time-dependent (TD)-DFT calculations were carried out on the optimized structures using the same functionals ((U)B3LYP) and basis set (6-31G(d)) as for the geometry optimization. The UV/vis spectra were simulated using the GaussView 5^[314] visualization software package. A half-width of 0.15 eV was assumed for proper simulation. For all calculations, the polarizable continuum model was employed with dichloromethane as solvent.

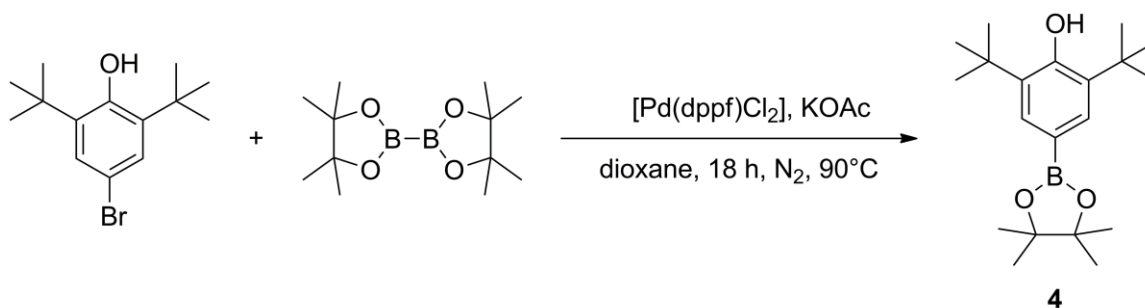
Single Crystal X-ray Diffraction. Single crystal X-ray diffraction data for **1** and **2** were collected at 100 K on a Bruker D8 Quest Kappa diffractometer with a Photon100 CMOS detector and multi-layered mirror monochromated CuK_α radiation. The structures were solved using direct methods, expanded with Fourier techniques and refined with the Shelx software package.^[315] All non-hydrogen atoms were refined anisotropically. Hydrogen atoms were included in the structure factor calculation on geometrically idealized positions. Crystallographic data have been deposited with the Cambridge Crystallographic Data Centre as supplementary publication no. CCDC 1582242 and CCDC 1582243. These data can be obtained free of charge from The Cambridge Crystallographic Data Centre via www.ccdc.ac.uk/data.request/cif.

EPR Spectroscopy. EPR measurements at X-band (9.38 GHz) were carried out using a Bruker ELEXSYS E580 CW EPR spectrometer equipped with an Oxford Instruments helium cryostat (ESR900) and a MercuryITC temperature controller. The spectral simulations were performed using MATLAB 8.6 and the EasySpin 5.0.18 toolbox.^[316]

8.1.2 Syntheses

N,N'-Bis(*rac*-2-ethylhexyl)-6-bromoisoindigo [**3a**] and *N,N'*-bis(*rac*-2-ethylhexyl)-6,6'-dibromoisoindigo [**3b**] were prepared according to literature known procedures.^[304, 317]

8.1.2.1 Synthesis of **4**

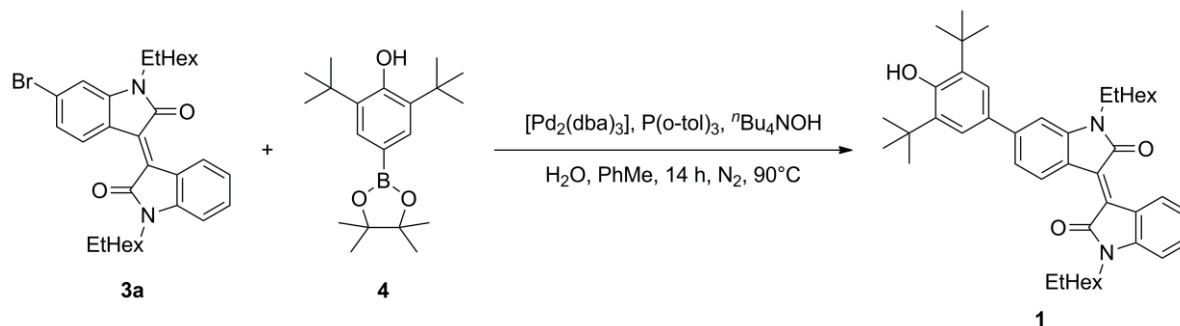


Scheme 8.1.1 | Synthesis of pinacol boronic acid ester **4** by Miyaura borylation.

Bis(diphenylphosphino)ferrocenyl palladium(0) (509 mg, 624 μ mol, 4.50 mol%), 4-bromo-2,6-di-*tert*-butylphenol (3.99 g, 14.0 mmol, 1.00 equivalent), bis(pinacolacto)diboron (4.83 g, 19.0 mmol, 1.36 equivalents) and potassium acetate (3.77 g, 38.0 mmol, 2.71 equivalents) were suspended in dioxane (170 mL) under an atmosphere of nitrogen. After stirring the reaction mixture at 90 °C for 18 h, the suspension was cooled down to room temperature. After filtration, the solvent was removed under reduced pressure and the crude product was purified by silica gel column chromatography (pentane/dichloromethane 2:1) to yield **4** as a colorless solid.

Yield: 3.16 g (9.51 mmol, 68 %). Melting point: 230–231 °C. ¹H NMR (400 MHz, CDCl₃): δ = 1.32 (C(CH₃)₂, 12 H, s), 1.46 (C(CH₃)₃, 18 H, s), 5.45 (OH, 1 H, s), 7.64 (aryl-CH, 2 H, s). ¹³C NMR (101 MHz, CD₂Cl₂): δ = 25.0, 30.5, 34.4, 83.5, 132.0, 135.2, 157.0. ¹¹B NMR (128 MHz, CD₂Cl₂): δ = 31.0. MS (MALDI-ToF, pos. mode, CHCl₃): m/z: calculated for C₂₀H₃₃BO₃: 332.252 [M]⁺, found: 332.219. HRMS (ESI-ToF, neg. mode, CH₂Cl₂/acetonitrile 1/1): m/z: calculated for C₂₀H₃₂BO₃: 331.2450 [M-H]⁻, found: 331.2450. Elemental Analysis: calculated for C₂₀H₃₃BO₃: C: 72.29%, H: 10.01%, found: C: 72.33%, H: 10.17%.

8.1.2.2 Synthesis of **1**

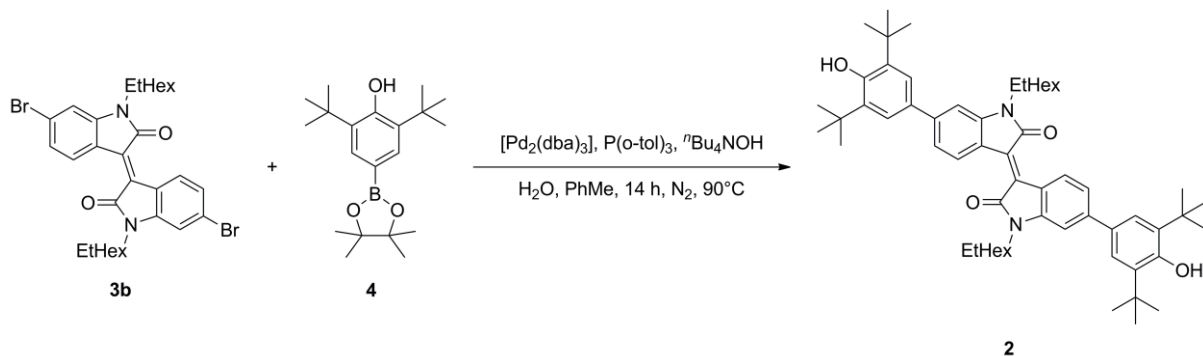


Scheme 8.1.2 | Synthesis of isoindio derivative **1** by Suzuki-Miyaura cross-coupling.

Tris(dibenzylideneacetone)dipalladium(0) (11.0 mg, 11.0 μmol , 3.50 mol%), **4** (153 mg, 460 μmol , 1.31 equivalents), tri(*o*-tolyl)phosphine (9.10 mg, 30.0 μmol , 9.50 mol%), **3a** (200 mg, 350 μmol , 1.00 equivalent) and tetrabutylammonium hydroxide (TBAH) (559 mg, 700 μmol , 2.00 equivalents) were suspended in a mixture of toluene (5 mL) and water (1 mL) under an atmosphere of nitrogen. After stirring the reaction mixture at 90°C for 14 h, the suspension was cooled down to room temperature. Subsequently, hydrochloric acid (1 M, 50 mL) was added and the crude product was extracted with dichloromethane (40 mL). The combined organic layers were washed with water, dried over Na_2SO_4 and the solvent was removed under reduced pressure. The crude product was purified by silica gel column chromatography (pentane/ dichloromethane 2:1) to yield **1** as a brown solid.

Yield: 159 mg (230 μmol , 66 %). Melting point: 155°C . ^1H NMR (400 MHz, CD_2Cl_2): δ = 0.86 – 1.00 (CH_3 , 12 H, m), 1.28 – 1.47 (CH_2 , 16 H, m), 1.50 ($\text{C}(\text{CH}_3)_3$, 18 H, s), 1.89 (alkyl- CH , 2 H, m), 3.71 (NCH_2 , 4 H, m), 5.43 (OH , 1 H, s), 6.82 ($\text{C}_7\text{-H}$, 1 H, dm, $^3J_{\text{HH}} = 7.7$ Hz), 6.99 ($\text{C}_7\text{-H}$, 1 H, d, $^4J_{\text{HH}} = 1.8$ Hz), 7.03 ($\text{C}_5\text{-H}$, 1 H, dd, $^4J_{\text{HH}} = 1.2$ Hz, $^3J_{\text{HH}} = 8.0$ Hz), 7.24 ($\text{C}_5\text{-H}$, 1 H, dd, $^4J_{\text{HH}} = 1.8$ Hz, $^3J_{\text{HH}} = 8.4$ Hz), 7.35 ($\text{C}_6\text{-H}$, 1 H, ddd, $^4J_{\text{HH}} = 1.2$ Hz, $^3J_{\text{HH}} = 7.7$ Hz, $^3J_{\text{HH}} = 7.7$ Hz), 7.50 (aryl- H , 2 H, s), 9.16 ($\text{C}_4\text{-H}$, 1 H, dm, $^3J_{\text{HH}} = 8.0$ Hz), 9.19 ($\text{C}_4\text{-H}$, 1 H, d, $^3J_{\text{HH}} = 8.4$ Hz). ^{13}C NMR (101 MHz, CD_2Cl_2): δ = 10.8 (CH_3), 11.0 (CH_3), 14.2 (CH_3), 14.3 (CH_3), 23.5 (CH_2), 23.5 (CH_2), 24.4 (CH_2), 24.6 (CH_2), 29.1 (CH_2), 29.5 (CH_2), 30.4 ($\text{C}(\text{CH}_3)_3$), 31.1 (CH_2), 31.4 (CH_2), 34.8 ($\text{C}(\text{CH}_3)_3$), 38.0 (alkyl- CH), 38.3 (alkyl- CH), 44.2 (NCH_2), 44.4 (NCH_2), 106.7 (C_7), 108.5 (C_7), 120.3 (C_5), 120.4 ($\text{C}_{9/9'}$), 122.1 (C_5), 122.2 ($\text{C}_{9/9'}$), 124.2 (aryl- C_{ortho}), 129.8 (C_4'), 130.5 (C_4), 131.9 (C_3), 132.3 (C_6), 132.6 (C_3), 133.5 (aryl- C_{ipso}), 136.9 (C_6), 145.5 (aryl- C_{meta}), 146.3 (C_8), 146.4 (C_8), 154.8 (aryl- C_{para}), 168.6 ($\text{C}_{2/2'}$), 169.0 ($\text{C}_{2/2'}$). HRMS (ESI-ToF, pos. mode, $\text{CH}_2\text{Cl}_2/\text{acetonitrile}$ 1/1): m/z : calculated for $\text{C}_{46}\text{H}_{63}\text{N}_2\text{O}_3^+$: 691.48332 $[\text{M}+\text{H}]^+$, found: 691.48498. Elemental Analysis: calculated for $\text{C}_{46}\text{H}_{62}\text{N}_2\text{O}_3$: C: 79.96%, H: 9.04%, N: 4.05% found: C: 79.95%, H: 9.32%, N: 3.78%.

8.1.2.3 Synthesis of 2

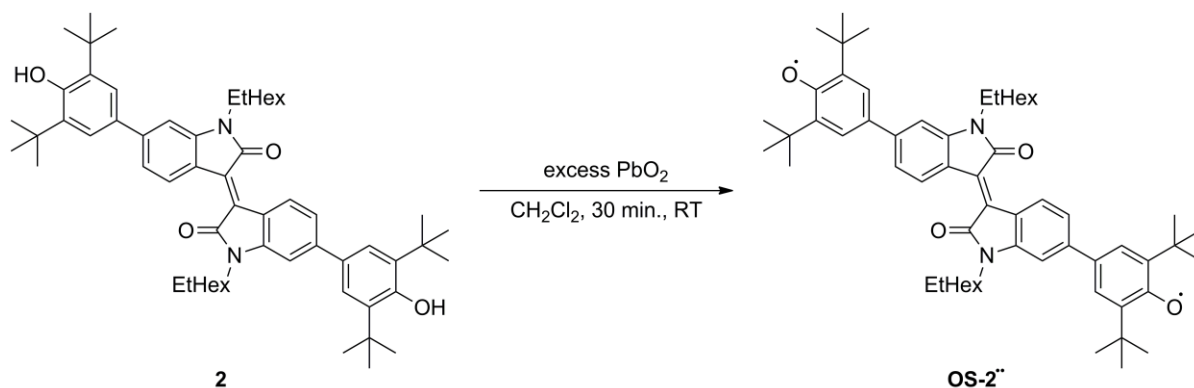


Scheme 8.1.3 | Synthesis of isoindigo derivative **2** by Suzuki–Miyaura cross–coupling.

Tris(dibenzylideneacetone)dipalladium(0) (11.0 mg, 11.0 μmol , 3.50 mol%), **4** (269 mg, 0.81 mmol, 2.61 equivalents), tri(*o*-tolyl)phosphine (9.10 mg, 30.0 μmol , 9.50 mol%), **3b** (200 mg, 310 μmol , 1.00 equivalent) and tetrabutylammonium hydroxide (TBAH) (496 mg, 590 μmol , 1.90 equivalents) were suspended in a mixture of toluene (5 mL) and water (1 mL) under an atmosphere of nitrogen. After stirring the reaction mixture at 90°C for 14 h the suspension was cooled down to room temperature. Subsequently, hydrochloric acid (1 M, 50 mL) was added and the crude product was extracted with dichloromethane (3 x 50 mL). The combined organic layers were washed with water, dried over Na_2SO_4 and the solvent was removed under reduced pressure. The crude product was purified by silica gel column chromatography (gradient of pentane/ dichloromethane from 4:1 to 2:1) to yield **2** as a brown solid.

Yield: 188 mg (210 μmol , 68 %). Melting point: 255°C . ^1H NMR (400 MHz, CD_2Cl_2): δ = 0.90 (CH_3 , 6 H, t, ${}^3J_{\text{HH}} = 7.3$ Hz), 0.97 (CH_3 , 6 H, t, ${}^3J_{\text{HH}} = 7.3$ Hz), 1.29–1.48 (CH_2 , 16 H, m), 1.51 ($\text{C}(\text{CH}_3)_3$, 36 H, s), 1.91 (alkyl- CH , 2 H, q_v), 3.74 (NCH_2 , 4 H, m), 5.42 (OH , 2 H, s), 7.00 ($\text{C}_7\text{-H}$, 2 H, d, ${}^4J_{\text{HH}} = 1.8$ Hz), 7.25 ($\text{C}_5\text{-H}$, 2 H, dd, ${}^4J_{\text{HH}} = 1.8$ Hz, ${}^3J_{\text{HH}} = 8.4$ Hz), 7.50 (aryl- CH , 4 H, s), 9.20 ($\text{C}_4\text{-H}$, 2 H, d, ${}^3J_{\text{HH}} = 8.4$ Hz). ^{13}C NMR (100 MHz, CD_2Cl_2): δ = 11.0 (CH_3), 14.3 (CH_3), 23.5 (CH_2), 24.7 (CH_2), 29.5 (CH_2), 30.4 ($\text{C}(\text{CH}_3)_3$), 31.4 (CH_2), 34.8 ($\text{C}(\text{CH}_3)_3$), 38.3 (alkyl- CH), 44.2 (NCH_2), 106.6 (C_7), 120.3 (C_5), 120.6 (C_3), 124.2 (aryl- C_{ortho}), 130.3 (C_4), 132.0 (C_6), 132.4 (C_9), 136.9 (aryl- C_{meta}), 146.1 (C_8), 146.1 (aryl- C_{para}), 154.8 (aryl- C_{ipso}), 169.1 (C_2). HRMS (ESI-ToF, pos. mode, $\text{CH}_2\text{Cl}_2/\text{acetonitrile}$ 1/1): m/z : calculated for $\text{C}_{60}\text{H}_{83}\text{N}_2\text{O}_4$: 895.63474 $[\text{M}+\text{H}]^+$, found: 895.63369. Elemental Analysis calculated for $\text{C}_{60}\text{H}_{82}\text{N}_2\text{O}_4$: C: 80.49%, H: 9.23%, N: 3.13% found: C: 80.32%, H: 9.63%, N: 3.06%.

8.1.2.4 Synthesis of OS-2^{••}



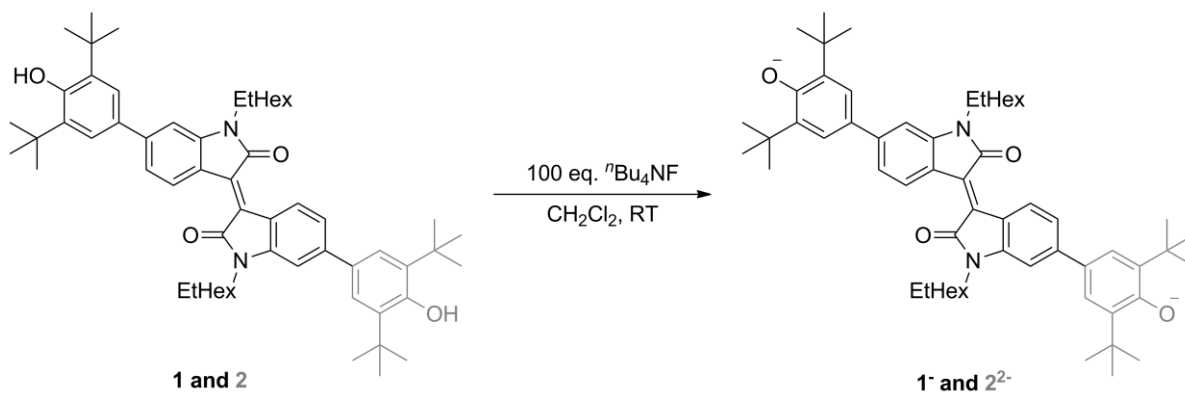
Scheme 8.1.4 | Synthesis of isoindigo biradical **OS-2^{••}** by proton coupled oxidation using PbO₂.

Lead(IV) oxide (89.6 mg, 375 μ mol, 70.8 equivalents) and **2** (4.73 mg, 5.29 μ mol, 1.00 equivalent) were suspended in dichloromethane (5 mL). After stirring the reaction mixture at room temperature for 30 minutes the excess lead(IV) oxide was filtered off and the solvent was removed under reduced pressure to yield **OS-2^{••}** as a green solid.

Yield: 4.59 mg (5.15 μ mol, 97 %). Melting point: 75 °C (decomposition). ¹H NMR (400 MHz, CD₂Cl₂, 300 K): δ = 0.91 (CH₃, 6 H, t, ³J_{HH} = 7.1 Hz), 1.00 (CH₃, 6 H, t, ³J_{HH} = 7.5 Hz), 1.29–1.46 (CH₂, C(CH₃)₃, 52 H, m), 1.83 (alkyl-CH, 2 H, q_v), 3.74 (NCH₂, 4 H, m). ¹H NMR (600 MHz, CD₂Cl₂, 200 K): δ = 0.81–0.94 (CH₃, 12 H, br), 1.22–1.44 (C(CH₃)₃, CH₂, 52 H, m), 1.64 (alkyl-CH, 2 H, br), 3.64 (NCH₂, 4 H, br), 7.00 (aryl-CH, 2 H, br), 7.59 (aryl-CH, 2 H, br), 7.70 (aryl-CH, 2 H, br), 7.79 (aryl-CH, 2 H, br), 7.99 (aryl-CH, 2 H, br). MS (MALDI-ToF, pos. mode, CHCl₃): m/z: calculated for C₆₀H₈₀N₂O₄: 892.612 [M]⁻, found: 892.557. (HRMS ESI-ToF, pos. mode, CH₂Cl₂/acetonitrile 1/1): m/z: calculated for C₆₀H₈₀N₂O₄: 892.6118 [M]⁺, found: 892.6109.

8.1.3 Sample preparation

8.1.3.1 Generation of (di)anions 1^- and 2^{2-}



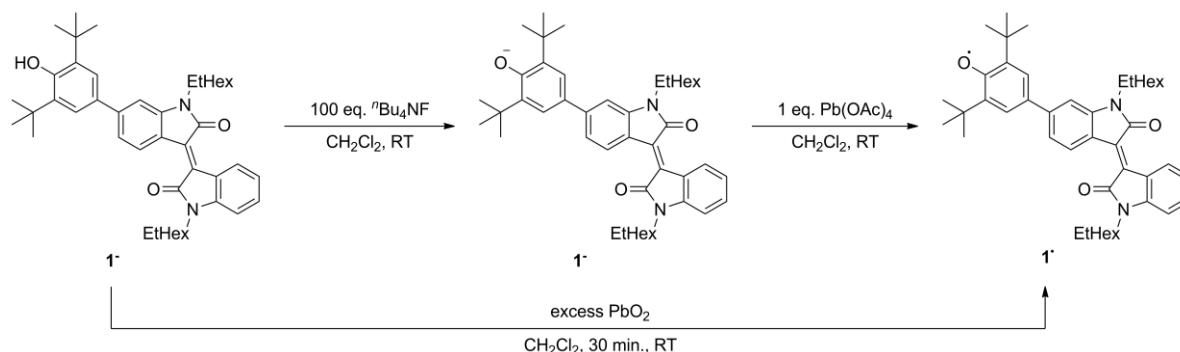
Scheme 8.1.5 | Generation of isoindigo (di)anions 1^- and 2^{2-} by deprotonation with tetrabutylammonium fluoride.

(Di)anions 1^- and 2^{2-} were obtained as its tetrabutylammonium salts dissolved in dichloromethane by deprotonation of **1** and **2** with an excess (100 equivalents) of tetrabutylammonium fluoride (TBAF):

To a solution of **1** (53.7 μg , 77.7 nmol, 1.00 equivalent) in dichloromethane (3.00 mL) a solution of TBAF (2.45 mg, 7.77 μmol , 100 equivalents) in dichloromethane (1.50 mL) is added to give 1^- as its tetrabutylammonium salt ($c = 17.1 \mu\text{M}$) dissolved in DCM.

To a solution of **2** (1.15 mg, 1.29 μmol , 1.00 equivalent) in dichloromethane (25.0 mL) a solution of TBAF (40.7 mg, 129 μmol , 100 equivalents) in dichloromethane (25.0 mL) is added to give 2^{2-} as its tetrabutylammonium salt ($c = 25.8 \mu\text{M}$) dissolved in DCM.

8.1.3.2 Generation of radical **1**'



Scheme 8.1.6 | Generation of isoindigo radical **1**' by successive deprotonation and chemical oxidation of **1**.

Isoindigo radical **1**' was generated either homogeneously by successive deprotonation and chemical oxidation using tetrabutylammonium fluoride (TBAF) and lead(IV) tetraacetate [Pb(OAc)₄] as oxidant (*Method A*) or heterogeneously using PbO₂ (*Method B*).

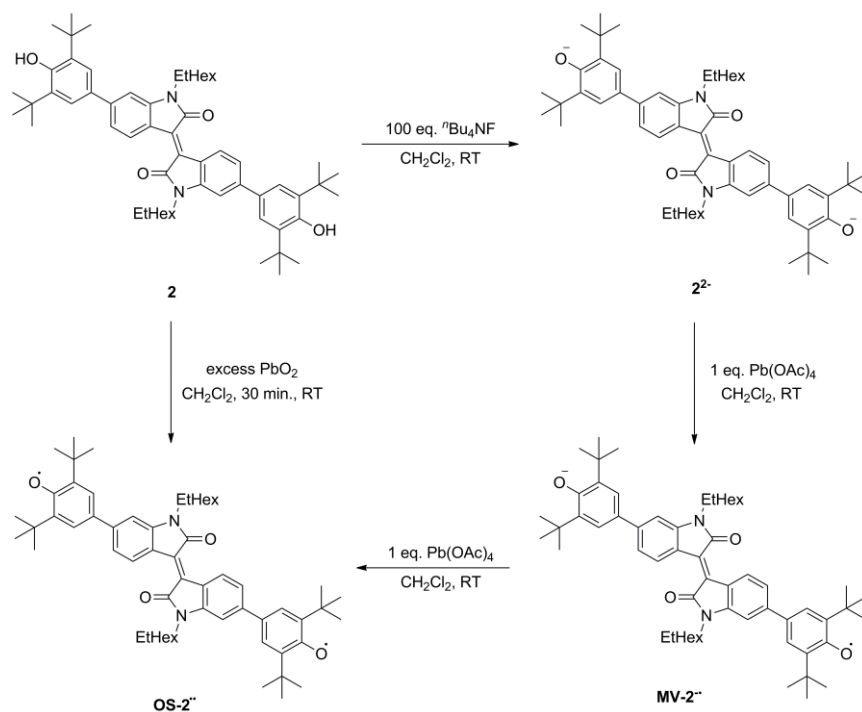
Method A:

To a solution of $7.73 \cdot 10^{-8}$ mol **1** (53.5 μg) in 2.5 mL dichloromethane 48 equivalents TBAF (in 0.5 mL dichloromethane, 3.71 μmol, 970 μg) were added and the solution was stirred for 5 minutes at room temperature. After adding four equivalents of [Pb(OAc)₄] dissolved in 0.5 mL dichloromethane (0.310 μmol, 137 μg), isoindigo radical **1**' is obtained as its dichloromethane solution.

Method B:

To a solution of $7.20 \cdot 10^{-5}$ mol **1** (49.8 mg) in 5 mL dichloromethane 39 equivalents PbO₂ (2.81 mmol, 0.670 g) were added and the resulting suspension was stirred for 30 minutes at room temperature. After filtration of the excess of PbO₂, isoindigo radical **1**' was obtained as its dichloromethane solution which is analytically pure according to MALDI- and ESI-ToF mass spectrometry, UV/vis/NIR absorption and ¹H NMR spectroscopy.

8.1.3.3 Generation of biradical OS-2^{••}



Scheme 8.1.7 | Generation of isoindigo biradical OS-2^{••} by successive deprotonation and chemical oxidation of 2.

Isoindigo biradical OS-2^{••} was generated either homogeneously by successive deprotonation and chemical oxidation using tetrabutylammonium fluoride (TBAF) and lead(IV) tetraacetate [Pb(OAc)₄] as oxidant (Method A) or heterogeneously using PbO₂ (Method B).

Method A:

To a solution of $5.14 \cdot 10^{-8}$ mol 2 (46.0 μ g) in 2.0 mL dichloromethane 200 equivalents TBAF (in 0.5 mL dichloromethane, 10.3 μ mol, 2.69 mg) were added and the solution was stirred for 5 minutes at room temperature. After adding five equivalents of [Pb(OAc)₄] dissolved in 0.5 mL dichloromethane (0.260 μ mol, 114 μ g), isoindigo biradical OS-2^{••} is obtained as its dichloromethane solution .

Method B:

To a solution of $2.89 \cdot 10^{-5}$ mol **2** (25.8 mg) in 5 ml dichloromethane 72 equivalents PbO₂ (2.09 mmol, 500 mg) were added and the resulting suspension was stirred for 30 minutes at room temperature. After filtration of the excess of PbO₂ isoindigo biradical **OS-2^{••}** was obtained as its dichloromethane solution, which is analytically pure according to MALDI- and ESI-ToF mass spectrometry, UV/vis/NIR absorption and ¹H NMR spectroscopy.

8.1.4 X-ray diffractometry

Single crystals of **1** were obtained by slow evaporation of a solution of **1** in chloroform/hexane. *Crystal data for 1* ($C_{46}H_{62}N_2O_3$): $M_r = 690.98$, $0.277 \times 0.118 \times 0.030 \text{ mm}^3$, triclinic space group $P\bar{1}$, $a = 10.9961(2) \text{ \AA}$, $\alpha = 89.1460(10)^\circ$, $b = 12.7659(3) \text{ \AA}$, $\beta = 89.8230(10)^\circ$, $c = 14.3683(3) \text{ \AA}$, $\gamma = 77.4880(10)^\circ$, $V = 1968.83(7) \text{ \AA}^3$, $Z = 2$, $\rho(\text{calcd}) = 1.166 \text{ g}\cdot\text{cm}^{-3}$, $\mu = 0.552 \text{ mm}^{-1}$, $F_{(000)} = 752$, $\text{Goof}(F^2) = 1.079$, $R_I = 0.0534$, $wR^2 = 0.1391$ for $I > 2\sigma(I)$, $R_I = 0.0612$, $wR^2 = 0.1444$ for all data, 7639 unique reflections [$\theta \leq 72.466^\circ$] with a completeness of 97.8 % and 583 parameters, 28 restraints.

Single crystals of **2** were obtained by slow evaporation of a solution of **2** in chloroform/hexane. *Crystal data for 2* ($C_{60}H_{83}N_2O_4$): $M_r = 895.27$, $0.441 \times 0.414 \times 0.385 \text{ mm}^3$, orthorhombic space group $Fddd$, $a = 17.5434(6) \text{ \AA}$, $\alpha = 90^\circ$, $b = 32.8551(15) \text{ \AA}$, $\beta = 90^\circ$, $c = 36.4785(15) \text{ \AA}$, $\gamma = 90^\circ$, $V = 21025.8(15) \text{ \AA}^3$, $Z = 16$, $\rho(\text{calcd}) = 1.131 \text{ g}\cdot\text{cm}^{-3}$, $\mu = 0.533 \text{ mm}^{-1}$, $F_{(000)} = 7808$, $\text{Goof}(F^2) = 1.055$, $R_I = 0.0458$, $wR^2 = 0.1174$ for $I > 2\sigma(I)$, $R_I = 0.0475$, $wR^2 = 0.1189$ for all data, 5204 unique reflections [$\theta \leq 72.295^\circ$] with a completeness of 99.9 % and 368 parameters, 14 restraints.

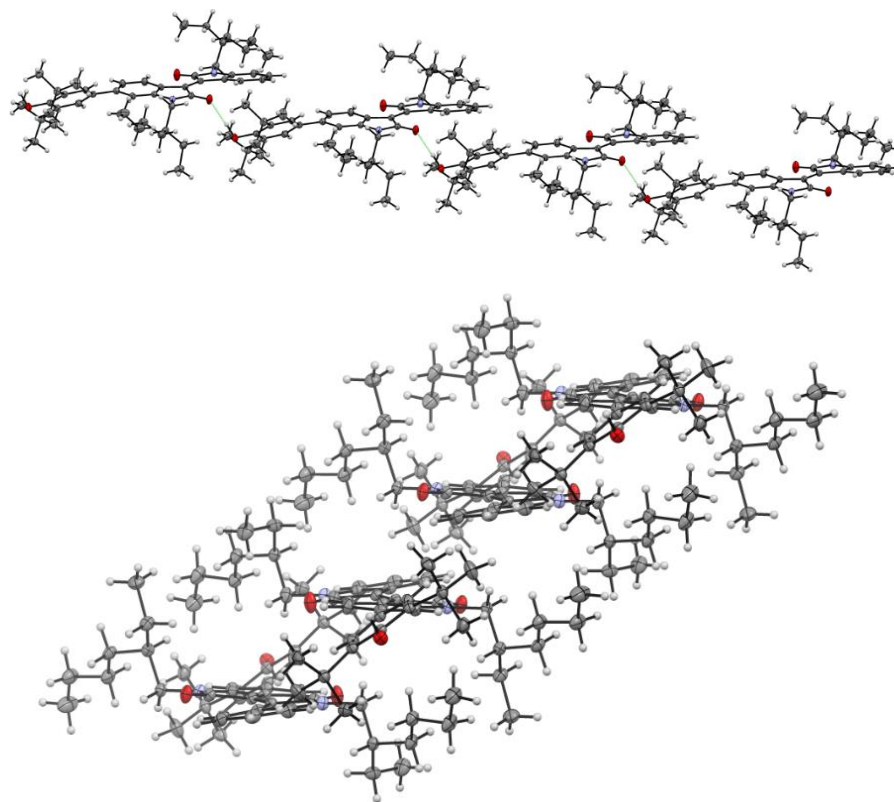
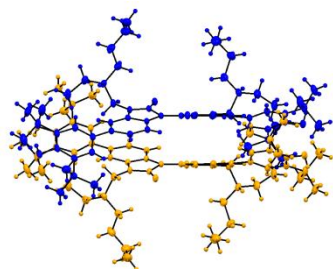


Figure 8.1.1 | Solid state molecular structure of **1** (ellipsoids set to 50 % probability) with intermolecular hydrogen bonding (top, dotted green line, carbon gray, nitrogen blue, oxygen red, hydrogen white) and staircase like packing arrangement (bottom).

(a)



(b)

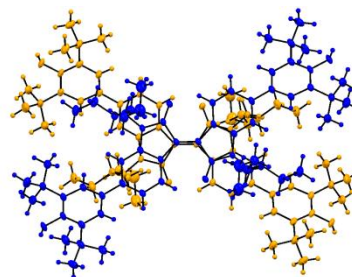


Figure 8.1.2 | Solid state molecular structure of **2** (ellipsoids set to 50 % probability) with side view (a) and top-view (b) an a rotoinverted dimer unit.

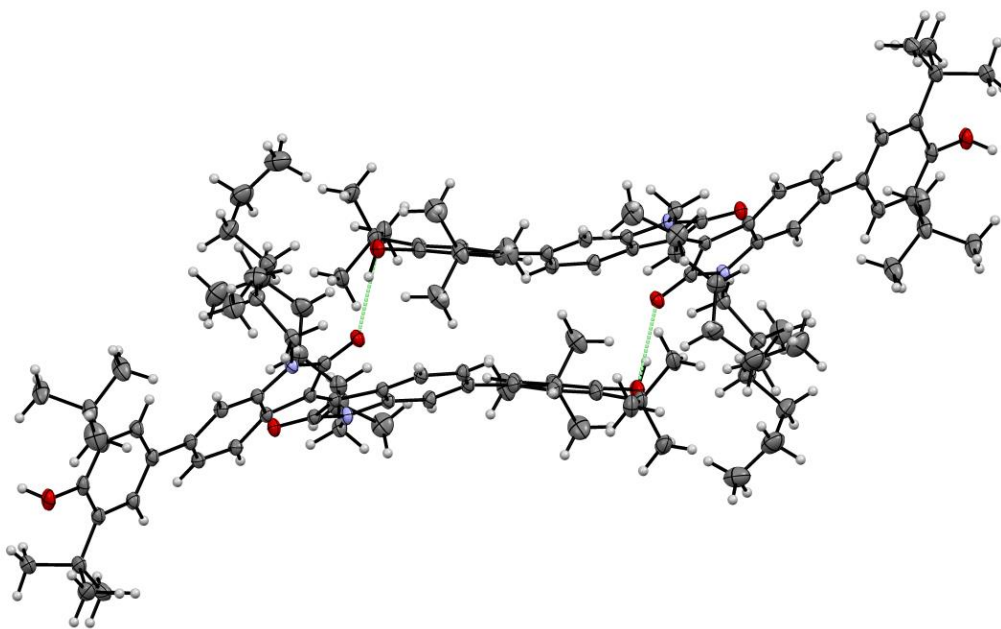


Figure 8.1.3 | Solid state molecular structure of **2** (ellipsoids set to 50 % probability) with double self-complementary intermolecular hydrogen bonding (dotted green line).

8.1.5 Mass spectrometry

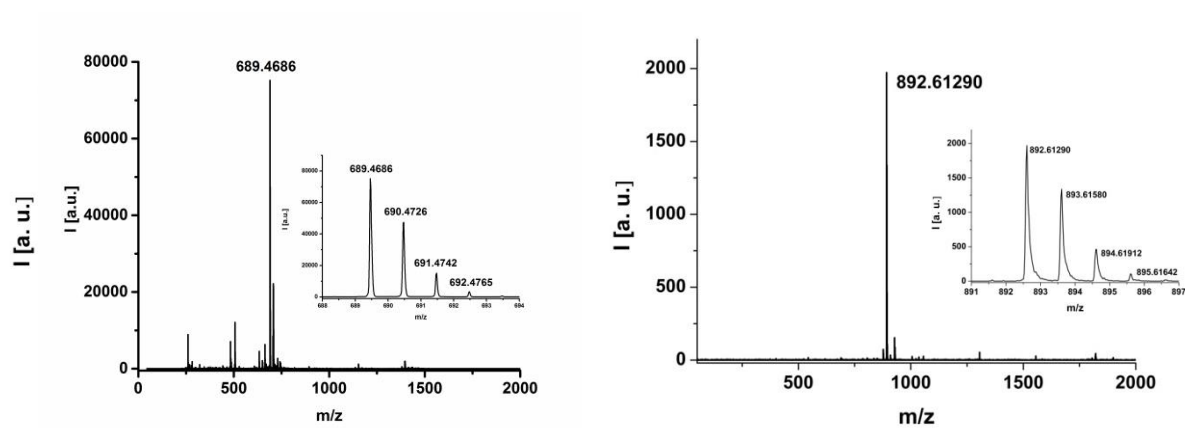


Figure 8.1.4 | ESI-ToF high resolution mass spectra of **1•** (left) and **OS-2••** (right). Inset: Isotopic distribution of (bi)radicals **1•** (left) and **OS-2••** (right).

8.1.6 UV/vis/NIR spectroscopy and spectroelectrochemistry

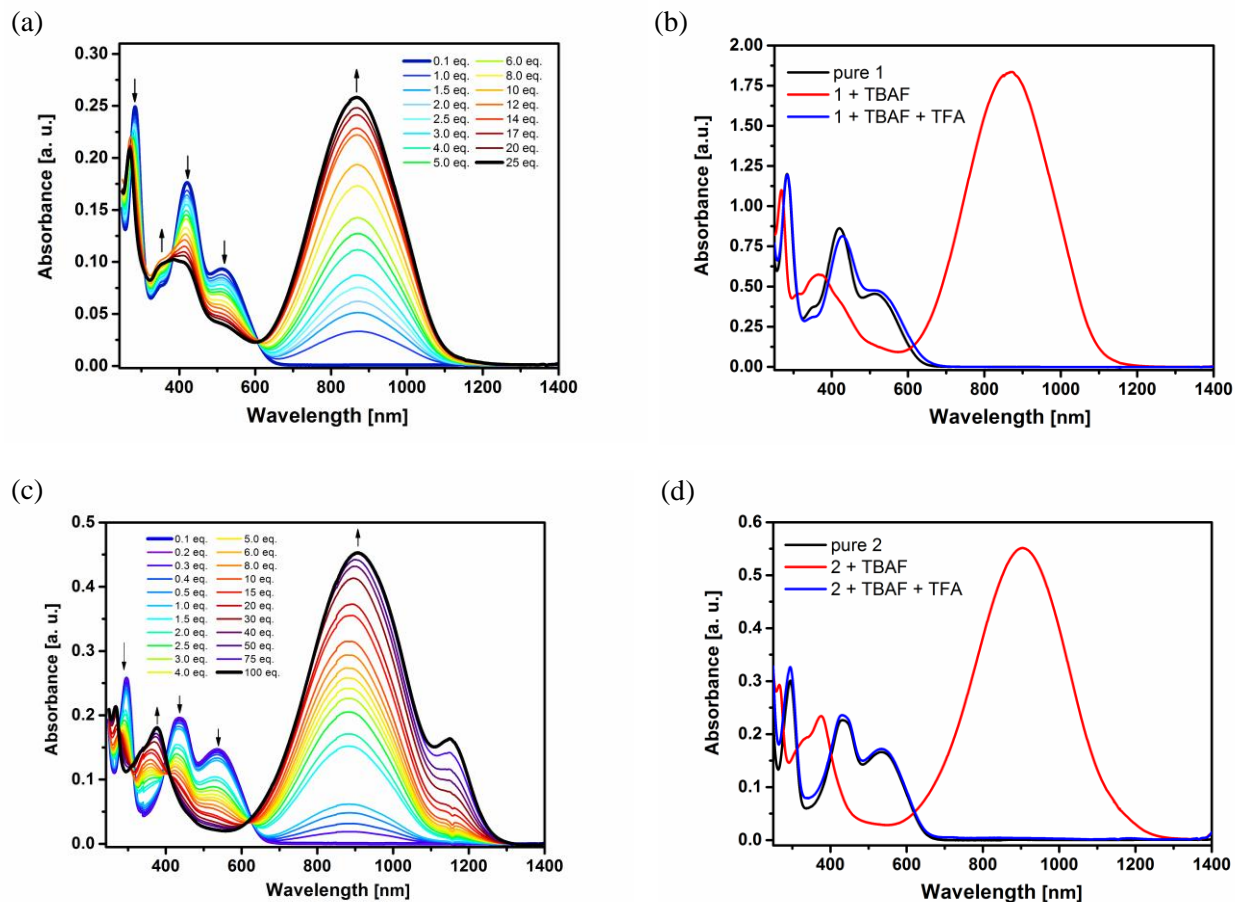


Figure 8.1.5 | UV/vis/NIR absorption spectral changes of **1** (a) ($c = 2.59 \cdot 10^{-5}$ M in CH_2Cl_2) and **2** (c) ($c = 2.98 \cdot 10^{-5}$ M in CH_2Cl_2) upon titration with ${}^n\text{Bu}_4\text{NF}$ solutions ($c = 5.14 \cdot 10^{-3}$ M in CH_2Cl_2) to form anions **1**⁻ and **2**²⁻. Arrows indicate spectral changes with ongoing deprotonation. UV/vis/NIR absorption spectrum of **1**⁻ (red, $c = 2.59 \cdot 10^{-5}$ M in CH_2Cl_2) freshly prepared by adding 100 eq. ${}^n\text{Bu}_4\text{NF}$ to a solution of **1** (black) and after addition of 100 eq. trifluoroacetic acid (TFA) (blue) in CH_2Cl_2 (b). UV/vis/NIR absorption spectrum of **2**²⁻ (red, $c = 2.98 \cdot 10^{-5}$ M in CH_2Cl_2) freshly prepared by adding 100 eq. ${}^n\text{Bu}_4\text{NF}$ to a solution of **2** (black) and after addition of 100 eq. trifluoroacetic acid (blue) in CH_2Cl_2 (d).

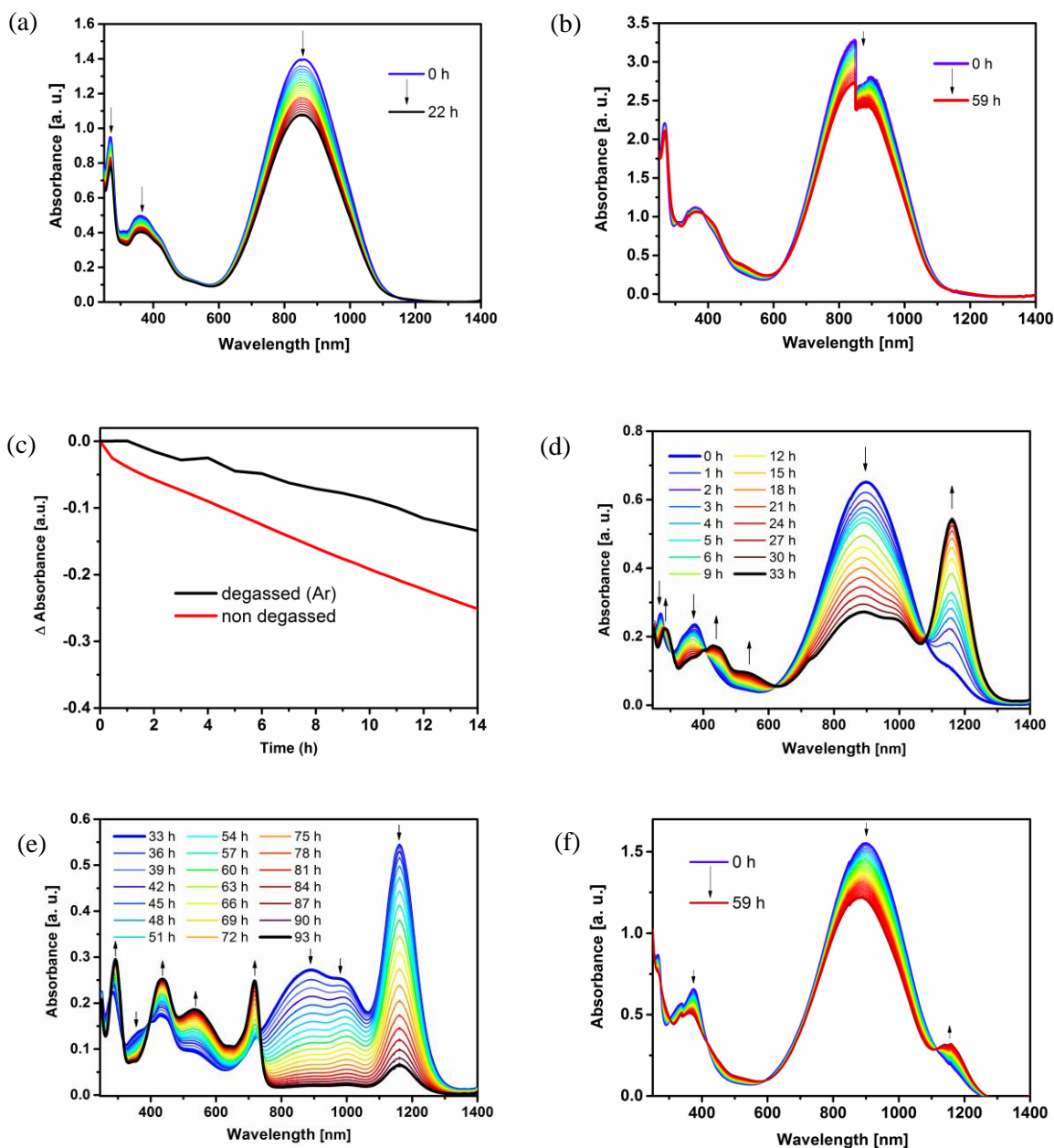


Figure 8.1.6 | Time-dependent UV/vis/NIR absorption spectral changes of \mathbf{I}^- ($c = 3.92 \cdot 10^{-5}$ M in CH_2Cl_2) under ambient conditions (a) and in degassed solution (b). Absorption decay at 848 nm over time for degassed (black) and non-degassed (red) solutions of \mathbf{I}^- (c). Time-dependent UV/vis/NIR absorption spectral changes of $\mathbf{2}^{2-}$ ($c = 1.7 \cdot 10^{-5}$ M in CH_2Cl_2) under ambient conditions (d, e) and in degassed solution ($c = 3.4 \cdot 10^{-5}$ M in CH_2Cl_2) (f). Arrows indicate spectral changes over time.

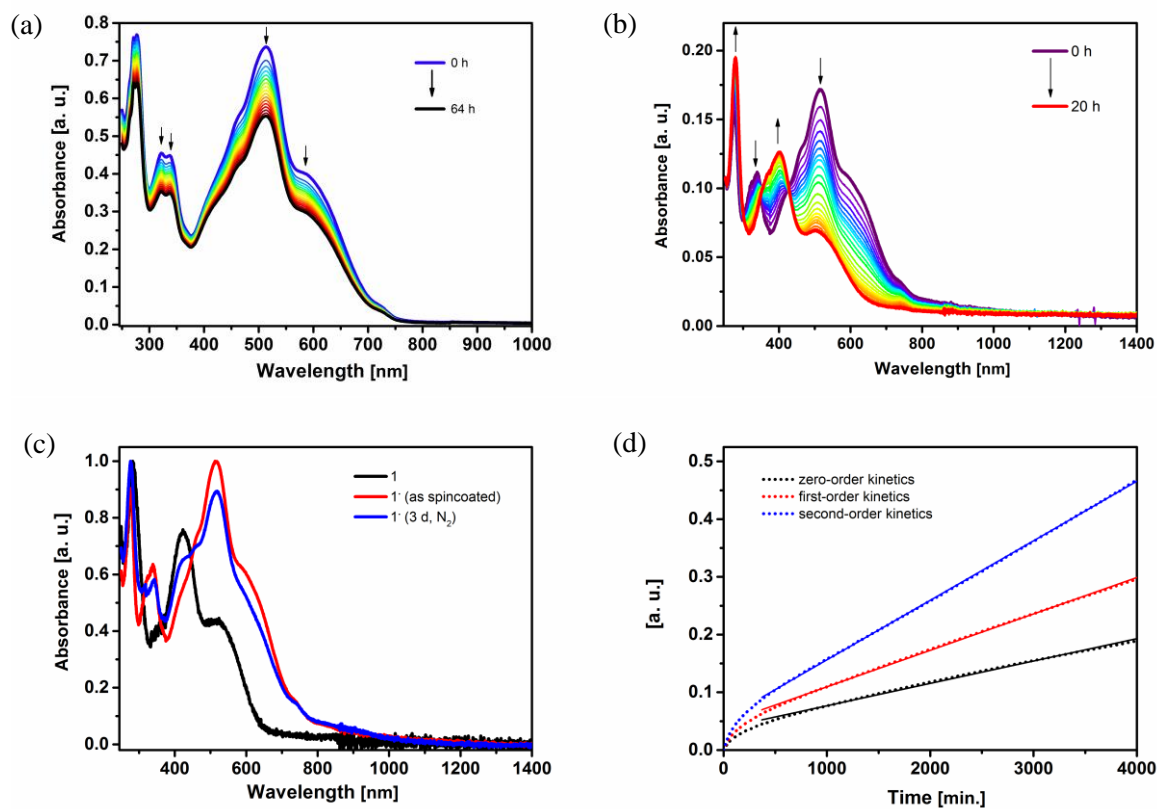


Figure 8.1.7 | Time-dependent UV/vis/NIR absorption spectral changes of a chloroform solution of $\mathbf{1}^*$ (a) ($c = 3.4 \cdot 10^{-5}$ M, ambient conditions). Time-dependent UV/vis/NIR absorption spectral changes of a spincoated thin film of $\mathbf{1}^*$ ($c = 1.4 \cdot 10^{-2}$ M in CHCl_3 , 25 μL , 3000 rpm, 30 s) upon decomposition under ambient conditions (b) and under an atmosphere of nitrogen (c). Arrows indicate spectral changes over time. Spectral changes of $\mathbf{1}^*$ (in CHCl_3) at 514 nm plotted versus time using zero-, first- and second-order rate equations (d).

Table 8.1.1 | Kinetic evaluation of the time-dependent UV/vis/NIR absorption spectral changes of **1*** ($c = 3.4 \cdot 10^{-5}$ M in CHCl_3) upon decomposition under ambient conditions.

rate law	equations		linear regression	rate constant k	half-life $\tau_{\frac{1}{2}}$ [d]	Pearson R^2
	rate equation	half-life				
0 ord.	$[A]_0 - [A]_t = kt$	$\tau_{\frac{1}{2}} = \frac{A_0}{2k}$	$y = 3.87605 \cdot 10^{-5}x + 0.03786$	$1.07 \cdot 10^{-7} \frac{\text{mol}}{\text{L h}}$	6.60	0.99685
1st ord.	$\ln \frac{[A]_0}{[A]_t} = kt$	$\tau_{\frac{1}{2}} = \frac{\ln 2}{k}$	$y = 6.31445 \cdot 10^{-5}x + 0.04631$	$3.79 \cdot 10^{-3} \frac{1}{\text{h}}$	7.62	0.99930
2nd ord.	$\frac{1}{[A]_t} - \frac{1}{[A]_0} = kt$	$\tau_{\frac{1}{2}} = \frac{1}{kA_0}$	$y = 1.03147 \cdot 10^{-4}x + 0.05302$	$134 \frac{\text{L}}{\text{mol h}}$	9.14	0.99991

After an initial period of time, no significant deviations from linearity can be observed for all applied rate equations. Therefore, the minimum half-life of **1*** has been estimated according to zero-order kinetics with a value of $\tau_{\frac{1}{2}} = 6.60$ d.

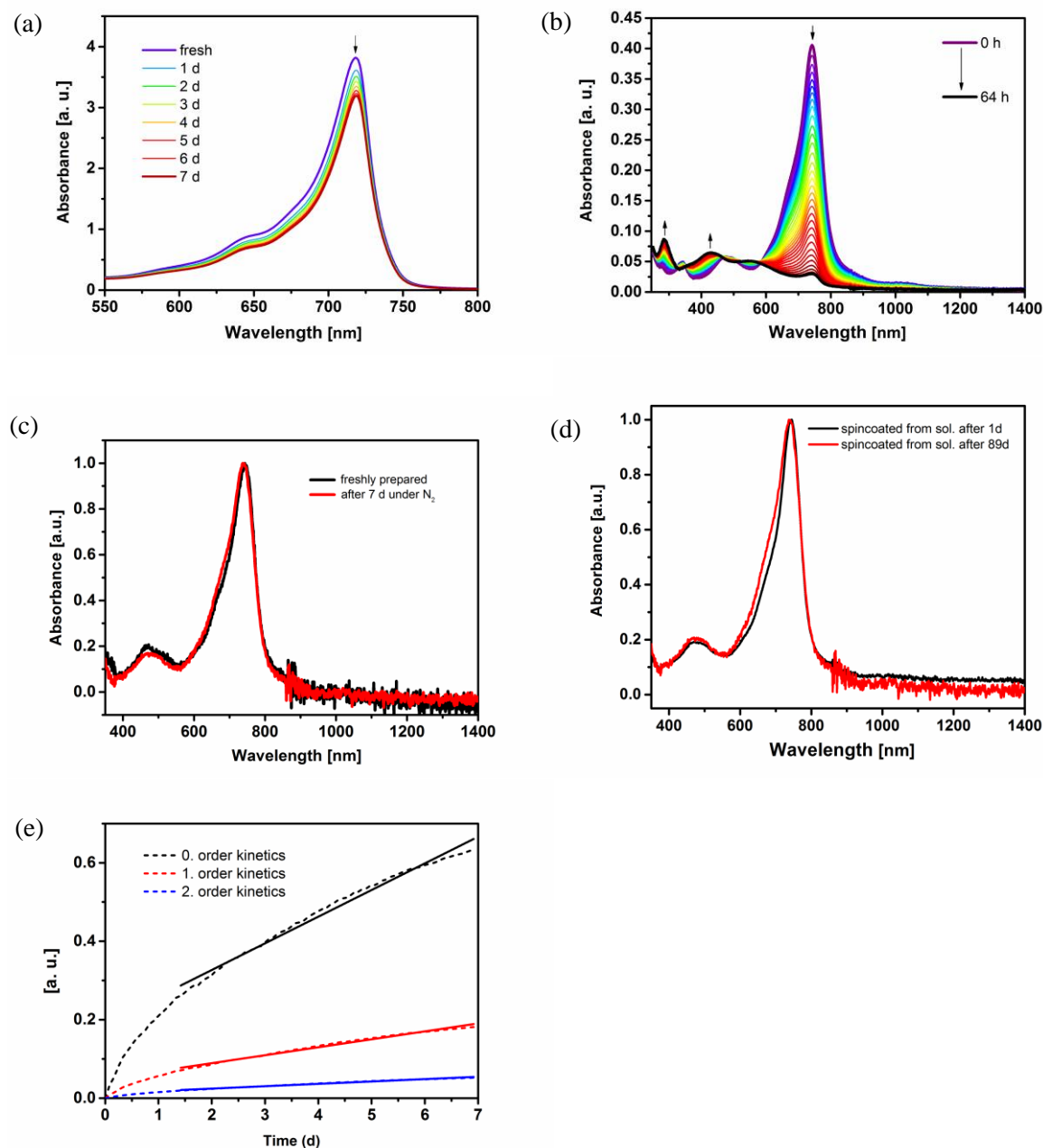


Figure 8.1.8 | Time-dependent UV/vis/NIR absorption spectral changes of a tetrachloromethane solution of **OS-2*** ($c = 3.1 \cdot 10^{-5}$ M, ambient conditions) (a). Time-dependent UV/vis/NIR absorption spectral changes of a spincoated thin film of **OS-2*** ($c = 5.8 \cdot 10^{-3}$ M in CH_2Cl_2 , 25 μL , 3000 rpm, 30 s) under ambient conditions (b) and under an atmosphere of nitrogen (c). UV/vis/NIR absorption spectra of a thin film spincoated under an atmosphere of nitrogen after 1d (black line) and after 89d (red line) from the same solution of **OS-2*** ($c = 5.8 \cdot 10^{-3}$ M in CH_2Cl_2 , 25 μL , 3000 rpm, 30 s) (d). Absorption spectral changes of **OS-2*** (in CCl_4) at 718 nm plotted versus time using zero-, first- and second-order rate equations (e). Arrows indicate spectral changes over time.

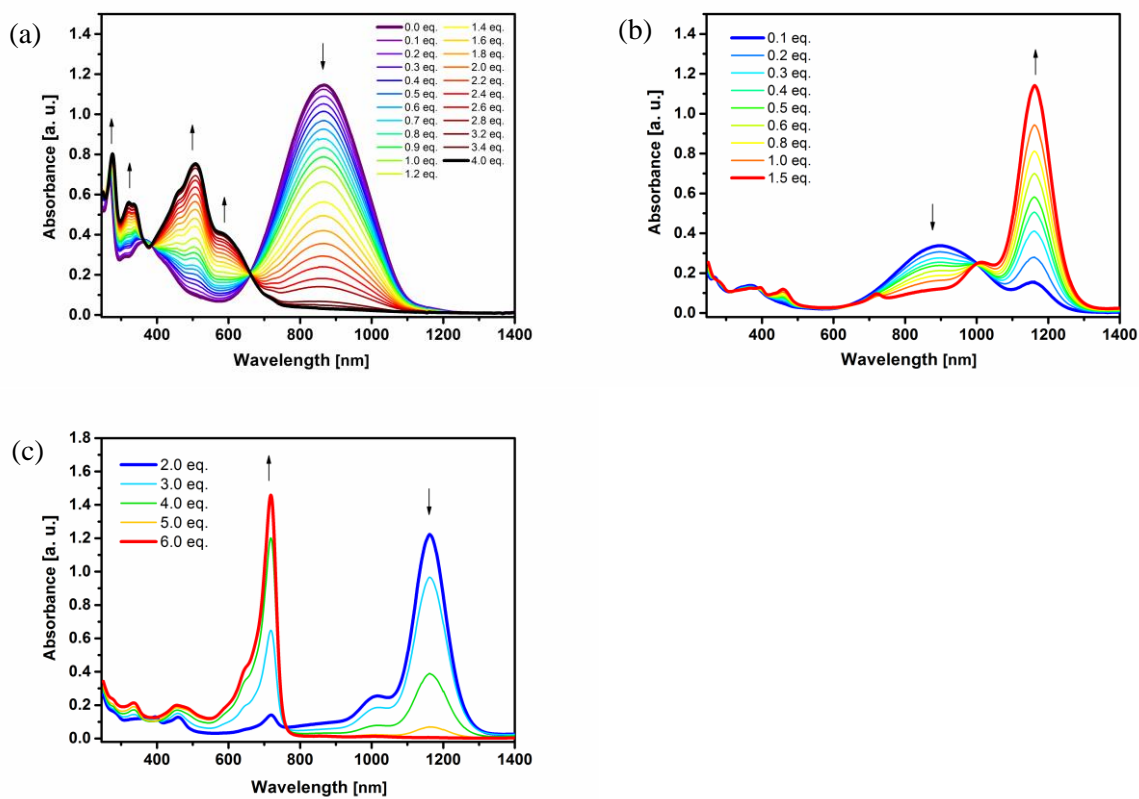


Figure 8.1.9 | UV/vis/NIR absorption spectral changes of 1^- (a) ($c = 3.1 \cdot 10^{-5} \text{ M}$ in CH_2Cl_2) and 2^{2-} (b, c) ($c = 3.0 \cdot 10^{-5} \text{ M}$ in CH_2Cl_2) upon oxidation with $[\text{Pb}(\text{OAc})_4]$. Arrows indicate spectral changes upon addition of $[\text{Pb}(\text{OAc})_4]$.

Table 8.1.2 | Kinetic evaluation of the time-dependent UV/vis/NIR absorption spectral changes of **OS-2^{••}** ($c = 3.1 \cdot 10^{-5}$ M in CCl_4) upon decomposition under ambient conditions.

rate law	equations		linear regression	rate constant k	half-life $\tau_{\frac{1}{2}}$ [d]	Pearson R^2
	rate equation	half-life				
zero order	$[A]_0 - [A]_t = kt$	$\tau_{\frac{1}{2}} = \frac{A_0}{2k}$	$y = 0.06795 x + 0.19086$	$2.29 \cdot 10^{-8} \frac{\text{mol}}{\text{L h}}$	28	0.98659
first order	$\ln \frac{[A]_0}{[A]_t} = kt$	$\tau_{\frac{1}{2}} = \frac{\ln 2}{k}$	$y = 0.02027 x + 0.04866$	$8.45 \cdot 10^{-4} \frac{1}{\text{h}}$	34	0.98947
second order	$\frac{1}{[A]_t} - \frac{1}{[A]_0} = kt$	$\tau_{\frac{1}{2}} = \frac{1}{kA_0}$	$y = 0.00605 x + 0.01225$	$31.1 \frac{\text{L}}{\text{mol h}}$	43	0.99195

The minimum half-life of **OS-2^{••}** has been estimated to be $\tau_{\frac{1}{2}} = 28$ d according to zero-order reaction kinetics.

Table 8.1.3 | Half-life of **OS-2** in different solvents determined by kinetic evaluation of the time-dependent UV/vis/NIR absorption spectral changes upon decomposition under ambient conditions.

solvent	$\tau_{\frac{1}{2}}$ (zero-order)	$\tau_{\frac{1}{2}}$ (first-order)	$\tau_{\frac{1}{2}}$ (second-order)
	Pearson R ²	Pearson R ²	Pearson R ²
benzene	7.3 d	9.1 d	12 d
C ₆ H ₆	0.99880	0.99956	0.99901
dichloromethane	21 d	29 d	41 d
CH ₂ Cl ₂	0.98691	0.98742	0.98790
tetrachloromethane	28 d	34 d	43 d
CCl ₄	0.98659	0.98947	0.99195

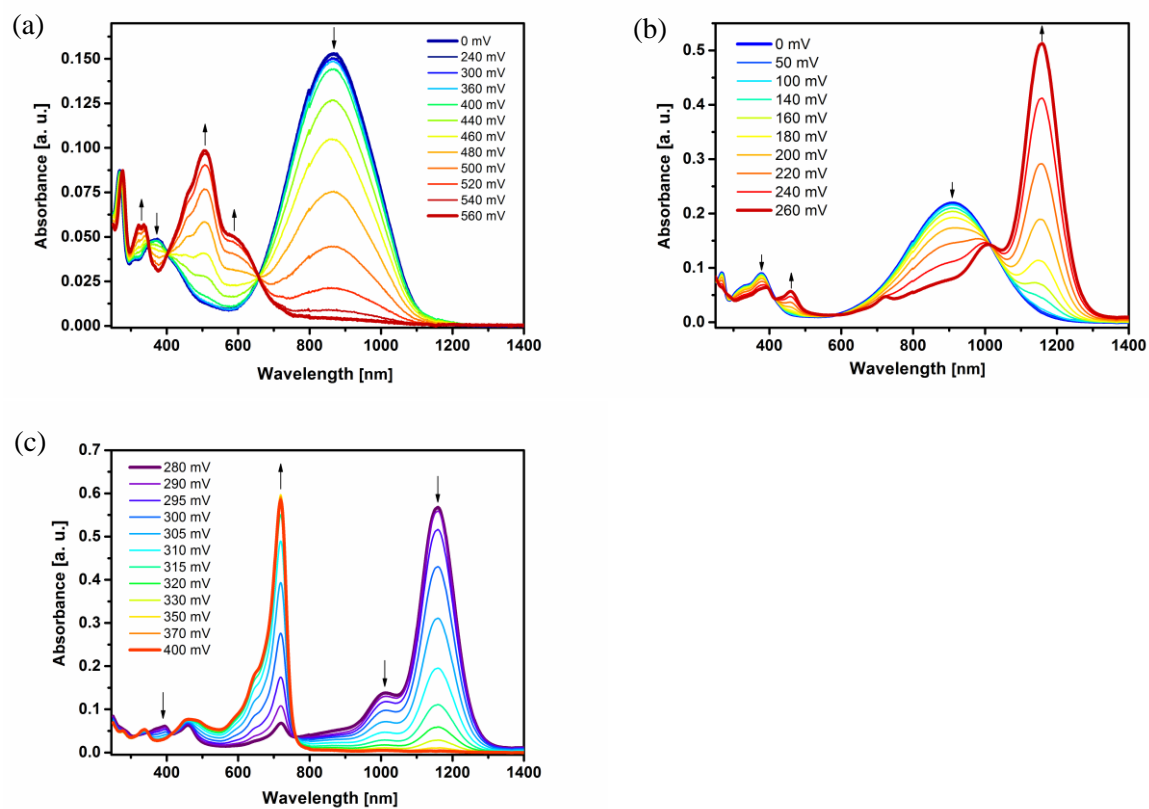


Figure 8.1.10 | UV/vis/NIR absorption spectral changes of 1^- (a) ($c = 1.7 \cdot 10^{-4} \text{ M}$ in CH_2Cl_2) and 2^{2-} (b, c) ($c = 1.9 \cdot 10^{-4} \text{ M}$ in CH_2Cl_2) upon electrochemical oxidation (0.2 M ${}^t\text{Bu}_4\text{NPF}_6$, RT). Arrows indicate spectral changes with increasing positive potential.

Table 8.1.4 | Absorption maxima of neutral isoindigo derivatives **1** and **2**, (di)anions **1⁻** and **2²⁻**, mixed valent intermediate **MV-2⁻**, and (bi)radicals **1[•]** and **OS-2^{••}** in dichloromethane solution.

Compound	λ_{max} [nm]	ϵ [M ⁻¹ cm ⁻¹] (λ)
1	284, 421, 514	17400 (421 nm)
1⁻	269, 374, 867	25600 (867 nm)
1[•]	276, 321, 336, 504, 590	16500 (504 nm)
2	296, 437, 537	19500 (437 nm)
2²⁻	267, 377, 905	45300 (905 nm)
MV-2⁻	394, 459, 720, 1011, 1158	117300 (1158 nm)
OS-2^{••}	277, 338, 463, 647, 719	123500 (719 nm)

8.1.7 NMR spectroscopy

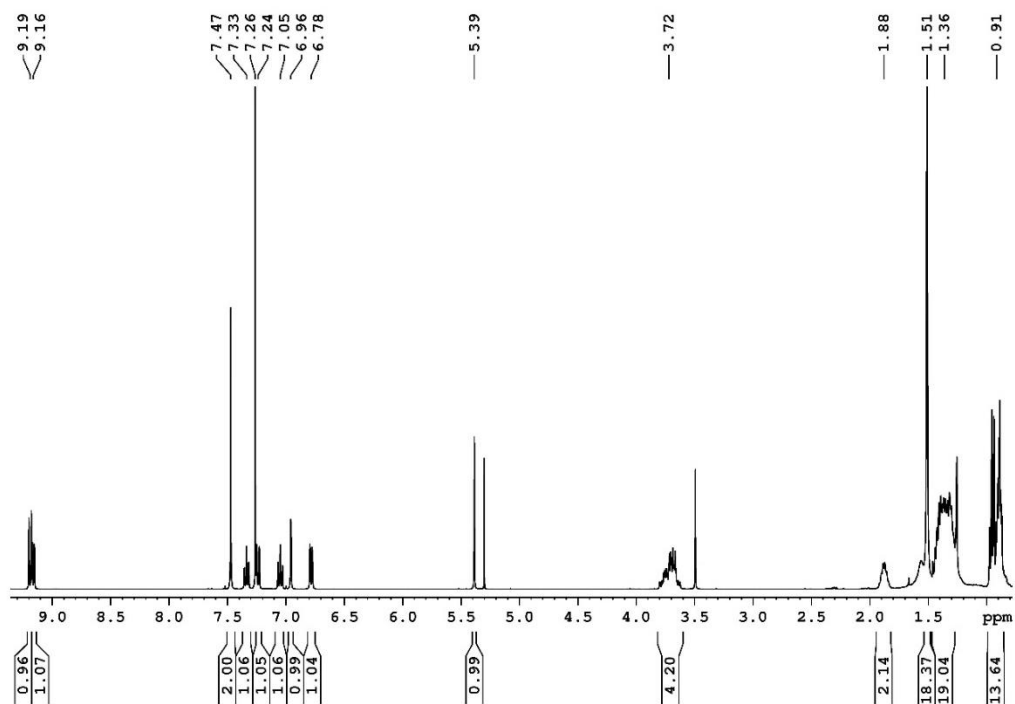


Figure 8.1.11 | ^1H NMR spectrum of **1** (400 MHz, CD_2Cl_2 , 300 K).

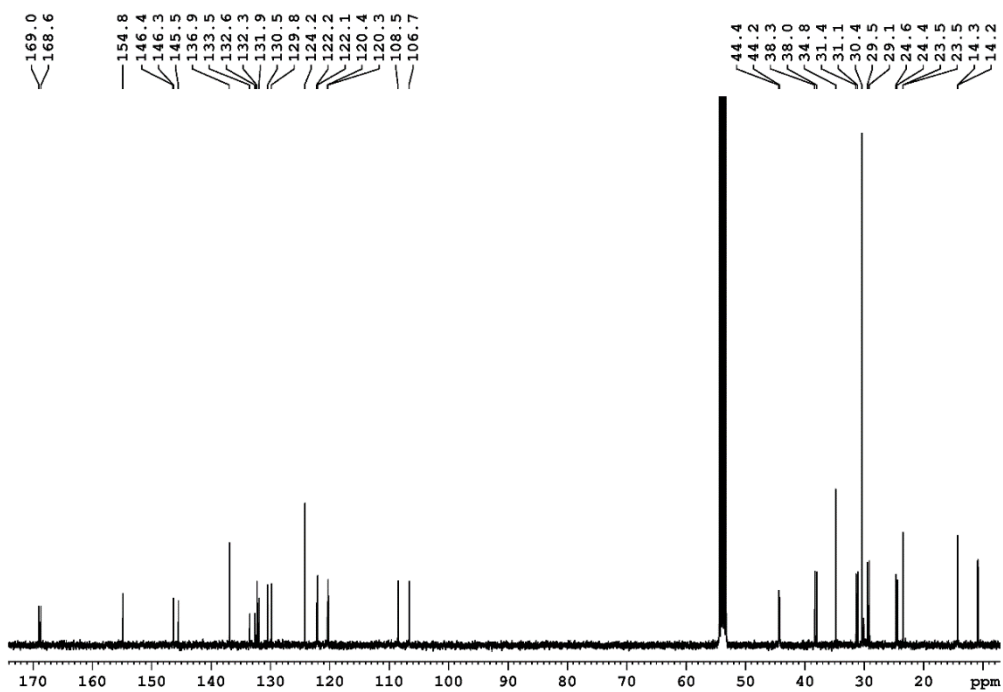


Figure 8.1.12 | ^{13}C NMR spectrum of **1** (101 MHz, CD_2Cl_2 , 300 K).

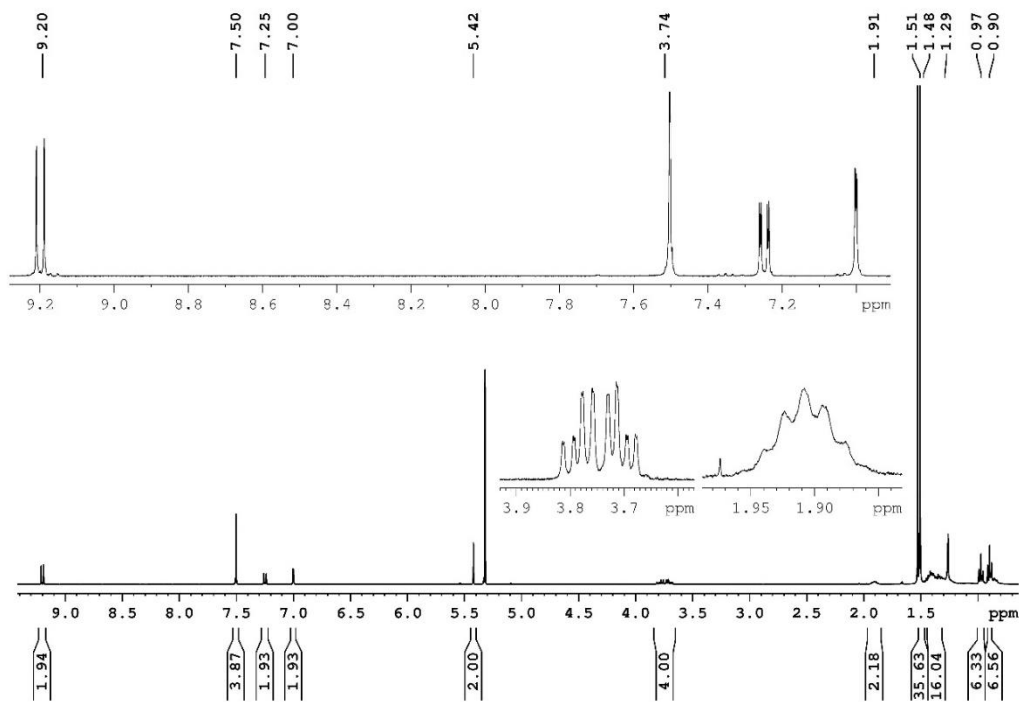


Figure 8.1.13 | ^1H NMR spectrum of **2** (400 MHz, CD_2Cl_2 , 300 K).

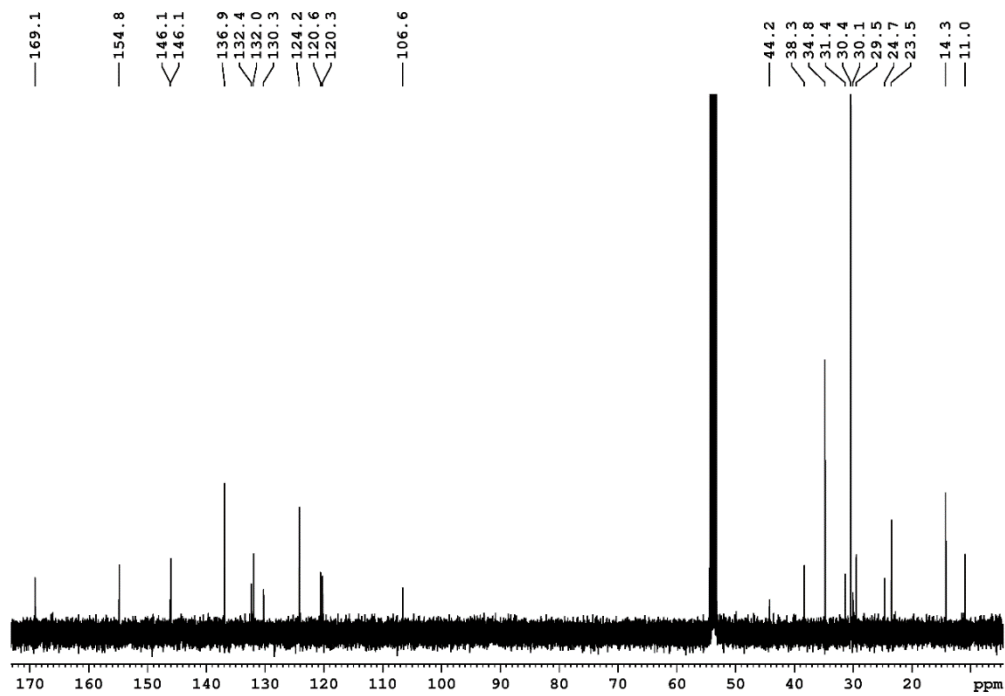


Figure 8.1.14 | ^{13}C NMR spectrum of **2** (101 MHz, CD_2Cl_2 , 300 K).

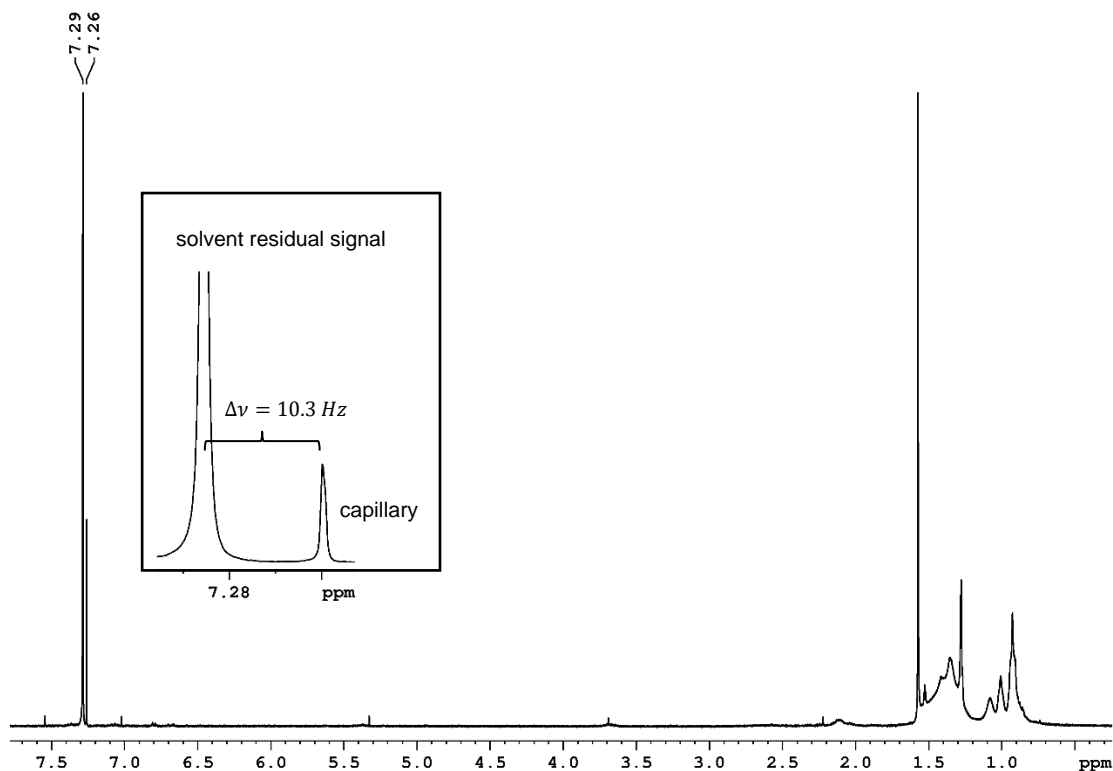


Figure 8.1.15 | ^1H NMR spectrum of isoindigo radical $\mathbf{1}^*$ in CDCl_3 (4.5 mM, 300 K, 400 MHz) containing a flame-sealed capillary of pure CDCl_3 . Inset: Solvent residual signals are magnified for better illustration.

Determination of the magnetic susceptibility in solution:

The magnetic susceptibility of $\mathbf{1}^*$ was determined using Evans method.^[208–212] Therefore, ^1H NMR spectroscopic experiments (Bruker Avance III HD 400, 400.1 MHz, spin rate 20 Hz, 300 K) were performed on a CDCl_3 solution of $\mathbf{1}^*$ (4.5 mM) containing a flame-sealed capillary of pure CDCl_3 . Due to the paramagnetic nature of $\mathbf{1}^*$ two individual and well separated resonances were detected for the solvent residual signals at 7.29 and 7.26 ppm beside the strongly broadened resonances of isoindigo radical $\mathbf{1}^*$, which have been assigned to the paramagnetic solution and the capillary, respectively. Based on the concentration of the solution (4.5 mM, CDCl_3) and the paramagnetic shift of the solvent residual signal (10.3 Hz shifted to lower field compared with the reference capillary), the paramagnetic susceptibility can be calculated according to equation (S1).

$$\chi_P = \chi_0 + \frac{3 \Delta\nu}{4 \pi \nu_0 m} + \frac{\chi_0(\rho_0 - \rho_s)}{m} \quad (\text{S1})$$

χ_P = mass susceptibility of the dissolved compound [$\text{cm}^3 \cdot \text{g}^{-1}$], χ_0 = mass susceptibility of the solvent [$\text{cm}^3 \cdot \text{g}^{-1}$], $\Delta\nu$ = paramagnetic shift [Hz], ν_0 = frequency of the spectrometer [Hz], m = concentration [$\text{g} \cdot \text{cm}^{-3}$], ρ_0 = density of the pure solvent [$\text{g} \cdot \text{cm}^{-3}$], ρ_s = density of the solution [$\text{g} \cdot \text{cm}^{-3}$].

By neglecting minor contributions of the diamagnetic susceptibility and density differences, the paramagnetic susceptibility can be calculated according to equation S2 after conversion in the SI system.

$$\chi_{para}^M = \frac{3 \cdot \Delta\nu}{10^3 \cdot \nu_0 \cdot c} \quad (\text{S2})$$

χ_{para}^M = molar susceptibility of the dissolved compound [$\text{m}^3 \cdot \text{mol}^{-1}$], $\Delta\nu$ = paramagnetic shift [Hz], ν_0 = frequency of the spectrometer [Hz], c = concentration [M].

Thus, the effective magnetic momentum can be expressed by equation S3.

$$\mu_{eff} = \sqrt{\frac{\chi_{para}^M \cdot 3 \cdot k \cdot T}{\mu_B^2 \cdot \mu_0 \cdot N_A}} \quad (\text{S3})$$

μ_{eff} = effective magnetic momentum [μ_B], χ_{para}^M = molar susceptibility of the dissolved compound [$\text{m}^3 \cdot \text{mol}^{-1}$], k = Boltzmann constant [$\text{J} \cdot \text{K}^{-1}$], T = temperature [K], μ_B = Bohr magneton [$\text{J} \cdot \text{T}^{-2}$], μ_0 = magnetic constant [$\text{N} \cdot \text{A}^{-2}$], N_A = Avogadro constant [mol^{-1}].

Neglecting orbital contributions to the effective magnetic moment assuming that the electron spin is prevailing for the magnetic behavior, the number of unpaired electrons correlates to the effective magnetic moment according to equation S4.

$$\mu_{eff,spin\ only} = \sqrt{n(n+2)} \quad (\text{S4})$$

$\mu_{eff,spin\ only}$ = effective magnetic moment neglecting orbital contributions [μ_B], n = number of unpaired electrons.

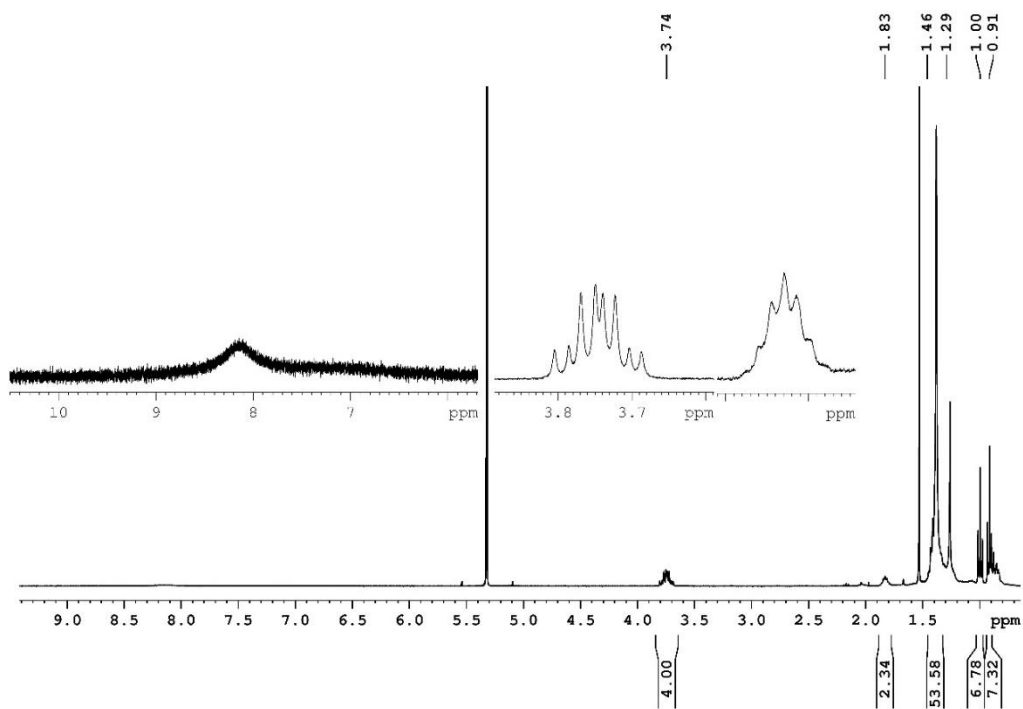


Figure 8.1.16 | ^1H NMR spectrum of OS-2'' (400 MHz, CD_2Cl_2 , 300 K).

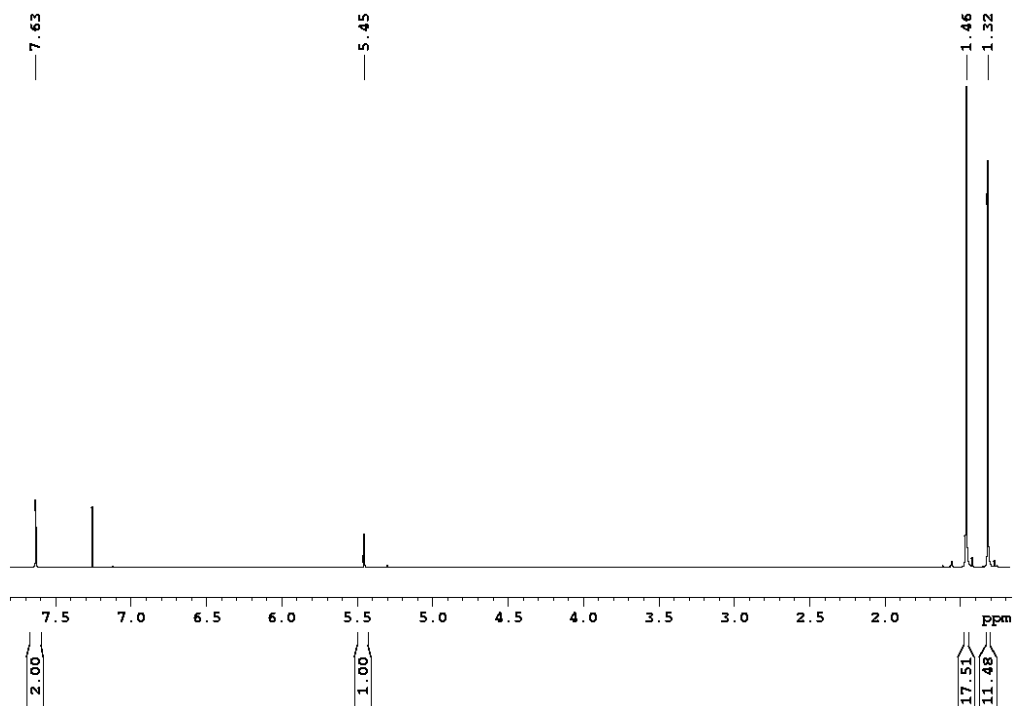


Figure 8.1.17 | ^1H NMR spectrum of 4 (400 MHz, CDCl_3 , 300 K).

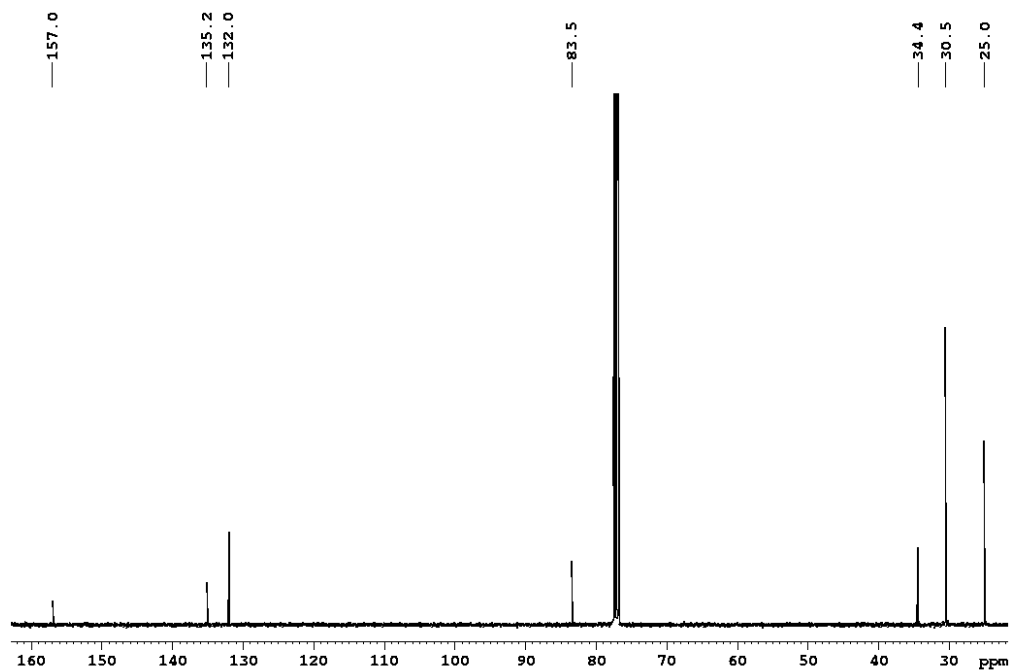


Figure 8.1.18 | ^{13}C NMR spectrum of **4** (101 MHz, CDCl_3 , 300 K).

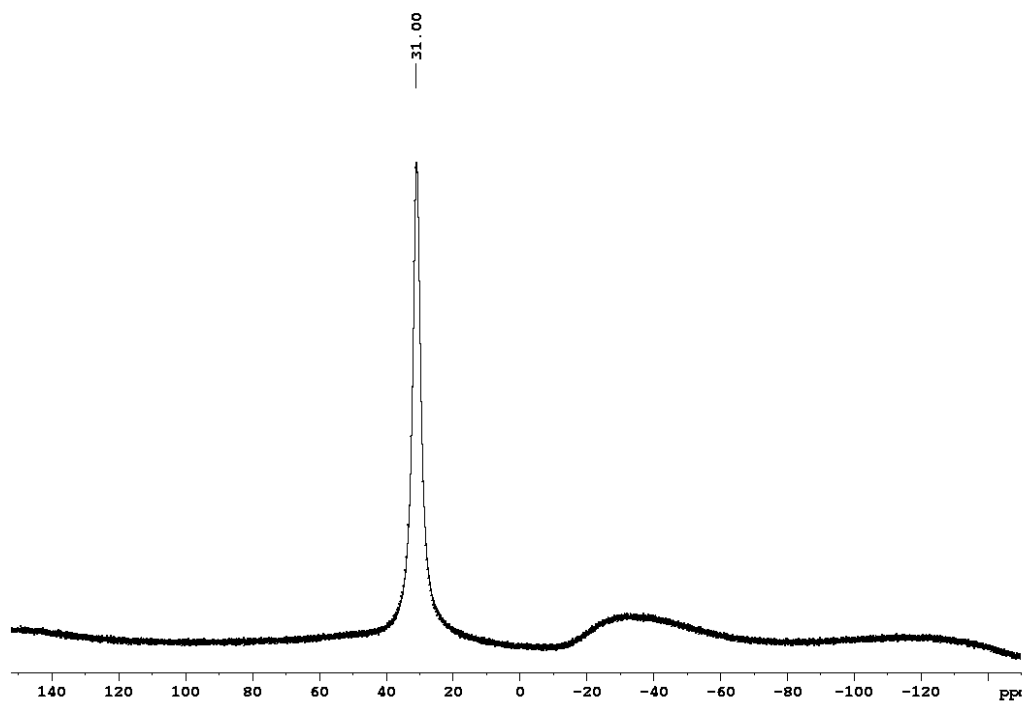


Figure 8.1.19 | ^{11}B NMR spectrum of **4** (128 MHz, CD_2Cl_2 , 300 K).

8.1.8 EPR spectroscopy

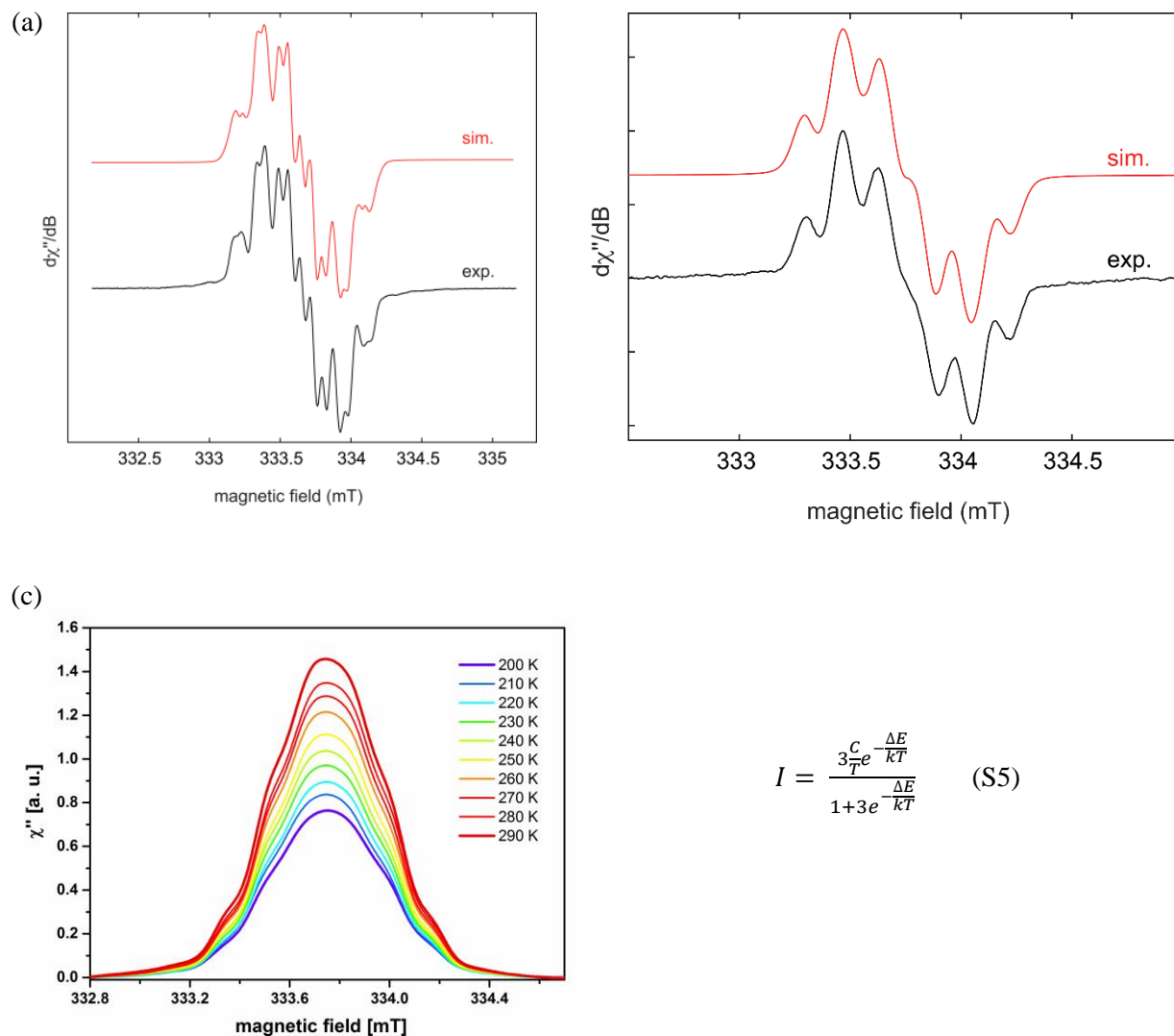


Figure 8.1.20 | Experimental (black) and simulated (red) continuous-wave (CW) X-band EPR spectra of 1^\bullet (a) and $\text{OS-2}^{\bullet\bullet}$ (b) in CH_2Cl_2 solution at room temperature. Integrated EPR spectra of $\text{OS-2}^{\bullet\bullet}$ (c) in CH_2Cl_2 solution at various temperatures (200 K up to 290 K). Bleaney Bowers equation^[213] S5 was used to experimentally determine the singlet-triplet energy gap.

8.1.9 DFT calculations

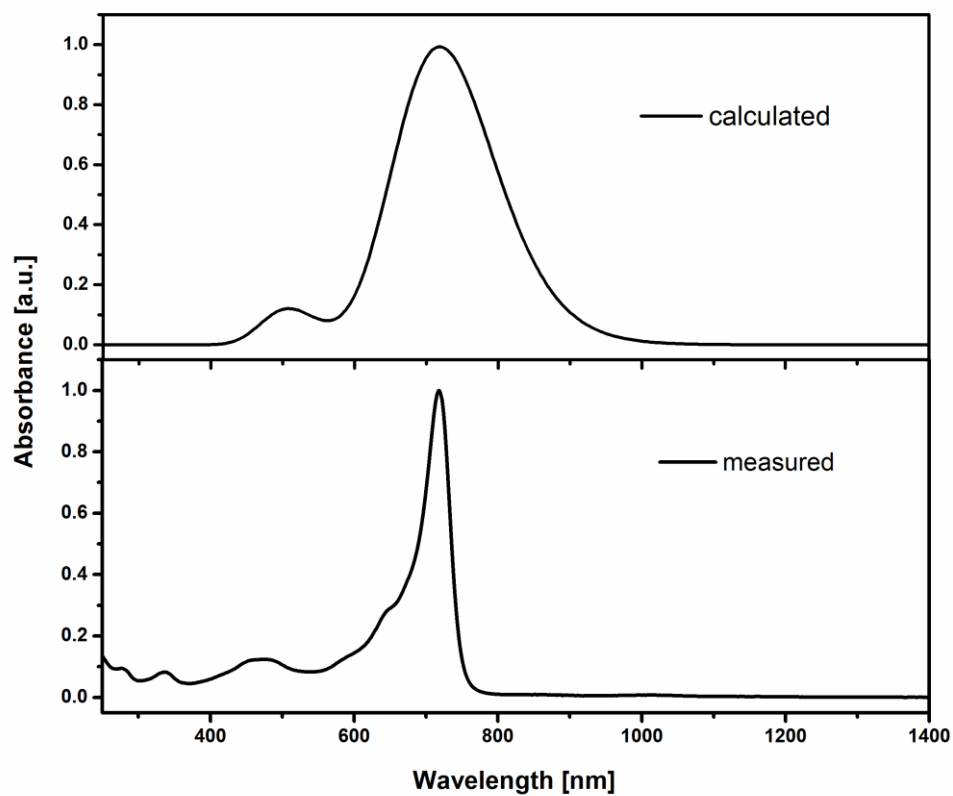


Figure 8.1.21 | Calculated (top, TD-DFT, UB3LYP/6-31G(d)) and measured (bottom, $c = 1.7 \cdot 10^{-5}$ M) UV/vis/NIR absorption spectra of **OS-2** in dichloromethane. The calculated spectrum was hypsochromically shifted by 0.23 eV.

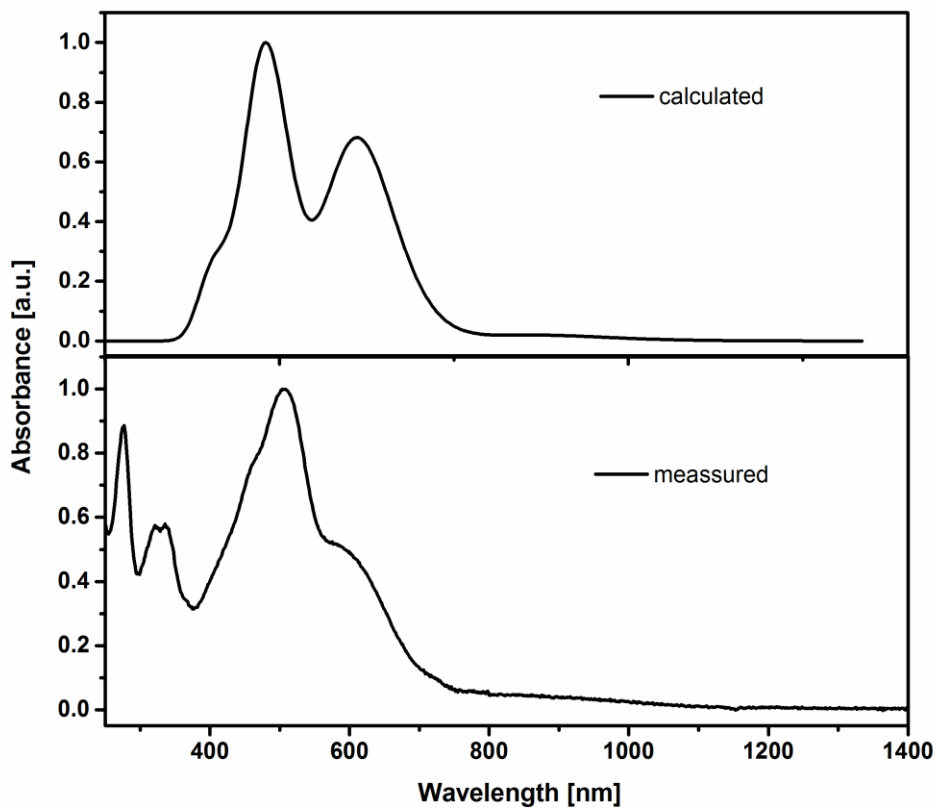


Figure 8.1.22 | Calculated (top, TD-DFT, UB3LYP/6-31G(d)) and measured (bottom, $c = 1.7 \cdot 10^{-5}$ M) UV/vis/NIR absorption spectra of **1*** in dichloromethane. The calculated spectrum was hypsochromically shifted by 0.24 eV.

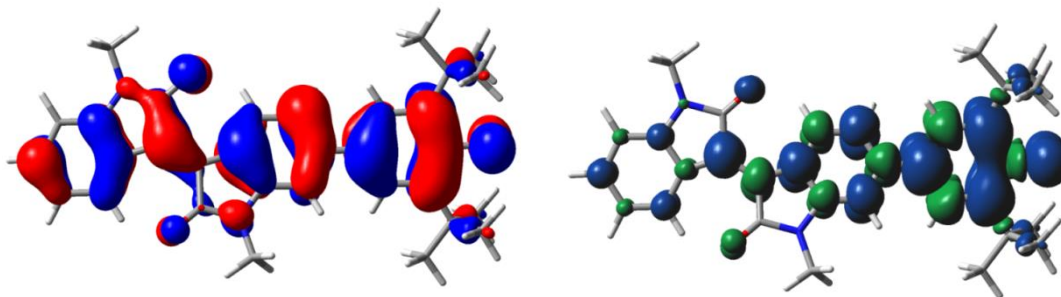
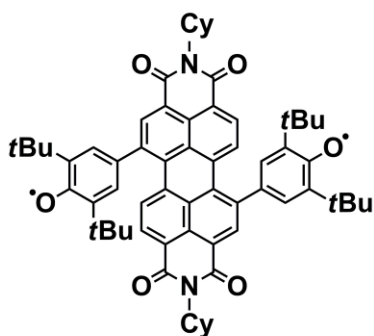


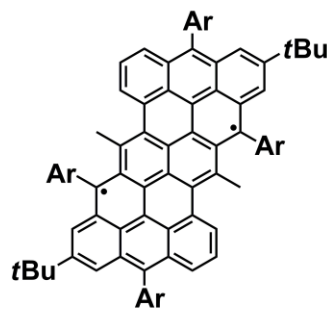
Figure 8.1.23 | Left: Calculated SOMO of **1*** (TD-DFT, UB3LYP/6-31G(d) isovalue 0.02 a. u.). Right: Calculated spin density distribution of **1*** (DFT, UB3LYP/6-31G(d) , isovalue 0.001 a. u.).

8.1.10 Examples for recent singlet open-shell biradicals



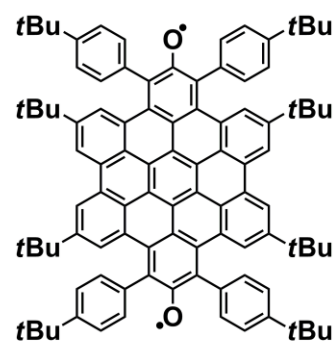
Kim, Würthner

$\tau_{1/2}$ solv. = 54 h
 Δ_{ST} = 0.041 eV
 y = 0.72



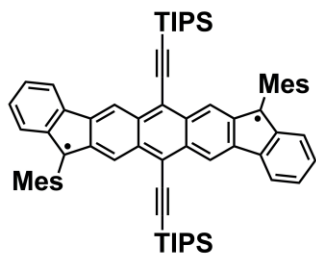
Ding, Wu

$\tau_{1/2}$ solv. = 4.34 h
 Δ_{ST} = 0.041 eV
 y = 0.64



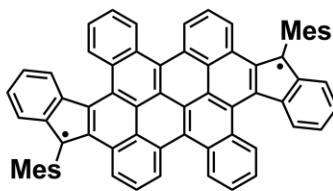
Ding, Wu

$\tau_{1/2}$ solv. = 33 h
 Δ_{ST} = 0.120 eV
 y = 0.21-0.40



**Nakano, Ottosson,
 Casado, Haley**

$\tau_{1/2}$ solv. = 64 d
 Δ_{ST} = 0.181 eV
 y = 0.50-0.74



Liu, Feng

$\tau_{1/2}$ solv. = 39 d
 Δ_{ST} = 0.080 eV
 y = 0.69

Figure 8.1.24 | Overview on recent examples of singlet open-shell biradicals with significant biradical character (Ar =3,5-di(trifluoromethyl)phenyl). Their singlet–triplet energy gaps and stabilities in solution are provided for comparison.

8.2 Supporting Information for Chapter 4

Please note: This section was partly communicated in *Chem. Sci.* **2021**, *12*, 793–802. The numeration of compounds in this part refers only to *Chapter 4* and is not necessarily the same as in *Chapter 1* and in particular in *Chapter 2*. Reprinted and adapted with permission from *Chem. Sci.* **2021**, *12*, 793–802. Published by The Royal Society of Chemistry. For the sake of unity of this thesis, several editorial changes have been made, which, however, do not affect substantive amendments.

8.2.1 Materials and methods

Materials. Chemicals, reagents and solvents were purchased from commercial suppliers. Column chromatography was performed on silica gel (particle size 0.040–0.063 mm) with freshly distilled solvents as eluents. Tetrabutylammonium fluoride was purchased as its trihydrate but had a significantly higher water content due to its hygroscopic character. DPP derivatives **1**^[305], **2**^[306], and **3**^[307] as well as boronic ester **4**^[173] were synthesized according to literature known procedure. All other commercially available reagents and solvents were of reagent grade and used without further purification.

NMR Spectroscopy. ¹H, ¹¹B and ¹³C NMR Spectra were recorded on a Bruker Avance III HD 400 or Bruker Avance III HD 600 spectrometer. ¹³C NMR Spectra are broad band proton decoupled. Chemical shifts (δ) are listed in parts per million (ppm) and are reported relative to tetramethylsilane (TMS). Spectra are referenced internally to residual proton solvent resonances (CDCl₃: δ = 7.26, DMSO-*d*₆: δ = 2.50, CD₂Cl₂: δ = 5.32) or natural abundance carbon resonances (CDCl₃: δ = 77.00, CD₂Cl₂: δ = 53.84). ¹¹B NMR spectra were referenced to external BF₃ · Et₂O. Coupling constants (*J*) are quoted in Hertz (Hz). The data are presented as follows: chemical shift, multiplicity (s = singlet, d = doublet, t = triplet, q = quartet, m = multiplet and/or multiple resonances, br = broad), coupling constant in Hertz (Hz), and integration.

Mass Spectrometry. MALDI–TOF mass spectra were recorded on a Bruker Daltronik GmbH (Autoflex II) mass spectrometer using trans-2-[3-(4-*tert*-butylphenyl)-2-methyl-2-propenylidene]malononitrile (DCTB) as matrix. High resolution ESI–TOF mass spectrometry was carried out on a microTOF focus instrument (Bruker Daltronik GmbH).

UV/vis/NIR Absorption Spectroscopy. The solvents for the spectroscopic measurements were of spectroscopic grade. UV/vis/NIR absorption spectra were recorded on a Perkin Elmer Lamda 950 or a Jasco V-670 spectrometer. Measurements in solution were carried out using quartz cuvettes with path lengths of 10 mm at ambient temperature. Measurements in solid state were performed on freshly spin

coated thin films on quartz wavers at ambient temperature ($c = 2 \cdot 10^{-3}$ M, 25 μ L, ambient temperature, $rpm = 3000$, $t = 30$ s).

UV/vis/NIR Spectroelectrochemistry. UV/vis/NIR spectroelectrochemical experiments in reflection mode were performed using an Agilent Cary 5000 Spectrometer and a self-made sample compartment with a layer thickness of 100 μ m, consisting of a cylindrical PTFE cell, a sapphire window and an adjustable three in one electrode (6 mm platinum disc working electrode, 1 mm platinum counter and pseudo reference electrode).

Titration Experiments. Unless otherwise specified, a solution of TBAF \cdot 3 H₂O ($c = 1.90 \cdot 10^{-3}$ M) in CH₂Cl₂ was added to the respective dye solution ($c \approx 2.85 \cdot 10^{-5}$ M) in CH₂Cl₂ at room temperature according to the below mentioned equivalents (1.00 equiv. = 15.0 μ L) and filled up to 3.00 mL with pure CH₂Cl₂. Due to a possibly increase water content of TBAF it cannot be excluded that the absolute TBAF amount was slightly lower than assumed.

Cyclic Voltammetry. Cyclic voltammetry (CV) and square wave voltammetry (SWV) were performed using a standard commercial electrochemical analyzer (EC epsilon; BAS Instruments, UK). A Pt disc electrode was used as a working electrode, platinum wire as a counter electrode and Ag⁺/Ag as a reference electrode, at a scan rate of 100 mV/s at room temperature. The compounds were dissolved in dichloromethane, and tetrabutylammonium hexafluorophosphate (^tBu₄NPF₆) was added as an electrolyte to give a concentration of 0.1 M. The supporting electrolyte was recrystallized from ethanol/water and dried under vacuum. The oxidation potentials were referenced against the ferrocenium/ferrocene redox couple (Fc⁺/Fc = 0.00 V).

Fluorescence Spectroscopy. Fluorescence spectra and fluorescence quantum yields were recorded with a PTI QM-4/2003 spectrometer (Photon Technology International, USA) as an average out of 4 equidistant excitation wavelengths relatively to the references *N*-(7-(diethylamino)-3*H*-phenoxazine-3-ylidene)-*N*-methylmethanaminium perchlorate^[309] ($\Phi_{Fl} = 0.11$ in EtOH) „Oxazin 1“ (for **DPP2** and **DPP3**) and *N,N*-(2,6-Di-*iso*-propylphenyl)-1,6,7,12-tetraphenoxyperylene-3,4:9,10-tetracarboxylic acid bisimide^[308] ($\Phi_{Fl} = 0.96$ in chloroform) „Perylene/ Lumogen red“ (for **DPP1**) in highly diluted solutions ($OD < 0.05$)^[318]. Measurements in solution were carried out using quartz cuvettes (Hellma optics, Germany) with path lengths of 10 mm and spectroscopic solvents at ambient temperature and atmosphere.

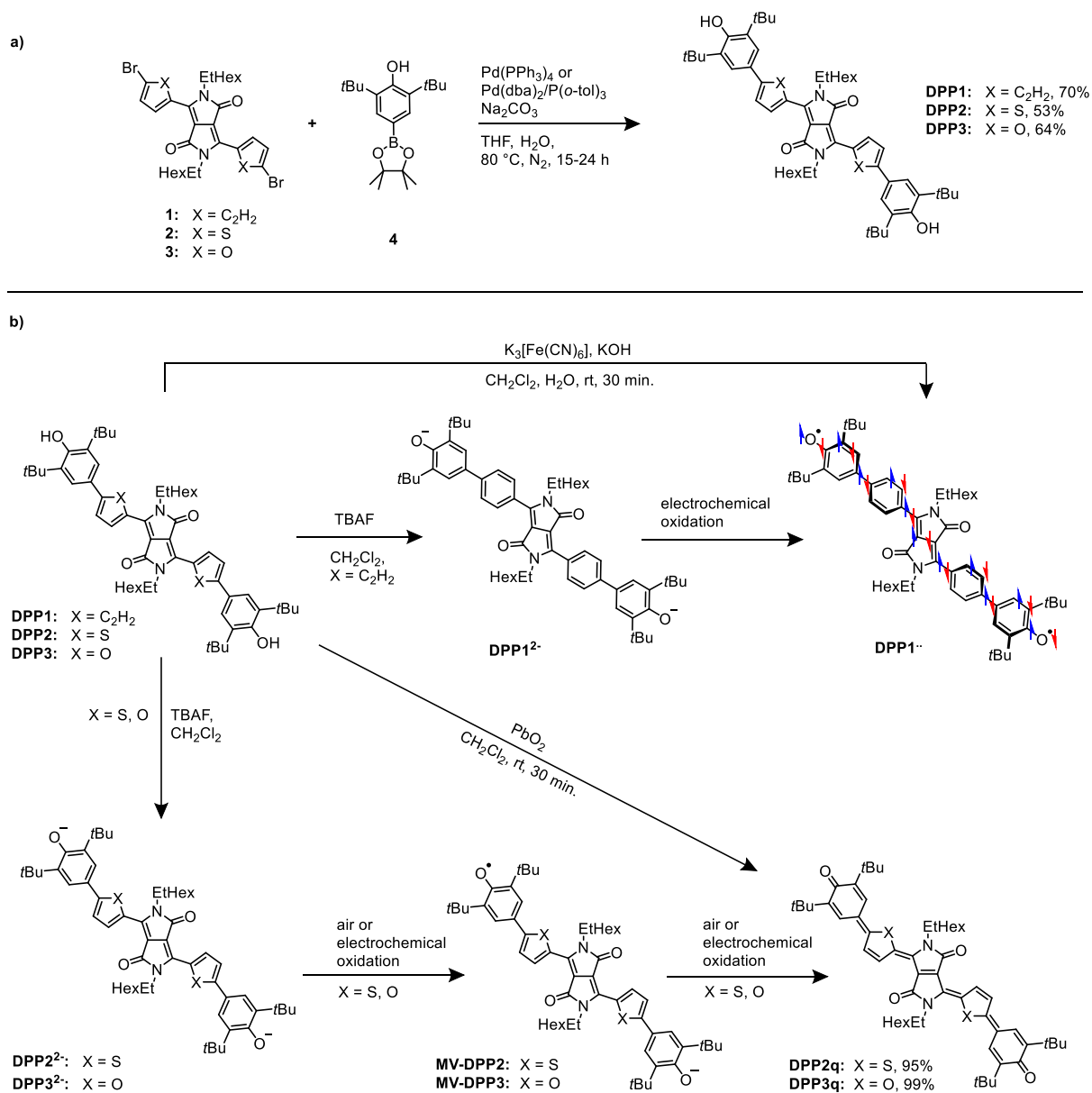
Computational chemistry. Spin-Flip TDDFT calculations have been carried out using the Q-Chem5.0 program package.^[319] For CASSCF calculations, the “Brilliantly Advanced General Electronic-structure Library” (BAGEL) by Shiozaki and coworkers^[320] has been employed. Starting orbitals have been

generated by performing HF calculations and in the case of excited state calculations, they have been optimized in a state-averaged manner with equal weights for S0 and S1 state.

Single Crystal X-ray Diffraction. Single crystal X-ray diffraction data for **DPP3q** were collected at 100 K on a Bruker X8APEX-II diffractometer with a CCD area detector and multi-layer mirror monochromated MoK α radiation. Single crystal X-ray diffraction data for **DPP1** were collected on a Bruker D8 Quest Kappa Diffractometer with a Photon100 CMOS detector and multi-layered mirror monochromated CuK α radiation. The structures were solved using direct methods, expanded with Fourier techniques and refined with the SHELX software package.^[315] All non-hydrogen atoms were refined anisotropically. Hydrogen atoms were included in the structure factor calculation on geometrically idealized positions. Crystallographic data have been deposited with the Cambridge Crystallographic Data Centre as supplementary publication no. CCDC 2001481 (**DPP3q**) and CCDC 2001480 (**DPP1**). These data can be obtained free of charge from The Cambridge Crystallographic Data Centre via www.ccdc.cam.ac.uk/data_request/cif.

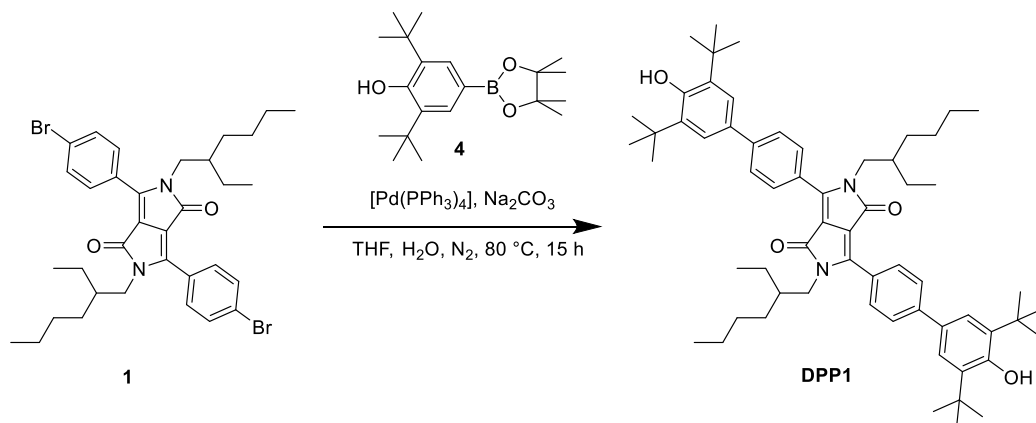
EPR Spectroscopy. EPR measurements at X-band (9.38 GHz) were carried out using a Bruker ELEXSYS E580 CW EPR spectrometer equipped with an Oxford Instruments helium cryostat (ESR900) and a MercuryITC temperature controller. The spectral simulations were performed using MATLAB 8.6 and the EasySpin 5.0.18 toolbox.^[316]

8.2.2 Syntheses



Scheme 8.2.1 | (a) Synthetic routes to diketopyrrolopyrrole derivatives **DPP1**, **DPP2** and **DPP3**. (b) Synthesis of biradical **DPP1^{••}** and quinones **DPP2q** and **DPP3q**, as well as generation of dianions **DPP1²⁻** and radicalanions **MV-DPP2** and **MV-DPP3**. Blue and red arrows in **DPP1^{••}** indicate spin polarization and illustrate antiferromagnetic coupling.

8.2.2.1 Synthesis of DPP1

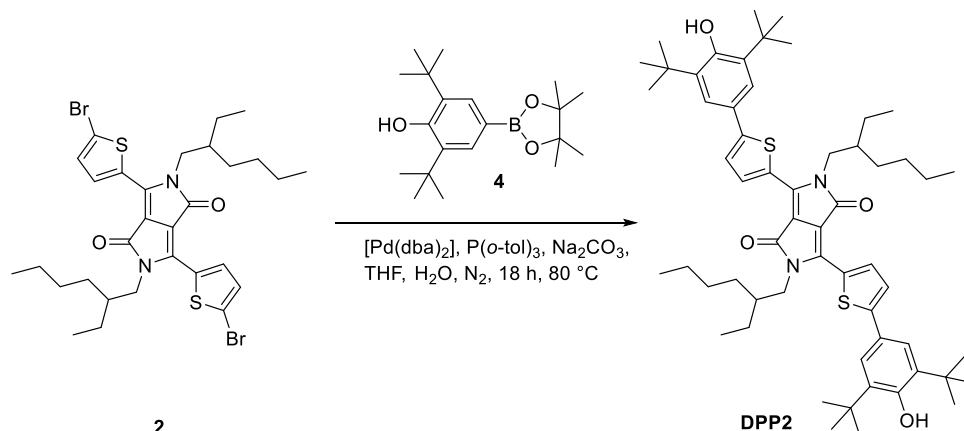


Scheme 8.2.2 | Synthesis of **DPP1** by Suzuki–Miyaura cross–coupling.

Sodium carbonate (490 mg, 4.60 mmol, 17.7 equiv.), **1** (175 mg, 261 μmol , 1.00 equiv.), and tetrakis(triphenylphosphine)palladium(0) (20.0 mg, 17.0 μmol , 6.67 mol%) were dissolved in a degassed mixture of THF/H₂O (10 mL/ 2mL) under an atmosphere of nitrogen. After the mixture was heated to 50 °C for 30 min., boronic ester **4** (176 mg, 530 μmol , 2.03 equiv.) dissolved in THF (5 mL) was added and the reaction mixture was stirred at 80 °C for 15 h. Subsequently, the suspension was cooled down to room temperature and the crude product was extracted with CH₂Cl₂ (3 x 20 mL). The combined organic layers were washed with hydrochloric acid (1 M), water, dried over MgSO₄ and the solvent was removed under reduced pressure. The crude product was purified by silica gel column chromatography (gradient from hexane/ CH₂Cl₂ (1:1) to pure CH₂Cl₂) to yield **DPP1** as a bright orange solid.

Yield: 168 mg (183 μmol , 70 %). Melting point: 290 – 291 °C. ¹H NMR (400 MHz, CD₂Cl₂): δ = 0.72 – 0.77 (m, 6 H, CH₃), 0.77 – 0.82 (m, 6 H, CH₃), 1.04 – 1.39 (m, 18 H, βCH , alkyl–CH₂), 1.51 (s, 36 H, C(CH₃)₃), 3.74 – 3.85 (m, 4 H, αCH_2), 5.40 (s, 2 H, OH), 7.50 (s, 4 H, aryl–CH), 7.73 (d, 4 H, aryl–CH, ³J_{HH} = 8.6 Hz), 7.86 (d, 4 H, aryl–CH, ³J_{HH} = 8.6 Hz). ¹³C NMR (101 MHz, CD₂Cl₂): δ = 10.7, 14.2, 23.2, 24.2, 28.8, 30.4, 30.7, 34.9, 39.0, 45.3, 110.2, 124.4, 127.0, 127.3, 129.5, 131.6, 137.0, 144.9, 148.4, 154.7, 163.1. HRMS (ESI–TOF, pos. mode, CHCl₃/MeCN 1/1): calculated for C₆₂H₈₄N₂O₄⁺: m/z 920.6426 [M]⁺, found 920.6410. MS (MALDI–TOF, pos. mode, DCTB 3:1 in CHCl₃): calculated for C₆₂H₈₄N₂O₄⁺: m/z 920.6426 [M]⁺, found 920.514. UV/Vis (DCM, c = 9.80 · 10^{–6} M): λ_{max} [nm] (ϵ_{max} [L mol^{–1} cm^{–1}]) = 269 (35000), 356 (20400), 486 (30100). IR (ATR): $\tilde{\nu}$ [cm^{–1}] = 3438 (s, $\nu_{\text{O–H, str}}$), 2951 (s, $\nu_{\text{C–H, str}}$), 2907 (s, $\nu_{\text{C–H, str}}$), 2855 (s, $\nu_{\text{C–H, str}}$), 1662 (vs, $\nu_{\text{C=O, str}}$). Fluorescence (DCM, λ_{ex} = 430 nm): λ_{max} = 565 nm (ϕ = 0.49 ± 0.07, standard: Perylene Orange).

8.2.2.2 Synthesis of DPP2

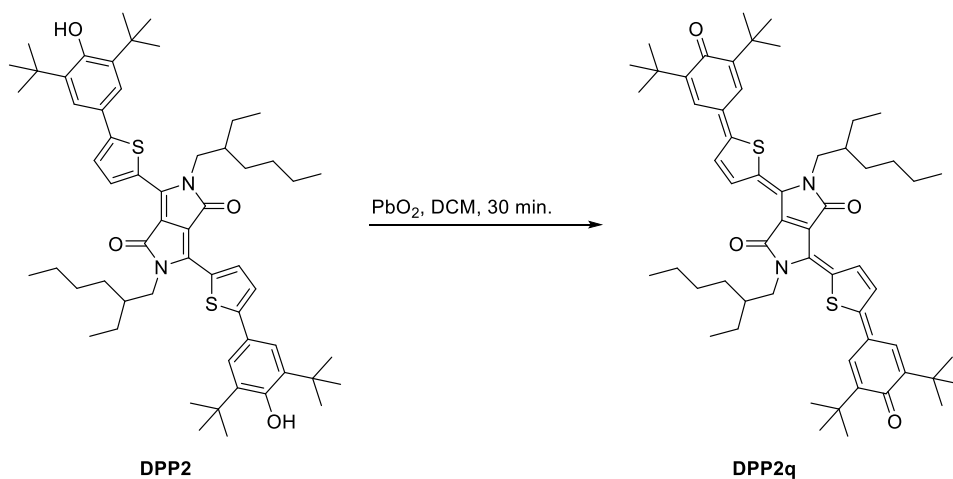


Scheme 8.2.3 | Synthesis of **DPP2** by Suzuki–Miyaura cross–coupling.

Sodium carbonate (825 mg, 7.78 mmol, 17.7 equiv.), **2** (300 mg, 440 μ mol, 1.00 equiv.), bis(dibenzylideneacetone)palladium(0) (17.0 mg, 29.4 μ mol, 6.67 mol%), boronic ester **4** (366 mg, 1.10 mmol, 2.50 equiv.) and tri(*o*-tolyl)phosphine (18.0 mg, 58.8 μ mol, 12.7 mol%) were dissolved in a degassed mixture of THF/H₂O (10 mL/ 2mL) under an atmosphere of nitrogen. After the mixture was heated to 80 °C for 18 h and cooled down to room temperature, water (30 mL) was added and the crude product was extracted with CH₂Cl₂ (3 x 20 mL). The combined organic layers were washed with hydrochloric acid (1 M), water, dried over MgSO₄ and the solvent was removed under reduced pressure. The crude product was purified by silica gel column chromatography (eluent: hexane/ CH₂Cl₂ (1:1)) to yield **DPP2** as a dark red solid.

Yield: 219 mg (235 μ mol, 53 %). Melting point: 247 – 248 °C. ¹H NMR (400 MHz, CD₂Cl₂): δ = 0.87 (t, 6 H, CH₃, ³J_{HH} = 7.2 Hz), 0.93 (t, 6 H, CH₃, ³J_{HH} = 7.6 Hz), 1.24 – 1.46 (m, 16 H, CH₂), 1.49 (s, 36 H, C(CH₃)₃), 1.90 – 2.03 (m, 2 H, β CH), 4.00 – 4.15 (m, 4 H, α CH₂), 5.49 (s, 2 H, OH), 7.38 (d, 2 H, heteroaryl–CH, ³J_{HH} = 4.1 Hz), 7.52 (s, 4 H, aryl–CH), 9.02 (d, 2 H, heteroaryl–CH, ³J_{HH} = 4.1 Hz). ¹³C NMR (101 MHz, CD₂Cl₂): δ = 10.8, 14.2, 23.5, 24.1, 25.0, 28.9, 30.3, 30.4, 34.8, 39.8, 46.1, 108.1, 123.4, 123.7, 125.1, 128.1, 132.1, 137.2, 137.3, 139.9, 151.7, 155.4, 162.1. HRMS (ESI–TOF, pos. mode, MeCN/ CHCl₃ 1/1): calculated for C₅₈H₈₀N₂O₄S₂⁺: m/z 932.5554 [M]⁺, found 932.5534. MS (MALDI–TOF, pos. mode, DCTB 3:1 in CHCl₃): calculated for C₅₈H₈₀N₂O₄S₂⁺: m/z 932.555 [M]⁺, found 932.437. UV/Vis (DCM, c = 1.01 · 10⁻⁵ M): λ_{\max} [nm] (ϵ_{\max} [L mol⁻¹ cm⁻¹]) = 572 (48300), 610 (55000). IR (ATR): $\tilde{\nu}$ [cm⁻¹] = 3625 (s, $\nu_{\text{O-H, str}}$), 2952 (s, $\nu_{\text{C-H, str}}$), 2926 (s, $\nu_{\text{C-H, str}}$), 2867 (s, $\nu_{\text{C-H, str}}$), 1660 (vs, $\nu_{\text{C=O, str}}$). Fluorescence (DCM, $\lambda_{\text{ex.}}$ = 540 nm): λ_{\max} = 638 nm (ϕ = 0.39 \pm 0.03, standard: Oxazine 1).

8.2.2.3 Synthesis of DPP2q

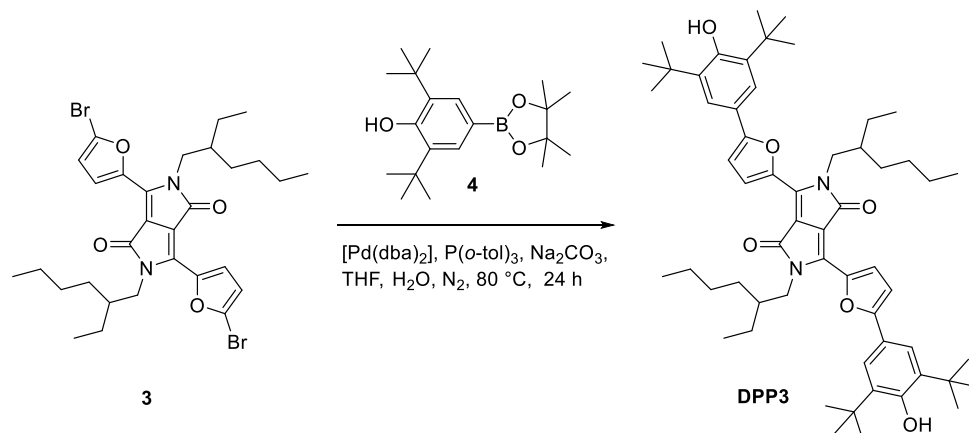


Scheme 8.2.4 | Synthesis of **DPP2q** by oxidation of **DPP2** with lead(IV)oxide.

Lead(IV) oxide (210 mg, 878 μmol , 14.0 equiv.) and **DPP2** (59.0 mg, 63.0 μmol , 1.00 equiv.) were suspended in dichloromethane (50 mL). After stirring the reaction mixture at room temperature for 30 minutes, the excess lead(IV) oxide was filtered off and the solvent was removed under reduced pressure to yield **DPP2q**.

Yield 56.0 mg (60.0 μmol , 95 %). Melting point 279 $^{\circ}\text{C}$. ^1H NMR (400 MHz, CD_2Cl_2): δ = 0.89 (t, 6 H, CH_3 , $^3J_{\text{HH}} = 7.1$ Hz), 0.97 (t, 6 H, CH_3 , $^3J_{\text{HH}} = 7.5$ Hz), 1.17 – 1.47 (m, 16 H, CH_2), 1.34 (s, 18 H, $(\text{CH}_3)_3$), 1.35 (s, 18 H, $\text{C}(\text{CH}_3)_3$), 1.95 – 2.05 (m, 2 H, βCH), 3.99 – 4.15 (m, 4 H, αCH_2), 7.30 (d, 2 H, aryl- CH , $^4J_{\text{HH}} = 2.5$ Hz), 7.47 (d, 2 H, aryl- CH , $^4J_{\text{HH}} = 2.5$ Hz), 7.62 (d, 2 H, heteroaryl- CH , $^3J_{\text{HH}} = 5.8$ Hz), 9.38 (d, 2 H, heteroaryl- CH , $^3J_{\text{HH}} = 5.8$ Hz). ^{13}C NMR (100.6 MHz, CD_2Cl_2): δ = 10.8, 14.2, 23.5, 23.9, 28.7, 29.7, 29.8, 30.8, 35.9, 36.1, 40.1, 46.5, 126.0, 126.5, 128.3, 129.3, 130.6, 131.4, 133.0, 142.5, 147.6, 149.8, 155.1, 162.1, 185.9. HRMS (ESI-TOF, pos. mode, MeCN/ CHCl_3 1/1): calculated for $\text{C}_{58}\text{H}_{78}\text{N}_2\text{O}_4\text{S}_2^+$: m/z 930.5398 $[\text{M}]^+$, found 930.5465. MS (MALDI-TOF, pos. mode, DCTB 3:1 in CHCl_3): calculated for $\text{C}_{58}\text{H}_{78}\text{N}_2\text{O}_4\text{S}_2^+$: m/z 930.540 $[\text{M}]^+$, found 930.420. UV/Vis (DCM, $c = 1.00 \cdot 10^{-5}$ M): λ_{max} [nm] (ϵ_{max} [$\text{L mol}^{-1} \text{cm}^{-1}$]) = 725 (67300), 782 (151800). IR (ATR): $\tilde{\nu}$ [cm^{-1}] = 2948 (s, $\nu_{\text{-C-H, str}}$), 2909 (s, $\nu_{\text{-C-H, str}}$), 2853 (s, $\nu_{\text{-C-H, str}}$), 1670 (vs, $\nu_{\text{-C=O, str}}$), 1584 (vs, $\nu_{\text{-C=O, str}}$).

8.2.2.4 Synthesis of DPP3

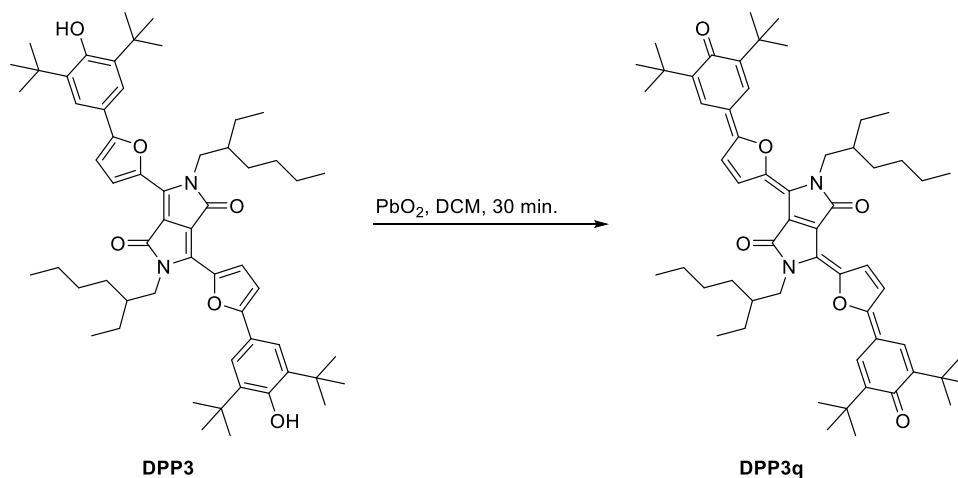


Scheme 8.2.5 | Synthesis of **DPP3** by Suzuki–Miyaura cross–coupling.

Sodium carbonate (590 mg, 5.57 mmol, 18.1 equiv.), **3** (200 mg, 307 μmol , 1.00 equiv.), bis(dibenzylideneacetone)palladium(0) (11.3 mg, 19.6 μmol , 6.67 mol%), boronic ester **4** (258 mg, 770 μmol , 2.50 equiv.) and tri(*o*-tolyl)phosphine (12.0 mg, 39.0 μmol , 12.7 mol%) were dissolved in a degassed mixture of THF/H₂O (10 mL/ 2mL) under an atmosphere of nitrogen. After the mixture was heated to 80 °C for 24 h and cooled down to room temperature, water (30 mL) was added and the crude product was extracted with CH₂Cl₂ (3 x 20 mL). The combined organic layers were washed with hydrochloric acid (1 M), water, dried over MgSO₄ and the solvent was removed under reduced pressure. The crude product was purified by silica gel column chromatography (eluent: hexane/ CH₂Cl₂ (1:1)) to yield **DPP3** as a dark red solid.

Yield: 177 mg (197 μmol , 64 %). Melting point: 126–127 °C. ¹H NMR (400 MHz, CD₂Cl₂): δ = 0.78 (t, 6 H, CH₃, ³J_{HH} = 7.0 Hz), 0.86 (t, 6 H, CH₃, ³J_{HH} = 7.4 Hz), 1.14 – 1.41 (m, 16 H, CH₂), 1.50 (s, 36 H, C(CH₃)₃), 1.78 – 1.89 (m, 2 H, β CH), 4.12 – 4.24 (m, 4 H, α CH₂), 5.52 (s, 2 H, OH), 6.85 (d, 2 H, heteroaryl–CH, ³J_{HH} = 3.8 Hz), 7.63 (s, 4 H, aryl–CH), 8.34 (d, 2 H, heteroaryl–CH, ³J_{HH} = 3.8 Hz). ¹³C NMR (101 MHz, CD₂Cl₂): δ = 10.9, 14.1, 23.4, 24.1, 29.0, 30.4, 30.8, 34.8, 39.9, 46.8, 106.8, 107.7, 121.6, 122.4, 122.6, 133.1, 137.2, 143.9, 155.4, 158.6, 161.4. HRMS (ESI–TOF, pos. mode, MeCN/ CHCl₃ 1/1): calculated for C₅₈H₈₀N₂O₆⁺: m/z 900.6011 [M]⁺, found 900.5951. MS (MALDI–TOF, pos. mode, DCTB 3:1 in CHCl₃): calculated for C₅₈H₈₀N₂O₆⁺: m/z 900.601 [M]⁺, found 900.445. UV/Vis (DCM, c = 9.50 · 10^{−6} M): λ_{max} [nm] (ϵ_{max} [M^{−1} cm^{−1}]) = 561 (49600), 607 (82500). IR (ATR): $\tilde{\nu}$ [cm^{−1}] = 3625 (s, $\nu_{\text{O–H, str}}$), 2950 (s, $\nu_{\text{C–H, str}}$), 2918 (s, $\nu_{\text{C–H, str}}$), 2855 (s, $\nu_{\text{C–H, str}}$), 1654 (vs, $\nu_{\text{C=O, str}}$). Fluorescence (DCM, λ_{ex} = 540 nm): λ_{max} = 624 nm (ϕ = 0.48 ± 0.08, standard: Oxazine 1).

8.2.2.5 Synthesis of DPP3q

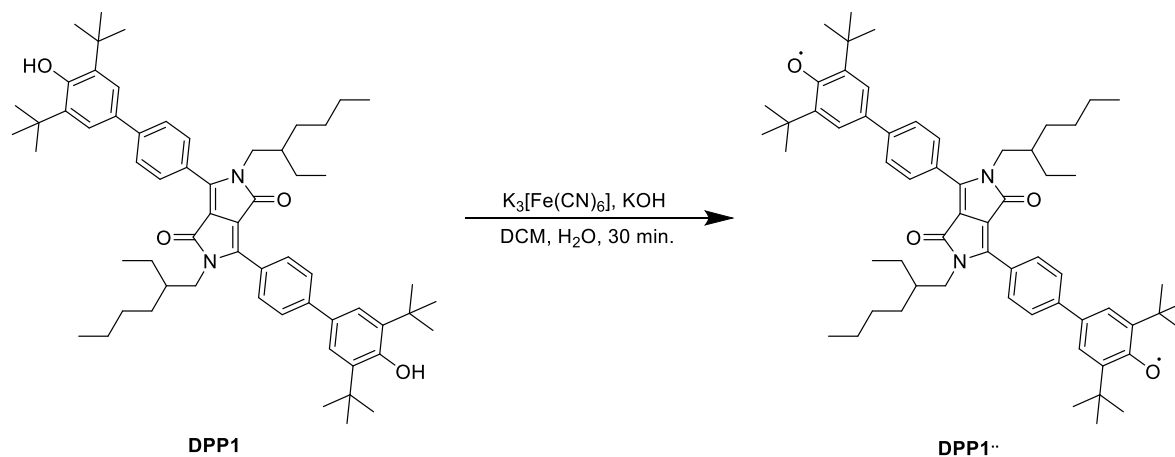


Scheme 8.2.6 | Synthesis of **DPP3q** by oxidation of **DPP3** with lead(IV)oxide.

Lead(IV) oxide (210 mg, 878 μmol , 14.0 equiv.) and **DPP3** (57.0 mg, 63.0 μmol , 1.00 equiv.) were suspended in dichloromethane (50 mL). After stirring the reaction mixture at room temperature for 30 minutes the excess lead(IV) oxide was filtered off and the solvent was removed under reduced pressure to yield **DPP3q**.

Yield: 56.0 mg (62.3 μmol , 99 %). Melting point: 274 $^{\circ}\text{C}$. ^1H NMR (400 MHz, CD_2Cl_2): δ = 0.84 (t, 6 H, CH_3 , $^3J_{\text{HH}} = 7.0$ Hz), 0.90 (t, 6 H, CH_3 , $^3J_{\text{HH}} = 7.4$ Hz), 1.20 – 1.53 (m, 16 H, CH_2), 1.35 (s, 18 H, $\text{C}(\text{CH}_3)_3$), 1.37 (s, 18 H, $\text{C}(\text{CH}_3)_3$), 1.84 – 1.95 (m, 2 H, βCH), 4.16 (d, 4 H, αCH_2 , $^3J_{\text{HH}} = 7.7$ Hz), 7.32 (d, 2 H, aryl- CH , $^4J_{\text{HH}} = 2.4$ Hz), 7.40 (d, 2 H, heteroaryl- CH , $^3J_{\text{HH}} = 5.5$ Hz), 7.60 (d, 2 H, aryl- CH , $^4J_{\text{HH}} = 2.4$ Hz), 8.85 (d, 2 H, heteroaryl- CH , $^3J_{\text{HH}} = 5.5$ Hz). ^{13}C NMR (100.6 MHz, CD_2Cl_2): δ = 10.9, 14.2, 23.4, 24.1, 28.9, 29.7, 29.9, 30.7, 35.9, 36.2, 39.6, 47.7, 115.5, 119.9, 123.6, 124.5, 126.9, 130.6, 133.6, 146.8, 148.4, 149.6, 161.3, 162.9, 185.8. HRMS (ESI-TOF, pos. mode, $\text{MeCN}/\text{CHCl}_3$ 1/1): calculated for $\text{C}_{58}\text{H}_{78}\text{N}_2\text{O}_6^+$: m/z 898.5854 $[\text{M}]^+$, found 898.5900. MS (MALDI-TOF, pos. mode, DCTB 3:1 in CHCl_3): calculated for $\text{C}_{58}\text{H}_{78}\text{N}_2\text{O}_6^+$: m/z 898.585 $[\text{M}]^+$, found 898.457. UV/Vis (DCM, $c = 1.00 \cdot 10^{-5}$ M): λ_{max} [nm] (ϵ_{max} [$\text{M}^{-1} \text{cm}^{-1}$]) = 695 (92200), 751 (172500). IR (ATR): $\tilde{\nu}$ [cm^{-1}] = 3105 (m, $\nu_{\text{C}=\text{O}, \text{str}, \text{ot}}$), 2953 (s, $\nu_{\text{C}-\text{H}, \text{str}}$), 2918 (s, $\nu_{\text{C}-\text{H}, \text{str}}$), 2860 (s, $\nu_{\text{C}-\text{H}, \text{str}}$), 1660 (vs, $\nu_{\text{C}=\text{O}, \text{str}}$), 1578 (vs, $\nu_{\text{C}=\text{O}, \text{str}}$).

8.2.2.6 Preparation of a DPP1^{••} sample



Scheme 8.2.7 | Synthesis of biradical **DPP1^{••}** by oxidation of **DPP1** with potassium ferricyanide(III).

DPP1 (3.00 mg, 3.26 μmol , 1.00 equiv.), potassium ferricyanide(III) (127 mg, 386 μmol , 118 equiv.) and potassium hydroxide (200 mg, 3.56 mmol, 1092 equiv.) were dissolved in a biphasic mixture of $\text{CH}_2\text{Cl}_2/\text{H}_2\text{O}$ (1.5 mL/ 2.0 mL) and vigorously stirred for 30 min. The organic layer was subsequently washed with water and dried over MgSO_4 to give a solution of **DPP1^{••}** in CH_2Cl_2 ($c = 2.17 \text{ mM}$).

HRMS (ESI-TOF, pos. mode, $\text{CH}_2\text{Cl}_2/\text{MeCN}$ 1/1): calculated for $\text{C}_{62}\text{H}_{82}\text{N}_2\text{O}_4^+$: m/z 918.6269 $[\text{M}]^+$, found 918.6250. UV/Vis (DCM, $c = 9.80 \cdot 10^{-6} \text{ M}$): λ_{max} [nm] (ϵ_{max} [$\text{L mol}^{-1} \text{ cm}^{-1}$]) = 269 (35000), 356 (20400), 486 (30100).

8.2.3 Mass spectrometry

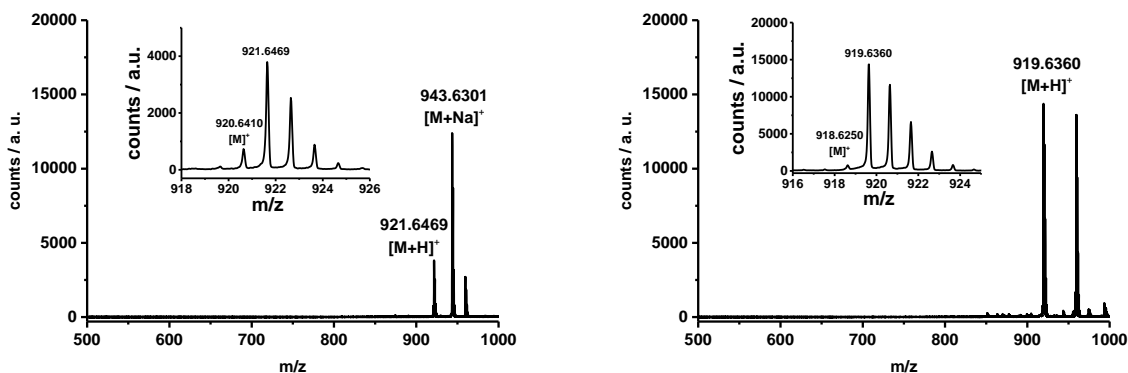


Figure 8.2.1 | ESI-TOF high resolution mass spectra of **DPP1** (left) and **DPP1*** (right). Inset: Isotopic distribution.

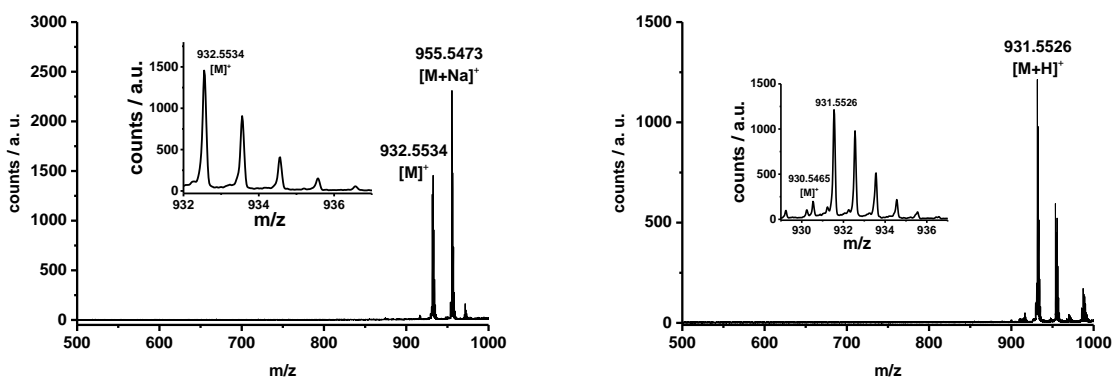


Figure 8.2.2 | ESI-TOF high resolution mass spectra of **DPP2** (left) and **DPP2q** (right). Inset: Isotopic distribution.

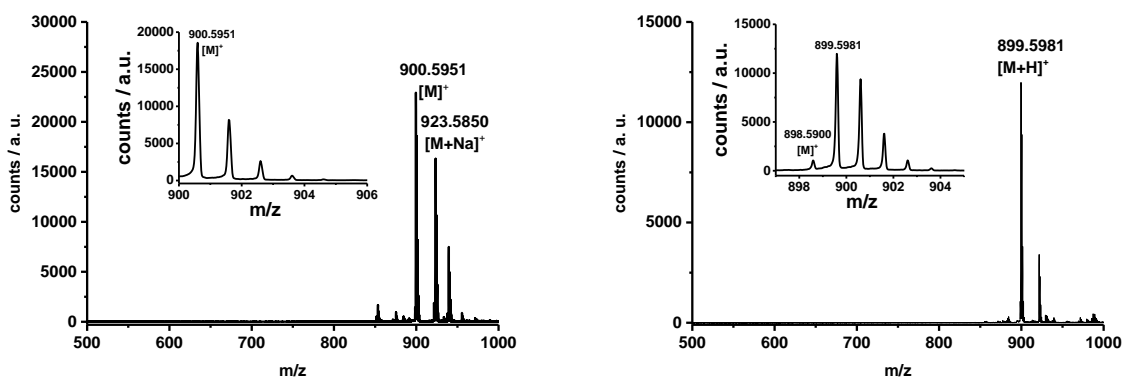


Figure 8.2.3 | ESI-TOF high resolution mass spectra of **DPP3** (left) and **DPP3q** (right). Inset: Isotopic distribution.

8.2.4 Single crystal X-ray diffraction

Single crystals of **DPP3q** were obtained by slow diffusion of methanol into a solution of **DPP3q** in CHCl_3 . Two almost identical structures were found with bond length deviations ≤ 0.5 pm.

Crystal data for DPP3q ($\text{C}_{58}\text{H}_{78}\text{N}_2\text{O}_6 \cdot 2 (\text{CH}_4\text{O})$): $M_r = 963.31$, $0.489 \times 0.361 \times 0.327 \text{ mm}^3$, monoclinic space group $P2_1/n$, $a = 15.3311(16) \text{ \AA}$, $\alpha = 90^\circ$, $b = 23.844(3) \text{ \AA}$, $\beta = 95.515(3)^\circ$, $c = 15.4674(16) \text{ \AA}$, $\gamma = 90^\circ$, $V = 5627.9(10) \text{ \AA}^3$, $Z = 4$, $\rho(\text{calcd}) = 1.137 \text{ g}\cdot\text{cm}^{-3}$, $\mu = 0.074 \text{ mm}^{-1}$, $F_{(000)} = 2096$, $\text{Goof}(F^2) = 1.037$, $R_I = 0.0591$, $wR^2 = 0.1454$ for $I > 2\sigma(I)$, $R_1 = 0.0860$, $wR^2 = 0.1599$ for all data, 11128 unique reflections [$\theta \leq 26.158^\circ$] with a completeness of 98.9 % and 718 parameters, 72 restraints.

Single crystals of **DPP1** were obtained slow diffusion of methanol into a solution of **DPP1** in CHCl_3 .

Crystal data for DPP1 ($\text{C}_{62}\text{H}_{84}\text{N}_2\text{O}_4$): $M_r = 921.31$, $0.281 \times 0.133 \times 0.114 \text{ mm}^3$, triclinic space group $P\bar{1}$, $a = 9.8347(4) \text{ \AA}$, $\alpha = 118.5760(10)^\circ$, $b = 12.6226(5) \text{ \AA}$, $\beta = 101.4230(10)^\circ$, $c = 12.8064(6) \text{ \AA}$, $\gamma = 94.6720(10)^\circ$, $V = 1339.49(10) \text{ \AA}^3$, $Z = 1$, $\rho(\text{calcd}) = 1.142 \text{ g}\cdot\text{cm}^{-3}$, $\mu = 0.537 \text{ mm}^{-1}$, $F_{(000)} = 502$, $\text{Goof}(F^2) = 1.041$, $R_I = 0.0464$, $wR^2 = 0.1195$ for $I > 2\sigma(I)$, $R_1 = 0.0492$, $wR^2 = 0.1220$ for all data, 5260 unique reflections [$\theta \leq 72.294^\circ$] with a completeness of 99.3 % and 426 parameters, 61 restraints.

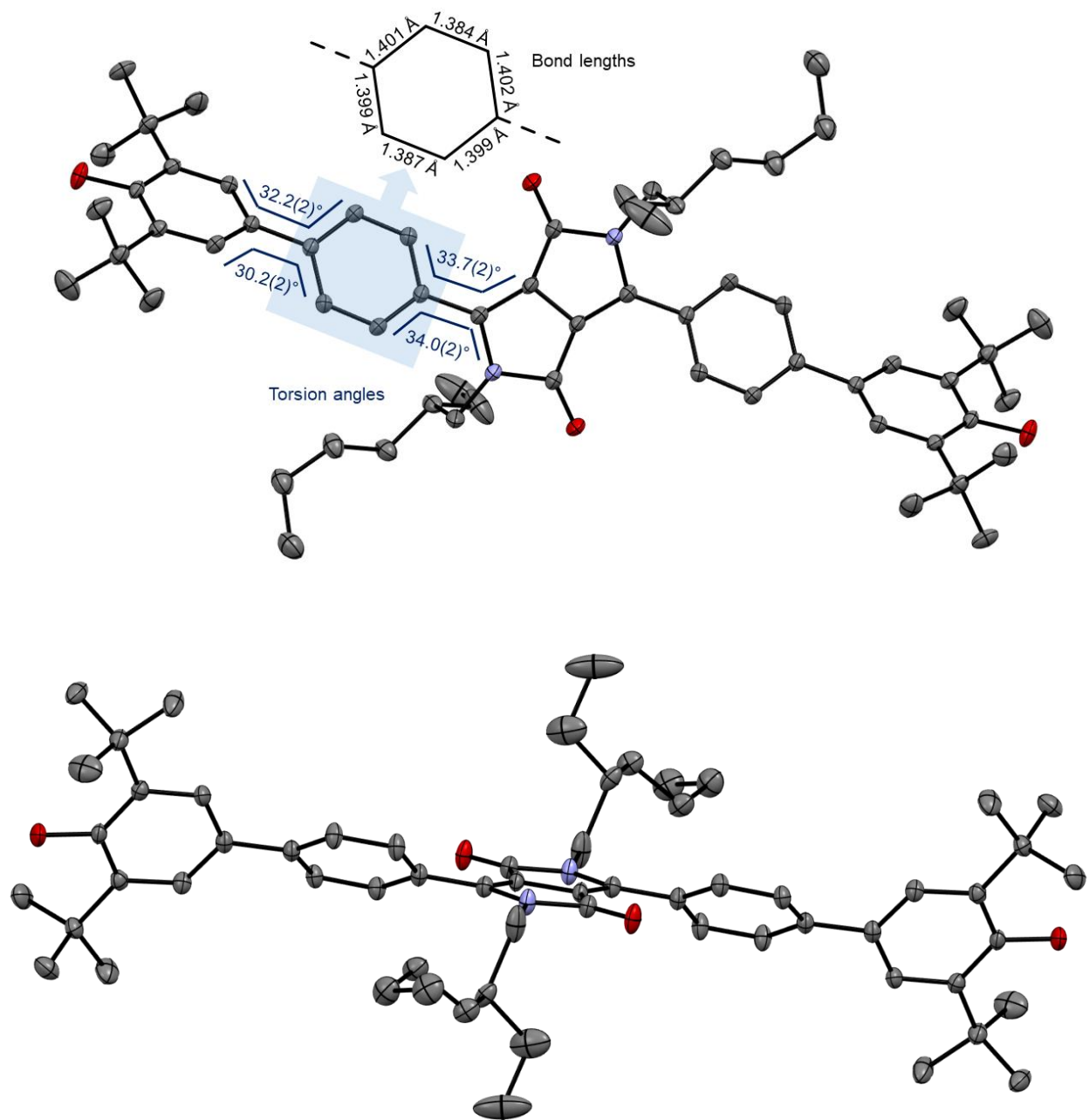


Figure 8.2.4 | Solid state molecular structure of **DPP1** in topview (top) and sideview (bottom) determined by single crystal X-ray diffraction (ellipsoids set to 50 % probability, carbon gray, nitrogen blue, oxygen red). Hydrogen omitted for clarity.

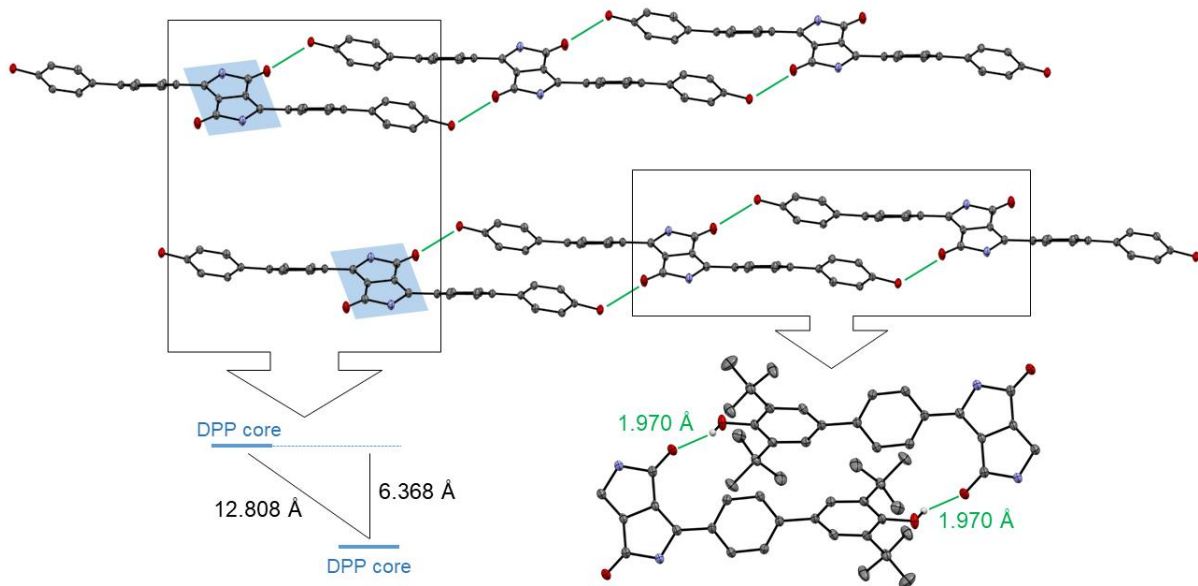


Figure 8.2.5 | Solid state molecular structure of **DPP1** determined by X-ray diffraction (ellipsoids set to 50 % probability) with intermolecular hydrogen bonding (hydrogen bond = green line, carbon gray, nitrogen blue, oxygen red, hydrogen white). Alkyl chains and hydrogen atoms partially omitted for clarity.

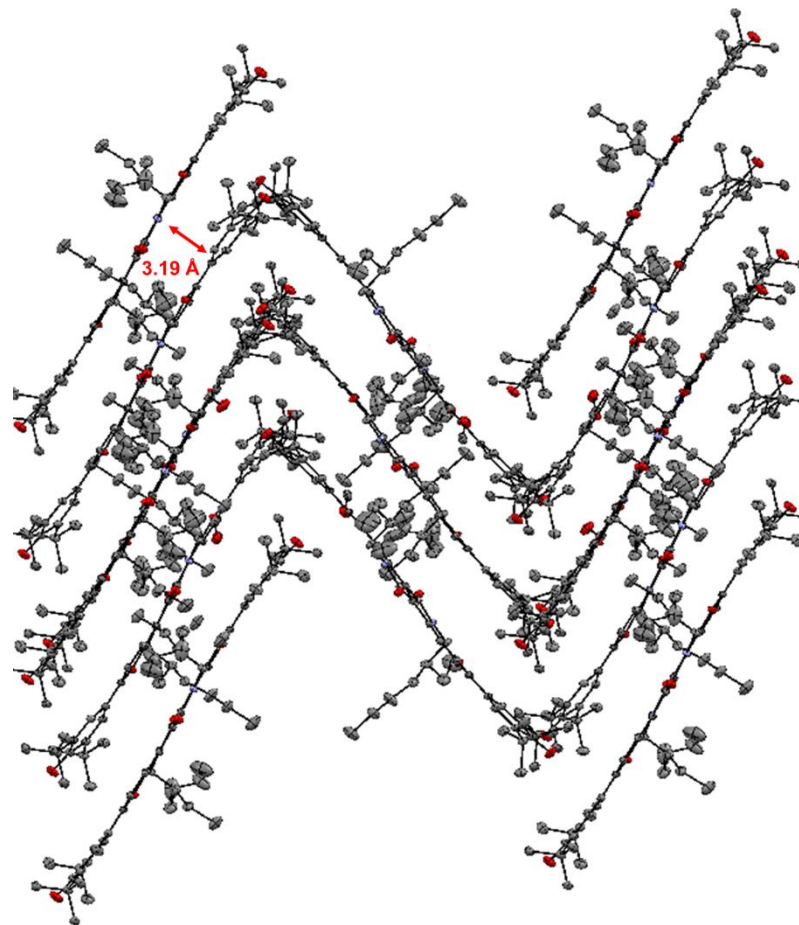


Figure 8.2.6 | Solid state molecular packing of **DPP3q** in herringbone type arrangement determined by single crystal X-ray diffraction (ellipsoids set to 50 % probability, carbon gray, nitrogen blue, oxygen red). Solvent molecules (methanol) and hydrogen atoms omitted for clarity.

8.2.5 UV/vis/NIR spectroscopy and spectroelectrochemistry

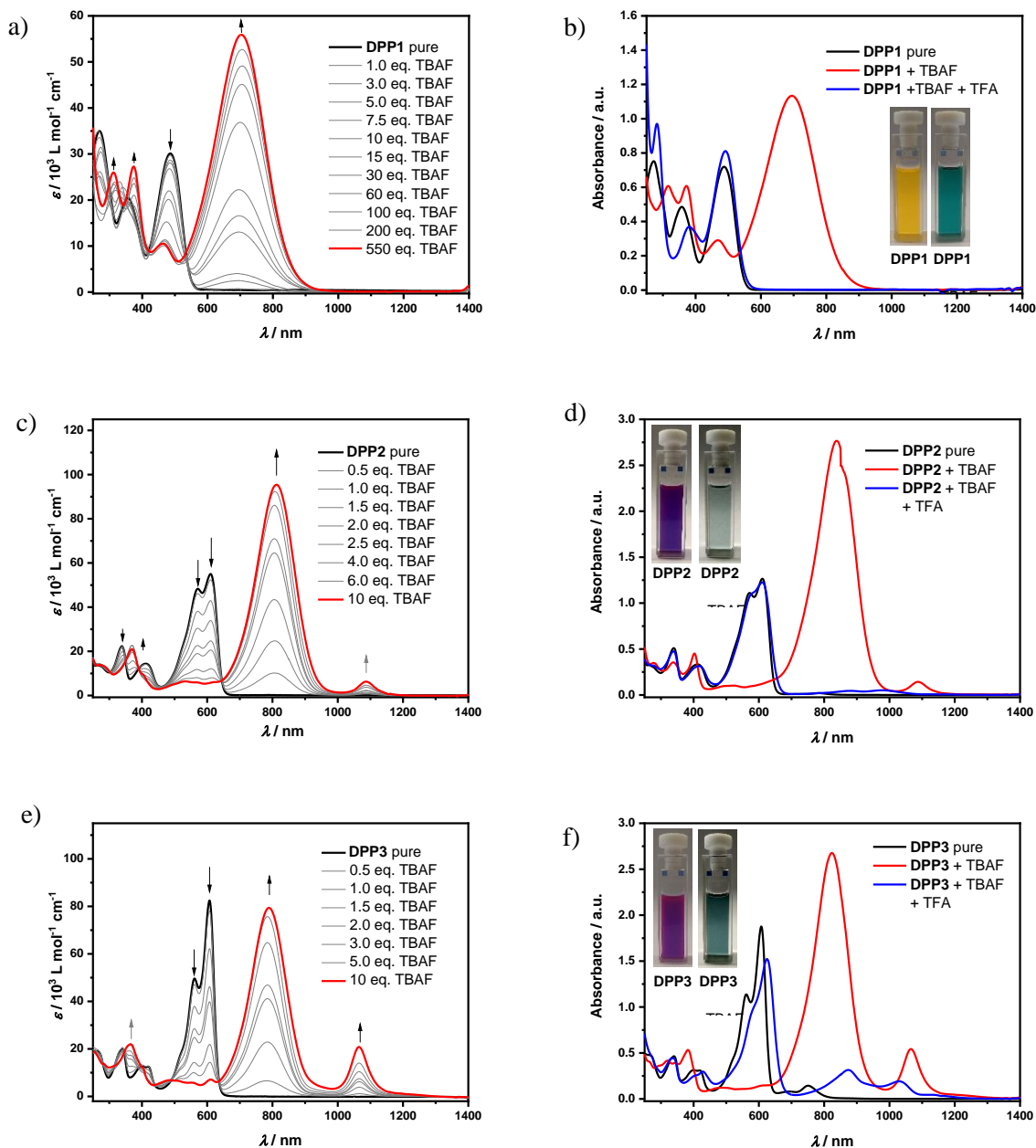


Figure 8.2.7 | UV/vis/NIR absorption spectral changes of (a) **DPP1** ($c = 1.01 \cdot 10^{-5} \text{ M}$ in CH_2Cl_2), (c) **DPP2** ($c = 9.30 \cdot 10^{-6} \text{ M}$ in CH_2Cl_2) and (e) **DPP3** ($c = 9.60 \cdot 10^{-6} \text{ M}$ in CH_2Cl_2) upon titration with ${}^t\text{Bu}_4\text{NF}$ (TBAF) solutions ($c = 7.50 \cdot 10^{-2} \text{ M}$ in CH_2Cl_2) to form dianions **DPP1**²⁻, **DPP2**²⁻ and **DPP3**²⁻, respectively. UV/vis/NIR absorption spectra of (b) **DPP1**²⁻ (red, $c = 2.44 \cdot 10^{-5} \text{ M}$ in CH_2Cl_2), (d) **DPP2**²⁻ (red, $c = 2.19 \cdot 10^{-5} \text{ M}$ in CH_2Cl_2) and (f) **DPP3**²⁻ (red, $c = 2.26 \cdot 10^{-5} \text{ M}$ in CH_2Cl_2) freshly prepared by adding 100 eq. ${}^t\text{Bu}_4\text{NF}$ to a solution of the respective neutral dye (black line) and after addition of 100 eq. trifluoroacetic acid (TFA) (blue line) in CH_2Cl_2 . Inset: Photographs of respective cuvettes.

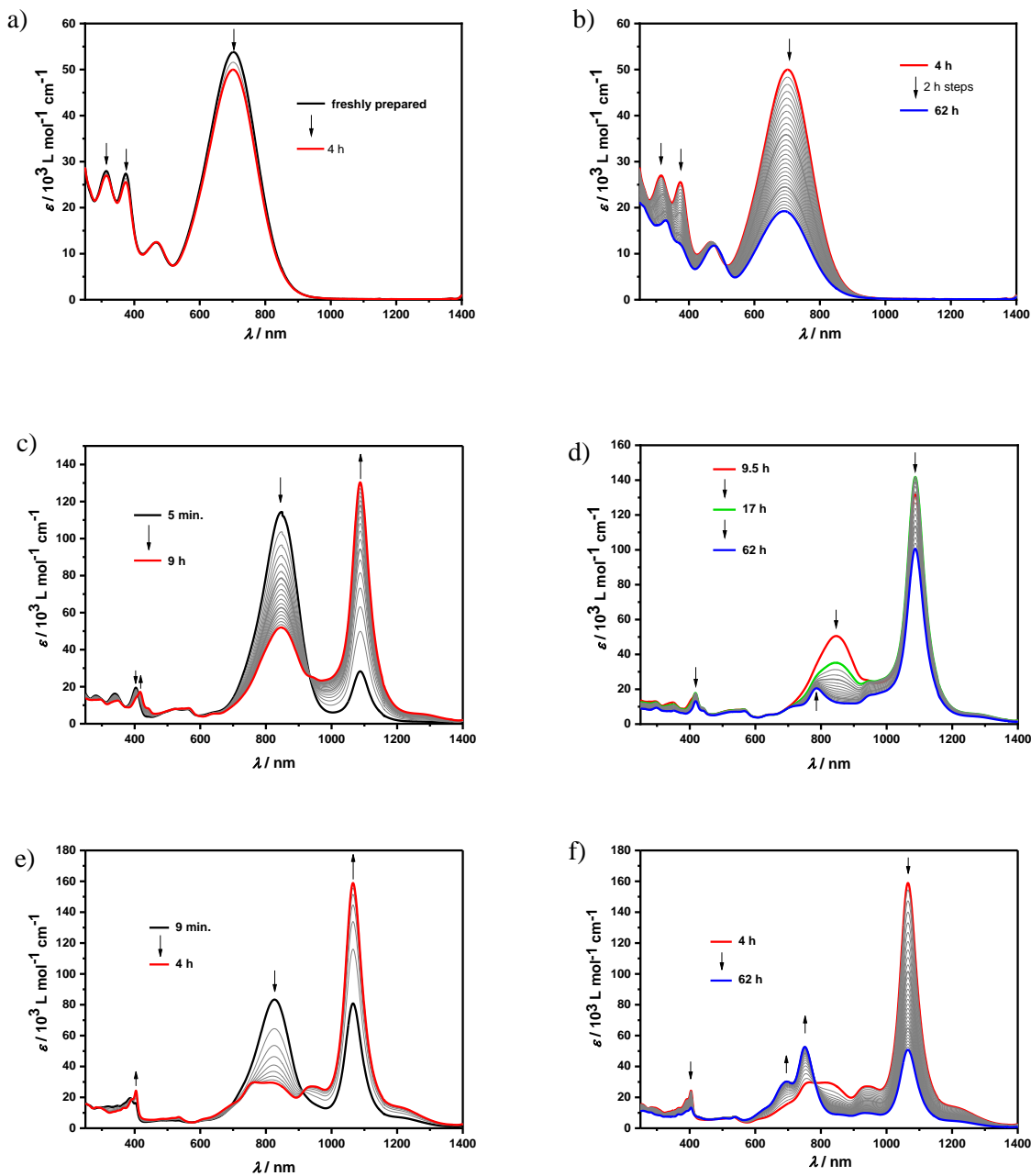


Figure 8.2.8 | Time-dependent UV/vis/NIR absorption spectral changes of (a, b) **DPP1²⁻**, (c, d) **DPP2²⁻** and (e, f) **DPP3²⁻** under ambient conditions ($c = 1.00 \cdot 10^{-5} \text{ M}$ in CH_2Cl_2 , counter ion: $^+\text{Bu}_4\text{N}$). Arrows indicate spectral changes over time.

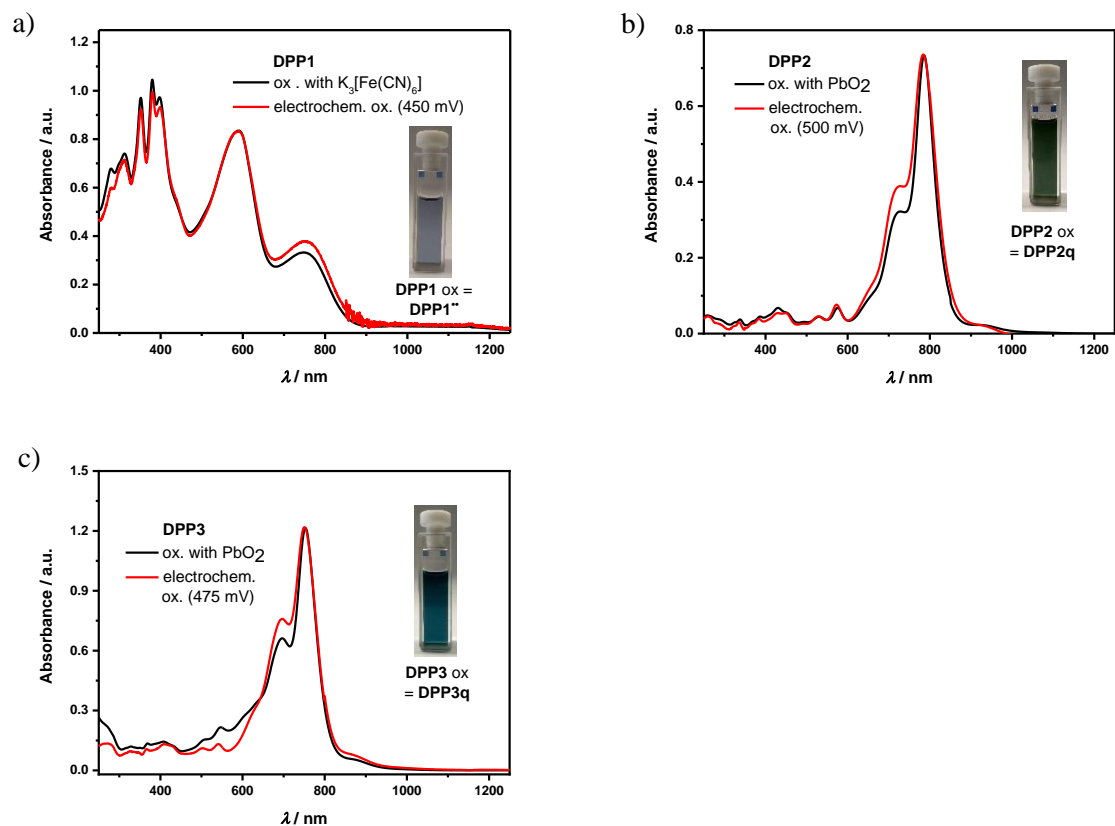


Figure 8.2.9 | Normalized UV/vis/NIR absorption spectra of (a) **DPP1^{ox}**, (b) **DPP2_q** and (c) **DPP3_q** obtained by chemical oxidation with $K_3[Fe(CN)_6]$ or PbO_2 (black solid line, $c \approx 10 \mu M$ in CH_2Cl_2) and electrochemical oxidation (red solid line, $c \approx 3 \text{ mM}$ in CH_2Cl_2) of the respective precursors **DPP1**, **DPP2** and **DPP3**. Inset: Photographs of respective cuvettes.

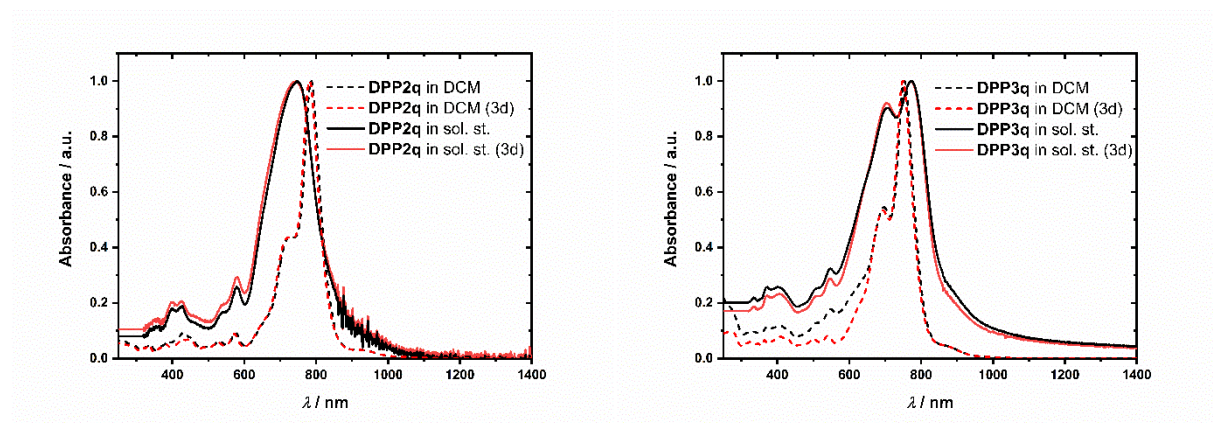


Figure 8.2.10 | Normalized UV/vis/NIR absorption spectra of **DPP2_q** (left) and **DPP3_q** (right) in solution (black dashed line, $c \approx 10 \mu M$ in CH_2Cl_2) and in the solid state ($c \approx 2 \text{ mM}$, $25 \mu L$, ambient temperature, $rpm = 3000$, $t = 30 \text{ s}$) as spincoated (red solid line) and after 3 days (black solid line) under ambient conditions.

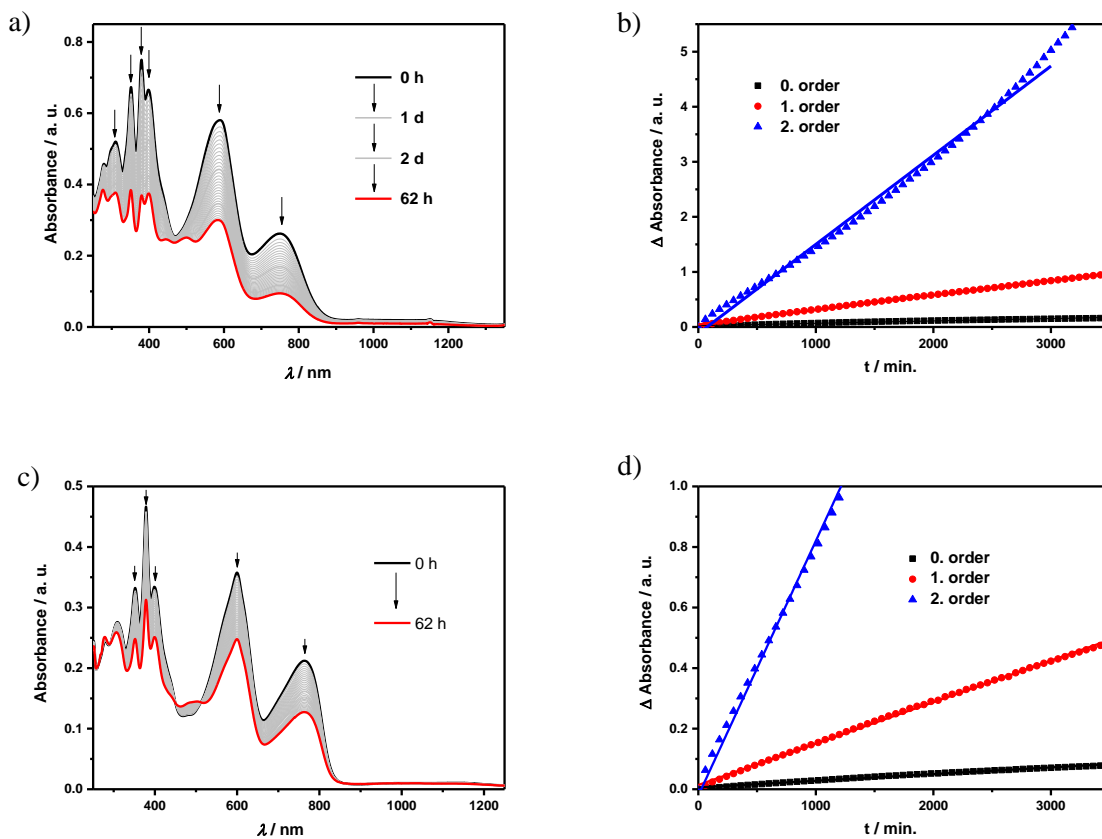


Figure 8.2.11 | Time-dependent UV/vis/NIR absorption spectral changes of **DPP1^{••}** ($c = 1.00 \cdot 10^{-5}$ M, ambient conditions) in (a) CH₂Cl₂ and (c) CCl₄. Absorption spectral changes of **DPP1^{••}** (in CCl₄) at 750 nm in (b) CH₂Cl₂ and (d) CCl₄ plotted versus time using zero-, first- and second-order rate equations. Arrows indicate spectral changes over time. Triangles, dots and circles represent the experimental results and the solid lines correspond to the respective fit.

Spectral changes observed were fitted with zero, first and second order kinetic models. As measurement data can be described with all three models with good accuracy, the minimum lifetime was chosen to be the lowest value obtained.

Table 8.2.1 | Kinetic evaluation of the time-dependent UV/vis/NIR absorption spectral changes of **DPP1^{••}** in CH₂Cl₂ (*c* = 1.00 · 10⁻⁵ M, ambient conditions) upon decomposition under ambient conditions. [A]₀ = initial absorption, [A]_t = time dependent absorption.

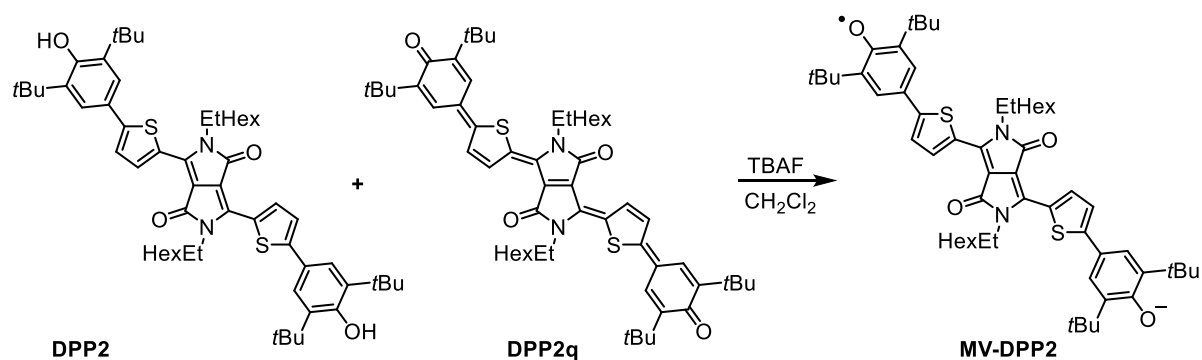
rate law	equations		linear regression	rate constant <i>k</i>	half-life $\tau_{\frac{1}{2}}$ [h]	Pearson R ²
	rate equation	half-life				
zero order	$[A]_0 - [A]_t = kt$	$\tau_{\frac{1}{2}} = \frac{A_0}{2k}$	$y = 0.0000430284x + 0.02372$	$2.58 \cdot 10^{-4} \frac{1}{h}$	51	0.97590
first order	$\ln \frac{[A]_0}{[A]_t} = kt$	$\tau_{\frac{1}{2}} = \frac{\ln 2}{k}$	$y = 0.000266114x + 0.04563$	$1.60 \cdot 10^{-2} \frac{1}{h}$	43	0.99894
second order	$\frac{1}{[A]_t} - \frac{1}{[A]_0} = kt$	$\tau_{\frac{1}{2}} = \frac{1}{kA_0}$	$y = 0.00162x - 0.11879$	$9.72 \cdot 10^{-2} \frac{1}{h}$	39	0.99410

Table 8.2.2 | Kinetic evaluation of the time-dependent UV/vis/NIR absorption spectral changes of **DPP1^{••}** in CCl₄ (*c* = 1.00 · 10⁻⁵ M, ambient conditions) upon decomposition under ambient conditions. [A]₀ = initial absorption, [A]_t = time dependent absorption.

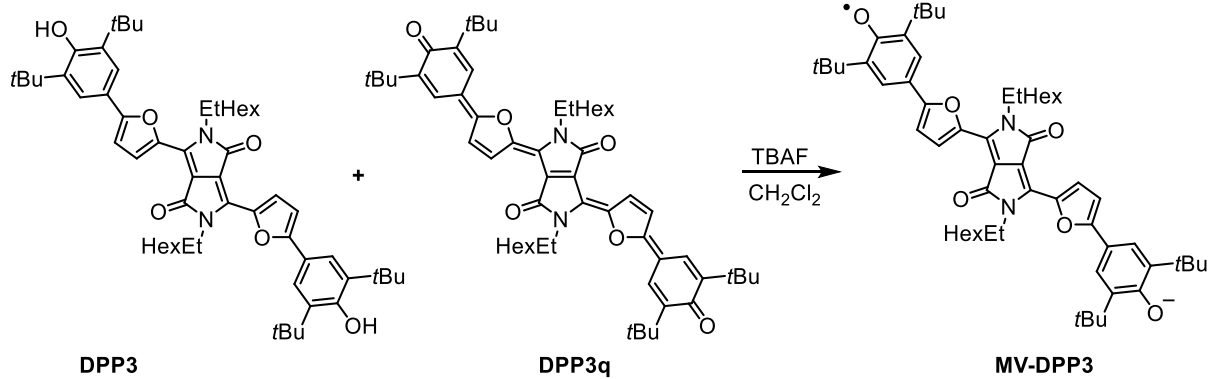
rate law	equations		linear regression	rate constant <i>k</i>	half-life $\tau_{\frac{1}{2}}$ [h]	Pearson R ²
	rate equation	half-life				
zero order	$[A]_0 - [A]_t = kt$	$\tau_{\frac{1}{2}} = \frac{A_0}{2k}$	$y = 0.0000220889x + 0.00586$	$1.33 \cdot 10^{-3} \frac{1}{h}$	78	0.99140
first order	$\ln \frac{[A]_0}{[A]_t} = kt$	$\tau_{\frac{1}{2}} = \frac{\ln 2}{k}$	$y = 0.000136849x + 0.01397$	$8.21 \cdot 10^{-3} \frac{1}{h}$	84	0.99901
second order	$\frac{1}{[A]_t} - \frac{1}{[A]_0} = kt$	$\tau_{\frac{1}{2}} = \frac{1}{kA_0}$	$y = 0.000840573x - 0.02077$	$50.4 \cdot 10^{-3} \frac{1}{h}$	96	0.99906

Table 8.2.3 | Absorption maxima of neutral diketopyrrolopyrrole derivatives **DPP1**, **DPP2** and **DPP3**, dianions **DPP1²⁻**, **DPP2²⁻** and **DPP3²⁻**, mixed valent intermediates **MV-DPP2** and **MV-DPP3**, biradical **DPP1^{••}** and quinones **DPP2q** and **DPP3q** in dichloromethane solution ($c \approx 10 \mu\text{M}$, ambient conditions).

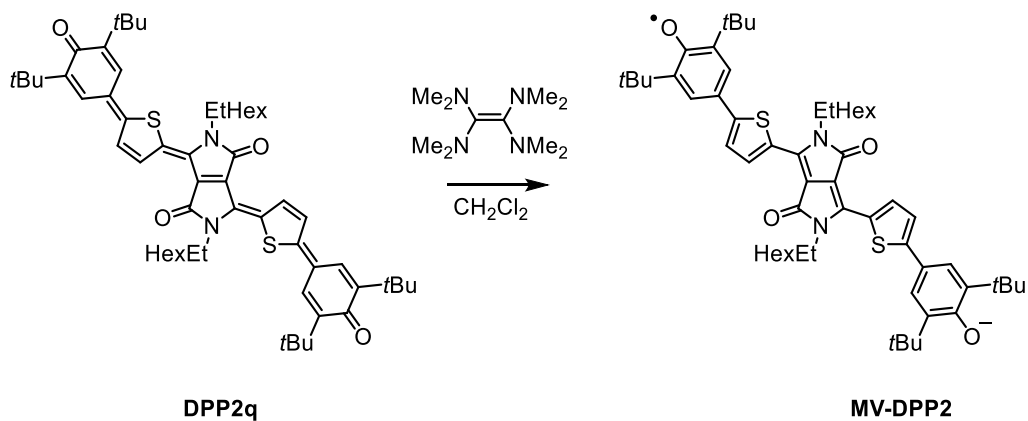
Compound	λ_{max} [nm]	ϵ [$\text{M}^{-1} \text{cm}^{-1}$] (λ)
DPP1	269, 356, 486	30100 (486 nm)
DPP1²⁻	312, 374, 704	55900 (704 nm)
DPP1^{••}	352, 380, 399, 588, 749	18500 (749 nm)
DPP2	572, 610	55000 (610 nm)
DPP2²⁻	813	95400 (813 nm)
MV-DPP2	1083	152600 (1083 nm)
DPP2q	725, 782	151800 (782 nm)
DPP3	561, 607	82500 (607 nm)
DPP3²⁻	789	79400 (789 nm)
MV-DPP3	1063	190800 (1063 nm)
DPP3q	695, 751	172500 (751 nm)



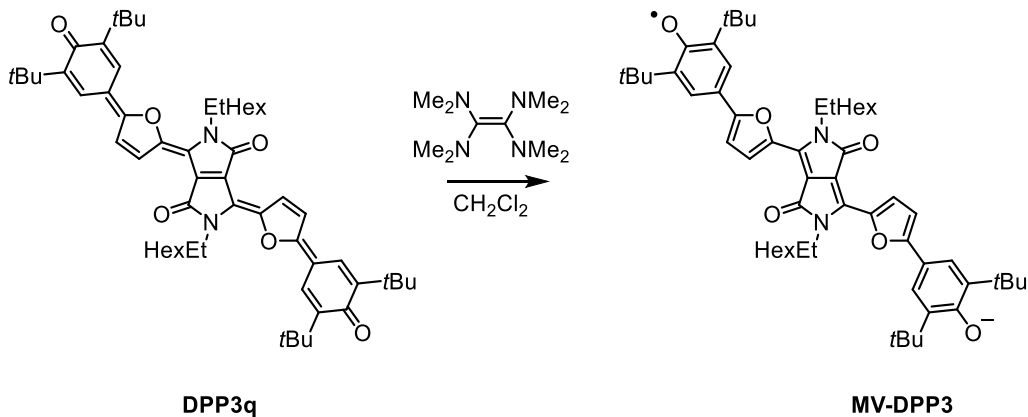
Scheme 8.2.8 | Generation of **MV-DPP2** by comproportionation of **DPP2q** and *in situ* generated **DPP2²⁻**.



Scheme 8.2.9 | Generation of **MV-DPP3** by comproportionation of **DPP3q** and *in situ* generated **DPP3²⁻**.



Scheme 8.2.10 | Generation of **MV-DPP2** by single electron transfer of TDMAE to **DPP2q**.



Scheme 8.2.11 | Generation of **MV-DPP3** by single electron transfer of TDMAE to **DPP3q**.

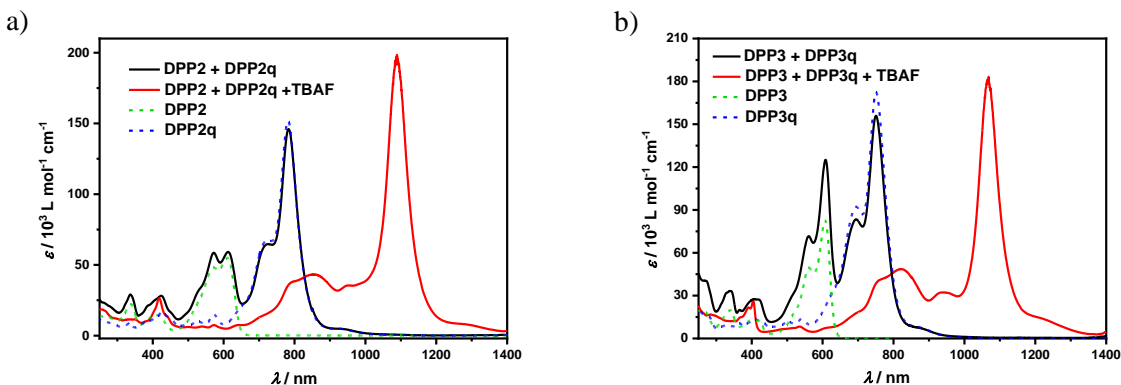


Figure 8.2.12 | UV/vis/NIR absorption spectra of equimolar mixtures of (a) **DPP2** and **DPP2q**, and (b) **DPP3** and **DPP3q** (each $c = 1.00 \cdot 10^{-5}$ M in CH_2Cl_2) before (black solid line) and after (red solid line, concentration corrected: Absorbance/2) addition of TBAF.

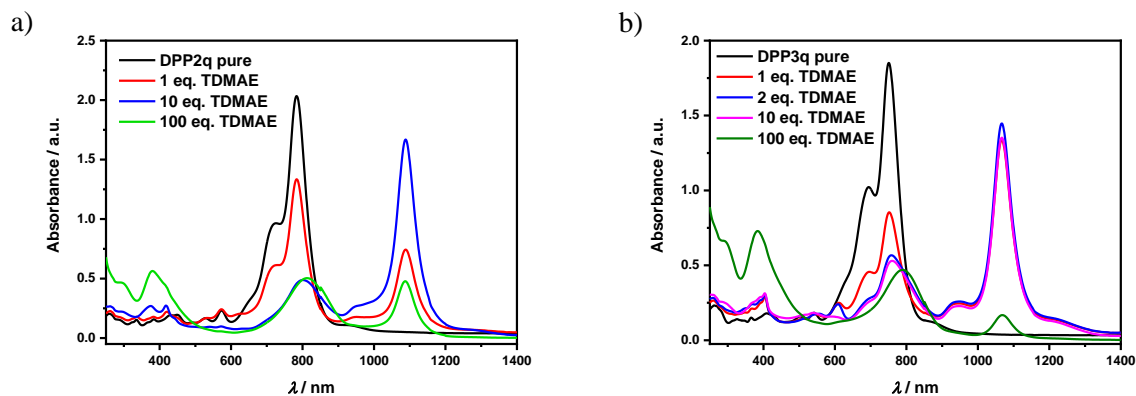


Figure 8.2.13 | UV/vis/NIR absorption spectral changes of (a) **DPP2q**, and (b) **DPP3q** (both $c = 1.00 \cdot 10^{-5}$ M in CH_2Cl_2) upon addition of tetrakis(dimethylamino)ethylene (TDMAE) solutions ($c = 2.00 \cdot 10^{-3}$ M in CH_2Cl_2) to form mixed valent **MV-DPP2** and **MV-DPP3**, respectively.

8.2.6 NMR spectroscopy

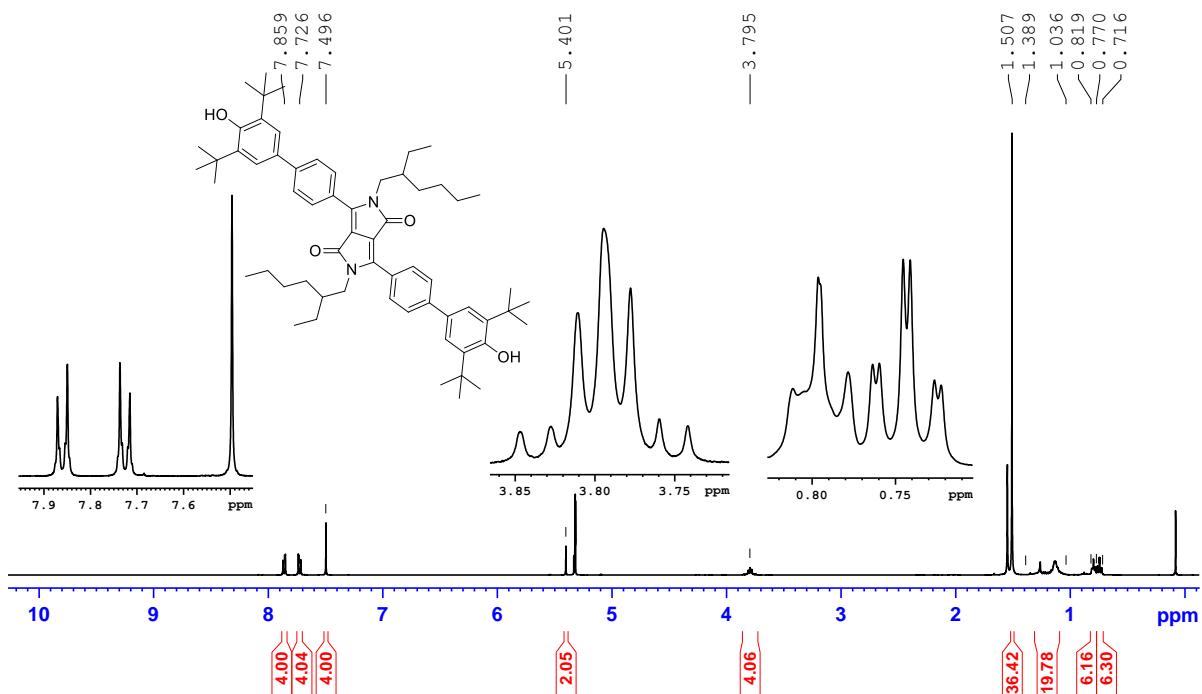


Figure 8.2.14 | ¹H NMR spectrum (400 MHz) of DPP1 in CD₂Cl₂ at 295 K.

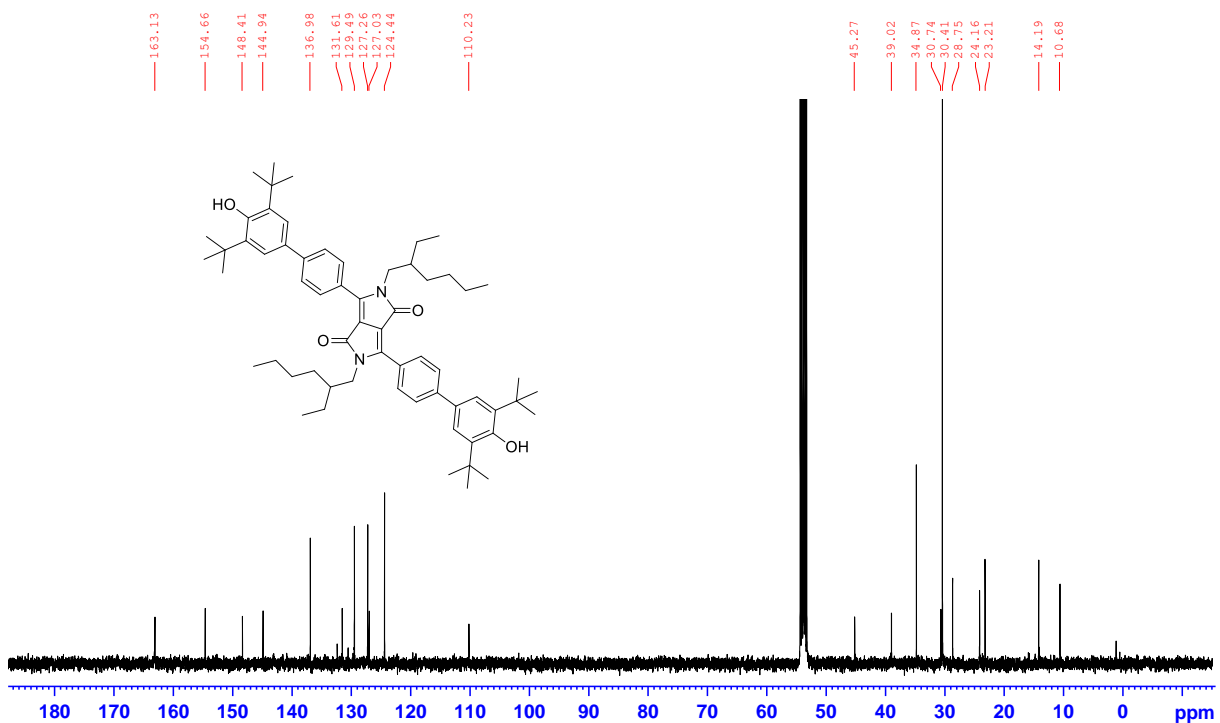


Figure 8.2.15 | ¹³C NMR spectrum (101 MHz) of DPP1 in CD₂Cl₂ at 295 K.

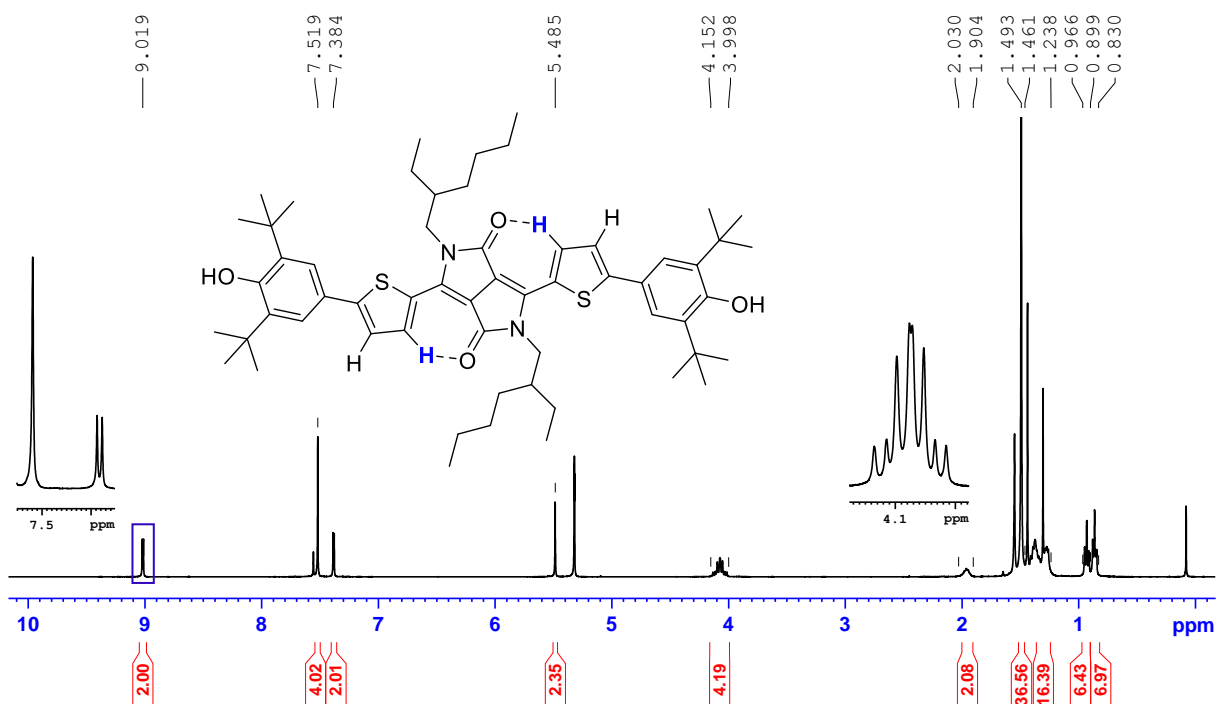


Figure 8.2.16 | ^1H NMR spectrum (400 MHz) of **DPP2** in CD_2Cl_2 at 295 K. Hydrogen bonded proton highlighted in blue.

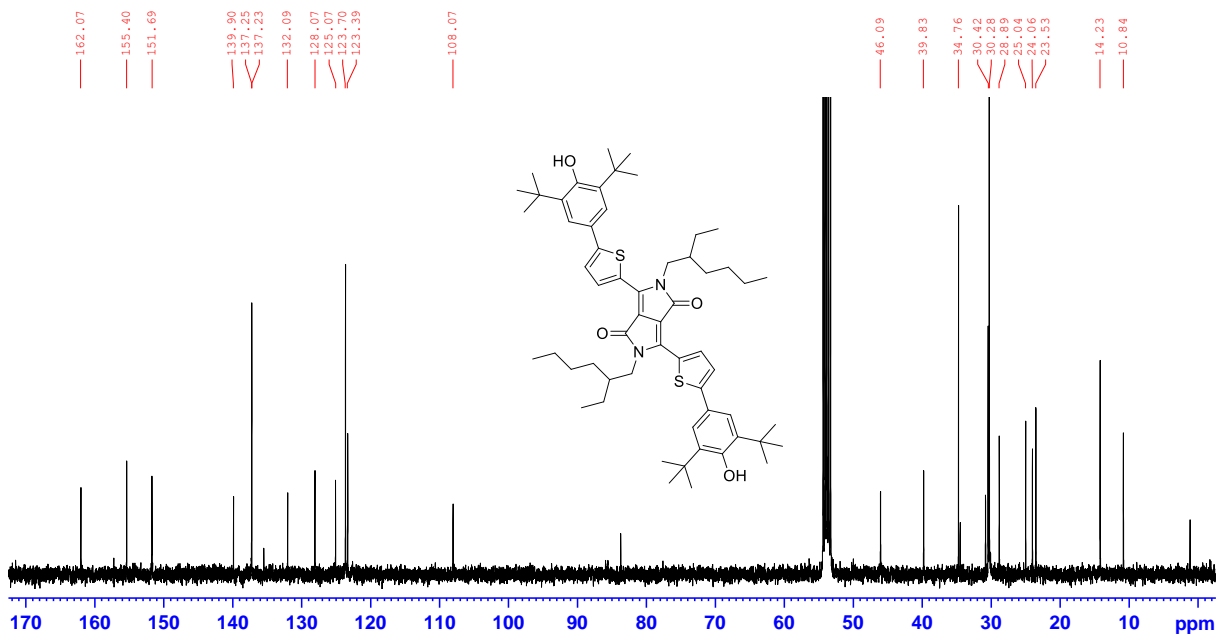


Figure 8.2.17 | ^{13}C NMR spectrum (101 MHz) of **DPP2** in CD_2Cl_2 at 295 K.

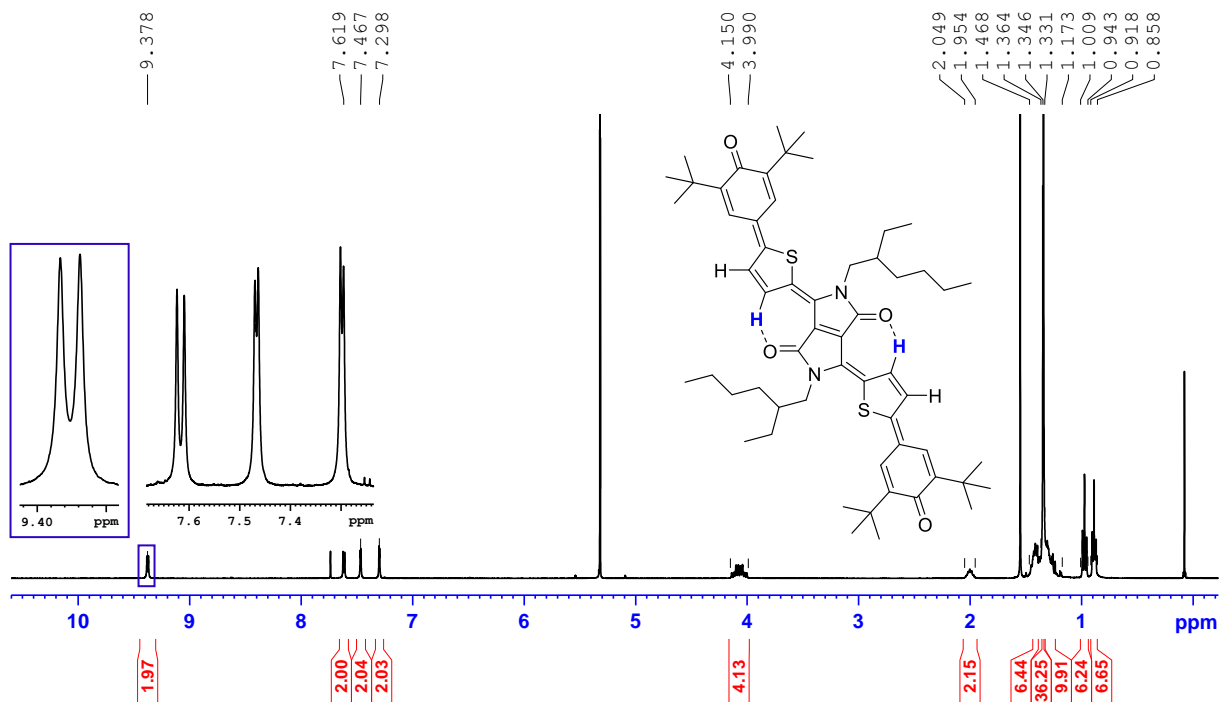


Figure 8.2.18 | ^1H NMR spectrum (400 MHz) of DPP2q in CD_2Cl_2 at 295 K. Hydrogen bonded proton highlighted in blue.

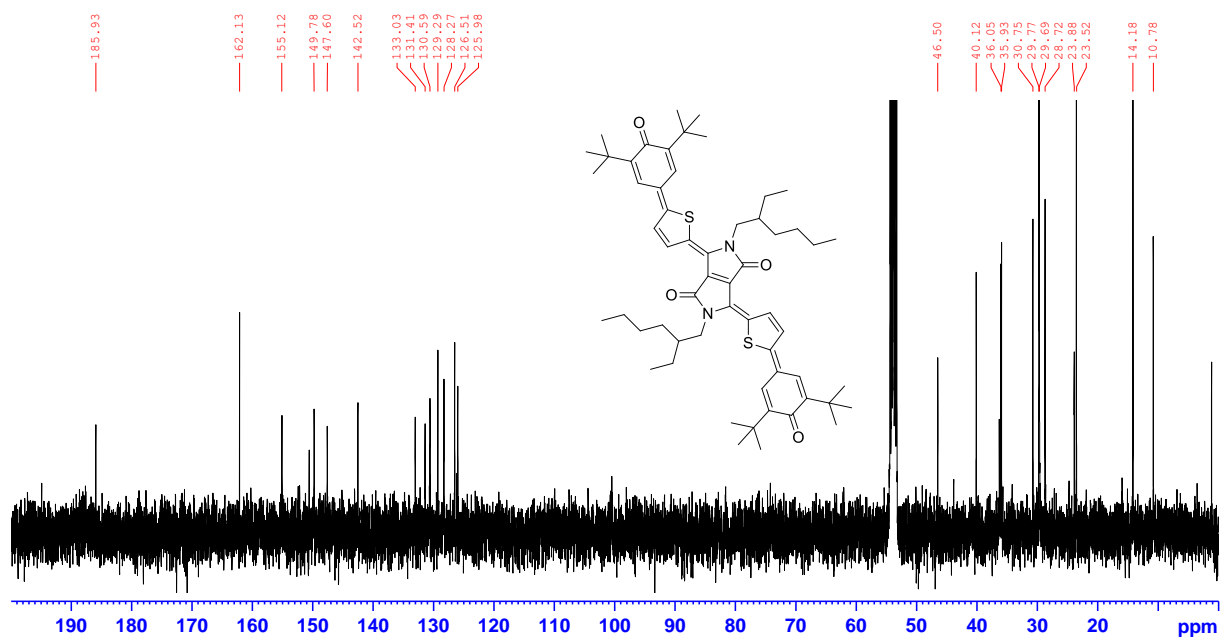


Figure 8.2.19 | ^{13}C NMR spectrum (101 MHz) of DPP2q in CD_2Cl_2 at 295 K.

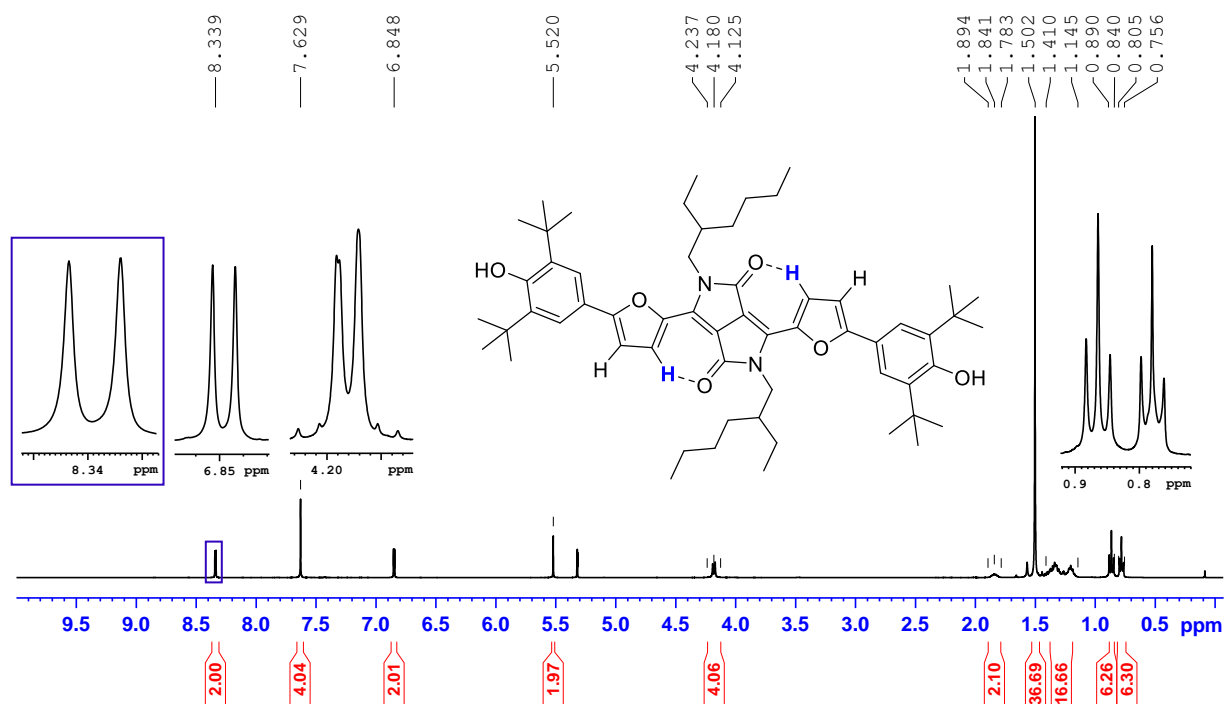


Figure 8.2.20 | ^1H NMR spectrum (400 MHz) of **DPP3** in CD_2Cl_2 at 295 K. Hydrogen bonded proton highlighted in blue.

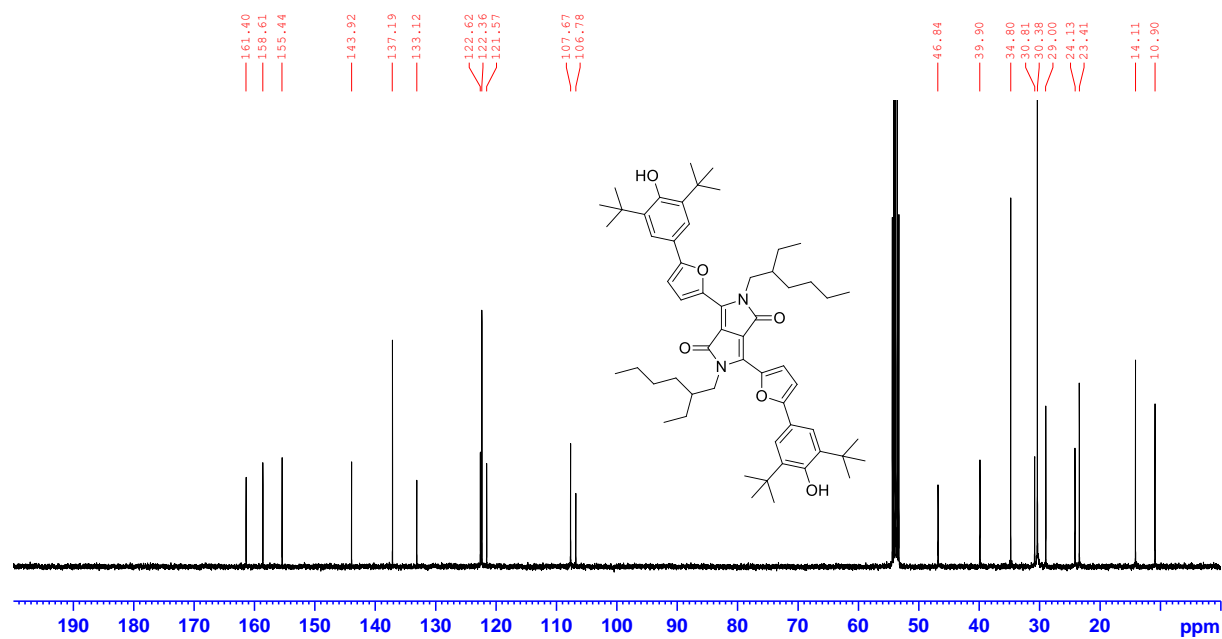


Figure 8.2.21 | ^{13}C NMR spectrum (101 MHz) of **DPP3** in CD_2Cl_2 at 295 K.

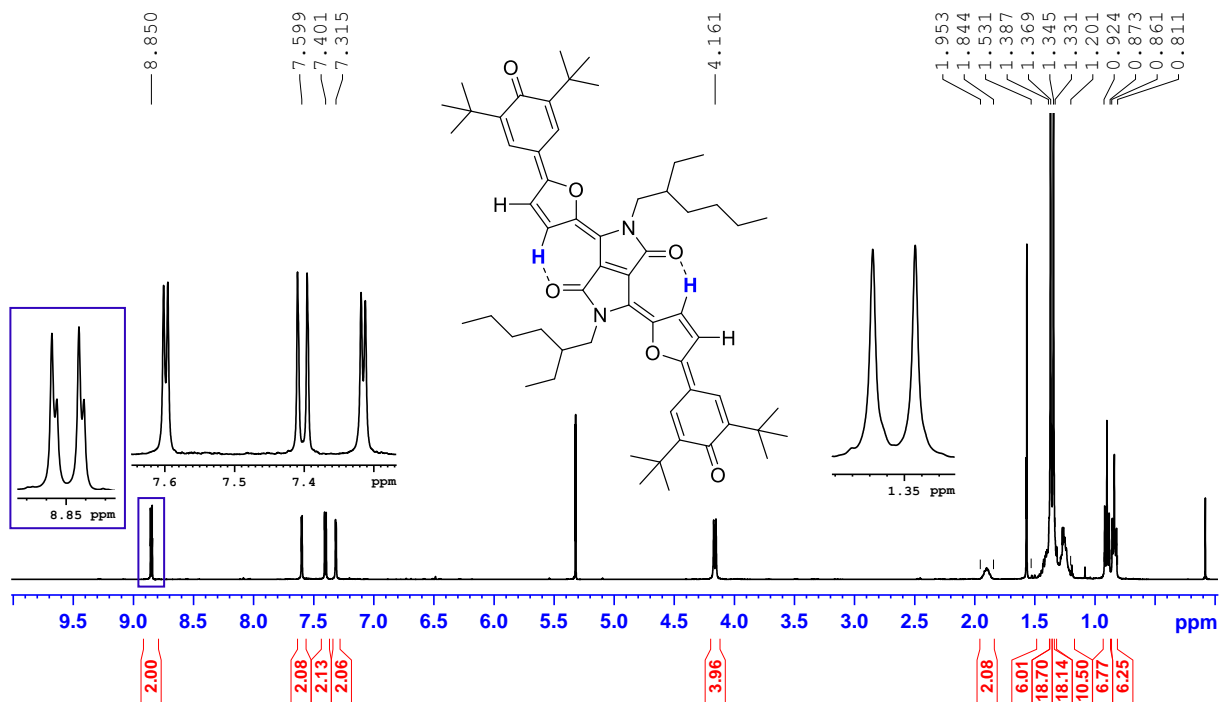


Figure 8.2.22 | ¹H NMR spectrum (400 MHz) of **DPP3q** in CD₂Cl₂ at 295 K. Hydrogen bonded proton highlighted in blue.

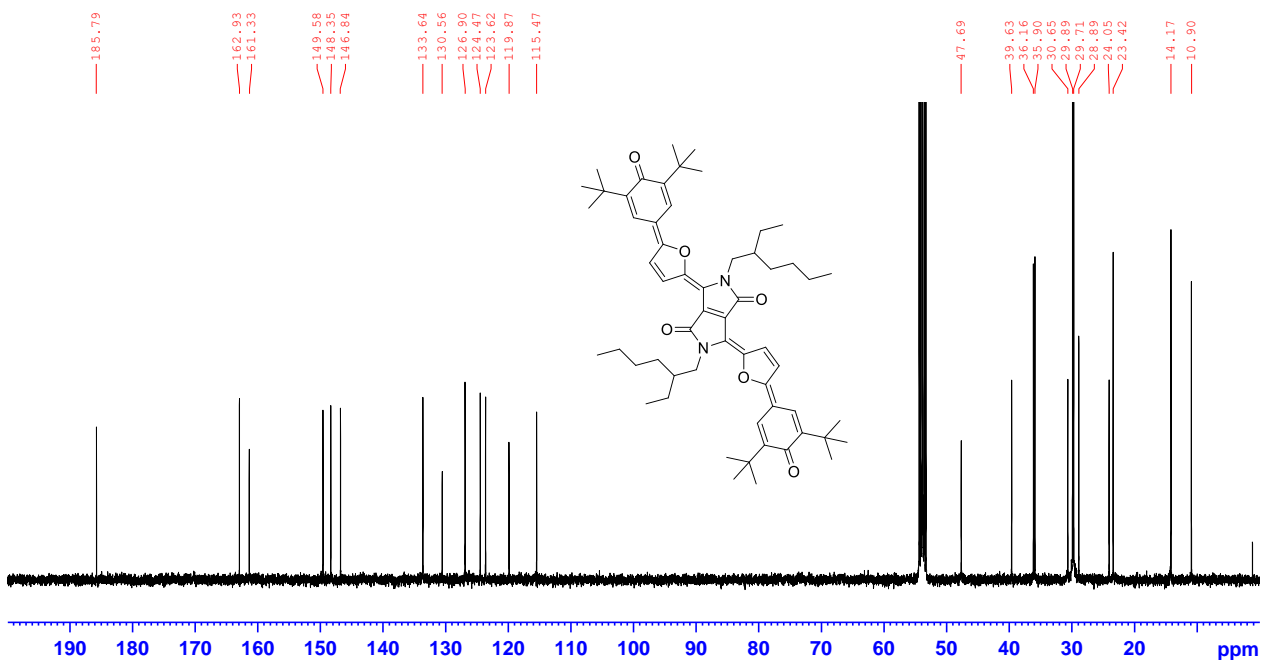


Figure 8.2.23 | ¹³C NMR spectrum (101 MHz) of **DPP3q** in CD₂Cl₂ at 295 K.

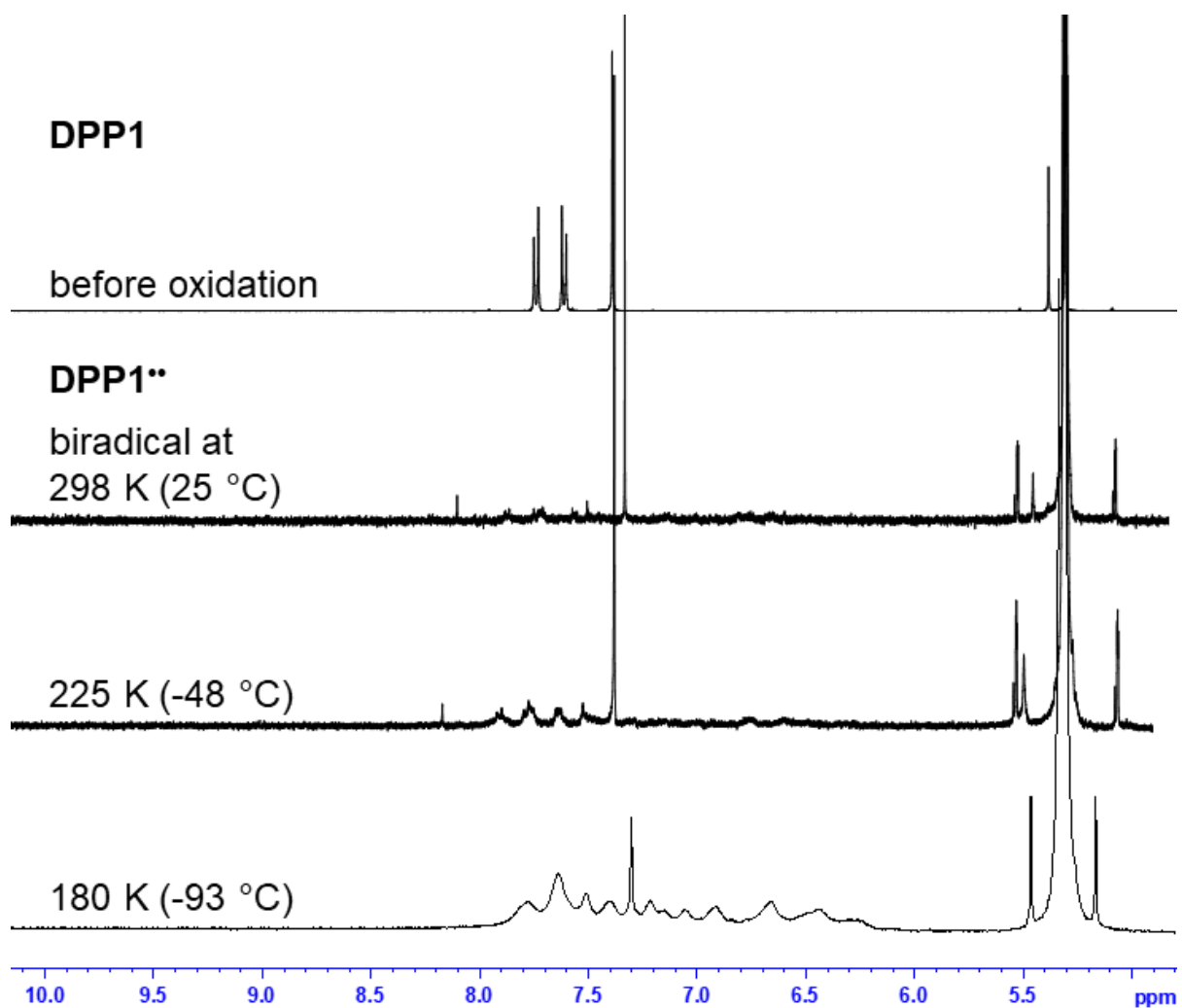


Figure 8.2.24 | Aromatic region of the ^1H NMR spectrum (600 MHz) of **DPP1** in CD_2Cl_2 before oxidation, and after oxidation to the biradical **DPP1^{••}** at 298 K, 225 K and 180 K (from the top).

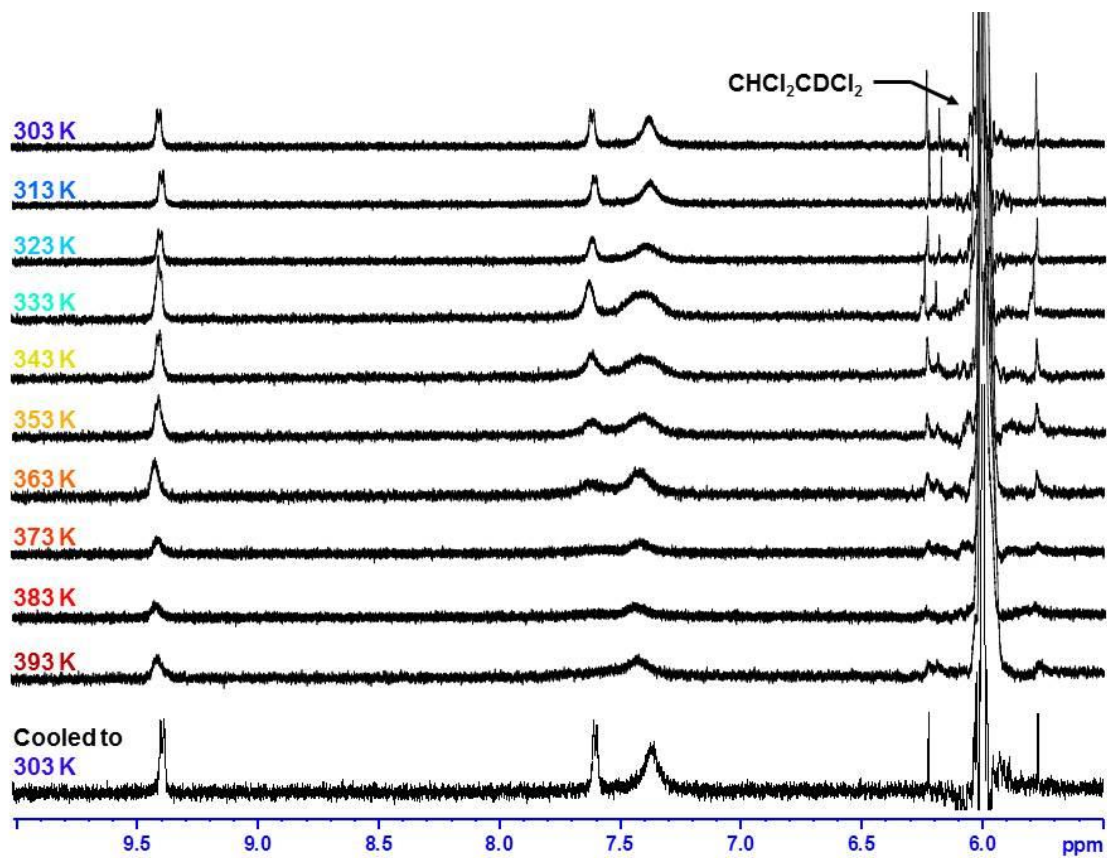


Figure 8.2.25 | Aromatic region of the ^1H NMR spectrum (400 MHz) of **DPP2q** in $\text{C}_2\text{D}_2\text{Cl}_4$ at various temperatures from 303 K to 393 K (from the top) and after cooling back to 303 K (bottom).

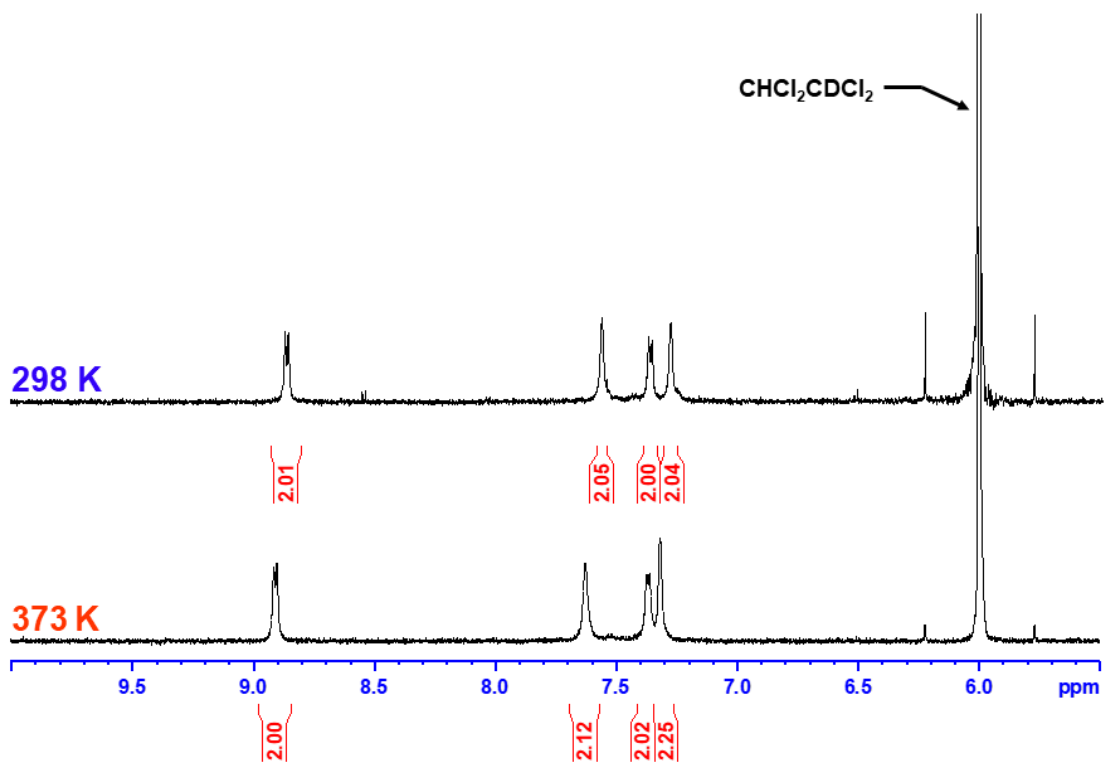


Figure 8.2.26 | Aromatic region of the ¹H NMR spectrum (400 MHz) of **DPP3q** in C₂D₂Cl₄ at 298 K (top) and at 373 K (bottom).

8.2.7 Band gap analysis and cyclic voltammetry (CV)

Tauc plot

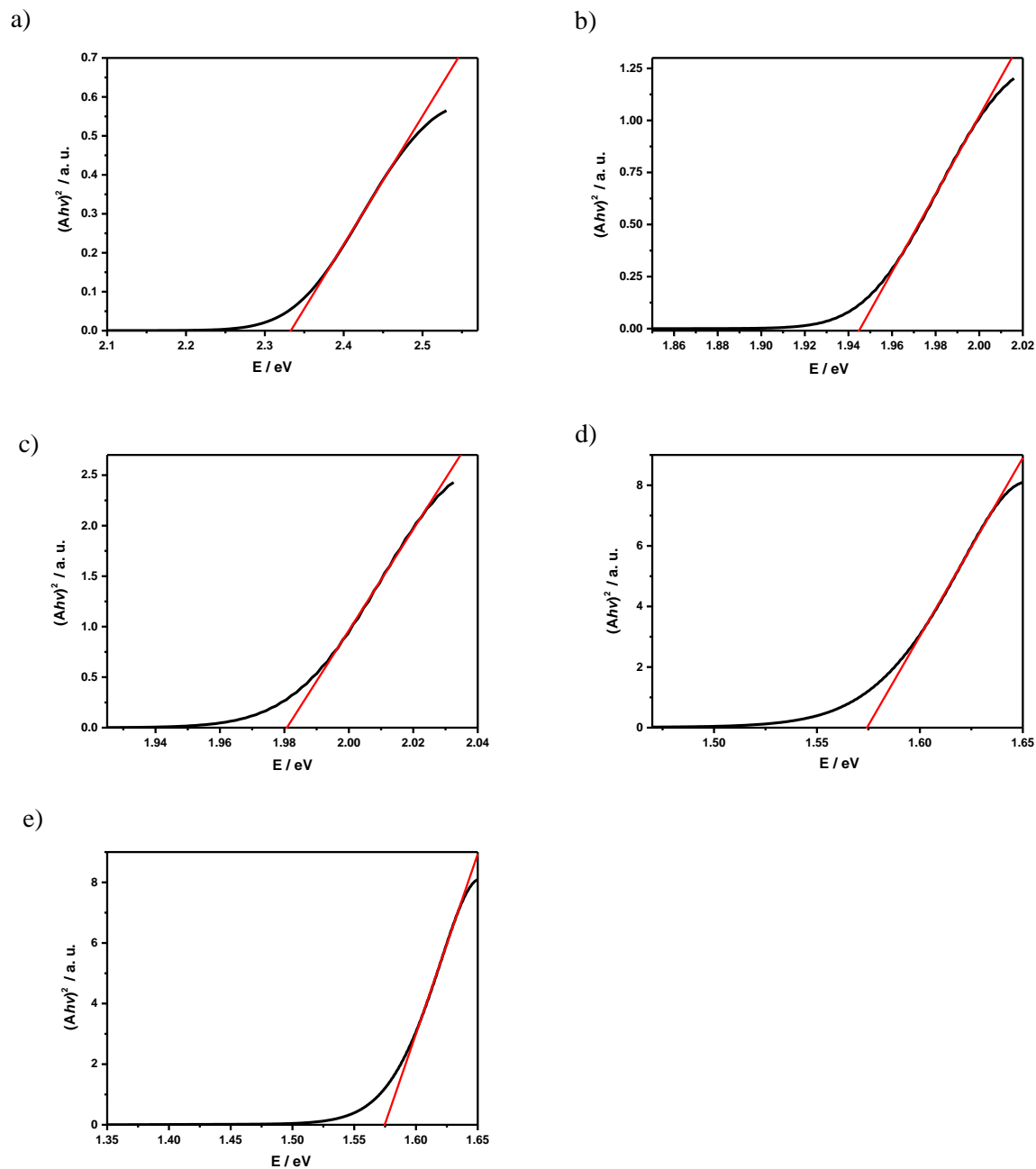


Figure 8.2.27 | Plot according to Tauc^[321–323] and optical energy gap determination of (a) DPP1, (b) DPP2, (c) DPP3, (d) DPP2q and (e) DPP3q.

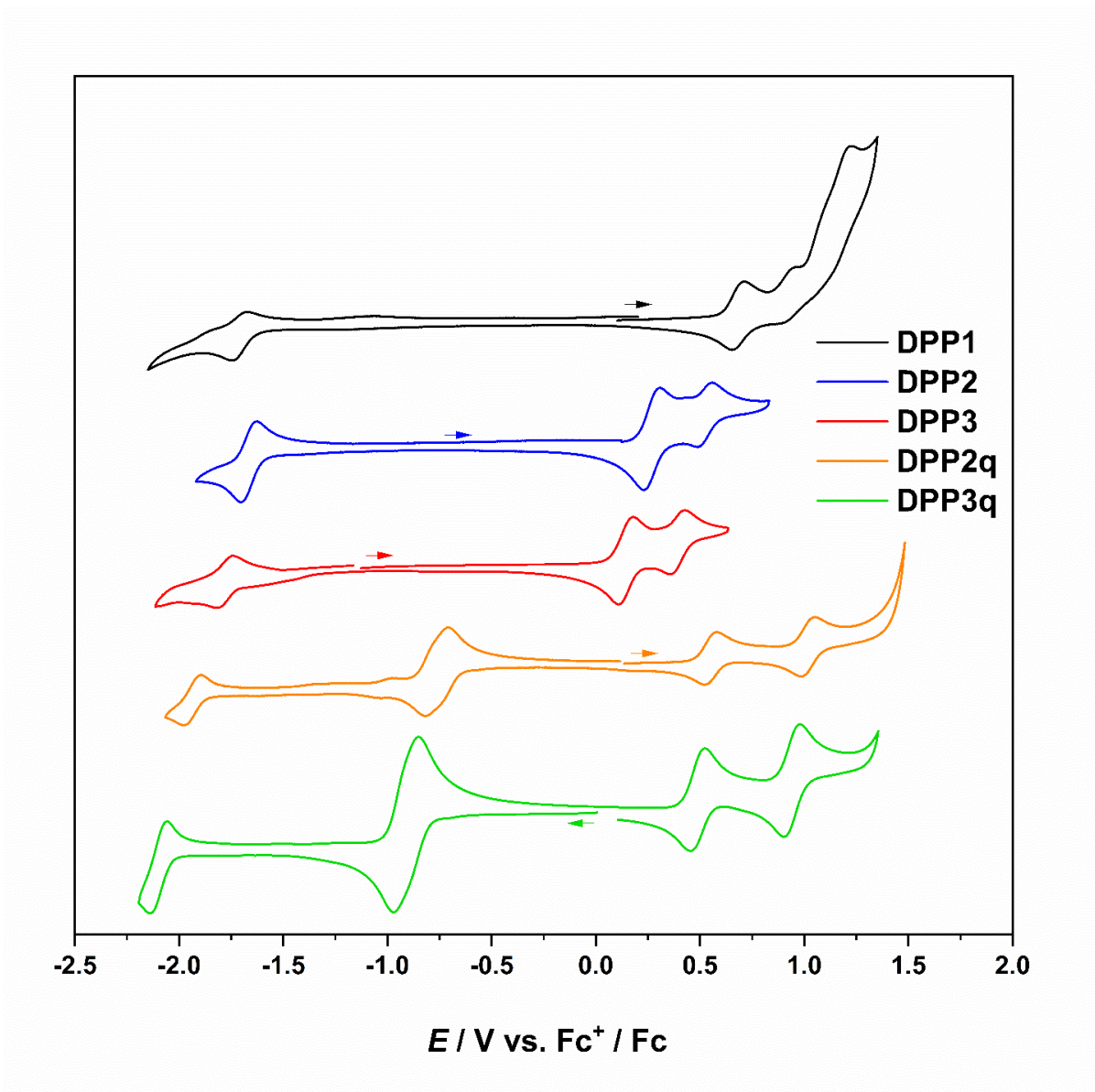


Figure 8.2.28 | Cyclic voltammetry of **DPP1**, **DPP2**, **DPP3**, **DPP2q** and **DPP3q** (from the top) in CH_2Cl_2 at room temperature ($c \approx 20 \mu M$, electrolyte: $0.1 M nBu_4NPF_6$, scan rate: $100 mVs^{-1}$).

Table 8.2.4 | Reduction potentials of **DPP1**, **DPP2**, **DPP3**, **DPP2q** and **DPP3q** versus the ferrocenium/ferrocene redox couple.

	$E_{1/2}^{\text{Red2}}$ [V]	$E_{1/2}^{\text{Red1}}$ [V]	$E_{1/2}^{\text{Ox1}}$ [V]	$E_{1/2}^{\text{Ox2}}$ [V]
DPP1		-1.711	0.683	
DPP2		-1.664	0.270	0.523
DPP3		-1.780	0.145	0.392
DPP2q	-1.937	-0.764	0.489	0.943
DPP3q	-2.098	-0.911	0.552	1.019

Fc⁺/Fc = 0.00 V

Table 8.2.5 | Frontier molecular orbital energies of **DPP1**, **DPP2**, **DPP3**, **DPP2q** and **DPP3q** as well as electrochemical and optical energy gap.

	$E(\text{HOMO})^{\text{a}}$ [eV]	$E(\text{LUMO})^{\text{b}}$ [eV]	E_g [eV] ^c	E_g^{opt} [eV] ^d
DPP1	-5.48	-3.09	2.39	2.33
DPP2	-5.07	-3.14	1.93	1.95
DPP3	-4.95	-3.02	1.93	1.98
DPP2q	-5.35	-4.04	1.31	1.57
DPP3q	-5.29	-3.89	1.40	1.57

a) $E(\text{HOMO}) = -4.80 \text{ eV} - E_{1/2}^{\text{Ox1}}$. b) $E(\text{LUMO}) = -4.80 \text{ eV} - E_{1/2}^{\text{Red1}}$. c) $E_g = E(\text{LUMO}) - E(\text{HOMO})$. d) E_g^{opt} according to Tauc.^[321–323]

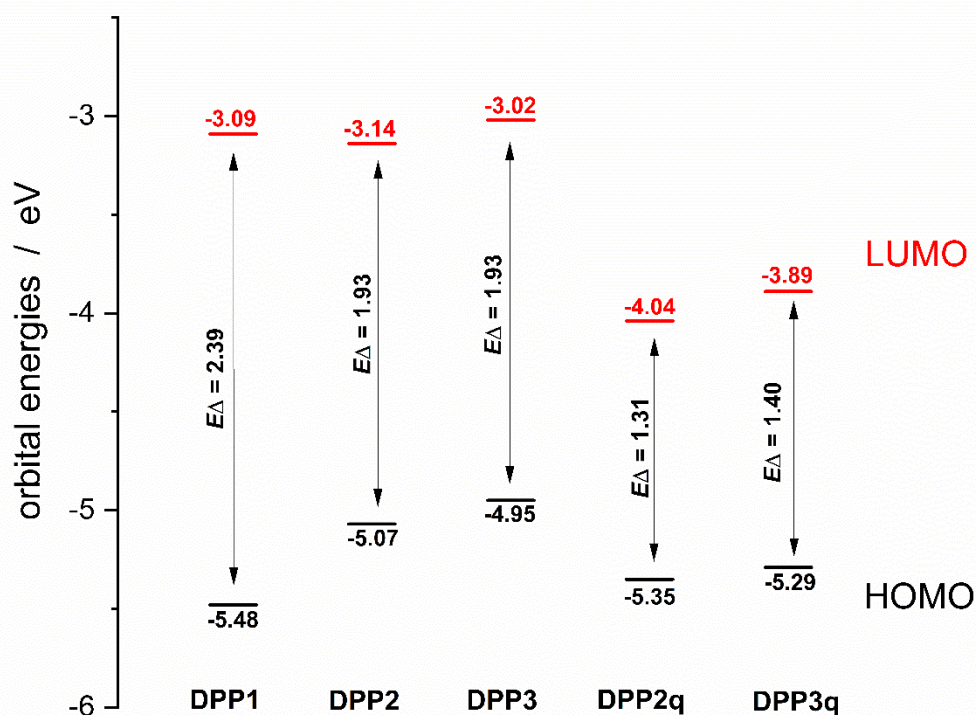


Figure 8.2.29 | Frontier orbital energies (in eV) of **DPP1**, **DPP2**, **DPP3**, **DPP2q** and **DPP3q** and electrochemical energy gap obtained from CV and differential pulse voltammetry (DP) data.

For the sake of completeness, the redox behavior of **DPP1**, **DPP2**, **DPP3**, **DPP2q** and **DPP3q** was additionally investigated by cyclic voltammetry (CV) experiments and the results compared to optical band gap analysis. The order of first oxidation potentials **DPP1** >> **DPP2** > **DPP3** can be explained by the more electron rich character of the heteroaromatic cores and is well in line with the higher autoxidation tendencies observed for **DPP2²⁻** and **DPP3²⁻** compared to **DPP1²⁻**. Frontier orbital energies derived from CV are in good accordance with the optical band gap (Fig. 8.2.27–8.2.29 and Table 8.2.5).

8.2.8 EPR spectroscopy

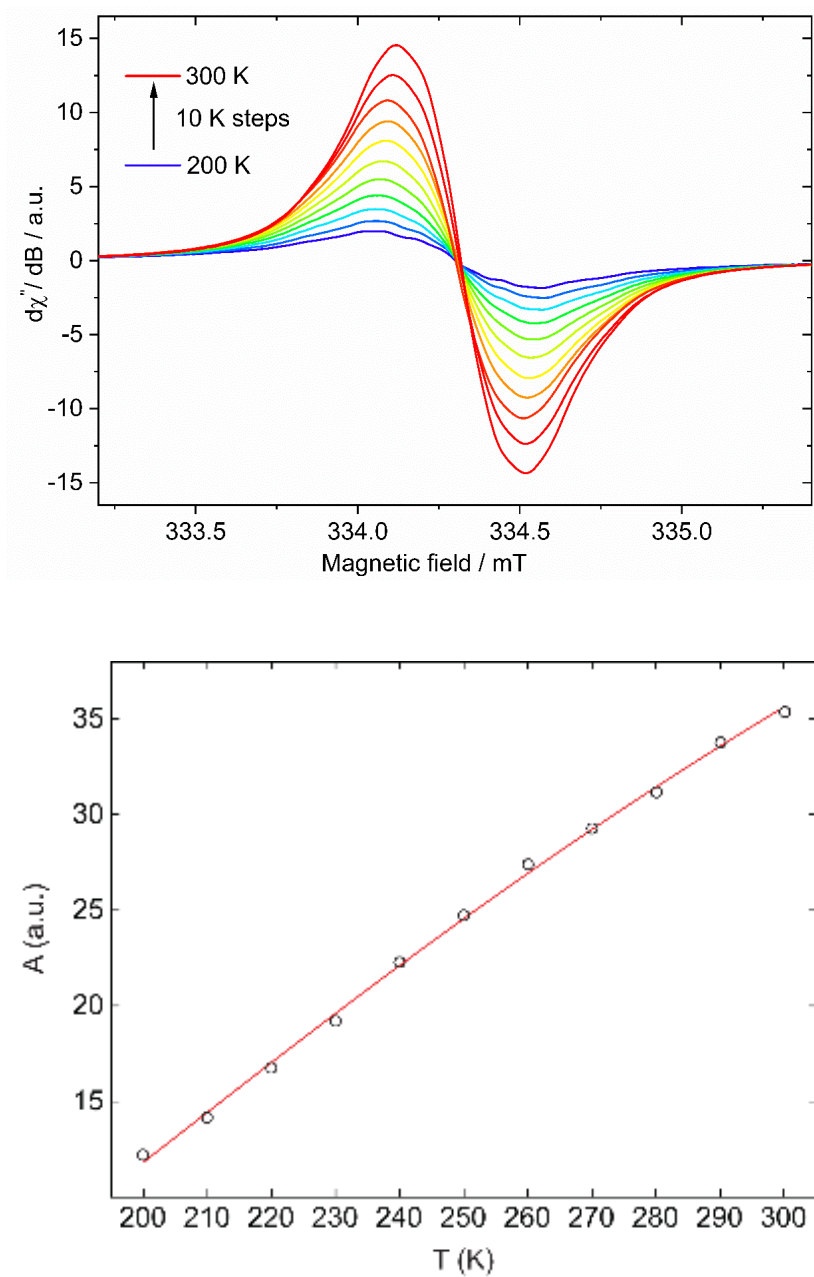


Figure 8.2.30 | Temperature dependence of the X-band EPR spectra of **DPPH•** in CH_2Cl_2 ($c \approx 1$ mM). The signal is centered at $g_{\text{iso}} = 2.0044$ with a peak-to-peak line width of 3.8 G (top). Temperature dependence of the double integral EPR intensity (A) of **DPPH•** in CH_2Cl_2 wherein circles (\bigcirc) represent the experimental results and the red line corresponds to the fit with the Bleaney–Bowers equation (bottom).^[213]

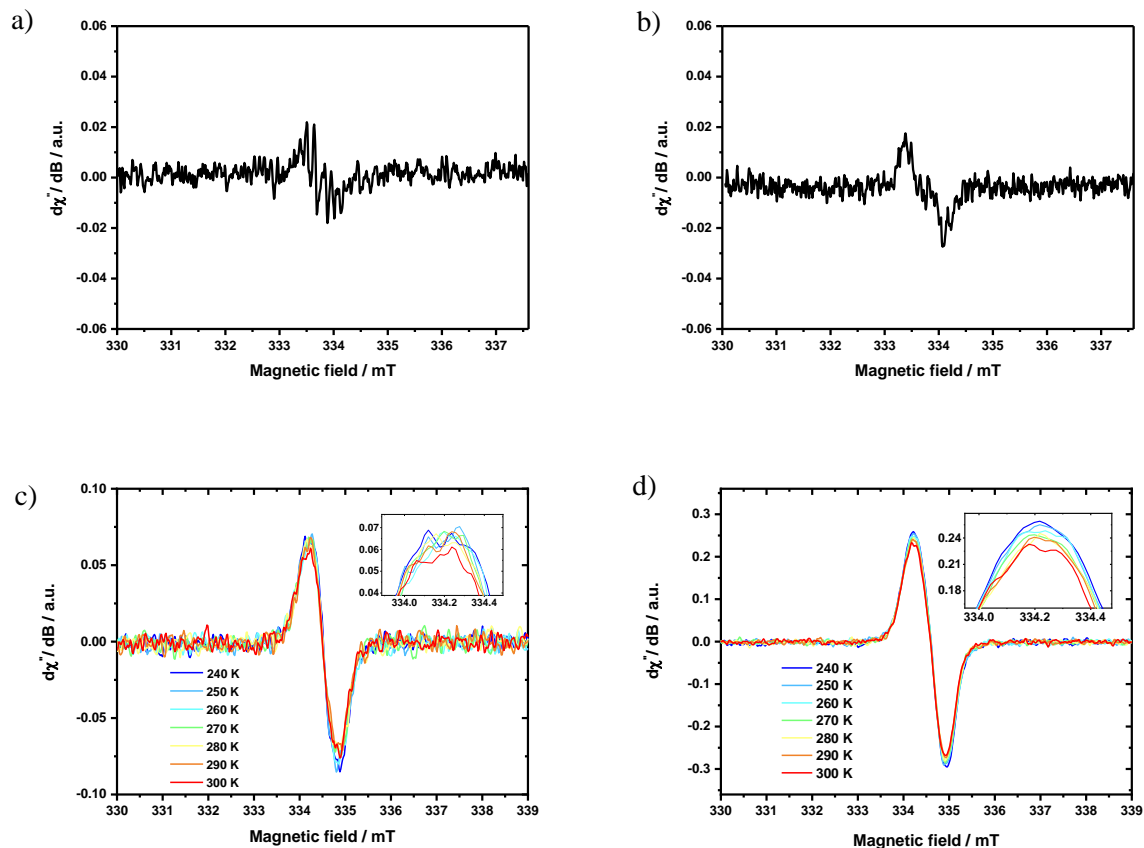


Figure 8.2.31 | Continuous-wave (CW) X-band EPR spectrum in CH₂Cl₂ solution ($c \approx 1$ mM) at 280 K of **DPP2q** (a) and **DPP3q** (b) as well as in the solid state at 240 to 300 K (diluted with KBr) of **DPP2q** (c) and **DPP3q** (d).

In the solid state VT-EPR measurements of **DPP2q** and **DPP3q**, no temperature dependence of the weak signal intensity could be observed. Accordingly, any fitting according to the Bleaney-Bowers equation^[213] is not justified as these signals are not attributable to triplet states of **DPP2q** and **DPP3q** but rather to impurities.

8.2.9 Computational chemistry

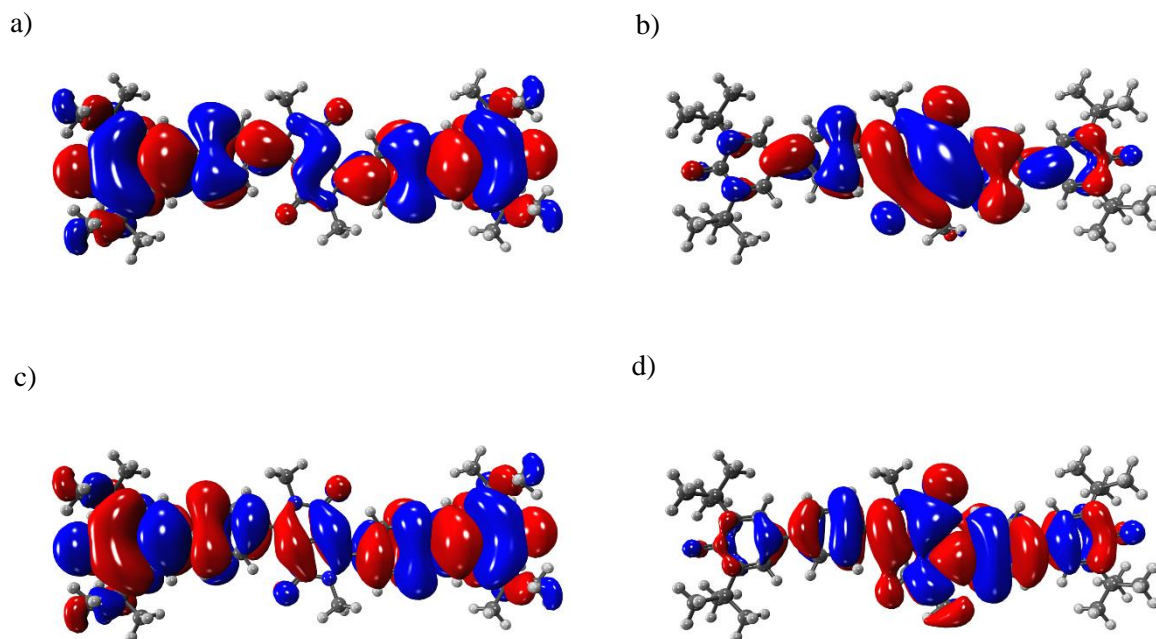


Figure 8.2.32 | Calculated frontier molecular orbital representations of **DPP1** (a) HOMO, (b) HOMO-1, (c) LUMO and (d) LUMO+1 (CASSCF(4,4)/def2-SVP level of theory).

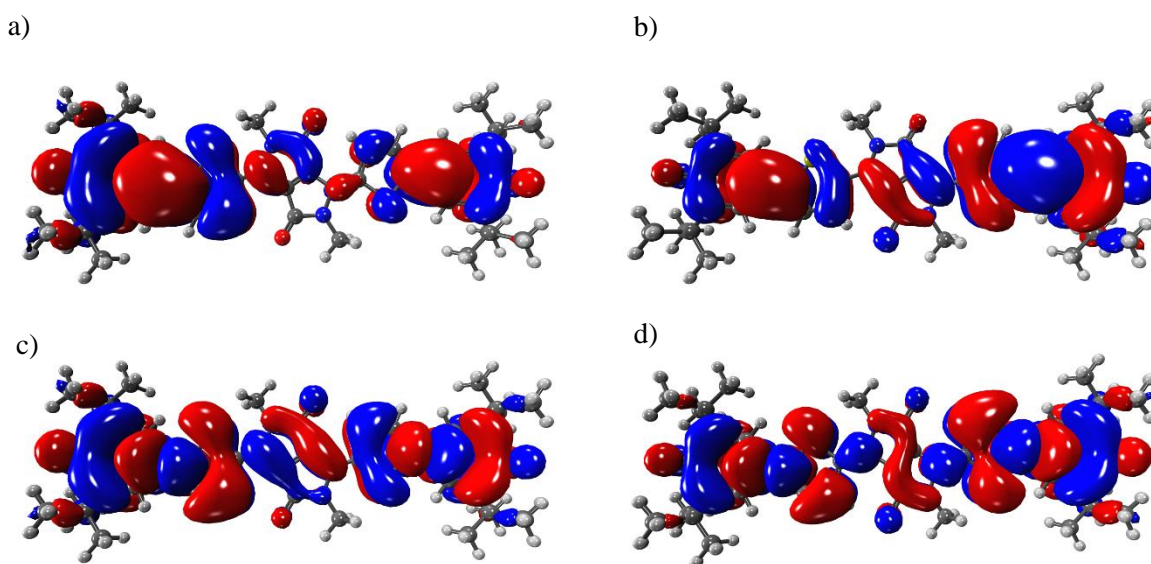


Figure 8.2.33 | Calculated frontier molecular orbital representations of **DPP2q** (a) HOMO, (b) HOMO-1, (c) LUMO and (d) LUMO+1 (CASSCF(4,4)/def2-SVP level of theory).

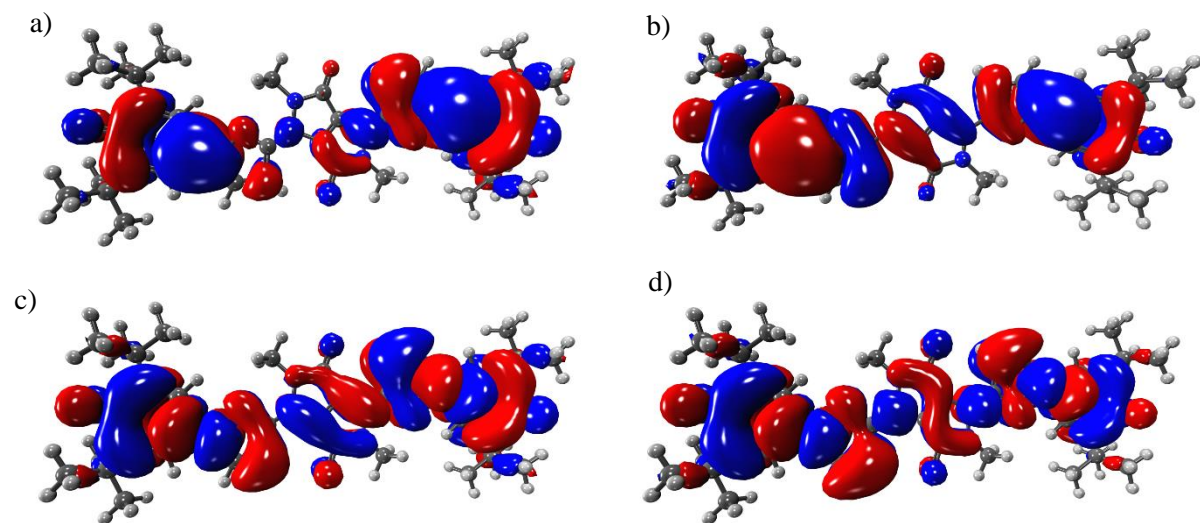


Figure 8.2.34 | Calculated frontier molecular orbital representations of **DPP3q** (a) HOMO, (b) HOMO-1, (c) LUMO and (d) LUMO+1 (CASSCF(4,4)/def2-SVP level of theory).

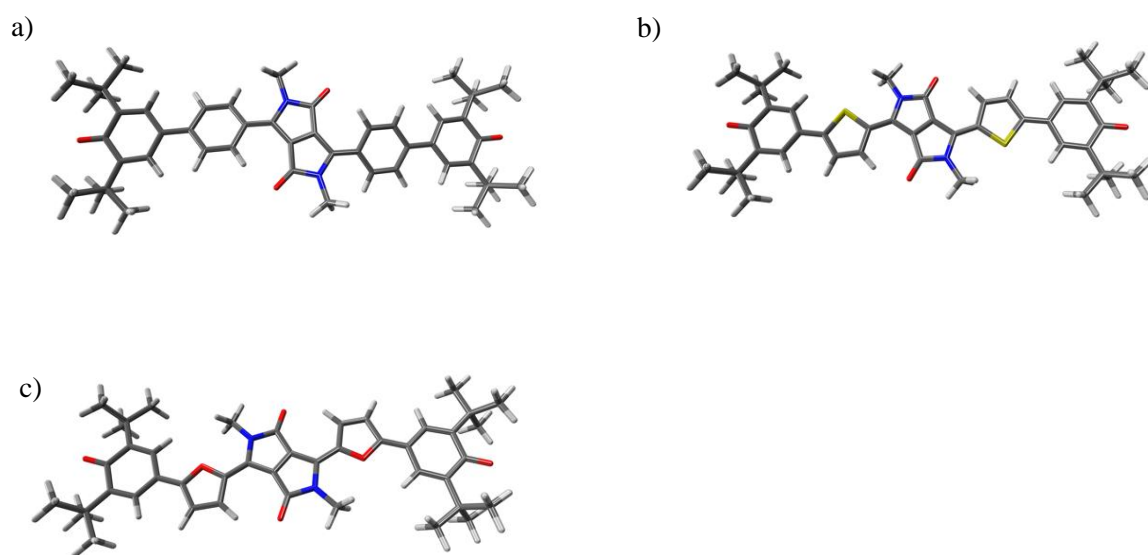


Figure 8.2.35 | Optimized geometries of (a) **DPP1***, (b) **DPP2q** and (c) **DPP3q** (SF-TDDFT (BHHLYP/def2-SVP) level of theory).

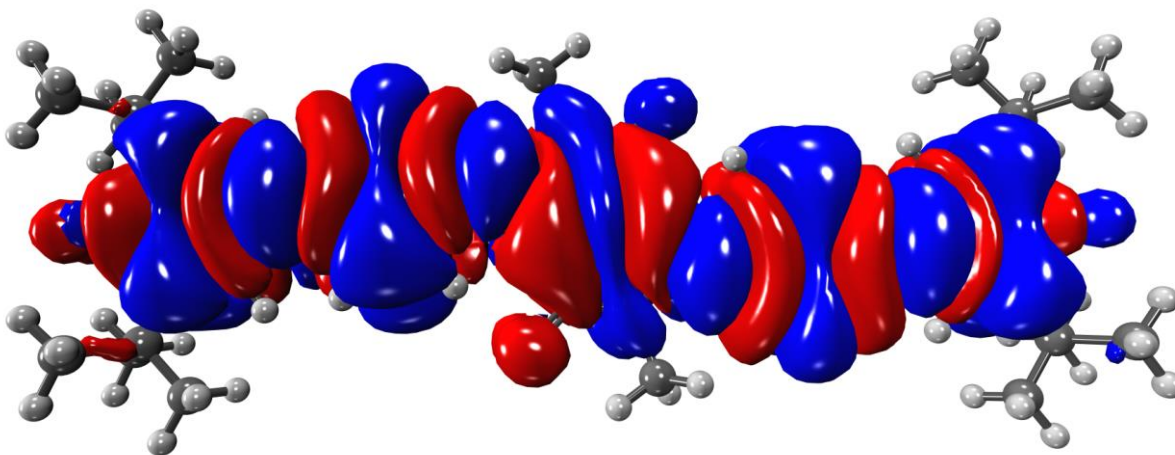


Figure 8.2.36 | Spin density distribution of **DPP1^{••}** calculated on the CASSCF(4,4)/def2-SVP level of theory.

Table 8.2.6 | Natural orbital occupation numbers (NOONs) of the frontier orbitals, singlet biradical character (y_0) and singlet–triplet energy gap (ΔE_{ST}) for **DPP1^{••}**, **DPP2q** and **DPP3q** at the level of CASSCF(4,4)/def2-SVP.

	HONO–1	HONO	LUNO	LUNO+1	y_0	ΔE_{ST} (eV)
DPP1^{••}	1.9111	1.1252	0.8754	0.0883	0.7540	0.0236
DPP2q	1.9227	1.9194	0.0818	0.0761	0.0035	1.2186
DPP3q	1.9555	1.9331	0.0707	0.0408	0.0025	1.3077

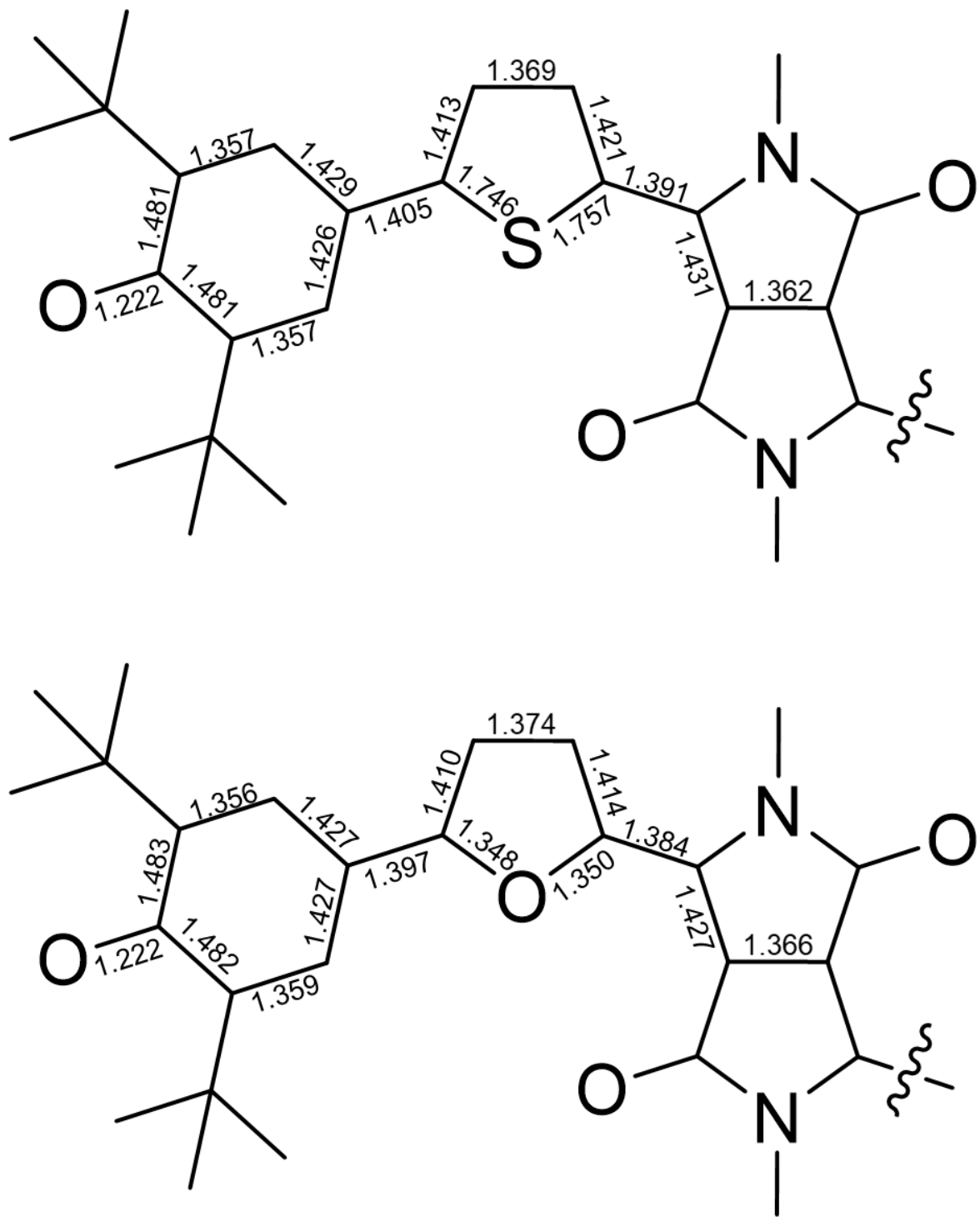
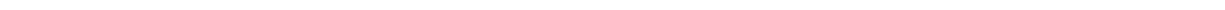


Figure 8.2.37 | Optimized *N,X-trans* geometries of **DPP2q** (top) and **DPP3q** (bottom) on the SF-TD-DFT (BHLYP/def2-SVP) level of theory with selected bond lengths in Å.



8.3 Supporting Information for Chapter 5

Please note: This section was partly communicated in *J. Org. Chem.* **2021**, *86*, 2447–2457. The numeration of compounds in this part refers only to *Chapter 5* and is not necessarily the same as in *Chapter 1* and in particular in *Chapter 2*. Reprinted and adapted with permission from *J. Org. Chem.* **2021**, *86*, 2447–2457. Copyright 2021 The American Chemical Society. For the sake of unity of this thesis, several editorial changes have been made, which, however, do not affect substantive amendments.

8.3.1 Materials and methods

Materials. Chemicals, reagents and solvents were purchased from commercial suppliers. Column chromatography was performed on silica gel (particle size 0.040–0.063 mm) with freshly distilled solvents as eluents. PBI, Isoindigo and DPP derivatives **2**^[303], **3**^[304], **4**^[305], **5**^[306] and **6**^[307] as well as boronic acid ester **1**^[202] were synthesized according to literature known procedure. All other commercially available reagents and solvents were of reagent grade and used without further purification.

NMR spectroscopy. ¹H, ¹¹B and ¹³C NMR spectra were recorded on a Bruker Avance III HD 400 or Bruker Avance III HD 600 spectrometer. ¹³C NMR Spectra are broad band proton decoupled. Chemical shifts (δ) are listed in parts per million (ppm) and are reported relative to tetramethylsilane (TMS). Spectra are referenced internally to residual proton solvent resonances (CDCl₃: δ = 7.26, CD₂Cl₂: δ = 5.32) or natural abundance carbon resonances (CDCl₃: δ = 77.16, CD₂Cl₂: δ = 53.84). Coupling constants (J) are quoted in Hertz (Hz). The data are presented as follows: chemical shift, multiplicity (s = singlet, d = doublet, t = triplet, q = quartet, m = multiplet and/or multiple resonances, br = broad), coupling constant in Hertz (Hz), and integration.

Mass spectrometry. MALDI–TOF mass spectra were recorded on a Bruker Daltronik GmbH (Autoflex II) mass spectrometer using trans–2–[3–(4–*tert*–butylphenyl)–2–methyl–2–propenylidene]malononitrile (DCTB) as matrix. High resolution ESI–TOF mass spectrometry was carried out on a microTOF focus instrument (Bruker Daltronik GmbH).

UV/vis absorption spectroscopy. The solvents for the spectroscopic measurements were of spectroscopic grade. UV/vis/NIR absorption spectra were recorded on a Perkin Elmer Lambda 950 or a Jasco V-670 spectrometer. Measurements in solution were carried out using quartz cuvettes with path lengths of 10 mm at ambient temperature. Measurements in solid state were performed on freshly spin coated thin films on quartz wafers at ambient temperature ($c = 2 \cdot 10^{-3}$ M, 25 μ L, ambient temperature, $rpm = 3000$, $t = 30$ s).

Cyclic voltammetry. Cyclic voltammetry (CV) and square wave voltammetry (SWV) were performed using a standard commercial electrochemical analyzer (EC epsilon; BAS Instruments, UK). A Pt disc electrode was used as a working electrode, platinum wire as a counter electrode and Ag^+/Ag as a reference electrode, at a scan rate of 100 mV/s at room temperature. The compounds were dissolved in dichloromethane, and tetra-*n*-butylammonium hexafluorophosphate (nBu_4NPF_6) was added as an electrolyte to give a concentration of 0.1 M. The supporting electrolyte was recrystallized from ethanol/water and dried under vacuum prior to use. The oxidation potentials were referenced against the ferrocenium/ferrocene redox couple ($Fc^+/Fc = 0.00$ V).

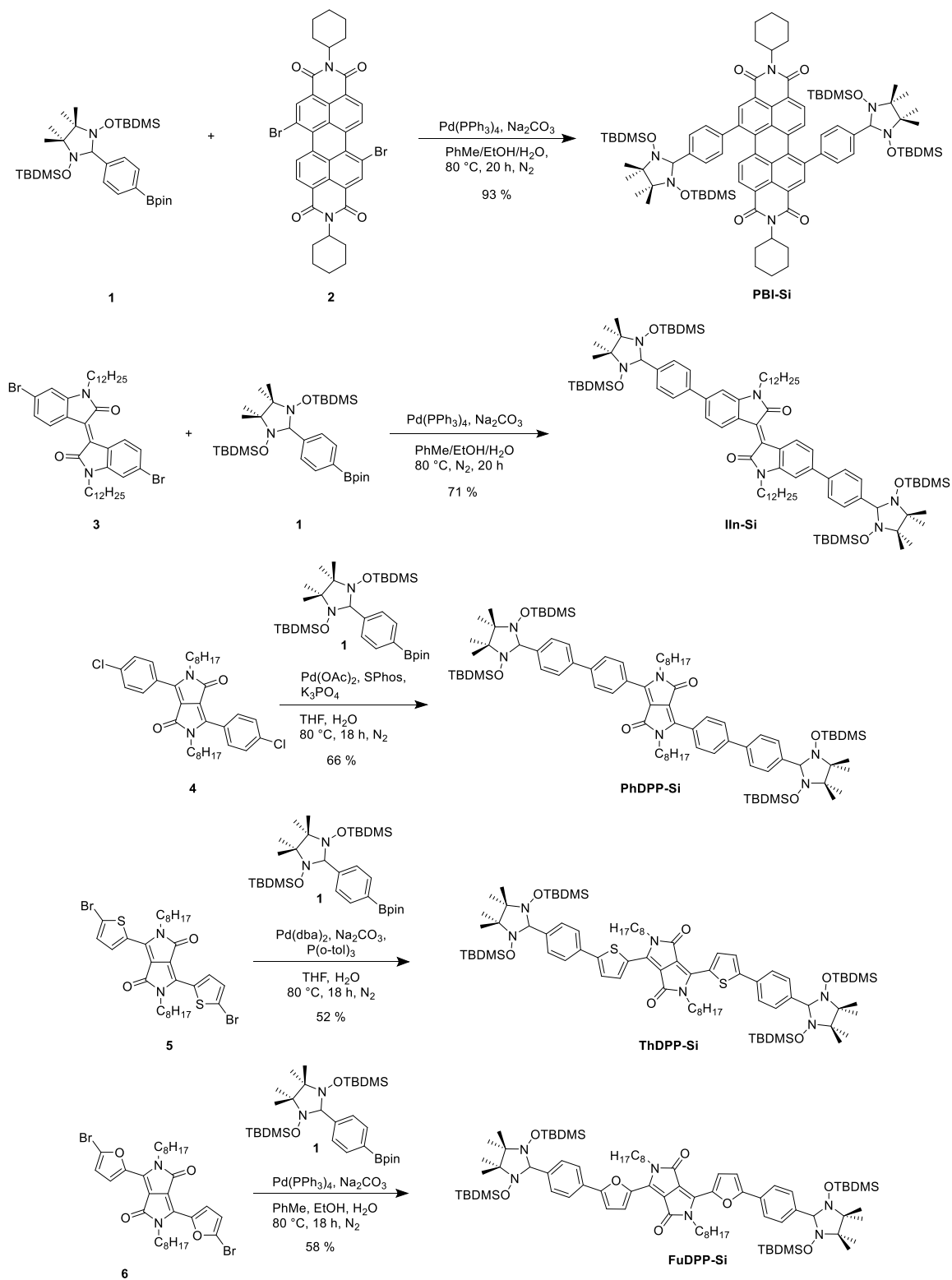
Fluorescence spectroscopy. Fluorescence spectra were recorded with a FLS980 Edinburgh Instrument fluorescence spectrometer. Fluorescence quantum yields were determined as an average out of 4 equidistant excitation wavelengths relatively to the references 3,7-bis(diethylamino)-phenoxazinium perchlorate („Oxazine 1“, CAS: 24796-94-9, $\Phi_{Fl} = 0.11$ in EtOH)^[309] for **FuDPP-Si** and **ThDPP-Si**; *N,N'*-bis(2,6-diisopropylphenyl)-3,4,9,10-perylenetetracarboxylic bisimide, “Lumogen/ perylene orange”, CAS: 82953-57-9, $\Phi_{Fl} = 1.00$ in $CHCl_3$)^[308] for **PhDPP-Si** and **PhDPP-NN** and *N,N'*-bis(2,6-diisopropylphenyl)-1,6,7,12-tetraphenoxy-3,4,9,10-perylenetetracarboxylic bisimide (“Lumogen/ perylene red”, CAS: 123174-58-3, $\Phi_{Fl} = 0.96$ in $CHCl_3$)^[308] for **PBI-Si** and **PBI-NN** in highly diluted solutions ($OD: 0.05-0.20$)^[318]. Measurements in solution were carried out using quartz cuvettes (Hellma optics, Germany) with path lengths of 10 mm and spectroscopic solvents at ambient temperature and atmosphere.

Single crystal X-ray diffraction. Single crystal X-ray diffraction data for **IIn-NN** were collected at 100 K on a Bruker D8 Quest Kappa diffractometer with a Photon II CPAD detector and multi-layered mirror monochromated CuK_α radiation. The structures were solved using direct methods, expanded with Fourier

techniques and refined with the Shelx software package.^[315] All non-hydrogen atoms were refined anisotropically. Hydrogen atoms were included in the structure factor calculation on geometrically idealized positions. Crystallographic data have been deposited with the Cambridge Crystallographic Data Centre as supplementary publication no. CCDC **2041555**. These data can be obtained free of charge from The Cambridge Crystallographic Data Centre via www.ccdc.cam.ac.uk/data_request/cif.

EPR spectroscopy. EPR measurements at X-band (9.38 GHz) were carried out using a Bruker ELEXSYS E580 CW EPR spectrometer equipped with an Oxford Instruments helium cryostat (ESR900) and a MercuryITC temperature controller. The spectral simulations were performed using MATLAB 8.6 and the EasySpin 5.0.18 toolbox.^[316] The nitrogen hyperfine couplings were determined by least-square fitting of the experimental data.

8.3.2 Syntheses



Scheme 8.3.1 | Synthesis of **PBI-Si**, **IIn-Si**, **PhDPP-Si**, **ThDPP-Si** and **FuDPP-Si**.

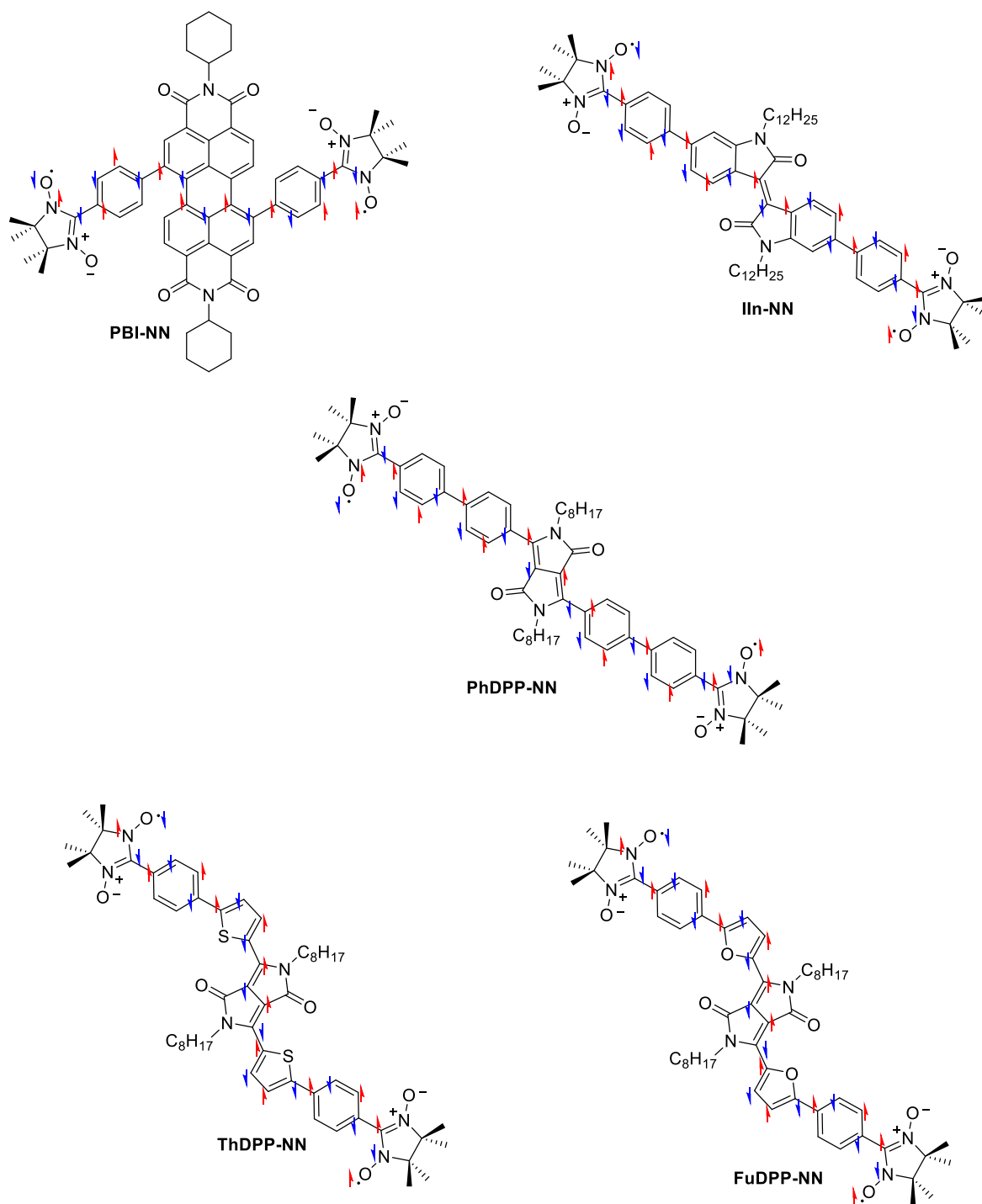


Chart 8.3.1 | Structures of nitronyl nitroxide biradicals **PBI-NN**, **IIn-NN**, **PhDPP-NN**, **ThDPP-NN** and **FuDPP-NN**. Red and blue arrows indicate spin polarization.

8.3.3 Mass spectrometry

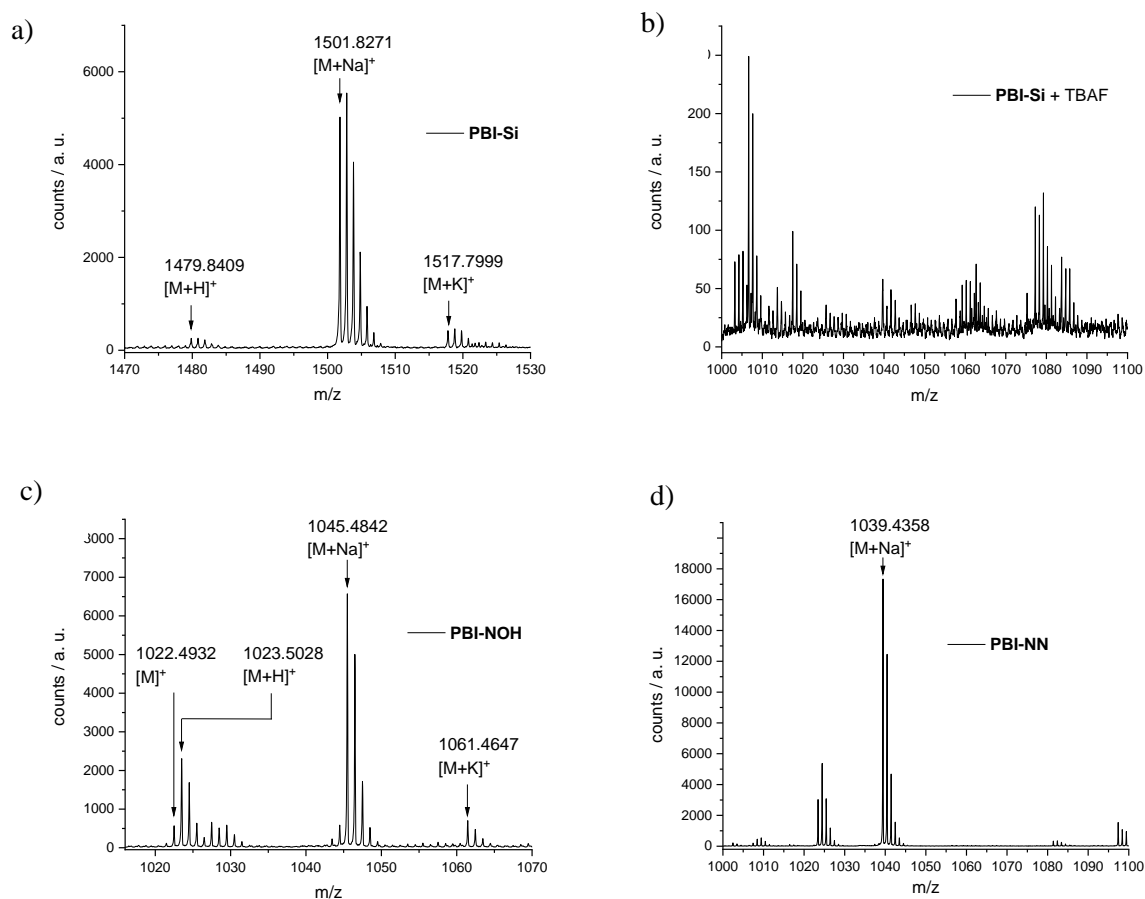
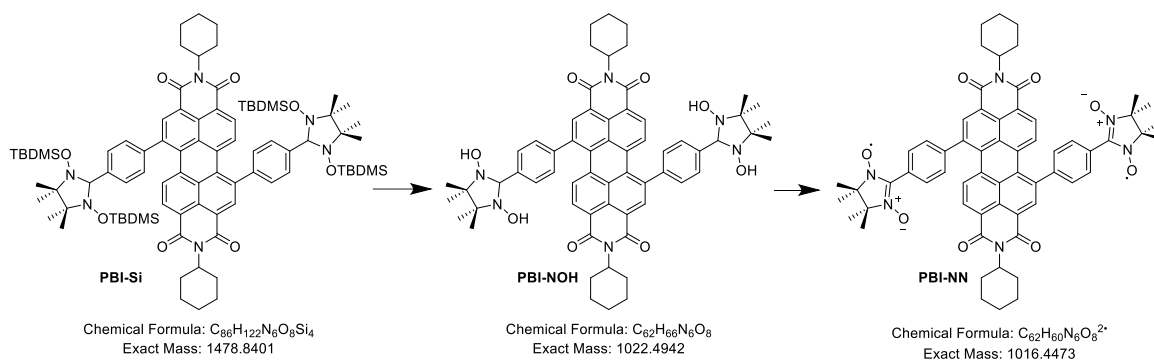


Figure 8.3.1 | ESI-TOF high resolution mass spectra of a) **PBI-Si**, b) **PBI-Si** after addition of TBAF, c) **PBI-Si** after addition of $BF_3 \cdot Et_2O$ and subsequent quenching with $Si(OEt)_4$ (resulting in the formation of **PBI-NOH**) and d) **PBI-NN**.

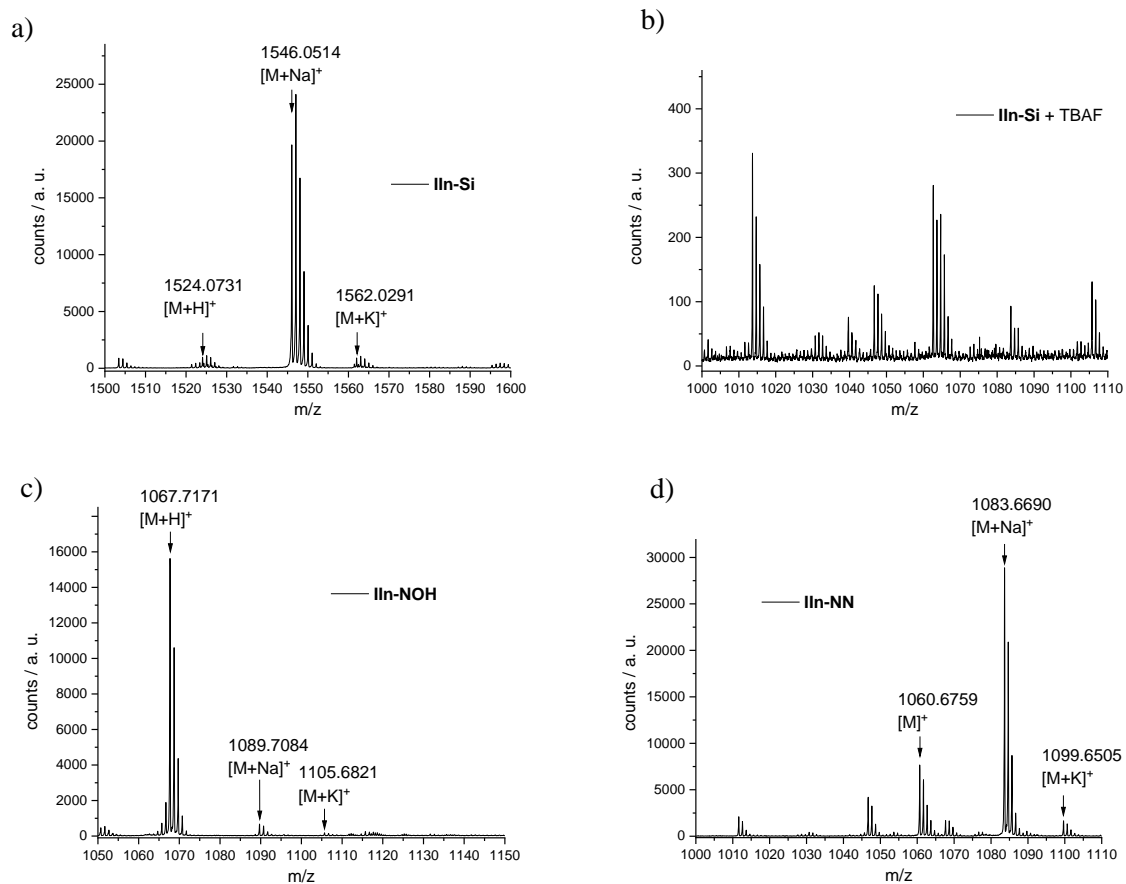
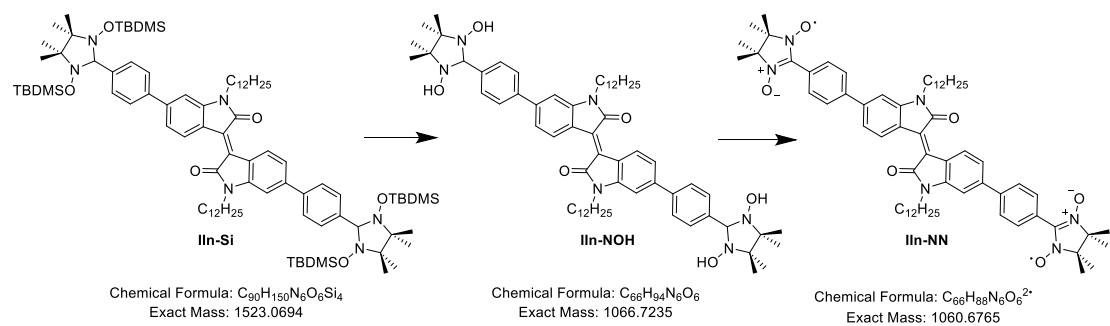


Figure 8.3.2 | ESI-TOF high resolution mass spectra of a) **II-Si**, b) **II-Si** after addition of TBAF, c) **II-Si** after addition of $BF_3 \cdot Et_2O$ and subsequent quenching with $Si(OEt)_4$ (resulting in the formation of **II-NOH**) and d) **II-NN**.

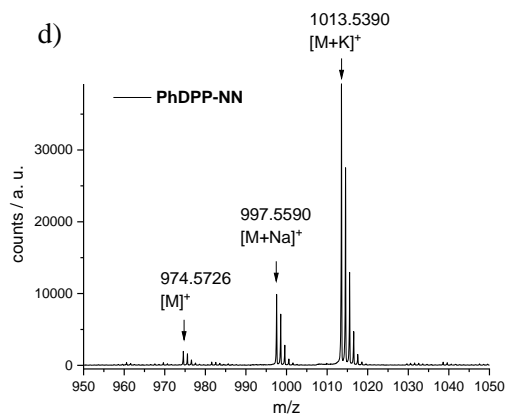
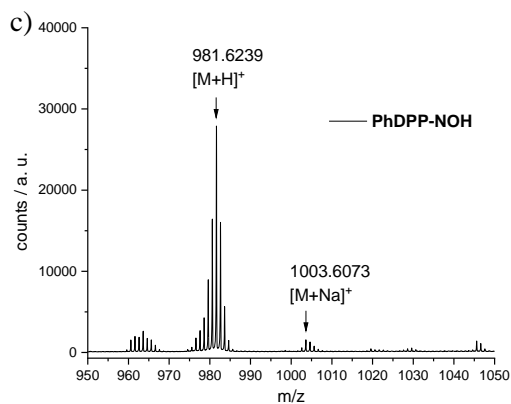
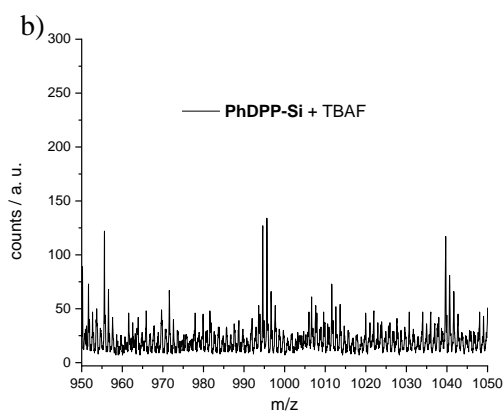
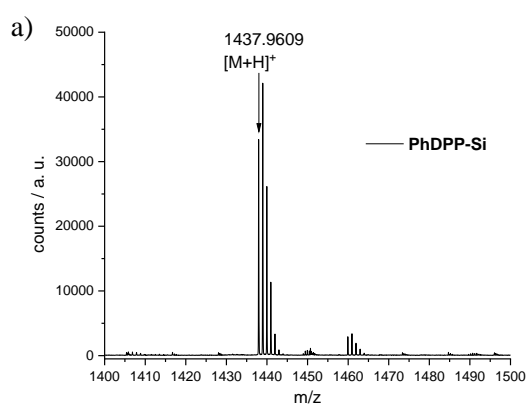
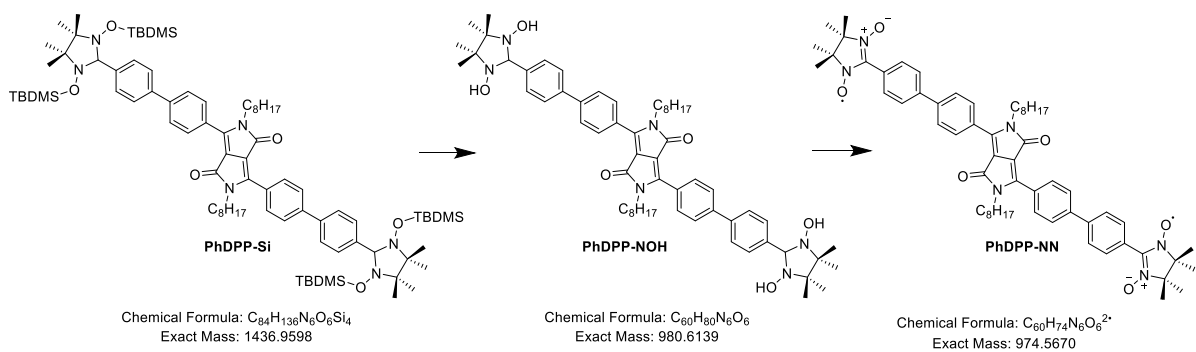


Figure 8.3.3 | ESI-TOF high resolution mass spectra of a) **PhDPP-Si**, b) **PhDPP-Si** after addition of TBAF, c) **PhDPP-Si** after addition of $BF_3 \cdot Et_2O$ and subsequent quenching with $Si(OEt)_4$ (resulting in the formation of **PhDPP-NOH**) and d) **PhDPP-NN**.

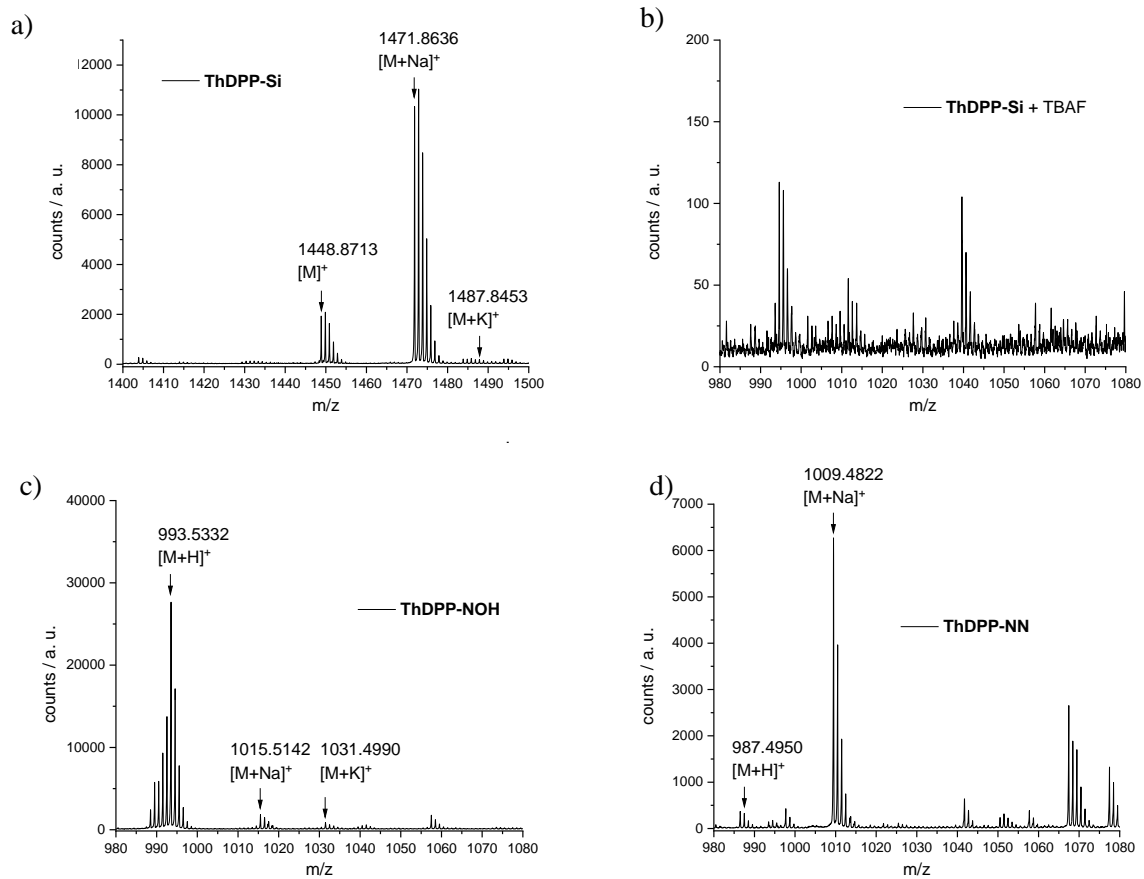
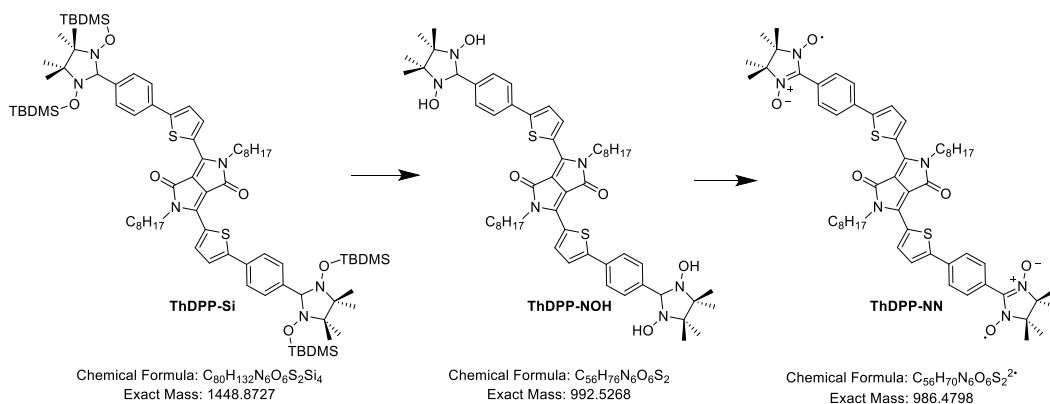


Figure 8.3.4 | ESI-TOF high resolution mass spectra of a) **ThDPP-Si**, b) **ThDPP-Si** after addition of TBAF, c) **ThDPP-Si** after addition of $BF_3 \cdot Et_2O$ and subsequent quenching with $Si(OEt)_4$ (resulting in the formation of **ThDPP-NOH**) and d) **ThDPP-NN**.

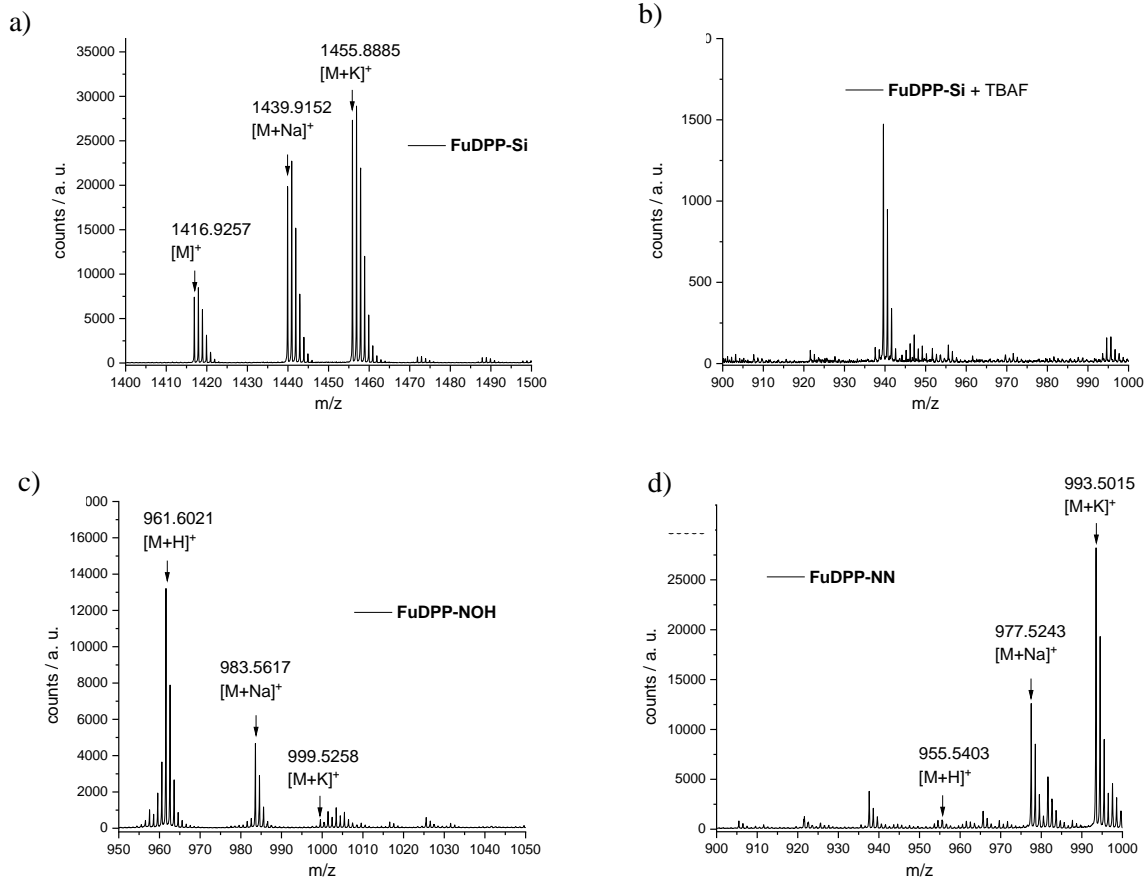
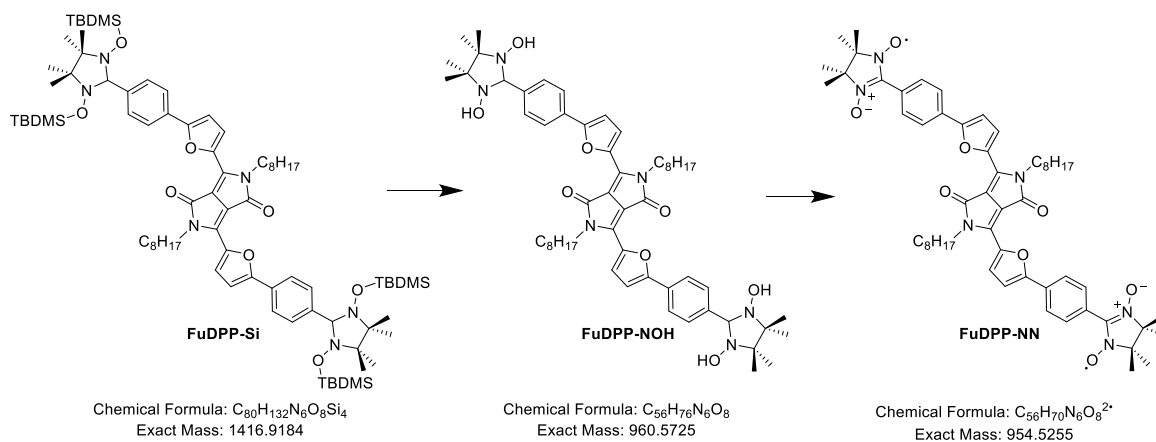


Figure 8.3.5 | ESI-TOF high resolution mass spectra of a) **FuDPP-Si**, b) **FuDPP-Si** after addition of TBAF, c) **FuDPP-Si** after addition of $BF_3 \cdot Et_2O$ and subsequent quenching with $Si(OEt)_4$ (resulting in the formation of **FuDPP-NOH**) and d) **FuDPP-NN**.

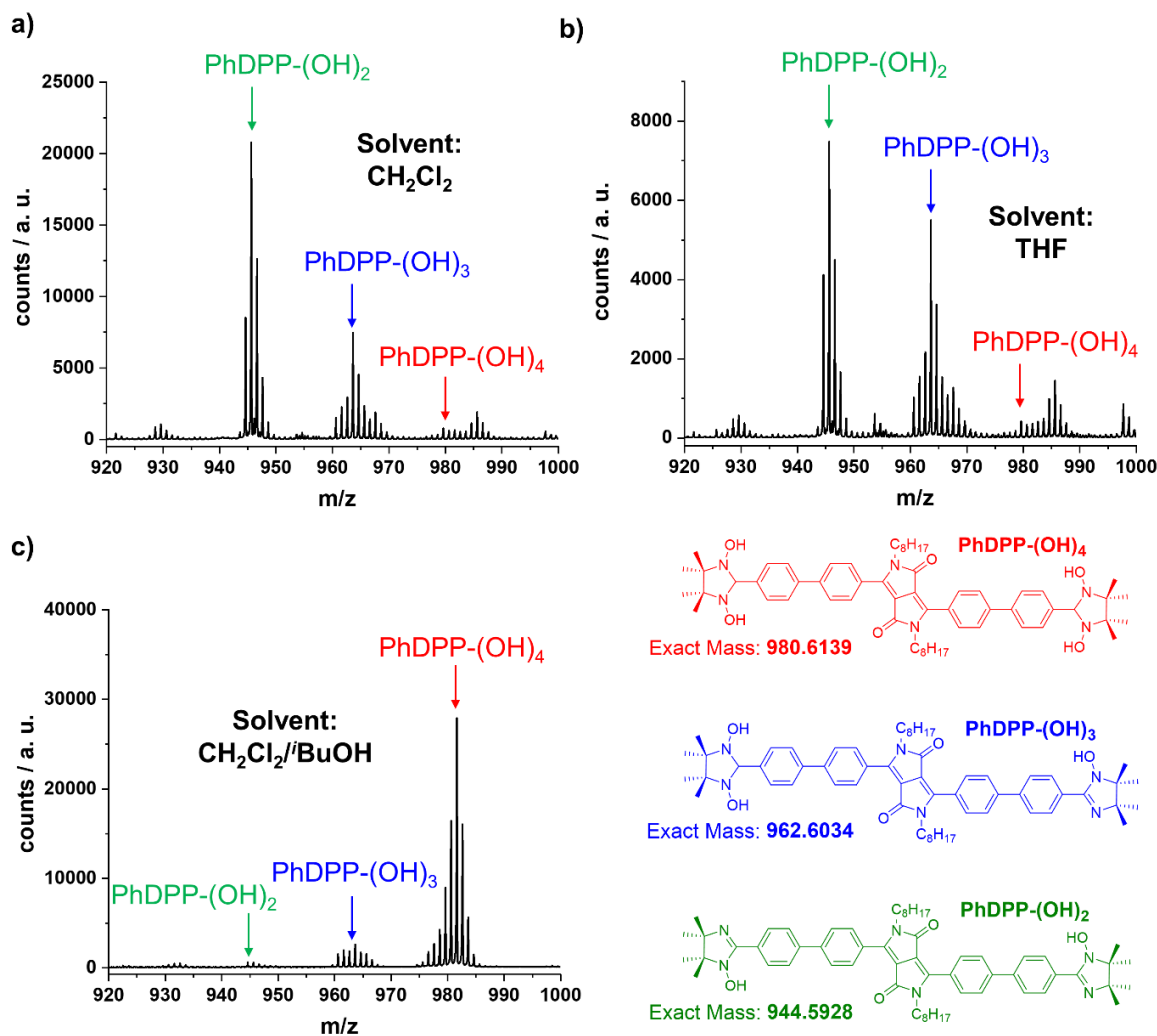


Figure 8.3.6 | ESI-HRMS spectra of crude reaction mixtures of **PhDPP-Si** with $\text{BF}_3 \cdot \text{Et}_2\text{O}$ in (a) CH_2Cl_2 , (b) THF and (c) $\text{CH}_2\text{Cl}_2/\text{BuOH}$ (20–25 Vol.-% ^tBuOH). Also shown are the formula and exact masses of bis(*N,N'*-dihydroxy imidazolidines) (red, PhDPP-(OH)₄), mixed *N*-hydroxy imidazolidines/*N,N'*-dihydroxy imidazolidines (blue, PhDPP-(OH)₃) and bis(*N*-hydroxy imidazolidines) (green, PhDPP-(OH)₂).

8.3.4 NMR spectroscopy

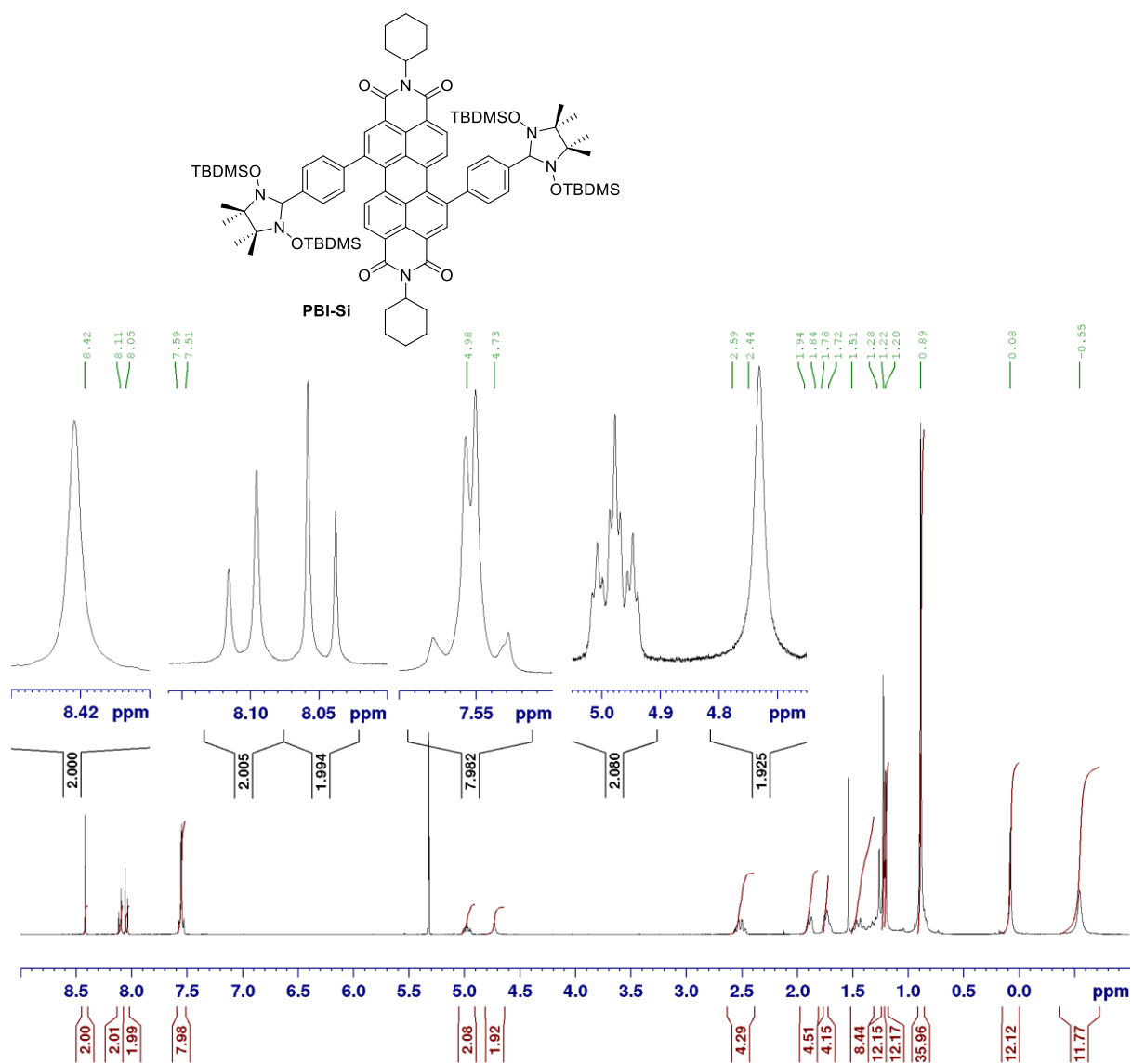


Figure 8.3.7 | ¹H NMR spectrum (400 MHz, CD₂Cl₂, 298 K) of PBI-Si.

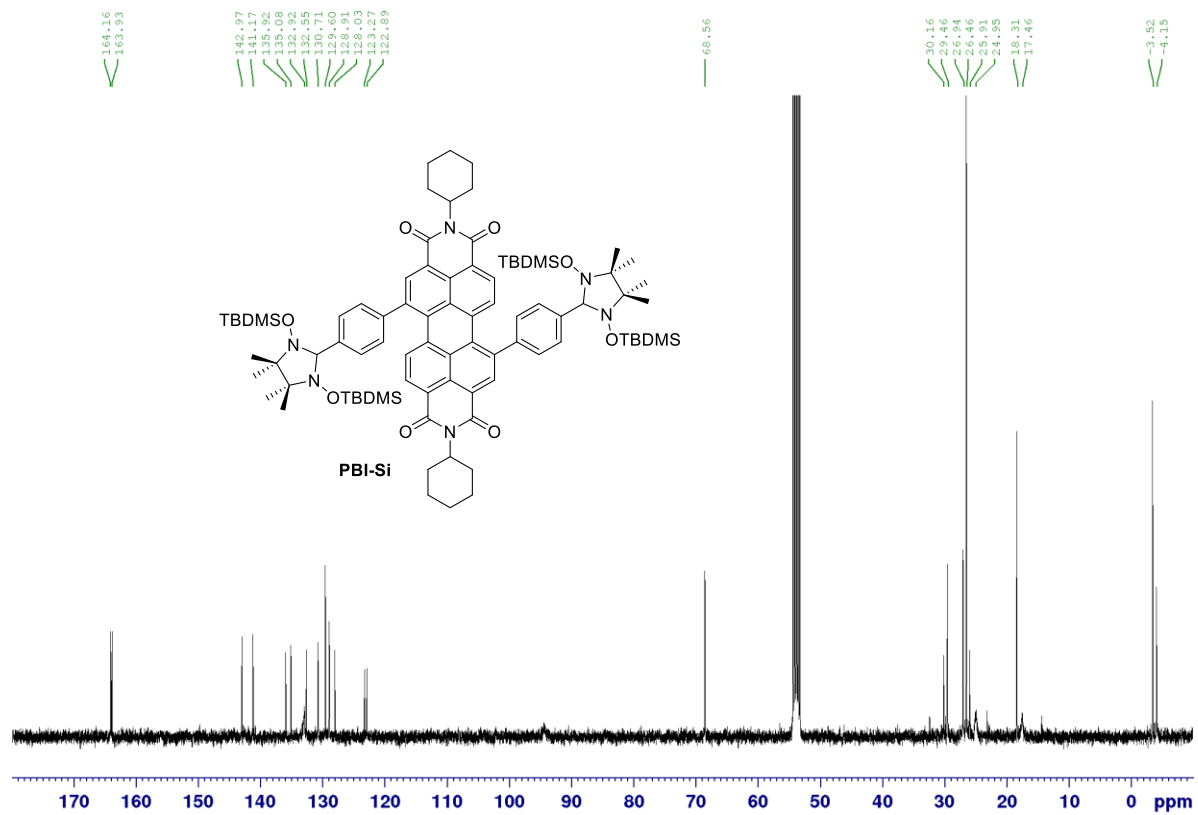


Figure 8.3.8 | ¹³C NMR spectrum (101 MHz, CD₂Cl₂, 298 K) of PBI-Si.

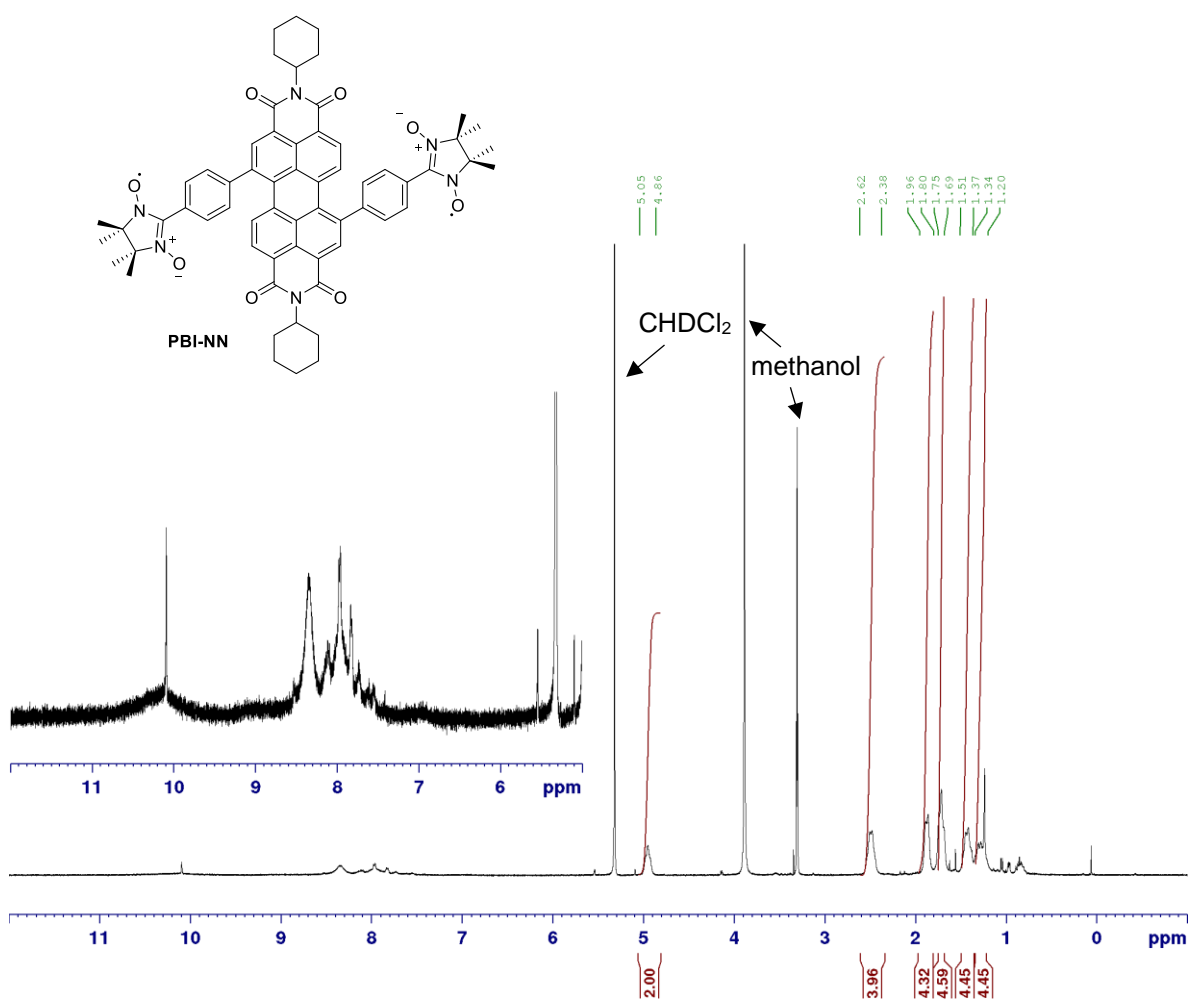


Figure 8.3.9 | ¹H NMR spectrum (400 MHz, CD₂Cl₂/CD₃OD (9:1), 298 K) of PBI-NN.

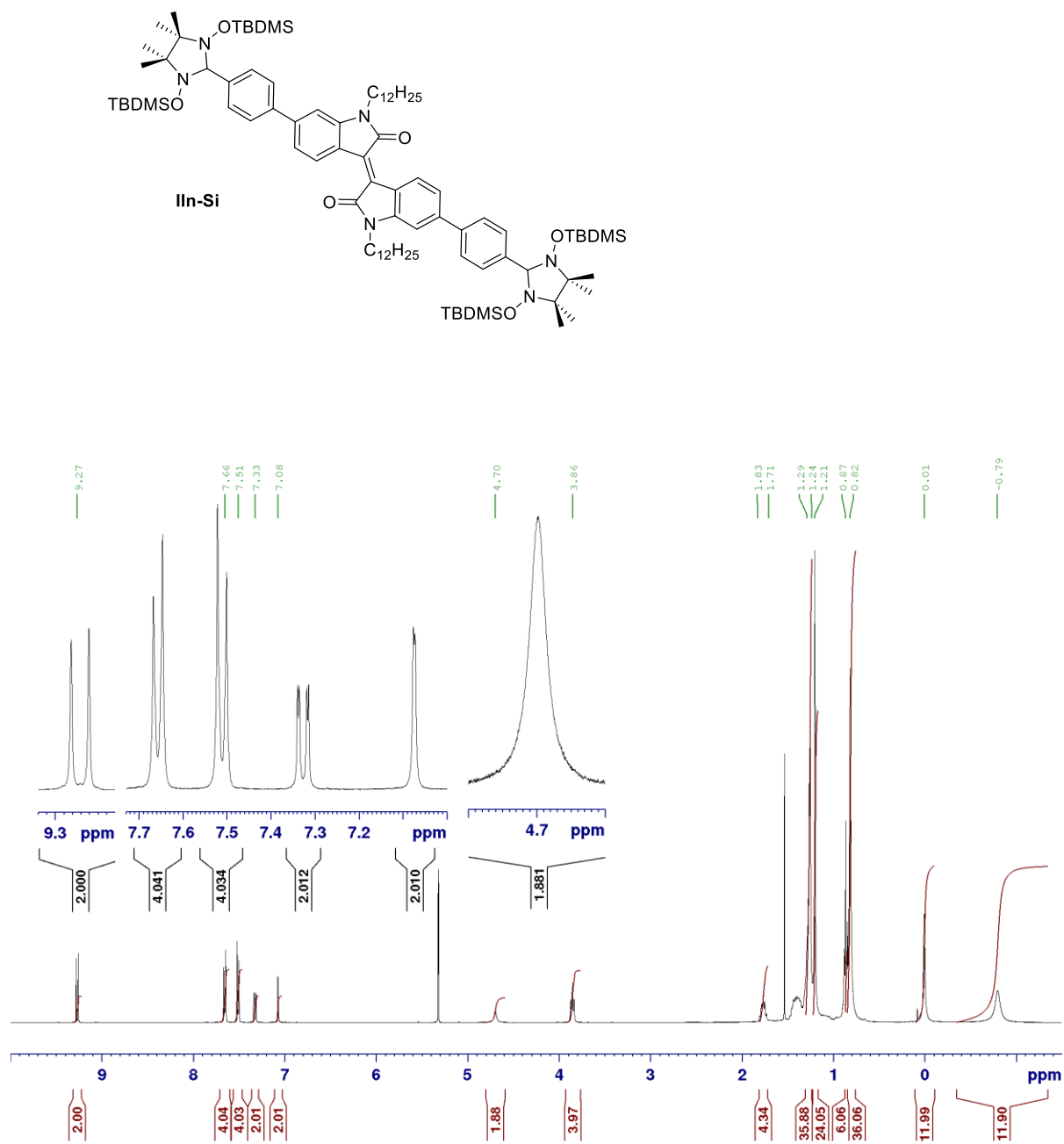


Figure 8.3.10 | ¹H NMR spectrum (400 MHz, CD₂Cl₂, 298 K) of **II_n-Si**.

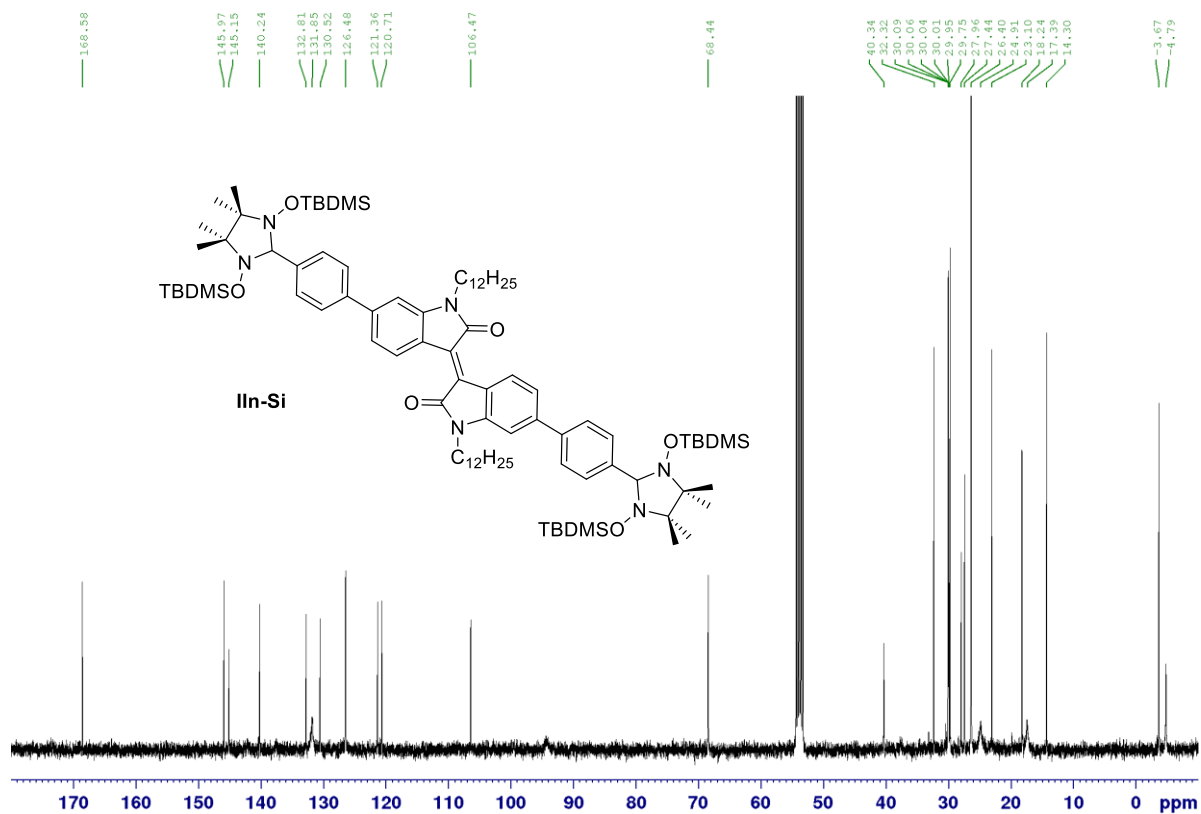


Figure 8.3.11 | ^{13}C NMR spectrum (101 MHz, CD_2Cl_2 , 298 K) of **IIIn-Si**.

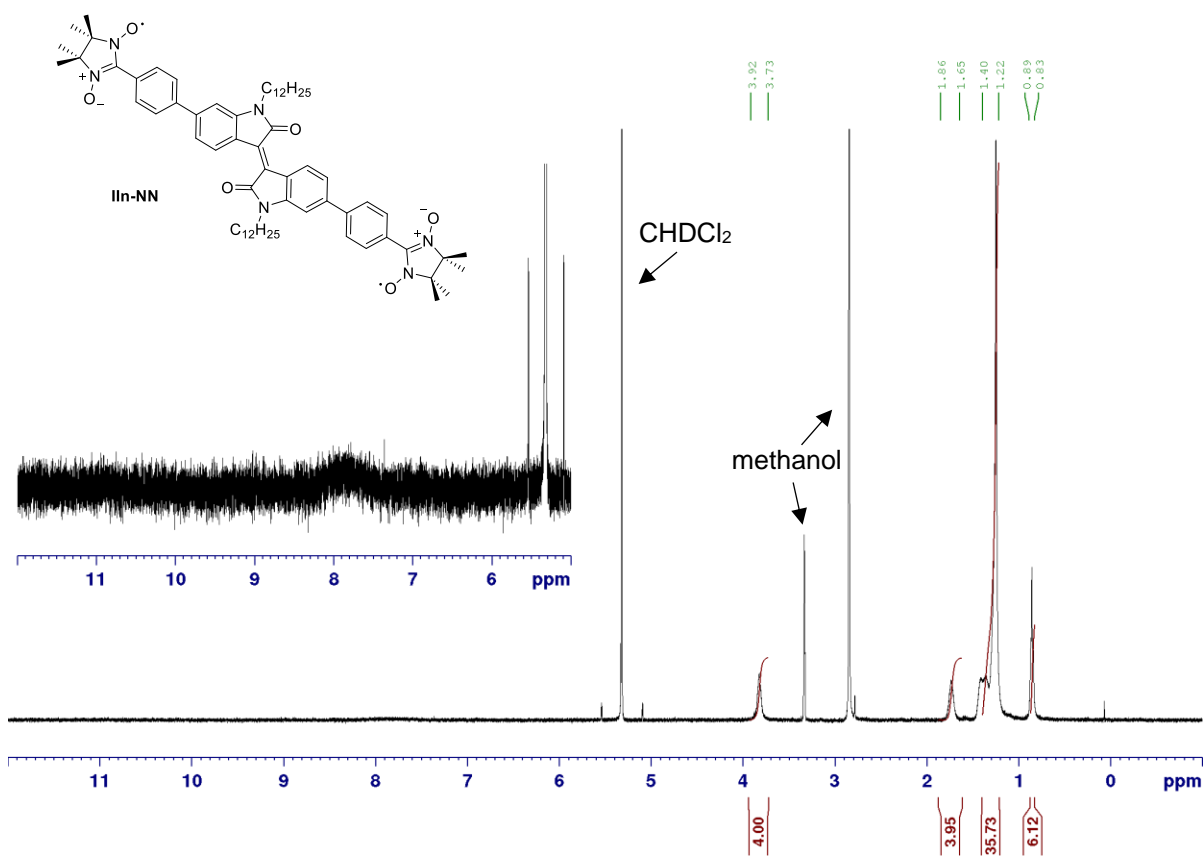


Figure 8.3.12 | 1H NMR spectrum (400 MHz, CD_2Cl_2/CD_3OD (9:1), 298 K) of **IIIn-NN**.

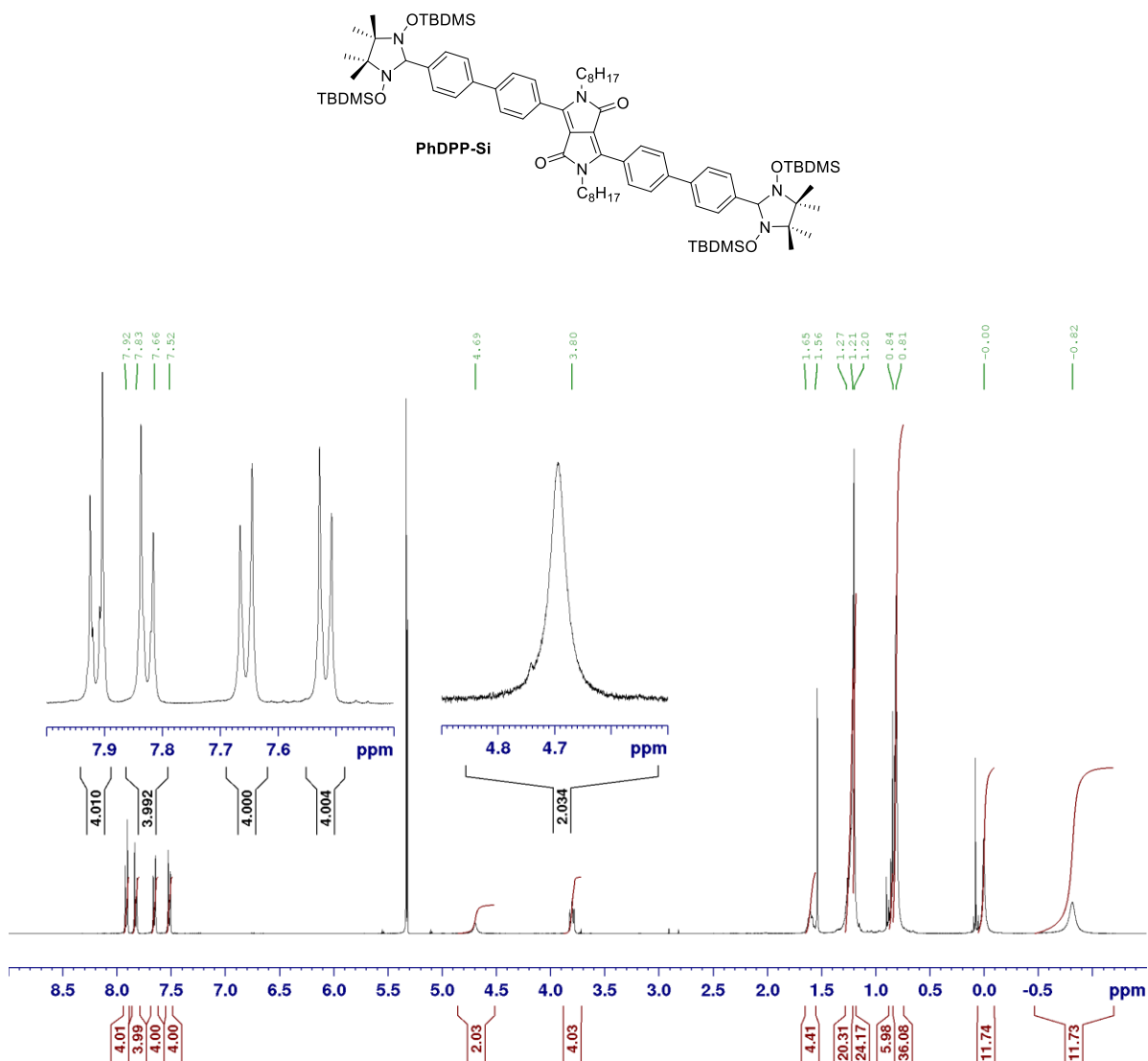


Figure 8.3.13 | 1H NMR spectrum (400 MHz, CD_2Cl_2 , 298 K) of **PhDPP-Si**.

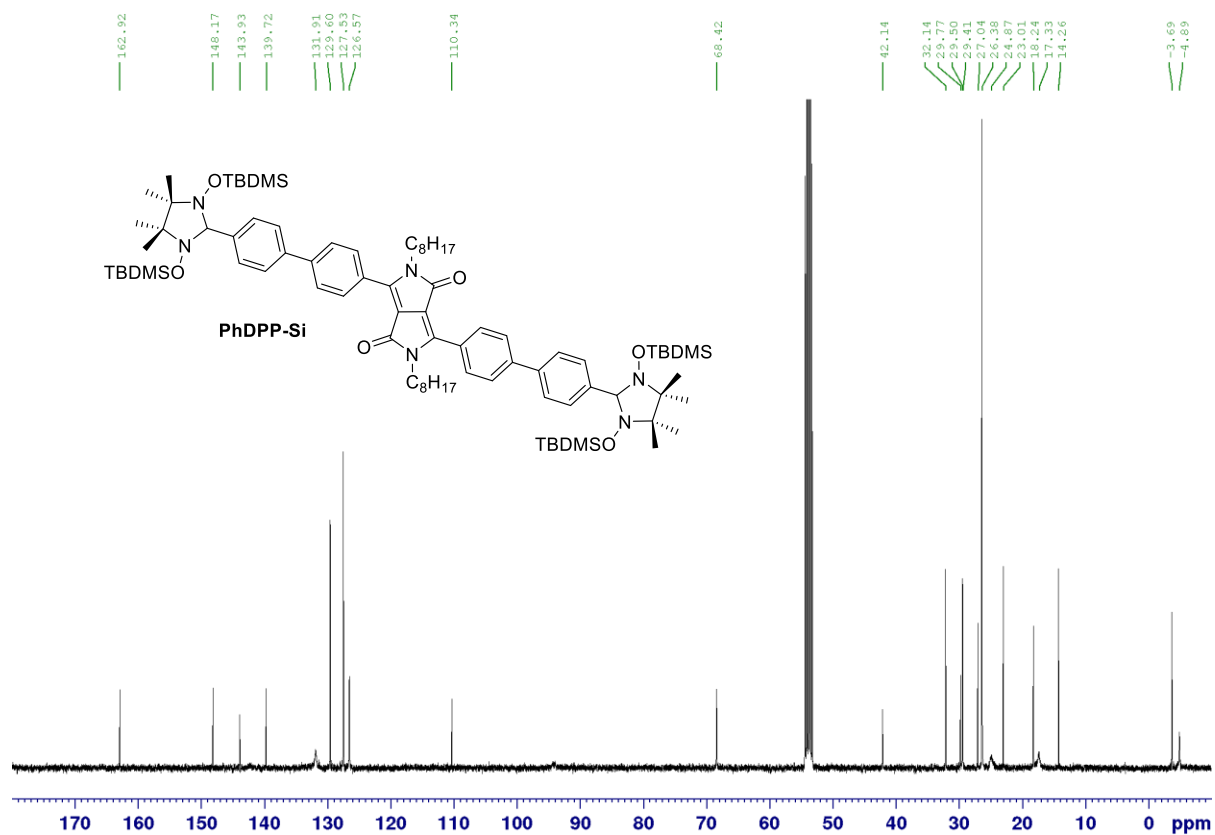


Figure 8.3.14 | ^{13}C NMR spectrum (101 MHz, CD_2Cl_2 , 298 K) of **PhDPP-Si**.

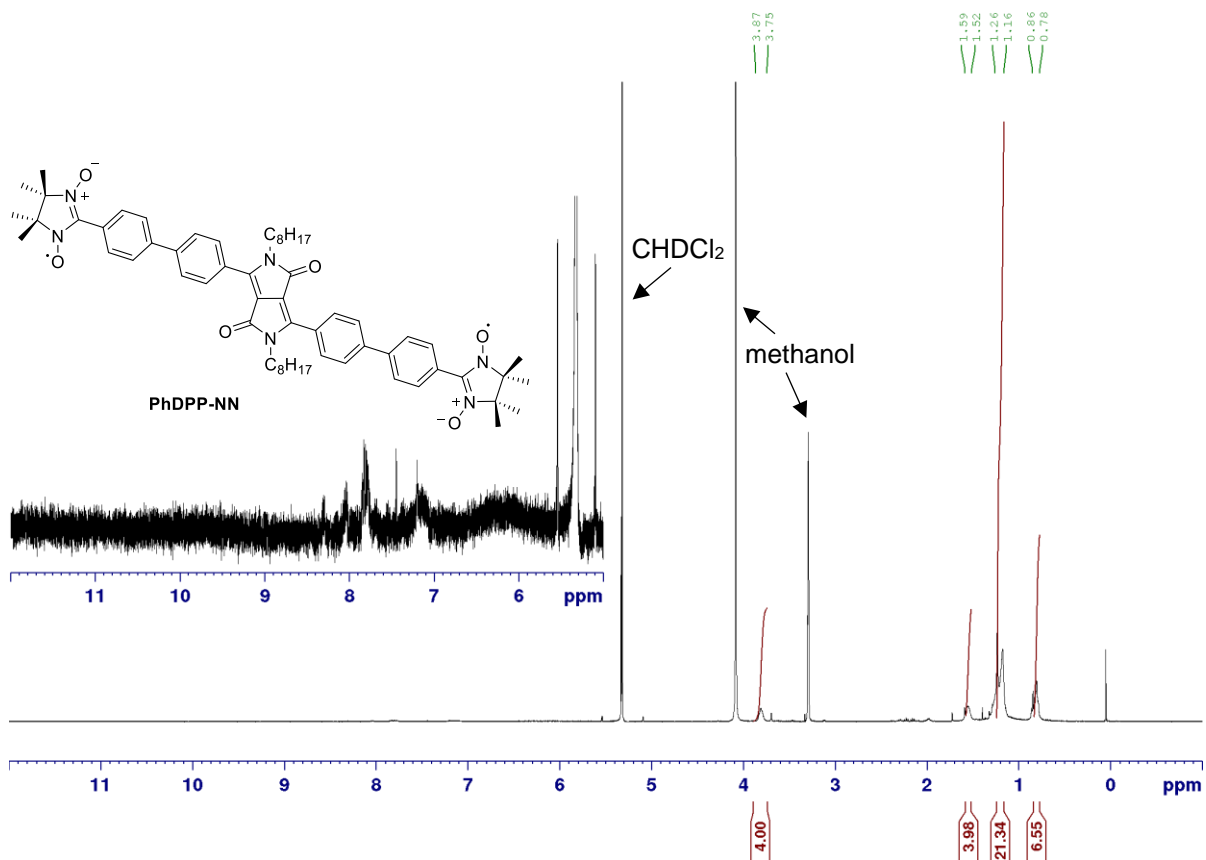


Figure 8.3.15 | ^1H NMR spectrum (400 MHz, $\text{CD}_2\text{Cl}_2/\text{CD}_3\text{OD}$ (9:1), 298 K) of **PhDPP-NN**.

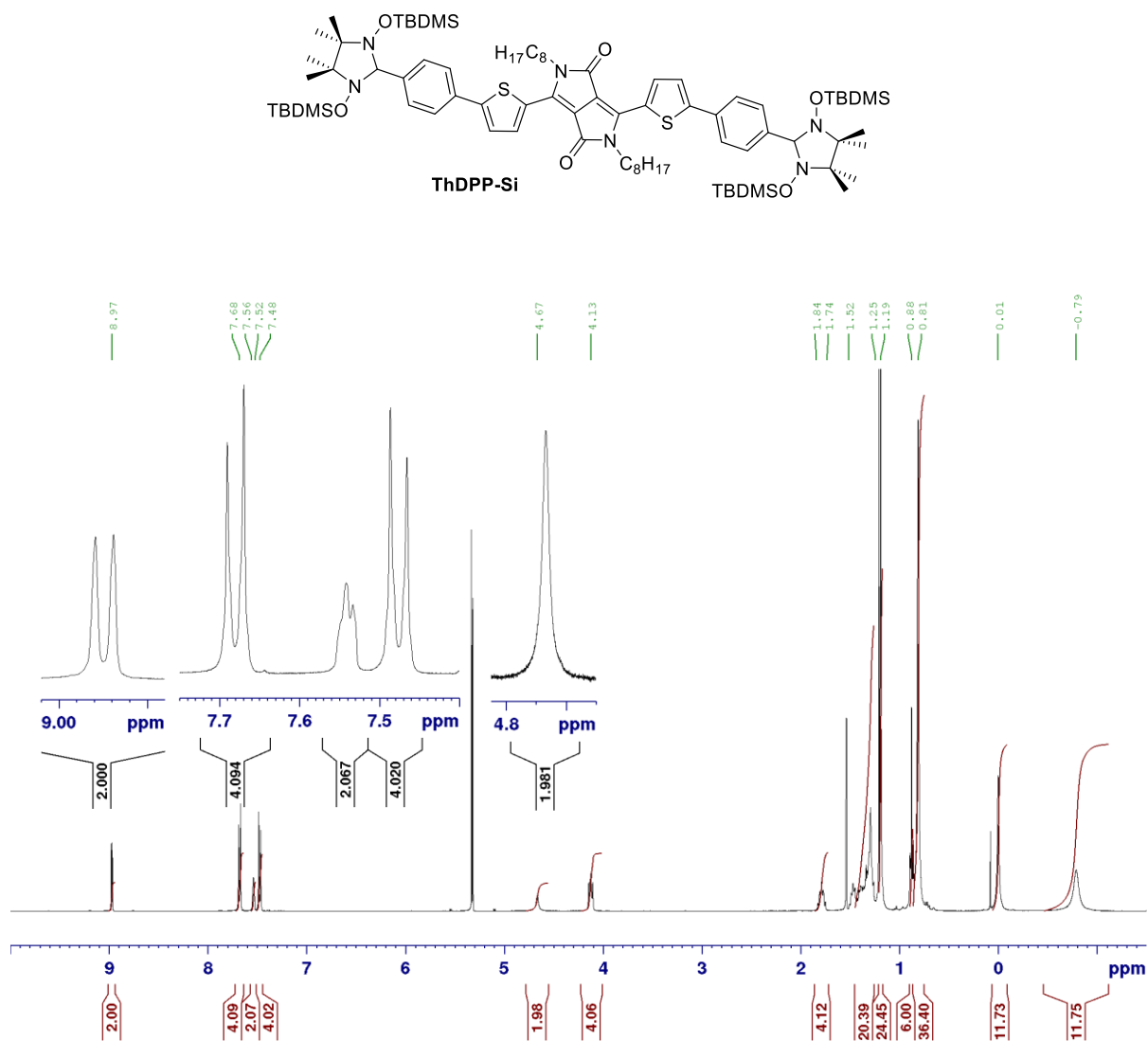


Figure 8.3.16 | ¹H NMR spectrum (400 MHz, CD₂Cl₂, 298 K) of ThDPP-Si.

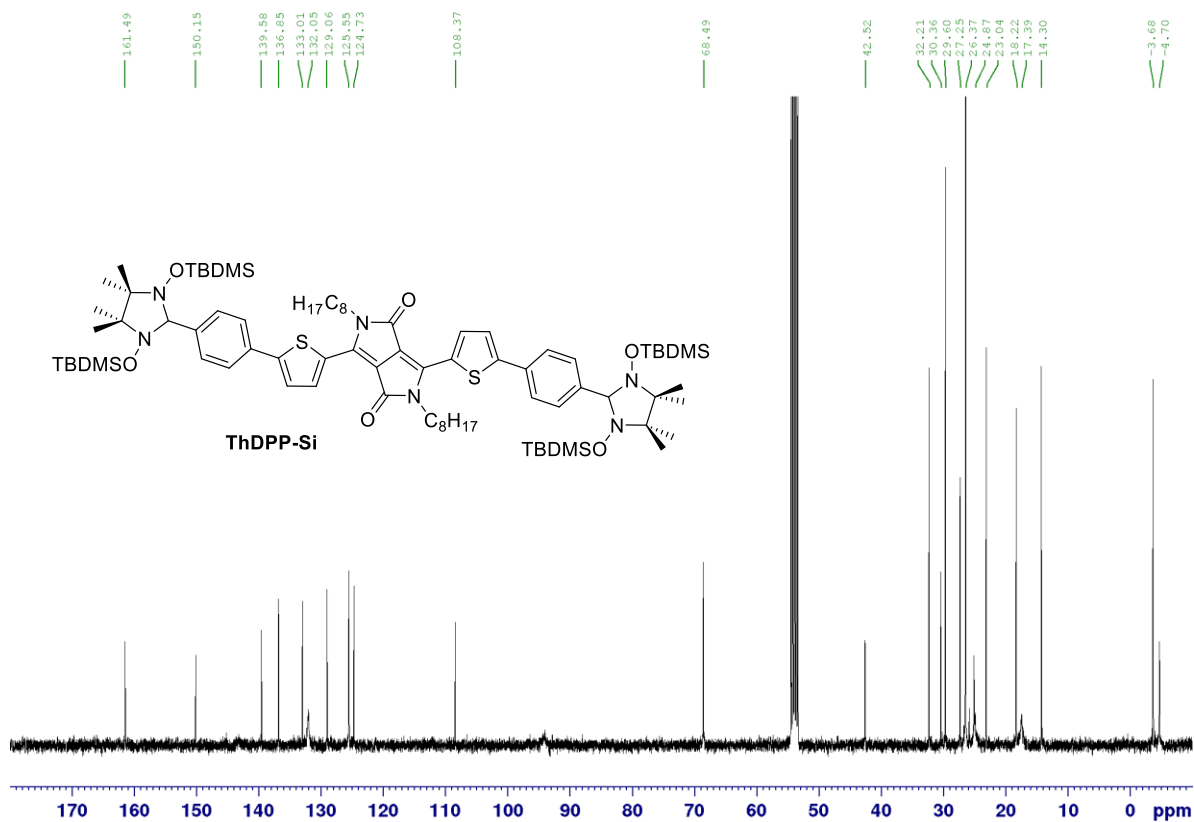


Figure 8.3.17 | ^{13}C NMR spectrum (101 MHz, CD_2Cl_2 , 298 K) of **ThDPP-Si**.

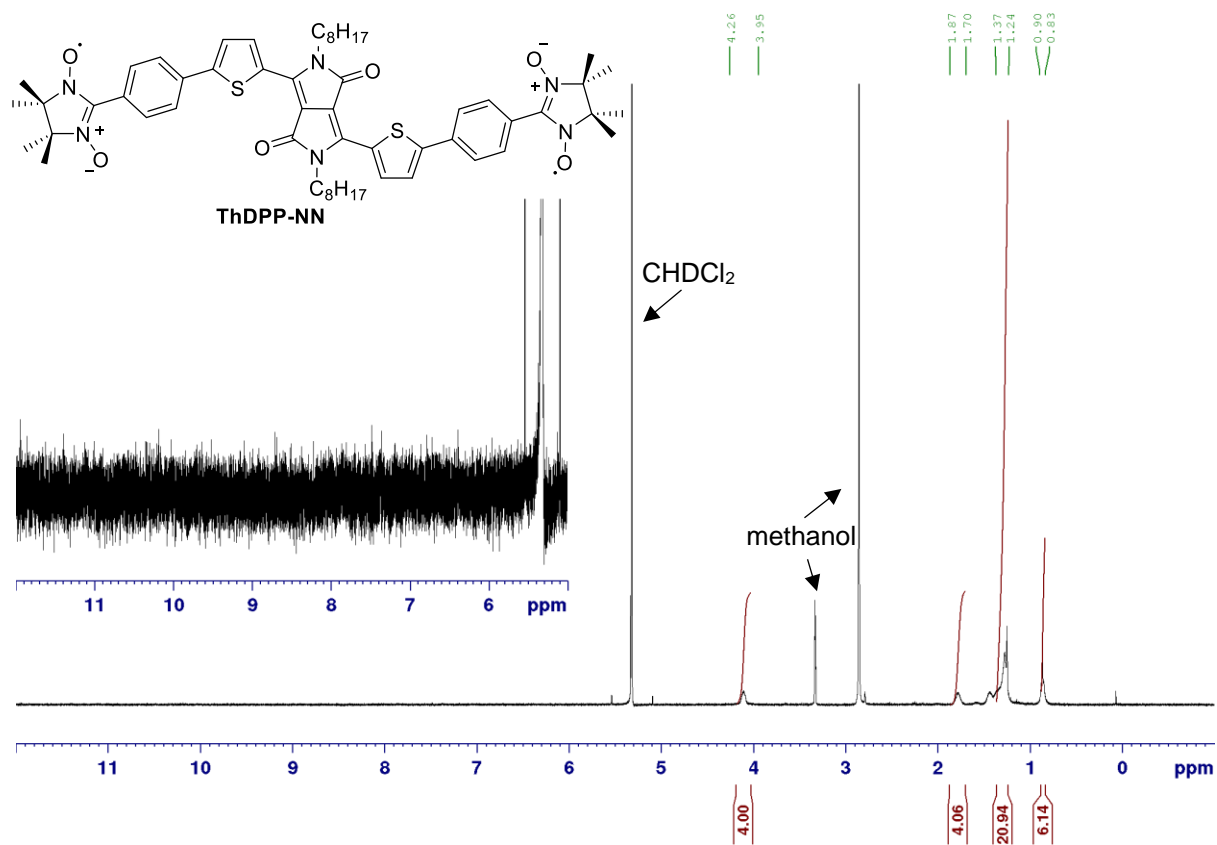


Figure 8.3.18 | ¹H NMR spectrum (400 MHz, CD₂Cl₂/CD₃OD (9:1), 298 K) of ThDPP-NN.

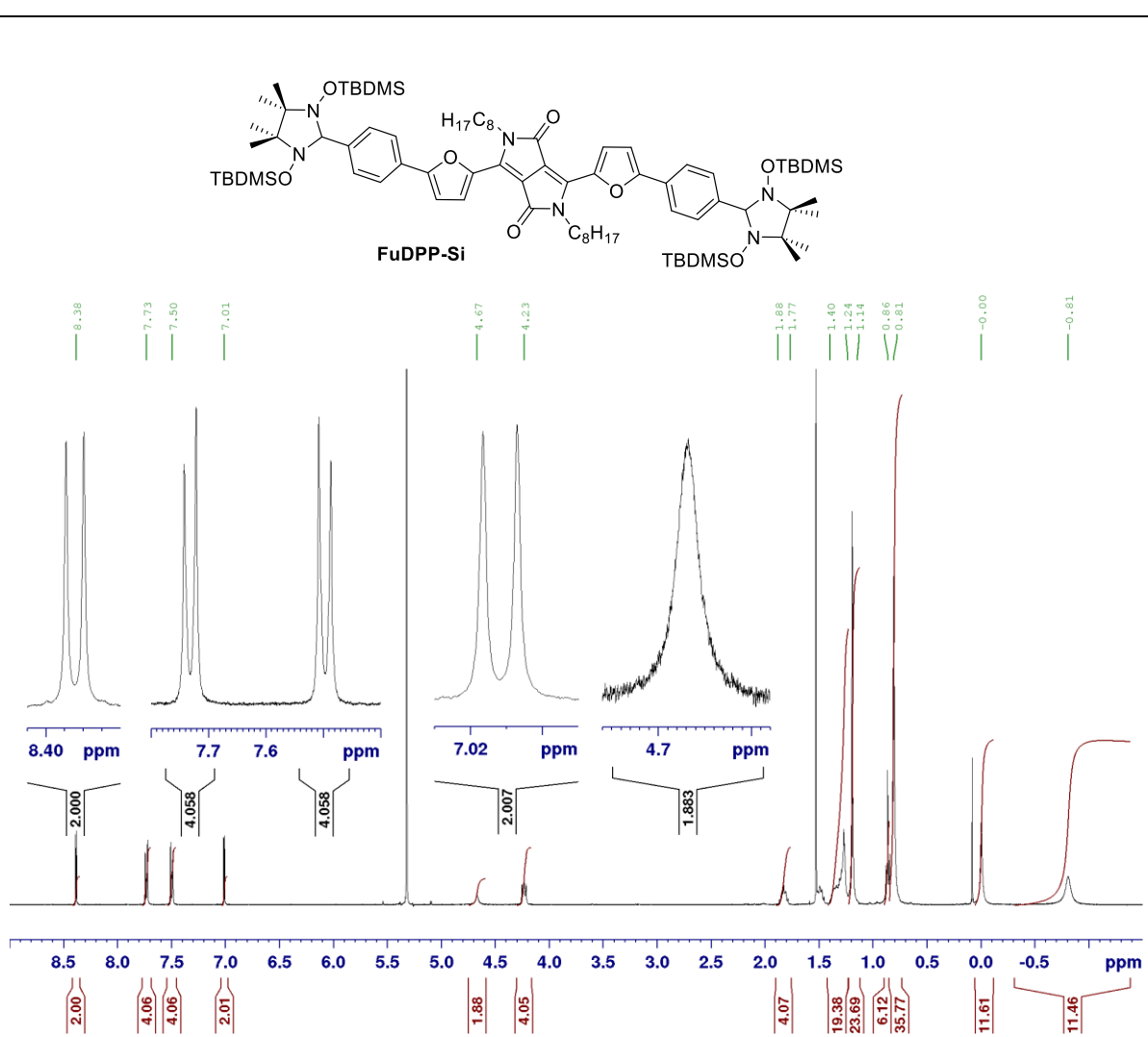


Figure 8.3.19 | ¹H NMR spectrum (400 MHz, CD₂Cl₂, 298 K) of FuDPP-Si.

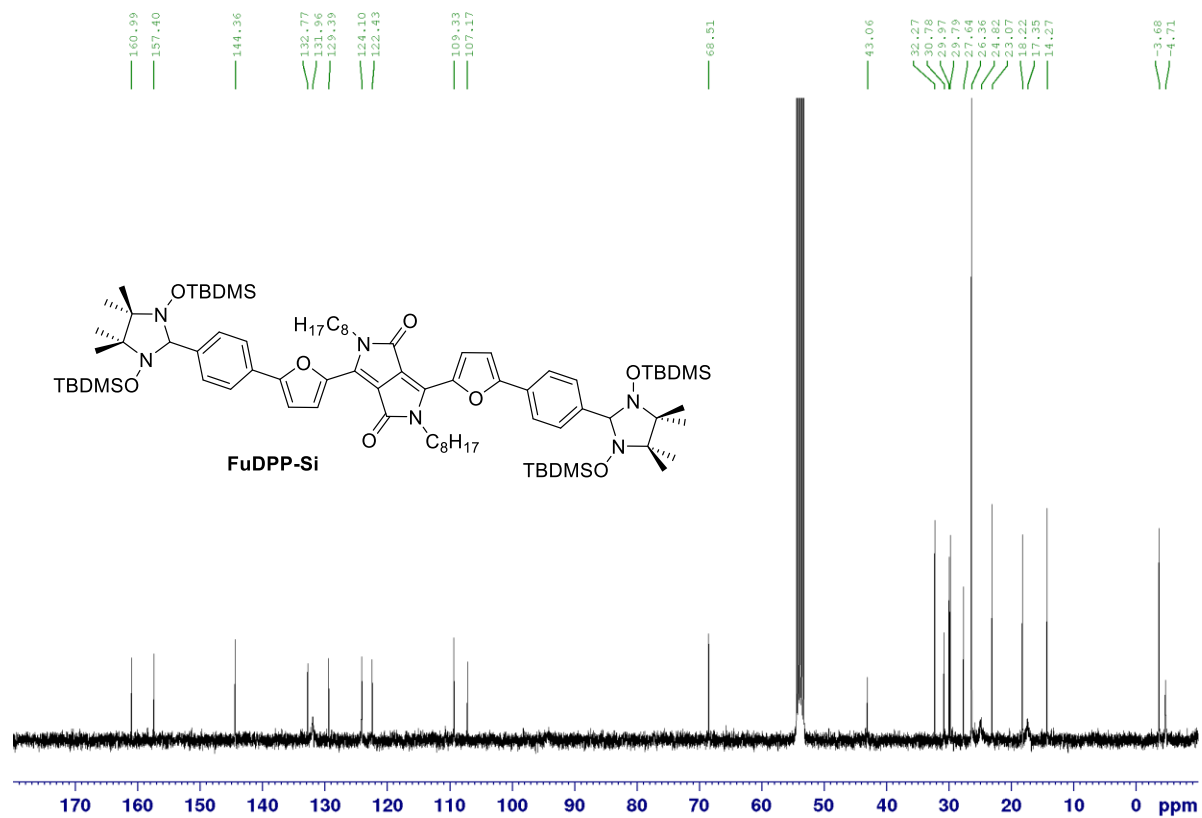


Figure 8.3.20 | ^{13}C NMR spectrum (101 MHz, CD_2Cl_2 , 298 K) of FuDPP-Si.

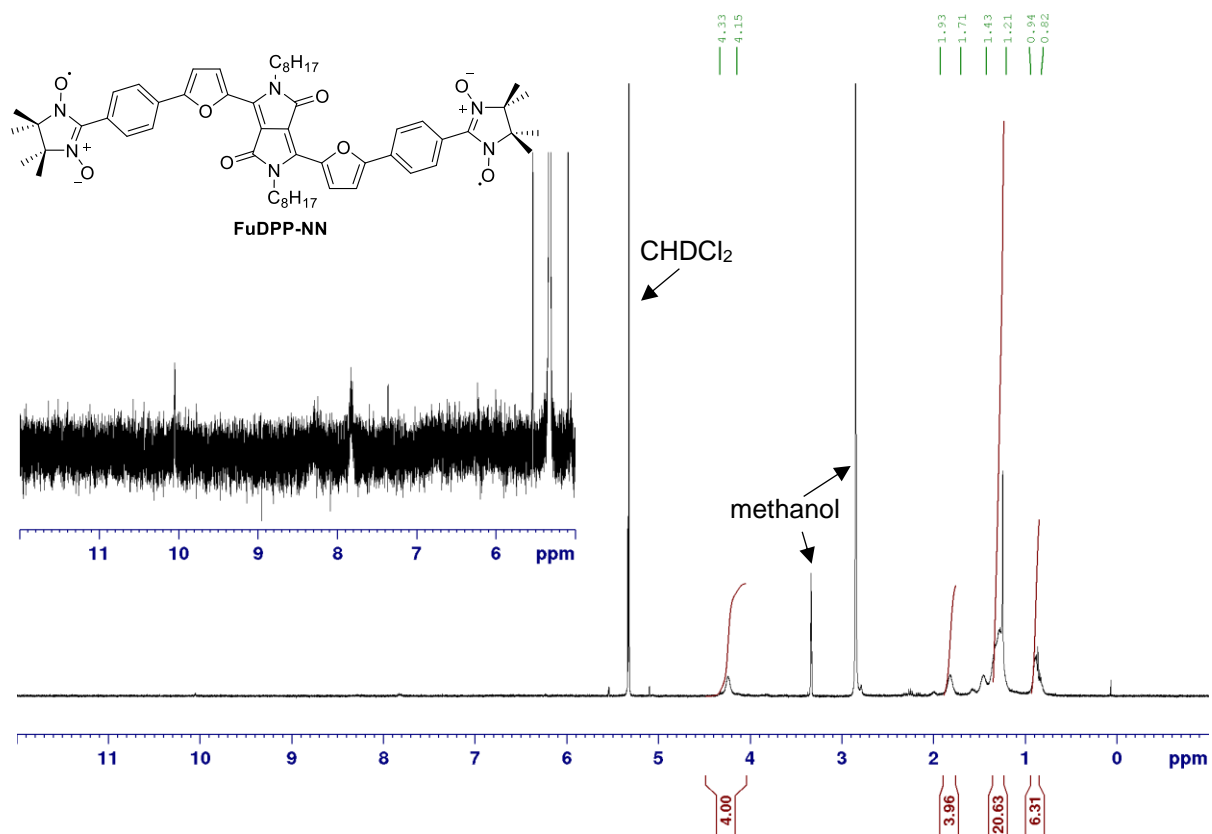


Figure 8.3.21 | ^1H NMR spectrum (400 MHz, $\text{CD}_2\text{Cl}_2/\text{CD}_3\text{OD}$ (9:1), 298 K) of **FuDPP-NN**.

8.3.5 X-ray analysis

Single crystals of **II_n-NN** were obtained by slow diffusion of methanol into a solution of **II_n-NN** in CH₂Cl₂. *Crystal data for II_n-NN* (C₆₆H₈₈N₆O₆: *Mr* = 1061.43, 0.360x0.200x0.021 mm³, triclinic space group P-1, *a* = 10.8585(5) Å, α = 66.505(6)°, *b* = 16.7866(15) Å, β = 73.610(4)° *c* = 18.2712(13) Å, γ = 80.928(5)°, *V* = 2926.3(4) Å³, *Z* = 2, ρ (*calcd*) = 1.205 g·cm⁻³, μ = 0.605 mm⁻¹, *F*₍₀₀₀₎ = 1148, *Goof*(*F*²) = 1.017, *R*_{*I*} = 0.0582, *wR*² = 0.1528 for *I* > 2σ(*I*), *R*₁ = 0.0791, *wR*² = 0.1723 for all data, 11588 unique reflections [$\theta \leq 72.791^\circ$] with a completeness of 99.9 % and 713 parameters, 0 restraints.

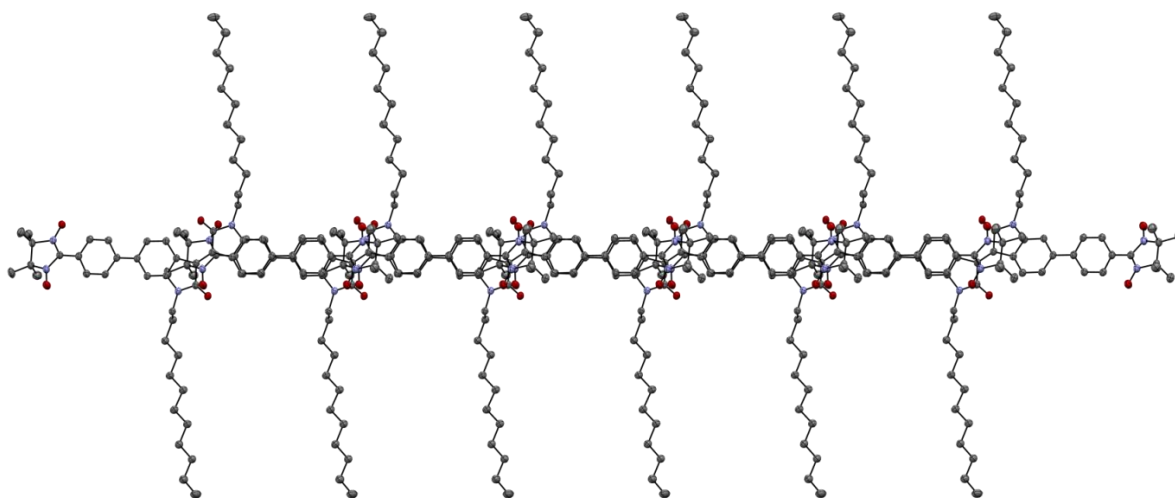


Figure 8.3.22a | Strand like side view of the solid state molecular packing of **II_n-NN** determined by single crystal X-ray diffraction (ellipsoids set to 50 % probability, carbon gray, nitrogen blue, oxygen red). Hydrogen atoms omitted for clarity.

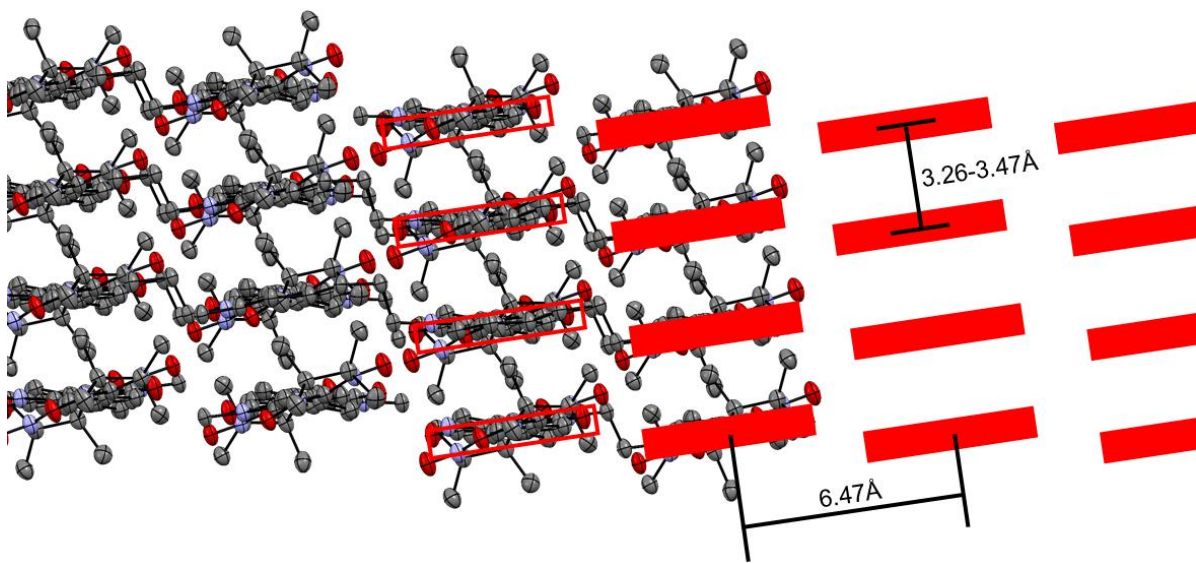


Figure 8.3.22b | Side view of the solid state molecular packing of **IIa-NN** determined by single crystal X-ray diffraction with schematic continuation for illustration and selected chromophore distances (ellipsoids set to 50 % probability, carbon gray, nitrogen blue, oxygen red). Hydrogen atoms omitted for clarity, “red bricks” represent the chromophore packing in cartoon.

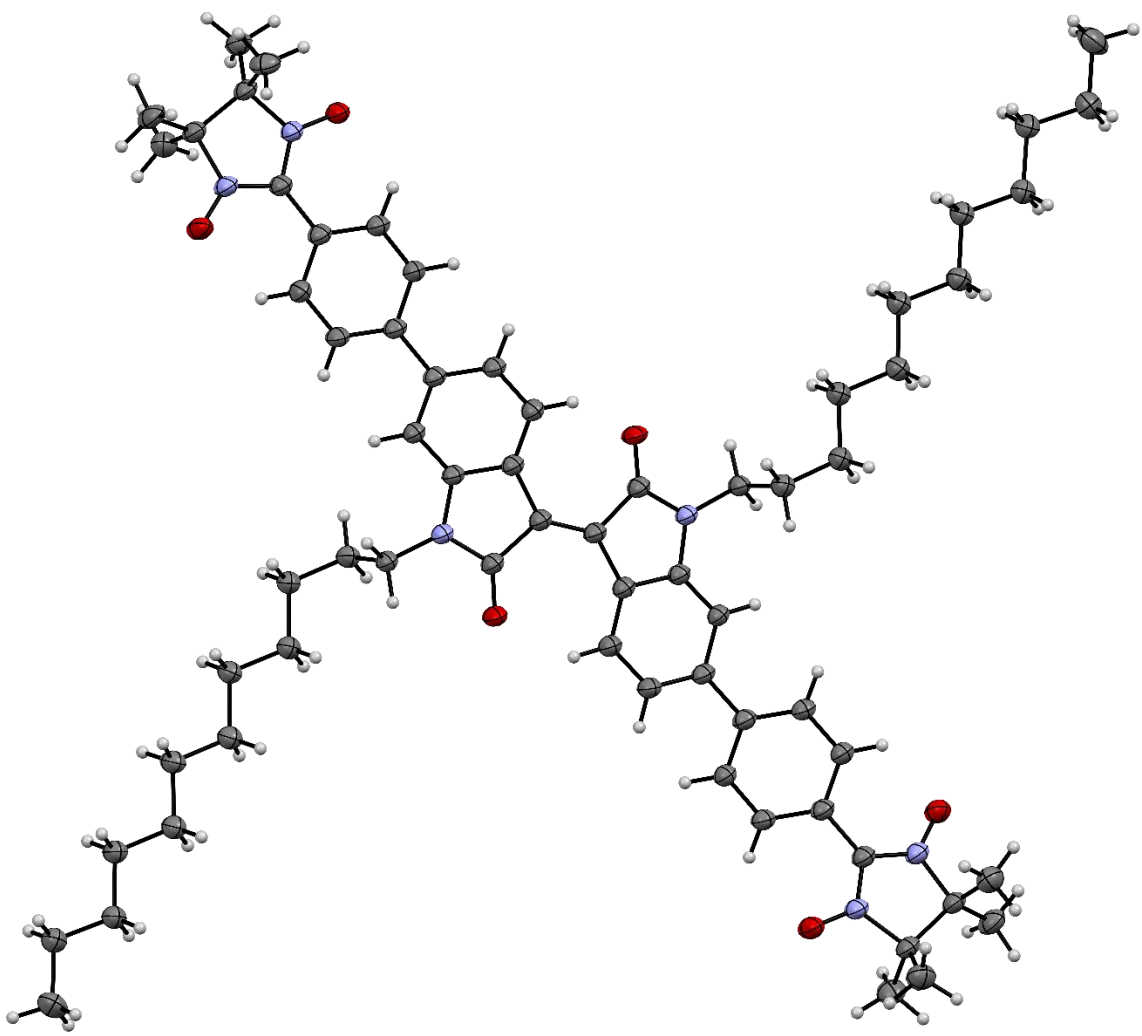


Figure 8.3.22c | Top view of the solid state molecular structure of **IIa-NN** determined by single crystal X-ray diffraction (ellipsoids set to 50 % probability, hydrogen white, carbon gray, nitrogen blue, oxygen red).

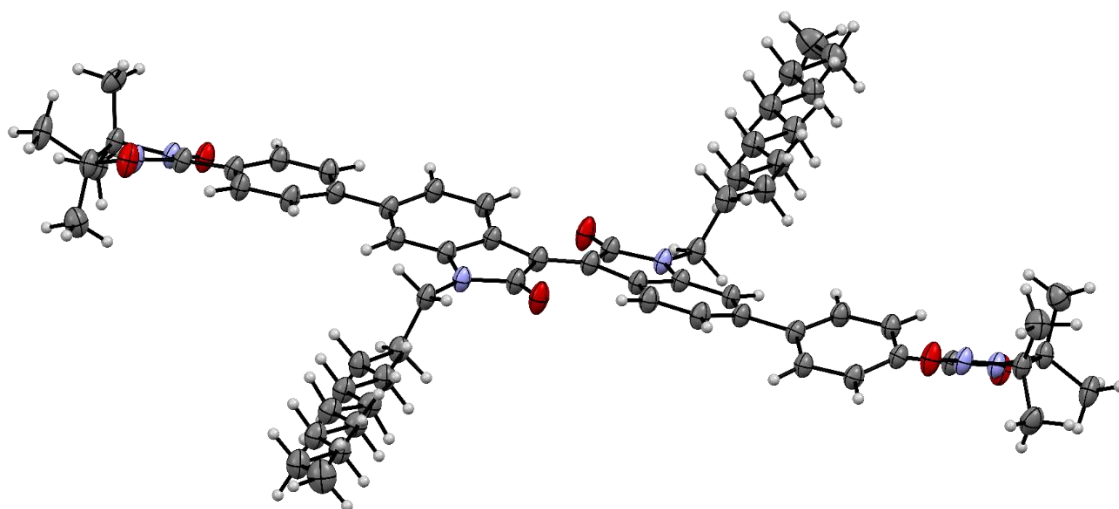


Figure 8.3.22d | Top view of the solid state molecular structure of **IIa-NN** determined by single crystal X-ray diffraction (ellipsoids set to 50 % probability, hydrogen white, carbon gray, nitrogen blue, oxygen red).

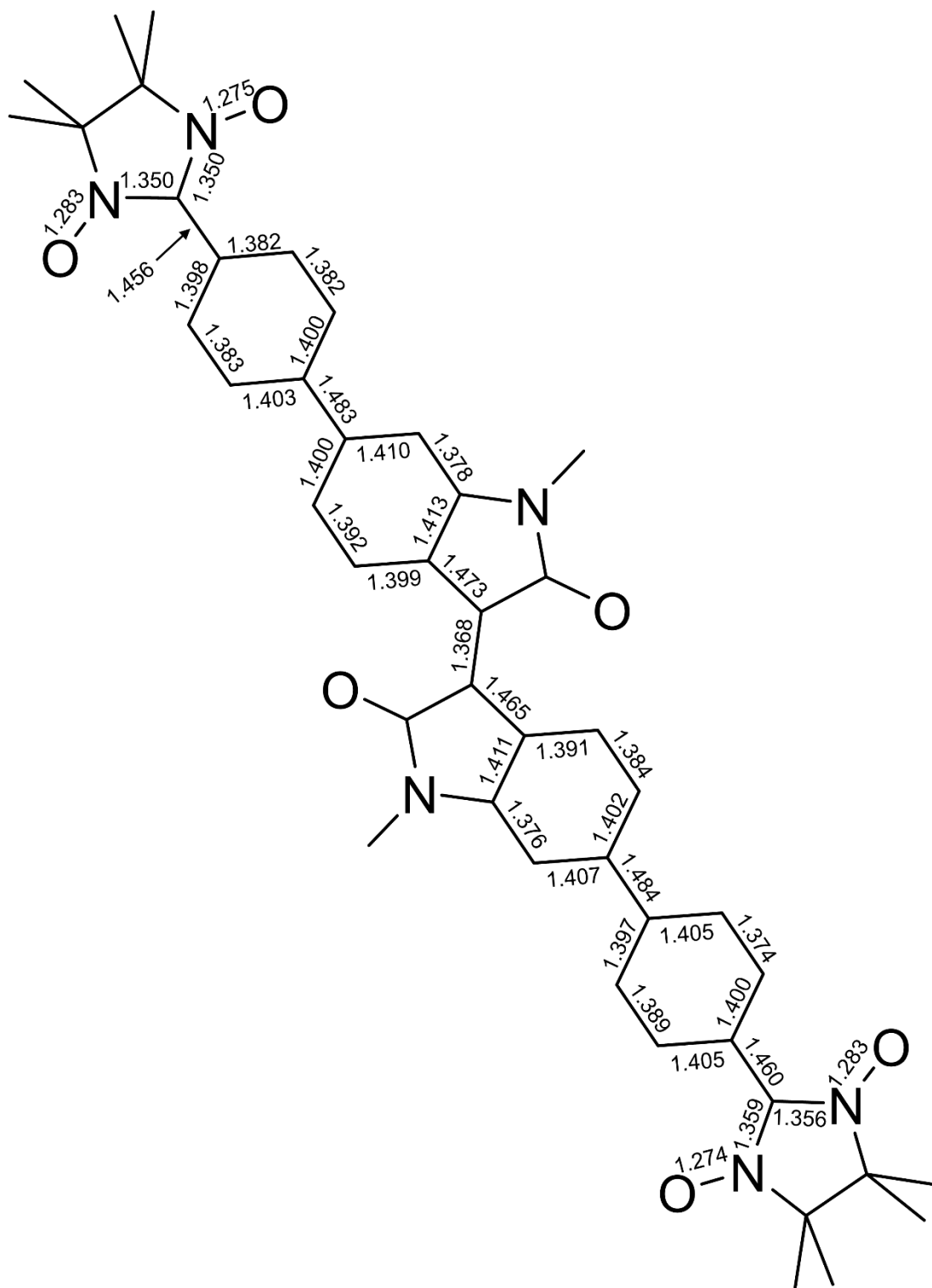


Figure 8.3.23 | Selected bond lengths of **II_n-NN** in Å determined by single crystal X-ray diffraction.

8.3.6 UV/vis/NIR spectroscopy

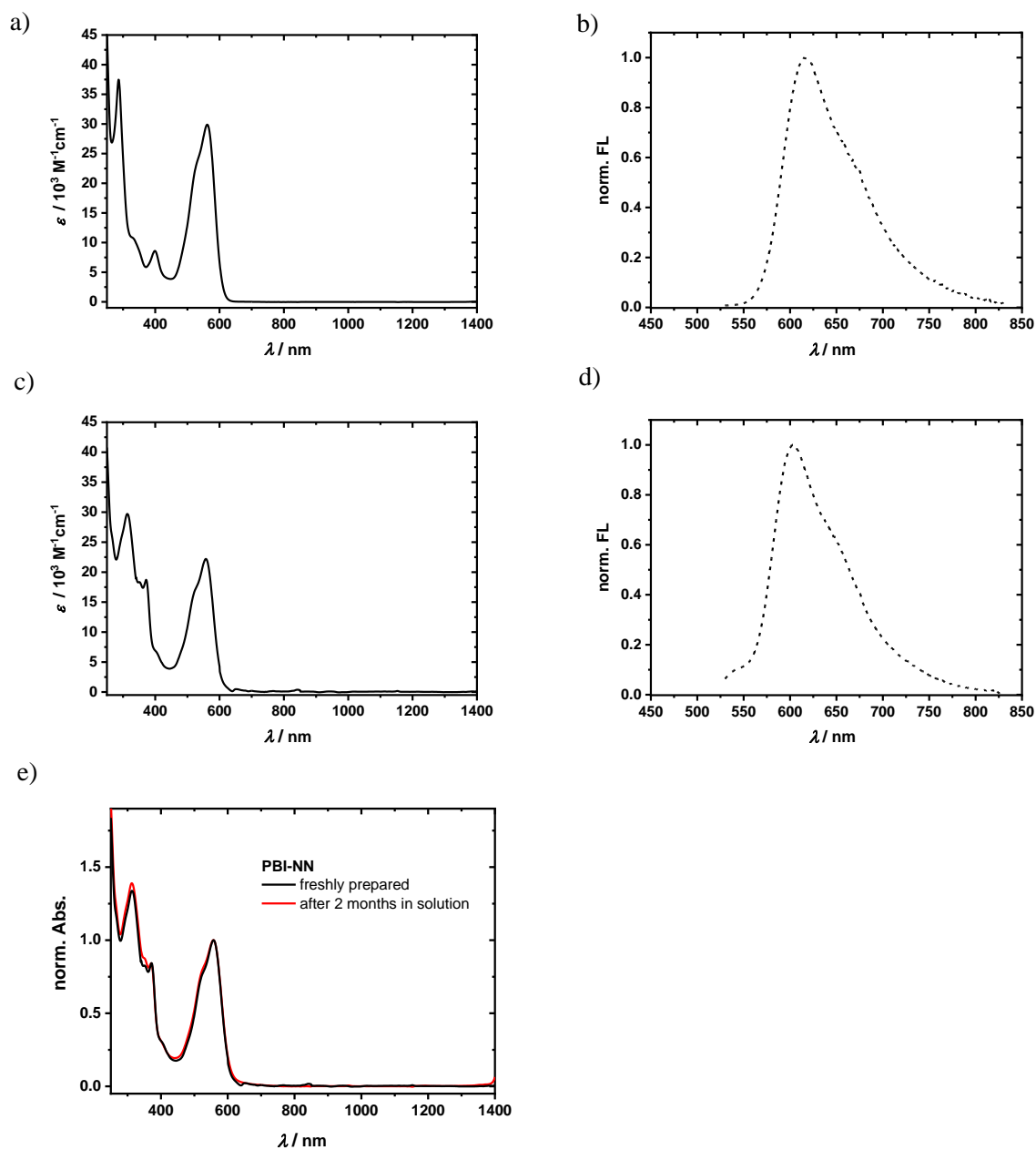


Figure 8.3.24 | UV/vis/NIR absorption spectra of **PBI-Si** (a), **PBI-NN** (c), and **PBI-NN** after storage for 2 months (e) in solution ($c \approx 10 \mu\text{M}$, CHCl_3 , RT) as well as fluorescence spectra of **PBI-Si** (b) and **PBI-NN** (d) in CHCl_3 .

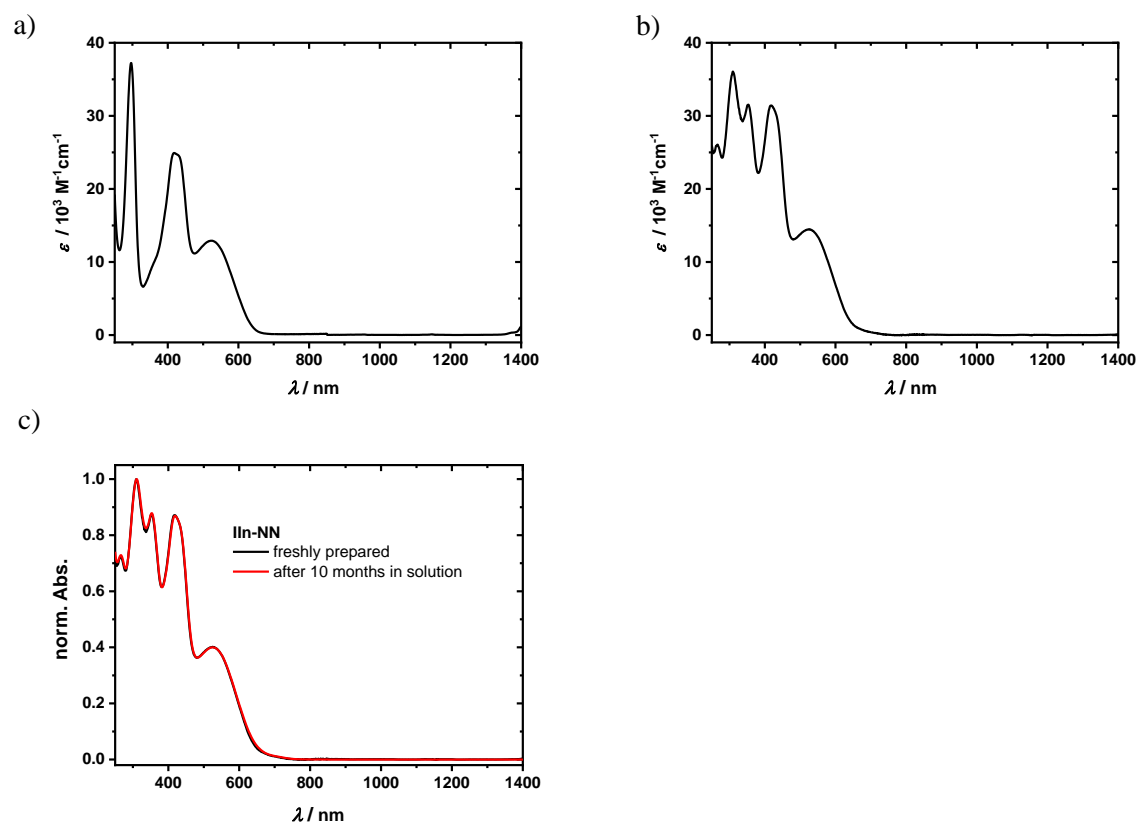


Figure 8.3.25 | UV/vis/NIR absorption spectra of **IIn-Si** (a), **IIn-NN** (b) and **IIn-NN** after storage for 10 months (c) in solution ($c \approx 10 \mu\text{M}$, CHCl_3 , RT). No emission detectable for **IIn-Si** and **IIn-NN**.

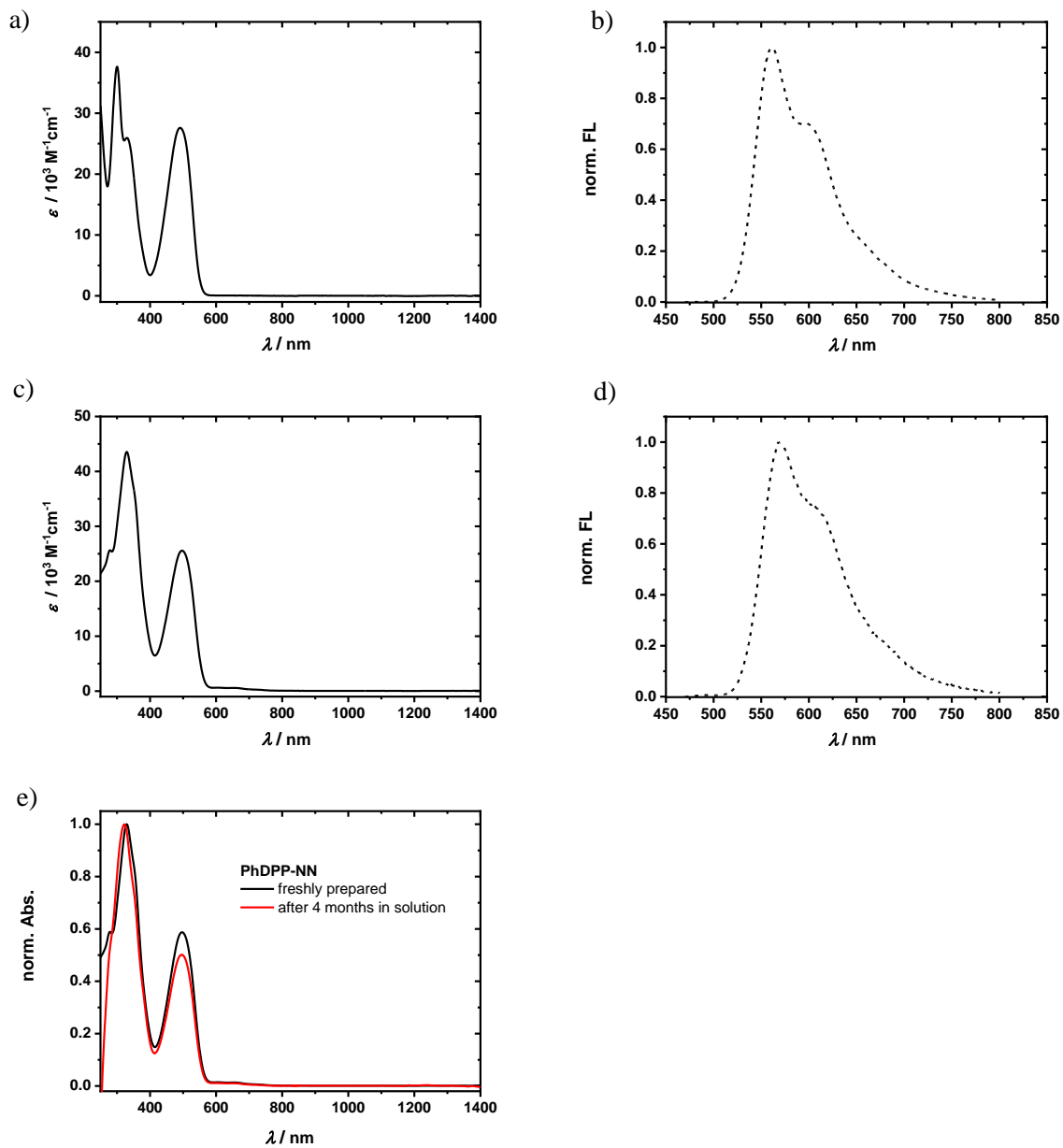


Figure 8.3.26 | UV/vis/NIR absorption spectra of **PhDPP-Si** (a), **PhDPP-NN** (c), and **PhDPP-NN** after storage for 4 months (e) in solution ($c \approx 10 \mu\text{M}$, THF, RT) as well as fluorescence spectra of **PhDPP-Si** (b) and **PhDPP-NN** (d) in THF.

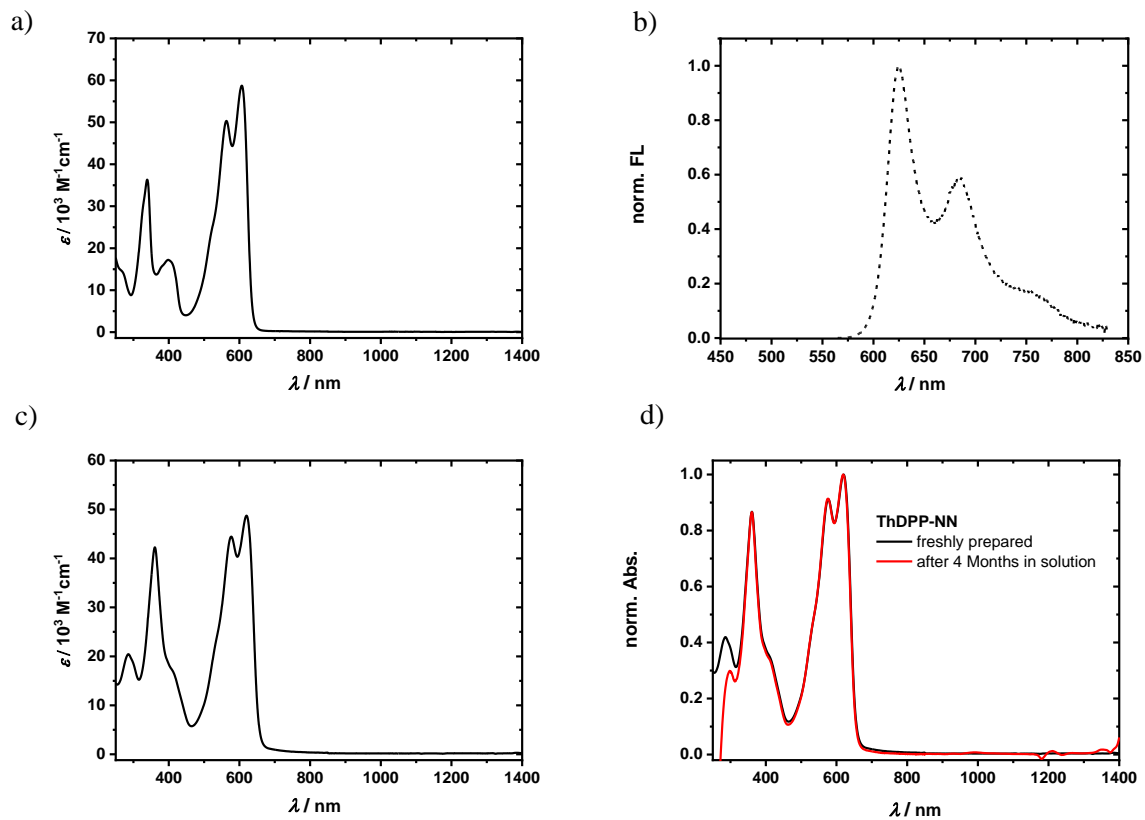


Figure 8.3.27 | UV/vis/NIR absorption spectra of **ThDPP-Si** (a), **ThDPP-NN** (c) and **ThDPP-NN** after storage for 4 months (d) in solution ($c \approx 10 \mu\text{M}$, THF, RT) as well as fluorescence spectrum of **ThDPP-Si** (b) in THF.

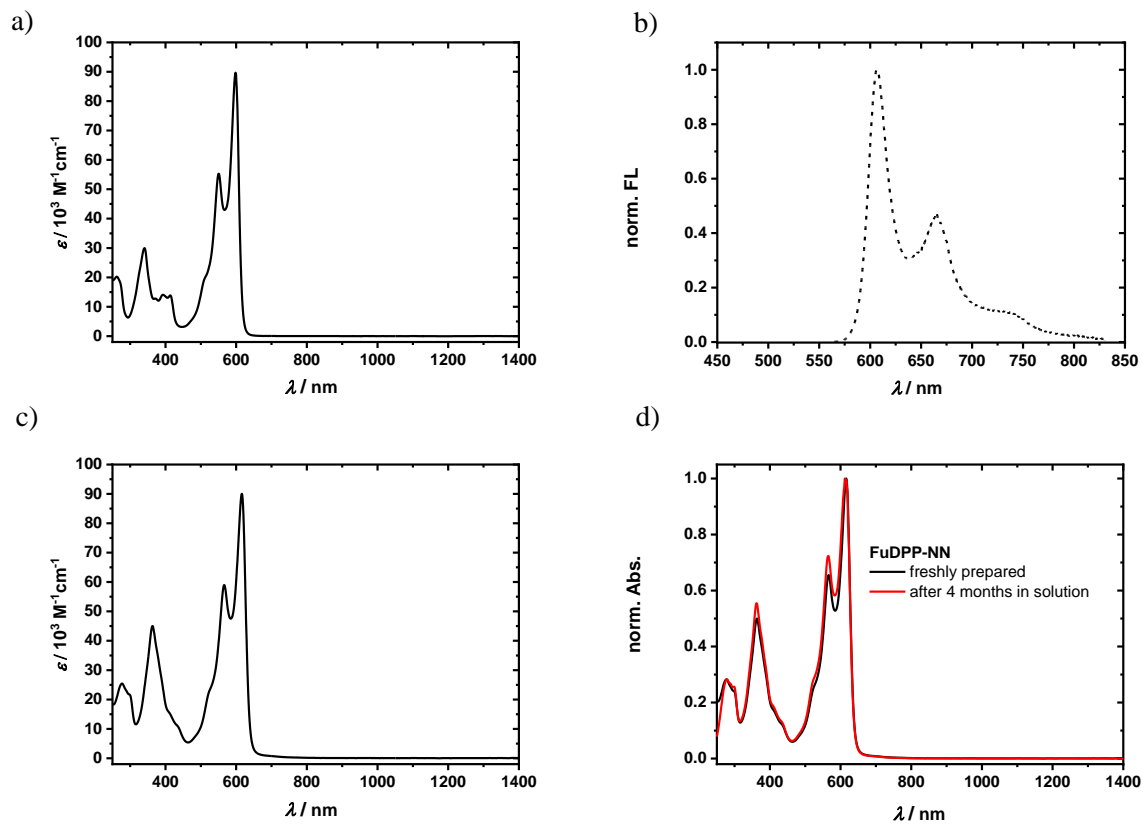


Figure 8.3.28 | UV/vis/NIR absorption spectra of **FuDPP-Si** (a), **FuDPP-NN** (c) and **FuDPP-NN** after storage for 4 months (d) in solution ($c \approx 10 \mu\text{M}$, THF, RT) as well as fluorescence spectrum of **FuDPP-Si** (b) in THF.

8.3.7 Cyclic voltammetry

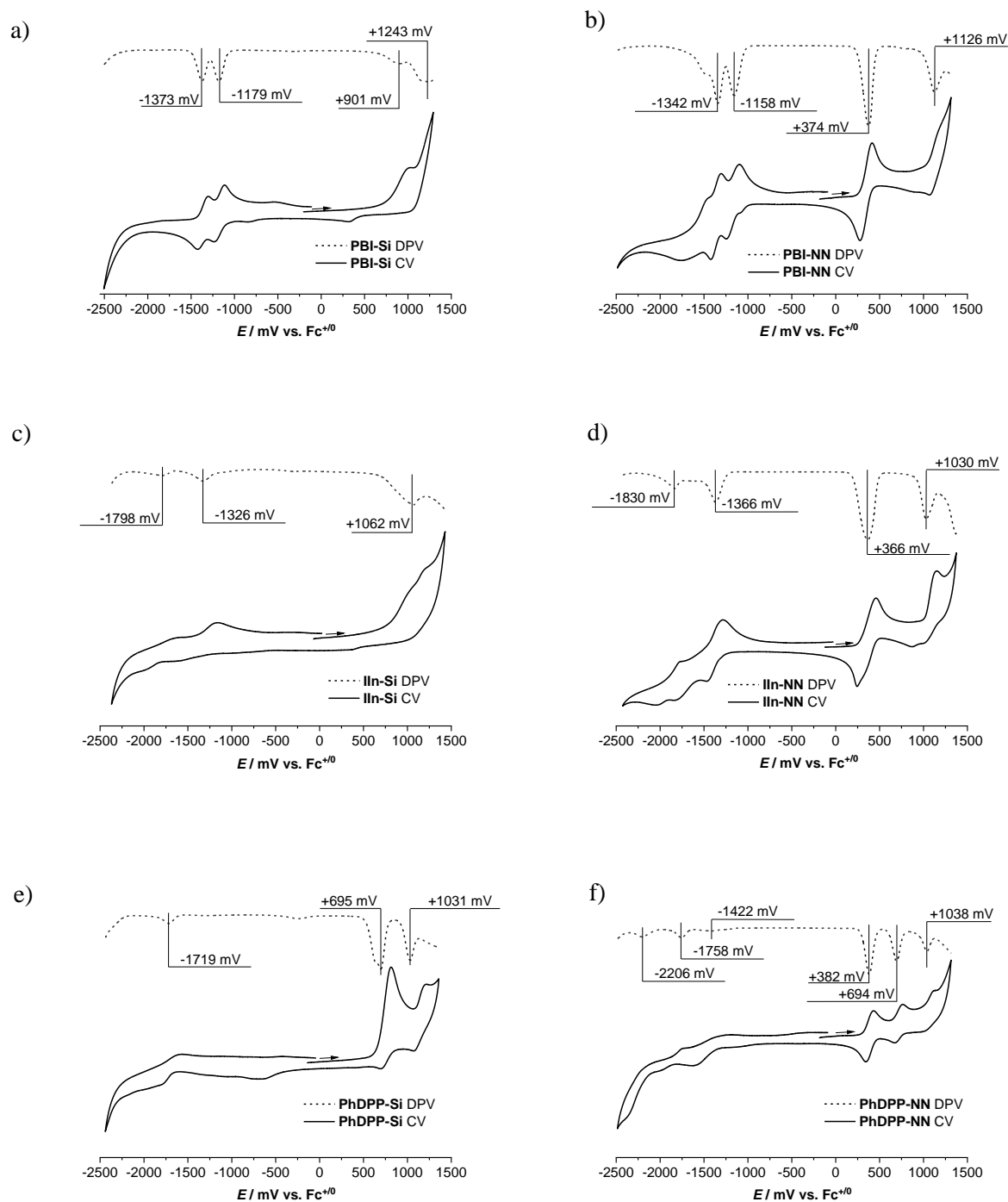


Figure 8.3.29 | Cyclic voltammograms (CV, solid line) and differential pulse voltammograms (DPV, dashed line) of a) **PBI-Si**, b) **PBI-NN**, c) **IIn-Si**, d) **IIn-NN**, e) **PhDPP-Si** and f) **PhDPP-NN** in CH_2Cl_2 ($c \approx 20 \mu\text{M}$, rt, electrolyte: $0.1 \text{ M } n\text{Bu}_4\text{NPF}_6$, scan rate: 100 mV s^{-1} , against $\text{Fc}^{0/+}$).

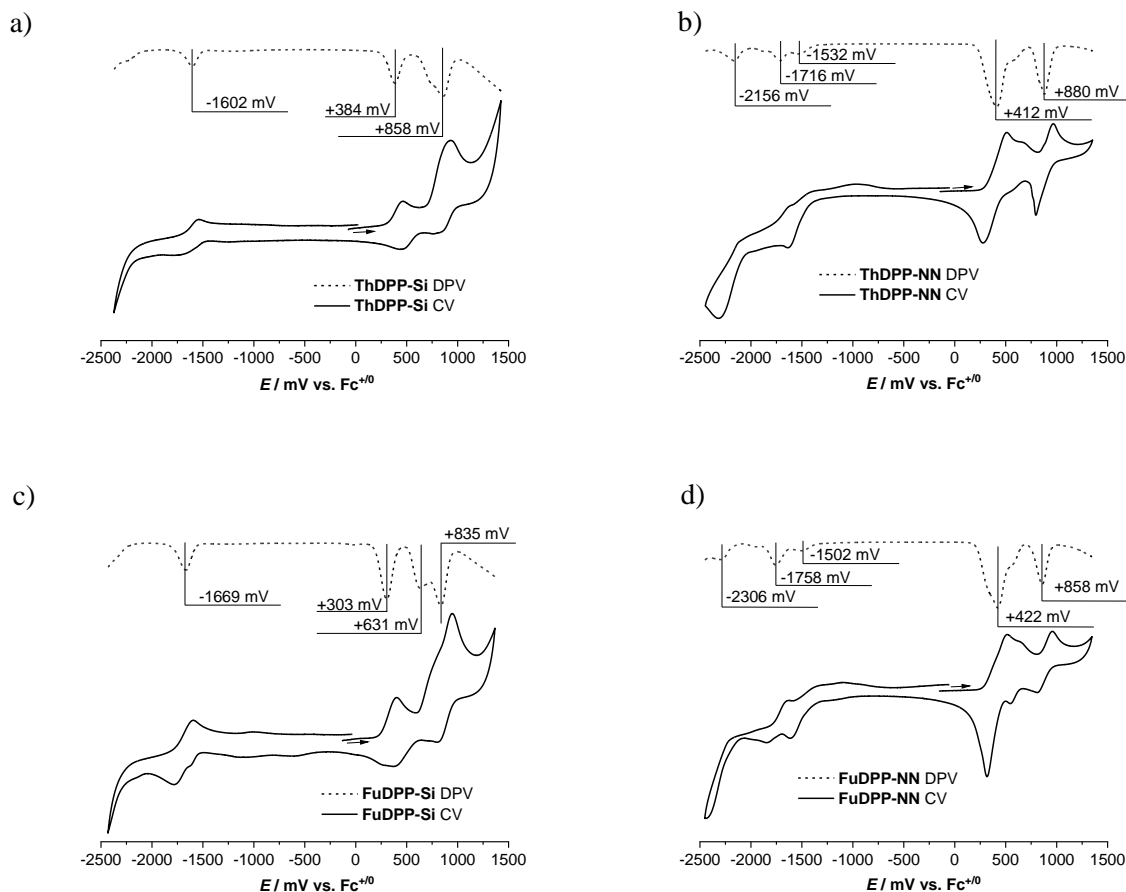


Figure 8.3.30 | Cyclic voltammograms (CV, solid line) and differential pulse voltammograms (DPV, dashed line) of a) **ThDPP-Si** b) **ThDPP-NN** c) **FuDPP-Si** and d) **FuDPP-NN** in CH_2Cl_2 ($c \approx 20 \mu\text{M}$, rt, electrolyte: $0.1 \text{ M } ^\text{t}\text{Bu}_4\text{NPF}_6$, scan rate: 100 mV s^{-1} , against $\text{Fc}^{0/+}$).

Table 8.3.1 | Redox potentials of **PBI-Si**, **IIn-Si**, **PhDPP-Si**, **ThDPP-Si** and **FuDPP-Si** versus the ferrocenium/ferrocene redox couple in CH_2Cl_2 .

	$E_{1/2}^{\text{Red}2}$ [V]	$E_{1/2}^{\text{Red}1}$ [V]	$E_{1/2}^{\text{Ox}1}$ [V]	$E_{1/2}^{\text{Ox}2}$ [V]	$E_{1/2}^{\text{Ox}3}$ [V]
PBI-Si	-1.373	-1.174	0.901	1.243	
IIn-Si	-1.798	-1.326	1.062		
PhDPP-Si		-1.719	0.695	1.031	
ThDPP-Si		-1.602	0.384	0.858	
FuDPP-Si		-1.669	0.303	0.631	0.835

$\text{Fc}^+/\text{Fc} = 0.00 \text{ V}$.

Table 8.3.2 | Redox potentials of **PBI–NN**, **IIn–NN**, **PhDPP–NN**, **ThDPP–NN** and **FuDPP–NN** versus the ferrocenium/ferrocene redox couple in CH₂Cl₂.

	$E_{1/2}^{\text{Red3}}$ [V]	$E_{1/2}^{\text{Red2}}$ [V]	$E_{1/2}^{\text{Red1}}$ [V]	$E_{1/2}^{\text{Ox1}}$ [V]	$E_{1/2}^{\text{Ox2}}$ [V]	$E_{1/2}^{\text{Ox3}}$ [V]
PBI–NN		–1.342	–1.158	0.374	1.126	
IIn–NN		–1.830	–1.366	0.366	1.030	
PhDPP–NN	–2.206	–1.758	–1.422	0.382	0.694	1.038
ThDPP–NN	–2.156	–1.716	–1.532	0.412	0.880	
FuDPP–NN	–2.306	–1.758	–1.502	0.422	0.858	

Fc⁺/Fc = 0.00 V.

8.3.8 EPR spectroscopy

Table 8.3.3 | g_{iso} and a values of **PBI–NN**, **IIn–NN**, **PhDPP–NN**, **ThDPP–NN** and **FuDPP–NN** determined by CW–EPR spectroscopy ($c \approx 1$ mM in $\text{CH}_2\text{Cl}_2/\text{MeOH}$ 9:1, rt).

Biradical	g_{iso}	$a(^{14}\text{N})$
PBI–NN	2.0066	10.3 MHz (3.7 G)
IIn–NN	2.0066	10.5 MHz (3.8 G)
PhDPP–NN	2.0067	10.4 MHz (3.7 G)
FuDPP–NN	2.0067	10.4 MHz (3.7 G)
ThDPP–NN	2.0066	10.6 MHz (3.8 G)

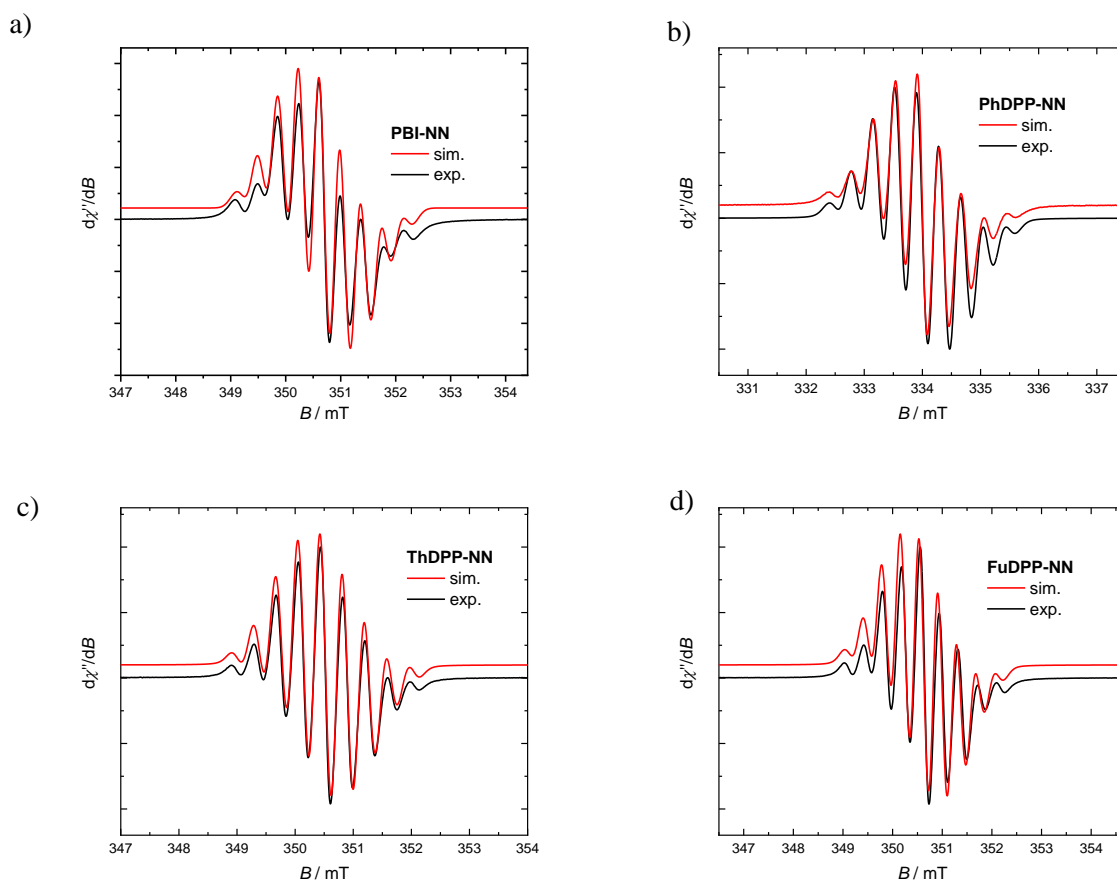


Figure 8.3.31 | Experimental (black) and simulated (red) continuous–wave (CW) X–band EPR spectra of a) **PBI–NN**, b) **PhDPP–NN**, c) **ThDPP–NN** and d) **FuDPP–NN** in a $\text{CH}_2\text{Cl}_2/\text{MeOH}$ (9:1) mixture at room temperature ($c \approx 1$ mM).



Chapter 9 – Individual contribution

The coauthors of the publications presented in this cumulative thesis are informed and agree with the reprint as well as with the individual contributions stated below.

Publikation: Stable Organic (Bi)Radicals by Delocalization of Spin Density into the Electron-Poor Chromophore Core of Isoindigo, *Chem. Eur. J.* **2018**, *24*, 3420–3424.

Autoren: Rodger Rausch (Hauptautor, RR), David Schmidt (Ko-Autor, DS), David Bialas (Ko-Autor, DB), Ivo Krummenacher (Ko-Autor, IK), Holger Braunschweig (Ko-Autor, HB), Frank Würthner (korrespondierender Autor, FW).

Detaillierte Darstellung der Anteile an der Veröffentlichung (in %)

Autor	RR	DS	DB	IK	HB	FW	Σ in Prozent
Forschungsdesign	60%	10%	–	–	–	30%	100%
Synthese	100%	–	–	–	–	–	100%
Charakterisierung der Verbindungen	90%	10%	–	–	–	–	100%
Röntgenographische Untersuchungen	–	100%	–	–	–	–	100%
Optische Untersuchungen (UV/vis)	90%	10%	–	–	–	–	100%
Elektronische Untersuchungen (CV/SWV)	100%	–	–	–	–	–	100%
DFT-Berechnungen	–	–	100%	–	–	–	100%
Spin-Untersuchungen/ EPR	–	–	–	90%	10%	–	100%
Verfassen der Veröffentlichung	65%	10%	–	–	–	25%	100%
Korrektur der Veröffentlichung	15%	25%	5%	–	–	55%	100%
Koordination der Veröffentlichung	20%	20%	–	–	–	60%	100%

Publikation: Tuning phenoxy-substituted diketopyrrolopyrroles from quinoidal to biradical ground states through (hetero-)aromatic linkers. *Chem. Sci.* **2021**, *12*, 793–802.

Autoren: Rodger Rausch (Hauptautor, RR), Merle I. S. Röhr (Ko-Autor, MR), David Schmidt (Ko-Autor, DS), Ivo Kruppenacher (Ko-Autor, IK), Holger Braunschweig (Ko-Autor, HB), Frank Würthner (korrespondierender Autor, FW).

Detaillierte Darstellung der Anteile an der Veröffentlichung (in %)

Autor	RR	MR	DS	IK	HB	FW	Σ in Prozent
Forschungsdesign	60%	–	10%	–	–	30%	100%
Synthese	100%	–	–	–	–	–	100%
Charakterisierung der Verbindungen	90%	–	10%	–	–	–	100%
Röntgenographische Untersuchungen	–	–	100%	–	–	–	100%
Optische Untersuchungen (UV/vis)	100%	–	–	–	–	–	100%
Elektronische Untersuchungen (CV/SWV)	100%	–	–	–	–	–	100%
DFT-Berechnungen	–	100%	–	–	–	–	100%
Spin-Untersuchungen/ EPR	–	–	–	90%	10%	–	100%
Verfassen der Veröffentlichung	60%	20%	–	–	–	20%	100%
Korrektur der Veröffentlichung	30%	–	–	–	–	70%	100%
Koordination der Veröffentlichung	30%	–	–	–	–	70%	100%

Publikation: Nitronyl Nitroxide Bifunctionalized Electron–Poor Chromophores: Synthesis of Stable Dye Biradicals by Lewis Acid Promoted Desilylation. *J. Org. Chem.* **2021**, 86, 2447–2457.

Autoren: Rodger Rausch (Hauptautor, RR), Ana–Maria Krause (Ko–Autor, AMK), Ivo Krummenacher (Ko–Autor, IK), Holger Braunschweig (Ko–Autor, HB), Frank Würthner (korrespondierender Autor, FW).

Detaillierte Darstellung der Anteile an der Veröffentlichung (in %)

Autor	RR	AMK	IK	HB	FW	∑ in Prozent
Forschungsdesign	70%	–	–	–	30%	100%
Synthese	100%	–	–	–	–	100%
Charakterisierung der Verbindungen	100%	–	–	–	–	100%
Röntgenographische Untersuchungen	–	100%	–	–	–	100%
Optische Untersuchungen (UV/vis)	100%	–	–	–	–	100%
Elektronische Untersuchungen (CV/DPV)	100%	–	–	–	–	100%
Spin–Untersuchungen/ EPR	–	–	90%	10%	–	100%
Verfassen der Veröffentlichung	70%	–	–	–	30%	100%
Korrektur der Veröffentlichung	30%	–	–	–	70%	100%
Koordination der Veröffentlichung	30%	–	–	–	70%	100%

Chapter 10 – Danksagung

Mein erster Dank gilt Herrn Prof. Dr. **Frank Würthner** für die interessante und spannende Themenstellung für diese Doktorarbeit, für die kompetente, engagierte, faire und vertrauensvolle Betreuung und Zusammenarbeit, für aufschlussreiche Diskussionen und für ein Arbeitsumfeld das hinsichtlich wissenschaftlicher Qualität, Professionalität, persönlichem Austausch und Zusammenhalt seinesgleichen sucht und Maßstäbe zu setzen vermag.

Besonders danken möchte ich auch dem Graduiertenkolleg 2112 „Molekulare Biradikale“ und stellvertretend dessen Sprecher, Herrn Prof. Dr. **Ingo Fischer** und der Administratorin Frau **Ursula „Uschi“ Rüppel**. Beiden und dem GRK verdanke ich die Möglichkeit zu und den Rahmen für intensiven Austausch mit Kollegiaten in zahlreichen Workshops und Seminaren, in Vorträgen und Konferenzen.

Für ihren steten Rat, für tiefgründige wissenschaftliche Diskussionen, für mühevollen Detailarbeit ebenso wie richtungsweisende Debatten und ihre persönliche Unterstützung bin ich gleichermaßen Herrn Dr. **David Schmidt** und Herrn Dr. **David Bialas** zu größtem Dank verpflichtet. Beide wirkten intensiv an der Abfassung und Korrektur meiner Manuskripte mit und übernahmen Verantwortung als Subgroupleiter.

Herrn Dr. **David Bialas** und Frau Dr. **Merle Röhr** danke ich sehr herzlich für ihre quantenchemischen Berechnungen und damit verbundene Diskussionen, die jeweils Einzug in ein Manuskript gefunden haben und durch ihre hohe Qualität insgesamt das Niveau der Arbeit gesteigert haben. Auch danke ich beiden sehr herzlich für ihre ständige Bereitschaft, Rückfragen ausführlich und geduldig zu beantworten.

Ebenso gilt mein Dank Herrn Dr. **Matthias Stolte**, Frau **Astrid Kudzus** und Herrn **Julius Albert** für die Möglichkeit, die Halbleitereigenschaften meiner Verbindungen in Transistoren und Solarzellen mit ihrer Unterstützung zu untersuchen. Wenngleich der „große Wurf“ hierbei ausgeblieben ist, so konnte ich dank der stets hervorragenden Arbeit dieser Kollegen immer versichert sein, dass es an der Untersuchung der Substanzen nicht lag, sondern viel mehr an den Materialeigenschaften selbst.

Frau **Ana-Maria Krause** und Dr. **David Schmidt** danke ich überdies für die sehr erfolgreiche röntgenographische Untersuchung einiger Kristalle aber gerade auch für die Inaugenscheinnahme so vieler weiterer „Quasikristalle“ (nicht i. e. S.), für die beide oft nur ein freundliches „weiter probieren“ übrig hatten.

Ein herzliches Dankeschön gilt auch Herrn Dr. **Ivo Krummenacher** und Prof. Dr. **Holger Braunschweig** für eine sehr produktive und durchwegs angenehme Kooperation im Rahmen des GRK 2112 und der damit verbundenen EPR–Messungen.

Auch gilt mein Dank allen MitarbeiterInnen der Analytikabteilungen für NMR–Spektroskopie und Massenspektrometrie sowie stellvertretend ihren Leitern Dr. **Matthias Grüne** und Dr. **Michael Büchner** für ihre zuverlässliche Arbeit und freundliche Art. Aufrichtigst danken möchte ich in diesem Zusammenhang gerade auch Frau **Juliane Adelmann**, der ich eine kompetente Einführung in die Bedienung des ESI–Massenspektrometers zu verdanken haben und welche nicht müde wurde, den Messbetrieb immer wieder in Gang zu setzen und Störungen desselben mit ihrem außergewöhnlichen technischen Sachverstand und unermüdlichen persönlichen Einsatz umgehend zu beheben. Vielen Dank, Juliane.

Dem geschätzten Herrn Dr. **Chantu R. Saha–Möller** danke ich für die zahlreichen Diskussionen, welche nicht nur wissenschaftlicher Natur waren, sondern thematisch von Schwarzriesling bis Van Gogh reichten. Großer Dank gebührt ihm zudem für die hervorragende Verköstigung während der vielen Weihnachtsfeiern der letzten Jahre.

Meinen werten Kollegen Herrn **Magnus Mahl** und Frau **Carina Mützel**, mit denen ich mir über Jahre einen Schreibtisch und so manches Leid geteilt habe, danke ich für ein immer offenes Ohr, große Geduld, eine wunderbare Zusammenarbeit und den unermesslichen Einsatz beider für das Wohl des ganzen Arbeitskreises; angefangen bei der zuverlässigen Gefahrgutentsorgung über Gloveboxwartung und SPS Management bis hin zur Versorgung der Gruppe mit Kaffee und die Pflege, bzw. Reparatur der unverzichtbaren Kaffeemaschine. Ich danke euch für eure Verlässlichkeit und Freundschaft; solche Menschen gibt es viel zu selten.

Mein herzlicher Dank gilt auch meiner Schreibraumkollegin Frau **Chia–An Shen** und unserer früheren Kollegin Dr. **Meike Sapotta** für ihre persönliche Unterstützung, viele gute Ratschläge, gemeinsam geteilten Ärger und die gegenseitige Motivation, auch bei gelegentlichen Tiefen nicht aufzugeben.

Besonders auch allen Laboranten (in alphabetischer Reihung des Vornamens) Frau **Anja Rausch**, Frau **Ann–Kathrin Lenz**, Frau **Astrid Kudzus**, Herrn **Christian Simon**, Frau **Jenny Begall**, Herrn **Joachim Bialas**, Herrn **Johannes Thein**, Herrn **Julius Albert**, Frau **Lisa Otter**, Frau **Olga Anhalt**, Frau **Petra Seufert–Baumbach** und Herrn **Maximilian Roth**, möchte ich für ihre unermüdliche Unterstützung, ihren Rat bei technischen und organisatorischen Problemstellungen und die produktive Zusammenarbeit danken. Ohne euch geriete das Labor aus den Fugen.

Dank gilt besonders auch meinen beiden Auszubildenden, Herrn **Maximilian Roth** und Frau **Carina Heer**, welche nicht nur großen Fleiß und bemerkenswertes Geschick an den Tag gelegt haben, sondern sich auch sozial sehr aktiv einzugliedern vermochten.

Herzlich danken möchte ich auch meinen Praktikanten Herrn **Julian Höcker**, Herrn **Lukas Gerstner**, Herrn **Matthias Maier** und Herrn **Christian Schmidle**, welche mich kompetent bei der Umsetzung so mancher Synthese unterstützt haben.

Für eine sehr kurze Zeit lang konnte ich auch die administrative Arbeit des Lehrstuhls für Organische Chemie II unterstützen. Bei den vielfältigsten Fragestellungen standen mir dabei Herr Dr. **Christian Stadler**, Frau **Christiana Toussaint**, Frau **Eleonore Klaus**, Frau **Anette Krug**, Herr Dipl. Ing. **Bernd Brunner** und Herr **Markus Braun** sowie zahllose Mitarbeiter der universitären Verwaltung und Sekretariate mit Rat und Tat zur Seite. Herzlichen Dank hierfür. Einige dieser Aufgaben wurden sodann von Frau **Sarah Bullheimer** und Frau **Lisa Weidner** übernommen, denen ich hierfür recht herzlich danken möchte und für die Zukunft alles Gute wünsche.

All der bescheidene Dank kann jedoch bestenfalls ansatzweise widerspiegeln, welche tolle kollegiale und produktive Atmosphäre auch durch die Vielfalt aller Mitarbeiter entsteht: Ich danke daher allen permanenten und temporären Mitarbeiterinnen und Mitarbeitern und Leitern der Arbeitsgruppen **Würthner, Beuerle** und **Nowak-Król**.

Nicht fehlen darf an dieser Stelle auch ein ganz großer Dank an all meine Freunde. Stellvertretend für sie möchte ich mich insbesondere bei **Thomas** für fruchtbare Diskussionen, lebhaftes Kritik, viele Momente des Lachens, wissenschaftliche und politische Debatten, verlässliche Hilfe mit Rat und Tat und für ganz viel herzliche Freude aufrichtig bedanken.

Mein ganz persönlicher Dank gilt meiner geliebten Frau **Anja**, meinen lieben **Eltern** und meinem lieben **Bruder**. Mein Weg zur und in der Wissenschaft begann schon im heimischen Hobby-Chemielabor, welches gerade meiner Familie ein äußerstes Maß an Geduld und Toleranz, aber auch an persönlichem Einsatz abverlangte – und das in vielerlei Hinsicht. Vielleicht ist es daher auch Ausdruck dieser Arbeit, dass all das nicht umsonst war. Vielen Dank für eure immerwährende Unterstützung!

Chapter 11 – List of Publications

1. Rausch, R., Schmidt, D., Bialas, D., Krummenacher, I., Braunschweig, H., Würthner, F. Stable Organic (Bi)Radicals by Delocalization of Spin Density into the Electron-Poor Chromophore Core of Isoindigo. *Chem. Eur. J.* **2018**, *24*, 3420–3424.
2. Rausch, R., Röhr, M. I. S., Schmidt, D., Krummenacher, I., Braunschweig, H., Würthner, F. Tuning phenoxy-substituted diketopyrrolopyrroles from quinoidal to biradical ground states through (hetero-)aromatic linkers. *Chem. Sci.* **2021**, *12*, 793–802.
3. Rausch, R., Krause, A.-M., Krummenacher, I., Braunschweig, H., Würthner, F. Nitronyl Nitroxide Bifunctionalized Electron-Poor Chromophores: Synthesis of Stable Dye Biradicals by Lewis Acid Promoted Desilylation. *J. Org. Chem.* **2021**, *86*, 2447–2457.

Chapter 12 – Bibliography

1. Aristotle. *Metaphysics*, **350 BC**, Book VIII, Part 6, translated by Ross, W. D., retrieved on the 31st of December 2020 from <http://classics.mit.edu/Aristotle/metaphysics.8.viii.html>.
2. Abe, M. Diradicals. *Chem. Rev.* **2013**, *113*, 7011–7088.
3. Bach, T., Aechtner, T., Neumüller, B. Enantioselective Norrish–Yang cyclization reactions of N-(omega-oxo-omega-phenylalkyl)-substituted imidazolidinones in solution and in the solid state. *Chem. Eur. J.* **2002**, *8*, 2464–2475.
4. Norrish, R. G. W., Bamford, C. H.. Photodecomposition of Aldehydes and Ketones. *Nature* **1937**, *31*, 195–196.
5. Kuzmanich, G., Vogelsberg, C. S., Maverick, E. F., Netto-Ferreira, J. C., Scaiano, J. C., Garcia-Garibay, M. A. Reaction Mechanism in Crystalline Solids: Kinetics and Conformational Dynamics of the Norrish Type II Biradicals from α -Adamantyl-*p*-Methoxyacetophenone. *J. Am. Chem. Soc.* **2012**, *134*, 1115–1123.
6. Renata, H., Zhou, Q. H., Baran, P. S. Strategic Redox Relay Enables A Scalable Synthesis of Ouabagenin, A Bioactive Cardenolide. *Science*, **2013**, *339*, 59–63.
7. Jones, R. R., Bergman, R. G. *p*-Benzyne. Generation as an intermediate in a thermal isomerization reaction and trapping evidence for 1,4-benzenediyl structure. *J. Am. Chem. Soc.* **1972**, *94*, 660–661.
8. Bergman, R. G. Reactive 1,4-dehydroaromatics. *Acc. Chem. Res.* **1973**, *6*, 25–31.
9. Darby, N., Kim, C. U., Salaün, J. A., Shelton, K. W., Takada, S., Masamune, S. Concerning the 1,5-didehydro[10]annulene system. *J. Chem. Soc. D*, **1971**, 1516–1517.
10. Wenk, H. H., Winkler, M., Sander, W. One century of aryne chemistry. *Angew. Chem. Int. Ed.* **2003**, *42*, 502–528.
11. Joshi, M. C., Rawat, D. S. Recent Developments in Eneidyne Chemistry. *Chem. Biodivers.* **2012**, *9*, 459–498.
12. Röder, A., Petersen, J., Issler, K., Fischer, I., Mitrić, R., Poisson, L. Exploring the Excited-State Dynamics of Hydrocarbon Radicals, Biradicals, and Carbenes Using Time-Resolved Photoelectron Spectroscopy and Field-Induced Surface Hopping Simulations. *J. Phys. Chem. A* **2019**, *123*, 10643–10662.
13. Pilling, M. J. Reactions of Hydrocarbon Radicals and Biradicals. *J. Phys. Chem. A* **2013**, *117*, 3697–3717.

14. Grosjean, E., Grosjean, D. Carbonyl products of the gas phase reaction of ozone with 1,1-disubstituted alkenes. *J. Atmos. Chem.* **1996**, *24*, 141–156.
15. Grosjean, D., Grosjean, E., Williams, E. L. Atmospheric Chemistry of Olefins: A Product Study of the Ozone–Alkene Reaction with Cyclohexane Added to Scavenge Hydroxyl Radical. *Environ. Sci. Technol.* **1994**, *28*, 186–196.
16. Ishida, M., Shin, J. Y., Lim, J. M., Lee, B. S., Yoon, M. C., Koide, T., Sessler, J. L., Osuka, A., Kim, D. Neutral Radical and Singlet Biradical Forms of Meso–Free, –Keto, and –Diketo Hexaphyrins(1.1.1.1.1.1): Effects on Aromaticity and Photophysical Properties. *J. Am. Chem. Soc.* **2011**, *133*, 15533–15544.
17. Nakano, M., Fukuda, K., Champagne, B. Third–Order Nonlinear Optical Properties of Asymmetric Non–Alternant Open-shell Condensed–Ring Hydrocarbons: Effects of Diradical Character, Asymmetry, and Exchange Interaction. *J. Phys. Chem. C* **2016**, *120*, 1193–1207.
18. Morita, Y., Nishida, S., Murata, T., Moriguchi, M., Ueda, A., Satoh, M., Arifuku, K., Sato, K., Takui, T. Organic tailored batteries materials using stable open-shell molecules with degenerate frontier orbitals. *Nat. Mater.* **2011**, *10*, 947–951.
19. Nesvadba, P., Bugnon, L., Maire, P., Novák, P. Synthesis of A Novel Spirobisnitroxide Polymer and its Evaluation in an Organic Radical Battery. *Chem. Mater.* **2010**, *22*, 783–788.
20. Varnavski, O., Abeyasinghe, N., Aragó, J., Serrano–Pérez, J. J., Ortí, E., Navarrete, J. T. L., Takimiya, K., Casanova, D., Casado, J., Goodson, T. High Yield Ultrafast Intramolecular Singlet Exciton Fission in a Quinoidal Bithiophene. *J. Phys. Chem. Lett.* **2015**, *6*, 1375–1384.
21. Shil, S., Bhattacharya, D., Misra, A., Klein, D. J. A high–spin organic diradical as a spin filter. *Phys. Chem. Chem. Phys.* **2015**, *17*, 23378–23383.
22. Sun, Z., Huang, K.–W., Wu, J. Soluble and Stable Heptazethrenebis(dicarboximide) with a Singlet Open-shell Ground State. *J. Am. Chem. Soc.* **2011**, *133*, 11896–11899.
23. Schmidt, D., Son, M., Lim, J. M., Lin, M. J., Krummenacher, I., Braunschweig, H., Kim, D., Würthner, F. Perylene Bisimide Radicals and Biradicals: Synthesis and Molecular Properties. *Angew. Chem. Int. Ed.* **2015**, *54*, 13980–13984.
24. Lee, S., Miao, F., Phan, H., Heng, T. S., Ding, J., Wu, J., Kim, D. Radical and Diradical Formation in Naphthalene Diimides through Simple Chemical Oxidation. *ChemPhysChem* **2017**, *18*, 591–595.
25. Ma, J., Liu, J. Z., Baumgarten, M., Fu, Y. B., Tan, Y.–Z., Schellhammer, K. S., Ortmann, F., Cuniberti, G., Komber, H., Berger, R., Müllen, K., Feng, X. A Stable Saddle–Shaped Polycyclic Hydrocarbon with an Open-shell Singlet Ground State. *Angew. Chem. Int. Ed.* **2017**, *56*, 3280–3284.
26. West, R., Jorgenson, J. A., Stearley, K. L., Calabrese, J. C. Synthesis, Structure and Semiconductivity of a *p*–Terphenoquinone. *J. Chem. Soc., Chem. Commun.* **1991**, 1234–1235.

27. Zhou, J., Rieker, A. Electrochemical and spectroscopic properties of a series of *tert*-butyl-substituted *para*-extended quinones. *J. Chem. Soc., Perkin Trans. 2*, **1997**, 2795–2795.
28. Hu, P., Wu, J. Modern zethrene chemistry. *Can. J. Chem.* **2017**, *95*, 223–233.
29. Li, Y., Heng, W.-K., Lee, B. S., Aratani, N., Zafra, J. L., Bao, N., Lee, R., Sung, Y. M., Sun, Z., Huang, K.-W., Webster, R. D., Navarrete, J. T. L., Kim, D., Osuka, A., Casado, J., Ding, J., Wu, J. Kinetically Blocked Stable Heptazethrene and Octazethrene: Closed-shell or Open-shell in the Ground State? *J. Am. Chem. Soc.* **2012**, *134*, 14913–14922.
30. Ravat, P., Šolomek, T., Häussinger, D., Blacque, O., Juríček, M. Dimethylcethrene: A Chiroptical Diradicaloid Photoswitch. *J. Am. Chem. Soc.* **2018**, *140*, 10839–10847.
31. Hu, P., Lee, S., Park, K. H., Das, S., Heng, T. S., Gonçalves, T.P., Huang, K.W., Ding, J., Kim, D., Wu, J. Octazethrene and Its Isomer with Different Diradical Characters and Chemical Reactivity: The Role of the Bridge Structure. *J. Org. Chem.* **2016**, *81*, 2911–2919.
32. Rudebusch, G. E., Zafra, J. L., Jorner, K., Fukuda, K., Marshall, J. L., Arrechea-Marcos, I., Espejo, G. L., Ortiz, R. P., Gómez-García, C. J., Zakharov, L. N., Nakano, M., Ottosson, H., Casado, J., Haley, M. M. Diindeno-fusion of an anthracene as a design strategy for stable organic biradicals. *Nat. Chem.* **2016**, *8*, 753–759.
33. Dressler, J. J., Zhou, Z., Marshall, J. L., Kishi, R., Takamuku, S., Wei, Z., Spisak, S. N., Nakano, M., Petrukhina, M. A., Haley, M. M. Synthesis of the Unknown Indeno[1,2-*a*]fluorene Regioisomer: Crystallographic Characterization of Its Dianion. *Angew. Chem. Int. Ed.* **2017**, *56*, 15363–15367.
34. Frederickson, C. K., Rose, B. D., Haley, M. M. Explorations of the Indenofluorenes and Expanded Quinoidal Analogues. *Acc. Chem. Res.* **2017**, *50*, 977–987.
35. Nieman, R., Silva, N. J., Aquino, A. J. A., Haley, M. M., Lischka, H. Interplay of Biradicaloid Character and Singlet/Triplet Energy Splitting for *cis*-/*trans*-Diindenoacenes and Related Benzothiophene-Capped Oligomers as Revealed by Extended Multireference Calculations. *J. Org. Chem.* **2020**, *85*, 3664–3675.
36. Dressler, J. J., Valdivia, A. C., Kishi, R., Rudebusch, G. E., Ventura, A. M., Chastain, B. E., Gómez-García, C. J., Zakharov, L. N., Nakano, M., Casado, J., Haley, M. M. Diindenoanthracene Diradicaloids Enable Rational, Incremental Tuning of Their Singlet–Triplet Energy Gaps. *Chem* **2020**, *6*, 1353–1368.
37. Canesi, E. V., Fazzi, D., Colella, L., Bertarelli, C., Castiglioni, C. Tuning the Quinoid versus Biradicaloid Character of Thiophene-Based Heteroquaterphenoquinones by Means of Functional Groups. *J. Am. Chem. Soc.* **2012**, *134*, 19070–19083.
38. Clar, E., Macpherson, I., Schulz-Kiesow, H. Die Bedeutung der Kekulé-Strukturen für die Stabilität der aromatischen Systeme, III. Benzozethren- und Dibenzozethren-Derivate. *Liebigs Ann. Chem.* **1963**, *669*, 44–52.
39. Clar, E. The Aromatic Sextet. **1972**, Wiley, London.

40. Clar, E., Lang, K. F., Schulz–Kiesow, H. Aromatische Kohlenwasserstoffe, LXX. Mitteil. Zethren (1.12;6.7–Dibenzotetracen. *Chem. Ber.* **1955**, 88, 1520–1527.
41. Müller, U. Dissertation, **2021**, Universität Würzburg.
42. Salem, L., Rowland, C. Electronic Properties of Diradicals. *Angew. Chem. Int. Ed.* **1972**, 11, 92–111.
43. Bonačić–Koutecký, V., Koutecký, J., Michl, J. Neutral and Charged Biradicals, Zwitterions, Funnels in S_1 , and Proton Translocation: Their Role in Photochemistry, Photophysics, and Vision. *Angew. Chem. Int. Ed.* **1987**, 26, 170–189.
44. Kanno, F., Inoue, K., Koga, N., Iwamura, H. 4,6–Dimethoxy–1,3–Phenylenebis(*N*–*tert*–butyl nitroxide) with a Singlet Ground State. Formal Violation of a Rule That *m*–Phenylene Serves as a Robust Ferromagnetic Coupling Unit. *J. Am. Chem. Soc.* **1993**, 115, 847–850.
45. Kolc, J. Michl, J. π,π –Biradicaloid Hydrocarbons. Pleiadene Family. I. Photochemical Preparation from Cyclobutene Precursors. *J. Am. Chem. Soc.* **1973**, 95, 7391–7401.
46. Muller, P. Glossary of Terms Used in Physical Organic–Chemistry. *Pure Appl. Chem.* **1994**, 66, 1077–1184.
47. Moss, G. P., Smith, P. A. S., Tavernier, D. Glossary of Class Names of Organic Compounds and Reactive Intermediates Based on Structure. *Pure Appl. Chem.* **1995**, 67, 1307–1375.
48. Braslavsky, S. E. Glossary of terms used in Photochemistry. *Pure Appl. Chem.* **2007**, 79, 293–465.
49. Schmidt, O. Die inneren Energie–Verhältnisse und die Substitutions–Regelmäßigkeiten bei aromatischen, carbocyclischen Substanzen. *Ber. Dtsch. Chem. Ges.* **1934**, 67, 1870–1888.
50. Montgomery, L. K., Huffman, J. C., Jurczak, E. A., Grendze, M. P. The Molecular Structures of Thiele’s and Chichibabin’s Hydrocarbons. *J. Am. Chem. Soc.* **1986**, 108, 6004–6011.
51. Gleicher, G. J., Newkirk, D. D., Arnold, J. C. Calculations on Quinonoid Compounds. I. Quinododimethides. *J. Am. Chem. Soc.* **1973**, 95, 2526–2531.
52. Döhnert, D., Koutecký, J. Occupation Numbers of Natural Orbitals as a Criterion for Biradical Character. Different Kinds of Biradicals. *J. Am. Chem. Soc.* **1980**, 102, 1789–1796.
53. Said, M., Maynau, D., Malrieu, J. P., Bach, M. A. G. A Nonempirical Heisenberg Hamiltonian for the Study of Conjugated Hydrocarbons. Ground–State Conformational Studies. *J. Am. Chem. Soc.* **1984**, 106, 571–579.
54. Slipchenko, L. V., Krylov, A. I. Electronic structure of the trimethylenemethane diradical in its ground and electronically excited states: Bonding, equilibrium geometries, and vibrational frequencies. *J. Chem. Phys.* **2003**, 118, 6874–6883.
55. Seeger, D. E., Lahti, P. M., Rossi, A. R., Berson, J. A. Synthesis of Two Bis–*m*–Quinomethanes. An Experimental Study of Connectivity Effects on the Equal–Parity Criterion for Low–Spin Ground–States in Alternant Non–Kekulé Molecules. *J. Am. Chem. Soc.* **1986**, 108, 1251–1265.

56. Doerr, R. G., Skell, P. S. Trimethylenemethane, $C(CH_2)_3$. *J. Am. Chem. Soc.* **1967**, *89*, 3062–3064.
57. Crawford, R. J., Chang, M. H. Evidence for Diazenyl Allyl Diradicals in the Thermolysis of 4-Alkylidene-1-Pyrazolines. *Tetrahedron* **1982**, *38*, 837–842.
58. LeFevre, G. N., Crawford, R. J. Intramolecular Steric Factors in the Thermolysis of 4-Alkylidene-1-Pyrazolines. *J. Am. Chem. Soc.* **1986**, *108*, 1019–1027.
59. Rottschäfer, D., Ho, N. K. T., Neumann, B., Stammler, H.–G., van Gastel, M., Andrada, D. M., Ghadwal, R. S. N-Heterocyclic Carbene Analogues of Thiele and Chichibabin Hydrocarbons. *Angew. Chem. Int. Ed.* **2018**, *57*, 5838–5842.
60. Rottschäfer, D., Neumann, B., Stammler, H.–G., Andrada, D. M., Ghadwal, R.S. Kekule diradicaloids derived from a classical N-heterocyclic carbene. *Chem. Sci.* **2018**, *9*, 4970–4976.
61. Rottschäfer, D., Busch, J., Neumann, B., Stammler, H.–G., van Gastel, M., Kishi, R., Nakano, M., Ghadwal, R. S. Diradical Character Enhancement by Spacing: N-Heterocyclic Carbene Analogues of Müller's Hydrocarbon. *Chem. Eur. J.* **2018**, *24*, 16537–16542.
62. Kamada, K., Ohta, K., Shimizu, A., Kubo, T., Kishi, R., Takahashi, H., Botek, E., Champagne, B., Nakano, M. Singlet Diradical Character from Experiment. *J. Phys. Chem. Lett.* **2010**, *1*, 937–940.
63. Thiele, J., Balhorn, H., Über einen chinoiden Kohlenwasserstoff. *Chem. Ber.* **1904**, *37*, 1463–1470.
64. Tschitschibabin, A. E. Über einige phenylierte Derivate des *p,p*-Ditolyls. *Ber. Dtsch. Chem. Ges.* **1907**, *40*, 1810–1819.
65. Gomberg, M., An Instance of Trivalent Carbon: Triphenylmethyl. *J. Am. Chem. Soc.* **1900**, *22*, 757–771.
66. Lankamp, H., Nauta, W. T., MacLean, C. A New Interpretation of Monomer–Dimer Equilibrium of Triphenylmethyl- and Alkylsubstituted–Diphenyl Methyl–Radicals in Solution. *Tetrahedron Lett.* **1968**, *9*, 249–254.
67. Smith, W. B. Hexaphenylethane Landmark Falls. *J. Chem. Educ.* **1970**, *47*, 535–536.
68. Sloan, G. J., Vaughan, W. R. Stable Organic Biradicals. *J. Org. Chem.* **1957**, *22*, 750–761.
69. Porter, W. W., Vaid, T. P., Rheingold, A. L. Synthesis and characterization of a highly reducing neutral "extended viologen" and the isostructural hydrocarbon 4,4''-Di-*n*-octyl-*p*-quaterphenyl. *J. Am. Chem. Soc.* **2005**, *127*, 16559–16566.
70. Müller, E., Pfanz, H. Über biradikaloide Terphenylderivate. *Ber. Dtsch. Chem. Ges.* **1941**, *74*, 1051–1074.
71. Schmidt, R., Brauer, H.–D. Energetic Positions of Lowest Singlet and Triplet State of Schlenk and of Müller Hydrocarbon. *Angew. Chem. Int. Ed.* **1971**, *10*, 506–507.

72. Veciana, J., Rovira, C., Crespo, M. I., Armet, O., Domingo, V. M., Palacio, F. Stable Polyradicals with High-Spin Ground-States. 1. Synthesis, Separation, and Magnetic Characterization of the Stereoisomers of 2,4,5,6-Tetrachloro- $\alpha,\alpha,\alpha',\alpha'$ -Tetrakis(Pentachlorophenyl)-*m*-Xylylene Biradical. *J. Am. Chem. Soc.* **1991**, *113*, 2552–2561.
73. Kanal, F., Ruetzel, S., Lu, H., Moos, M., Holzapfel, M., Brixner, T., Lambert, C. Measuring Charge-Separation Dynamics via Oligomer Length Variation. *J. Phys. Chem. C* **2014**, *118*, 23586–23598.
74. Zeng, Z., Sung, Y. M., Bao, N., Tan, D., Lee, R., Zafra, J. L., Lee, B. S., Ishida, M., Ding, J., Navarrete, J. T. L., Li, Y., Zeng, W., Kim, D., Huang, K.-W., Webster, R. D., Casado, J., Wu, J. Stable Tetrabenzochichibabin's Hydrocarbons: Tunable Ground State and Unusual Transition between Their Closed-shell and Open-shell Resonance Forms. *J. Am. Chem. Soc.* **2012**, *134*, 14513–14525.
75. Nishiuchi, T., Ito, R., Stratmann, E., Kubo, T. Switchable Conformational Isomerization of an Overcrowded Trisicyclic Aromatic Ene. *J. Org. Chem.* **2020**, *85*, 179–186.
76. Xiao, S., Kang, S. J., Wu, Y., Ahn, S., Kim, J. B., Loo, Y.-L., Siegrist, T., Steigerwald, M. L., Li, H., Nuckolls, C. Supersized contorted aromatics. *Chem. Sci.* **2013**, *4*, 2018–2023.
77. Lim, Z., Zheng, B., Huang, K.-W., Liu, Y., Wu, J. Quinoidal Oligo(9,10-anthryl)s with Chain-Length-Dependent Ground States: A Balance between Aromatic Stabilization and Steric Strain Release. *Chem. Eur. J.* **2015**, *21*, 18724–18729.
78. Zade, S. S., Bendikov, M. Reactivity of acenes: mechanisms and dependence on acene length. *J. Phys. Org. Chem.* **2012**, *25*, 452–461.
79. Schleyer, P. v. R., Manoharan, M., Jiao, H., Stahl, F. The acenes: Is there a relationship between aromatic stabilization and reactivity? *Org. Lett.* **2001**, *3*, 3643–3646.
80. Hückel, E. Quantentheoretische Beiträge zum Benzolproblem. *Z. Phys.* **1931**, *70*, 204–286.
81. Doering, W. v. E., Detert, F. L. Cycloheptatrienylium Oxide. *J. Am. Chem. Soc.* **1951**, *73*, 876–877.
82. Hückel, E. Quantentheoretische Beiträge zum Problem der aromatischen und ungesättigten Verbindungen. *Z. Phys.* **1932**, *76*, 628–648.
83. Setiawan, D., Kraka, E., Cremer, D. Quantitative Assessment of Aromaticity and Antiaromaticity Utilizing Vibrational Spectroscopy. *J. Org. Chem.* **2016**, *81*, 9669–9686.
84. Kalescky, R., Kraka, E., Cremer, D. Description of Aromaticity with the Help of Vibrational Spectroscopy: Anthracene and Phenanthrene. *J. Phys. Chem. A* **2014**, *118*, 223–237.
85. (a) Bendikov, M., Duong, H. M., Starkey, K., Houk, K. N., Carter, E. A., Wudl, F. Oligoacenes: Theoretical prediction of open-shell singlet diradical ground states (vol 126, pg 7416, 2004). *J. Am. Chem. Soc.* **2004**, *126*, 10493–10493; (b) Würthner, F., Schmidt, R. Electronic and Crystal Engineering of Acenes for Solution-Processible Self-Assembling Organic Semiconductors. *ChemPhysChem* **2006**, *7*, 793–797.

86. Krüger, J., García, F., Eisenhut, F., Skidin, D., Alonso, J. M., Guitián, E., Pérez, D., Cuniberti, G., Moresco, F., Peña, D. Decacene: On–Surface Generation. *Angew. Chem. Int. Ed.* **2017**, *56*, 11945–11948.
87. Zuzak, R., Dorel, R., Kolmer, M., Szymonski, M., Godlewski, S., Echavarren, A. M. Higher Acenes by On–Surface Dehydrogenation: From Heptacene to Undecacene. *Angew. Chem. Int. Ed.* **2018**, *57*, 10500–10505.
88. Shen, B., Tatchen, J., Sanchez–Garcia, E., Bettinger, H. F. Evolution of the Optical Gap in the Acene Series: Undecacene. *Angew. Chem. Int. Ed.* **2018**, *57*, 10506–10509.
89. Mondal, R., Tönshoff, C., Khon, D., Neckers, D. C., Bettinger, H. F. Synthesis, Stability, and Photochemistry of Pentacene, Hexacene, and Heptacene: A Matrix Isolation Study. *J. Am. Chem. Soc.* **2009**, *131*, 14281–14289.
90. Müller, M., Maier, S., Tverskoy, O., Rominger, F., Freudenberg, J., Bunz, U. H. F. Tetrabenzononacene: "Butterfly Wings" Stabilize the Core. *Angew. Chem. Int. Ed.* **2020**, *59*, 1966–1969.
91. Kaur, I., Jazdyk, M., Stein, N. N., Prusevich, P., Miller, G. P. Design, Synthesis, and Characterization of a Persistent Nonacene Derivative. *J. Am. Chem. Soc.* **2010**, *132*, 1261–1263.
92. Purushothaman, B., Bruzek, M., Parkin, S. R., Miller, A.–F., Anthony, J. E. Synthesis and Structural Characterization of Crystalline Nonacenes. *Angew. Chem. Int. Ed.* **2011**, *50*, 7013–7017.
93. Bunz, U. H. F. The Larger Linear N–Heteroacenes. *Acc. Chem. Res.* **2015**, *48*, 1676–1686.
94. Liu, Y.–Y., Song, C.–L., Zeng, W.–J., Zhou, K.–G., Shi, Z.–F., Ma, C.–B., Yang, F., Zhang, H.–L., Gong, X. High and Balanced Hole and Electron Mobilities from Ambipolar Thin–Film Transistors Based on Nitrogen–Containing Oligoacenes. *J. Am. Chem. Soc.* **2010**, *132*, 16349–16351.
95. Shi, X., Kueh, W., Zheng, B., Huang, K.–W., Chi, C. Dipolar Quinoidal Acene Analogues as Stable Isoelectronic Structures of Pentacene and Nonacene. *Angew. Chem. Int. Ed.* **2015**, *54*, 14412–14416.
96. Ye, Q., Chang, J., Shi, X., Dai, G., Zhang, W., Huang, K.–W., Chi, C. Stable 7,14–Disubstituted–5,12–Dithiapentacenes with Quinoidal Conjugation. *Org. Lett.* **2014**, *16*, 3966–3969.
97. Dressler, J. J., Teraoka, M., Espejo, G. L., Kishi, R., Takamuku, S., Gómez–García, C. J., Zakharov, L. N., Nakano, M., Casado, J., Haley, M. M. Thiophene and its sulfur inhibit indenoindenodibenzothiophene diradicals from low–energy lying thermal triplets. *Nat. Chem.* **2018**, *10*, 1134–1140.
98. Motomura, S., Nakano, M., Fukui, H., Yoneda, K., Kubo, T., Carion, R., Champagne, B. Size dependences of the diradical character and the second hyperpolarizabilities in dicyclopenta–fused acenes: relationships with their aromaticity/antiaromaticity. *Phys. Chem. Chem. Phys.* **2011**, *13*, 20575–20583.

99. Fix, A. G., Chase, D. T., Haley, M. M. Indenofluorenes and Derivatives: Syntheses and Emerging Materials Applications. Polyarenes I, *Top. Curr. Chem.* **2014**, *349*, 159–195.
100. Shimizu, A., Tobe, Y. Indeno[2,1-*a*]fluorene: An Air-Stable *ortho*-Quinodimethane Derivative. *Angew. Chem. Int. Ed.* **2011**, *50*, 6906–6910.
101. Shimizu, A., Kishi, R., Nakano, M., Shiomi, D., Sato, K., Takui, T., Hisaki, I., Miyata, M., Tobe, Y. Indeno[2,1-*b*]fluorene: A 20- π -Electron Hydrocarbon with Very Low-Energy Light Absorption. *Angew. Chem. Int. Ed.* **2013**, *52*, 6076–6079.
102. Ovchinnikov, A. A. Multiplicity of Ground-State of Large Alternant Organic-Molecules with Conjugated Bonds. *Theor. Chim. Acta* **1978**, *47*, 297–304.
103. Barker, J. E., Dressler, J. J., Valdivia, A. C., Kishi, R., Strand, E. T., Zakharov, L. N., MacMillan, S. N., Gómez-García, C. J., Nakano, M., Casado, J., Haley, M. M. Molecule Isomerism Modulates the Diradical Properties of Stable Singlet Diradicaloids. *J. Am. Chem. Soc.* **2020**, *142*, 1548–1555.
104. Zeidell, A. M., Jennings, L., Frederickson, C. K., Ai, Q., Dressler, J. J., Zakharov, L. N., Risko, C., Haley, M. M., Jurchescu, O. D. Organic Semiconductors Derived from Dinaphtho-Fused *s*-Indacenes: How Molecular Structure and Film Morphology Influence Thin-Film Transistor Performance. *Chem. Mater.* **2019**, *31*, 6962–6970.
105. Dressler, J. J., Haley, M. M. Learning how to fine-tune diradical properties by structure refinement. *J. Phys. Org. Chem.* **2020**, *33*, e4114.
106. Ravat, P., Ribar, P., Rickhaus, M., Häussinger, D., Neuburger, M., Juriček, M. Spin-Delocalization in a Helical Open-shell Hydrocarbon. *J. Org. Chem.* **2016**, *81*, 12303–12317.
107. Kubo, T., Shimizu, A., Uruichi, M., Yakushi, K., Nakano, M., Shiomi, D., Sato, K., Takui, T., Morita, Y., Nakasuji, K. Singlet biradical character of phenalenyl-based Kekule hydrocarbon with naphthoquinoid structure. *Org. Lett.* **2007**, *9*, 81–84.
108. Koike, H., Chikamatsu, M., Azumi, R., Tsutsumi, J., Ogawa, K., Yamane, W., Nishiuchi, T., Kubo, T., Hasegawa, T., Kanai, K. Stable Delocalized Singlet Biradical Hydrocarbon for Organic Field-Effect Transistors. *Adv. Funct. Mater.* **2016**, *26*, 277–283.
109. Kubo, T., Shimizu, A., Sakamoto, M., Uruichi, M., Yakushi, K., Nakano, M., Shiomi, D., Sato, K., Takui, T., Morita, Y., Nakasuji, K. Synthesis, intermolecular interaction, and semiconductive behavior of a delocalized singlet biradical hydrocarbon. *Angew. Chem. Int. Ed.* **2005**, *44*, 6564–6568.
110. Shimizu, A., Hirao, Y., Matsumoto, K., Kurata, H., Kubo, T., Uruichi, M., Yakushi, K. Aromaticity and π -bond covalency: prominent intermolecular covalent bonding interaction of a Kekulé hydrocarbon with very significant singlet biradical character. *Chem. Commun.* **2012**, *48*, 5629–5631.
111. Wu, T.-C., Chen, C.-H., Hibi, D., Shimizu, A., Tobe, Y., Wu, Y.-T. Synthesis, Structure, and Photophysical Properties of Dibenzo[*de,mn*]naphthacenes. *Angew. Chem. Int. Ed.* **2010**, *49*, 7059–7062.

112. Sun, Z., Huang, K.-W., Wu, J. Soluble and Stable Zethrenebis(dicarboximide) and Its Quinone. *Org. Lett.* **2010**, *12*, 4690–4693.
113. Feng, J., Gopalakrishna, T. Y., Phan, H., Wu, J. Hexakis(3,6-di-*tert*-butyl-4-oxo-2,5-cyclohexadien-1-ylidene)cyclohexane: Closed-shell [6]Radialene or Open-shell Hexa-Radicaloid? *Chem. Eur. J.* **2018**, *24*, 9499–9503.
114. Kikuchi, A., Iwahori, F., Abe, J. Definitive evidence for the contribution of biradical character in a closed-shell molecule, derivative of 1,4-bis-(4,5-diphenylimidazol-2-ylidene)cyclohexa-2,5-diene. *J. Am. Chem. Soc.* **2004**, *126*, 6526–6527.
115. Melidonie, J., Dmitrieva, E., Zhang, K., Fu, Y., Popov, A. A., Pisula, W., Berger, R., Liu, J., Feng, X. Dipyrrene-Fused Dicyclopenta[*a,f*]naphthalenes. *J. Org. Chem.* **2020**, *85*, 215–223.
116. Segura, J. L., Martín, N. *o*-Quinodimethanes: Efficient intermediates in organic synthesis. *Chem. Rev.* **1999**, *99*, 3199–3246.
117. Sato, C., Suzuki, S., Kozaki, M., Okada, K. 2,11-Dibromo-13,14-dimesityl-5,8-dioxapentaphene: A Stable and Twisted Polycyclic System Containing the *o*-Quinodimethane Skeleton. *Org. Lett.* **2016**, *18*, 1052–1055.
118. Zeng, W., Sun, Z., Herng, T. S., Gonçalves, T. P., Gopalakrishna, T. Y., Huang, K.-W., Ding, J., Wu, J. Super-heptazethrene. *Angew. Chem. Int. Ed.* **2016**, *55*, 8615–8619.
119. Zeng, W., Gopalakrishna, T. Y., Phan, H., Tanaka, T., Herng, T. S., Ding, J., Osuka, A., Wu, J. Superoctazethrene: An Open-shell Graphene-like Molecule Possessing Large Diradical Character but Still with Reasonable Stability. *J. Am. Chem. Soc.* **2018**, *140*, 14054–14058.
120. Huang, R., Phan, H., Herng, T. S., Hu, P., Zeng, W., Dong, S.-Q., Das, S., Shen, Y., Ding, J., Casanova, D., and Wu, J. Higher Order π -Conjugated Polycyclic Hydrocarbons with Open-shell Singlet Ground State: Nonazethrene versus Nonacene. *J. Am. Chem. Soc.* **2016**, *138*, 10323–10330.
121. Casado, J. *Para*-Quinodimethanes: A Unified Review of the Quinoidal-Versus-Aromatic Competition and its Implications. *Top. Curr. Chem.* **2017**, *375*, 73.
122. Hirsch, F., Pachner, K., Fischer, I., Issler, K., Petersen, J., Mitrić, R., Bakels, S., Rijs, A. M. Do Xylylenes Isomerize in Pyrolysis? *ChemPhysChem* **2020**, *21*, 1515–1518.
123. Hirsch, F., Flock, M., Fischer, I., Bakels, S., Rijs, A. M. The Gas-Phase Infrared Spectra of Xylyl Radicals. *J. Phys. Chem. A* **2019**, *123*, 9573–9578.
124. Iwatsuki, S. Polymerization of Quinodimethane Compounds. *Adv. Polym. Sci.* **1984**, *58*, 93–120.
125. Reilly, N. J., da Silva, G., Wilcox, C. M., Ge, Z., Kokkin, D. L., Troy, T. P., Nauta, K., Kable, S. H., McCarthy, M. C., Schmidt, T. W. Interconversion of Methyltropylium and Xylyl Radicals: A Pathway Unavailable to the Benzyl-Tropylium Rearrangement. *J. Phys. Chem. A* **2018**, *122*, 1261–1269.

126. Li, Z., Gopalakrishna, T. Y., Han, Y., Gu, Y., Yuan, L., Zeng, W., Casanova, D., Wu, J. [6]Cyclo-*para*-phenylmethine: An Analog of Benzene Showing Global Aromaticity and Open-shell Diradical Character. *J. Am. Chem. Soc.* **2019**, *141*, 16266–16270.
127. Liu, C., Sandoval–Salinas, M. E., Hong, Y., Gopalakrishna, T. Y., Phan, H., Aratani, N., Herng, T. S., Ding, J., Yamada, H., Kim, D., Casanova, D., Wu, J. Macrocyclic Polyradicaloids with Unusual Super–ring Structure and Global Aromaticity. *Chem* **2018**, *4*, 1586–1595.
128. Baird, N. C. Quantum Organic Photochemistry. II. Resonance and Aromaticity in Lowest $^3\pi\pi^*$ State of Cyclic Hydrocarbons. *J. Am. Chem. Soc.* **1972**, *94*, 4941–4948.
129. Ottosson, H. Organic photochemistry: Exciting excited–state aromaticity. *Nat. Chem.* **2012**, *4*, 969–971.
130. Mandado, M., Graña, A. M., Pérez–Juste, I. Aromaticity in spin–polarized systems: Can rings be simultaneously alpha aromatic and beta antiaromatic? *J. Chem. Phys.* **2008**, *129*, 164114.
131. Takahashi, T., Matsuoka, K.–I., Takimiya, K., Otsubo, T., Aso, Y. Extensive quinoidal oligothiophenes with dicyanomethylene groups at terminal positions as highly amphoteric redox molecules. *J. Am. Chem. Soc.* **2005**, *127*, 8928–8929.
132. Asoh, T., Kawabata, K., Takimiya, K. Carbonyl–Terminated Quinoidal Oligothiophenes as *p*–Type Organic Semiconductors. *Materials* **2020**, *13*, 3020.
133. Takimiya, K., Kawabata, K. Thienoquinoidal System: Promising Molecular Architecture for Optoelectronic Applications. *J. Synth. Org. Chem., Jpn.* **2018**, *76*, 1176–1184.
134. Lin, Z., Chen, L., Xu, Q., Shao, G., Zeng, Z., Wu, D., Xia, J. Tuning Biradical Character to Enable High and Balanced Ambipolar Charge Transport in a Quinoidal π –System. *Org. Lett.* **2020**, *22*, 2553–2558.
135. Zeng, Z., Ishida, M., Zafra, J. L., Zhu, X., Sung, Y. M., Bao, N., Webster, R. D., Lee, B. S., Li, R.–W., Zeng, W., Li, Y., Chi, C., Navarrete, J. T. L., Ding, J., Casado, J., Kim, D., Wu, J. Pushing Extended *p*–Quinodimethanes to the Limit: Stable Tetracyano–oligo(*N*–annulated perylene)quinodimethanes with Tunable Ground States. *J. Am. Chem. Soc.* **2013**, *135*, 6363–6371.
136. Zeng, Z., Lee, S., Zafra, J. L., Ishida, M., Bao, N., Webster, R. D., Navarrete, J. T. L., Ding, J., Casado, J., Kim, D., Wu, J. Turning on the biradical state of tetracyano–perylene and quaterrylenequinodimethanes by incorporation of additional thiophene rings. *Chem. Sci.* **2014**, *5*, 3072–3080.
137. Zeng, Z., Lee, S., Zafra, J. L., Ishida, M., Zhu, X., Sun, Z., Ni, Y., Webster, R. D., Li, R.–W., Navarrete, J. T. L., Chi, C., Ding, J., Casado, J., Kim, D., Wu, J. Tetracyanoquaterrylene and Tetracyanohexarylenequinodimethanes with Tunable Ground States and Strong Near–Infrared Absorption. *Angew. Chem. Int. Ed.* **2013**, *52*, 8561–8565.
138. Zeng, Z., Lee, S., Son, M., Fukuda, K., Burrezo, P. M., Zhu, X., Qi, Q., Li, R.–W., Navarrete, J. T. L., Ding, J., Casado, J., Nakano, M., Kim, D., Wu, J. Push–Pull Type Oligo(*N*–annulated

- perylene)quinodimethanes: Chain Length and Solvent-Dependent Ground States and Physical Properties. *J. Am. Chem. Soc.* **2015**, *137*, 8572–8583.
139. Wang, C., Zang, Y., Qin, Y., Zhang, Q., Sun, Y., Di, C.-A., Xu, W., Zhu, D. Thieno[3,2-*b*]thiophene-Diketopyrrolopyrrole-Based Quinoidal Small Molecules: Synthesis, Characterization, Redox Behavior, and n-Channel Organic Field-Effect Transistors. *Chem. Eur. J.* **2014**, *20*, 13755–13761.
140. Qiao, Y., Guo, Y., Yu, C., Zhang, F., Xu, W., Liu, Y., Zhu, D. Diketopyrrolopyrrole-Containing Quinoidal Small Molecules for High-Performance, Air-Stable, and Solution-Processable n-Channel Organic Field-Effect Transistors. *J. Am. Chem. Soc.* **2012**, *134*, 4084–4087.
141. Ray, S., Sharma, S., Salzner, U., Patil, S. Synthesis and Characterization of Quinoidal Diketopyrrolopyrrole Derivatives with Exceptionally High Electron Affinities. *J. Phys. Chem. C* **2017**, *121*, 16088–16097.
142. Re, R., Pellegrini, N., Proteggente, A., Pannala, A., Yang, M., Rice-Evans, C. Antioxidant activity applying an improved ABTS radical cation decolorization assay. *Free Radic. Biol. Med.* **1999**, *26*, 1231–1237.
143. Traber, M. G., Atkinson, J. Vitamin E, antioxidant and nothing more. *Free Radic. Biol. Med.* **2007**, *43*, 4–15.
144. Barnes, S., Prasain, J., D'Alessandro, T., Arabshahi, A., Botting, N., Lila, M. A., Jackson, G., Janle, E. M., Weaver, C. M. The metabolism and analysis of isoflavones and other dietary polyphenols in foods and biological systems. *Food Funct.* **2011**, *2*, 235–244.
145. Ueda, K., Kawabata, R., Irie, T., Nakai, Y., Tohya, Y., Sakaguchi, T. Inactivation of Pathogenic Viruses by Plant-Derived Tannins: Strong Effects of Extracts from Persimmon (*Diospyros kaki*) on a Broad Range of Viruses. *Plos One* **2013**, *8*, e55343.
146. Trumpower, B. L. The Protonmotive Q-Cycle – Energy Transduction by Coupling of Proton Translocation to Electron-Transfer by the Cytochrome-Bc1 Complex. *J. Biol. Chem.* **1990**, *265*, 11409–11412.
147. Slater, E. C. The Q-Cycle, an Ubiquitous Mechanism of Electron-Transfer. *Trends Biochem. Sci.* **1983**, *8*, 239–242.
148. Iverson, F. Phenolic Antioxidants – Health Protection Branch Studies on Butylated Hydroxyanisole. *Cancer Lett.* **1995**, *93*, 49–54.
149. Burton, G. W., Ingold, K. U. Autoxidation of Biological Molecules. 1. The Antioxidant Activity of Vitamin-E and Related Chain-Breaking Phenolic Antioxidants In Vitro. *J. Am. Chem. Soc.* **1981**, *103*, 6472–6477.
150. Babu, B., Wu, J.-T. Production of Natural Butylated Hydroxytoluene as an Antioxidant by Freshwater Phytoplankton. *J. Phycol.* **2008**, *44*, 1447–1454.

151. Frauscher, M., Agocs, A., Besser, C., Rögner, A., Allmaier, G., Dörr, N. Time-Resolved Quantification of Phenolic Antioxidants and Oxidation Products in a Model Fuel by GC–EI–MS/MS. *Energy Fuels* **2020**, *34*, 2674–2682.
152. Yehye, W. A., Rahman, N. A., Ariffin, A., Hamid, S. B. A., Alhadi, A. A., Kadir, F. A., Yaeghoobi, M. Understanding the chemistry behind the antioxidant activities of butylated hydroxytoluene (BHT): A review. *Eur. J. Med. Chem.* **2015**, *101*, 295–312.
153. Karavalakis, G., Stournas, S. Impact of Antioxidant Additives on the Oxidation Stability of Diesel/Biodiesel Blends. *Energy Fuels* **2010**, *24*, 3682–3686.
154. Campos–Martin, J. M., Blanco–Brieva, G., Fierro, J. L. G. Hydrogen peroxide synthesis: An outlook beyond the anthraquinone process. *Angew. Chem. Int. Ed.* **2006**, *45*, 6962–6984.
155. Takahashi, K., Gunji, A., Yanagi, K., Miki, M. Synthesis of novel heteroquaterphenoquinones and their electrochemical, structural, and spectroscopic characterization. *J. Org. Chem.* **1996**, *61*, 4784–4792.
156. Fazzi, D., Canesi, E. V., Negri, F., Bertarelli, C., Castiglioni, C. Biradicaloid Character of Thiophene-Based Heterophenoquinones: The Role of Electron–Phonon Coupling. *ChemPhysChem* **2010**, *11*, 3685–3695.
157. Tampieri, F., Colella, L., Maghsoumi, A., Martí–Rujas, J., Parisini, E., Tommasini, M., Bertarelli, C., Barbon, A. Meeting the Challenging Magnetic and Electronic Structure of Thiophene-Based Heterophenoquinones. *J. Phys. Chem. C* **2016**, *120*, 5732–5740.
158. Di Motta, S., Negri, F., Fazzi, D., Castiglioni, C., Canesi, E. V. Biradicaloid and Polyenic Character of Quinoidal Oligothiophenes Revealed by the Presence of a Low–Lying Double–Exciton State. *J. Phys. Chem. Lett.* **2010**, *1*, 3334–3339.
159. Intorp, S. N., Hodecker, M., Müller, M., Tverskoy, O., Rosenkranz, M., Dmitrieva, E., Popov, A. A., Rominger, F., Freudenberg, J., Dreuw, A., Bunz, U. H. F. Quinoidal Azaacenes: 99 % Diradical Character. *Angew. Chem. Int. Ed.* **2020**, *59*, 12396–12401.
160. Intorp, S. N., Kushida, S., Dmitrieva, E., Popov, A. A., Rominger, F., Freudenberg, J., Hinkel, F., Bunz, U. H. F. True Blue Through Oxidation—A Thiazulenenic Heterophenoquinone as Electrochrome. *Chem. Eur. J.* **2019**, *25*, 5412–5415.
161. Mitsuoka, M., Sakamaki, D., Fujiwara, H. Tetrathiafulvalene–Inserted Diphenquinone: Synthesis, Structure, and Dynamic Redox Property. *Chem. Eur. J.* **2020**, *26*, 14144–14151.
162. Zhang, K., Huang, K.–W., Li, J., Luo, J., Chi, C., Wu, J. A Soluble and Stable Quinoidal Bisanthene with NIR Absorption and Amphoteric Redox Behavior. *Org. Lett.* **2009**, *11*, 4854–4857.
163. Ueda, A., Nishida, S., Fukui, K., Ise, T., Shiomi, D., Sato, K., Takui, T., Nakasuji, K., Morita, Y. Three–Dimensional Intramolecular Exchange Interaction in a Curved and Nonalternant π –Conjugated System: Corannulene with Two Phenoxy Radicals. *Angew. Chem. Int. Ed.* **2010**, *49*, 1678–1682.

164. Lin, M.-J., Fimmel, B., Radacki, K., Würthner, F. Halochromic Phenolate Perylene Bisimides with Unprecedented NIR Spectroscopic Properties. *Angew. Chem. Int. Ed.* **2011**, *50*, 10847–10850.
165. López-Carballeira, D., Zubiria, M., Casanova, D., Ruipérez, F. Improvement of the electrochemical and singlet fission properties of anthraquinones by modification of the diradical character. *Phys. Chem. Chem. Phys.* **2019**, *21*, 7941–7952.
166. Miao, F., Phan, H., Wu, J. A BODIPY–Bridged Bisphenoxy Diradicaloid: Solvent–Dependent Diradical Character and Physical Properties. *Molecules* **2019**, *24*, 1446.
167. Yang, N. C., Castro, A. J. Synthesis of a Stable Biradical. *J. Am. Chem. Soc.* **1960**, *82*, 6208–6208.
168. Chandross, E. A. Bisgalvinoxyl, a Stable Triplet. *J. Am. Chem. Soc.* **1964**, *86*, 1263–1264.
169. Mukai, K., Tamaki, T. Synthesis and Magnetic–Properties of Stable Crystalline *p*–Phenylenebis(Galvinoxyl) Biradical. *J. Chem. Phys.* **1978**, *68*, 2006–2007.
170. Gallagher, N. M., Olankitwanit, A., Rajca, A. High–Spin Organic Molecules. *J. Org. Chem.* **2015**, *80*, 1291–1298.
171. Wautelet, P., Turek, P., Le Moigne, J. Synthesis of phenyl ethynylene coupled biradicals and polyradicals based on galvinoxyl. *Synthesis* **2002**, 1286–1292.
172. Shultz, D. A., Knox, D. A., Morgan, L. W., Sandberg, K., Tew, G. N. Preparation of *Meso*–Tetra(4–Galvinolphenyl)Porphyrin – a Building Block for Molecular Magnetic Materials. *Tetrahedron Lett.* **1993**, *34*, 3975–3978.
173. Rausch, R., Schmidt, D., Bialas, D., Krummenacher, I., Braunschweig, H., Würthner, F. Stable Organic (Bi)Radicals by Delocalization of Spin Density into the Electron–Poor Chromophore Core of Isoindigo. *Chem. Eur. J.* **2018**, *24*, 3420–3424.
174. Boldt, P., Bruhnke, D., Gerson, F., Scholz, M., Jones, P. G., Bär, F. Synthesis and Structure of a *p*–Terphenoquinone and Paramagnetic Species Derived Therefrom. *Helv. Chim. Acta* **1993**, *76*, 1739–1751.
175. Nelsen, S. F., Weaver, M. N., Telo, J. P. Charge localization in a 17–bond mixed–valence quinone radical anion. *J. Phys. Chem. A* **2007**, *111*, 10993–10997.
176. Beugelmans, R., Bois–Choussy, M. Phenoxide and Naphthoxide Ions as Nucleophiles for $S_{RN}1$ Reactions – Synthesis of Biphenyl and Phenyl naphthyl Derivatives. *Tetrahedron Lett.* **1988**, *29*, 1289–1292.
177. Xue, G., Hu, X., Chen, H., Ge, L., Wang, W., Xiong, J., Miao, F., Zheng, Y. Understanding the nature of quinoidal and zwitterionic states in carbazole-based diradicals. *Chem. Commun.* **2020**, *56*, 5143–5146.

178. Mukai, K. ESR Studies of Phenoxy Radicals Produced by PbO₂ Oxidation of Hindered Polyphenols. III. *p*- and *m*-Phenylenebisgalvinoxyls, Stable Triplets. *Bull. Chem. Soc. Jpn.* **1975**, *48*, 2405–2408.
179. Kolanji, K., Postulka, L., Wolf, B., Lang, M., Schollmeyer, D., Baumgarten, M. Planar Benzo[1,2-*b*:4,5-*b'*]dithiophene Derivatives Decorated with Nitronyl and Imino Nitroxides. *J. Org. Chem.* **2019**, *84*, 140–149.
180. Ravat, P., Ito, Y., Gorelik, E., Enkelmann, V., Baumgarten, M. Tetramethoxypyrene-Based Biradical Donors with Tunable Physical and Magnetic Properties. *Org. Lett.* **2013**, *15*, 4280–4283.
181. Shimono, S., Tamura, R., Ikuma, N., Takimoto, T., Kawame, N., Tamada, O., Sakai, N., Matsuura, H., Yamauchi, J. Preparation and characterization of new chiral nitronyl nitroxides bearing a stereogenic center in the imidazolyl framework. *J. Org. Chem.* **2004**, *69*, 475–481.
182. Hirel, C., Vostrikova, K. E., Pécaut, J., Ovcharenko, V. I., Rey, P. Nitronyl and imino nitroxides: Improvement of Ullman's procedure and report on a new efficient synthetic route. *Chem. Eur. J.* **2001**, *7*, 2007–2014.
183. Shimizu, A., Ito, A., Teki, Y. Photostability enhancement of the pentacene derivative having two nitronyl nitroxide radical substituents. *Chem. Commun.* **2016**, *52*, 2889–2892.
184. Akpınar, H., Schlueter, J. A., Cassaro, R. A. A., Friedman, J. R., Lahti, P. M. Rigid Core Anthracene and Anthraquinone Linked Nitronyl and Imino Nitroxide Biradicals. *Cryst. Growth Des.* **2016**, *16*, 4051–4059.
185. Ullman, E. F., Osiecki, J. H., Boocock, D. G. B., Darcy, R. Stable Free Radicals. X. Nitronyl Nitroxide Monoradicals and Biradicals as Possible Small Molecule Spin Labels. *J. Am. Chem. Soc.* **1972**, *94*, 7049–7059.
186. Hosokoshi, Y., Tamura, M., Sawa, H., Kato, R., Kinoshita, M. 2-Dimensional Ferromagnetic Intermolecular Interactions in Crystals of the *p*-Cyanophenyl Nitronyl Nitroxide Radical. *J. Mater. Chem.* **1995**, *5*, 41–46.
187. Tanimoto, R., Suzuki, S., Kozaki, M., Okada, K. Nitronyl Nitroxide as a Coupling Partner: Pd-Mediated Cross-coupling of (Nitronyl nitroxide-2-ido)(triphenylphosphine)gold(I) with Aryl Halides. *Chem. Lett.* **2014**, *43*, 678–680.
188. Haraguchi, M., Tretyakov, E. V., Gritsan, N., Romanenko, G., Gorbunov, D., Bogomyakov, A., Maryunina, K., Suzuki, S., Kozaki, M., Shiomi, D., Sato, K., Takui, T., Nishihara, S., Inoue, K., Okada, K. (Azulene-1,3-diyl)-bis(nitronyl nitroxide) and (Azulene-1,3-diyl)-bis(iminonitroxide) and Their Copper Complexes. *Chem. Asian J.* **2017**, *12*, 2929–2941.
189. Tahara, T., Suzuki, S., Kozaki, M., Shiomi, D., Sugisaki, K., Sato, K., Takui, T., Miyake, Y., Hosokoshi, Y., Nojiri, H., Okada, K. Triplet Diradical-Cation Salts Consisting of the Phenothiazine Radical Cation and a Nitronyl Nitroxide. *Chem. Eur. J.* **2019**, *25*, 7201–7209.

190. Suzuki, S., Nakamura, F., Naota, T. A direct synthetic method for (nitronyl nitroxide)-substituted π -electronic compounds *via* a palladium-catalyzed cross-coupling reaction with a zinc complex. *Mater. Chem. Front.* **2018**, 2, 591–596.
191. Yamada, K., Zhang, X., Tanimoto, R., Suzuki, S., Kozaki, M., Tanaka, R., Okada, K. Radical Metalloids with *N*-Heterocyclic Carbene and Phenanthroline Ligands: Synthesis, Properties, and Cross-Coupling Reaction of [(Nitronyl Nitroxide)-2-ido]metal Complexes with Aryl Halides. *Bull. Chem. Soc. Jpn.* **2018**, 91, 1150–1157.
192. Suzuki, S., Nakamura, F., Naota, T. Environmentally Benign Strategy for Arylation of Nitronyl Nitroxide Using a Non-Transition Metal Nucleophile. *Org. Lett.* **2020**, 22, 1350–1354.
193. Fedyushin, P. A., Panteleeva, E. V., Bagryanskaya, I. Y., Maryunina, K., Inoue, K., Stass, D. V., Tretyakov, E. V. An approach to fluorinated phthalonitriles containing a nitronyl nitroxide or iminonitroxide moiety. *J. Fluor. Chem.* **2019**, 217, 1–7.
194. Tretyakov, E. V., Fedyushin, P. A., Panteleeva, E. V., Stass, D. V., Bagryanskaya, I. Y., Beregovaya, I. V., Bogomyakov, A. S. Substitution of a Fluorine Atom in Perfluorobenzonitrile by a Lithiated Nitronyl Nitroxide. *J. Org. Chem.* **2017**, 82, 4179–4185.
195. Nishide, H., Hozumi, Y., Nii, T., Tsuchida, E. Poly(1,2-phenylenevinylene)s bearing nitronyl nitroxide and galvinoxyl at the 4-position: π -conjugated and non-Kekulé-type polyradicals with a triplet ground state. *Macromolecules* **1997**, 30, 3986–3991.
196. Suga, T., Sugita, S., Ohshiro, H., Oyaizu, K., Nishide, H. p- and n-Type Bipolar Redox-Active Radical Polymer: Toward Totally Organic Polymer-Based Rechargeable Devices with Variable Configuration. *Adv. Mater.* **2011**, 23, 751–754.
197. Kurata, T., Koshika, K., Kato, F., Kido, J., Nishide, H. An unpaired electron-based hole-transporting molecule: Triarylamine-combined nitroxide radicals. *Chem. Commun.* **2007**, 2986–2988.
198. Shinomiya, M., Higashiguchi, K., Matsuda, K. Evaluation of the β Value of the Phenylene Ethynylene Unit by Probing the Exchange Interaction between Two Nitronyl Nitroxides. *J. Org. Chem.* **2013**, 78, 9282–9290.
199. Roques, N., Gerbier, P., Teki, Y., Choua, S., P. Lesniakovà, Sutter, J.-P., Guionneau, P., Guérin, C. Towards a better understanding of photo-excited spin alignment processes using silole diradicals. *New J. Chem.* **2006**, 30, 1319–1326.
200. Maekawa, K., Shiomi, D., Ise, T., Sato, K., Takui, T. A guanine-substituted nitronyl nitroxide radical forming a one-dimensional ferromagnetic chain. *Org. Biomol. Chem.* **2007**, 5, 1641–1645.
201. Okamoto, A., Inasaki, T., Saito, I. Synthesis and ESR studies of nitronyl nitroxide-tethered oligodeoxynucleotides. *Tetrahedron Lett.* **2005**, 46, 791–795.
202. Kolanji, K., Ravat, P., Bogomyakov, A. S., Ovcharenko, V. I., Schollmeyer, D., Baumgarten, M. Mixed Phenyl and Thiophene Oligomers for Bridging Nitronyl Nitroxides. *J. Org. Chem.* **2017**, 82, 7764–7773.

203. Gallagher, N., Zhang, H., Junghoefer, T., Giangrisostomi, E., Ovsyannikov, R., Pink, M., Rajca, S., Casu, M. B., Rajca, A. Thermally and Magnetically Robust Triplet Ground State Diradical. *J. Am. Chem. Soc.* **2019**, *141*, 4764–4774.
204. Wang, D., Ma, Y., Wolf, B., Kokorin, A. I., Baumgarten, M. Temperature-Dependent Intramolecular Spin Coupling Interactions of a Flexible Bridged Nitronyl Nitroxide Biradical in Solution. *J. Phys. Chem. A* **2018**, *122*, 574–581.
205. Matsuda, K., Irie, M. A diarylethene with two nitronyl nitroxides: Photoswitching of intramolecular magnetic interaction. *J. Am. Chem. Soc.* **2000**, *122*, 7195–7201.
206. Matsuda, K., Matsuo, M., Irie, M. Photoswitching of intramolecular magnetic interaction using diarylethene with oligothiophene π -conjugated chain. *J. Org. Chem.* **2001**, *66*, 8799–8803.
207. Matsuda, K., Irie, M. Photochromism of diarylethenes with two nitronyl nitroxides: Photoswitching of an intramolecular magnetic interaction. *Chem. Eur. J.* **2001**, *7*, 3466–3473.
208. Evans, D. F. The Determination of the Paramagnetic Susceptibility of Substances in Solution by Nuclear Magnetic Resonance. *J. Chem. Soc.* **1959**, 2003–2005.
209. Sur, S. K. Measurement of Magnetic Susceptibility and Magnetic Moment of Paramagnetic Molecules in Solution by High-Field Fourier Transform NMR Spectroscopy. *J. Magn. Reson.* **1989**, *82*, 169–173.
210. Grant, D. H. Paramagnetic Susceptibility by NMR: the “Solvent Correction” Reexamined. *J. Chem. Educ.* **1995**, *72*, 39–40.
211. Schubert, E. M. Utilizing the Evans Method with a Superconducting NMR Spectrometer in the Undergraduate Laboratory. *J. Chem. Educ.* **1992**, *69*, 62–62.
212. Hoppeé, J. I. Effective Magnetic Moment. *J. Chem. Educ.* **1972**, *49*, 505–505.
213. Bleaney, B., Bowers, K. D. Anomalous Paramagnetism of Copper Acetate. *Proc. R. Soc. Lond. A* **1952**, *214*, 451–465.
214. Orms, N., Krylov, A. I. Singlet-triplet energy gaps and the degree of diradical character in binuclear copper molecular magnets characterized by spin-flip density functional theory. *Phys. Chem. Chem. Phys.* **2018**, *20*, 13127–13144.
215. Wang, W., Ge, L., Xue, G., Miao, F., Chen, P., Chen, H., Lin, Y., Ni, Y., Xiong, J., Hu, Y., Wu, J., Zheng, Y. Fine-tuning the diradical character of molecular systems *via* the heteroatom effect. *Chem. Commun.* **2020**, *56*, 1405–1408.
216. Shao, Y., Head-Gordon, M., Krylov, A. I. The spin-flip approach within time-dependent density functional theory: Theory and applications to diradicals. *J. Chem. Phys.* **2003**, *118*, 4807–4818.
217. Rudebusch, G. E., Espejo, G. L., Zafra, J. L., Peña-Alvarez, M., Spisak, S. N., Fukuda, K., Wei, Z., Nakano, M., Petrukhina, M. A., Casado, J., Haley, M. M. A Biradical Balancing Act: Redox

- Amphoterism in a Diindenoanthracene Derivative Results from Quinoidal Acceptor and Aromatic Donor Motifs. *J. Am. Chem. Soc.* **2016**, *138*, 12648–12654.
218. Sun, Z., Ye, Q., Chi, C., Wu, J. Low band gap polycyclic hydrocarbons: from closed-shell near infrared dyes and semiconductors to open-shell radicals. *Chem. Soc. Rev.* **2012**, *41*, 7857–7889.
219. Fukuda, K., Fujiyoshi, J.–Y., Matsui, H., Nagami, T., Takamuku, S., Kitagawa, Y., Champagne, B., Nakano, M. A theoretical study on quasi–one–dimensional open-shell singlet ladder oligomers: multi–radical nature, aromaticity and second hyperpolarizability. *Org. Chem. Front.* **2017**, *4*, 779–789.
220. Kamada, K., Ohta, K., Kubo, T., Shimizu, A., Morita, Y., Nakasuji, K., Kishi, R., Ohta, S., Furukawa, S., Takahashi, H., Nakano, M. Strong two–photon absorption of singlet diradical hydrocarbons. *Angew. Chem. Int. Ed.* **2007**, *46*, 3544–3546.
221. Chikamatsu, M., Mikami, T., Chisaka, J., Yoshida, Y., Azumi, R., Yase, K., Shimizu, A., Kubo, T., Morita, Y., Nakasuji, K. Ambipolar organic field–effect transistors based on a low band gap semiconductor with balanced hole and electron mobilities. *Appl. Phys. Lett.* **2007**, *91*, 043506.
222. Ravat, P., Baumgarten, M. "Tschitschibabin type biradicals": benzenoid or quinoid? *Phys. Chem. Chem. Phys.* **2015**, *17*, 983–991.
223. Li, G., Phan, H., Heng, T. S., Gopalakrishna, T. Y., Liu, C., Zeng, W., Ding, J., Wu, J. Toward Stable Superbenzoquinone Diradicaloids. *Angew. Chem. Int. Ed.* **2017**, *56*, 5012–5016.
224. Xia, D., Keerthi, A., An, C., Baumgarten, M. Synthesis of a quinoidal dithieno[2,3–*d*;2',3'–*d*]benzo[2,1–*b*;3,4–*b'*]–dithiophene-based open-shell singlet biradicaloid. *Org. Chem. Front.* **2017**, *4*, 18–21.
225. Zeng, W., Lee, S., Son, M., Ishida, M., Furukawa, K., Hu, P., Sun, Z., Kim, D., Wu, J. Phenalenyl–fused porphyrins with different ground states. *Chem. Sci.* **2015**, *6*, 2427–2433.
226. Kubo, T. Phenalenyl-Based Open-shell Polycyclic Aromatic Hydrocarbons. *Chem. Rec.* **2015**, *15*, 218–232.
227. Zeng, W., Sun, Z., Heng, T. S., Gonçalves, T. P., Gopalakrishna, T. Y., Huang, K.–W., Ding, J., Wu, J. Super–heptazethrene. *Angew. Chem. Int. Ed.* **2016**, *55*, 8615–8619.
228. Zollinger, H. Color Chemistry, Wallimann, P. M. (Editor), 3rd ed., Wiley–VCH, Weinheim, **2003**.
229. Ashizawa, M., Masuda, N., Higashino, T., Kadoya, T., Kawamoto, T., Matsumoto, H., Mori, T. Ambipolar organic transistors based on isoindigo derivatives. *Org. Electron.* **2016**, *35*, 95–100.
230. Estrada, L. A., Stalder, R., Abboud, K. A., Risko, C., Brédas, J.–L., Reynolds, J. R. Understanding the Electronic Structure of Isoindigo in Conjugated Systems: A Combined Theoretical and Experimental Approach. *Macromolecules* **2013**, *46*, 8832–8844.
231. Yue, W., Li, C., Tian, X., Li, W., Neophytou, M., Chen, H., Du, W., Jellett, C., Chen, H.–Y., Onwubiko, A., McCulloch, I. Diazaisoindigo Bithiophene and Terthiophene Copolymers for

- Application in Field-Effect Transistors and Solar Cells. *J. Polym. Sci. Pol. Chem.* **2017**, *55*, 2691–2699.
232. Baumgarten, M. Tuning the Magnetic Exchange Interactions in Organic Biradical Networks. *Phys. Status Solidi B* **2019**, *256*, 1800642.
233. Ratera, I., Veciana, J. Playing with organic radicals as building blocks for functional molecular materials. *Chem. Soc. Rev.* **2012**, *41*, 303–349.
234. Konishi, A., Kubo, T. Benzenoid Quinodimethanes in: Physical organic chemistry of quinodimethanes, Tobe, Y., Kubo, T. (Editors), Springer, Berlin Heidelberg New York, **2018**, p. 69–80.
235. Qiu, S., Wang, C., Xie, S., Huang, X., Chen, L., Zhao, Y., Zeng, Z. Toward helical-shaped diradicaloids: cyclobutenyl *o*-quinodimethane-bridged indeno[1,2-*b*]fluorenes. *Chem. Commun.* **2018**, *54*, 11383–11386.
236. Wang, Q., Hu, P., Tanaka, T., Gopalakrishna, T. Y., Heng, T. S., Phan, H., Zeng, W., Ding, J., Osuka, A., Chi, C., Siegel, J., Wu, J. Curved π -conjugated corannulene dimer diradicaloids. *Chem. Sci.* **2018**, *9*, 5100–5105.
237. Zhou, J., Rieker, A. Electrochemical and spectroscopic properties of a series of *tert*-butyl-substituted *para*-extended quinones. *J. Chem. Soc., Perkin Trans. 2* **1997**, 931–938.
238. Liu, J., Ravat, P., Wagner, M., Baumgarten, M., Feng, X., Müllen, K. Tetrabenz[a,f,j,o]perylene: A Polycyclic Aromatic Hydrocarbon With An Open-shell Singlet Biradical Ground State. *Angew. Chem. Int. Ed.* **2015**, *54*, 12442–12446.
239. Grzybowski, M., Gryko, D. T. Diketopyrrolopyrroles: Synthesis, Reactivity, and Optical Properties. *Adv. Optical Mater.* **2015**, *3*, 280–320.
240. Kaur, M., Choi, D. H. Diketopyrrolopyrrole: brilliant red pigment dye-based fluorescent probes and their applications. *Chem. Soc. Rev.* **2015**, *44*, 58–77.
241. Zhao, C., Guo, Y., Zhang, Y., Yan, N., You, S., Li, W. Diketopyrrolopyrrole-based conjugated materials for non-fullerene organic solar cells. *J. Mater. Chem. A* **2019**, *7*, 10174–10199.
242. Pieczykolan, M., Sadowski, B., Gryko, D. T. An Efficient Method for the Programmed Synthesis of Multifunctional Diketopyrrolopyrroles. *Angew. Chem. Int. Ed.* **2020**, *59*, 7528–7535.
243. Bürckstümmer, H., Weissenstein, A., Bialas, D., Würthner, F. Synthesis and Characterization of Optical and Redox Properties of Bithiophene-Functionalized Diketopyrrolopyrrole Chromophores. *J. Org. Chem.* **2011**, *76*, 2426–2432.
244. Data, P., Kurowska, A., Pluczyk, S., Zassowski, P., Pander, P., Jedrysiak, R., Czwartosz, M., Otulakowski, L., Suwinski, J., Lapkowski, M., Monkman, A. P. Exciplex Enhancement as a Tool to Increase OLED Device Efficiency. *J. Phys. Chem. C* **2016**, *120*, 2070–2078.
245. Gao, X., Hu, Y. Development of n-type organic semiconductors for thin film transistors: a viewpoint of molecular design. *J. Mater. Chem. C* **2014**, *2*, 3099–3117.

246. Zhang, Y., Kim, C., Lin, J., Nguyen, T.-Q. Solution-Processed Ambipolar Field-Effect Transistor Based on Diketopyrrolopyrrole Functionalized with Benzothiadiazole. *Adv. Funct. Mater.* **2012**, *22*, 97–105.
247. He, T., Leowanawat, P., Burschka, C., Stepanenko, V., Stolte, M., Würthner, F. Impact of 2-Ethylhexyl Stereoisomers on the Electrical Performance of Single-Crystal Field-Effect Transistors. *Adv. Mater.* **2018**, *30*, 1804032.
248. Li, W., Hendriks, K. H., Wienk, M. M., Janssen, R. A. J., Diketopyrrolopyrrole Polymers for Organic Solar Cells. *Acc. Chem. Res.* **2016**, *49*, 78–85.
249. Cuesta, V., Vartanian, M., Malhotra, P., Biswas, S., de la Cruz, P., Sharma, G. D., Langa, F. Increase in efficiency on using selenophene instead of thiophene in π -bridges for D- π -DPP- π -D organic solar cells. *J. Mater. Chem. A* **2019**, *7*, 11886–11894.
250. Yue, W., Suraru, S.-L., Bialas, D., Müller, M., Würthner, F. Synthesis and Properties of a New Class of Fully Conjugated Azahexacene Analogues. *Angew. Chem. Int. Ed.* **2014**, *53*, 6159–6162.
251. Grzybowski, M., Glodkowska-Mrowka, E., Stoklosa, T., Gryko, D. T. Bright, Color-Tunable Fluorescent Dyes Based on π -Expanded Diketopyrrolopyrroles. *Org. Lett.* **2012**, *14*, 2670–2673.
252. Fischer, G. M., Daltrozzo, E., Zumbusch, A. Selective NIR chromophores: Bis(Pyrrolopyrrole) Cyanines. *Angew. Chem. Int. Ed.* **2011**, *50*, 1406–1409.
253. Wang, C., Qin, Y., Sun, Y., Guan, Y.-S., Xu, W., Zhu, D. Thiophene-Diketopyrrolopyrrole-Based Quinoidal Small Molecules as Solution-Processable and Air-Stable Organic Semiconductors: Tuning of the Length and Branching Position of the Alkyl Side Chain toward a High-Performance n-Channel Organic Field-Effect Transistor. *ACS Appl. Mater. Interfaces* **2015**, *7*, 15978–15987.
254. Wu, H., Wang, Y., Qiao, X., Wang, D., Yang, X., Li, H. Pyrrolo[3,2-*b*]pyrrole-Based Quinoidal Compounds For High Performance n-Channel Organic Field-Effect Transistor. *Chem. Mater.* **2018**, *30*, 6992–6997.
255. Ren, L., Liu, F., Shen, X., Zhang, C., Yi, Y., Zhu, X. Developing Quinoidal Fluorophores with Unusually Strong Red/Near-Infrared Emission. *J. Am. Chem. Soc.* **2015**, *137*, 11294–11302.
256. Parts of this work were presented at the 18th International Symposium on Novel Aromatic Compounds (ISNA-18) in July 2019 in Sapporo, Japan.
257. Mizuguchi, J., Grubenmann, A., Wooden, G., Rihs, G. Structures of 3,6-Diphenylpyrrolo[3,4-*c*]Pyrrole-1,4-Dione and 2,5-Dimethyl-3,6-Diphenylpyrrolo[3,4-*c*]Pyrrole-1,4-Dione. *Acta Crystallogr. B* **1992**, *48*, 696–700.
258. Celik, S., Ergun, Y., Alp, S. Synthesis and Spectroscopic Studies of 3,6-Diphenyl-2,5-Dihydropyrrolo[3,4-*c*]Pyrrole-1,4-Dione's *N,N'*-Dialkyl Derivatives. *J. Fluoresc.* **2009**, *19*, 829–835.

259. Murai, M., Ku, S.-Y., Treat, N. D., Robb, M. J., Chabynyc, M. L., Hawker, C. J. Modulating structure and properties in organic chromophores: influence of azulene as a building block. *Chem. Sci.* **2014**, *5*, 3753–3760.
260. Kumar, Y., Kumar, S., Bansal, D., Mukhopadhyay, P. Synthesis and Isolation of a Stable Perylenediimide Radical Anion and Its Exceptionally Electron-Deficient Precursor. *Org. Lett.* **2019**, *21*, 2185–2188.
261. Slater, J. C. Quantum Theory of Molecules and Solids, McGraw-Hill, New York, **1974**.
262. Becke, A. D. Density-Functional Exchange-Energy Approximation with Correct Asymptotic-Behavior. *Phys. Rev. A* **1988**, *38*, 3098–3100.
263. Vosko, S. H., Wilk, L., Nusair, M. Accurate Spin-Dependent Electron Liquid Correlation Energies for Local Spin-Density Calculations: a Critical Analysis. *Can. J. Phys.* **1980**, *58*, 1200–1211.
264. Lee, C., Yang, W., Parr, R. G. Development of the Colle-Salvetti Correlation-Energy Formula into a Functional of the Electron-Density. *Phys. Rev. B* **1988**, *37*, 785–789.
265. Weigend, F., Ahlrichs, R. Balanced basis sets of split valence, triple zeta valence and quadruple zeta valence quality for H to Rn: Design and assessment of accuracy. *Phys. Chem. Chem. Phys.* **2005**, *7*, 3297–3305.
266. Roos, B. O. The Complete Active Space Self-Consistent Field Method and its Applications in Electronic Structure Calculations. *Adv. Chem. Phys.* **1987**, *69*, 399–445.
267. Werner, H.-J., Knowles, P. J. A second Order Multiconfiguration SCF Procedure with Optimum Convergence. *J. Chem. Phys.* **1985**, *82*, 5053–5063.
268. Busch, T., Degli Esposti, A., Werner, H.-J. Analytical Energy Gradients for Multiconfiguration Self-Consistent Field Wave-Functions with Frozen Core Orbitals. *J. Chem. Phys.* **1991**, *94*, 6708–6715.
269. Knowles, P. J. Werner, H.-J. An Efficient Second-Order MC SCF Method for Long Configuration Expansions. *Chem. Phys. Lett.* **1985**, *115*, 259–267.
270. Kruszewski, J., Krygowski, T. M. Definition of Aromaticity Basing on Harmonic Oscillator Model. *Tetrahedron Lett.* **1972**, 3839–3842.
271. Krygowski, T. M. Crystallographic Studies of Intermolecular and Intramolecular Interactions Reflected in Aromatic Character of π -Electron Systems. *J. Chem. Inf. Comput. Sci.* **1993**, *33*, 70–78.
272. Ravat, P., Šolomek, T., Rickhaus, M., Häussinger, D., Neuburger, M., Baumgarten, M., Juríček, M. Cethrene: A Helically Chiral Biradicaloid Isomer of Heptazethrene. *Angew. Chem. Int. Ed.* **2016**, *55*, 1183–1186.
273. Giamarchi, T., Rüegg, C., Tchernyshyov, O. Bose-Einstein condensation in magnetic insulators. *Nat. Phys.* **2008**, *4*, 198–204.

274. Petunin, P. V., Rybalova, T. V., Trusova, M. E., Uvarov, M. N., Kazantsev, M. S., Mostovich, E. A., Postulka, L., Eibisch, P., Wolf, B., Lang, M., Postnikov, P. S., Baumgarten, M. A Weakly Antiferromagnetically Coupled Biradical Combining Verdazyl with Nitronyl Nitroxide Units. *ChemPlusChem* **2020**, *85*, 159–162.
275. Nakazaki, J., Chung, I., Matsushita, M. M., Sugawara, T., Watanabe, R., Izuoka, A., Kawada, Y. Design and preparation of pyrrole-based spin-polarized donors. *J. Mater. Chem.* **2003**, *13*, 1011–1022.
276. Sanvito, S. Molecular spintronics. *Chem. Soc. Rev.* **2011**, *40*, 3336–3355.
277. Hiraoka, S., Okamoto, T., Kozaki, M., Shiomi, D., Sato, K., Takui, T., Okada, K. A stable radical-substituted radical cation with strongly ferromagnetic interaction: Nitronyl nitroxide-substituted 5,10-diphenyl-5,10-dihydrophenazine radical cation. *J. Am. Chem. Soc.* **2004**, *126*, 58–59.
278. Nagata, A., Hiraoka, S., Suzuki, S., Kozaki, M., Shiomi, D., Sato, K., Takui, T., Tanaka, R., Okada, K. Redox-Induced Modulation of Exchange Interaction in a High-Spin Ground-State Diradical/Triradical System. *Chem. Eur. J.* **2020**, *26*, 3166–3172.
279. Jaumann, E. A., Steinwand, S., Klenik, S., Plackmeyer, J., Bats, J. W., Wachtveitl, J., Prisner, T. F. A combined optical and EPR spectroscopy study: azobenzene-based biradicals as reversible molecular photoswitches. *Phys. Chem. Chem. Phys.* **2017**, *19*, 17263–17269.
280. Anghel, M., Magnan, F., Catingan, S. D., McCready, M. A., Aawani, E., Wong, V., Singh, D., Fanchini, G., Gilroy, J. B. Redox polymers incorporating pendant 6-oxoverdazyl and nitronyl nitroxide radicals. *J. Polym. Sci.* **2020**, *58*, 309–319.
281. Slota, M., Keerthi, A., Myers, W. K., Tretyakov, E. V., Baumgarten, M., Ardavan, A., Sadeghi, H., Lambert, C. J., Narita, A., Müllen, K., Bogani, L. Magnetic edge states and coherent manipulation of graphene nanoribbons. *Nature* **2018**, *557*, 691–695.
282. Stass, D., Tretyakov, E. V. Estimation of Absolute Spin Counts in Nitronyl Nitroxide-Bearing Graphene Nanoribbons. *Magnetochemistry* **2019**, *5*, 32.
283. Stroh, C., Mayor, M., von Hänisch, C. Suzuki reactions with stable organic radicals – Synthesis of biphenyls substituted with nitronyl-nitroxide radicals. *Eur. J. Org. Chem.* **2005**, 3697–3703.
284. Stroh, C., Mayor, M., von Hänisch, C. Rigid nitronyl-nitroxide-labelled anchoring molecules: syntheses, structural and magnetic investigations. *Tetrahedron Lett.* **2004**, *45*, 9623–9626.
285. Gsänger, M., Bialas, D., Huang, L., Stolte, M., Würthner, F. Organic Semiconductors based on Dyes and Color Pigments. *Adv. Mater.* **2016**, *28*, 3615–3645.
286. Huang, Y., Xu, Z., Jin, S., Li, C., Warncke, K., Evangelista, F. A., Lian, T., Egap, E. Conjugated Oligomers with Stable Radical Substituents: Synthesis, Single Crystal Structures, Electronic Structure, and Excited State Dynamics. *Chem. Mater.* **2018**, *30*, 7840–7851.

287. Önal, E., Yerli, Y., Cosut, B., Pilet, G., Ahsen, V., Luneau, D., Hirel, C. Nitronyl and imino nitroxide free radicals as precursors of magnetic phthalocyanine and porphyrin building blocks. *New J. Chem.* **2014**, *38*, 4440–4447.
288. Barton, T. J., Tully, C. R. Sterically Hindered Silyl Perchlorates as Blocking Reagents. *J. Org. Chem.* **1978**, *43*, 3649–3653.
289. Servis, K. L., Jao, L. Nuclear Magnetic Resonance Studies of Methanol–Boron Trifluoride Complexes. *J. Phys. Chem.* **1972**, *76*, 329–334.
290. Poon, N. L., Satchell, D. P. N. Kinetics and Mechanism of the Addition of Alcohols to Ketenes in Diethyl–Ether Solution in the Presence of Boron–Trifluoride. *J. Chem. Soc., Perkin Trans. 2* **1984**, 1083–1087.
291. Burg, A. B., Bickerton, J. H. Trimethylamine Oxide Boron Fluoride. *J. Am. Chem. Soc.* **1945**, *67*, 2261–2261.
292. Prabhakar, S., Lobo, A. M., Tavares, M. R. Boron Complexes as Control Synthons in Photocyclizations: Improved Phenanthridine Synthesis. *J. Chem. Soc., Chem. Commun.* **1978**, 884–885.
293. Würthner, F. Perylene bisimide dyes as versatile building blocks for functional supramolecular architectures. *Chem. Commun.* **2004**, 1564–1579.
294. Huang, C., Barlow, S., Marder, S. R. Perylene–3,4,9,10–tetracarboxylic Acid Diimides: Synthesis, Physical Properties, and Use in Organic Electronics. *J. Org. Chem.* **2011**, *76*, 2386–2407.
295. Ryu, H. G., Mayther, M. F., Tamayo, J., Azarias, C., Espinoza, E. M., Banasiewicz, M., Łukasiewicz, L. G., Poronik, Y. M., Jeżewski, A., Clark, J., Derr, J. B., Ahn, K. H., Gryko, D. T., Jacquemin, D., Vullev, V. I. Bidirectional Solvatofluorochromism of a Pyrrolo[3,2-*b*]pyrrole–Diketopyrrolopyrrole Hybrid. *J. Phys. Chem. C* **2018**, *122*, 13424–13434.
296. Kolanji, K., Baumgarten, M. Dithienopyrrole Derivatives with Nitronyl Nitroxide Radicals and Their Oxidation to Cationic High–Spin Molecules. *Chem. Eur. J.* **2020**, *26*, 3626–3632.
297. Sun, Z., Lee, S., Park, K. H., Zhu, X., Zhang, W., Zheng, B., Hu, P., Zeng, Z., Das, S., Li, Y., Chi, C., Li, R.–W., Huang, K.–W., Ding, J., Kim, D., Wu, J. Dibenzoheptazethrene Isomers with Different Biradical Characters: An Exercise of Clar's Aromatic Sextet Rule in Singlet Biradicaloids. *J. Am. Chem. Soc.* **2013**, *135*, 18229–18236.
298. Tretyakov, E. V., Okada, K., Suzuki, S., Baumgarten, M., Romanenko, G., Bogomyakov, A., Ovcharenko, V., Synthesis, structure and properties of nitronyl nitroxide diradicals with fused–thiophene couplers. *J. Phys. Org. Chem.* **2016**, *29*, 725–734.
299. Hasegawa, T., Ashizawa, M., Matsumoto, H. Design and structure–property relationship of benzothienoisindigo in organic field effect transistors. *RSC Adv.* **2015**, *5*, 61035–61043.
300. Bernstein, H. J. Bond Distances in Hydrocarbons. *Trans. Faraday Soc.* **1961**, *57*, 1649–1656.

301. Orpen, A. G., Brammer, L., Allen, F. H., Kennard, O., Watson, D. G., Taylor, R. Appendix A: Typical Interatomic Distances in: Organic Compounds and Organometallic Compounds and Coordination Complexes of the d- and f-block metals, in: Bürgi, H.-B., Dunitz, J. D. (Editors), *Structure Correlation*, Vol. 2., Wiley-VCH, Weinheim, **1994**.
302. Arjona-Esteban, A., Stolte, M., Würthner, F. Conformational Switching of π -Conjugated Junctions from Merocyanine to Cyanine States by Solvent Polarity. *Angew. Chem. Int. Ed.* **2016**, *55*, 2470–2473.
303. Würthner, F., Stepanenko, V., Chen, Z., Saha-Möller, C. R., Kocher, N., Stalke, D. Preparation and characterization of regioisomerically pure 1,7-disubstituted perylene bisimide dyes. *J. Org. Chem.* **2004**, *69*, 7933–7939.
304. Mei, J., K. R., Graham, Stalder, R., Reynolds, J. R. Synthesis of Isoindigo-Based Oligothiophenes for Molecular Bulk Heterojunction Solar Cells. *Org. Lett.* **2010**, *12*, 660–663.
305. Li, Y., Li, H., Chen, H., Wan, Y., Li, N., Xu, Q., He, J., Chen, D., Wang, L., Lu, J. Controlling Crystallite Orientation of Diketopyrrolopyrrole-Based Small Molecules in Thin Films for Highly Reproducible Multilevel Memory Device: Role of Furan Substitution. *Adv. Funct. Mater.* **2015**, *25*, 4246–4254.
306. Huo, L., Hou, J., Chen, H.-Y., Zhang, S., Jiang, Y., Chen, T. L., Yang, Y. Bandgap and Molecular Level Control of the Low-Bandgap Polymers Based on 3,6-Dithiophen-2-yl-2,5-dihydropyrrolo[3,4-c]pyrrole-1,4-dione toward Highly Efficient Polymer Solar Cells. *Macromolecules* **2009**, *42*, 6564–6571.
307. Woo, C. H., Beaujuge, P. M., Holcombe, T. W., Lee, O. P., Fréchet, J. M. J. Incorporation of Furan into Low Band-Gap Polymers for Efficient Solar Cells. *J. Am. Chem. Soc.* **2010**, *132*, 15547–15549.
308. Seybold, G., Wagenblast, G. New Perylene and Violanthrone Dyestuffs for Fluorescent Collectors. *Dyes Pigm.* **1989**, *11*, 303–317.
309. Sens, R., Drexhage, K. H. Fluorescence Quantum Yield of Oxazine and Carbazine Laser-Dyes. *J. Lumin.* **1981**, *24*, 709–712.
310. Frisch, M. J., Schlegel, H. B., Scuseria, G. E., Robb, M. A., Cheeseman, J. R., Scalmani, G., Barone, V., Mennucci, B., Petersson, G. A., Nakatsuji, H., Caricato, M., Li, X., Hratchian, H. P., Izmaylov, A. F., Bloino, J., Zheng, G., Sonnenberg, J. L., Hada, M., Ehara, M., Toyota, K., Fukuda, R., Hasegawa, J., Ishida, M., Nakajima, T., Honda, Y., Kitao, O., Nakai, H., Vreven, T., Montgomery, Jr., J. A., Peralta, J. E., Ogliaro, F., Bearpark, M., Heyd, J. J., Brothers, E., Kudin, K. N., Staroverov, V. N., Kobayashi, R., Normand, J., Raghavachari, K., Rendell, A., Burant, J. C., Iyengar, S. S., Tomasi, J., Cossi, M., Rega, N., Millam, J. M., Klene, M., Knox, J. E., Cross, J. B., Bakken, V., Adamo, C., Jaramillo, J., Gomperts, R., Stratmann, R. E., Yazyev, O., Austin, A. J., Cammi, R., Pomelli, C., Ochterski, J. W., Martin, R. L., Morokuma, K., Zakrzewski, V. G., Voth, G. A., Salvador, P., Dannenberg, J. J., Dapprich, S., Daniels, A. D., Farkas, Ö., Foresman, J. B., Ortiz, J. V., Cioslowski, J., Fox D. J., *Gaussian 09*. Gaussian, Inc., Wallingford CT, **2009**.

311. Miehlich, B., Savin, A., Stoll, H., Preuss, H. Results Obtained with the Correlation–Energy Density Functionals of Becke and Lee, Yang and Parr. *Chem. Phys. Lett.* **1989**, *157*, 200–206.
312. Petersson, G. A., Al–Laham, M. A. A Complete Basis Set Model Chemistry. II. Open-shell Systems and the Total Energies of the first–Row Atoms. *J. Chem. Phys.* **1991**, *94*, 6081–6090.
313. Petersson, G. A., Bennett, A., Tensfeldt, T. G., Al–Laham, M. A., Shirley, W. A., Mantzaris, J. A Complete Basis Set Model Chemistry. I. The Total Energies of Closed-shell Atoms and Hydrides of the first–Row Elements. *J. Chem. Phys.* **1988**, *89*, 2193–2218.
314. Dennington, R., Millam, J. GaussView, Semichem Inc., Shawnee Mission KS, **2009**.
315. Sheldrick, G. M. A short history of SHELX. *Acta Cryst. A* **2008**, *64*, 112–122.
316. Stoll, S., Schweiger, A. EasySpin, a comprehensive software package for spectral simulation and analysis in EPR. *J. Magn. Reson.* **2006**, *178*, 42–55.
317. Ji, C., Yin, L., Xie, B., Wang, X., Li, X., Zhang, J.–J., Ni, J., Li, Y. Narrow band gap isoindigo–based small molecules for solution–processed organic solar cells with high open–circuit voltage. *Synth. Met.* **2016**, *220*, 448–454.
318. Lakowitz, J. R. Principles of Fluorescence Spectroscopy, 2nd ed., Kluwer Academic/Plenum, New York, **1999**.
319. Shao, Y. H., Gan, Z. T., Epifanovsky, E., Gilbert, A. T. B., Wormit, M., Kussmann, J., Lange, A. W., Behn, A., Deng, J., Feng, X. T., Ghosh, D., Goldey, M., Horn, P. R., Jacobson, L. D., Kaliman, I., Khaliullin, R. Z., Kuś, T., Landau, A., Liu, J., Proynov, E. I., Rhee, Y. M., Richard, R. M., Rohrdanz, M. A., Steele, R. P., Sundstrom, E. J., Woodcock, H. L., Zimmerman, P. M., Zuev, D., Albrecht, B., Alguire, E., Austin, B., Beran, G. J. O., Bernard, Y. A., Berquist, E., Brandhorst, K., Bravaya, K. B., Brown, S. T., Casanova, D., Chang, C. M., Chen, Y. Q., Chien, S. H., Closser, K. D., Crittenden, D. L., Diedenhofen, M., DiStasio, R. A., Do, H., Dutoi, A. D., Edgar, R. G., Fatehi, S., Fusti–Molnar, L., Ghysels, A., Golubeva–Zadorozhnaya, A., Gomes, J., Hanson–Heine, M. W. D., Harbach, P. H. P., Hauser, A. W., Hohenstein, E. G., Holden, Z. C., Jagau, T. C., Ji, H. J., Kaduk, B., Khistyayev, K., Kim, J., Kim, J., King, R. A., Klunzinger, P., Kosenkov, D., Kowalczyk, T., Krauter, C. M., Lao, K. U., Laurent, A. D., Lawler, K. V., Levchenko, S. V., Lin, C. Y., Liu, F., Livshits, E., Lochan, R. C., Luenser, A., Manohar, P., Manzer, S. F., Mao, S. P., Mardirossian, N., Marenich, A. V., Maurer, S. A., Mayhall, N. J., Neuscammann, E., Oana, C. M., Olivares–Amaya, R., O’Neill, D. P., Parkhill, J. A., Perrine, T. M., Peverati, R., Prociuk, A., Rehn, D. R., Rosta, E., Russ, N. J., Sharada, S. M., Sharma, S., Small, D. W., Sodt, A., Stein, T., Stuck, D., Su, Y. C., Thom, A. J. W., Tsuchimochi, T., Vanovschi, V., Vogt, L., Vydrov, O., Wang, T., Watson, M. A., Wenzel, J., White, A., Williams, C. F., Yang, J., Yeganeh, S., Yost, S. R., You, Z. Q., Zhang, I. Y., Zhang, X., Zhao, Y., Brooks, B. R., Chan, G. K. L., Chipman, D. M., Cramer, C. J., Goddard, W. A., Gordon, M. S., Hehre, W. J., Klamt, A., Schaefer, H. F., Schmidt, M. W., Sherrill, C. D., Truhlar, D. G., Warshel, A., Xu, X., Aspuru–Guzik, A., Baer, R., Bell, A. T., Besley, N. A., Chai, J. D., Dreuw, A., Dunietz, B. D., Furlani, T. R., Gwaltney, S. R., Hsu, C. P., Jung, Y. S., Kong, J., Lambrecht, D. S., Liang, W. Z., Ochsenfeld, C., Rassolov, V. A., Slipchenko, L. V., Subotnik, J. E., Van Voorhis, T.,

- Herbert, J. M., Krylov, A. I., Gill P. M. W., Head–Gordon, M. Advances in molecular quantum chemistry contained in the Q–Chem 4 program package. *Mol. Phys.* **2015**, *113*, 184–215.
320. Shiozaki, T. BAGEL: Brilliantly Advanced General Electronic–structure Library. *WIREs Comput. Mol. Sci.* **2018**, *8*, e1331.
321. Tauc, J., Grigorovici, R., Vancu, A. Optical Properties and Electronic Structure of Amorphous Germanium. *Phys. Status Solidi* **1966**, *15*, 627–637.
322. Seguy, I., Jolinat, P., Destruel, P., Mamy, R., Allouchi, H., Courseille, C., Cotrait, M., Bock, H. Crystal and electronic structure of a fluorescent columnar liquid crystalline electron transport material. *ChemPhysChem* **2001**, *2*, 448–452.
323. Cardona, C. M., Li, W., Kaifer, A. E., Stockdale, D., Bazan, G. C. Electrochemical Considerations for Determining Absolute Frontier Orbital Energy Levels of Conjugated Polymers for Solar Cell Applications. *Adv. Mater.* **2011**, *23*, 2367–2371.